Національна академія наук України
Головна астрономічна обсерваторія

Кваліфікаційна наукова праця
у формі наукової доповіді

ЕЛИЇВ АНДРІЙ АНДРІЙОВИЧ

УДК 524.7+52-735

КОСМІЧНІ ВОЙДИ: СТРУКТУРА І ФІЗИЧНІ ПРОЦЕСИ В НИХ ТА НАВКОЛО

01.03.02 – Астрофізика, радіоастрономія
10 – Природничі науки; 104 – Фізика та астрономія

Подається на здобуття наукового ступеня доктора фізико-математичних наук

Дисертація містить результати власних досліджень.
Використання ідей, результатів і текстів інших авторів
мають посилання на відповідне джерело.
А.А. Елиїв

Науковий консультант: Вавилова Ірина Борисівна,
доктор фізико-математичних наук, професор,
член-кореспондент НАН України, завідувач відділу
позагалактичної астрономії та астроінформатики
Головної астрономічної обсерваторії
Національної академії наук України

Київ – 2022

АНОТАЦІЯ

Елиїв А. А. Космічні войди: структура і фізичні процеси в них та навколо. – Кваліфікаційна наукова праця у формі наукової доповіді.

Дисертація на здобуття наукового ступеня доктора фізико-математичних наук за спеціальністю 01.03.02 – Астрофізика, радіоастрономія (104 – Фізика та астрономія). – Головна астрономічна обсерваторія Національної академії наук України, Київ, 2022.

Робота присвячена дослідженню космічних войдів, або порожнин - областей у Всесвіті з низькою концентрацією галактик. Застосовано кілька методів виділення войдів та розглянуто населення космічних порожнин. Досліджено населення галактик, що оточує войди і скупчення. Визначено відстані до галактик Місцевого Всесвіту методами машинного навчання. Застосовано методи кореляційної функції та пошуку надлишків густини для вивчення оточення різних типів активних ядер галактик (АЯГ), відібраних у рентгенівському діапазоні. Застосовано метод мозаїки Вороного другого та третього порядків для виокремлення пар і триплетів галактик та проаналізовано їхні властивості з точки зору ізольованості системи. Проведено пошук гравітаційно-лінзованих систем квазарів у рентгенівському полі. Проаналізована можливість вимірювання магнітного поля у войдах, виходячи зі спостережень вторинного випромінювання від електромагнітних лавин, що проходять крізь них.

Метою дисертаційної роботи є комплексне дослідження властивостей космічних порожнеч, а саме: розробка методів виокремлення порожнин у розподілі великомасштабних структур Всесвіту; аналіз високоенергетичних процесів, що відбуваються у войдах. Робота охоплює дослідження властивостей великомасштабних структур (галактик, АЯГ, скупчень галактик, войдів, філаментів), а також їх оточення в різних діапазонах електромагнітного випромінювання.

Методи дослідження. У роботі використовувалися методи чисельного моделювання, зокрема, метод Монте-Карло; машинного навчання - моделі різних типів регресій та нейронних мереж; 2D і 3D методи мозаїки Вороного для просторового розподілу великомасштабних структур Всесвіті, ієрархічний метод виділення груп/агломератів галактик та АЯГ; методи обробки спостережуваних даних та статистичних оцінок для встановлення достовірності отриманих результатів, а також методи порівняння змодельованих параметрів зі спостережуваними даними.

Було запропоновано два методи пошуку войдів, які базуються на динамічних критеріях виділення порожнеч у лагранжевих координатах: LZVF, що використовує наближення Лагранжа-Зельдовича для відстеження зворотних у часі орбіт галактик та UVF – використовує метод послаблення кореляційної функції галактика-галактика для доведення розподілу об’єктів до однорідного. В обох випадках порожнечі визначаються як області негативної дивергенції зміщень, які можна розглядати як стоки трейсерів маси. Вперше показано, що значимість сигналу дивергенції в центральних частинах войдів, отриманих обома шукачами, на 60% вища, ніж для надлишку профілю густини, отриманим геометричним методом.

Вперше доведено, що запропоновані шукачі войдів є перспективними альтернативами до існуючих, і є ефективними для покращення точності космологічних тестів, що базуються на статистиці войдів та виміряних асиметричностей накладених войдів – наприклад, тесту Алькока-Пачинського для уточнення космічних параметрів, насамперед Ω_m.

Було застосовано п’ять моделей машинного навчання для визначення модуля відстані галактик за їхніми спостережуваними даними, такими як видимі зоряні величини у кількох смугах, кутовий діаметр, поверхнева яскравість, показники кольору та координати галактик, променева швидкістю, а також відомий модуль відстані. Було показано, що модель регресії нейронної мережі з двома прихованими шарами дає точніший результат, ніж інші моделі. Показано, що запропонована модель є конкурентоспроможною у порівнянні з

загальновживаними вторинними методами вимірювань модуля відстані, такими як метод фундаментальної площини (FP) та відношення Таллі-Фішера.

Було проведено аналіз двоточкової кореляційної функції вибірки точкових джерел поля XMM-LSS (11 кв. град) зі 94 спостережуваних полів XMM-Newton (d=30’), що містять понад п’ять тисяч точкових джерел у м’якому (0.5– 2 keV) та жорсткому (2–10 keV) діапазонах. Було знайдено, що амплітуда двоточкової кореляційної функції значно більша у жорсткому діапазоні, ніж у м’якому. Показано, що АЯГ з жорстким рентгенівським спектром (здебільшого АЯГ 2 типу) більш кластеризовані, ніж ті, що мають м'який спектр (АЯГ 1 типу). Це може означати, що два основних типи АЯГ перебувають в різних середовищах, а саме АЯГ з м'яким рентгенівським спектром тяжіють до більш розріджених областей Всесвіту, якими є межі космічних войдів.

Дослідження властивостей близького (<0.4–1 Мпк) та далекого (> 1 Мпк) оточення рентгенівських АЯГ поля XXL до $z = 1$ показало, що АЯГ обох типів можуть знаходитися як у тісному, так у розрідженому оточенні. Було знайдено, що рентгенівські АЯГ, що мають також радіо ототожнення є більш затьмареними (жорсткими у X-діапазоні), ніж джерела, що не випромінюють в радіо діапазоні. Ніякої значної різниці в великомасштабному оточенні різних типів АЯГ (1 та 2 типів, радіо і не радіо об’єктами, світними і тм’яними) знайдено не було. Однак, було підтверджено, що АЯГ здебільшого розташовані у локальних надлишках густини, порівняно з рентгенівськими галактиками. Такі результати підтверджують уніфіковану схему АЯГ, але не виключають, що оточення може мати вплив на еволюцію АЯГ.

Було застосовано геометричний метод Вороного вищих порядків для виділення галактик, пар та триплетів з вибірки огляду SDSS. Було знайдено, що галактики в ізольованих парах та триплетах мають світність у два рази вищу, ніж ізольовані галактики. Також, групи галактик у більш тісному оточені - наприклад, що знаходяться у скупченнях, мають більшу дисперсію швидкостей та відношення маси до світності.

Було розраховано очікувані статистичні властивості для виявлення оптичних ототожнень множинних зображень квазарів з рентгенівського огляду XXL, враховуючи параметри спостережень супутника. Серед 11 тисяч квазарів очікується знайти ~20 гравітаційно-лінзових квазарів з більше ніж двома зображеннями. Візуальний перегляд оптичних g, r та i зображень 5500 рентгенівських АЯГ, розташованих на 11 кв. градусах огляду XMM-LSS та аналіз кольорів об’єктів дозволив знайти 3 кандидати у лінзовані АЯГ.

Вперше доведено, що властивості електромагнітної лавини та зображення блазарів в гамма-променях сильно залежать від магнітного поля в космічних войдах, через які поширюється лавина, та від частки об'єму Всесвіту, зайнятої войдами. Така залежність може бути використана для виявлення та оцінки екстремально малого магнітного поля в космічних порожнинах.

Було вивчено морфологічні властивості гамма зображень блазарів методами чисельних моделювань. Досліджено характеристики протяжного зображення, а саме форму, розподіл поверхневої яскравості та їхню залежність від характеристик міжгалактичного магнітного поля. Показано, що гамма випромінювання від протяжної частини зображення затримується близько на 10 млн. років по відношенню до прямих фотонів від джерела. Така довга затримка означає, що протяжні гало навколо можуть спостерігатися навколо блазарів, які вже не активні. Вперше доведено, що електрон-позитронні пучки в космічних порожнинах є стабільними на масштабах набагато більших, ніж час розвитку електромагнітного каскаду. З цього випливає, що електрон-позитронні пучки від блазарів не впливають на міжгалактичне середовище.

Ключові слова: войди, космічні порожнечі, шукач войдів, методи вимірювання відстаней до галактик, метод Вороного, машинне навчання, АЯГ, блазари, електромагнітні лавини, міжгалактичне магнітне поле, ефект гравітаційного лінзування.

ANNOTATION

Elyiv A. A. – Cosmis voids: structure and physical processes in and around them. - Qualifying scientific work in the form of a scientific report.
Dissertation for a Doctor of Sciences degree in Physics and Mathematics, speciality 01.03.02 – Astrophysics, Radio Astronomy (104 – Physics and Astronomy). Main Astronomical Observatory of the National Academy of Sciences of Ukraine, Kyiv, 2022.

The work is devoted to the study of cosmic voids or cavities - regions in the Universe with a low concentration of galaxies. Several methods of void detection have been applied and the population of cosmic cavities has been considered. The population of galaxies surrounding voids and clusters has been studied.

Distances to galaxies of the Local Universe are determined by machine learning methods. Methods of correlation function and search for overdensities were used to study the environment of different types of active galaxy nuclei (AGN) selected in the X-ray range.

The second- and third-order Voronoi tessellation methods were used to find isolated pairs and triplets of galaxies; their properties were analyzed in terms of system isolation. The search for gravitational-lens systems of quasars in the X-ray field is carried out.

The possibility of measuring the magnetic field in voids is analyzed, based on observations of secondary emission from electromagnetic cascades passing through them.

The purpose of the dissertation is a comprehensive study of the properties of the cosmic voids, namely: development of methods for voids detection in the distribution of Large-Scale Structures of the Universe; analysis of high-energy processes occurring in voids. The work covers the study of the properties of large-scale structures (galaxies, AGN, galaxy clusters, voids and filaments), as well as their environment in different ranges of electromagnetic radiation.

Research methods: The methods of numerical modeling, in particular, the Monte Carlo method; machine learning - models of different types of regressions and neural networks; 2D and 3D methods of Voronoi's mosaic for spatial distribution of large-scale structures of the Universe, hierarchical method of selection of groups / agglomerates of galaxies and AGN; methods of processing the observational data, in particular aperture photometry and modeling of the point spread function, as well as statistical estimates to establish the reliability of the results and methods of comparing the simulated parameters with the observed data.

Two methods of searching for voids based on dynamic criteria for the selection of voids in Lagrangian coordinates were applied: the LZVF, which uses the Lagrange-Zeldovich approximation to trace back in time the orbits of galaxies located in voids and their surroundings, and the UVF that uses the observed galaxy–galaxy correlation function to relax the objects' spatial distribution to homogeneity and isotropy. In both cases voids are defined as regions of the negative velocity divergence, which can be regarded as sinks of the back-in-time streamlines of the mass tracers. The significance of the divergence signal in the central parts of the voids obtained from both finders is 60% higher than for the excess density profile obtained by the geometric method.

It is shown that the proposed void finders are promising alternatives to the existing ones as well as effective for improving the accuracy of cosmological tests based on void statistics and measuring the asymmetries of superimposed voids, for example, the Alcock-Paczynski test to improve the accuracy of cosmological parameters.

Five machine learning models have been used to determine the distance modulus of galaxies based on their observed data, such as visual magnitudes, angular diameter, surface brightness, galaxy color and coordinates, radial velocity, and known distance modulus. It was found that the regression model of a neural network with two hidden layers gives a more accurate result than other models. This model is competitive in comparison with commonly used secondary methods of measuring the distance moduli, such as the Fundamental Plane and the Tully-Fisher ratio.

An analysis of the two-point correlation function of a sample of XMM-LSS X-ray point sources (11 sq. deg) from 94 observed XMM-Newton fields (d = 30') containing more than five thousand point sources in soft (0.5– 2 keV) and hard (2–10 keV) ranges was performed. The amplitude of the two-point correlation function was found to be much larger in the hard than in the soft range. It has been shown that hard X-ray spectra (mostly type 2 AGN) are more clustered than soft spectra (type 1 AGN). This may mean that the two main types of AGN are in different environments, namely the AGN with a soft X-ray spectrum tend to more sparse areas of the universe, which are the boundaries of space voids.

The study of the properties of the near (<0.4-1 Mpc) and far (> 1 Mpc) environment of X-ray AGN of the XXL field up to z = 1 showed that the AGN of both types can be located in both close and sparse environments. It was found that X-ray AGN that also have radio counterparts are more obscured than sources that do not emit in the radio range. No significant differences were found in the large-scale environments of the different types of AGN (types 1 and 2, radio and non-radio objects, luminous and faint). However, it has been confirmed that AGN are mostly located in local overdensities compared to X-ray galaxies. Such results confirm the universal scheme of AGN but do not exclude that the environment may influence their evolution.

The higher-order Voronoi tessellation geometric method was used to select galaxies, pairs, and triplets from the SDSS survey sample. It has been found that galaxies in isolated pairs and triplets have a luminosity twice as high as isolated galaxies. Also, groups of galaxies in a closer environment - for example, in clusters, have a greater velocity dispersion and the mass to luminosity ratio.

The statistical expectations to detect optical counterparts of multiple images of quasars were estimated on X-ray XXL survey, taking into account the parameters of satellite observations. Among the 11,000 point-like sources, ~20 gravitational-lens quasars with more than two images are expected. Visual inspection of optical g, r and i images of 5500 X-ray AGN located on 11 sq. deg. of XMM-LSS survey and color analysis allowed to find three promising candidates for lensed AGN.

It was found that the properties of the electromagnetic cascades and the image of blazars in gamma rays strongly depend on the magnetic field in the cosmic voids through which the cascade propagates, and on the proportion of the volume of the Universe occupied by the voids. This dependence can be used to detect and estimate extremely small magnetic fields in space cavities. The morphological properties of gamma images of blazars were studied by numerical simulations. The characteristics of the extended image are studied, namely the shape, distribution of surface brightness and their dependence on the characteristics of the intergalactic magnetic field. It is shown that the gamma radiation from the extended part of the image is delayed by about 10 million years relative to the direct photons from the source. Such a long delay means that extended halos can be observed around blazars that are no longer active. It is proved that electron-positron beams in voids are stable on a scale much larger than the time of development of the electromagnetic cascade. It follows that electron-positron beams from blazars do not affect the intergalactic medium.

Keywords: voids, cosmic cavities, void finder, methods for measuring distances to galaxies, Voronoi tessellation, machine learning, AGN, blazars, electromagnetic cascades, intergalactic magnetic field, gravitational lensing effect.

СПИСОК ОПУБЛІКОВАНИХ ПРАЦЬ ЗА ТЕМОЮ ДИСЕРТАЦІЇ

Основні наукові праці (у реферованих журналах першого квартилю (Q1) відповідно до класифікації SCImago Journal and Country Rank або Journal Citation Reports), окрім статей із *:

Скорочення: A&A – Astronomy and Astrophysics; MNRAS – Monthly Notices of the Royal Astronomical Society; ApJ – Astrophysical Journal; Phys. Rev. D – Physical Review D.

1. Elyiv, A., Marulli, F., Pollina, G., Baldi, M., Branchini, E., Cimatti, A., Moscardini, L., 2015. Cosmic voids detection without density measurements. MNRAS, 448, pp. 642–653.
2. Elyiv, A. A., Melnyk, O. V., Vavilova, I. B., Dobrycheva, D. V., Karachentseva, V. E., 2020. Machine-learning computation of distance modulus for local galaxies. A&A, 635A, 124E (7 pp.).
3. Elyiv, A., Clerc, N., Plionis, M., Surdej, J., Pierre, M., Basilakos, S., Chiappetti, L., Gandhi, P., Gosset, E., Melnyk, O., Pacaud, F., 2012. Angular correlation functions of X-ray point-like sources in the full exposure XMM-LSS field. A&A, 537, id. A131 (14 pp.).
4. Miniati, F., Elyiv, A., 2012. Relaxation of Blazar-induced Pair Beams in Cosmic Voids. ApJ, 770, 1 (9 pp.).
5. Schlickeiser, R., Elyiv, A., Ibscher, D., Miniati, F., 2012. The pair beam production spectrum from photon-photon annihilation in cosmic voids. ApJ, 758, 101 (18 pp.).
6. Elyiv, A., Neronov, A., Semikoz, D. V., 2010. Gamma-ray induced cascades and magnetic fields in the intergalactic medium, Phys. Rev. D., 80, 023010 (11 pp.).
7. Neronov, A., Semikoz, D., Kachelriess, M., Ostapchenko, S., Elyiv, A., 2010. Degree-scale GeV "Jets" from Active and Dead TeV Blazars. ApJ Journal Letters, 719, pp. L130–L133.
8. Finet, F., Elyiv, A., Melnyk, O., Wertz, O., Horellou, C., Surdej, J., 2015. Predicted multiply imaged X-ray AGNs in the XXL survey. MNRAS, 452, pp. 1480-1492.

9. Ricci D., Poels J., Elyiv A., Finet F., Sprimont P. G., Anguita T., Bozza V., Browne P. , Burgdorf M., Calchi Novati S., Dominik M., Dreizler S., Glitrup M., Grundahl F., Harpsøe K., Hessman F., Hinse T. C., Hornstrup A., Hundertmark M., Jørgensen U. G., Liebig C., Maier G., Mancini L., Masi G., Mathiasen M., Rahvar S., Scarpetta G., Skottfelt J., Snodgrass C., Southworth J., Teuber J., Thöne C. C., Wambsganß J., Zimmer F., Zub M., Surdej J., 2011. Flux and color variations of the quadruply imaged quasar HE 0435-1223. A&A, V. 528, id.A42.

10. Ricci D., Elyiv A., Finet F., Wertz O., Alsubai, K., Anguita, T., Bozza, V., Browne, P., Burgdorf, M., Calchi Novati, S., Dodds, P., Dominik, M., Dreizler, S., Gerner, T., Glitrup, M., Grundahl, F., Hardis, S., Harpsøe, K., Hinse, T. C., Hornstrup, A., Hundertmark, M., Jørgensen, U. G., Kains, N., Kerins, E., Liebig, C., Maier, G., Mancini, L., Masi, G., Mathiasen, M., Penny, M., Proft, S., Rahvar, S., Scarpetta, G., Sahu, K., Schäfer, S., Schönebeck, F., Schmidt, R., Skottfelt, J., Snodgrass, C., Southworth, J., Thöne, C. C., Wambsganss, J., Zimmer, F., Zub, M., Surdej, J., 2013. Flux and color variations of the doubly imaged quasar UM673, A&A, 551, A104.

11. Elyiv, A., Melnyk, O., Finet, F., Pospieszalska-Surdej, A., Chiappetti, L., Pierre, M., Sadibekova, T., Surdej, J., 2013. Search for gravitational lens candidates in the XMM-LSS/CFHTLS common field. MNRAS, 434, pp. 3305–3309.

12. Elyiv, A., Melnyk, O., Vavilova, I., 2009. High-order 3D Voronoi tessellation for identifying isolated galaxy pairs and triplets. MNRAS, 394, pp. 1409–1418.

13. Melnyk, O., Elyiv, A., Smolčić, V., Plionis, M., Koulouridis, E., Fotopoulou, S., Chiappetti, L., Adami, C., Baran, N., Butler, A., Delhaize, J., Delvecchio, I., Finet, F., Huynh, M., Lidman, C., Pierre, M., Pompei, E., Vignali, C., Surdej, J., 2018. The XXL Survey. XXI. The environment and clustering of X-ray AGN in the XXL-South field. A&A, 620, id.A6 (14 pp.).

Наукові праці, які додатково висвітлюють тему дисертації:

а) Наукові праці у реферованих журналах першого квартилю (Q1) відповідно до класифікації SCImago Journal and Country Rank або Journal Citation Reports, окрім статей з *

14. Nwaokoro, E., Phillipps, S., Young, A. J., Baldry, I., Bongiorno, A., Bremer, M. N., Brown, M. J. I., Chiappetti, L., De Propris, R., Driver, S. P., Elyiv, A., Fotopoulou, S., Giles, P. A., Hopkins, A. M., Maughan, B., McGee, S., Pacaud, F., Pierre, M., Plionis, M., Poggianti, B. M., Vignali, C., 2021. GAMA/XXL: X-ray point sources in low-luminosity galaxies in the GAMA G02/XXL-N field. MNRAS, 502, pp. 3101–3112.

15. Koulouridis, E., Ricci, M., Giles, P., Adami, C., Ramos-Ceja, M., Pierre, M., Plionis, M., Lidman, C., Georgantopoulos, I., Chiappetti, L., Elyiv, A., Ettori, S., Faccioli, L., Fotopoulou, S., Gastaldello, F., Pacaud, F., Paltani, S., Vignali, C., 2018. The XXL Survey. XXXV. The role of cluster mass in AGN activity. A&A, 620, id. A20 (10 pp.).

16. Chiappetti, L., Fotopoulou, S., Lidman, C., Faccioli, L., Pacaud, F., Elyiv, A., Paltani, S., Pierre, M., Plionis, M., Adami, C., Alis, S., Altieri, B., Baldry, I., Bolzonella, M., Bongiorno, A., Brown, M., Driver, S., Elmer, E., Franzetti, P., Grootes, M., Guglielmo, V., Iovino, A., Koulouridis, E., Lefèvre, J. P., Liske, J., Maurogordato, S., Melnyk, O., Owers, M., Poggianti, B., Polletta, M., Pompei, E., Ponman, T., Robotham, A., Sadibekova, T., Tuffs, R., Valtchanov, I., Vignali, C., Wagner, G., 2018. The XXL Survey: XXVII. The 3XLSS point source catalogue, A&A, 620, A12 (18 pp.).

17. Guglielmo, V., Poggianti, B. M., Vulcani, B., Moretti, A., Fritz, J., Gastaldello, F., Adami, C., Caretta, C. A., Willis, J., Koulouridis, E., Ramos, Ceja, M. E., Giles, P., Baldry, I., Birkinshaw, M., Bongiorno, A., Brown, M., Chiappetti, L., Driver, S., Elyiv, A., Evrard, A., Grootes, M., Guennou, L., Hopkins, A., Horellou, C., Iovino, A., Maurogordato, S., Owers, M., Pacaud, F., Paltani, S.,

Pierre, M., Plionis, M., Ponman, T., Robotham, A., Sadibekova, T., Smolčić, V., Tuffs, R., Vignali, C., 2018. The XXL Survey: XXX. Characterisation of the XLSSsC N01 supercluster and analysis of the galaxy stellar populations. A&A, 620, id. A15 (15 pp.).

18. Guglielmo, V., Poggianti, B. M., Vulcani, B., Adami, C., Gastaldello, F., Ettori, S., Fotoupoulou, S., Koulouridis, E., Ramos, Ceja, M. E., Giles, P., McGee, S., Altieri, B., Baldry, I., Birkinshaw, M., Bolzonella, M., Bongiorno, A., Brown, M., Chiappetti, L., Driver, S., Elyiv A., Evrard, A., Garilli, B., Grootes, M., Guennou, L., Hopkins, A., Horellou, C., Iovino, A., Lidman, C., Liske, J., Maurogordato, S., Owers, M., Pacaud, F., Paltani, S., Pierre, M., Plionis, M., Ponman, T., Robotham, A., Sadibekova, T., Scodeggio, M., Sereno, M., Smolčić, V., Tuffs, R., Valtchanov, I., Vignali, C., Willis J., 2018. The XXL Survey: XXII. The XXL-North spectrophotometric sample and galaxy stellar mass function in X-ray detected groups and cluster. A&A, 620, id.A7 (20 pp.).

19. Pierre, M., Adami, C., Birkinshaw, M., Chiappetti, L., Ettori, S., Evrard, A., Faccioli, L., Gastaldello, F., Giles, P., Horellou, C., Iovino, A., Koulouridis, E., Lidman, C., Le Brun, A., Maughan, B., Maurogordato, S., McCarthy, I., Miyazaki, S., Pacaud, F., Paltani, S., Plionis, M., Reiprich, T., Sadibekova, T., Smolcic, V., Snowden, S., Surdej, J., Tsirou, M., Vignali, C., Willis, J., Alis, S., Altieri, B., Baran, N., Benoist, C., Bongiorno, A., Bremer, M., Butler, A., Cappi, A., Caretta, C., Ciliegi, P., Clerc, N., Corasaniti, P. S., Coupon, J., Delhaize, J., Delvecchio, I., Democles, J., Desai, Sh., Devriendt, J., Dubois, Y., Eckert, D., Elyiv, A., Farahi, A., Ferraril, C., Fotopoulou, S., Forman, W., Georgantopoulos, I., Guglielmo, V., Huynh, M., Jerlin, N., Jones, Ch., Lavoie, S., Le Fevre, J.-P., Lieu, M., Kilbinger, M., MaruIli, F., Mantz, A., McGee, S., Melin, J.-B., Melnyk, O., Moscardini, L., Novak, M., Piconcelli, E., Poggianti, B., Pomarede, D., Pompei, E., Ponman, T., Ramos, Ceja, M. E., Rana, P., Rapetti, D., Raychaudhury, S., Ricci, M., Rottgering, H., Sahlen, M., Sauvageot, J.-L., Schimd, C., Sereno, M., Smith, G. P., Umetsu, K., Valageas, P., Valotti, A., Valtchanov, I., Veropalumbo, A., Ascaso, B., Barnes, D., De Petris, M., Durret, F., Donahue, M., Ithana, M., Jarvis, M., Johnston-Hollitt, M.,

Kalfountzou, E., Kay, S., La Franca, F., Okabe, N., Muzzin, A., Rettura, A., Ricci, F., Ridl, J., Risaliti, G., Takizawa, M., Thomas, P., Truong, N., 2017. The XXL survey: First results and future, Astronomische Nachrichten, 338, pp. 334–341.

20. Lavoie, S., Willis, J. P., Démoclès, J., Eckert, D., Gastaldello, F., Smith, G. P., Lidman, C., Adami, C., Pacaud, F., Pierre, M., Clerc, N., Giles, P., Lieu, M., Chiappetti, L., Altieri,B., Ardila, F., Baldry, I., Bongiorno, A., Desai, S., Elyiv, A., Faccioli, L., Gardner, B., Garilli, B., Groote, M. W., Guennou, L., Guzzo, L., Hopkins, A. M., Liske, J., McGee, S., Melnyk, O., Owers, M. S., Poggianti, B., Ponman, T. J., Scodeggio, M., Spitler, L., Tuffs, R. J., 2016. The XXL survey XV: evidence for dry merger driven BCG growth in XXL-100-GC X-ray clusters. MNRAS, 2016, 462, pp. 4141–4156.

21. Koulouridis, E., Poggianti, B., Altieri, B., Valtchanov, I., Jaffé, Y., Adami, C., Elyiv, A., Melnyk, O., Fotopoulou, S., Gastaldello, F., Horellou, C., Pierre, M., Pacaud, F., Plionis, M., Sadibekova, T., Surdej, J., 2016. The XXL Survey. XII. Optical spectroscopy of X-ray-selected clusters and the frequency of AGN in superclusters. A&A, 592, id. A11 (11 pp.).

22. Fotopoulou, S., Pacaud, F., Paltani, S., Ranalli, P., Ramos-Ceja, M. E., Faccioli, L., Plionis, M., Adami, C., Bongiorno, A., Brusa, M., Chiappetti, L., Desai, S., Elyiv, A., Lidman, C., Melnyk, O., Pierre, M., Piconcelli, E., Vignali, C., Alis, S., Ardila, F., Arnouts, S., Baldry, I., Bremer, M., Eckert, D., Guennou, L., Horellou, C., Iovino, A., Koulouridis, E., Liske, J., Maurogordato, S., Menanteau, F., Mohr,J. J., Owers, M., Poggianti, B., Pompei, E., Sadibekova, T., Stanford, A., Tuffs, R., Willis, J., 2016. The XXL Survey. VI. The 1000 brightest X-ray point sources. A&A, id.A5 (30 pp.).

23. Pierre, M., Pacaud, F., Adami, C., Alis, S., Altieri, B., Baran, N., Benoist, C., Birkinshaw, M., Bongiorno, A., Bremer, M. N., Brusa, M., Butler, A., Ciliegi, P., Chiappetti, L., Clerc, N., Corasaniti, P. S., Coupon, J., De Breuck, C., Democles, J., Desai, S., Delhaize, J., Devriendt, J., Dubois, Y., Eckert, D., Elyiv, A., Ettori, S., Evrard, A., Faccioli, L., Farahi, A., Ferrari, C., Finet, F., Fotopoulou, S., Fourmanoit, N., Gandhi, P., Gastaldello, F., Gastaud, R., Georgantopoulos, I., Giles, P., Guennou,

L., Guglielmo, V., Horellou, C., Husband, K., Huynh, M., Iovino, A., Kilbinger, M., Koulouridis, E., Lavoie, S., Le Brun, A. M. C., Le Fevre, J. P., Lidman, C., Lieu, M., Lin, C. A., Mantz, A., Maughan, B. J., Maurogordato, S., McCarthy, I. G., McGee, S., Melin, J. B., Melnyk, O., Menanteau, F., Novak, M., Paltani, S., Plionis, M., Poggianti, B. M., Pomarede, D., Pompei, E., Ponman, T. J., Ramos-Ceja, M. E., Ranalli, P., Rapetti, D., Raychaudury, S., Reiprich, T. H., Rottgering, H., Rozo, E., Rykoff, E., Sadibekova, T., Santos, J., Sauvageot, J. L., Schimd, C., Sereno, M., Smith, G. P., Smolčić, V., Snowden, S., Spergel, D., Stanford, S., Surdej, J., Valageas, P., Valotti, A., Valtchanov, I., Vignali, C., Willis, J., Ziparo, F., 2016. The XXL Survey. I. Scientific motivations – XMM-Newton observing plan – Follow-up observations and simulation program. A&A, 592, id. A1 (16 pp.).

24. Lidman, C., Ardila, F., Owers, M., Adami, C., Chiappetti, L., Civano, F., Elyiv, A., Finet, F., Fotopoulou, S., Goulding, A., Koulouridis, E., Melnyk, O., Menanteau, F., Pacaud, F., Pierre, M., Plionis, M., Surdej, J., Sadibekova, T., 2016. The XXL Survey XIV. AAOmega Redshifts for the Southern XXL Field, Publications of the Astronomical Society of Australia, 33, e001 (7 pp.).

25. Koulouridis, E., Plionis, M., Melnyk, O., Elyiv, A., Georgantopoulos, I., Clerc, N., Surdej, J., Chiappetti, L., Pierre, M., 2014. X-ray AGN in the XMM-LSS galaxy clusters: no evidence of AGN suppression. A&A, 567, id. A83 (15pp.).

26. Chiappetti, L., Clerc, N., Pacaud, F., Pierre, M., Guéguen, A., Paioro, L., Polletta, M., Melnyk, O., Elyiv, A., Surdej, J., Faccioli, L., 2013. The XMM-Large Scale Structure catalogue - II. X-ray sources and associated multiwavelength data. MNRAS, 429, pp. 1652–1673.

27. Finet, F., Elyiv, A., & Surdej, J., 2012. Detection of bright imaged quasar with Gaia. Memorie della Societa Astronomica Italiana. 83, pp. 944-988.*

28. Akhunov, T. A., Wertz, O., Elyiv, A., Gaisin, R., Artamonov, B. P., Dudinov, V. N., Nuritdinov, S. N., Delvaux, C., Sergeyev, A. V., Gusev, A. S., Bruevich, V. V., Burkhonov, O., Zheleznyak, A. P., Ezhkova, O., Surdej, J., 2017. Adaptive PSF fitting - a highly performing photometric method and light curves of the GLS H1413+117: time delays and micro-lensing effects, MNRAS, 465, pp. 3607–3621.

29. Giannini, E., Schmidt, R. W., Wambsganss, J., Alsubai, K., Andersen, J. M., Anguita, T., Bozza, V., Bramich, D. M., Browne, P., Calchi, Novati, S., Damerdji, Y., Diehl, C., Dodds, P., Dominik, M., Elyiv, A., Fang, X., Figuera, Jaimes, R., Finet, F., Gerner, T., Gu, S., Hardis, S., Harpsøe, K., Hinse, T. C., Hornstrup, A., Hundertmark, M., Jessen-Hansen, J., Jørgensen, U. G., Juncher, D., Kains, N., Kerins, E., Korhonen, H., Liebig, C., Lund, M. N., Lundkvist, M. S., Maier, G., Mancini, L., Masi, G., Mathiasen, M., Penny, M., Proft, S., Rabus, M., Rahvar, S., Ricci, D., Scarpetta, G., Sahu, K., Schäfer, S., Schönebeck, F., Skottfelt, J., Snodgrass, C., Southworth, J., Surdej, J., Tregloan-Reed, J., Vilela, C., Wertz, O., Zimmer, F., 2017. MiNDSTEp differential photometry of the gravitationally lensed quasars WFI 2033-4723 and HE 0047-1756: microlensing and a new time delay, A&A, 597, 16.

30. Vavilova I.B., Dobrycheva D.V., Vasylenko M.Yu., Elyiv A.A., Melnyk O.V., and Khramtsov V., 2021. Machine learning technique for morphological classification of galaxies from the SDSS I. Photometry-based approach, A&A, 648, A122 (14 pp.).

31. Vavilova I. B., Khramtsov V. , Dobrycheva D. V., Vasylenko M. Yu., Elyiv A.A., Melnyk O.V., 2022. Machine learning technique for morphological classification of galaxies from SDSS. II. The image-based morphological catalogs of galaxies at 0.02<z<0.1, Space Science & Technology, 28 (1), pp. 03-22.*

32. Dobrycheva, D.V., Melnyk, O.V., Vavilova, I.B., Elyiv, A.A., 2015. Environmental Density vs. Colour Indices of the Low Redshifts Galaxies, Astrophysics, 58, pp. 168–180.*

33. Melnyk, O., Plionis, M., Elyiv, A., Salvato, M., Chiappetti, L., Clerc, N., Gandhi, P., Pierre, M., Sadibekova, T., Pospieszalska-Surdej, A., Surdej, J., 2013. Classification and environmental properties of X-ray selected point-like sources in the XMM-LSS field. A&A, 557, id. A81 (14 pp.).

б) Розділи у монографіях

34. Elyiv A.A., Melnyk O.V., Vavilova I.B. Dark and baryonic matter distribution in the sparsely populated galaxy groups, p. 129–158. In: Vavilova I.B., Bolotin Yu.L., Boyarsky A.M. et al. Dark matter: Observational manifestation and experimental searches. Kyiv: Akademperiodyka, 2015, 375 p., Vol. 3 of the "Dark energy and dark matter in the Universe", in three volumes, Ed. V. Shulga. ISBN 978-966-360-287-5.

35. Vavilova I., Elyiv A., Dobrycheva D., Melnyk O. The Voronoi Tessellation Method in Astronomy. In: Zelinka I., Brescia M., Baron D. (eds). Intelligent Astrophysics. Emergence, Complexity and Computation, vol 39. Springer, Cham, 2021. Chapter 3, p. 57–79. ISBN 978-3-030-65867-0.

36. Vavilova I., Dobrycheva D., Vasylenko M., Elyiv A., Melnyk O. Multiwavelength Extragalactic Surveys: Examples of Data Mining. In: Knowledge Discovery in Big Data from Astronomy and Earth Observation, 1st Edition. Edited by Petr Skoda and Fathalrahman Adam. Elsevier, 2020, p. 307–323. ISBN 978-0-128-19154-5.

37. Vavilova I., Pakuliak L., Babyk I., Elyiv A., Dobrycheva D., Melnyk O. Surveys, Catalogues, Databases, and Archives of Astronomical Data. In: Knowledge Discovery in Big Data from Astronomy and Earth Observation, 1st Edition. Edited by Petr Skoda and Fathalrahman Adam. Elsevier, 2020, p.57–102. ISBN 978-0-128-19154-5.

в) Матеріали та тези конференцій

38. Vavilova I.B., Elyiv A.A., Dobrycheva D.V., Melnyk O.V. Voronoi tessellation in a spatial galaxy distribution. Abstracts of the Institute of Mathematics Conferences, Sixth International Conference on Analytic Number Theory and Spatial Tessellations, 24–28 Sept., 2018, Kyiv, Ukraine. P. 68.

39. Dobrycheva D., Melnyk O., Elyiv A., Vavilova I. Environmental density of galaxies from SDSS via Voronoi tessellation The Zeldovich Universe: Genesis and Growth of the Cosmic Web, Proceedings of the International Astronomical Union, Cambridge: Cambridge University Press, 2016, Vol. 308, pp. 248–249 (Scopus).

40. Elyiv A. X-ray surveys – Correlation function analyses of X-ray point-like sources in the XMM-LSS and XXL fields Half a Century of X-ray Astronomy, Proceedings of the conference held 17–21 September, 2012 in Mykonos Island, Greece. Online at http://www.astro.noa.gr/xcosmo/, id.107.

41. Dobrycheva D.V., Melnyk O.V., Vavilova I.B., Elyiv A.A. Environmental properties of galaxies at z<0.1 from the SDSS via the Voronoi tessellation. Odessa Astronomical Publications, 2014, vol. 27(1), p. 26–27.

42. Melnyk O.V., Elyiv A.A., Vavilova I.B. 3-D Voronoi's Tessellation as a Tool for Identifying Galaxy Groups. In: Galaxy Evolution Across the Hubble Time, Edited by F.Combes and J. Palous, Proceedings of the International Astronomical Union, Cambridge: Cambridge University Press, 2007, vol. 235, p. 223.

43. Melnyk O., Elyiv A. Clustering and environmental studies of AGN in the XMM – LSS and XXL fields. Абстракти "Астрономія та фізика космосу в Київському університеті", Міжнародна конференція в рамках VIII Всеукраїнського фестивалю науки, 27–30 травня 2014 року, Київ. С. 29.

44. Dobrycheva D., Vavilova I., Elyiv A., Melnyk O. Scaling properties of new sample of galaxies with z<0.1 from SDSS DR9. Абстракти "Астрономія та фізика космосу в Київському університеті", Міжнародна конференція в рамках VIII Всеукраїнського фестивалю науки, 27–30 травня 2014 року, Київ. С. 18.

ЗМІСТ

ПЕРЕЛІК УМОВНИХ ПОЗНАЧЕНЬ

FP – метод Фундаментальної площини

АЯГ – активні ядра галактик

ZOBOV – ZOnes Bordering On Voidness шукач войдів [47]

LZVF – Lagrangian Zeldovich Void Finder

UVF – Uncorrelated Void Finder

SDSS – Sloan Digital Sky Survey www. sdss.org

NASA/IPAC – NASA/IPAC Extragalactic Database http://ned.ipac.caltech.edu/ [49]

HYPERLEDA – Database for physics of galaxies http://leda.univ-lyon1.fr/ [50]

ROSAT – The Roentgen Satellite, was launched on June 1, 1990 and operated for almost 9 years

XMM-COSMOS – 2 кв. град. глибокий огляд неба рентгенівським супутником XMM-Newton, що має ототожнення об'єктів у більш ніж 30 фотометричних смугах

XXL – рентгенівський огляд неба 50 кв. град., 25 кв градусів у північній півкулі і 25 кв градусів у південній півкулі

XMM-LSS – рентгенівський огляд неба у 11 кв. град., частина північного огляду XXL

CFHTLS – Canada-France-Hawaii Telescope Legacy Survey

ВСТУП

Актуальність теми. Космічні войди, або порожнечі, займають гігантські простори Всесвіту з низькою концентрацією галактик. Вони були виявлені близько 40 років тому назад, але їхнє систематичне вивчення стало можливим лише в останнє десятиріччя з появою сучасних спектроскопічних оглядів галактик всього неба. Через свої гігантські об’єми, характерну форму, динаміку і низьку густину видимої матерії, вони є унікальними лабораторіями для позагалактичної астрофізики та космології. Складна ієрархія войдів, взаємні перетини, піно-подібна структура на різних масштабах Всесвіту роблять їх цікавими об’єктами з точки зору застосування геометричних і топографічних методів та технологій нейромереж.

У дослідженнях з астрофізики високих енергій войди розглядають як “шосе” для поширення релятивістських частинок, де присутність ненульового магнітного поля та позагалактичного фонового інфрачервоного випромінювання є відкритим питанням. Войди є важливими для тестування еволюційних моделей, оскільки вони дозволяють вивчати ізольовані галактики і малонаселені групи без впливу оточення та порівнювати їх з галактиками, що знаходяться у галактикчних скупченнях. Войди можуть бути використані для ефективного тестування космологічних моделей та оцінки космологічних параметрів. Зокрема спостережуваний дефіцит карликових галактик у близьких войдах суперечить космологічному сценарію з холодною темною матерією. Їхні фізичні властивості залежать від природи темної енергії та зародкового поля густини, з якого вони розвинулися, зокрема форма войдів дуже чутлива до рівняння стану темної енергії та вмісту темної матерії.

Точність космологічних тестів і еволюційних моделей Великомасштабної структури Всесвіту залежить від критеріїв виокремлення цих космічних порожнеч. Підтвердженням цьому є велика кількість розроблених алгоритмів для їх пошуку. Ключовим параметром для всіх типів шукачів войдів є положення галактик в просторі з добре виміряними відстанями, в ідеалі, не збуреними пекулярними і

колективним рухами галактик. Тому важливими є розробка методів встановлення модулів відстаней до галактик, що окреслюють войди або знаходяться у них, з точністю кращою, ніж може забезпечити метод червоного зміщення.

Відомо, що оточення галактик впливає не тільки такі їхні властивості як колір, морфологічний тип, світність, темп зореутворення, а також і на наявність активного ядра у центрі галактики (АЯГ) та, власне, на спектральні особливості випромінювання АЯГ. На сьогодні відсутня остаточна відповідь на запитання, що грає домінантну роль в еволюції галактик та активності ядра – внутрішня еволюція чи оточення галактик. Однак, очевидно, що універсальна схема АЯГ, згідно з якою всі типи АЯГ повинні знаходитися в однакових оточеннях, не враховує вікової еволюції і активно переглядається. З цієї точки зору випливає актуальність дослідження властивостей АЯГ у войдах, філаментах, скупченнях галактик та в інших структурах у контексті еволюції галактик, а також і зворотного ефекту впливу АЯГ, а особливо їхнього підтипу – блазарів, на процеси всередині космічних порожнеч.

Зв'язок роботи з науковими програмами, планами, темами. Дослідження виконувалися під час роботи здобувача в Головній астрономічній обсерваторії НАН України за такими програмами і темами:

відомчі теми НАН України «Великомасштабна структура Всесвіту за даними багатохвильових оглядів окремих її складників» (№ держ. реєстрації 0119U000393, 2019–2023 рр.), «Чисельний аналіз фізичних характеристик і еволюції скупчень галактик, галактик і галактичних підсистем» (№ держ. реєстрації 0113U008323, 2014–2018 рр.), «Розвиток та застосування кластерних технологій для мультимасштабного динамічного моделювання та аналізу структури локального Всесвіту» (№ держ. реєстрації 0110U007860, 2011–2013 рр.);

цільова комплексна програма НАН України «Астрофізичні і космологічні проблеми прихованої маси і темної енергії Всесвіту» (шифр «Космомікрофізика-2»), у межах науково-дослідних робіт «Властивості ізольованих галактик з активними ядрами і оцінка мас їх центральних чорних дір» (№ держ. реєстрації 0113U008053, 2013 р.), «Властивості баріонної і небаріонної матерії в галактиках і

скупченнях галактик» (№ держ. реєстрації 0112U004455, 2012 р.) і «Астрофізичні прояви темної матерії» (№ держ. реєстрації 0110U003747, 2010–2011 рр.);

цільова комплексна програма НАН України «Дослідження структури та складу Всесвіту, прихованої маси і темної енергії» (шифр «Космомікрофізика»), у межах науково-дослідної роботи «Спостережні прояви баріонної і небаріонної компонент матерії» (№ держ. реєстрації 0107U009720, 2007–2009 рр.);

наукові проекти Державного фонду фундаментальних досліджень України «Популяція галактик в близьких космічних лакунах» (№ держ. реєстрації 0113U004477, 2013 р.), «Просторовий розподіл та фізичні властивості галактик в областях з екстремально низькою густиною матерії» (№ держ. реєстрації 0111U006527, 2011–2012 рр.);

стипендія Президента України для молодих учених (2011–2012 рр.);

наукові проекти «АЯГ та їхнє оточення» під час стажування в Університеті м. Льєж впродовж 2009–2013 рр., “Виявлення космічних порожнеч без вимірювань густини” в Університеті м. Болонья впродовж 2013–2015 рр., «Застосування методів машинного навчання для визначення відстаней до галактик», INAF, Мілан (2016-2021).

Метою дисертаційної роботи є комплексне дослідження властивостей космічних порожнеч, а саме: розробка методів виокремлення порожнин у розподілі великомасштабних структур Всесвіту; аналіз високоенергетичних процесів, що відбуваються у войдах, у тому числі, моделювання магнітного поля та властивостей і стійкості електромагнітних лавин; визначення багатохвильових властивостей галактик у порожнечах та навколо. Робота охоплює дослідження великомасштабних структур (галактик, скупчень галактик, войдів, філаментів) у широкому спектральному діапазоні від інфрачервоного до гамма-випромінювання.

Відповідно до поставленої мети були запропоновані і вирішені такі **завдання**:

- Розроблено алгоритм пошуку войдів, який показує кращу точність за існуючі аналоги.

- Вперше розроблено метод відновлення відстаней до галактик за доступними спостережуваними даними на основі методів машинного навчання.
- Створено інструменти та програмне забезпечення для чисельного моделювання розвитку електромагнітних лавин у войдах та формування зображень блазарів у гамма-діапазоні.
- Доведено стабільність релятивістських електрон-позитронних пучків, викликаних гамма-фотонами від блазарів.
- Вперше досліджено кореляційні властивості АЯГ, спостережуваних у глибокому рентгенівському огляді неба XMM-LSS космічного телескопу XMM-Newton.
- Виконано пошук кандидатів у гравітаційно-лінзові системи у рентгенівському полі XXL
- Застосовано метод мозаїки Вороного другого та третього порядків для виділення пар і триплетів галактик, що дало можливість проаналізувати їхні властивості у залежності від ступеня ізольованості системи

Об'єкти дослідження: войди, галактики, скупчення галактик, гравітаційно-лінзовані квазари, АЯГ, квазари, великомасштабна структура Всесвіту.

Предмет дослідження: властивості космічних войдів на червоних зміщеннях від Місцевого Всесвіту до z = 2; електромагнітні лавини від блазарів та вимірювання магнітного поля в войдах; кореляційні властивості галактик з активними ядрами та їхнє оточення; гравітаційно-лінзові системи квазарів та їх пошук; кінематичні і динамічні властивості галактик Місцевого Всесвіту; методи встановлення відстаней до галактик та виділення структур галактик/АЯГ.

Методи дослідження. У роботі використовувалися методи чисельного моделювання, зокрема, метод Монте-Карло; машинного навчання - моделі різних типів регресій та нейронних мереж; 2D і 3D методи мозаїки Вороного для просторового розподілу великомасштабних структур Всесвіті, ієрархічний метод виділення груп/агломератів галактик та АЯГ; методи обробки спостережуваних даних та статистичних оцінок для встановлення достовірності отриманих

результатів, а також методи порівняння змодельованих параметрів зі спостережуваними даними.

Наукова новизна отриманих результатів.

Розроблено алгоритми для пошуку космічних войдів на основі динамічних властивостей великомасштабної структури Всесвіту.

Застосована апроксимація Лагранжа-Зельдовича для відтворення поля густини матерії низької концентрації та для виокремлення космічних порожнин; створено та апробовано відповідне програмне забезпечення.

Розроблено геометричний шукач порожнин та виділено в Місцевому Всесвіті войди та гіпервойди, створено алгоритми для виділення агломератів галактик. Досліджено населення космічних войдів Місцевого Всесвіту.

Вперше запропоновано використовувати метод редукції двоточкової кореляційної функції для відновлення орбіт галактик під час еволюції та формування космічних структур.

Вперше запропоновано метод мозаїки Вороного вищих порядків для виділення ізольованих галактик, пар та триплетів галактик.

Проведено обробку та аналіз даних позагалактичного рентгенівського огляду XXL/XMM-LSS, виконаного супутником XMM-Newton. Створено програмне забезпечення для аналізу кореляційних властивостей розподілу АЯГ, порівняно оточення АЯГ 1го та 2го типів, а також радіо і не-радіо АЯГ, з високою світністю і тмяних. Створено інструмент для пошуку надлишку густини навколо точкових рентгенівських джерел в оптичному діапазоні. Виявлено особливості просторового розподілу АЯГ щодо великомасштабних структур Всесвіту. Проведено оцінку кількості та пошук гравітаційно-лінзових систем в рентгенівському огляді XXL.

Проведено дослідження високоенергетичних процесів в космічних войдах, а саме електромагнітних лавин від гамма-фотонів, випромінених особливим типом АЯГ — блазарами. Виконано аналітичний опис основних характеристик лавини. Створено чисельні моделі лавин, фотон фотонної анігіляції та релятивістських електрон-позитронних пучків. За результатами вперше проведених моделювань показано, що за спостереженнями гало навколо блазарів в гамма діапазоні можна

оцінити величину магнітного поля в космічних войдах та характеристики самих блазарів, чим самим доводиться ненульове значення магнітного поля в войдах. Доведена стійкість пучків електрон-позитронних пар в космічних порожнинах Показано, що електромагнітні лавини від блазарів не впливають на термічну історію міжгалактичного простору войдів, крізь які вони поширюються.

Практичне значення одержаних результатів. Розроблено алгоритми та програмне забезпечення, яке може бути використане для обробки майбутніх оглядів позагалактичних джерел, отриманих за даними наземних і космічних телескопів, для уточнення космологічних параметрів Всесвіту та його картини великомасштабної структури.

Розроблений шукач войдів запропоновано для обробки спостережних даних космічній місії телескопа «Евклід».

Запропоновані та розвинуті у роботі математичні методи досліджень розподілу войдів, галактик і їхніх угруповань та спектрофотометричні методи обробки спостережних даних галактик достовірно відтворюють властивості цих об'єктів і можуть бути застосовані у подальших наукових дослідженнях, зокрема і при постановці конкурсної тематики, бакалаврських, магістерських і дисертаційних робіт.

Монографія «Dark Energy and Dark Matter in the Universe» у трьох томах, де том 3 «Dark matter: Observational manifestation and experimental searches» підготовлено за участі здобувача, визнана переможцем у категорії «Basic Science Book Awards» Міжнародної академії астронавтики у 2016 р. (https://iaaweb.org/content/view/144/244/).

Робота «Космічні войди великомасштабної структури Всесвіту: виокремлення, населення, активні ядра галактик та магнітні поля» отримала Премію Президента України для молодих вчених у 2018 році.

Результати дослідження використовуються в астрономічних установах національних університетів України, Інституті теоретичної фізики ім. М.М. Боголюбова НАН України, Інституті прикладних проблем механіки і математики ім. Я.С. Підстригача НАН України та за кордоном (наприклад, в Національній

обсерваторії Афін, на факультеті фізики та астрономії Болонського університету, французькому науково-дослідницькому інституті CEA-Sacley), у міжнародному проекті дослідження багатохвильового огляду неба XXL-XMM (THE ULTIMATE XMM EXTRAGALACTIC SURVEY), що охоплює 50 кв. градусів. Мета проекту - дослідження еволюції скупчень галактик та АЯГ і уточнення космологічних параметрів. Над проектом працює колаборація з більше ніж ста наукових співробітників з різних міжнародних установ. Також результати було використано у проекті Galaxy And Mass Assembly (GAMA) – вивчення властивостей та еволюції галактик та їх скупчень на малих червоних зміщеннях – і проекті MiNDSTEp (Microlensing Network for the Detection of Small Terrestrial Exoplanets), де здобувач приймав участь у спостереженнях АЯГ.

Достовірність та обґрунтованість наукових положень, висновків та рекомендацій. Достовірність і обґрунтованість результатів досліджень базуються на застосуванні загальноприйнятих та добре перевірених фізичних, математичних та чисельних методів, зокрема $\chi 2$, найменших квадратів, тестами Колмогорова-Смірнова та Стьюдента, а також порівнянням різних методів, застосованих до однієї вибірки. Наукові положення обґрунтовано та підтверджено публікацією результатів у рецензованих фахових журналах і матеріалах міжнародних конференцій та посиланнями на ці статті іншими авторами.

Особистий внесок здобувача. Результати дисертаційної роботи опубліковано в основних статтях [1–13], додаткових статтях [14–33], що висвітлюють тему дисертації, розділах у монографіях [34–37], а також в матеріалах і тезах конференцій [37–44]. У всіх статтях, де здобувач є першим автором, здобувачу належить постановка дослідження, розробка математичних методів дослідження і основна частина написання програмних кодів, участь у обґрунтуванні отриманих результатів та інтерпретації фізичних процесів, що відбуваються в досліджуваних об’єктах Всесвіту.

Додатково по статтям подано нижче.

У статті [1] здобувач виконував усі розрахунки і комп’ютерні програми, написав 90 % тексту статті та інтерпретував результати.

У статті [2] здобувач виконував розрахунки і комп’ютерні програми, писав текст статті, брав участь в обговоренні та інтерпретації результатів.

У статті [3] здобувач брав участь у постановці задачі, виконував усі розрахунки і комп’ютерні програми, написав текст статті.

У статті [4] здобувач виконав постановку задачі, розрахунки і комп’ютерні програми, написав текст статті.

У статті [5] здобувач приймав участь у постановці задачі, виконав усі розрахунки і комп’ютерні програми, написав текст статті.

У статті [6] здобувач приймав участь у постановці задачі, виконав 90% розрахунків і програмного забезпечення, написав текст статті.

У статті [7] здобувач приймав участь у постановці задачі, виконав 50 % розрахунків та усі комп’ютерні програми, приймав участі у написанні тексту статті.

У статті [8] здобувач приймав участь у постановці задачі, виконав усі розрахунки і комп’ютерні програми, написав текст статті, приймав участь в обговоренні результатів.

У статтях [9, 10] здобувач виконав 50 % розрахунків і комп’ютерних програм, приймав участь в обговоренні результатів.

У статті [11] здобувач створив комп'ютерну програму, написав текст статті, приймав участь в обговоренні та інтерпретації результатів.

У статті [12] здобувач брав участь у постановці задачі, створив комп’ютерну програму для методу Вороного вищих порядків, брав участь в обговоренні та інтерпретації результатів і написанні тексту статті.

У статті [13] здобувач брав участь у створенні комп'ютерних програм, зокрема ієрархічного методу для виділення агломератів, обговоренні та інтерпретації результатів.

У статтях [14–26] здобувач брав участь в обговоренні та інтерпретації результатів в рамках колаборацій проєктів XXL та GAMA як один із координаторів цих проєктів.

У статтях [27, 28] здобувач брав участь в обчисленнях, обговоренні та інтерпретації результатів.

У статті [29] здобувач брав участь в спостереженнях, обговоренні та інтерпретації результатів у якості колаборатора проєкту MiNDSTEp.

У статтях [30, 31] здобувач брав участь в обчисленнях, обговоренні та інтерпретації результатів.

У статті [32] здобувач брав участь в постановці задачі, обчисленнях, а також у обговоренні та інтерпретації результатів.

У статті [33] здобувач брав участь у створенні комп'ютерних програм, обговоренні та інтерпретації результатів.

Апробація результатів дисертації. Основні результати дослідження доповідалися на міжнародних наукових конференціях, семінарах ГАО НАН Укараїни та інших установ в Україні та за кордоном.

Зокрема на таких *конференціях* як

—IAU Symposium 362 Predictive Power of Computational Astrophysics as a Discovery Tool, VirtualMeeting, France, 2021;

—The European Week of Astronomy and Space Science (EWASS), Prague, Czech Republic, 2017; Lyon, France, 2019; Leiden, The Netherlands, 2020-2021;

—XIII-XV, XIX, XXI Gamov Summer School “Astronomy and beyond: Astrophysics, Cosmology, Cosmomicrophysics, Astroparticle Physics, Radioastronomy and Astrobiology”, Odessa, Ukraine, 2013-2015, 2019, 2021;

—The International Symposium “Astronomical Surveys and Big Data 2” (ASBD-2), Byurakan, Armenia, 2020;

— XX International Scientific and Technical Conference “Artificial Intelligence and Intellegent Systems", Kyiv, Ukraine, 2020;

— International Conference "Astronomy and Space Physics", Kyiv, Ukraine, 2020, 2021;

—XIII-Всеукраїнській студентській конференції “Фізика та науково-технічний прогрес”, Харків, Україна, 23-24 квітня 2019;

— Institute of Mathematics Conferences, Sixth International Conference on Analytic Number Theory and Spatial Tessellations, Kyiv, Ukraine, 2018;

— Meeting of XXL collaboration, Florence, Italy, 2016 p.;

— IAU Symposium No. 308 The Zeldovich Universe: Genesis and Growth of the Cosmic Web in Tallinn, Estonia, 2016;

— Advanced Workshop on Cosmological Structures from Reionization to Galaxies: Combining Efforts from Analytical and Numerical Methods, Trieste, Italy, 2015 p.;

— Euclid clustering meeting, London, UK, 2015 p.;

— Cosmic voids in the next generation of galaxy surveys workshop, Columbus, USA, 2015 p.;

— Астрономія та фізика космосу в Київському університеті. Міжнародна конференція в рамках VIII Всеукраїнського фестивалю науки 27 - 30 травня 2014 року. Київ;

— Meeting of XXL collaboration, Sesto, Italy, 2014 p.;

— International symposium "Multiwavelength-surveys: Galaxy Formation and Evolution from the early universe to today", Dubrovnik, Croatia, 2014 p.;

— AGN meeting of XXL collaboration, Athens, Greece, 2014 p.;

— Meeting of XXL collaboration, Bonn, Germany, 2013 p.;

— Conference "Half a century of X-ray Astronomy, Mykonos, Greece, 2012 p.;

— Space and ground-based imaging in astrophysics, "Actions de recherche concertées" annual meeting, Liege, Belgium, 2012 p.;

— Meeting of XXL collaboration, Meudon, France, 2012 p.;

— Meeting of XXL collaboration, Bonifacio, France, 2011 p.;

— Meeting of XXL collaboration, Sacley, France, 2011 p.;

— 17th Young Scientists' Conference on Astronomy and Space Physics, Kyiv, Ukraine, 2010 p.;

— X International Conference Relativistic Astrophysics, Gravitation and Cosmology, Kyiv, Ukraine, 2010 p.;

та семінарах:

— семінари департаменту астрофізики, геофізики і океанографії Льєжського університету, Льєж, Бельгія, 2011 р., 2012 р.;

— семінар інституту теоретичної фізики Рурського університету, Бохум, Німеччина, 2012 р.;

— семінари відділу позагалактичної астрономії та астроінформатики Головної астрономічної обсерваторії НАН України, Київ, Україна, 2009, 2010, 2011, 2013, 2015, 2018, 22020, 2021 р.;

— семінар астрономічної обсерваторії Ягеллонського університету, Краків, Польща, 2008 р.;

— семінари департаменту фізики та астрономії Болонського університету, Болонья, Італія, 2013, 2014, 2015 р.;

— семінар Національного Інституту Астрофізики INAF, Мілан, Італія 2019 р.;

— семінар ISDC відділення астрономічного департаменту Женевського університету, Версуа, Швейцарія, 2008 р.;

Розділ 1. ВОЙДИ ЯК СКЛАДНИК ВЕЛИКОМАСШТАБНОГО РОЗПОДІЛУ НЕБЕСНИХ ОБ'ЄКТІВ ВСЕСВІТУ

Космічними войдами називають області у Всесвіті з низькою концентрацією галактик. Ці космічні порожнини оточені волокнами та стінками, до яких концентруються галактики, а на їх перетині формуються багаті скупчення галактик. Згідно з [69] еволюція войдів тісно пов'язана з навколишнім середовищем: менші порожнечі мають тенденцію з'являтися у середині надщільного середовища, тоді як більші порожнечі справді антикорельовані щодо розподілу матерії. Таким чином, менші порожнечі мають тенденцію руйнуватися з часом, тоді як більші порожнечі продовжують розширюватися. Ближче до центрів войдів більш поширеними є маломасивні галактики зі слабким темпом зореутворення, хоча воно більш ефективне, ніж у відповідних галактиках у регіонах з щільною густиною оточення [75].

Властивості войдів використовуються для тестування космологічних моделей. Зокрема, однозначна та об'єктивна ідентифікація войдів є важливою для здійснення тесту Алькок-Пачинського [45], де вимірюється розмір багатьох накладених войдів вздовж і поперек променя зору в супутніх космологічних координатах. Можливі відхилення від сферичності такого складеного войду говорять про застосування некоректної космологічної моделі чи її параметрів. Точність цього тесту сильно залежить від надійності методу виділення космічних порожнин.

Відомі шукачі можна розбити на три класи в залежності від типу критеріїв виокремлення войдів.

Перший клас базується на безпосередньому вимірюванні густини галактик в певному об'ємі, де войд є областю простору без галактик, або з концентрацією галактик нижче певної границі. Другий клас використовує критерії, де войди є геометричними фігурами, наприклад, сферами,

багатогранниками тощо. Шукачі войдів третього класу базуються на динамічних критеріях, де галактики розглядаються як тестові частинки для космічного поля швидкостей.

Шукачі перших двох класів виділяють войди з Ейлерових координатах. Попри простоту методів, такі стратегії мають два недоліки. По перше, галактики використовуються як трейсери маси, і припускається певна невизначеність у зв'язку між полем концентрації галактик і полем густини видимої матерії. По-друге, за означенням войди – це області з низькою концентрацією галактик, тому будь-який метод, що безпосередньо використовує розподіл галактик для ідентифікації войдів, піддається впливу статистичного шуму. Однак, ці фактори мають більше значення, якщо мова йде про великі об'єми (великий розкид червоних зміщень), а для невеликих войдів, ці методи досить ефективні при невеликому задіяні обчислювальних ресурсів. В роботі [1] запропоновано новий алгоритм виділення войдів третього класу, що базується на динамічних і кластерних критеріях опису войдів у Лагранжевих координатах, – вони мінімізують вклад фактору низької концентрації галактик у войдах (див. Розділ 1.1).

Потрібно зазначити, що визначення войдів у всіх авторів дещо різне [71, 72]. Отже, недоліком всіх шукачів є те, що вибрані порожнечі не можна легко порівняти з тими, які отримані за допомогою інших методів [1, 80]. Тому задачею усіх авторів є намагання порівняти войди, отримані різними методами та створити універсальний шукач, результати роботи якого не залежали б від початкових умов вибірки та його параметрів.

1.1. Динамічний та некорельований шукач войдів

У роботі [46] показано, що наївний підхід вимірювання концентрації галактик у сферичних шарах навколо войдів призводить до великої кількості порожніх шарів без галактик і, як наслідок, до систематичної недооцінки профілю густини. Перевагою шукачів войдів третього класу є те, що войди можуть бути визначені в Лагранжевих координатах, що значно покращує проблему статистичного шуму та полегшує теоретичну інтерпретацію результатів.

У роботі [1] нами запропоновано новий алгоритм виділення войдів третього класу. Основна ідея методу полягає в спеціальній рандомізації вибірки галактик для досягнення однорідного первинного розподілу галактик та подальшого використання індивідуальних векторів зміщення галактик після даної процедури. Під зміщенням тут розуміється вектор, який з'єднує спостережувані координати галактик з отриманими положеннями після рандомізації. Така процедура відповідає зворотній в часі еволюції великомасштабної структури Всесвіту.

Описаний у роботі шукач LZVF (Lagrangian Zeldovich Void Finder) використовує апроксимацію Лагранжа-Зельдовича для відновлення взаємного розташування галактик на початку еволюції. Він полягає в припущенні, що рух галактик відбувається з дотриманням умови мінімізації дії S, яка є інтегралом Лагранжіана по часу. На практиці, застосування цього підходу вимагає генерацію вибірки випадкових галактик розміром і об'ємом, що відповідають реальній вибірці. З'єднання реальних галактик з випадковими відбувається таким чином, щоб сума квадратів відстаней всіх пар «реальна – ипадкова» галактика була мінімальною, що дає змогу побудувати векторне поле зміщення.

Для верифікації даного підходу був розроблений так званий некорельований шукач войдів UVF (Uncorrelated Void Finder), в якому поле зміщень будувалося, виходячи лише з геометричних міркувань. Результати, отримані двома методами, добре узгоджуються між собою.

Для тестування методу було використано каталог гало холодної темної матерії з N-тіл моделювання CODECs для стандартної космологічної моделі ΛCDM, де частинки темної матерії є основними трейсерами локальної густини маси.

Отримані результати порівняно з класичним шукачем войдів ZOBOV (ZOnes Bordering On Voidness), створеного на основі виділення концентрацій галактик за допомогою мозаїки Вороного [47]. Показано, що структури, виділені методами LZVF і UVF, краще накладаються на неоднорідності великомасштабної структури Всесвіту, ніж виділенні шукачем ZOBOV.

Monthly Notices of the ROYAL ASTRONOMICAL SOCIETY
MNRAS **448,** 642–653 (2015) doi:10.1093/mnras/stv043

Cosmic voids detection without density measurements

Andrii Elyiv,[1,2]★ Federico Marulli,[1,3,4] Giorgia Pollina,[1,5] Marco Baldi,[1,3,4] Enzo Branchini,[6,7,8] Andrea Cimatti[1] and Lauro Moscardini[1,3,4]

[1]*Dipartimento di Fisica e Astronomia, Università di Bologna, viale Berti Pichat 6/2, I-40127 Bologna, Italy*
[2]*Main Astronomical Observatory, Academy of Sciences of Ukraine, 27 Akademika Zabolotnoho St., UA-03680 Kyiv, Ukraine*
[3]*INAF – Osservatorio Astronomico di Bologna, via Ranzani 1, I-40127 Bologna, Italy*
[4]*INFN – Sezione di Bologna, viale Berti Pichat 6/2, I-40127 Bologna, Italy*
[5]*University Observatory Munich, Ludwig-Maximilian University, Scheinerstr. 1, D-81679, Munich, Germany*
[6]*Dipartimento di Fisica, Universit degli Studi Roma Tre, via della Vasca Navale 84, I-00146 Rome, Italy*
[7]*INAF – Osservatorio Astronomico di Roma, Monte Porzio Catone, Italy*
[8]*INFN – Sezione di Roma Tre, via della Vasca Navale 84, I-00146 Rome, Italy*

Accepted 2015 January 7. Received 2015 January 3; in original form 2014 October 16

ABSTRACT

Cosmic voids are effective cosmological probes to discriminate among competing world models. Their identification is generally based on density or geometry criteria that, because of their very nature, are prone to shot noise. We propose two void finders that are based on dynamical criterion to select voids in Lagrangian coordinates and minimize the impact of sparse sampling. The first approach exploits the Zel'dovich approximation to trace back in time the orbits of galaxies located in voids and their surroundings; the second uses the observed galaxy–galaxy correlation function to relax the objects' spatial distribution to homogeneity and isotropy. In both cases voids are defined as regions of the negative velocity divergence, which can be regarded as sinks of the back-in-time streamlines of the mass tracers. To assess the performance of our methods we used a dark matter halo mock catalogue CODECS, and compared the results with those obtained with the ZOBOV void finder. We find that the void divergence profiles are less scattered than the density ones and, therefore, their stacking constitutes a more accurate cosmological probe. The significance of the divergence signal in the central part of voids obtained from both our finders is 60 per cent higher than for overdensity profiles in the ZOBOV case. The ellipticity of the stacked void measured in the divergence field is closer to unity, as expected, than what is found when using halo positions. Therefore, our void finders are complementary to the existing methods, which should contribute to improve the accuracy of void-based cosmological tests.

Key words: methods: data analysis – large-scale structure of Universe.

1 INTRODUCTION

Cosmic voids are regions of low density that occupy a significant fraction of the volume in the Universe. The first observational evidence of giant voids was obtained more than 30 years ago (Gregory & Thompson 1978; Joeveer, Einasto & Tago 1978). However, their systematic and quantitative study came later with the advent of the first large spectroscopic surveys (Huchra et al. 1988; Geller & Huchra 1989; Bahcall 1995). Now it is well established that void sizes span a wide range of scales, from minivoids with diameters of about 3–5 Mpc in the Local Universe (Tikhonov & Karachentsev 2006) to the supervoids with diameters of about 200 Mpc (Lindner et al. 1995; Szapudi et al. 2014). Due to large volume filling factor, characteristic shape, dynamics and low density, they constitute unique laboratories for astrophysics and cosmology.

In the framework of high-energy astrophysics, voids can be regarded as *highways* for propagating particles like cosmic rays and neutrinos (Schlickeiser et al. 2012; Miniati & Elyiv 2013; Krakau & Schlickeiser 2014), in which the presence of non-zero extragalactic magnetic fields or extragalactic light is still an open issue (Elyiv, Neronov & Semikoz 2009; DeLavallaz & Fairbairn 2012; Arlen & Vassiliev 2013; Beck et al. 2013). Voids are also important for testing galaxy evolution models since they allow us to study the evolution of isolated objects and assess, by comparison, the influence of the environment (Peebles 2001; Patiri et al. 2006; Vavilova, Melnyk & Elyiv 2009; Stanonik et al. 2010; Karachentsev et al. (2011); Nicholls et al. 2014). Indeed, the deficit of dwarf galaxies in nearby voids (Peebles 2001; Kreckel et al. 2011; Elyiv et al. 2013) with respect to the theoretical prediction, often dubbed as the

★ E-mail: andrii.elyiv@unibo.it

Void Phenomenon, is still regarded as a potential evidence against the cold dark matter (CDM) scenario.

Finally, and most importantly, voids are very relevant for cosmology. They have an impact on the cosmic microwave background and on the weak lensing signal. Anomalies like the Cold Spot could be explained as the result of the Integrated Sachs–Wolfe effect over large voids (Rees & Sciama 1968; Kovács et al. 2014; Szapudi et al. 2014). Next-generation galaxy surveys like those that will be carried out by the Large Synoptic Survey Telescope (Kaiser et al. 2002) and by the Euclid satellite (Laureijs et al. 2011; Amendola et al. 2013) are expected to detect gravitational lensing from medium-sized voids with which one can constrain the void's mass density profile without using galaxies and assumptions on their bias (Izumi et al. 2013; Krause et al. 2013; Clampitt & Jain 2014; Melchior et al. 2014).

Indeed, voids can be used as effective cosmological probes. Their physical properties depend on the nature of dark energy (DE) and on the primordial density field from which they have evolved (Odrzywołek 2009; D'Amico et al. 2011; Bos et al. 2012; Spolyar, Sahlén & Silk 2013; Gibbons et al. 2014). In particular, it has been realized that their shape is very sensitive to the equation of state of the DE component and that spurious ellipticity could be used to constrain the amount of dark matter (DM) (Lavaux & Wandelt 2010). Additional constraints on DM can also be obtained by measuring the outflow velocities from voids in the nearby Universe (Courtois et al. 2012; Tully et al. 2013). Finally, voids' expansion history and shape have been used to test modified gravity models (Li 2011; Clampitt, Cai & Li 2013; Cai, Padilla & Li 2014; Zivick & Sutter 2014).

Perhaps their most common and effective cosmological application is through the so-called Alcock–Paczynski (AP) test (Alcock & Paczynski 1979), in which one measures the size of the stacked void along and across the line of sight and looks for a possible mismatch that would arise from assuming an incorrect cosmological model (Sutter et al. 2012, 2014a). The accuracy of the AP test has been discussed in comparison to that of other cosmological tests by Lavaux & Wandelt (2012). The first application of the method by Sutter et al. (2012) considered voids extracted from the SDSS DR-7 galaxy survey (Abazajian et al. 2009) using a modified version of the ZOnes Bordering On Voidness (ZOBOV) algorithm (Neyrinck 2008). With 10 stacked voids detected out to $z = 0.36$ they failed to detect any significant distortions. In a more recent attempt by Sutter, Pisani & Wandelt (2014b) that used the SDSS-DR10 LOWZ and CMASS galaxy samples (Ahn et al. 2014), the AP signal corresponding to a mass density parameter $\Omega_{\rm M} \simeq 0.15$ has been detected.

The accuracy of the AP test depends on the ability to identify voids in a reliable and robust way. This is not an easy task, as demonstrated by the fact that many different void finders have been proposed over the years, many of which cross-compared in the Aspen-Amsterdam contest (Colberg et al. 2008). Lavaux & Wandelt (2010) proposed to classify void finders in three different categories depending on the type of criterion adopted for the identification. The first class is based on a density criterion and defines voids as regions empty of galaxies or with local density well below the mean (Gottlöber et al. 2003; Colberg et al. 2005; Brunino et al. 2007; Elyiv et al. 2013). The second class uses geometry criteria and identifies voids as geometrical structures like e.g. spherical cells, polyedra, etc. (Plionis & Basilakos 2002; Colberg et al. 2005; Shandarin et al. 2006; Platen, van de Weygaert & Jones 2007; Neyrinck 2008; Leclercq et al. 2014). The third class is that of finders based on dynamical criteria in which galaxies are considered as test particles of the cosmic velocity field and not as tracers of the underlying mass distribution (Hahn et al. 2007; Lavaux & Wandelt 2010).

Finders of the first two classes identify voids from galaxies' Eulerian positions. This strategy has two disadvantages. First of all, galaxies are used as mass tracers and some biasing prescription has to be adopted to specify the relation between the galaxy and the mass density field. This might play a significant role when attempting to use cosmic voids to distinguish different cosmological scenarios, in particular different theories of gravity or couplings in the dark sector, as these models might feature a non-standard evolution of the halo bias (Pollina et al., in preparation). Secondly, voids are by definition low-density regions. Any method that uses galaxies to identify voids is then prone to shot noise error. Nadathur et al. (2014) showed that the naive strategy of measuring density in spherical shells around voids leads to a large number of empty shells and, consequently, a systematic underestimate of the density profile. An additional drawback related to the Eulerian nature of these methods is that they identify structures in a broad range of dynamical regimes, which complicates the comparison with theoretical predictions.

An advantage of void finders of the third class is that they can be defined in Lagrangian coordinates, which greatly alleviates the shot noise problem and eases the theoretical interpretation of the results. The disadvantage, however, is that voids selected cannot be readily compared with those obtained with the other methods. Perhaps, the best worked out example of dynamical Lagrangian void finder is the DIVA method proposed by Lavaux & Wandelt (2010). This technique uses the Monge–Ampère–Kantorovitch method (Brenier et al. 2003) to reconstruct galaxy orbits back in time starting from their Eulerian position, and identifies voids in Lagrangian coordinates by looking at the regions where the divergence of the displacement field is positive. Assuming approximate correspondence between the divergence field and linearly extrapolated initial density field, they made predictions on void statistics and local ellipticities defined from the curvature of the divergence field. Dynamical void finders from the last class are very promising for the probe of precision cosmology.

In this work we propose two dynamical void finders of the third class. Both methods aim at reconstructing galaxies' Lagrangian positions by randomizing the Eulerian ones. The randomization, however, is achieved in two different ways. The first exploits galaxy clustering, and more specifically the observed two-point correlation function, and relaxes the system to a homogeneous and isotropic distribution using, in reverse, an annealing scheme similar to the one proposed by Rintoul & Torquato (1997) and commonly used in solid-state physics to create samples with specified spatial correlation properties. The second method is not completely new and actually quite similar to the DIVA method, except that it uses the Path Interchange Zel'dovich Approximation (PIZA) (Croft & Gaztanaga 1997) to reconstruct galaxy orbits that, in this case, are simply straight lines. In this respect, more accurate reconstruction schemes could be used, like those that minimize the action of a non-linear system (Peebles 1989; Nusser & Branchini 2000). However, we decided to adopt the PIZA scheme since it is fast, and easy to implement.

The randomization procedure allows us to build a displacement field which approximates the cosmic velocity field and enables us to trace the build up of cosmic structures, including voids. The latter are defined as sinks in the time reverse streamline of galaxies. This is the criterion that we use to locate voids in the Lagrangian coordinates Sahni & Shandarin 1996). We test our void finders using the catalogue of DM haloes extracted from a high-resolution N-body simulation (Baldi 2012) at $z = 0$, and compare our results

with those obtained when we use the ZOBOV void finder (Neyrinck 2008). The quantitative comparison focuses on voids' statistics, as well as on physical properties such as their mass density profile and ellipticities.

The paper is organized as follows. In Section 2 we describe the halo catalogues used in this work. In Section 3 we present the two proposed void finders based on the two-point correlation function (Section 3.1) and on the Lagrangian Zel'dovich approximation (Section 3.2). The procedure used for the final void identification is described in Section 4. In Section 5 we analyse the properties of the voids selected with the two methods, and compare them with the ones detected by the ZOBOV finder. The conclusions are drawn in Section 6.

2 THE DM HALO CATALOGUE

In order to test our void finder algorithms, and to compare them with those obtained with the public code ZOBOV, we use a halo catalogue extracted from the CoDECS simulations (Baldi et al. 2010; Baldi 2012), which are the largest suite of publicly available[1] cosmological and hydrodynamical simulations of interacting DE cosmologies (Wetterich 1995; Amendola 2000) to date. The CoDECS runs include five different models of DE interaction, plus a reference ΛCDM run.

In this work we focus on the standard ΛCDM run and plan to explore the other interacting DE models included in the CoDECS Project in a future work aimed at assessing the impact of the dark sector interactions on voids' properties (Pollina et al., in preparation). Specifically, we have considered the H-CoDECS run, a hydrodynamical N-body simulation with a comoving box size of 80 Mpc h^{-1} and a total number of particles (gas + CDM) of $N_{\rm p} = 2 \times 512^3 \approx 2.7 \times 10^8$. The CDM mass resolution is $m_{\rm c} = 2.39 \times 10^8\ {\rm M}_\odot\, h^{-1}$, and the gravitational softening was set to $\epsilon_g = 3.5$ kpc h^{-1}, corresponding to about 1/40th of the mean inter-particle separation, $\bar{d}$. CDM haloes have been identified by means of a Friends-of-Friends (FoF) algorithm (Davis et al. 1985) with linking length $\lambda = 0.2 \times \bar{d}$. This procedure has been applied to the particle distribution by linking the CDM particles as primary tracers of the local mass density, and then attaching baryonic particles to the FoF group of their nearest neighbour. The CoDECS public repository provides also spherical overdensity catalogues computed with the SUBFIND algorithm (Springel et al. 2001), but for the present analysis we will consider only the FoF catalogues. In this work we focus on the $z = 0$ output. At this epoch the halo catalogue consists of 116 129 haloes with a minimum mass of $7.657 \times 10^{10}\ {\rm M}_\odot\, h^{-1}$, corresponding to an average halo density of $\rho_{\rm h} = 0.23\ ({\rm Mpc}\, h^{-1})^{-3}$ and to a corresponding mean inter-halo separation of 1.64 Mpc h^{-1}. The average halo density is high enough to identify small voids with sizes above 3Mpc h^{-1}, while the large volume of the sample, $5.12 \times 10^5 {\rm Mpc}^3\, h^{-3}$, may provide a wide range of void sizes up to ∼20 Mpc h^{-1}.

3 DYNAMICAL VOID FINDERS

The basic idea behind the two dynamical void finders that we present in this section is rather simple. Let us consider a volume of the Universe characterized by large-scale structures in the DM component and probed by 'particles' like haloes or galaxies. Here we propose to use these as test particles, not mass tracers, and trace their orbits back in time to a homogeneous and isotropic initial distribution, that is to reconstruct their Lagrangian positions $\boldsymbol{q}$. This is done in two ways: (i) by exploiting the different correlation properties of the initial and final particle distributions and (ii) by assuming some dynamical approximation that allows us to solve the mixed boundary problem of a system of particles with known final positions and well-defined initial statistical properties. The practical implementation of these ideas is described in Sections 3.1 and 3.2, respectively.

After reconstructing Lagrangian positions, $\boldsymbol{q}$, we obtain the particle displacement field, $\boldsymbol{\Psi}$, by simply connecting them to the Eulerian positions, $\boldsymbol{v}$, hence assuming straight orbits: $\boldsymbol{q} - \boldsymbol{v} = \boldsymbol{\Psi}(\boldsymbol{q})$. The divergence of the displacement field, $\Theta \equiv \nabla \cdot \boldsymbol{\Psi}$, is associated with the mass density field and used to identify voids as sinks of mass streamlines in time reverse variables. We note that this approach is similar to that of Ricciardelli, Quilis & Planelles (2013), in which a positive divergence in the galaxy flow was one of the conditions used to identify voids.

3.1 The uncorrelating void finder

At the present epoch the spatial distribution of galaxies is highly inhomogeneous. Deviations from the homogeneity are conveniently and readily characterized by their spatial two-point correlation function that measures the departure from a purely Poisson distribution. On the other hand, at early epochs the distribution of matter and of any test particles like galaxies is supposed to be highly homogeneous, with no spatial correlation. This suggests that a practical way to trace galaxy orbits back in time, at least in a statistical sense, could be that of relaxing their present spatial distribution to homogeneity, practically defined as a state in which the correlation function at all separations is zero. An effective way to achieve this is by applying the annealing method of Rintoul & Torquato (1997) in reverse, effectively moving the system away from its minimum energy configuration. We note that this method has been used to generate mock galaxy catalogues with a specified two-point correlation function (Soares-Santos et al. 2011). In our iterative algorithm we allow for a small random displacement of one halo along a random direction with the length 0.5 Mpc h^{-1}. If the amplitude of the two-point correlation function decreases then we place the halo at the new position. Otherwise we keep it at the original position. Then we move to the next halo and repeat the procedure for all haloes in the catalogue. Then we move to the next iteration and start again with the first halo. Iterations stop when the amplitude of the two-point correlation function is consistent with zero within the uncertainties at all separations. More quantitatively, iterations stop when $\sum_{i=1}^{N} \xi(r_i)^2 / N_{\rm b} < \varepsilon_{\rm lim}$, where $\xi(r_i)$ is the amplitude of the two-point correlation function at separation r_i, and $N_{\rm b}$ is the total number of bins. In this work we used $N = 50$ logarithmic bins over the range of scales $0.5 < r[{\rm Mpc}\, h^{-1}] < 50$. We set the tolerance parameter empirically to the value $\varepsilon_{\rm lim} = 10^{-6}$, as a compromise between reconstruction accuracy and computational cost. For a fast measurement of the two-point correlation function, we use a linked-list based algorithm (Marulli et al. 2012, 2013), specifically modified to update at each iteration step only the number of pairs associated with the halo that is moved in the procedure.[2]

At the various steps of the iteration the haloes describe a random walk from high-density regions to low-density ones. We compute

[1] See http://www.marcobaldi.it/CoDECS

[2] Using ∼116 000 haloes as test particles, the code requires ∼100 h of CPU time to detect the voids, with an Intel Core i5, 520M@2.4 GHz CPU.

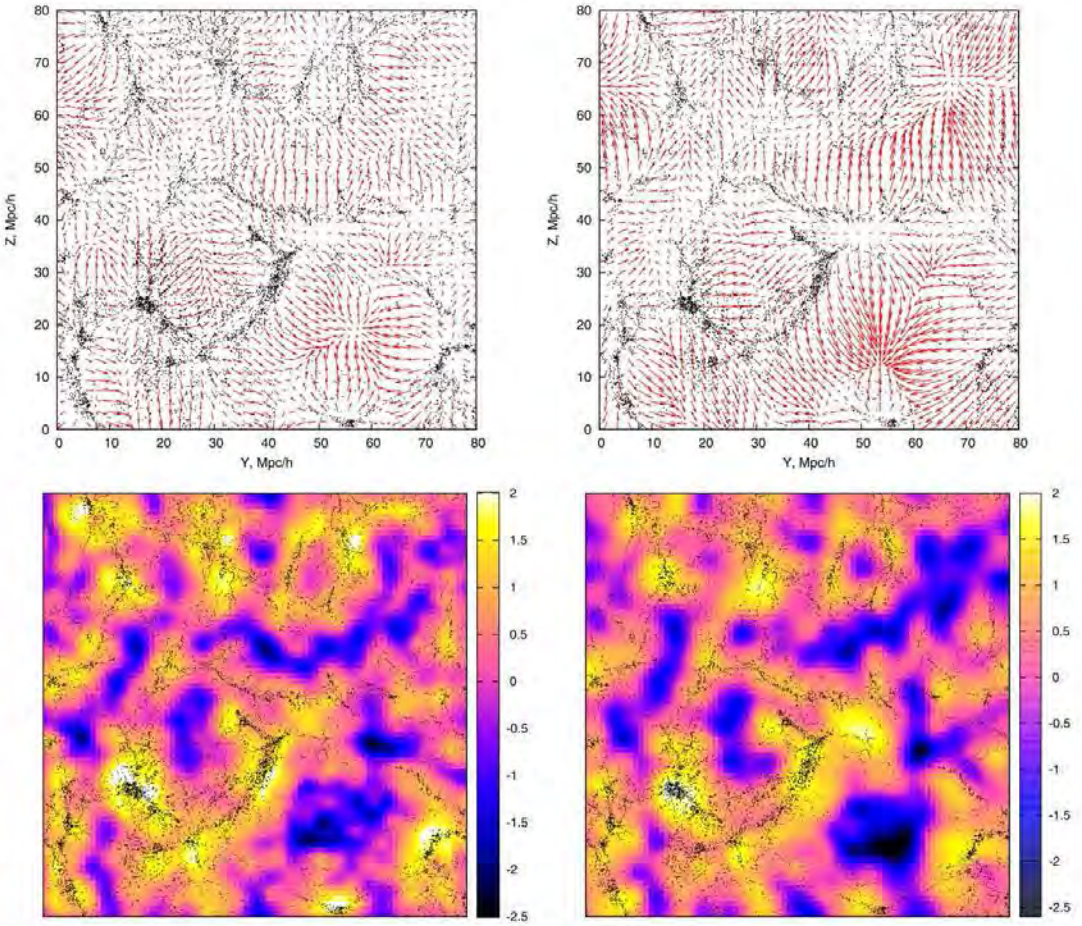

Figure 1. The reconstructed displacement field Ψ (top panels) and its divergence Θ (bottom panels) obtained with the two void finders proposed in this work, the UVF (left-hand panels) and the LZVF (right-hand panels). The size of the displayed region is $80 \times 80\,\mathrm{Mpc}\,h^{-1}$, with a thickness of $5\,\mathrm{Mpc}\,h^{-1}$. Black dots represent DM haloes. The amplitude of the vector field components (red arrows) is reduced by a factor of 0.75, for visual clarity.

the displacement vector Ψ that connects the Eulerian and the reconstructed Lagrangian positions at the end of the iteration. Since the reconstruction is not unique, the Lagrangian positions, and consequently the displacement field, depend on the random seed. We perform 10 reconstructions using different seeds and obtain the average displacement field at the given position $\boldsymbol{q}$ by Gaussian-weighting the individual displacement vectors at the different reconstructed Lagrangian positions, that is

$$\langle \Psi(\boldsymbol{q}) \rangle = \sum_j \Psi_j \cdot \exp\left(-d_j^2/2\sigma^2\right) / \sum_j \exp\left(-d_j^2/2\sigma^2\right). \quad (1)$$

Here the subscript j identifies the reconstructed Lagrangian positions in any of the 10 reconstructions and the sum runs over all haloes' Lagrangian positions in the 10 reconstructions, d_j is the distance of the halo j to the given position $\boldsymbol{q}$. Such a Gaussian smoothing is a needed procedure to convert discrete displacement vectors which are computed at the Lagrangian positions of galaxies to a contiguous vector field. The most direct way is Gaussian smoothing with kernel scale $\sigma = 1.5\,\mathrm{Mpc}\,h^{-1}$, which corresponds to the mean inter-halo distance. Finally, the displacement field is used to build the divergence field $\Theta = \nabla \cdot \Psi$ at the generic position (x, y, z) which, for convenience, we place at the nodes of a cubic grid of size $1\,\mathrm{Mpc}\,h^{-1}$. We shall call this method the UNCORRELATING VOID FINDER (UVF).

Fig. 1 shows a slice of thickness $5\,\mathrm{Mpc}\,h^{-1}$ across the computational cube. The top left panel shows the Eulerian positions of the haloes (black dots) superimposed to the projected displacement field $\langle \Psi \rangle$ (red arrows). In the bottom panel the same black dots are superimposed to the divergence field. The colour code is set according to the amplitude of Θ, as indicated by the colour bar.

3.2 The Lagrangian Zel'dovich void finder

The second void finder that we consider here is based on the Zel'dovich approximation (Zel'dovich 1970) to the growth of density fluctuations. More specifically, we implement the PIZA method

of Croft & Gaztanaga (1997) to trace the orbit of the objects in a self-gravitating system by minimizing its action, under the Zel'dovich approximation. Since objects have straight orbits, we simply connect their Eulerian positions to those of a randomly distributed sample. In each iteration we modify the connection, hence setting a new path to a different grid point, and accept it if the total path, obtained by summing the square of the individual paths, decreases. Since the total path is proportional to the action, this system is relaxed to the correct dynamical configuration. We will refer to this finder as the LAGRANGIAN ZEL'DOVICH VOID FINDER (LZVF).

Again, the reconstructed positions depend on the choice of the random seed used in the iterative procedure. The displacement fields obtained from 10 different reconstructions were smoothed by a Gaussian kernel of radius 1.5 Mpc h^{-1}, i.e. the same one used in the UVF finder.

The result is shown in the right panels of Fig. 1, which are analogous to their counterpart on the left. Clearly, both the divergence and the displacement fields obtained with the two methods are qualitatively similar. The main features (coherent flows, regions of large positive/negative divergence) are seen on both reconstructions. However, their amplitude and spatial location do not always coincide. We shall see in the next sections what are the impacts of these differences on the properties of the voids.

4 VOID IDENTIFICATION AND CHARACTERIZATION

By definition the divergence of the vector field represents the density, Θ, of sources or sinks of that field at a given point:

$$\Theta = \nabla\boldsymbol{\Psi} = \sum_{i=1}^{3} \frac{\partial \Psi_i}{\partial x_i}, \tag{2}$$

where x_i are the Cartesian coordinates. We calculate the divergence numerically in a grid with step 1 Mpc h^{-1}. The colour maps in the lower panels of Fig. 1 show the divergence field assessed with the two proposed void finders, UVF (left) and LZVF (right). Clearly, there is a strong correlation between the distribution of the Eulerian halo positions and the magnitude of divergence calculated in Lagrangian coordinates.

We use the dimensionless quantity Θ to characterize the voids, instead of the local density. Specifically, the local minima of the divergence field are used to localize the voids. In our approach, a local minimum is a grid node where Θ is lower than in all the adjacent $3^3 - 1$ nodes around it. Moreover, we consider only the local minima with negative divergence. Each local minimum identifies a subvoid. To determine its shape we use the well-known watershed technique (Platen et al. 2007). We fill the basin starting from the local minimum. When the 'water' level of a subvoid reaches the ones of adjacent subvoids, we do not join these regions but just put a wall between them and continue by filling until all grid nodes with $\Theta < 0$ are not involved. In such a way the divergence field divides the space between subvoids around each local minimum. We do not use any other additional parameters or criteria for the void identification, as the average or minimum halo density. This approach provides a strict definition of subvoids, which can be considered as the sinks of the back-in-time streamlines of the mass tracers. The subvoids are the roots in the tree hierarchy, and have no parent voids (Aragon-Calvo & Szalay 2013). We do not consider subvoids that lie close to the boundary of the sample, as their volumes would be underestimated.

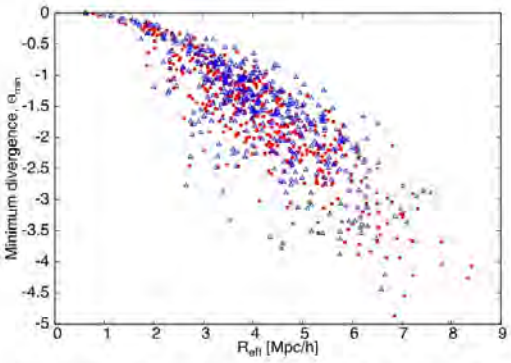

Figure 2. Relation between the effective subvoid radii, $R_{\rm eff}$, and the divergence minima, $\Theta_{\rm min}$, for the two void finders, UVF (blue triangles) and LZVF (red circles).

To assess the subvoid as well as void sizes, we estimate the spherical equivalent radius $R_{\rm eff} = \left(\frac{3V_{\rm void}}{4\pi}\right)^{1/3}$, where $V_{\rm void}$ is the volume of the void. We find a moderate correlation between the values of minimum divergence, $\Theta_{\rm min}$, and the effective radii of the corresponding subvoids, as shown in Fig. 2. This is expected: the smaller is the minimum divergence, the larger is the subvoid volume around. It can be interpreted according to the large-scale structure growing scenario. The larger is a galaxy escaping velocity at a given place, the more effective is the void expanding there, as confirmed theoretically for isolated perturbations of the density field (Bardeen et al. 1986; Sheth & van de Weygaert 2004). This result is in agreement with the findings by Nadathur et al. (2014), obtained using the ZOBOV watershed transform algorithm.

The construction of the void hierarchical tree is not unique. Here we have adopted a procedure based on merging adjacent voids and set the minimum effective radius of accepted voids, $R_{\rm lim}$. Voids are said to be adjacent when they have been assigned two nearby grid points. The procedure is the following.

– Voids are sorted by their effective radius from the largest to the smallest.
– Voids with an effective radius larger than $R_{\rm lim}$ are kept.
– Voids with radius below $R_{\rm lim}$ that are isolated (that is with no adjacent void) are discarded.
– Voids with radius below $R_{\rm lim}$ with one or more adjacent voids are merged to the adjacent one with the largest radius. The effective radius of the new merged void is calculated from the sum of the void volumes that are included in the merged void. We repeat this procedure until all adjacent voids have radii below $R_{\rm lim}$.
– After the merging procedure we keep all objects with radius larger than $R_{\rm lim}$.

A crucial issue to be addressed when reconstructing void profiles and stacking is how to define the void centres. We consider four alternative definitions. The first one is the geometrical centre defined as follows:

$$\boldsymbol{r}_G = \frac{\sum_{i=1}^{n} \boldsymbol{r}_i}{n}, \tag{3}$$

where $\boldsymbol{r}_i$ are the coordinates of all n grid nodes that belong to the void, that is $\boldsymbol{r}_G$ is the centre of mass if the void density is uniform.

Table 1. Main properties of the void samples selected with UVF, LZVF (for different values of $R_{\rm lim}$) and ZOBOV.

Void sample, $R_{\rm lim}$ (Mpc h^{-1})	Number of voids	$R_{\rm eff}$ range (Mpc h^{-1})	Median $R_{\rm eff}$ (Mpc h^{-1})
UVF finder			
All subvoids	427	0.6–7.4	4.0
2	405	2.0–7.4	4.1
3	344	3.0–7.4	4.4
4	211	4.0–8.0	5.4
5	103	5.0–11.6	6.8
5.3	82	5.3–12.6	7.0
6	34	6.0–17.1	8.3
7	8	7.0–28.7	12.0
8	7	8.0–28.7	12.5
LZVF finder			
All subvoids	433	0.6–8.4	4.1
2	412	2.0–8.4	4.2
3	358	3.0–8.5	4.4
4	233	4.0–8.5	5.3
5	117	5.0–12.2	6.9
5.3	96	5.3–12.6	7.3
6	46	6.0–17.9	8.5
7	15	7.0–26.5	9.0
8	5	8.0–32.2	17.5
ZOBOV	87	3.9–15.1	8.2

The second definition is the barycentre of the haloes hosted in the void:

$$\boldsymbol{r}_{\rm B} = \frac{\sum_{j=1}^{N} v_j}{N}, \tag{4}$$

where v_j are the coordinates of the N haloes in the void.

The third void centre is defined as the weighted centre over the divergence field inside a given void:

$$\boldsymbol{r}_{\rm W} = \frac{\sum_{i=1}^{n} \Theta(r_i) r_i}{\sum_{i=1}^{n} \Theta_i(r_i)}, \tag{5}$$

where $\boldsymbol{r}_i$ are the coordinates of all n grid nodes that belong to the void.

The last definition considered in this work is the position of the minimum of the divergence field inside a given void, $\boldsymbol{r}_M$. In the following figures, we will refer to these four different definitions of void centres as G, B, W, M, respectively.

5 RESULTS

Applying our two finders, UVF (Section 3.1) and LZVF (Section 3.2), to the $z = 0$ DM halo sample described in Section 2, we construct a set of void catalogues. In the following sections we present the main properties of the selected voids, and compare them to the ones detected by the ZOBOV finder in Section 5.5.

5.1 Void statistics

Using the two void finders, UVF and LZVF, we find in total 427 and 433 subvoids, respectively, with effective radii up to ~8.4 Mpc h^{-1}. We construct different void samples by cutting at different $R_{\rm lim}$. The main properties of the selected void catalogues are summarized in Table 1.

Fig. 3 compares the cumulative distributions of voids selected with different finders, as a function of the effective radius $R_{\rm eff}$, and

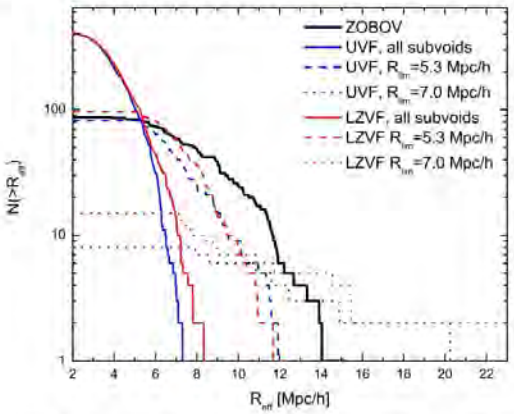

Figure 3. The cumulative distribution of selected voids as a function of $R_{\rm eff}$, for different values of $R_{\rm lim}$, as indicated by the labels. Blue, red and black lines show the results obtained with UVF, LZVF and ZOBOV, respectively.

for three different values of $R_{\rm lim}$. As expected, these distributions become steeper as $R_{\rm lim}$ decreases. The results obtained with the two finders UVF and LZVF appear in reasonable agreement.

The use of a grid and of a smoothing of the displacement field could in principle introduce a numerical bias in our results. We investigate the impact of these issues by changing the grid steps and the smoothing scale. An increasing of the grid step from 1 to 2 Mpc has the effect of enhancing the median subvoid radii by ~10 per cent, while the size of the larger merged voids and the divergence profiles are almost unaffected. When increasing the smoothing scale from 1.5 to 3 Mpc h^{-1}, the median radii of subvoids are enhanced by ~30(70) per cent for $R_{\rm lim} = 4(0)$ Mpc h^{-1}, while the sizes of larger voids are unchanged.

5.2 Divergence profiles

Fig. 4 shows the mean divergence profiles (left panel) and associated 1σ deviations (right panel) as a function of the normalized distance $d/R_{\rm eff}$ from the void centres. In particular, this figure shows the impact of the different definitions of void centres considered in this work. As it can be seen in the left panel, the divergence profiles obtained with the M centring, that is by defining the void centres as the minima of the divergence field, are the steepest in the central part and the least noisy. Therefore, in the following analysis we will consider only this definition.

Fig. 5 compares the results obtained with UVF and LZVF for three different values of $R_{\rm lim} = 0$, 5.3 and 7Mpc h^{-1} (with M centring). While the mean divergence profiles of the two void finders are in close agreement, we note that the ones provided by UVF are the least noisy, independent of $R_{\rm lim}$. As the selected voids are not exactly spherical, the outer parts of these profiles can include also regions outside the voids. The effect is however low, and does not significantly impact our results.

5.3 Overdensity profiles

Fig. 6 compares the mean overdensity profiles and corresponding 1σ deviations of the subvoids, moderate ($R_{\rm lim} = 5.3$ Mpc h^{-1}) and large voids ($R_{\rm lim} = 7$ Mpc h^{-1}) detected by our two finders, assuming the

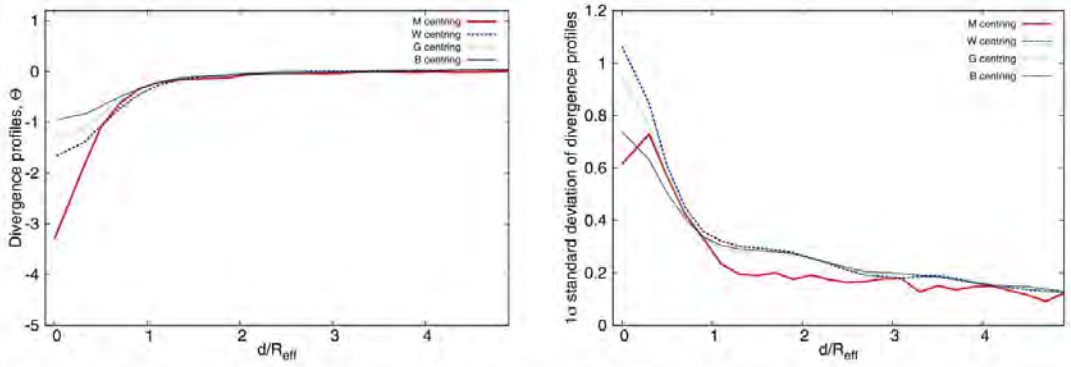

Figure 4. Mean divergence profiles (left-hand panel) and corresponding 1σ deviations (right-hand panel) of the voids detected by the LZVF, as a function of the normalized radial distance, $d/R_{\rm eff}$, and for different centrings, as indicated by the labels.

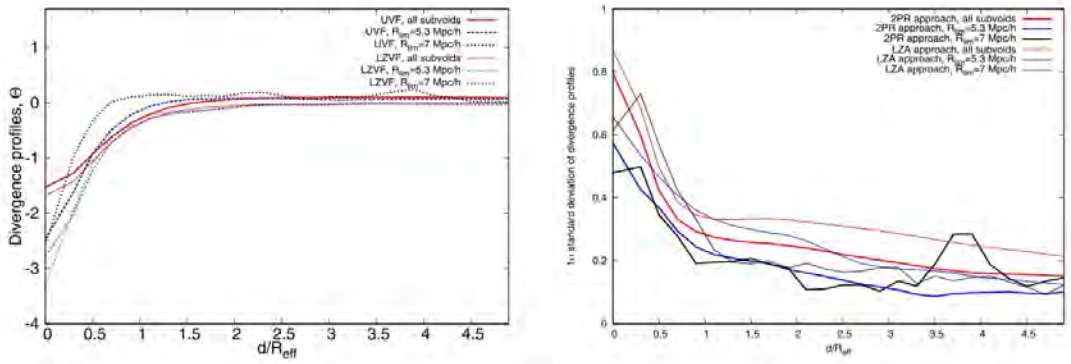

Figure 5. Mean divergence profiles (left-hand panel) and corresponding 1σ deviations (right-hand panel) of the voids detected by the two finders UVF and LZVF, as a function of the normalized radial distance, $d/R_{\rm eff}$, and for three different values of $R_{\rm lim}$ (M centring), as indicated by the labels.

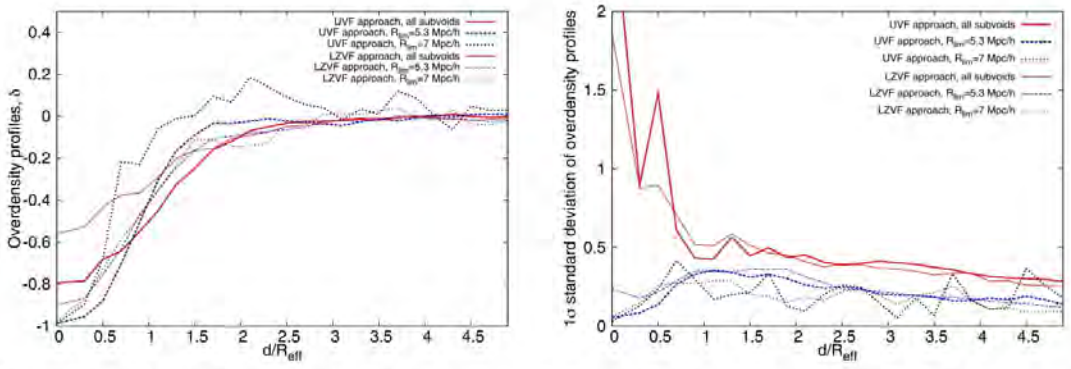

Figure 6. Mean overdensity profiles (left-hand panel) and corresponding 1σ deviations (right-hand panel) of the voids detected by the two finders UVF and LZVF, as a function of the normalized radial distance, $d/R_{\rm eff}$, and for three different values of $R_{\rm lim}$ (M centring), as indicated by the labels.

Table 2. Main parameters of the selected void samples. First and second columns are the names of the void finders and the values of $R_{\rm lim}$. Third and fourth columns show the average amplitudes of overdensity and divergence profiles in the central part of voids within $0.2 \cdot R_{\rm eff}$ with 1σ standard deviation. The values in bracket show the ratio between the average values and their standard deviations (that is the significance of the signal). Fifth and sixth columns show the radius range of the voids used for stacking and their numbers, respectively. Seventh and eighth columns represent the average ellipticities $<e>$ of individual voids with 1σ standard deviation, and the ellipticities of stacked voids $e^{(s)}$, respectively. Ellipticities are measured using the divergence field for UVF and LZVF voids, and using halo positions for ZOBOV voids.

Void finder	$R_{\rm lim}$	Overdensity (δ)	Divergence (Θ)	Radius range (Mpc)	N	$\langle e_{1,2}\rangle$, $\langle e_{1,3}\rangle$	$e^{(s)}_{1,2}$ and $e^{(s)}_{1,3}$
UVF	0	-0.79 ± 2.71 (0.3)	-1.53 ± 0.80 (1.9)	4–7	212	0.82 ± 0.11, 0.58 ± 0.18	0.99 ± 0.01, 0.97 ± 0.01
UVF	5.3	-0.99 ± 0.05 (20)	-2.47 ± 0.57 (4.3)	7–10	33	0.79 ± 0.12, 0.52 ± 0.21	0.98 ± 0.04, 0.97 ± 0.05
UVF	7	-0.99 ± 0.03 (33)	-2.57 ± 0.48 (5.4)	>7	7	0.70 ± 0.16, 0.47 ± 0.09	0.63 ± 0.24, 0.46 ± 0.21
LZVF	0	-0.56 ± 1.86 (3.3)	-1.68 ± 0.87 (1.7)	4–7	222	0.84 ± 0.11, 0.64 ± 0.19	0.99 ± 0.01, 0.98 ± 0.01
LZVF	5.3	-0.90 ± 0.23 (3.9)	-2.78 ± 0.66 (4.2)	7–10	50	0.81 ± 0.11, 0.61 ± 0.17	0.97 ± 0.03, 0.96 ± 0.03
LZVF	7	-0.98 ± 0.06 (16.3)	-3.29 ± 0.61 (5.4)	>7	15	0.79 ± 0.10, 0.47 ± 0.18	0.89 ± 0.09, 0.83 ± 0.11
ZOBOV		-0.87 ± 0.33 (2.6)	-0.37 ± 1.00 (0.4)	7–10	34	0.76 ± 0.10, 0.59 ± 0.11	0.94 ± 0.04, 0.89 ± 0.04

M centring. The profiles appear quite smooth, flattening at around $2R_{\rm eff}$. Most of them are not compensated, differently from what is obtained using void finders based on density measurements (see Section 5.5). We find also very few voids with positive overdensity in the central radial bin, due to the cloud-in-void mode of the void hierarchy (Sheth & van de Weygaert 2004). The 1σ deviations of the overdensity profiles decrease for larger values of $R_{\rm lim}$, especially at small radial distances. Overall, the mean void profiles obtained with the two finders UVF and LZVF appear in good agreement. Divergence, overdensity and shape parameters of the selected void samples are reported in Table 2.

5.4 Void ellipticities

To further investigate the characteristics of the selected samples, we estimate the ellipticity of stacked voids. We consider three subsamples: subvoids with $4 < r_{\rm eff}[{\rm Mpc}\,h^{-1}] < 7$, moderate voids with $7 < r_{\rm eff}[{\rm Mpc}\,h^{-1}] < 10$ and $R_{\rm lim} = 5.3\,{\rm Mpc}\,h^{-1}$, and large voids with $r_{\rm eff} > 7\,{\rm Mpc}\,h^{-1}$ and $R_{\rm lim} = 7\,{\rm Mpc}\,h^{-1}$. To measure the ellipticity in the divergence field, we use the second moments of the Θ distribution at the void position. The components of the inertial tensor are defined in Lagrangian space with respect to the void centres:

$$I_{i,j} = \sum \chi_i \chi_j \Theta(\boldsymbol{q})\,, \tag{6}$$

where the smoothed divergence field Θ is defined over the nodes of a cubic grid with 1 Mpc h^{-1} spacing. The sum runs over all grid points within a distance of $0.7 \cdot R_{\rm max}$ from the void centre, where $R_{\rm max}$ is the radius of the largest selected void. The quantity χ_i represents the ith Cartesian component of the grid point in Lagrangian space with respect to the void centre. The conservative choice of considering points within $0.7 \cdot R_{\rm max}$ was proposed by Sutter et al. (2014b) to balance between the need to consider a large number of grid points to maximize the signal-to-noise ratio and that of avoiding fluctuations that are effectively outside the void boundaries. We define the ellipticity, e, as the axial ratio of the eigenvalues Λ_i of the matrix $I_{i,j}$ given by equation (9):

$$e_{1,2} = \sqrt{\Lambda_2/\Lambda_1},\ e_{1,3} = \sqrt{\Lambda_3/\Lambda_1}\,, \tag{7}$$

where $\Lambda_1 \geq \Lambda_2 \geq \Lambda_3$. The same definition has already been used by Plionis, Barrow & Frenk (1991), de Theije et al. (1995) and Splinter et al. (1997). The errors on the stacked void ellipticities are computed using the jackknife technique (Efron 1982). The average and stacked void ellipticities are reported in Table 2. The average ellipticity and its variance provide information on individual void shapes. Voids detected by our two finders have similar ellipticities, almost independent of $R_{\rm lim}$. The ratio between major and medium axes is in the range 0.70–0.84 with $rms \sim 0.1$, and between major and minor axes in 0.47–0.64 with $rms \sim 0.15$. Voids look like elongated tri-axial ellipsoids. Overall, the void shape appears approximately similar, independently on which of our finders (UVF or LZVF) we use. Ellipticities of the stacked voids are close to unity, as expected, because our sample is not redshift-space distorted. Finally, we note that subvoids have on average a more spherical shape than larger voids.

5.5 Comparison with ZOBOV finder

We compare our results with those obtained with ZOBOV (Neyrinck 2008), a publicly available and widely used void finder algorithm that searches for depressions in the density distribution of a set of points. Applying a Voronoi tessellation, the algorithm associates a cell at each point, defined as the region that is closer to that point than to any other point of the sample. ZOBOV then identifies the local density minima, searching for the Voronoi-cells whose density is lower than that of all the other adjacent cells. The Voronoi-cells surrounding the local density minima are eventually joined, adding cells with larger and larger densities. Voids are identified as unions of these Voronoi-cells.

However, local density minima can be found also in overdense regions. To exclude the latter, we consider only regions with an overdensity minimum smaller than -0.8 (Neyrinck 2008). To assess the statistical significance for each void, ZOBOV provides also the *fakeness probability*, that is the probability that a void is simply generated by Poisson fluctuations in the distribution of points. In this analysis, we consider only the voids with a significance level larger than 2σ, as commonly assumed.

To assess ZOBOV void centres, we use the following definition:

$$\boldsymbol{x}_v = \frac{1}{V_{\rm void}} \sum_{i=1}^{N_{\rm V}} \boldsymbol{x}_i^{\rm halo} \cdot V_i^{\rm halo}\,, \tag{8}$$

where $\boldsymbol{x}_v$ is the baricentre, $\boldsymbol{x}_i$ and $V_i^{\rm halo}$ are the position of the ith halo in the void and the volume of the associated Voronoi cell, respectively, and $V_{\rm void}$ is the volume provided by ZOBOV. The main properties of the ZOBOV void catalogue are reported in Tables 1 and 2. To compare our void finders with ZOBOV, we consider subsamples selected with $R_{\rm lim} = 5.3\ {\rm Mpc}\,h^{-1}$. This choice has no particular

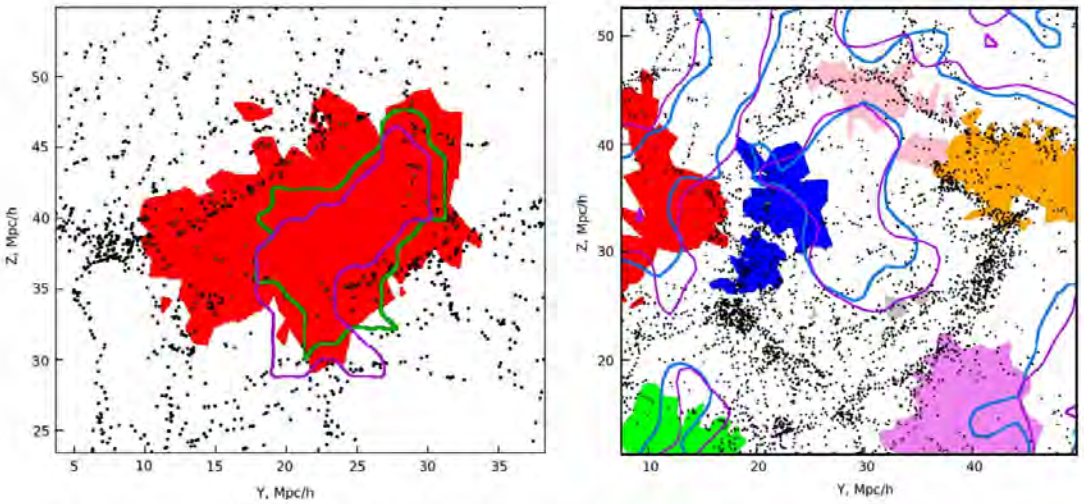

Figure 7. Zoom of two regions of the slice shown in Fig. 1. Thick and thin lines show the shapes of voids selected by UVF and LZVF finders, respectively. Filled coloured areas show the voids found by ZOBOV. The underdense regions selected by UVF and LZVF appear always similar. On the other hand, voids selected by ZOBOV are in some cases similar to the ones detected by the other two finders (left-hand panel), while in other cases are very different (right-hand panel).

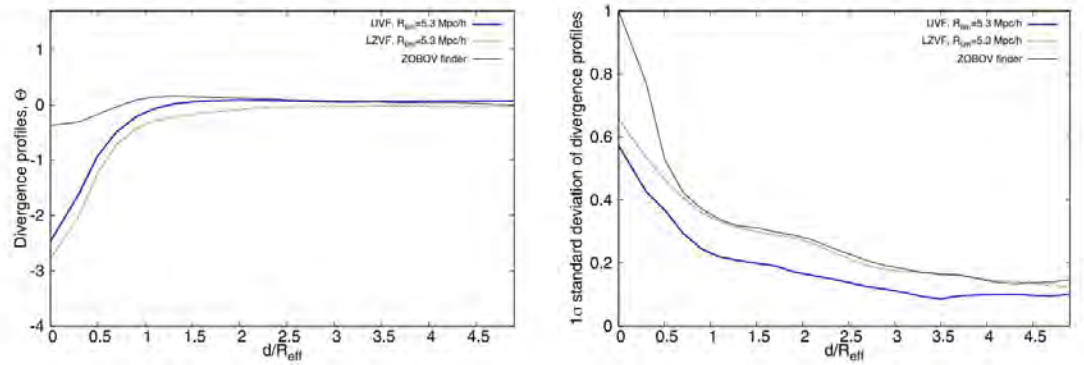

Figure 8. Comparison between the mean divergence profiles (left-hand panel) and corresponding 1σ deviations (right-hand panel) of the voids detected by the two finders UVF and LZVF and the ones detected by ZOBOV, as a function of the normalized radial distance, $d/R_{\rm eff}$.

physical meaning. It just ensures that the number and effective radii of the voids selected with the three different finders are similar (see Table 1), and thus the statistical errors are similar as well. The interesting issue of how to determine the optimal value of $R_{\rm lim}$ for a specific cosmological analysis is deferred to a forthcoming paper.

The black line in Fig. 3 shows the cumulative distribution of the ZOBOV voids compared to our findings. While the total numbers of voids selected by UVF, LZVF and ZOBOV are similar, the ZOBOV voids appear systematically larger than the others. The median radii of UVF, LZVF (for $R_{\rm lim} = 5.3\,{\rm Mpc}\,h^{-1}$) and ZOBOV are 7.0, 7.3 and 8.2 $\rm Mpc\,h^{-1}$, respectively. The filling factor of the ZOBOV voids is 56.4 per cent, larger than the ones of our finders, 41 per cent for UVF and 47 per cent for LZVF.

A one-by-one comparison of the voids selected by the three finders is rather complicated, if not impossible, since different methods can select very different topological underdense structures. The two zoomed regions displayed in Fig. 7 show representative examples of two extreme cases. On the left-hand panel we zoom on a large void detected by all the three finders, approximately at the same positions. On the contrary, the region shown on the right-hand panel demonstrates that, in some cases, the underdense regions selected by ZOBOV can be entirely different from the ones detected by UVF and LZVF, while the latter are always in close agreement with each other. This is due to the significant differences in the methods. For example, the overdensity in the central part of the large void selected by UVF and LZVF (and not by ZOBOV) in the centre of the right-hand panel of Fig. 7 is -0.70 ± 0.07, thus larger than the overdensity threshold used in ZOBOV.

Figs 8 and 9 compare the mean divergence and overdensity profiles, and the corresponding 1σ deviations, of the voids detected by the three finders UVF, LZVF and ZOBOV. As it can be seen, the UVF and LZVF profiles are steeper at small radial distances, and less scattered, especially the UVF one, consistent with the universality of the void shapes (Nadathur et al. 2014). The different profile shapes are caused by the very different approaches of the analysed Eulerian and Lagrangian void finders.

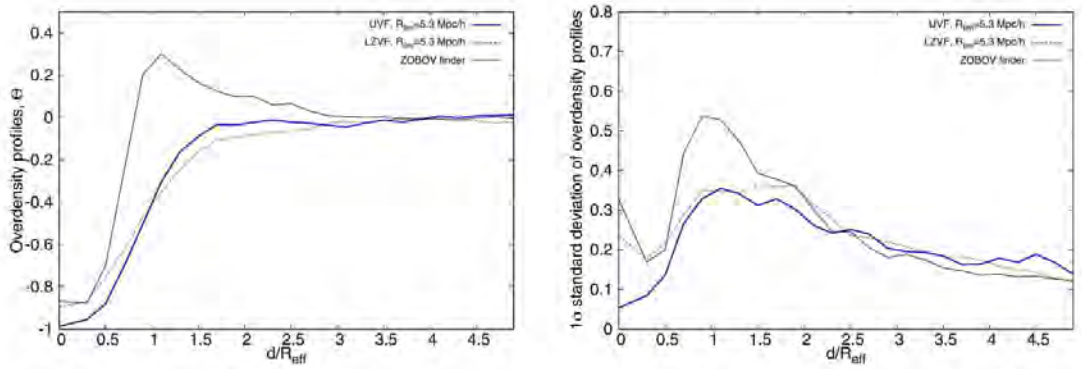

Figure 9. Comparison between the mean overdensity profiles (left-hand panel) and corresponding 1σ deviations (right-hand panel) of the voids detected by the two finders UVF and LZVF and the ones detected by ZOBOV, as a function of the normalized radial distance, $d/R_{\rm eff}$.

In Table 2 we compare the significance of the signal at the first radial bin, within $0.2 \cdot R_{\rm eff}$, for both overdensity and divergence profiles. As it can be seen, the most prominent signal is in the overdensity profiles for ZOBOV, and in the divergence profiles for UVF and LZVF. However, the significance of the divergence signal obtained from both of our finders is 60 per cent higher than for overdensity profiles of ZOBOV voids. This may be explained by the fact that, for the calculation of the divergence field and corresponding void selection, we use randomized samples of haloes that are less biased by shot-noise in the central, extremely underdense, void regions.

For the ZOBOV voids we calculate the inertial tensor using the Eulerian coordinates of haloes within $0.7 \cdot R_{\rm max}$ and assuming that all the haloes have equal masses, $m = 1$:

$$I_{i,j} = \sum_k \chi_{i,k}\chi_{j,k} \,. \tag{9}$$

where the index k corresponds to the index of the considered halo. UVF and LZVF have ellipticities closer to unity than ZOBOV ($e^2_{1,2} = 0.98, 0.97$ and 0.94, respectively), and the same $rms \sim 0.04$. For the ratio of major and minor axes, we also find systematically closer results to unity for UVF and LZVF than ZOBOV (0.97, 0.96 and 0.89, respectively).

6 SUMMARY AND CONCLUSIONS

Present and upcoming next-generation galaxy redshift surveys, such as SDSS (Abazajian et al. 2009), BigBOSS (Schlegel et al. 2009), WFIRST (Green et al. 2012), HETDEX (Hill et al. 2008), and Euclid (Laureijs et al. 2011), will provide spectroscopic data with unprecedented large statistics, allowing the use of underdense regions as effective cosmological probes. One of the most promising applications for cosmology is to exploit void ellipticities (Lavaux & Wandelt 2010; Sutter et al. 2012).

The identification of cosmic voids, however, is not trivial, due to their large sizes and peculiar structures. Generally, void finders are based on density or geometric criteria, which can be affected by large shot noise. In this work we implemented two dynamical void finders, not affected by this weakness, and characterized by a minimal number of free parameters and additional assumptions. The proposed void finders are based on sample randomization. One uses the Zel'dovich approximation to trace back in time the orbits of matter tracers. The second uses the observed two-point correlation function to relax the objects' spatial distribution to homogeneity. The Lagrangian Zel'dovich Void Finder is similar to the DIVA procedure for what concerns the displacement field reconstruction (Lavaux & Wandelt 2010). On the other hand, the Uncorrelating Void Finder adopts a new technique based on the measurement of the two-point correlation function of the sample. The two independent dynamical void finders considered in this work are thus complementary, and allowed us to strengthen our main results and conclusions.

We defined voids as sinks of the back-in-time streamlines of the mass tracers in Lagrangian coordinates using the divergence of the displacement field. With a watershed technique (Platen et al. 2007) we identified hundreds of subvoids around the local minima of the divergence field. These subvoids are parents of larger voids, which we constructed using criteria of minimal effective void radius. Moreover, we considered four different approaches for the definition of void centres, a crucial issue for a proper void stacking. We found that the most convenient option is the stacking of voids centred on their minimum divergence. To test our finders we used a halo catalogue from the CoDECS simulations.

We compared our results with those obtained with the publicly available Eulerian class ZOBOV finder, using the same halo catalogue at $z = 0$. We found that the overdensity profiles of both UVF and LZVF are more self-similar than the ZOBOV ones, thus their stacking should provide more accurate cosmological probes. The significance of the signal in the central part of the voids ($<0.2R_{\rm eff}$) is 60 per cent higher for the divergence profiles of our voids than for overdensity profiles of ZOBOV voids, when using Eulerian halo positions. We measured the ellipticities of both individual voids and stacked ones. We found a good agreement between individual void shapes for all the three finders with average axis ratios $<e_{1,2}> \sim 0.8 \pm 0.1$, $<e_{1,3}> \sim 0.55 \pm 0.15$. The void shape appears approximately universal, independent of the fact that voids are detected using overdensities or divergences. Stacked voids from both of our finders have much more spherical shape than ZOBOV ones. The voids' properties of both our finders are in good agreement with each other. The two proposed void finders can thus complement the existing set of finders and contribute to improve the accuracy of cosmological probes.

The forthcoming Euclid survey will be very promising for the application of our dynamical void finders. The expected spectroscopic survey will cover 15 000 deg^2 and will contain around 5×10^7 galactic redshifts, mainly in the range $0.7 < z < 2.1$, up to visual

magnitude $m_H = 24$ (Laureijs et al. 2011). At such redshift range the mean spacing will rise just from 4 to 15 Mpc h^{-1} (Biswas, Alizadeh & Wandelt 2010). This makes the Euclid spectroscopic survey an ideal laboratory for the studying of voids' evolution. The volume of the Euclid spectroscopic survey will be larger than that of SDSS by a factor of 500. So we expect 300 times more galaxies and a few hundred times more voids in comparison to SDSS.

In the work by Biswas et al. (2010) it has been shown that such a high statistics of void ellipticities, combined with other traditional methods, is expected to improve the DE task force figure of merit (FoM) on the DE parameters by orders of hundreds. The simulation of Lavaux & Wandelt (2012) showed the effectiveness of the Euclid stacked voids for the AP test and further DE probes. The FoM of stacked voids from the Euclid survey may double all the other DE probes derived from the Euclid data alone (combined with *Planck* priors). Moreover, the Euclid voids could in principle improve the outcomes from baryon acoustic oscillations by an order of magnitude. The cosmological constraints that can be obtained with the cosmic microwave background gravitational lensing on cosmic voids for a Euclid-like survey have been investigated by Chantavat et al. (2014). The authors found that the latter could be comparable to the constraints from *Planck* data alone.

In a forthcoming paper we plan to further investigate the characteristics of the cosmic voids detected by the proposed finders, in particular the redshift evolution of the void number density, size distribution and ellipticities, and their dependence on the cosmological model. We will also investigate the effect of redshift-space distortions in the divergence field.

ACKNOWLEDGEMENTS

We acknowledge the grants ASI n.I/023/12/0 'Attività relative alla fase B2/C per la missione Euclid' and MIUR PRIN 2010-2011 'The dark Universe and the cosmic evolution of baryons: from current surveys to Euclid'. MB is supported by the Marie Curie Intra European Fellowship 'SIDUN' within the 7th Framework Programme of the European Commission. The numerical simulations presented in this work have been performed and analysed on the Hydra cluster at the RZG supercomputing centre in Garching, and on the BladeRunner cluster at the Bologna University, partly funded by the Marie Curie Intra European Fellowship 'SIDUN'. We acknowledge financial support from PRIN INAF 2012 'The Universe in the box: multiscale simulations of cosmic structure.

REFERENCES

Abazajian K. N. et al., 2009, ApJS, 182, 543
Ahn C. P. et al., 2014, ApJS, 211, 17
Alcock C., Paczynski B., 1979, Nature, 281, 358
Amendola L., 2000, Phys. Rev. D, 62, 043511
Amendola L. et al., 2013, Living Rev. Relativ., 16, 6
Aragon-Calvo M. A., Szalay A. S., 2013, MNRAS, 428, 3409
Arlen T. C., Vassiliev V. V., 2013, preprint (arXiv:1303.2121)
Bahcall N. A., 1995, PASP, 107, 790
Baldi M., 2012, MNRAS, 422, 1028
Baldi M., Pettorino V., Robbers G., Springel V., 2010, MNRAS, 403, 1684
Bardeen J. M., Bond J. R., Kaiser N., Szalay A. S., 1986, ApJ, 304, 15
Beck A. M., Hanasz M., Lesch H., Remus R.-S., Stasyszyn F. A., 2013, MNRAS, 429, L60
Biswas R., Alizadeh E., Wandelt B. D., 2010, Phys. Rev. D, 82, 023002
Bos E. G. P., van de Weygaert R., Dolag K., Pettorino V., 2012, MNRAS, 426, 440
Brenier Y., Frisch U., Hénon M., Loeper G., Matarrese S., Mohayaee R., Sobolevskii A., 2003, MNRAS, 346, 501
Brunino R., Trujillo I., Pearce F. R., Thomas P. A., 2007, MNRAS, 375, 184
Cai Y.-C., Padilla N., Li B., 2014, preprint (arXiv:1410.1510)
Chantavat T., Sawangwit U., Sutter P. M., Wandelt B. D., 2014, preprint (arXiv:1409.3364)
Clampitt J., Jain B., 2014, preprint (arXiv:1404.1834)
Clampitt J., Cai Y.-C., Li B., 2013, MNRAS, 431, 749
Colberg J. M., Sheth R. K., Diaferio A., Gao L., Yoshida N., 2005, MNRAS, 360, 216
Colberg J. M. et al., 2008, MNRAS, 387, 933
Courtois H. M., Hoffman Y., Tully R. B., Gottlöber S., 2012, ApJ, 744, 43
Croft R. A. C., Gaztanaga E., 1997, MNRAS, 285, 793
D'Amico G., Musso M., Noreña J., Paranjape A., 2011, Phys. Rev. D, 83, 023521
Davis M., Efstathiou G., Frenk C. S., White S. D. M., 1985, ApJ, 292, 371
de Theije P. A. M., Katgert P., van Kampen E., 1995, MNRAS, 273, 30
DeLavallaz A., Fairbairn M., 2012, Phys. Rev. Lett., 108, 171301
Efron B., 1982, The Jackknife, the Bootstrap, and other Resampling Plans. Society of Industrial and Applied Mathematics CBMS-NSF Monographs. SIAM, Philadelphia, p. 38
Elyiv A., Neronov A., Semikoz D. V., 2009, Phys. Rev. D, 80, 023010
Elyiv A. A., Karachentsev I. D., Karachentseva V. E., Melnyk O. V., Makarov D. I., 2013, Astrophys. Bull., 68, 1
Geller M. J., Huchra J. P., 1989, Science, 246, 897
Gibbons G. W., Werner M. C., Yoshida N., Chon S., 2014, MNRAS, 438, 1603
Gottlöber S., Łokas E. L., Klypin A., Hoffman Y., 2003, MNRAS, 344, 715
Green J. et al., 2012, preprint (arXiv:1208.4012)
Gregory S. A., Thompson L. A., 1978, ApJ, 222, 784
Hahn O., Porciani C., Carollo C. M., Dekel A., 2007, MNRAS, 375, 489
Hill G. J. et al., 2008, ASP Conf. Ser. Vol. 399, Panoramic Views of Galaxy Formation and Evolution. Astron. Soc. Pac., San Francisco, p. 115
Huchra J. P., Geller M. J., de Lapparent V., Burg R., 1988, Large Scale Structures of the Universe, Symposium no. 130, International Astronomical Union Symposium. Kluwer Academic Publishers, Dordrecht, p. 105
Izumi K., Hagiwara C., Nukajima K., Kitamura T., Asada H., 2013, Phys. Rev. D, 88, 024049
Joeveer M., Einasto J., Tago E., 1978, MNRAS, 185, 357
Kaiser N. et al., 2002, Proc. SPIE, 4836, 154
Karachentsev I. D., Makarov D. I., Karachentseva V. E., Melnyk O. V., 2011, Astrophys.l Bull., 66, 1
Kovács A. et al., 2014, preprint (arXiv:1407.1470)
Krakau S., Schlickeiser R., 2014, ApJ, 789, 84
Krause E., Chang T.-C., Doré O., Umetsu K., 2013, ApJ, 762, L20
Kreckel K., Peebles P. J. E., van Gorkom J. H., van de Weygaert R., van der Hulst J. M., 2011, AJ, 141, 204
Laureijs R. et al., 2011, preprint (arXiv:1110.3193)
Lavaux G., Wandelt B. D., 2010, MNRAS, 403, 1392
Lavaux G., Wandelt B. D., 2012, ApJ, 754, 109
Leclercq F., Jasche J., Sutter P. M., Hamaus N., Wandelt B., 2014, preprint (arXiv:1410.0355)
Li B., 2011, MNRAS, 411, 2615
Lindner U., Einasto J., Einasto M., Freudling W., Fricke K., Tago E., 1995, A&A, 301, 329
Marulli F., Bianchi D., Branchini E., Guzzo L., Moscardini L., Angulo R. E., 2012, MNRAS, 426, 2566
Marulli F. et al., 2013, A&A, 557, A17
Melchior P., Sutter P. M., Sheldon E. S., Krause E., Wandelt B. D., 2014, MNRAS, 440, 2922
Miniati F., Elyiv A., 2013, ApJ, 770, 54
Nadathur S. et al., 2014, preprint (arXiv:1407.1295)
Neyrinck M. C., 2008, MNRAS, 386, 2101
Nicholls D. C., Jerjen H., Dopita M. A., Basurah H., 2014, ApJ, 780, 88
Nusser A., Branchini E., 2000, MNRAS, 313, 587
Odrzywołek A., 2009, Phys. Rev. D, 80, 103515

Patiri S. G., Betancort-Rijo J. E., Prada F., Klypin A., Gottlöber S., 2006, MNRAS, 369, 335
Peebles P. J. E., 1989, ApJ, 344, L53
Peebles P. J. E., 2001, ApJ, 557, 495
Platen E., van de Weygaert R., Jones B. J. T., 2007, MNRAS, 380, 551
Plionis M., Basilakos S., 2002, MNRAS, 330, 399
Plionis M., Barrow J. D., Frenk C. S., 1991, MNRAS, 249, 662
Rees M. J., Sciama D. W., 1968, Nature, 217, 511
Ricciardelli E., Quilis V., Planelles S., 2013, MNRAS, 434, 1192
Rintoul M. D., Torquato S., 1997, J. Colloid Interface Sci., 186, 467
Sahni V., Shandarin S., 1996, MNRAS, 282, 641
Schlegel D. J. et al., 2009, preprint (arXiv:0904.0468)
Schlickeiser R., Elyiv A., Ibscher D., Miniati F., 2012, ApJ, 758, 101
Shandarin S., Feldman H. A., Heitmann K., Habib S., 2006, MNRAS, 367, 1629
Sheth R. K., van de Weygaert R., 2004, MNRAS, 350, 517
Soares-Santos M. et al., 2011, ApJ, 727, 45
Splinter R. J., Melott A. L., Linn A. M., Buck C., Tinker J., 1997, ApJ, 479, 632
Spolyar D., Sahlén M., Silk J., 2013, Phys. Rev. Lett., 111, 241103
Springel V., White S. D. M., Tormen G., Kauffmann G., 2001, MNRAS, 328, 726
Stanonik K. et al., 2010, ASP Conf. Ser. 421, Galaxies in Isolation: Exploring Nature Versus Nurture, Astron. Soc. Pac., San Francisco, p. 107
Sutter P. M., Lavaux G., Wandelt B. D., Weinberg D. H., 2012, ApJ, 761, 187
Sutter P. M., Lavaux G., Wandelt B. D., Weinberg D. H., Warren M. S., 2014a, MNRAS, 438, 3177
Sutter P. M., Pisani A., Wandelt B. D., Weinberg D. H., 2014b, MNRAS, 443, 2983
Szapudi I. et al., 2014, preprint (arXiv:1406.3)
Tikhonov A. V., Karachentsev I. D., 2006, ApJ, 653, 969
Tully R. B. et al., 2013, ApJ, 146, 86
Vavilova I. B., Melnyk O. V., Elyiv A. A., 2009, Astron. Nachr., 330, 1004
Wetterich C., 1995, A&A, 301, 321
Zel'dovich Y. B., 1970, A&A, 5, 84
Zivick P. M., Sutter S., 2014, preprint (arXiv:1410.0133)

This paper has been typeset from a TEX/LATEX file prepared by the author.

1.2. Висновки до розділу 1

Було запропоновано два методи пошуку войдів, які базуються на динамічних критеріях виділення порожнеч у лагранжевих координатах.

Перший підхід LZVF використовує наближення Лагранжа-Зельдовича для відстеження зворотних у часі орбіт галактик; другий UVF використовує метод послаблення кореляційної функції галактика-галактика для доведення розподілу об’єктів до однорідного та відповідного відстеження зворотних у часі орбіт галактик. У обох випадках порожнечі визначаються як області негативної дивергенції зміщень, які можна розглядати як стоки трейсерів маси. Значимість сигналу дивергенції в центральних частинах войдів, отриманих з обидвох шукачів, на 60 % вища, ніж для надлишку профіля густини, отриманого геометричним методом ZOBOV.

Показано, що запропоновані шукачі войдів є хорошими альтернативами до існуючих і є ефективними для покращення точності космологічних тестів, що базуються на статистиці войдів та вимірюванні асиметричностей накладених войдів, – наприклад, тесту Алькока-Пачинського [45] для уточнення космічних параметрів, насамперед густини матерії Ω_{m}.

Індивідуальні войди, вибрані нашими шукачами та ZOBOV, мають подібну форму тривісниxx еліпсоїдів. Еліптичність войда, отриманого після накладання багатьох войдів з подібними ефективними радіусами, виміряна в полі дивергенції (0.97±0.04), є ближчою до очікуваної одиниці, ніж виміряна для класичних ZOBOV войдів у полі густини галактик (0.92±0.04).

Було також показано, що динамічний алгоритм пошуку порожнин, в якому немає залежності від положень частинок, може зменшувати внесок статистичного шуму при ідентифікації войдів.

Важливість цього висновку також було відмічено авторами [46, 70–73], які зокрема цитують роботу [1]. У [70] автори зробили спробу визначити взаємозв’язки між яскравими трейсерами великомасштабної структури та відповідним розподілом речовини у пустотах, щоб перевірити гіпотезу про лінійне зміщення. Автори [71] вивчали динамічні властивості войдів, зокрема було показано, що нелінійна динаміка внутрішніх областей пустот може залежати від еволюції оточуючих структур. У роботах [46], [72] та [73] обговорюються властивості войдів, отриманих шукачем ZOBOV, ZOBOV-VIDE та VIDE [80] відповідно.

У цілому, властивості войдів залежать від алгоритму, який їх визначає, це було підкреслено також авторами [74, 78]. Варто зазначити, що ефект спотворення у просторі червоних зміщень (RSD, redshift-space distortions), який обговорюється у статті [76], не вплинув на висновки роботи, оскільки було використано так звані мок-каталоги, а не реальні дані спостережень.

Майбутній позагалактичний огляд великомасштабних структур Всесвіту космічною обсерваторією «Евклід» Європейського Космічного Агентства стане багатообіцяючим для застосування розроблених нами динамічних шукачів войдів. Очікуване покриття спектрального огляду галактик (15000 кв. гр.) буде містити більше 50 млн. галактик з виміряними променевими швидкостями на червоних зміщеннях $0.7<z<2.1$ до граничної зоряної величини $m_{\mathrm{H}} = 24$, типова відстань між галактиками очікується від 4 to 15 Мпк/h, обсяг огляду буде в 500 раз більшим за обсяг вибірки галактик Слоунівського огляду неба SDSS. Це зробить спектральний огляд «Евклід» ідеальною лабораторією для вивчення властивостей та еволюції космічних порожнин, зокрема, запропонованими шукачами войдів.

Крім цієї космічної місії, розроблені шукачі войдів можна застосувати до даних сучасних та майбутніх місій DESI, SPHEREx та

Nancy Grace Roman Space Telescope, які будуть продукувати величезні обсяги даних, охоплюючи об’єми простору на різних червоних зміщеннях, у тому числі, і для задачі незалежного визначення маси нейтрино у войдах [77]. Окрім вишеназваних задач, ідентифікація войдів важлива для вивчення розподілу та взаємодії темної матерії та темної енергії у них [79].

Розділ 2. МОДУЛЬ ВІДСТАНІ ДО ГАЛАКТИК ТА ОЦІНКИ ІЗОЛЬОВАНОСТІ МАЛОНАСЕЛЕНИХ СИСТЕМ ГАЛАКТИК

Вимірювання відстаней до галактик із застосуванням фотометричних, спектроскопічних та інших методів із високою точністю є важливим напрямом досліджень астрофізики і позагалактичної астрономії, зокрема для виокремлення войдів, груп та скупчень галактик, тестування космологічних моделей. Реконструкція поля швидкостей галактик має вирішальне значення для картографування Всесвіту, дослідження складників великомасштабної структури Всесвіту.

Традиційно відстані для галактик вимірюються за модулем відстані $m-M$, різницею між їхніми видимою та абсолютною зоряними величинами. Теоретичні оцінки абсолютної зоряної величини M галактик, зірок чи їхніх скупчень використовують як індикатори (свічки) відстаней. Первинні індикатори базуються на стандартних свічках, що представляють собою спеціальні типи зірок із відомими світностями: цефеїди, RR Lyrae, наднові типу Ia тощо. Ці методи дають відстані з похибкою від 4 % для галактик Місцевої групи [48] та до 10 % для більш віддалених галактик. Вторинними індикаторами є емпіричні відношення Таллі-Фішера та Фундаментальної Площини (FP) з типовими точностями відстаней ~20 %, які зазвичай застосовуються для галактик на $z \sim 0.1 - 0.2$.

2.1. Оцінки модуля відстані до галактик методами машинного навчання

Основна ідея, висвітлена в роботі [2], полягає у використанні максимально доступних спостережуваних даних для масивів галактик з червоним зміщенням $z < 0.2$. Для відновлення модуля відстані $m - M$ ми використовували різні спостережувані характеристики, такі як видимі

зоряні величини в різних фотометричних смугах, поверхневу яскравість, кутові розміри, променеву швидкість, показники кольору як аналог морфологічних типів, та положення галактик на небі. Вплив деяких із уих параметрів не є безпосереднім, але ми враховували їх, оскільки вони могли б мати неявний вплив на точність вимірювання модуля відстані.

У цій роботі ми використали каталог відстаней, незалежних від червоного зміщення, з позагалактичної бази даних NASA/IPAC [49]. Також каталог містить відстані для 141249 галактик, що отримані за допомогою вторинних методів, таких як Таллі-Фішера, Фундаментальної площини та інших. Зокрема ці методи були використані для порівняння точності із запропонованим нами методом. Вищеназвані характеристики галактик для тренування моделей машинного навчання ми завантажили з бази даних HyperLeda [50]. Радіальні швидкості галактик обмежувались з урахуванням швидкості Місцевої групи 1500км/с < V_{LG} < 60000 км/с.

До досліджуваної вибірки галактик ми застосували 5 моделей машинного навчання, де у якості пояснювальних змінних використали спостережувані характеристики галактик, а у якості цільової змінної – модуль відстані, отриманий з точністю краще ніж 0.50 зоряних величин. Ми порівняли результати 5-ти регресійних моделей: лінійної, поліноміальної, k-найближчих сусідів, регресії градієнтного підсилення та нейромережевої (багатошаровий перцептрон).

Ми розглянули переваги та недоліки кожного з них і оцінили похибку отримання модуля відстані $m-M$ з каталогу відстаней, визначених незалежно від червоних зміщень. Також ми розглянули випадок, коли радіальна швидкість недоступна, намагаючись відновити $m-M$ з доступних даних спостережень. Перевагою нашого підходу є те, що ми використовуємо зручні для спостереження базові параметри галактик, відомі для великого масиву галактик.

A&A 635, A124 (2020)
https://doi.org/10.1051/0004-6361/201936883

Astronomy & Astrophysics

Machine-learning computation of distance modulus for local galaxies

A. A. Elyiv[1], O. V. Melnyk[1], I. B. Vavilova[1], D. V. Dobrycheva[1,2], and V. E. Karachentseva[1]

[1] Main Astronomical Observatory, National Academy of Sciences of Ukraine, 27 Akademika Zabolotnoho St., 04103 Kyiv, Ukraine
e-mail: andrii.elyiv@gmail.com
[2] Bogolyubov Institute for Theoretical Physics of the NAS of Ukraine, 14-b Metrolohichna St., Kyiv 03143, Ukraine

Received 10 October 2019 / Accepted 13 February 2020

ABSTRACT

Context. Quickly growing computing facilities and an increasing number of extragalactic observations encourage the application of data-driven approaches to uncover hidden relations from astronomical data. In this work we raise the problem of distance reconstruction for a large number of galaxies from available extensive observations.
Aims. We propose a new data-driven approach for computing distance moduli for local galaxies based on the machine-learning regression as an alternative to physically oriented methods. We use key observable parameters for a large number of galaxies as input explanatory variables for training: magnitudes in U, B, I, and K bands, corresponding colour indices, surface brightness, angular size, radial velocity, and coordinates.
Methods. We performed detailed tests of the five machine-learning regression techniques for inference of $m-M$: linear, polynomial, k-nearest neighbours, gradient boosting, and artificial neural network regression. As a test set we selected 91 760 galaxies at $z < 0.2$ from the NASA/IPAC extragalactic database with distance moduli measured by different independent redshift methods.
Results. We find that the most effective and precise is the neural network regression model with two hidden layers. The obtained root–mean–square error of 0.35 mag, which corresponds to a relative error of 16%, does not depend on the distance to galaxy and is comparable with methods based on the Tully–Fisher and Fundamental Plane relations. The proposed model shows a 0.44 mag (20%) error in the case of spectroscopic redshift absence and is complementary to existing photometric redshift methodologies. Our approach has great potential for obtaining distance moduli for around 250 000 galaxies at $z < 0.2$ for which the above-mentioned parameters are already observed.

Key words. galaxies: statistics – galaxies: distances and redshifts – galaxies: photometry – methods: data analysis

1. Introduction

Better-quality measurements of galaxy distances than those purely dependent on redshift are a fundamental goal in astronomy. Such measurements are important for establishing the extragalactic distance scale, estimating the Hubble constant and cosmological models (Zaninetti 2019; Hartnett 2006), and studying peculiar velocities of galaxies with respect to the Hubble flow (Karachentsev et al. 2015, 2006; Dupuy et al. 2019). Furthermore, reconstruction of the velocity field of galaxies is crucial for mapping the Universe, and will pave the way for exploration of the large-scale structure (LSS) elements such as galaxy groups (Melnyk et al. 2006; Makarov & Karachentsev 2011; Wang et al. 2012; Shen et al. 2016; Pulatova et al. 2015; Vavilova et al. 2005), clusters, filaments, and voids (Bertschinger et al. 1990; Erdoğdu et al. 2006; Courtois et al. 2012; Elyiv et al. 2015; Tully et al. 2019), including the zone of avoidance of our galaxy (Sorce et al. 2017; Vavilova et al. 2018; Jones et al. 2019).

Traditionally, distances to galaxies have been measured using the distance modulus $m-M$ which is the difference between absolute and apparent stellar magnitudes. Theoretical estimations of the absolute magnitude M of a whole galaxy or some objects inside it could be performed through primary and secondary indicators. Primary indicators are based on the standard candles, which are stars with known luminosity of which there are several types: Cepheids, RR Lyrae, Type Ia supernovae, and so on. These methods provide distances with errors ranging from 4% for the Local Group galaxies (Riess et al. 2012) to 10% for more distant galaxies. Secondary indicators, the Tully–Fisher (TF) and fundamental plane (FP) empirical relationships, provide distance errors of ~20% and are usually applied for galaxies at $z \sim 0.1-0.2$, where individual stars are not resolved.

Despite the machine learning technique being applied in astrophysics since the 1990s (Storrie-Lombardi et al. 1992), only in the last 10 years has computing power been sufficient to allow its widespread use (Bogdanos & Nesseris 2009; Nesseris & Shafieloo 2010; Nesseris & García-Bellido 2012; VanderPlas et al. 2012; Murrugarra-LLerena & Hirata 2017; Dobrycheva et al. 2017; Baron 2019). Such a trend is also seen in rapidly increasing observational data and the development of data-driven science, where mining of datasets uncovers new knowledge. Regression analysis occupies an important place among statistical techniques and is widely used for estimation of functional relationships between variables (Isobe et al. 1990) for spectroscopic (Bukvić et al. 2008) and photometric (Ascenso et al. 2012) data processing. A machine learning genetic algorithm was used to build model-independent reconstructions of the luminosity distance and Hubble parameter as a function of redshift using supernovae type Ia data by Arjona & Nesseris (2019), Bogdanos & Nesseris (2009). A detailed analysis and classification of contemporary published literature on machine learning in astronomy is presented by Fluke & Jacobs (2020).

The redshift could be approximately reconstructed from the photometric redshift calculation technique (Bolzonella et al. 2000). Supervised machine learning regression is commonly applied for this task (Salvato et al. 2019). Sets of galaxies with multi-band photometry and known spectroscopic redshifts are used in training regression models to map between high-dimensional photometric band space and redshifts. It is also possible to input new data into the trained model where spectroscopy is not available. The most popular computational tools for photometric redshift inferences are the Random Forests (Carliles et al. 2010, 2008; Carrasco Kind & Brunner 2013) and neural network regressions (Cavuoti et al. 2012; Bonnett 2015) including deep machine learning techniques (D'Isanto & Polsterer 2018).

Regression in a Bayesian framework was considered by Kügler & Gianniotis (2016) and was used to model the multi-modal photometric redshifts. Zhou et al. (2019) published a catalogue of calibrated photometry of galaxies from the Extended Groth Strip field. These latter authors improved photometric redshift accuracy with an algorithm based on Random Forest regression.

The principle aim of our work is to exploit available observations for galaxy datasets at redshifts $z < 0.2$ in order to complement existing methods of distance measurement. For distance modulus $m-M$ (angular size distance) reconstruction we used different observational characteristics such as photometry of galaxies, their surface brightness and angular sizes, radial velocity, colour indices as analogues of morphological types, and celestial coordinates.

The influence of some parameters is not direct but we took them into account because of their possible confounding effect on $m-M$. We also took into consideration the celestial coordinates of galaxies, which are distributed in a non-random manner in the Universe, forming a large-scale structure web, and so we assumed that direction in the sky is important. The probability density function (PDF) of distance to galaxy depends on the direction of observation because many galaxies are concentrated in clusters and filaments, whereas empty regions or cosmic voids occupy more than half of the volume of the Local Universe. Previously, the galaxy coordinates were taken into account for photometric redshift computations by maximizing the spatial cross-correlation signal between the unknown and the reference samples with redshifts (Newman 2008; Rahman et al. 2015). Aragon-Calvo et al. (2015) computed photometric redshifts from the product of PDFs obtained from the colours, the cosmic web, and the local density field.

The machine learning regression approach uses a data sample for which a target value, distance modulus in our case, has already been measured with some accuracy using another direct or indirect method. The model should be trained on a "training" sample to be able to make a regression on a new "test" sample that has never been input into the model. Award of training is getting minimal difference between predicted and real target value, which is an error of the model. Training of the model consists in a numerical minimisation of error by changing the model parameters. One important step is an error generalisation, where the model is evaluated on the test sample (Goodfellow et al. 2016).

We applied and compared the performances of five regression models: linear, polynomial, k-nearest-neighbour regression, gradient boosting, and artificial neural network (ANN). By comparing their respective benefits and disadvantages we evaluated the $m-M$ error from the redshift-independent galaxy distance catalogue from the NASA/IPAC extragalactic database (Steer et al. 2017). We also considered a case where the radial velocity is not available, trying to recover $m-M$ from the available observational data.

One advantage of our approach is that we do not cut the sample by luminosity or apparent magnitude and do not impose restrictions on galaxy distribution in space in order to avoid losing useful information. Also, we used easily observable basic parameters, which are known for a myriad of galaxies.

In Sect. 2 we describe the sample of local galaxies used in this work and training sample. In Sect. 3 we discuss the main principles of machine-learning regression on the basis of linear regression. Sections 4–7 represent the application of polynomial, k-nearest neighbour, gradient boosting, and neural network regressions, respectively. We present a discussion and our main conclusions in Sect. 8.

2. Local galaxy sample

We used the catalogue of redshift-independent distances from the NASA/IPAC extragalactic database (Steer et al. 2017). This is a compilation of distance measurements made using 75 different methods taken from more than 2000 refereed articles. The latest version 15.1.0[1] (December 2018) contains 66 388 distance measurements for 7156 galaxies. These are based on primary methods that use the standard candles such as Cepheids and Type Ia supernova, or standard rulers such as globular cluster radii and masers, among others. Also, the catalogue contains 204 038 distances for 141 249 galaxies based on secondary methods like TF, FP relations, and others. The following information is available for each galaxy: identity (ID), distance modulus in mag $m-M$, one-sigma statistical error of the distance modulus, distance indicator method, reference to a published article, reference to a published distance, and other parameters.

In order to obtain galaxy coordinates and other available observational parameters we matched them by galaxy ID with the Lyon–Meudon Extragalactic Database[2] (HyperLeda Makarov et al. 2014). We considered both the northern and southern sky, except for the low galactic latitudes $|b| < 15^{\circ}$ (Zone of Avoidance). Radial velocities of galaxies were limited to $1500\,\mathrm{km\,s^{-1}} < V_{\mathrm{LG}} < 60\,000\,\mathrm{km\,s^{-1}}$. We did not use the nearby galaxies with $V_{\mathrm{LG}} < 1500\,\mathrm{km\,s^{-1}}$ to avoid selection effects as the population of nearby galaxies mainly consists of dwarf galaxies (including dwarf galaxies of low surface brightness Tully et al. 2014; Makarov & Uklein 2012; Karachentseva & Vavilova 1994; Einasto 1991), which are not common among galaxy populations with $V_{\mathrm{LG}} > 1500\,\mathrm{km\,s^{-1}}$. Also, the distribution of galaxies at small redshifts is very inhomogeneous due to the presence of the Virgo cluster and Tully void. This could create a bias for the model when the galaxy coordinates are used as input explanatory variables for regression. An upper limit at $V_{\mathrm{LG}} = 60\,000\,\mathrm{km\,s^{-1}}$ was chosen since the number of galaxies with known distances drops dramatically at this velocity; see Fig. 1.

We reduced all of the distance moduli to the common Hubble constant $H_0 = 70\,\mathrm{km\,s^{-1}\,Mpc^{-1}}$, since this is the default value used by the Supernova Cosmology Project and the Supernova Legacy Survey (Steer et al. 2017). Distance modulus error depends on the method used and varies in a wide range from 0.06 mag for Cepheids and RR Lyrae Stars to 0.42 mag for the FP and TF methods (Fig. 2). We used measurements made with

[1] https://ned.ipac.caltech.edu/Library/Distances/
[2] http://leda.univ-lyon1.fr

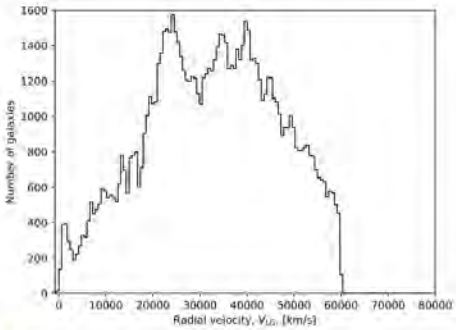

Fig. 1. Radial velocity distribution of galaxies that meet the criteria described in Sect. 2. The sample of galaxies is based on the catalogue of redshift-independent distances from the NASA/IPAC extragalactic database (Steer et al. 2017).

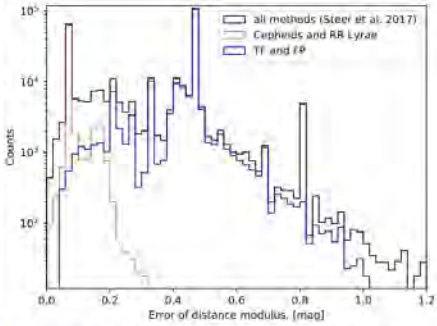

Fig. 2. Distribution of distance modulus errors for all galaxies from Steer et al. (2017) (black line). As an example, the distributions are shown for typical methods: Cepheids and RR Lyrae (red thin line), TF and FP relations methods (blue thick line).

primary[3] and secondary[4] methods with a mean error of less than 0.50 mag to train our models. However, all the individual measurements with error above 0.50 mag were removed from the sample. Some galaxies have several distance measurements taken by different authors using different methods. We aggregated such distances for each galaxy and calculated the weighted mean $m-M$ with the weight inversely proportional to the square of the error.

Finally, we obtained an initial sample of 91 760 galaxies, $S_{0.50}$, with the following information: Supergalactic coordinates (SGB, SGL); radial velocity with respect to the Local Group, $V_{\rm LG}$; the decimal logarithm of the projected major axis length of the galaxy at the isophotal level of 25 mag arcsec^{-2} in the B-band $\log d25$; mean surface brightness within 25 mag isophote in the B-band, $bri25$; the apparent total U, B, I, and K magnitudes; and U–I and B–K colours, which represent a morphological type of galaxy. We did not use other observational parameters like 21 cm line flux and velocity rotation since these are only available for <3% galaxies in our sample.

We created the second sample of galaxies limiting with $m-M$ error of <0.25 mag and 1500 km s^{-1} < $V_{\rm LG}$ < 30 000 km s^{-1}. This sample contains 9360 galaxies with distances calculated mostly using accurate Cepheids and RR Lyrae methods. We refer to this sample as $S_{0.25}$.

For the correct application of the machine-learning algorithms we reduced $V_{\rm LG}$ to magnitude units using the following conversions.

$$m-M = 5 * \log\left(\frac{d_{\rm A}}{10\,{\rm pc}}\right), \tag{1}$$

where angular size distance for the ΛCDM cosmological model:

$$d_{\rm A} = cH_0^{-1}(1+z)^{-1}\int_0^{z'} {\rm d}z'/\sqrt{\Omega_m(1+z')^3+\Omega_\Lambda}, \tag{2}$$

[3] Maser, SNII optical, the old globular cluster luminosity function method (GCLF), planetary nebulae luminosity function (PNLF), surface brightness fluctuations (SBF) method, Miras, SNIa SDSS, TypeII Cepheids, SNIa, HII region diameter, Horizontal Branch, colour-magnitude diagram (CMD), Eclipsing Binary, tip of the red giant branch (TRGB), RR Lyrae, Cepheids, Red Clump.

[4] FP, Brightest Stars, TF, Tertiary, D-Sigma, brightest cluster galaxy (BCG), colour-magnitude diagram (CMD), Faber–Jackson, Active galactic nucleus (AGN) time lag, Sosies, Magnitude.

with parameters $H_0 = 70\,{\rm km\,s^{-1}\,Mpc^{-1}}$, $\Omega_{\rm m} = 0.3089$, $\Omega_\Lambda = 0.6911$. Finally, the redshift could be expressed as a radial velocity $V_{\rm LG}$ as:

$$1+z = \sqrt{\frac{1+V_{\rm LG}/c}{1-V_{\rm LG}/c}}. \tag{3}$$

We do not consider the K-correction here because it is significantly smaller than a typical error of distance modulus at redshifts <0.2. We used a diameter of $\log d25$ because it is already in logarithmic scale. Because supergalactic coordinates are periodic, as are any spherical coordinates, we converted them to 3D Cartesians with unit radial vector for all galaxies.

Here, we considered 12 attributes of galaxies, which are the input explanatory variables to predict our desired target: distance modulus $m-M$. We chose these variables because they are easily accessible for observation and are available for a large number of galaxies. In particular, galaxy coordinates provide information about the LSS, colour indices correlate with a morphological type, and photometric data and angular diameters correlate with distance modulus. Therefore, we used a compilation of different parameters, some of which, such as for example position in the sky, surface brightness, and colour indices, have never been used before for distance modulus estimation.

3. Linear regression

We explain the main principles of machine-learning regression on a linear model. This is a basic regression model that deals with linear combinations of input variables (also referred to as features or attributes). Multidimensional linear regression is a system that takes an n-size vector of input explanatory variables $\boldsymbol{x} \in R^n$ and predicts a scalar, so-called dependent variable, $y \in R$, with some approximation $\hat{y}$:

$$\hat{y} = \boldsymbol{w}^\top \boldsymbol{x} + b = w_1 x_1 + \cdots + w_n x_n + b, \tag{4}$$

where the vector of model parameters is $\boldsymbol{w} \in R^n$ and $b \in R$ is the intercept term (bias). Parameters $\boldsymbol{w}$ could be interpreted as the weights of the contribution of certain features to the composed output value $\hat{y}$. The larger the absolute weight of a feature, w_i, the larger the impact of the ith feature on the prediction.

Table 1. Applied regression models with $RMSE_{test}$ errors using all the attributes of galaxies and without the V_{LG} value.

Model	All attributes	Without V_{LG}	SGB SGL	V_{LG}	log $d25$	$bri25$	U	B	I	K	U–I	B–K
Linear	0.38	0.52	0.48	37	0.22	0.64	0.01	0	0	0.01	0.14	0.02
Polynomial	0.37	0.49	0.87	32	0.27	1.16	0.78	0.06	0	0.05	1.67	0.05
k-NN	0.37	0.50	0	35	0.01	0	0	0.01	0.02	0	0	0
Gradient boosting	0.36	0.44	1.51	22	0.18	0	0.04	1.02	0.95	0	0	0
ANN	0.35	0.44	1.09	26	0.33	0	0.16	0.01	0.47	0.11	0.71	0.22

Notes. The last ten columns show the importance of each attribute for a given regression model, which is given as an increase in error as a percentage when leaving out a given attribute.

The mean squared error (MSE) of the predicted output values $\hat{y}$ with respect to the real y,

$$\mathrm{MSE} = 1/m \sum_{i}^{m} (\hat{y}_i - y_i)^2, \tag{5}$$

is widely used as an indicator of model performance; here m is the size of the sample. In other words, the model performance could be expressed as the Euclidean distance between predicted m-dimension vectors $\hat{y}$ and y.

The main requirement of the machine learning regression is that the algorithm work well on new inputs that were not involved in the training stage. Therefore, we split our data into training and test samples. Typically, the test sample represents a randomly selected 20–35% subsample of the observations from the primary sample. It is important that the training and test samples be independent and have the same unbiased distributions.

The model should optimise its parameters on a training sample with minimisation MSE_{train} and evaluate the obtained $(\boldsymbol{w}, b)$ parameters on a test sample. The test error MSE_{test} should be minimised as well. This error with its variation reflects the expected level of error of y for the new inputs $\boldsymbol{x}$. Such a procedure is called "generalisation" and differentiates the machine learning technique from a simple fitting. There are two main problems, which may appear during the training: underfitting, when the training error is too large, and overfitting, when the training error is small but the test error is still large (Goodfellow et al. 2016).

Linear regression is one of the simplest models, with a small capacity but a high parsimony and learning speed. For training of linear regression and all the models considered here, we used the free machine-learning library Scikit-learn[5]. To prevent very large parameters $\boldsymbol{w}$, we applied the Ridge regularisation (Greiner 2004), where the loss function for minimisation is $MSE_{train} + \|\boldsymbol{w}\|^2$. We normalised all features before training by removing the mean and scaling to unit variance, which is a common requirement for many machine-learning estimators. To evaluate the accuracy of our predictive model with the new data, we used the k-folds cross-validation technique (Kohavi 1995): we randomly split our sample into five equally sized subsamples and trained the model five times, sequentially using one subsample as the test sample and the other four as the training samples, rotating the test subsample each time. This gave us five independent estimations of MSE_{test} from which we calculated the mean and its standard deviation.

For the larger $S_{0.50}$ sample, a linear regression gives the test root–mean–square error $RMSE_{test} = 0.376 \pm 0.003$ mag. Using Eq. (1) this error was converted to a linear relative distance error of 17.3% ± 0.2%. We obtained the following coefficients of linear regression $\boldsymbol{w}$ in decreasing order of absolute value: $w_{V_{LG}} = 0.713$, $w_K = 0.134$, $w_{\log d25} = -0.110$, $w_{bri25} = 0.103$, $w_U = -8.92 \times 10^{-2}$, $w_{B-K} = 6.75 \times 10^{-2}$, $w_{U-I} = 6.37 \times 10^{-2}$, $w_{Y_{SG}} = 3.08 \times 10^{-2}$, $w_{X_{SG}} = 1.25 \times 10^{-3}$, $w_{Z_{SG}} = -7.45 \times 10^{-5}$, $w_B = 0$, $w_I = 0$. The most important parameter here is the radial velocity V_{LG}, and those with the least significance are the K magnitude, angular diameter, and surface brightness. The remaining parameters provide a smaller contribution to the distance estimation.

In cases where we do not have a redshift or V_{LG} value, it is still possible to recover distance using other data with an accuracy of 0.52 mag or 24% of the angular size distance. The errors for different models considered in this paper can be found in Table 1. For the sample of nearby galaxies with more accurate measurements of distance modulus $S_{0.25}$, we obtained $RMSE_{test} = 0.288 \pm 0.019$ mag (13%±0.9%). In the case of radial velocity estimation, we obtained an error of 0.644 ± 0.029 mag (30% ± 1.3%).

4. Polynomial regression

A polynomial regression is an extension of a linear regression, where a kth degree polynomial relation between the input explanatory variables $\boldsymbol{x}$ and the dependent variable y is used. We considered second- and third-order polynomial regressions.

For the second-order polynomial regression we obtained $RMSE_{test} = 0.366 \pm 0.003$ mag (16.9% ± 0.1%) for $S_{0.50}$ sample. For the third-order, $RMSE^{3pol}_{test} = 0.362 \pm 0.037$ mag (16.7% ± 1.7%). As the third-order regression offers only a small improvement with respect to the second-order regression but with a greater uncertainty, we did not consider it. For the $S_{0.25}$ sample we obtained an error of 0.276 ± 0.017 mag (13% ± 0.9%). When we eliminate the radial velocity, the test error is 0.607 ± 0.021 mag (28% ± 1%).

5. A k-nearest neighbours regression

The k-nearest neighbours (k-NN) regression uses the k closest training points around the test point in the feature nD space. The predicted variable $\hat{y}$ in this case is the weighted average of the values y of the k nearest neighbours (Altman 1992). A k-NN algorithm computes distances or similarities between the new instance and the training instances to make a decision. Normally, it uses weighted averaging, where each neighbour among the closest k neighbours has a weight of $1/d$, where d is the distance to the neighbour.

k-NN regression is a type of instance-based learning. Contrary to this approach, a linear regression and many other function-based approaches use explicit generalisation.

[5] https://scikit-learn.org

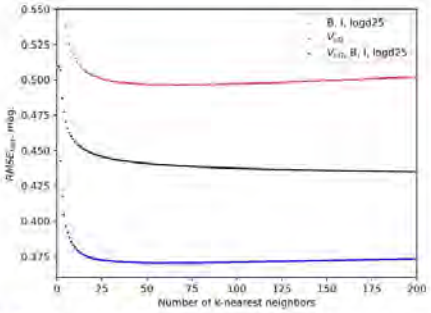

Fig. 3. Dependence of $RMSE_{test}$ of k-NN regression on k number of neighbours for different sets of input features: I, B bands and angular diameter (red dots), radial velocity (black), I, B bands, angular diameter, and radial velocity (blue).

k-NN regression has one hyperparameter, k, which allows the number of near neighbours to be taken into account. We obtained our best results for the $S_{0.50}$ sample for the case where distance weight to neighbour was inverse to the distance with Euclidean metric, with $k = 56$ near neighbours. We obtained an error of $RMSE_{test} = 0.370 \pm 0.003$ mag ($17.0\% \pm 0.1\%$) using radial velocity, angular diameters, and photometry in B and I bands. As can be seen from Fig. 3, the minimum error forms a plateau in the range $40 < k < 80$. A combination of photometric data and angular diameter, simultaneously excluding radial velocity, provides an error of 0.50 (23%). The test errors of regression for the $S_{0.25}$ sample are listed in Table 1.

6. Gradient-boosting regression

The gradient-boosting regression is a kind of ensemble algorithm, which is widely used in machine learning. The ensemble algorithm is a stack of simple prediction models, like decision tree, linear regression, and so on, joined together to make a final prediction. The theory behind this method is that many weak models predict a target variable with independent individual error. Superposition of these models could show better results than any single predictor alone.

There are two main approaches of forming the ensemble algorithm; "bagging", where all simple models are independent and the final result is averaged over each model output. The second approach is referred to as boosting, where the predictors are lined up sequentially and each subsequent predictor learns from the errors of the previous one, reducing these errors. We applied gradient-boosting regression (Mason et al. 1999) using the open-source software library XGBoost[6]. This algorithm minimises the error function by iteratively choosing a function that points to the negative gradient direction in the space of model parameters.

To prevent overfitting we applied DART (Dropouts meet Multiple Additive Regression Trees) technique, which decreases the effect of overspecialisation when adding new trees. We found the optimal hyperparameters when using gradient-boosting regression and obtained a test error of $RMSE_{test} = 0.355 \pm 0.003$ mag ($16.3\% \pm 0.1\%$).

7. Neural-network regression

The Multilayer Perceptron is a type of feedforward ANN consisting of neurons grouped in parallel layers: an input layer, a hidden layer or layers, and an output layer. All the neurons of adjacent layers are connected. The main characteristic of an ANN is the ability to transmit a numerical signal from one artificial neuron to another in a "feedforward" direction from the input layer to the output layer. In a regression model, the output layer is a single neuron that computes the target value $\hat{y}$. The output of each neuron is transformed by some non-linear activation function of the sum of its inputs. The outputs of the neurons from one layer are the input for neurons of the next layer, and so on. The connection between neurons has a weight that adjusts as learning proceeds. This weight corresponds to the importance of a signal at its transmission.

The neural network is a very powerful tool for machine-learning regression since it can approximate the continuous function of many variables with any accuracy under certain conditions (Cybenko 1989). The ANN regression utilises a supervised learning technique called backpropagation of error (loss function) for its training. In this study, we used the mean squared error (Eq. (5)) as a loss function.

For our regression task we took all 12 input features mentioned in Sect. 2 as neurons of the input layer. The best model performance was reached by shallow ANN with two hidden layers with 24 and 228 neurons, respectively. As an activation function we used rectified linear unit function "relu", $f(x) = \max(0, x)$. The Broyden–Fletcher–Goldfarb–Shanno algorithm is considered to be the most appropriate for our task; it is one of the quasi-Newton methods for solving ANN optimisation problems (Curtis & Que 2015). The regularisation term of L2 penalty was chosen as 0.0005 to avoid over-fitting. The learning rate was in mode "invscaling".

Finally, we obtained a test error $RMSE_{test} = 0.354 \pm 0.003$ mag ($16.3\% \pm 0.1\%$), which is comparable to the gradient-boosting result. The plot of predicted versus true values is shown in Fig. 4.

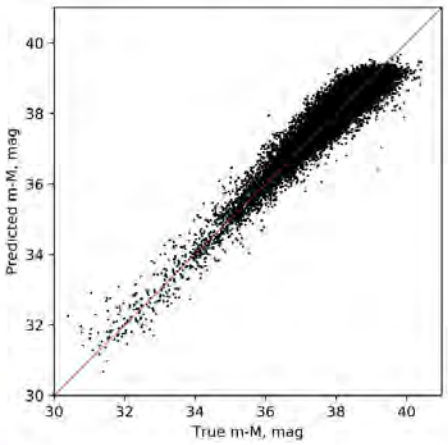

Fig. 4. Dependence of the predicted distance moduli versus the true distance moduli for an ANN regression model using all the attributes for the $S_{0.5}$ sample.

8. Discussion and conclusions

Table 1 presents root–mean–square test errors for the sample $S_{0.5}$ (described in Sect. 2) after applying regression models for

[6] https://xgboost.ai

two sets of input attributes. The first set includes all attributes: photometric data, angular diameter, surface brightness, colour indices, radial velocity, and position of a galaxy in the sky (second column). The second set has the same attributes but without radial velocity (third column). The lowest errors are for the gradient-boosting and the neural network regressions. However, the ANN model has a smaller complexity than the gradient-boosting model and we chose ANN regression as the most appropriate model according to Occam's razor principle, i.e. ANN regression has a good trade-off between simplicity and accuracy.

The last ten columns of Table 1 show the importance of each observable galaxy attribute. We quantified this importance as the increase in test error, as a percentage, due to leaving out a given attribute. The most important contribution comes from radial velocity, especially for linear, polynomial, and k-NN regressions (32–37%). At the same time, a radial velocity is less important for the gradient-boosting and ANN models (22–26%), as these approaches effectively also use information from other attributes. For ANN regression, the most important after V_{LG} is Supergalactic coordinates of galaxy (1.09%), $U-I$ colour (0.71%), I mag (0.47%), and angular diameter (0.33%). The rest of attributes individually have importance less than 0.22%.

Table 2 shows the mean errors of various methods for $m-M$ computing applied to the $S_{0.50}$ sample using all attributes. As can be seen, the ANN regression has an error of 0.35 mag, which lies between the values of the errors of the BCG[7] and TF relation[8] methods, and shows a better result than the FP relation (0.42 mag). Direct conversion of a radial velocity to $m-M$ according to Eqs. (1)–(3) gives a mean error of 0.40 mag (Conv. $V_{LG} \rightarrow m-M$ in Table 2). Therefore, usage of all available attributes improves the uncertainty from 0.40 to 0.35 mag.

When we exclude V_{LG} from consideration, our method gives an error of 0.44 mag (20%), which is still acceptable for studying the LSS web and galaxy evolution. The case of using all the attributes but without radial velocity of galaxies is analogous to photometric redshift computation. The only difference is that the dependent variable is distance modulus instead of radial velocity. The relative RMSE test error of 20% will also apply to the redshift predictions. As can be seen from the second column of Table 2, the ANN regression (all attributes) could potentially be applied to 393 359 galaxies, which is the number of unique galaxies from the Lyon–Meudon Extragalactic Database for which all ten observational parameters needed for this model are available. The catalogue of distance modulus (Steer et al. 2017) contains 183 058 unique galaxies. Therefore, we expect to contribute an additional 210 301 distance moduli computed with an accuracy of 0.35 mag at $z < 0.2$. Furthermore, the Lyon–Meudon Extragalactic Database contains 436 140 galaxies with nine of the required observational parameters but with unknown radial velocity. We expect to compute $m-M$ with an accuracy of 0.44 mag, and redshift with an accuracy of 20% for around 40 000 galaxies with unknown radial velocities.

We demonstrate how the ANN regression reconstructs $m-M$ at different distances in Fig. 5. The black line represents one-sigma statistical error from the NASA/IPAC extragalactic database for galaxies from the $S_{0.5}$ sample. The error increases from 0.2 to 0.4 at radial velocities below 10 000 km s^{-1}. This can be explained by the decreased contribution of high-accuracy Cepheid and RR Lyrae measurements of $m-M$. The error reaches 0.46 mag for galaxies with $V_{LG} > 30\,000$ km s^{-1}. The majority of the distance moduli for those galaxies were estimated using the FP method with an error of 0.46 mag.

Direct use of the radial velocity as an analogue of linear distance according to Eqs. (1)–(3) causes large errors of 0.5–0.6 mag for $V_{LG} < 7000$ km s^{-1} due to the influence of collective motions caused by local galaxy clusters and voids. At larger distances, this kind of distance measurement provides almost constant error of around 0.40 mag.

Our ANN regression method, even without information about V_{LG}, could improve the accuracy of distance measurements for nearby galaxies and provides RMSE 0.44 mag for all distances. Addition of the radial velocity to our ANN regression model decreases the error to 0.35 mag for all distances. The performance of our ANN model demonstrates the fact that the influence of velocity at small radial velocities should be decreased in favour of other parameters such as angular diameter, photometry, and so on. This is why for our model the influence of local clusters and voids is negligible and the distance modulus error is almost constant at 0.35 mag for all V_{LG} (blue thick line Fig. 5).

Our approach is especially useful for measuring distances for galaxies with $V_{LG} > 10\,000$ km s^{-1}, where primary methods are not working. Therefore, the regression model developed here is competitive against widely used secondary methods for $m-M$ measurement such as the FP and TF relation.

Table 2. Comparison of one-sigma statistical error of the distance modulus for different methods from the NASA/IPAC Extragalactic Database with three cases considered in our work: the ANN regression using all attributes and without radial velocity, and using direct conversation radial velocity to $m-M$ according to Eqs. (1)–(3).

Method	N	Error, mag
Primary methods		
TRGB	475	0.05
Cepheids	87	0.08
PNLF	72	0.12
GC radius	107	0.13
HII region diameter	44	0.13
SNIa	3179	0.14
SNIa SDSS	1771	0.16
SNII optical	184	0.17
SBF	539	0.18
AGN time lag	20	0.18
GCLF	213	0.18
Masers	10	0.22
BCG	239	0.35
Secondary methods		
Sosies	344	0.20
Tertiary	283	0.30
D-Sigma	566	0.33
ANN regr. (all attributes)	393 359	0.35
TF	12 244	0.38
Conv. V_{LG} to $m-M$	120 9871	0.40
FP	129 038	0.42
ANN regr. (without V_{LG})	436 140	0.44

Notes. Errors are only for the $S_{0.50}$ sample ranked in ascending order separately for primary and secondary methods. The column N represents the number of galaxies for which distance modulus was defined by a given method from Steer et al. (2017). For the ANN regression and conversion of V_{LG} to $m-M$ models we give the number of galaxies for which it is possible to compute distance modulus using the corresponding method.

[7] A secondary distance indicator by the brightest galaxies in galaxy clusters as standard candles (Hoessel 1980).

[8] Standard candles based on the absolute blue magnitudes of spiral galaxies (Tully & Fisher 1977).

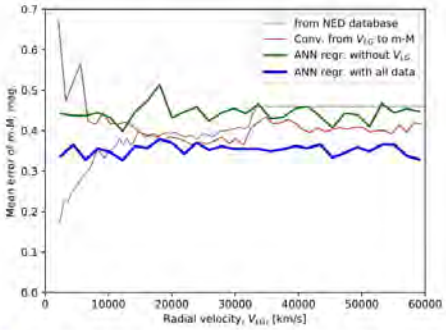

Fig. 5. Root-mean-square errors of $m-M$ for various measurements of galaxies with different radial velocities. In order of line width increasing: distance modulus statistical errors from the NASA/IPAC extragalactic database used in our study (black line), after conversion V_{LG} to $m-M$ (red line), using the ANN regression without V_{LG} (green line), using the ANN regression with all available attributes (blue line).

We proposed the new data-driven approach for computing distance moduli to local galaxies based on ANN regression. In addition to traditionally used photometric data we also involved the surface brightness, angular size, radial velocity, and the position in the sky of galaxies to predict $m-M$. Applying our method to the test sample of randomly selected galaxies from the NASA/IPAC Extragalactic Database we obtained a root–mean–square error of 0.35 mag (16%), which does not depend on the distance to a galaxy and is comparable with the mean errors from the TF and FP methods. Our model provides an error of 0.44 mag (20%) in cases where radial velocity is not taken into consideration.

In the future we plan to make a more detailed comparison of our ANN regression approach with other physically based methods. Namely, we are going to build an analogue of the 2D redshift space correlation function with distance modulus instead of redshift. More accurate methods should reveal the smaller effects of distortion caused by both random peculiar velocities of galaxies and by the coherent motions of galaxies in the LSS. Also, we will apply our ANN model to measure $m-M$ for galaxies with unknown distance moduli in the range of radial velocities $1500 < V_{LG} < 60\,000\,\mathrm{km\,s^{-1}}$ and release a corresponding catalogue. This catalogue will include distance moduli computed for around a quarter of a million galaxies with $z < 0.2$.

Acknowledgements. We would like to thank very much referee for kind advices and useful remarks. This work was partially supported in frame of the budgetary program of the NAS of Ukraine "Support for the development of priority fields of scientific research" (CPCEL 6541230).

References

Altman, N. 1992, Am. Stat., 46, 175
Aragon-Calvo, M. A., van de Weygaert, R., Jones, B. J. T., & Mobasher, B. 2015, MNRAS, 454, 463
Arjona, R., & Nesseris, S. 2019, ArXiv e-prints [arXiv:1910.01529]
Ascenso, J., Lombardi, M., Lada, C. J., & Alves, J. 2012, A&A, 540, A139
Baron, D. 2019, ArXiv e-prints [arXiv:1904.07248]
Bertschinger, E., Dekel, A., Faber, S. M., Dressler, A., & Burstein, D. 1990, ApJ, 364, 370
Bogdanos, C., & Nesseris, S. 2009, JCAP, 0905, 006
Bolzonella, M., Miralles, J. M., & Pelló, R. 2000, A&A, 363, 476
Bonnett, C. 2015, MNRAS, 449, 1043
Bukvić, S., Spasojević, D., & Žigman, V. 2008, A&A, 477, 967
Carliles, S., Budavári, T., Heinis, S., Priebe, C., & Szalay, A. 2008, ASP Conf. Ser., 521, 394
Carliles, S., Budavári, T., Heinis, S., Priebe, C., & Szalay, A. S. 2010, ApJ, 712, 511
Carrasco Kind, M., & Brunner, R. J. 2013, MNRAS, 432, 1483
Cavuoti, S., Brescia, M., Longo, G., & Mercurio, A. 2012, A&A, 546, A13
Courtois, H. M., Hoffman, Y., Tully, R. B., & Gottlöber, S. 2012, ApJ, 744, 43
Curtis, F., & Que, X. 2015, Math. Prog. Comp., 7, 399
Cybenko, G. 1989, Math. Control Signals Syst., 2, 303
D'Isanto, A., & Polsterer, K. L. 2018, A&A, 609, A111
Dobrycheva, D. V., Vavilova, I. B., Melnyk, O. V., & Elyiv, A. A. 2017, ArXiv e-prints [arXiv:1712.08955]
Dupuy, A., Courtois, H. M., & Kubik, B. 2019, MNRAS, 486, 440
Einasto, M. 1991, MNRAS, 250, 802
Elyiv, A., Marulli, F., Pollina, G., et al. 2015, MNRAS, 448, 642
Erdoğdu, P., Lahav, O., Huchra, J. P., et al. 2006, MNRAS, 373, 45
Fluke, C. J., & Jacobs, C. 2020, WIREs Data Mining and Knowledge Discovery, in press [arXiv:1912.02934]
Goodfellow, I., Bengio, Y., & Courville, A. 2016, Deep Learning (MIT Press), 781
Greiner, R. 2004, in Feature Selection, L1 vs. L2 Regularization, and Rotational Invariance, Proceedings of the Twenty-first International Conference on Machine Learning, 78
Hartnett, J. G. 2006, Found. Phys., 36, 839
Hoessel, J. G. 1980, ApJ, 241, 493
Isobe, T., Feigelson, E. D., Akritas, M. G., & Babu, G. J. 1990, ApJ, 364, 104
Jones, D., Schroeder, A., & Nitschke, G. 2019, ArXiv e-prints [arXiv:1903.07461]
Karachentseva, V. E., & Vavilova, I. B. 1994, Bull. Spec. Astrophys. Obs., 37, 98
Karachentsev, I. D., Kudrya, Y. N., Karachentseva, V. E., & Mitronova, S. N. 2006, Astrophysics, 49, 450
Karachentsev, I. D., Tully, R. B., Makarova, L. N., Makarov, D. I., & Rizzi, L. 2015, ApJ, 805, 144
Kohavi, R. 1995, Morgan Kaufmann, 1, 1137
Kügler, S. D., & Gianniotis, N. 2016, ArXiv e-prints [arXiv:1607.06059]
Makarov, D., & Karachentsev, I. 2011, MNRAS, 412, 2498
Makarov, D. I., & Uklein, R. I. 2012, Astrophys. Bull., 67, 135
Makarov, D., Prugniel, P., Terekhova, N., Courtois, H., & Vauglin, I. 2014, A&A, 570, A13
Mason, L., Baxter, J., Bartlett, P. L., & Frean, M. 1999, Advances in Neural Information Processing Systems (MIT Press), 512
Melnyk, O. V., Elyiv, A. A., & Vavilova, I. B. 2006, Kinematika i Fizika Nebesnykh Tel, 22, 283
Murrugarra-LLerena, J. H., & Hirata, N. S. T. 2017, in Galaxy Image Classification, eds. R. P. Torchelsen, E. R. D. Nascimento, D. Panozzo, et al., Conference on Graphics, Patterns and Images (SIBGRAPI), 30
Nesseris, S., & García-Bellido, J. 2012, JCAP, 1211, 033
Nesseris, S., & Shafieloo, A. 2010, MNRAS, 408, 1879
Newman, J. A. 2008, ApJ, 684, 88
Pulatova, N. G., Vavilova, I. B., Sawangwit, U., Babyk, I., & Klimanov, S. 2015, MNRAS, 447, 2209
Rahman, M., Ménard, B., Scranton, R., Schmidt, S. J., & Morrison, C. B. 2015, MNRAS, 447, 350
Riess, A. G., Fliri, J., & Valls-Gabaud, D. 2012, ApJ, 745, 156
Salvato, M., Ilbert, O., & Hoyle, B. 2019, Nat. Astron., 3, 212
Shen, S.-Y., Argudo-Fernández, M., Chen, L., et al. 2016, Res. Astron. Astrophys., 16, 43
Sorce, J. G., Colless, M., Kraan-Korteweg, R. C., & Gottlöber, S. 2017, MNRAS, 471, 3087
Steer, I., Madore, B. F., & Mazzarella, J. M. 2017, AJ, 153, 37
Storrie-Lombardi, M. C., Lahav, O., Sodre, Jr., L., & Storrie-Lombardi, L. J. 1992, MNRAS, 259, 8P
Tully, R. B., & Fisher, J. R. 1977, A&A, 54, 661
Tully, R. B., Courtois, H., Hoffman, Y., & Pomarède, D. 2014, Nature, 513, 71
Tully, R. B., Pomarède, D., Graziani, R., et al. 2019, ApJ, 880, 24
VanderPlas, J., Connolly, A. J., Ivezic, Z., & Gray, A. 2012, Proceedings of Conference on Intelligent Data Understanding (CIDU), 47
Vavilova, I. B., Karachentseva, V. E., Makarov, D. I., & Melnyk, O. V. 2005, Kinematika i Fizika Nebesnykh Tel, 21, 3
Vavilova, I. B., Elyiv, A. A., & Vasylenko, M. Y. 2018, Russ. Radio Phys. Radio Astron., 23, 244
Wang, H., Mo, H. J., Yang, X., & van den Bosch, F. C. 2012, MNRAS, 420, 1809
Zaninetti, L. 2019, Int. J. Astron. Astrophys., 9, 51
Zhou, R., Cooper, M. C., Newman, J. A., et al. 2019, MNRAS, 488, 4565

2.2. Метод мозаїки Вороного вищих порядків для виявлення впливу оточення на характеристики галактик та їх малонаселених систем

Мозаїка Вороного [56] є зручним і універсальним геометричним інструментом, що широко використовувалась в астрофізиці для різних задач, наприклад, виділення войдів у великомасштабній структурі Всесвіту [46, 57], моделювання анізотропії мікрохвильового фону [58], виділення груп галактик різної населеності [59]. В роботі [30] мозаїка Вороного була застосована для виявлення “сфери впливу” галактики на своє оточення, де “сфера впливу” рахувалася як об’єм комірки Вороного, див. також дискусії у [32–35].

У алгоритмі найпростішої мозаїки Вороного першого порядку ключовим параметром є об’єм комірки Вороного. Цей параметр характеризує густину оточення даної галактики - чим менше об’єм комірки, тим ближче до галактики знаходяться її сусідні галактики, і навпаки – галактики у великих за об’ємом комірках є ізольованими. У роботі [12] ми вперше застосували 3D метод мозаїки Вороного другого та третього порядків для виділення пар і триплетів галактик, відповідно, з вибірки 6786 галактик спектроскопічного огляду SDSS DR5 з обмеженням $3000 \leq V_{\mathrm{LG}} \leq 9500$ км/с по променевій швидкості.

На відміну від методу Вороного першого порядку, метод Вороного другого порядку передбачає пошук комірки, яка належить не одній галактиці, а зразу двом галактикам, причому всі точки об’єму цієї комірки просторово ближче до цих двох галактик, ніж до будь якої іншої галактики вибірки. Аналогічно, у методі Вороного третього порядку ми шукали комірки, що містять одночасно три галактики. Об’єми комірок, як і в

методі мозаїки Вороного першого порядку, відповідали за ступінь ізольованості даної пари чи триплету галактик.

Mon. Not. R. Astron. Soc. **394**, 1409–1418 (2009) doi:10.1111/j.1365-2966.2008.14150.x

High-order 3D Voronoi tessellation for identifying isolated galaxies, pairs and triplets

A. Elyiv,[1⋆] O. Melnyk[1,2] and I. Vavilova[1,3]

[1]*Main Astronomical Observatory, Academy of Sciences of Ukraine, 27 Akademika Zabolotnoho St., 03680 Kyiv, Ukraine*
[2]*Astronomical Observatory, Kyiv National University, 3 Observatorna St., 04053 Kyiv, Ukraine*
[3]*Space Research Institute, National Space Agency of Ukraine, National Academy of Sciences of Ukraine, 40 Akademika Glushkova av., 03680 Kyiv, Ukraine*

Accepted 2008 October 25. Received 2008 October 5; in original form 2008 April 8

ABSTRACT

A geometric method based on the high-order 3D Voronoi tessellation is proposed for identifying single galaxies, pairs and triplets. This approach allows us to select small galaxy groups and isolated galaxies in different environments and to find the isolated systems. The volume-limited sample of galaxies from the Sloan Digital Sky Survey Data Release 5 spectroscopic survey was used. We conclude that in such small groups as pairs and triplets, segregation by luminosity is clearly observed: galaxies in isolated pairs and triplets are on average two times more luminous than isolated galaxies. We consider the dark matter content in different systems. The median values of mass-to-luminosity ratio are $12\,M_{\odot}/L_{\odot}$ for the isolated pairs and $44\,M_{\odot}/L_{\odot}$ for the isolated triplets, and 7 (8) $M_{\odot}/L_{\odot}$ for the most compact pairs (triplets). We also found that systems in denser environments have greater rms velocity and mass-to-luminosity ratio.

Key words: galaxies: general – galaxies: kinematics and dynamics – dark matter.

1 INTRODUCTION

The physical properties of galaxies depend on the formation conditions and evolution. In addition to intrinsic evolution, galaxies are exposed to environmental influence (see, among others, Dressler 1980; Lewis et al. 2002; Gomez et al. 2003; Einasto et al. 2003; Blanton et al. 2005; Martinez & Muriel 2006; Weinmann et al. 2006; Park et al. 2007, 2008). The density of galaxies (number of galaxies per volume unit) or luminosity density and the number of galaxies in group/cluster or distance to the nearest galaxy are often assumed to reflect the environment. The influence of an environment can be found up to 1 Mpc and even farther (Kauffmann et al. 2004; Blanton et al. 2005; Park et al. 2007, 2008), where small galaxy groups are observed. The study of 'environmental effects' in such poor galaxy groups is helpful for understanding the galaxy evolution on intermediate scales between isolated galaxies and rich groups/clusters.

The isolated galaxies that have not sufficiently undergone the influence of environment allow us to consider them as 'autonomous laboratories' for studying the evolutionary processes in the galaxies. Individual properties of isolated galaxies (mass, luminosity, morphology, colour-index, etc.) can be regarded as the standard when studying galaxies in different environments (see e.g. Karachentseva 1973, hereafter KIG; Prada et al. 2003; Reda et al. 2004; Stocke et al. 2004; Verley et al. 2007). To study galaxy properties in different environments, it is also important to define the galaxy's isolation degree which can be described by some parameter. For example, Karachentsev & Kasparova (2005) used the tidal index for each galaxy to study global properties of nearest galaxies in different environments. Verley et al. (2007) quantified the isolation degree of KIG galaxies by two parameters: local number density and tidal strength.

It is known that with the increase in galaxy system richness from individual galaxies to clusters, their mass increases more quickly than luminosity (Karachentsev 1966; Girardi et al. 2002). The dark matter in small groups seems to be distributed in the whole volume of the system in the case of compact groups and to be concentrated in the halo of individual galaxies in the case of loose groups (Mulchaey et al. 2003; Melnyk & Vavilova 2006; Da Rocha, Ziegler & Mendes de Oliveira 2008). At the same time, the amount of dark matter in galaxy groups is not enough for the standard cosmological model (Makarov & Karachentsev 2007).

As a rule, for identifying groups by different selection methods, the principle of overdensity in comparison with the background is used. The richer the group population, the stronger the overdensity and therefore the more likely that such a group is physically bound. Identification of poor groups depends strongly on the limiting parameters of the method. These systems can be easily confused with the random physically unbound systems. For this reason, many authors prefer to study rich groups/clusters only. That is why the elaboration of the reliable methods for identifying small groups will allow us to pay more attention to these structures.

Karachentsev (1972, 1987), Karachentseva, Karachentsev & Sherbanobsky (1979) and Karachentseva & Karachentsev (2000)

⋆E-mail: elyjuw@ukr.net

used a 2D method for pair and triplet selection taking into account the isolation degree in comparison with the foreground and background. The environment of each pair and triplet was inspected using Palomar Observatory Sky Survey (POSSI and POSSII) and European Southern Observatory SERC plates. This method selects effectively the isolated systems, which are compact in projection with characteristic distance between galaxies $R \sim 50$ and 100 kpc. With the appearance of the large data bases and surveys [Lyon–Meudon Extragalactic Database (LEDA), NASA/IPAC Extragalactic Database (NED), Sloan Digital Sky Survey (SDSS), The Center for Astrophysics Redshift Survey 2 (CfA2), The Second Southern Sky Redshift Survey (SSRS2), The DEEP2 Redshift Survey (DEEP2), Two-Degree Field Redshift Survey (2dF)] and information about the radial velocities of galaxies, the application of 3D methods of selection became generally accepted. 3D methods of group identification use as a rule two limited parameters: projected distance between galaxies R and radial velocity difference ΔV. For example, Barton, Geller & Kenyon (2000, 2003), Geller et al. (2006) and Woods, Geller & Barton (2006) selected close pairs of galaxies from the CfA2 catalogue with $R < 50$ kpc and $\Delta V < 1000\,\mathrm{km\,s^{-1}}$; the isolation criterion was ignored. Patton et al. (2000) investigated galaxy pairs from SSRS2. They considered all pairs with $R < 100$ kpc and did not find pairs with signs of interaction with $\Delta V > 600\,\mathrm{km\,s^{-1}}$, but most pairs with interaction signs had $R < 20$ kpc and $\Delta V < 500\,\mathrm{km\,s^{-1}}$ (see also Patton et al. 2002; Xu, Sun & He 2004; Patton, Grant & Simard 2005; De Propris et al. 2007). Nikolic, Cullen & Alexander (2004) obtained similar results for SDSS pairs. The authors found that the star formation rate is significantly enhanced for projected separations less than 30 kpc. Lambas et al. (2003) and Alonso et al. (2004) considered galaxy pairs with $R < 1$ Mpc and $\Delta V < 1000\,\mathrm{km\,s^{-1}}$ from the 2dF survey. They analysed the star formation activity in the pairs as a function of both relative projected distance and relative radial velocity, and found that the star formation activity in galaxy pairs is significantly enhanced over that in isolated galaxies at similar redshifts for $R < 25$ kpc and $\Delta V < 100\,\mathrm{km\,s^{-1}}$. Soares (2007) showed that more than half of the simulated pairs with projected distance $R \leq 50$ kpc have 3D separations greater than 50 kpc. Therefore for the selection of real physical pairs, it is important to take into account the signs of interaction, but that is not always possible.

Triplets of galaxies are less studied than pairs. Mainly triplets have been selected from the catalogues of groups of different populations (Trofimov & Chernin 1995). For example, Karachentseva et al. (2005), Vavilova et al. (2005), Melnyk (2006) and Melnyk & Vavilova (2006) compared the kinematic, dynamical, configurational and morphological properties of triplets from samples formed by the different methods. They showed that physical properties of galaxy groups strongly depend on selection criteria.

The main goal of our paper is to provide the uniform selection of single galaxies, pairs and triplets from SDSS[1] for later analysis of their properties: mass-to-luminosity ratio, colour indices, morphology and others. Such an investigation can be helpful for the study of the environmental influence and dark matter content on small scales (galaxy – pair – triplet). To meet this goal, we made selection of not only the most isolated galaxies and systems, but also single galaxies, pairs and triplets with different isolation degrees.

Most authors mentioned above used simple selection algorithms for pair identification: they consider all pairs with the fixed limitation parameters R and ΔV, which describe properties of the galaxy pair only as a separate system, without information about their neighbours. Contrary to this, we propose another approach. We use the second-order Voronoi tessellation for galaxy pair identification where the fundamental elements are pairs, and the third-order Voronoi tessellation for galaxy triplet identification where the fundamental elements are triplets. The geometric properties of the high-order tessellations give information about the relative location of neighbouring galaxies. This allows us to analyse the correlations of group properties with environment. The high-order (second- or third-order) Voronoi tessellation method has not been applied earlier for group detection, unlike the first-order Voronoi tessellation. Using the galaxies from the SDSS DR5 survey with known redshifts allows us to realize the 3D approach.

The outline of the paper is as follows. In Section 2, we present the method and parameters. The sample of galaxies is described in Section 3. In Section 4, we discuss our results and compare them with other works. Our conclusions are presented in Section 5.

2 THE METHOD AND PARAMETERS

The Voronoi diagram was introduced by Voronoi (1908). The most popular is the first-order Voronoi diagram (so-called Voronoi tessellation), Fig. 1(a). It is a geometric method of space partition on regions. Each region consists of one nucleus and all the points of space that are closer to a given nucleus than to other nuclei (Matsuda & Shima 1984; Lindenbergh 2002). Kiang (1966) found an analytic function of the Voronoi cell volume distribution for random points in 2D and 3D space. The Voronoi tessellation is used widely in astrophysics, especially for modelling the galaxy and void large-scale structure distribution (Icke & van de Weygaert 1987; van de Weygaert & Icke 1989; van de Weygaert 1994; Zaninetti 2006; van de Weygaert & Schaap 2007), for studying periodicities in deep pencil-beam sky surveys (Ikeuchi & Turner 1991; van de Weygaert 1991; Williams, Peacock & Heavens 1991; SubbaRao & Szalay 1992; Gonzales et al. 2000), for the extragalactic radio source distribution (Benn & Wall 1995) and for modelling of the cosmic microwave background anisotropy (Coles & Barrow 1990; SubbaRao et al. 1994) etc. Ebeling & Wiedenmann (1993) were the first to apply the Voronoi tessellation for finding groups and clusters of galaxies in the 2D case. Later such an approach was used by Ramella et al. (2001), Kim et al. (2002), Lopes et al. (2004), Barrena et al. (2005) and Panko & Flin (2006). The 3D Voronoi tessellation for galaxy group identification was realized by Marinoni et al. (2002) and Cooper et al. (2005). The application of the 3D Voronoi tessellation to the DEEP2 survey was introduced by Gerke et al. (2005). Melnyk, Elyiv & Vavilova (2006) applied the first-order 3D Voronoi tessellation for the identification of galaxy groups in the local supercluster. The authors demonstrated that the first-order tessellation is more useful for searching the rich clusters of galaxies than the small groups. In the first-order Voronoi tessellation, the key parameter is the volume of the galaxy's Voronoi cell V. This parameter characterizes a galaxy environmental density. The condition of cluster/group membership of a certain galaxy is the relatively small value of V. This condition is true when the galaxy is surrounded by close neighbouring galaxies. That is why the first-order Voronoi tessellation is not corrected for the identification of small isolated galaxy systems (see Melnyk et al. 2006 for details). In this paper, we propose the high-order 3D Voronoi tessellation method for identification of pairs and triplets. Let us consider this method below.

Contrary to the first-order tessellation (Fig. 1a), the second-order tessellation for set S distribution of nuclei is the partition of the

[1] http://www.sdss.org

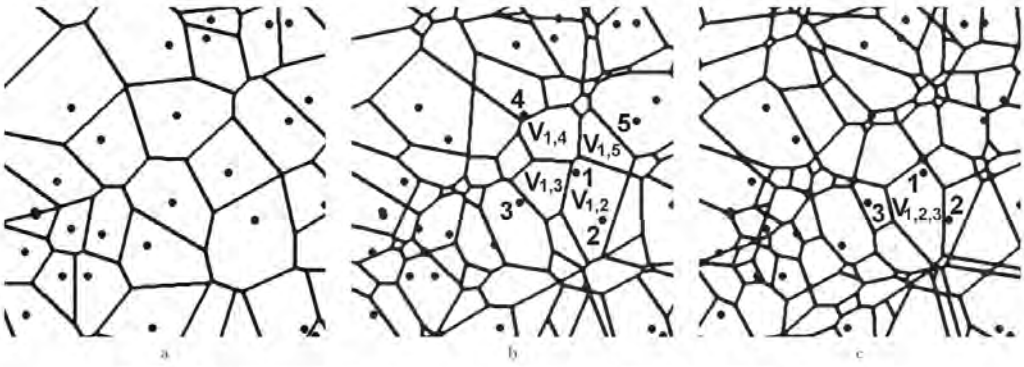

Figure 1. 2D Voronoi tessellation of the first (a), second (b) and third (c) order for the same distribution of random nuclei.

space which associates a region $V_{1,2}$ with each pair of nuclei 1 and 2 from S in such a way that all points in $V_{1,2}$ are closer to 1 and 2 than other nuclei from S (Fig. 1b). Region $V_{1,2}$ is a *common cell* for nuclei 1 and 2.[2] In such a way, the second-order Voronoi tessellation is available for the identification of single galaxies and pairs.

The third-order Voronoi tessellation is appropriate for the identification of triplets. It is the partition of the space which associates a region $V_{1,2,3}$ with each triplet of nuclei 1, 2, 3 in such a way that all points in $V_{1,2,3}$ are closer to nuclei 1, 2, 3 than other nuclei from S (Lindenbergh 2002), Fig. 1(c).

Since we work with a sample of galaxies, we use galaxies as the nuclei of the Voronoi tessellation taking into account equatorial coordinates α, δ and radial velocities of galaxies V_h only. For the construction of the 3D Voronoi tessellations, it is necessary to determine the distances in 3D space. The spatial distance between two galaxies can be decomposed into projected (tangential) distance r and radial component v (difference of the radial velocities). We can determine the projected distance with a relatively high accuracy, while the radial component has errors owing to inaccuracy of radial velocity measurement of each galaxy and existing strong peculiar velocities (due to virial motions of galaxies in groups and clusters). As a result the galaxy distribution in space of radial velocities is extended along the radial component, the so-called fingers-of-God effect. This is attributed to the random velocity dispersions in a galaxy volume-limited sample that cause a galaxy's velocity to deviate from pure Hubble flow, stretching out a group of galaxies in redshift space (Jackson 1972). Various authors take into account this effect in their own way depending on the specifics of their problem. For example, Marinoni et al. (2002) chose some cylindrical window of clustering which is extended along the radial component. We propose a different way that is based on introduction of weight for a radial component (see Appendix A). Such an approach allows us to avoid the problem of tangential and radial distance inequivalence and to apply the high-order 3D Voronoi tessellation method.

[2] However, it is not necessary that these nuclei lie in the common cell. For example, nuclei 1 and 5 create the common cell $V_{1,5}$ and they do not lie in this cell.

2.1 Second-order Voronoi tessellation: pairs and single galaxies

The second-order Voronoi tessellation was applied for the identification of pairs and single galaxies in the following way. Each galaxy i from set S forms common cells with a certain number of neighbouring galaxies (Fig. 1b). So we define the *neighbouring galaxies* of galaxy i as only galaxies that create common cells with this galaxy. For example, galaxy 1 creates only four common cells ($V_{1,2}$, $V_{1,3}$, $V_{1,4}$, $V_{1,5}$) with neighbouring galaxies 2, 3, 4 and 5, respectively. Each pair of galaxies i, j is characterized by the dimensionless parameters $p_{i,j}$:

$$p_{i,j} = \frac{\sqrt[D]{V_{i,j}}}{m_{i,j}}, \tag{1}$$

where D is the space dimension, $V_{i,j}$ is the area (for 2D) or volume (for 3D) of the cell, and $m_{i,j}$ is the distance between galaxies i and j (see Appendix A).

Each galaxy has a set of $p_{i,j}$ parameters. For example, galaxy 1 has the set $p_{1,2}$, $p_{1,3}$, $p_{1,4}$, $p_{1,5}$. We choose the maximum value from the set of parameters for galaxy 1: $p_{\max}(1) = \max(p_{1,2}, p_{1,3}, p_{1,4}, p_{1,5})$. In the general case for galaxy i: $p_{\max}(i) = \max(p_{i,j})$, where j assumes numbers of k neighbours.

We define the *geometric pair* in the second-order Voronoi tessellation as such a pair which contains two galaxies with a common cell that have the same $p_{\max}$ parameters, $p_{\max}(1) = p_{\max}(2) = p$. The parameter p characterizes a *degree of geometric pair isolation*. By a degree of pair isolation, we mean the overdensity relative to the background. We used the principle which was applied by Karachentsev (1987) for the selection of isolated galaxy pairs: if all galaxies have the same angular diameter, a neighbour of a pair of galaxies should be located on the sky more than five times farther from a pair than the separation of the pair members from each other. In our 3D approach, the degree of pair isolation is described by the relation between volume $V_{1,2}$ of the common cell (it characterizes distance to neighbours) and the distance $m_{1,2}$ between pair members according to equation (1). For example, a strongly isolated pair has a large value of p due to a large $V_{1,2}$ and small $m_{1,2}$ (1), see also Fig. 2(a).

We also introduce the parameter p_e which describes only the *pair environment* and does not depend on distance between pair members directly. We define it as the mean value of the $p_j(1)$ and

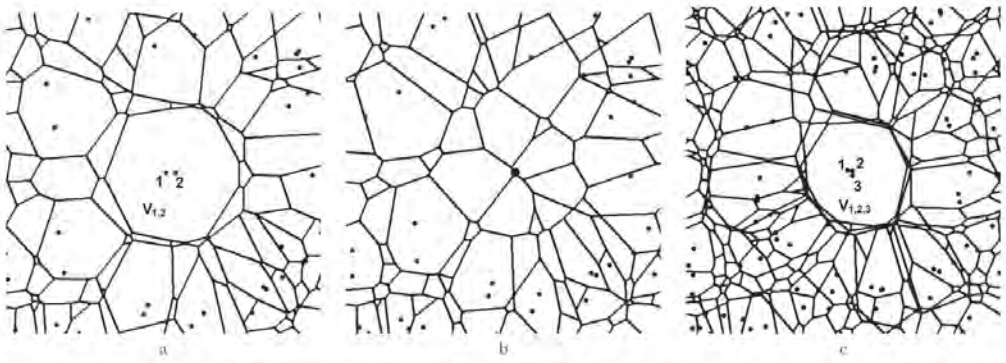

Figure 2. Different configurations of the galaxies: isolated close pair (a) and isolated single galaxy (b) in the second-order tessellation, and isolated close triplet in the third-order tessellation (c).

$p_l(2)$ parameters of the first and second galaxy, excepting p from both sets:

$$p_e = \frac{\sum_{j=2}^{k} p_j(1) + \sum_{l=2}^{n} p_l(2)}{k+n-2}, \tag{2}$$

where k and n are the numbers of neighbouring galaxies for 1 and 2 galaxies of the geometric pair, respectively. We start the sums from $j = 2$ and $l = 2$ for excepting $2p$, because the first galaxy is a neighbour of the second galaxy and vice versa. Therefore, $k + n-2$ is the sum of neighbouring galaxies of pair members excepting pair galaxies as being neighbours for each other. Parameter p_e depends on the distribution of neighbouring galaxies. A small value of p_e points out that such a pair is located in a loose environment. In such a case, the average volume of common cells of pair components with neighbouring galaxies is relatively small, and distance between them is large, see formula (1) and Fig. 2(a).

A *single galaxy* is a galaxy which is not a member of any geometric pair. The single galaxies are field galaxies in the environment of geometric pairs. Every single galaxy has its own neighbours; single galaxies and geometric pair members can be among them. According to the second-order Voronoi tessellation, the larger the degree of galaxy isolation, the greater is the number of neighbours (see Fig. 1b in comparison with Fig. 2b), but these neighbours are located farther away. The best parameter that describes the isolation degree of a single galaxy is the mean value of all parameters p_j of this galaxy:

$$s = \frac{\sum_{j=1}^{k} p_j}{k}, \tag{3}$$

where k is the number of neighbours. Therefore, the smaller the value of s, the more isolated is the single galaxy.

2.2 Third-order Voronoi tessellation: triplets

The method of the third-order Voronoi tessellation can be introduced in the same way as the second-order approach (Fig. 1c). All points of the common triplet's cell are closer to galaxies of this triplet than to other galaxies. Similarly to the parameter $p_{i,j}$ for pairs, we set up the parameter $t_{i,j,u}$ for triplets:

$$t_{i,j,u} = \frac{\sqrt[D]{V_{i,j,u}}}{\max(m_{i,j}, m_{i,u}, m_{j,u})}, \tag{4}$$

where D is the space dimension, $V_{i,j,u}$ is the area (for 2D) or volume (for 3D) of the cell, and $m_{i,j}$, $m_{i,u}$, $m_{j,u}$ are the distances between galaxies in the triplet.

A *geometric triplet* in the third-order Voronoi tessellation contains three galaxies that have a common cell and the same maximal parameters $t_{\max}(1) = t_{\max}(2) = t_{\max}(3) = t$. The parameter t characterizes a *degree of geometric triplet isolation*. We define the parameter of *triplet environment* t_e as the mean value of parameters $t_i(1)$, $t_j(2)$ and $t_u(3)$, except t from three sets:

$$t_e = \frac{\sum_{i=2}^{k} t_i(1) + \sum_{j=2}^{n} t_j(2) + \sum_{u=2}^{q} t_u(3)}{k+n+q-3}; \tag{5}$$

here in the case of the third-order Voronoi tessellation, k, n and q denote the number of *neighbouring triplets* which contain galaxies 1, 2 and 3, respectively. Therefore, $k + n + q - 3$ is the number of neighbouring triplets for a certain triplet that contain at least one galaxy from this triplet.

It can be seen from Fig. 2(c) and equations (4) and (5) that for the triplet with the highest degree of standing out against a background, the isolation parameter t has the highest value. At the same time, if the triplet neighbours are located far from it, parameter t_e has a small value.

Parameters p, s, t are the basic ones and define the isolation degree of a galaxy pair, single galaxy or triplet in comparison with the background, respectively. Parameters p_e and t_e are additional ones and contain information about the distribution of the neighbouring galaxies (environment).

Similarly to the second- and third-order Voronoi tessellations, it is possible to apply more high-order Voronoi tessellations for the identification of galaxy quartets, quintets and so on.

3 THE SAMPLE

For our investigation, we used the Northern part of the SDSS DR5 spectroscopic survey. Our sample is volume limited and consists of objects that are classified as galaxies. The primary sample had contained approximately 11 000 galaxies with radial velocities from 2500 to 10 000 km s^{-1}, $H_0 = 75$ km s^{-1} Mpc^{-1}. It is known that the completeness of the SDSS is poor for the bright galaxies because of spectroscopic selection criteria and the difficulty of obtaining correct photometry for objects with large angular size. We tried to

decrease the influence of this effect due to limiting of our sample $V_h > 2500\,\mathrm{km\,s^{-1}}$, i.e. so as not to take into account nearest objects with large angular diameter. Such a volume limiting also helps us to avoid influence of the Virgo cluster where strong peculiar motion exists. We checked additionally all pairs of galaxies with a small angular resolution and excluded identical objects (parts of galaxies), which are presented twice and more in the SDSS survey. All galaxy velocities V_h were corrected for the Local Group centroid V_{LG} according to Karachentsev & Makarov (1996). When we had applied the high-order Voronoi tessellation method to the SDSS catalogue, we limited our sample to $3000 \leq V_{LG} \leq 9500\,\mathrm{km\,s^{-1}}$. We did not consider also galaxies that are located within 2° near borders, because the correct estimation of the Voronoi cell volume is not possible in this case. Our volume-limited sample is complete up to 17.7 mag but contains also about 100 more fainter galaxies. The final number of galaxies in the sample is 6786.

4 THE RESULTS

We applied the second-order 3D Voronoi tessellation to our sample of 6786 galaxies and obtained 2196 geometric pairs and 2394 single galaxies (65 per cent galaxies of whole sample are in pairs and 35 per cent are singles). We divided our samples of geometric pairs and singles into four equal parts by the parameters of isolation p and s, respectively. A quarter of each sample with the highest isolation degree we called *isolated* (549 pairs and 598 singles). It means that the isolated pairs and singles have $p > Q_3$ and $s < Q_1$, respectively; Q_3 is the third quartile and Q_1 is the first quartile. See values of quartiles in Table 1.

Fig. 3 shows the distributions of number of neighbouring galaxies for galaxies that are members of pairs and singles. We can see from Fig. 3 that number of neighbours is varied through the range from 4 to 30 galaxies. Isolated galaxies have more neighbours than galaxies in other samples on average. It is a feature of the second-order Voronoi tessellation (see above). Galaxies in isolated pairs have approximately half as many neighbours as isolated galaxies because the pair's neighbours distribute between two members.

Table 1. Quartiles of isolation parameters.

	Parameters	Q_1	Q_2	Q_3
Singles	s	0.57	0.77	1.08
Pairs	p	3.59	5.72	10.17
Triplets	t	1.90	2.62	3.90

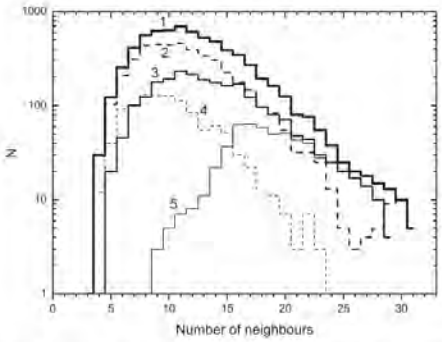

Figure 3. Distributions of number of neighbouring galaxies: (1) all galaxies of the sample, (2) galaxies in geometric pairs, (3) single galaxies, (4) galaxies in isolated pairs and (5) isolated galaxies.

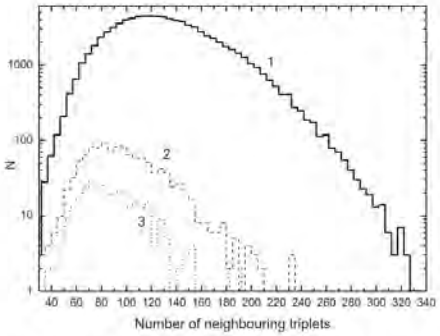

Figure 4. Distributions of number of neighbouring triplets: (1) all triplets of the sample, (2) geometric triplets and (3) isolated triplets.

Independently, we applied the third-order 3D Voronoi tessellation to our galaxy sample and obtained 1182 geometric triplets (52 per cent of the whole sample). The quarter (297) of the triplet sample with the highest isolation degree $t > Q_3$ we called *isolated*. Values of all quartiles for triplets can be found in Table 1. The distribution of numbers of neighbouring triplets is shown in Fig. 4. As can be seen, this picture looks the same as for the distribution of number of neighbouring galaxies in the case of the second-order Voronoi tessellation (Fig. 3).

4.1 Comparison with other samples

We cross-correlated our results with other samples. To first order, we compared pairs and triplets of our sample with Tago et al. (2008) groups selected by the modified friends-of-friends method using the same release of SDSS. From 965 galaxies of Tago's pairs that are located in our region of investigation, 686 galaxies (343 pairs or 71 per cent) coincide with our pairs with different isolation degree. The median value of the isolation parameter p is 9.89 which does not differ strongly from our isolation limit ($Q_3 = 10.17$). Another 121 galaxies coincide with one of our pair members; the median value of p for these pairs is 3.94. We can conclude that they are located in the field. The remaining 158 galaxies coincide with our single galaxies having isolation degree $s = 0.87$, i.e. also associated with the field galaxies (our isolation limit is less than $Q_1 = 0.57$). 63 triplets (51 per cent) of the Tago et al. (2008) triplets that fall in our region coincide with our triplets. The median value of isolation degree for these triplets $t = 4.83$ is higher than our isolation limit $Q_3 = 3.90$. We also compared our pairs with 28 isolated Karachentsev (1987) pairs that are located in our region of investigation: 16 pairs coincide with our pairs (the median value of isolation degree $p = 21.16$ is very high). Among seven of our 'pairs', one of the components is an interacting galaxy which corresponds to Karachentsev's pair, the second component is a fainter galaxy, these 'pairs' are not isolated (median value of p is 3.95). Such cases appear because of difficulties in the spectroscopic measurement of interacting (very close) galaxies in the SDSS. The remaining five pairs coincide by components with different pairs and single galaxies with small isolation degree because these pairs are surrounded by fainter satellites. We found

that 10 out of 36 KIG galaxies coincided with our single galaxies, but 24 KIG galaxies fall in our pairs with different isolation degree (the median value is not very high, $p = 5.8$). Such a difference can be explained by the presence of a fainter galaxy in the immediate vicinity of the KIG galaxy. Actually, all 34 isolated galaxies with fainter satellites from Prada et al. (2003), which locate in our region, coincide with our pairs and triplets.

We can conclude that our singles, pairs and triplets of galaxies obtained by the high-order Voronoi tessellation are in good agreement with other samples, especially concerning the systems with high isolation degrees. Some lack of coincidence can be explained by the differences in primary catalogues, for example, by the magnitude depth or spectroscopy of interacting galaxies in the SDSS.

4.2 Isolation and main parameters

In addition to the isolation and environmental parameters p, p_c, s, t and t_c, we calculated also other characteristics (Karachentsev, Karachentseva & Lebedev 1989; Vavilova et al. 2005): rms velocity of galaxies with respect to the group centre (in km s^{-1}), $S_v = [\frac{1}{N}\sum_{i=1}^{N}(V_{LG}^i - \langle V_{LG_i}\rangle)^2]^{1/2}$, $S_v = \Delta V/2$ for pairs, N is the number of galaxies in the group; harmonic mean radii of the system (in kpc) – $R_h = (\frac{1}{2}\sum_{i,k} R_{ik}^{-1})^{-1}$, where $R_{ik} = X_{ik}\,\langle V_{LG}\rangle\, H_0^{-1}$ and X_{ik} is the relative angular distance; R is the maximal distance between galaxies in triplets, for galaxy pair $R_h = R$; dimensionless crossing-time

$$\tau = 2H_0 R_h/S_v \tag{6}$$

expressed in units of the cosmological time H_0^{-1}; virial mass

$$M_{vir} = 3\pi N(N-1)^{-1}G^{-1}S_v^2 R_h \tag{7}$$

in $M_\odot$; galaxy luminosity L_r, which corresponds to the Petrosian magnitude in the r band, $L_\odot$; and mass-to-luminosity ratio $M_{vir}/L = M_{vir}/\sum L_r$ in $M_\odot/L_\odot$.

First of all we investigated how the values of rms velocity and mean harmonic radius of pairs and triplets depend on their isolation degree. Table 2 presents the median values and quartiles of S_v and R_h for pairs and triplets in dependence on isolation parameters p and t: all geometric pairs, pairs with $p > Q_1$, $p > Q_2$, $p > Q_3$; all geometric triplets, triplets with $t > Q_1$, $t > Q_2$, $t > Q_3$, where Q_1, Q_2, Q_3 is the first, second (median value), third quartile, respectively. See values of p and t quartiles in Table 1. It can be seen from Table 2 that all geometric samples have largest values of S_v and R_h and largest interquartile range (IQR). With the increase in isolation degree, the medians and IQR of S_v and R_h decrease. Pairs and triplets selected by a dynamical method (Makarov & Karachentsev 2000) have medians $S_v = 24^{+22}_{-13}$ km s^{-1}, $R_h = 170^{+185}_{-114}$ kpc and 41^{+19}_{-18} km s^{-1}, 191^{+157}_{-98} kpc, respectively. The sample of triplets from Vavilova et al. (2005) has medians $S_v = 30^{+18}_{-12}$ km s^{-1} and $R_h = 160^{+117}_{-77}$ kpc. These values better agree with samples which have $p, t > Q_2$ (i.e. $p > 5.72$ and $t > 2.62$ for pairs and triplets, respectively).

Table 2. Physical properties of pairs and triplets: dependence on isolation parameters.

Pairs	N	S_v	R_h
	Pairs		
All geometric	2196	22^{+18}_{-11}	354^{+536}_{-199}
$p > Q_1$	1677	20^{+15}_{-11}	252^{+217}_{-130}
$p > Q_2$	1038	18^{+12}_{-10}	182^{+156}_{-91}
$p > Q_3$	549	16^{+8}_{-8}	106^{+73}_{-47}
	Triplets		
All geometric	1182	41^{+20}_{-15}	390^{+333}_{-184}
$t > Q_1$	893	38^{+16}_{-14}	330^{+216}_{-148}
$t > Q_2$	582	35^{+14}_{-12}	275^{+194}_{-109}
$t > Q_3$	297	31^{+11}_{-10}	212^{+132}_{-83}

We also considered how the isolation degree of pairs and triplets depends on S_v and R_h. Tables 3 and 4 give values of parameters p, p_c, t, t_c for pairs and triplets at the fixed values of S_v and R_h, which correspond to intervals: $S_v, R_h < Q_1$; $Q_1 < S_v, R_h < Q_2$; $Q_2 < S_v, R_h < Q_3$; $S_v, R_h > Q_3$; All S_v, R_h.

Most compact pairs with R_h less than the first quartile have medians of p 2.5 times greater and IQR almost three times greater than the values for sample 'All S_v, R_h'. This means that compact pairs are more isolated (or higher contrast in comparison with the background) than in average galaxies in the whole sample, but also they are characterized by different isolation degree. At $R_h < Q_1$ and $p, t > Q_3$, 65 per cent of pairs (47 per cent of triplets) coincide.

Parameter p_c for the compact pairs has a large dispersion also. This means that similar compact pairs are in both densest and loose environments. Thus, the isolation degree and IQR change depending on the values of rms velocities: the most compact pairs with rms velocity less than the first quartile are most isolated. For these pairs, parameter p is almost five times greater than the median of the 'All R_h, S_v' sample and IQR is 4.5 times greater. Most compact pairs with $S_v > Q_3$ have an isolation degree the same as galaxies of the whole sample. The values of isolation parameter decrease with increasing of R_h and S_v, thus, at R_h greater than third quartile the p becomes almost two times less than the median of the whole sample. It means that these pairs are less isolated. It is necessary to note that p significantly changes in dependence on R_h, compared with S_v. But all of the pairs with $S_v > 40\,\mathrm{km\,s^{-1}}$ (Q_3) are characterized by small isolation degree, compared with pairs with $S_v < 40\,\mathrm{km\,s^{-1}}$. The additional parameter p_c also decreases with R_h increasing and for $R_h > Q_3$ it has the minimum value with a small variation (p is also minimal). So, all wide pairs ($R_h > Q_3$) are in low-density environments. It is obvious that there is not enough free space for the widest pairs to be isolated (without galaxies). Most probably, these pairs are the accidental ones in the common field. From Table 4, it is easy to be convinced that all of the above-mentioned tendencies are similar for triplets but with their own values.

4.3 The luminosity content

Considering the luminosity–density relation (e.g. Park et al. 2007, 2008, and references therein), we can note the following: galaxies are more luminous in the high-density regions than in the field. Karachentseva et al. (2005) showed that galaxies even in such poor groups as the triplets are more luminous than the isolated galaxies. We compared the luminosities of single/isolated galaxies with the luminosities of galaxies in pairs and triplets. Their medians with quartiles and mean values with standard deviations are presented in Table 5. Fig. 5 shows the distribution of galaxy luminosities.

It can be seen from Table 5 and Fig. 5 that the median and mean values of luminosities are greater for galaxies in pairs and triplets than for single/isolated galaxies. The mean values of luminosities of isolated galaxies and galaxies in isolated pairs differ significantly (with a probability of >0.99 by the t-criterion), but differences for 'All' samples are not statistically significant. The same conclusions

Table 3. Parameters p and p_ε at fixed values S_v and R_0 for geometric pairs.

Pairs		$S_v < 10$	$10 < S_v < 22$	$22 < S_v < 40$	$S_v > 40$	All S_v
$R_0 < 155$	p	$27.61^{+17.57}_{-12.68}$	$18.90^{+13.44}_{-6.65}$	$11.84^{+5.62}_{-3.88}$	$6.14^{+2.91}_{-1.38}$	$14.67^{+13.09}_{-5.93}$
	p_ε	$0.90^{+0.38}_{-0.20}$	$0.94^{+0.55}_{-0.30}$	$0.87^{+0.38}_{-0.24}$	$0.63^{+0.19}_{-0.14}$	$0.85^{+0.37}_{-0.24}$
	N	149	153	144	103	549
$155 \leq R_0 < 354$	p	$8.85^{+5.37}_{-2.74}$	$8.47^{+4.72}_{-2.49}$	$7.05^{+2.57}_{-2.18}$	$4.87^{+1.71}_{-1.10}$	$7.36^{+3.18}_{-2.51}$
	p_ε	$0.83^{+0.25}_{-0.18}$	$0.83^{+0.32}_{-0.20}$	$0.82^{+0.19}_{-0.18}$	$0.66^{+0.14}_{-0.12}$	$0.78^{+0.23}_{-0.18}$
	N	146	154	133	116	549
$354 \leq R_0 < 690$	p	$5.45^{+1.65}_{-1.43}$	$5.23^{+2.34}_{-1.39}$	$4.73^{+1.79}_{-1.18}$	$4.03^{+1.31}_{-0.93}$	$4.84^{+1.84}_{-1.21}$
	p_ε	$0.64^{+0.17}_{-0.13}$	$0.63^{+0.18}_{-0.10}$	$0.69^{+0.34}_{-0.12}$	$0.59^{+0.15}_{-0.15}$	$0.64^{+0.15}_{-0.13}$
	N	153	130	139	127	549
$R_0 \geq 690$	p	$3.12^{+1.32}_{-0.82}$	$3.27^{+1.21}_{-0.81}$	$3.05^{+1.17}_{-0.70}$	$2.42^{+0.90}_{-0.43}$	$2.83^{+1.10}_{-0.65}$
	p_ε	$0.47^{+0.14}_{-0.09}$	$0.46^{+0.09}_{-0.09}$	$0.52^{+0.07}_{-0.10}$	$0.47^{+0.10}_{-0.08}$	$0.48^{+0.10}_{-0.09}$
	N	101	112	133	203	549
All R_0	p	$7.27^{+6.74}_{-2.78}$	$7.57^{+6.47}_{-3.32}$	$5.63^{+3.77}_{-1.94}$	$3.81^{+1.92}_{-1.24}$	$5.72^{+4.45}_{-2.13}$
	p_ε	$0.71^{+0.25}_{-0.20}$	$0.70^{+0.29}_{-0.19}$	$0.69^{+0.26}_{-0.16}$	$0.55^{+0.15}_{-0.12}$	$0.65^{+0.24}_{-0.15}$
	N	549	549	549	549	2196

Table 4. Parameters i and i_ε at fixed values S_v and R_0 for geometric triplets.

Triplets		$S_v < 26$	$26 < S_v < 41$	$41 < S_v < 61$	$S_v > 61$	All S_v
$R_0 < 205$	i	$5.22^{+2.24}_{-2.12}$	$4.33^{+2.64}_{-1.42}$	$3.47^{+1.40}_{-1.11}$	$2.25^{+0.71}_{-0.79}$	$3.75^{+2.53}_{-1.23}$
	i_ε	$0.43^{+0.14}_{-0.08}$	$0.41^{+0.09}_{-0.06}$	$0.36^{+0.05}_{-0.06}$	$0.29^{+0.05}_{-0.05}$	$0.38^{+0.10}_{-0.07}$
	N	91	92	70	43	296
$205 \leq R_0 < 390$	i	$3.44^{+1.74}_{-0.82}$	$3.36^{+1.13}_{-1.04}$	$2.84^{+1.05}_{-1.64}$	$2.25^{+0.69}_{-0.79}$	$3.11^{+1.17}_{-0.85}$
	i_ε	$0.41^{+0.05}_{-0.07}$	$0.38^{+0.05}_{-0.07}$	$0.37^{+0.04}_{-0.06}$	$0.32^{+0.03}_{-0.04}$	$0.37^{+0.06}_{-0.06}$
	N	81	87	83	44	295
$390 \leq R_0 < 723$	i	$2.96^{+0.83}_{-0.78}$	$2.47^{+0.92}_{-0.57}$	$2.50^{+0.74}_{-0.47}$	$2.03^{+0.58}_{-0.44}$	$2.42^{+0.79}_{-0.54}$
	i_ε	$0.31^{+0.09}_{-0.04}$	$0.32^{+0.05}_{-0.04}$	$0.33^{+0.06}_{-0.04}$	$0.29^{+0.05}_{-0.03}$	$0.32^{+0.08}_{-0.05}$
	N	71	65	76	83	295
$R_0 \geq 723$	i	$1.92^{+0.92}_{-0.36}$	$1.97^{+0.33}_{-0.25}$	$1.89^{+0.61}_{-0.35}$	$1.74^{+0.69}_{-0.31}$	$1.88^{+0.64}_{-0.38}$
	i_ε	$0.25^{+0.04}_{-0.05}$	$0.27^{+0.03}_{-0.05}$	$0.27^{+0.04}_{-0.04}$	$0.24^{+0.02}_{-0.03}$	$0.25^{+0.03}_{-0.04}$
	N	53	51	66	126	296
All R_0	i	$3.23^{+1.96}_{-0.97}$	$3.08^{+1.37}_{-1.01}$	$2.65^{+1.02}_{-0.65}$	$2.03^{+0.57}_{-0.44}$	$2.62^{+1.28}_{-0.71}$
	i_ε	$0.37^{+0.09}_{-0.09}$	$0.35^{+0.08}_{-0.07}$	$0.33^{+0.07}_{-0.05}$	$0.27^{+0.05}_{-0.04}$	$0.32^{+0.07}_{-0.06}$
	N	296	295	295	296	1182

Table 5. Comparison between the luminosities of the galaxies from different samples.

Sample of galaxies	$L_r \times 10^9$ ($L_\odot$)	
	Median	Mean (SD)
All single	$2.23^{+3.66}_{-1.15}$	5.17 (8.00)
All geometric pairs	$2.38^{+4.27}_{-1.29}$	5.79 (8.66)
All geometric triplets	$2.48^{+1.96}_{-0.14}$	6.00 (8.77)
Isolated	$1.80^{+3.10}_{-0.77}$	3.52 (4.47)
Isolated pairs	$2.89^{+7.20}_{-1.73}$	6.74 (9.46)
Isolated triplets	$2.68^{+6.80}_{-1.52}$	6.53 (9.97)

can be drawn from the comparison of the sample of single/isolated galaxies with galaxies in triplets.

So, galaxies in isolated pairs and triplets are two times more luminous than isolated galaxies. It is necessary to note that our method of group identification does not take into account individual physical characteristics of galaxies, therefore the effects of selection are absent here. The fact that for 'All' samples the mean values have a small difference may serve as evidence of the influence of non-physical (accidental) groups in these samples; the wide systems are dominant among them.

4.4 Mass-to-luminosity ratio

For studying the presence and distribution of dark matter in small galaxy groups, we used the mass-to-luminosity ratio ($M_{\rm vir}/L$) as the quantitative indicator of dark matter contribution. We checked the mass-to-luminosity ratio in dependence on the isolation degree of pairs and triplets. We plotted the dependences of system isolation p, i on $M_{\rm vir}/L$ in narrow bins of R, because the isolation parameters p, i and virial mass $M_{\rm vir}$ depend on the projected distance between the galaxies R (see equations 1, 4 and 7). Fig. 6 presents the dependence of slope α in the p, i–$M_{\rm vir}/L$ relation on R, and Fig. 7 presents

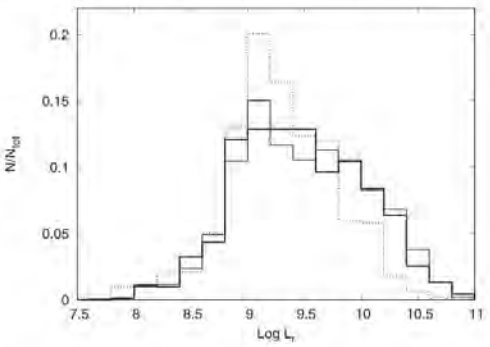

Figure 5. Luminosity distributions of isolated galaxies (dotted line), galaxies in isolated pairs (solid line) and galaxies in isolated triplets (thick line).

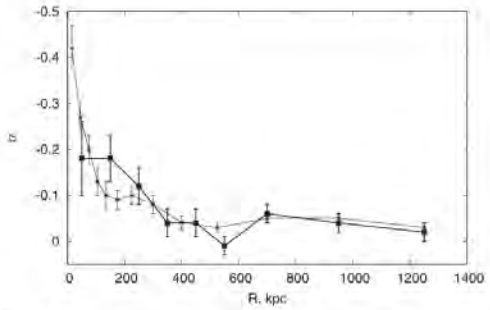

Figure 6. Dependence between slope α and R; for the pairs $\log(p) = \alpha \log(M_{\rm vir}/L) + b$ (thin line) and for the triplets $\log(t) = \alpha \log(M_{\rm vir}/L) + b$ (thick line).

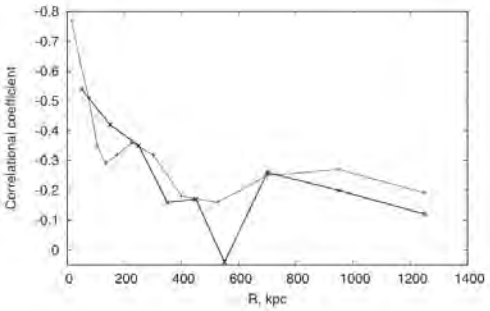

Figure 7. Dependence of correlation coefficient in relations from Fig. 6 on R; for the pairs (thin line) and for the triplets (thick line).

the dependence of correlation coefficient on R (details in legends to the figures).

We see from Figs 6 and 7 that if the system is located in a denser environment, it has a greater value of $M_{\rm vir}/L$ ($\alpha < -0.1$, correlation coefficient < -0.3). Moreover, such dependences are true only on scales approximately up to 150–200 kpc for pairs and up to 250–300 kpc for triplets. For greater values of R, the p, t–$M_{\rm vir}/L$ dependences were not observed. This conclusion only confirms our results (Sections 4.2 and 4.3) where we showed that the widest systems most probably are accidental formations, because they do not stand out against a background.

Our results agree with the work of Park, Gott & Yun-Young (2008) who studied the dependence of morphology and luminosity on environment. A strong dependence of morphology on the nearest neighbour was found at distances of about 200 h^{-1} kpc. On the other hand, authors (see e.g. Patton et al. 2000; Lambas et al. 2003; Alonso et al. 2004; Woods et al. 2006; De Propris et al. 2007) on the basis of analysis of physical properties such as star formation rate and colour indices concluded that differences between galaxies in pairs and field galaxies are significant in pairs with $R < 20$–50 kpc. The dependence on velocity dispersion is weaker, but Lambas et al. (2003) and Alonso et al. (2004) found significant differences in $\Delta V < 100$ km s^{-1}.

Because the maximal distance R is a constant, the enhancement of the $M_{\rm vir}/L$ value is a result of the increase in rms velocities in groups. In other words, if the relatively compact pairs and triplets are located in a denser environment, then they have a greater value of mass-to-luminosity ratio due to larger virial motions. The same result was obtained by Einasto et al. (2003). The authors found that loose groups in the neighbourhood of a rich cluster are typically 2.5 times more massive and 1.6 times more luminous than groups on average, and these loose groups have velocity dispersions 1.3 times greater than groups on average.

Table 6 presents the medians and quartiles of system crossing time τ and mass-to-luminosity ratio $M_{\rm vir}/L$ for samples of pairs and triplets that are characterized by different isolation degree and compactness.

From Table 6 it follows that values of $M_{\rm vir}/L$ at $R < 50$ kpc for pairs and $R < 100$ kpc for triplets are 7–8 $M_\odot/L_\odot$ and increase with enhancement of R_h faster for triplets than for pairs.

The values of $M_{\rm vir}/L$ are in good agreement with the corresponding values within the IQR for groups that were selected by a dynamical method. The values of $M_{\rm vir}/L$ are $18^{+39}_{-14}\,M_\odot/L_\odot$ and $32^{+34}_{-22}\,M_\odot/L_\odot$ for pairs and triplets, respectively (Makarov & Karachentsev 2000), and for triplets (from Vavilova et al. 2005) $35^{+50}_{-23}\,M_\odot/L_\odot$. The median of most compact triplets is in agreement with the median $M_{\rm vir}/L = 13^{+16}_{-11}\,M_\odot/L_\odot$ obtained for interacting triplets, where the star formation rate is high (Melnyk 2006). The median of isolated triplets is in good agreement with the median $M_{\rm vir}/L = 47^{+48}_{-33}\,M_\odot/L_\odot$ which corresponds to the sample of isolated Northern (Karachentseva, Karachentsev & Sherbanovsky 1979) and Southern (Karachentseva & Karachentsev 2000) triplets.

Table 6. Medians and quartiles of the system crossing time and mass-to-luminosity ratio for pairs and triplets.

Pairs	N	τ	$M_{\rm vir}/L$	Triplets*	N	τ	$M_{\rm vir}/L$
$p > Q_3$	519	$1.12^{+1.24}_{-0.59}$	12^{+37}_{-10}	$t > Q_3$	297	$1.06^{+0.88}_{-0.42}$	44^{+60}_{-28}
$R < 50$	133	$0.18^{+0.20}_{-0.07}$	7^{+28}_{-6}	$R < 100$	16	$0.24^{+0.07}_{-0.08}$	8^{+16}_{-3}
$R < 100$	335	$0.40^{+0.47}_{-0.21}$	9^{+31}_{-8}	$R < 200$	70	$0.43^{+0.49}_{-0.24}$	20^{+46}_{-13}
$R < 150$	549	$0.61^{+0.63}_{-0.32}$	14^{+44}_{-11}	$R < 300$	136	$0.70^{+0.33}_{-0.28}$	24^{+41}_{-16}
$R < 200$	684	$0.70^{+0.75}_{-0.34}$	17^{+50}_{-14}	$R < 400$	240	$0.71^{+0.39}_{-0.30}$	31^{+49}_{-18}

*Maximal distance R correlates with R_h : $R = 1.41\,R_h + 266$; the correlation coefficient is 0.87 for triplets and $R = R_h$ for pairs.

An observable agreement with previous results is additional evidence of the correctness of applying the high-order Voronoi tessellation method for the identification of pairs and triplets.

5 CONCLUSIONS

For the first time we have introduced and applied the high-order 3D Voronoi tessellation method for the identification of isolated galaxies, pairs and triplets.

We used a volume-limited sample of 6786 galaxies from the Northern part of the SDSS DR5 spectroscopic survey ($3000 \leq V_{\rm LG} \leq 9500\,{\rm km\,s^{-1}}$). We selected single galaxies and pairs by the second-order Voronoi tessellation, as well as triplets by the third-order Voronoi tessellation method. As a result we formed 2196 geometric pairs, 1182 triplets and 2394 single galaxies. Then, we introduced parameters p, t and s to characterize the isolation degree of pairs, triplets and single galaxies, respectively. We did not make a clear division between physical gravitationally bound systems and non-physical ones, following the supposition that the more isolated a system is, the higher probability that it is physical. We denoted the subsets of our single galaxies, pairs and triplets with $s < Q_1$, $p > Q_3$ and $t > Q_3$, respectively, as 'isolated' (i.e. with the highest isolation degree). The values of quartiles are in Table 1. So, we consider the properties of single galaxies, pairs and triplets in dependence on their isolation degree (in different environments).

Our main conclusions are outlined below.

Compact pairs ($R_{fl} < 150$ kpc) and triplets ($R_{fl} < 200$ kpc) are more isolated on average than systems in geometric samples, thus they are characterized by different isolation degrees. The wider the pair (triplet), the smaller isolation degree is observed. Small values of parameters p_6 and t_6 are evidence of a loose environment of these systems (they do not have enough 'free space' to be isolated groups). Thus, we consider wide geometric pairs and triplets as accidental ones in the common field.

We compared the luminosities of single galaxies and galaxies in geometric pairs and triplets. It was shown that galaxies in isolated pairs and triplets are two times more luminous than isolated galaxies. On the one hand, it is evidence of the accuracy of our geometric method. On the other hand, we can conclude that in such small groups as pairs and triplets the luminosity–density relation is observed.

We considered the dark matter content in our groups. The median values of M_{vir}/L for our samples limited by different criteria are $12\,{\rm M_\odot/L_\odot}$ for isolated pairs, $44\,{\rm M_\odot/L_\odot}$ for isolated triplets and 7 (8) $\rm M_\odot/L_\odot$ for the most compact pairs (triplets) with $R < 50$ (100) kpc. Note that for the most compact (close or interacting) systems there is not a very large difference in dark matter content for pairs and triplets, but for isolated triplets the M_{vir}/L is three times larger than for pairs. These results are in agreement with the studies of other authors. We also found that the pair/triplet is a less isolated system (in a denser environment), when M_{vir}/L is greater. This relation testifies that galaxy systems in denser environments have greater rms velocity (because of $M_{vir} \sim S_v^2$ at fixed distance between galaxies). The p, t–M_{vir}/L dependences are observed only for compact systems (up to 150–200 kpc for pairs and up to 250–300 kpc for triplets).

We conclude that the 3D Voronoi high-order tessellation method is an effective tool for the identification of small groups and the study of their properties in dependence on environment. In our next paper, we will present results on morphological content and colour indices of galaxies in pairs and triplets in comparison with isolated galaxies and their environment.

ACKNOWLEDGMENT

This work was partially supported by the Cosmomicrophysics Program of the NAS of Ukraine. We are also grateful to the Ukrainian Virtual Roentgen and Gamma-Ray Observatory VIRGO.UA, the computing clusters of Main Astronomical Observatory and Bogolyubov Institute for Theoretical Physics, for use of their computing resources.

REFERENCES

Alonso M. S., Tissera B., Coldwell G., Lambas D., 2004, MNRAS, 352, 1081
Barrena R., Ramella M., Boschin W., Nonino M., Biviano A., Mediavilla E., 2005, A&A, 444, 685
Barton E. G., Geller M. J., Kenyon S. J., 2000, ApJ, 530, 660
Barton E. G., Geller M. J., Kenyon S. J., 2003, ApJ, 582, 668
Benn C., Wall J., 1995, MNRAS, 272, 678
Blanton M., Eisenstein D., Hogg D., Schlegel D., Brinkmann J., 2005, ApJ, 629, 143
Ceccarelli M., Valotto C., Lambas D., Padilla N., Giovanelli R., Haynes M., 2005, ApJ, 622, 853
Coles P., Barrow J., 1990, MNRAS, 244, 557
Cooper M., Newman J., Madgwick D., Gerke B., Yan R., Davis M., 2005, ApJ, 634, 833
Da Rocha C., Ziegler B. L., Mendes de Oliveira C., 2008, MNRAS, 388, 1433
De Propris R., Conselice Ch., Liske J., Driver S., Patton D., Graham A., Allen P., 2007, ApJ, 666, 212
Dressler A., 1980, ApJ, 236, 351
Ebeling H., Wiedenmann G., 1993, Phys. Rev., 47, 704
Einasto M., Einasto J., Muller V., Heinamaki P., Tucker D. L., 2003, A&A, 401, 851
Geller M. J., Kenyon S. J., Barton E. G., Jarrett T. H., Kewley L. J., 2006, AJ, 132, 2243
Gerke B. F. et al., 2005, ApJ, 625, 6
Girardi M., Manzato P., Mezzetti M., Giuricin G., Limboz F., 2002, ApJ, 569, 720
Gomez P. et al., 2003, ApJ, 584, 210
Gonzales J. A., Quevedo H., Salgado M., Sudarsky D., 2000, A&A, 362, 835
Icke V., van de Weygaert R., 1987, A&A, 184, 16
Ikeuchi S., Turner E., 1991, MNRAS, 250, 519
Jackson J., 1972, MNRAS, 156, 1
Karachentsev I., 1966, Astrofizika, 2, 81
Karachentsev I., 1972, Soobshch. Spets. Astrofiz. Obs., 7, 1
Karachentsev I., 1987, Double Galaxies. Nauka, Moscow (in Russian)
Karachentseva V., 1973, Soobshch. Spets. Astrofiz. Obs., 8, 3 (KIG)
Karachentsev I., Makarov D., 1996, AJ, 111, 794
Karachentseva V. E., Karachentsev I. D., 2000, Astron. Rep., 44, 501
Karachentsev I. D., Kasparova A. V., 2005, Astron. Lett., 31, 152
Karachentseva V. E., Karachentsev I. D., Sherbanobsky A. L., 1979, Izv. SAO, 11, 3
Karachentsev I., Karachentseva V., Lebedev V., 1989, Izv. SAO, 27, 67
Karachentseva V. E., Melnyk O. V., Vavilova I. B., Makarov D. I., 2005, Kin. Phys. Celest. Bodies, 21, 217
Kauffmann G., White S., Heckman T., Menard B., Brinchmann J., Charlot S., Tremonti C., Brinkmann J., 2004, MNRAS, 353, 713
Kiang T., 1966, Z. Astrophys., 64, 433
Kim R. et al., 2002, AJ, 123, 20
Lambas D. S., Tissera P. B., Alonso M. S., Coldwell G., 2003, MNRAS, 346, 1189
Lewis J. et al., 2002, MNRAS, 334, 673
Lindenbergh R. C., 2002, PhD thesis, Univ. Utrecht
Lopes P., de Carvalho R., Gal R., Djorgovski S. G., Odewahn S. C., Mahabal A. A., Brunner R. J., 2004, AJ, 128, 1017

Makarov D. I., Karachentsev I. D., 2000, in Valtonen M. J., Flynn C., eds, ASP Conf. Ser. Vol. 209, Small Galaxy Groups. Astron. Soc. Pac., San Francisco, p. 40
Makarov D. I., Karachentsev I. D., 2007, in Davies J. I., Disney M. J., eds, Proc. IAU Symp. 244, Cambridge Univ. Press, Cambridge, p. 370
Marinoni C., Davis M., Newman J., Coil A., 2002, ApJ, 580, 122
Martinez H., Muriel H., 2006, MNRAS, 370, 1003
Matsuda T., Shima E., 1984, Prog. Theor. Phys., 71, 205
Melnyk O. V., 2006, Astron. Lett., 32, 302
Melnyk O. V., Vavilova I. B., 2006, Kinematika Fiz. Nebesnykh Tel, 22, 422
Melnyk O. V., Elyiv A. A., Vavilova I. B., 2006, Kinematika Fiz. Nebesnykh Tel, 22, 283
Mulchaey J., Davis D., Mushotzky R., Burstein D., 2003, ApJS, 145, 39
Nikolic B., Cullen H., Alexander P., 2004, MNRAS, 355, 874
Panko E., Flin P., 2006, J. Astron. Data, 12, 1
Park C., Choi Y., Vogeley S., Gott J., III, Blanton M., 2007, ApJ, 658, 898
Park C., Gott R., III, Yun-Young C., 2008, ApJ, 674, 784
Patton D. R., Carlberg R. G., Marzke R. O., Pritchet C. J., da Costa L. N., Pellegrini P. S., 2000, ApJ, 536, 153
Patton D. R. et al., 2002, AJ, 565, 208
Patton D. R., Grant J. K., Simard L., 2005, AJ, 130, 2043
Prada F. et al., 2003, ApJ, 598, 260
Ramella M., Boschin W., Fadda D., Nonino M., 2001, A&A, 368, 776
Reda F., Forbes D., Beasley A., O'Sullivan E., Goudfrooij P., 2004, MNRAS, 354, 851
Soares D. S. L., 2007, AJ, 134, 71
Stocke J., Keeney B., Lewis A., Epps H., Schild R., 2004, AJ, 127, 1336
SubbaRao M., Szalay A., 1992, ApJ, 391, 483
SubbaRao M., Szalay A., Gulkis S., von Gronefeld P., 1994, ApJ, 420, 474
Tago E., Einasto J., Saar E., Tempel E., Einasto M., Vennik J., Muller V., 2008, A&A, 479, 927
Trofimov A. V., Chernin A. D., 1995, AZh, 72, 308
van de Weygaert R., 1991, MNRAS, 249, 159
van de Weygaert R., 1994, A&A, 283, 361
van de Weygaert R., Icke V., 1989, A&A, 213, 1
van de Weygaert R., Schaap W., 2007, preprint (arXiv:0708.1441v1)
Vavilova I. B., Karachentseva V. E., Makarov D. I., Melnyk O. V., 2005, Kinematika Fiz. Nebesnykh Tel, 21, 3
Verley S. et al., 2007, A&A, 472, 121
Voronoi G., 1908, Reine Angew. Math., 134, 198
Weinmann S., van den Bosch F., Yang X., Mo H., 2006, MNRAS, 366, 2
Williams B., Peacock J., Heavens A., 1991, MNRAS, 252, 43
Woods D. F., Geller M. J., Barton E. J., 2006, AJ, 132, 197
Xu C. K., Sun Y. C., He X. T., 2004, ApJ, 603, L73
Zamnetti L., 2006, Chin. J. Astron. Astrophys., 6, 387

APPENDIX A: RADIAL AND PROJECTED DISTANCE

To avoid the fingers-of-God effect, we used the correction factor in the calculation of space distance between galaxies. If the projected r and radial v distances were equivalent, we should calculate a space distance between two galaxies as

$$d^2 = v^2 + r^2. \tag{A1}$$

Obviously, we work in the space of radial velocities and by r we mean $r \times H_0$. We inserted the certain factor $k < 1$ as a weight of the radial component. This factor is responsible for the relative virial motion of galaxies. In that case, the modified distance is $m^2 = v^2k^2 + r^2$. After some transformations, we obtained the equation of an ellipse:

$$v^2\frac{k^2}{m^2} + r^2\frac{1}{m^2} = 1, \tag{A2}$$

where m is the minor semiaxis and $\frac{m}{k}$ is the major semiaxis of the ellipse. We took into account some tolerance v_p in measuring v. For that we labelled the major semiaxis as $\frac{m}{k} = d + v_p$, where d^2 is a distance in the space of radial velocities according to equation (A1). So the weight of the radial component is $k = \frac{m}{d+v_p}$. Since the new distance m is a part of the formula for k, therefore for the simplification we used here $m = d$ and obtained the new distance

$$m^2 = \frac{v^2}{\left(1+\frac{v_p}{d}\right)^2} + r^2. \tag{A3}$$

In the case of $v_p = 0$, the formula (A3) changes to (A1). If the galaxies are located at a great distance $d \gg v_p$, formula (A3) also changes to (A1). So in these cases, the virial velocities have a weak action on the distance measurement accuracy. If $d \sim v_p$, then $1 + \frac{v_p}{d} > 1$, i.e. the weight of the radial distance decreases. In the case $d \ll v_p$, the denominator $(1 + \frac{v_p}{d})^2$ tends to infinity and the radial component loses significance, while the projected distance r keeps it. For our calculations, we used $v_p = 300\,\mathrm{km\,s^{-1}}$ as the value of typical relative velocities in small galaxy systems (Ceccarelli et al. 2005). Moreover, Karachentsev et al. (1989) showed that the majority of physically bound triplets have rms velocity $S_v < 300\,\mathrm{km\,s^{-1}}$.

To test the robustness of our method, we compared the main parameters in the cases of different v_p. Table 7 presents the medians and quartiles of S_v and R_h for the obtained galaxy pairs at $v_p = 100$ and $500\,\mathrm{km\,s^{-1}}$, respectively. The dependences S_v, R_h on v_p are not significant (see Table 2 for comparison). Increasing v_p by five times produces a change of rms velocity and projected distance between galaxies by 1.4 times only. In our paper, we choose the compromise value $v_p = 300\,\mathrm{km\,s^{-1}}$. So, such an approach lets us avoid the mistaken identification of wide pairs with a small velocity difference.

Table 7. Physical properties of pairs in dependence on isolation parameter and v_p.

Pairs	N	S_v	R_h
	$v_p = 100\,\mathrm{km\,s^{-1}}$		
All geometric	2211	19^{+15}_{-10}	399^{+360}_{-219}
$p > 2.93$	1658	17^{+14}_{-9}	308^{+226}_{-164}
$p > 4.72$	1005	14^{+8}_{-8}	222^{+163}_{-115}
$p > 8.15$	553	12^{+7}_{-6}	142^{+92}_{-66}
	$v_p = 500\,\mathrm{km\,s^{-1}}$		
All geometric	2210	24^{+21}_{-13}	338^{+331}_{-191}
$p > 3.83$	1657	22^{+17}_{-12}	237^{+200}_{-120}
$p > 6.15$	1105	20^{+15}_{-10}	167^{+139}_{-84}
$p > 11.19$	553	17^{+10}_{-9}	100^{+65}_{-45}

This paper has been typeset from a TEX/LATEX file prepared by the author.

2.3 Висновки до розділу 2

У роботі [2] для визначення модуля відстані галактик тренувалися п’ять моделей машинного навчання. Використовувалися спостережувані дані, такі як видимі зоряні величини у кількох смугах, кутовий діаметр, поверхнева яскравість, показники кольору та координати галактик, променева швидкість, а також відомий модуль відстані у якості цільової змінної. Було показано, що модель нейронної мережі з двома прихованими шарами дає точніший результат, ніж інші моделі. Отримана середньоквадратична похибка становить 0.35 зоряних величин, що відповідає відносний похибці 16 % (таблиця 2 у роботі [2]) для розглянутих червоних зміщень $z < 0.2$. Це співмірно з похибками методів Таллі-Фішера та Фундаментальної площини. Зауважимо, що для близьких галактик метод дає ще кращу точність: похибка зростає з 0.2 до 0.4 при радіальних швидкостях менших 10000 км/с. Це можна пояснити зменшенням внеску високоточних вимірювань відстаней методами зірок типу цефеїди та RR Ліри на визначення модуля відстані.

У разі відсутності даних щодо швидкостей V_{LG}, наш метод дає похибку 0.44 з.в. (20 %), яка все ще прийнятна для оцінки модуля відстані і дослідження великомасштабної структури Всесвіту та еволюції галактик. Зокрема, цей альтернативний підхід корисний тоді, коли у нас немає даних про радіальні швидкості галактик, але достатньо фотометричних та інших даних. Як відомо, отримання спектроскопічних відстаней за червоним зміщенням галактик потребує більшого часу спостережень (експозиції), що не завжди прийнятно під час проведення широких за площею небесної сфери оглядів неба, орієнтованих на отримання якомога більшого за кількістю масиву фотометричних даних про галактики.

Запропонований метод машинного навчання корисний, зокрема, для вимірювання відстаней до галактик з $V_{\mathrm{LG}} > 10000$ км/с, де основні методи

не працюють. Тому регресійна модель на основі нейронної мережі, розроблена в роботі [2], є конкурентоспроможною у порівнянні з загальновживаними вторинними методами вимірювань $m - M$, такими, як Фундаментальна площина та відношення Таллі-Фішера.

Загалом, методи машинного навчання в сучасній науці відіграють величезну роль під час каталогізації великої кількості будь-яких астрофізичних об'єктів і особливо корисні при класифікації з використанням оглядів всього неба. Зокрема, машинне навчання активно застосовують для пошуку та класифікації наднових, екзопланет, відстеження змінності яскравості зірок, для знаходження важливих коливаннь активності Сонця, визначення місцезнаходження астероїдів, комет та інших слабких об’єктів у Сонячній системі, а також морфологічної класифікації галактик. Зокрема верифікацію різних методів машинного навчання для морфологічної класифікації галактик огляду неба SDSS DR9 за фотометричними даними і зображеннями виконано в роботах [30] та [31].

У роботі [30] зроблено порівняння результатів бінарної класифікації галактик на ранні E та пізні L типи, отриманих традиційними методами, такими як візуальна класифікація, колір-колір діаграми та ін. з результатами, отриманими методами машинного навчання. Було показано, що методи машинного навчання, такі як метод опорних векторів та випадкового лісу, продемонстрували значно меншу упередженість, ніж оцінка морфології, заснована на вищеназваних загальноприйнятих методах. Зокрема, точність класифікації становила 96,4 % для методу опорних векторів та 95,5% для випадкового лісу.

У роботі [31] було застосовано нейронну мережу до вибірки зображень галактик на малих червоних зміщеннях з метою визначення наступних морфологічніх класів галактик: округлі, майже округлі, гладкі сигароподібні, видимі з ребра, спіральні. Точність класифікації 216148

галактик цієї вибірки становить 93 %. Крім того, створено каталоги з визначеними 34 детальними морфологічні особливостями галактик, такими як наявність бару, кілець, кількість спіральних рукавів, ознаки злиття тощо для понад 160000 галактик. Вперше показано, що застосування моделі нейронної мережі покращує морфологічну класифікацію слабкіших за $m_r < 17.7$ галактик огляду SDSS.

Було застосовано геометричний метод Вороного вищих порядків для виділення галактик, пар та триплетів з вибірки огляду SDSS [12]. Такий підхід дозволив визначити ступінь ізольованості групи галактик. Було знайдено, що галактики в ізольованих парах та триплетах мають світність у два рази вищу, ніж ізольовані галактики. Також, групи галактик у більш тісному оточені – наприклад, що знаходяться у скупченнях, мають більшу дисперсію швидкостей та відношення маси до світності. Завдяки визначенню ступеня ізольованості галактики методом Вороного, було підтверджено відмінності в оточенні галактик ранніх та пізніх типів у малонаселених системах: чим щільніше оточення навколо галактики, тим ймовірніше, що вона має ранній тип, ніж пізній. Цей висновок є підтвердженням відомого співвідношення «морфологія-густина» [81].

Відмітимо декілька із цитувань нашого дослідження [12]. У роботі [82] було зазначено, що даний підхід здатен знаходити складні структури у розташуванні найближчих сусідів. У роботі [83] було акцентовано нашу роботу як одну з небагатьох, де досліджувалися триплети галактик SDSS; автори роботи [84], які вивчали критерії ізольованості та властивості дуже ізольованих галактик, та роботи [85] враховували результати нашого застосування мозаїк Вороного вищих порядків для виділення малонаселених систем галактик як обґрунтування доцільності обраних критеріїв ізольованості.

Розділ 3. ГАЛАКТИКИ З АКТИВНИМИ ЯДРАМИ ТА ОСОБЛИВОСТІ ЇХНЬОГО ВЕЛИКОМАСШТАБНОГО РОЗПОДІЛУ

Вивчення об’єктів великомасштабної структури Всесвіту на далеких відстанях призводить до необхідності створення глибоких оглядів позагалактичних об'єктів. Такі спостереження проводяться практично у всіх доступних діапазонах довжин хвиль. Рентгенівські спостереження становлять важливу їхню частину через слабке міжгалактичне поглинання при таких високих енергіях. Більше 95 % всіх виявлених об'єктів в рентгенівському діапазоні далеко від площини Галактики є точковими джерелами, переважно галактики з активними ядрами (АЯГ), інші, в основному, це протяжні джерела – насамперед скупчення і групи галактик. Завдяки високій рентгенівської світності, АЯГ можуть бути виявлені в широкому діапазоні червоних зміщень, аж до $z = 4$, на відміну від нормальних галактик. Отже, ці об'єкти є відмінними мітками космічної веб-структури (войдів, філаментів, стін, скупчень галактик) і зручним інструментом для вивчення еволюційних явищ у Всесвіті.

Для всебічного вивчення АЯГ необхідним є створення статистично репрезентативних вибірок, спостережуваних єдиним інструментом у неперервній ділянці неба. З цією метою у різні роки було проведено декілька десятків спостережуваних програм протягом останніх 25 років з різним покриттям та глибиною: наприклад, неглибокий огляд неба ROSAT нараховував 670 АЯГ, більша частина яких мать червоні зміщення до z=0.5 [37, 52], глибокий огляд XMM-COSMOS, спостережуваний на двох кв. градусах, містить ~ 1800 АЯГ здебільшого до $z = 4$ [37, 53]. Безпрецедентну глибину до $z = 6$ функції світності по всьому небу забезпечує німецько-

російська обсерваторія eROSITA [54], але спостережувані дані залишаться недоступні принаймні наступні декілька років.

Поле рентгенівського огляду проміжної глибини XXL складається з двох ділянок у північній і південній півкулях по 25 кв. гр. кожна, спостережуваних з експозицією близько 10 год космічним телескопом XMM-Newton. Огляд містить близько 40000 джерел у м'якому (0.5-2 кеВ) та 25000 в жорсткому (2–10 кеВ) рентгенівському діапазоні до граничних потоків як: $F_{0.5\text{-}2\ keV} = 3\cdot10^{-15}$ ерг/(с·см^2) та $F_{2\text{-}10keV} = 1\cdot10^{-14}$ ерг/(с·см^2) при ймовірності детектування 50 % [19, 23]. Огляд налічує декілька тисяч АЯГ з повнотою до $z = 1$ [13].

Огляд XXL є унікальною лабораторією для вивчення АЯГ та скупчень/груп галактик, оскільки крім рентгенівського покриття огляд містить дані про багатохвильові спостереження небесних об’єктів від радіо та інфрачервоного до ультрафіолетового діапазонів [16, 22, 26, 27], а також спектральні спостереження червоних зміщень [18, 24]. Зокрема, вивчення кластеризації АЯГ (розділ 3.1) надає інформацію про флуктуації густини речовини на різних масштабах, важливу для уточнення космологічних параметрів, з’ясування впливу оточення на галактики та АЯГ, як і дозволяє уточнити уніфіковану схему АЯГ [51] та зробити висновки щодо еволюції цих об’єктів (розділ 3.2). XXL огляд є також плацдармом для пошуку та дослідження гравітаційно-лінзових об’єктів, – таку спробу ми зробили, вона описана у підрозділі 3.4.

Аналіз населення скупчень галактик на $z \sim 1$ актуальний для розуміння еволюції галактик та АЯГ у тісному оточенні та впливу оточення на зорeутворення в галактиках [14, 15, 17, 20, 21, 25]. Наприклад, у роботі [21] було показано, що кількість АЯГ у надскупченнях значно перевищує очікувану кількість АЯГ серед населення поля (низька щільність галактик), а частка

АЯГ у скупченнях антикорелює з масою скупчення [15]. При цому, АЯГ у скупченнях проміжних мас не є активнішими, ніж у загальному полі [25]. Було також показано, що оточення грає головну роль у кількості галактик з активних зореутворенням у скупченнях [17], а злиття галактик – у зростанні маси центральної найяскравішої галактики скупчення [20].

3.1 Кореляційні властивості розподілу АЯГ в рентгенівському огляді XXL

Найпростіша версія уніфікованої моделі [51] передбачає, що різні типи АЯГ, такі як Сейферти 1 та 2 типів, а також АЯГ з широкими та вузькими емісійними лініями (їх ще називають незатмарені та затьмарені або 1 та 2 типів) є одними і тими ж самими об’єктами, по-різному орієнтованими до променя зору. Однак, багато авторів, цитованих у [5, 13, 33], знаходили різні відмінності у властивостях та оточенні двох типів АЯГ, що може бути пояснено 1) спостережуваними ефектами селекції, 2) насправді різними властивостями цих об’єктів або 3) різними стадіями еволюції одних і тих самих об’єктів. Таким чином, дослідження оточення та властивостей АЯГ є актуальним для уточнення уніфікованої схеми АЯГ.

Найбільш поширеним підходом для вивчення кластеризації АЯГ є вимірювання двоточкової кутової кореляційної функції. Також, схема кластеризації популяції АЯГ може надати важливу інформацію щодо космографії флуктуацій густини матерії на різних масштабах та космологічних параметрів. Метою роботи [3] було вивчення великомасштабної структури незатмарених та затьмарених рентгенівських АЯГ (5700 точкових джерел, вибраних у м'якому рентгенівському діапазоні 0.5 – 2 кеВ і близько 2500 в жорсткому 2 – 10 кеВ) за допомогою глибокого рентгенівського огляду XMM–LSS розміром 11 кв. гр., що знаходиться у

північному полі XXL, за допомогою метода двоточкової кореляційної функції. Для обчислення кутової кореляційної функції було згенеровано випадкові каталоги джерел для врахування селекційних ефектів при спостереженнях та були розраховані ймовірності детектування об’єктів з чисельних моделювань.

A&A 537, A131 (2012)
DOI: 10.1051/0004-6361/201117983

Astronomy & Astrophysics

Angular correlation functions of X-ray point-like sources in the full exposure XMM-LSS field*

A. Elyiv[1,2], N. Clerc[3], M. Plionis[4,5], J. Surdej[1], M. Pierre[3], S. Basilakos[6,7], L. Chiappetti[8], P. Gandhi[9], E. Gosset[1], O. Melnyk[1,10], and F. Pacaud[11]

[1] Institut d'Astrophysique et de Géophysique, Université de Liège, 4000 Liège, Belgium
e-mail: elyiv@astro.ulg.ac.be
[2] Main Astronomical Observatory, Academy of Sciences of Ukraine, 27 Akademika Zabolotnoho St., 03680 Kyiv, Ukraine
[3] DSM/Irfu/SAp, CEA/Saclay, 91191 Gif-sur-Yvette Cedex, France
[4] Institute of Astronomy & Astrophysics, National Observatory of Athens, Thessio 11810, Athens, Greece
[5] Instituto Nacional de Astrofísica, Óptica y Electrónica, 72000 Puebla, Mexico
[6] Academy of Athens, Research Center for Astronomy and Applied Mathematics, Soranou Efesiou 4, 11527 Athens, Greece
[7] High Energy Physics Group, Dept. ECM, Universitat de Barcelona, Av. Diagonal 647, 08028 Barcelona, Spain
[8] INAF-IASF Milano, via Bassini 15, 20133 Milano, Italy
[9] Institute of Space and Astronautical Science (ISAS), Japan Aerospace Exploration Agency, 3-1-1 Yoshinodai, Chuo-ku, Sagamihara, Kanagawa 252-5210, Japan
[10] Astronomical Observatory, Kyiv National University, 3 Observatorna St., 04053 Kyiv, Ukraine
[11] Argelander Institut für Astronomie, Universität Bonn, Germany

Received 31 August 2011 / Accepted 13 November 2011

ABSTRACT

Aims. Our aim is to study the large-scale structure of different types of AGN using the medium-deep XMM-LSS survey.
Methods. We measure the two-point angular correlation function of ~5700 and 2500 X-ray point-like sources over the ~11 sq. deg. XMM-LSS field in the soft (0.5–2 keV) and hard (2–10 keV) bands. For the conversion from the angular to the spatial correlation function we used the Limber integral equation and the luminosity-dependent density evolution model of the AGN X-ray luminosity function.
Results. We have found significant angular correlations with the power-law parameters $\gamma = 1.81 \pm 0.02$, $\theta_0 = 1.3'' \pm 0.2''$ for the soft, and $\gamma = 2.00 \pm 0.04$, $\theta_0 = 7.3'' \pm 1.0''$ for the hard bands. The amplitude of the correlation function $w(\theta)$ is higher in the hard than in the soft band for $f_x \lesssim 10^{-14}$ erg s^{-1} cm^{-2} and lower above this flux limit. We confirm that the clustering strength θ_0 grows with the flux limit of the sample, a trend which is also present in the amplitude of the spatial correlation function, but only for the soft band. In the hard band, it remains almost constant with $r_0 \simeq 10\ h^{-1}$ Mpc, irrespective of the flux limit. Our analysis of AGN subsamples with different hardness ratios shows that the sources with a hard-spectrum are more clustered than soft-spectrum ones. This result may be a hint that the two main types of AGN populate different environments. Finally, we find that our clustering results correspond to an X-ray selected AGN bias factor of ~2.5 for the soft band sources (at a median $\bar{z} \simeq 1.1$) and ~3.3 for the hard band sources (at a median $\bar{z} \simeq 1$), which translates into a host dark matter halo mass of $\sim 10^{13}\ h^{-1} M_\odot$ and $\sim 10^{13.7}\ h^{-1} M_\odot$ for the soft and hard bands, respectively.

Key words. X-rays: galaxies – galaxies: active – surveys

1. Introduction

The study of the large-scale structure for the universe and of structure formation processes makes it necessary to carry out wide-field surveys of extragalactic objects. These surveys are performed in almost all accessible wavelength bands. X-ray surveys constitute an important part of these surveys because of the weak absorption at such high energies. The most recent and prominent observational X-ray results have been obtained with the *XMM-Newton* and *Chandra* space observatories (Brandt & Hasinger 2005). More than 95% of all detected objects in X-ray surveys away from the galactic plane are point-like and predominantly active galactic nuclei (AGN), the rest are mostly extended sources (groups and clusters of galaxies and relatively nearby galaxies). Owing to their high X-ray luminosity, AGN can be detected over a wide range of redshifts in contrast to normal galaxies (Hartwick & Schade 1989), and therefore these objects are excellent tracers of the cosmic web and a convenient tool for studying evolutionary phenomena in the Universe. It is known that the optical and X-ray classification of type 2 (obscured) AGN agree quite well, see for example Garcet et al. (2007) and references therein. X-ray selected AGN also provide a relatively unbiased census of the AGN phenomenon because obscured AGN, which are largely missed in optical surveys, are included in X-ray surveys.

The clustering pattern of the AGN population can provide important information regarding the cosmography of matter density fluctuations at different scales and the cosmological parameters (e.g., Hickox et al. 2007; Engels et al. 1999; Plionis et al. 2010; Ebrero et al. 2009; Basilakos & Plionis 2009, 2010), the evolution of the AGN phenomenon (e.g., Comastri & Brusa 2008; Koulouridis et al. 2011; Allevato et al. 2011), the relation

* This paper is dedicated to the memory of Olivier Garcet who has initiated the present work just before his sudden death.

between AGN activity and their dark matter halo hosts, supermassive black hole formation (e.g., Mandelbaum et al. 2009; Miyaji et al. 2011; Allevato et al. 2011), and so on. The most common approach to quantify AGN clustering, without redshift information is to measure the AGN two-point angular correlation function (ACF; Akylas et al. 2000; Yang et al. 2003; Manners et al. 2003; Basilakos et al. 2005; Gandhi et al. 2006; Puccetti et al. 2006; Miyaji et al. 2007; Carrera et al. 2007; Garcet et al. 2007; Ebrero et al. 2009), which provides an estimate of how significant the excess of AGN pairs is, within some projected angular separation over that of a random distribution. Once the angular correlation function is measured, it is possible to reconstruct the spatial clustering, under some specific assumptions, using the Limber integral equation (Limber 1953; Peebles 1980). However, spectroscopic follow-up as well as multiwavelength photometric observations in a number of different bands allow us to measure or estimate redshifts for a large number of AGN and to apply the direct spatial correlation analysis (e.g., Gilli et al. 2005; Yang et al. 2006; Gilli et al. 2009; Coil et al. 2009; Cappelluti et al. 2010; Miyaji et al. 2011).

Clustering analyses of the various surveys of X-ray selected AGN in the soft and hard bands have provided a wide range of angular and spatial clustering lengths. Strong indications for a flux-limit clustering dependence appear to reconcile most of the diverse results, however (Plionis et al. 2008; Ebrero et al. 2009; Krumpe et al. 2010).

Another important question is whether the clustering of X-ray selected AGN evolves with time. Gilli et al. (2009) did not find any significant difference between the X-ray AGN clustering below and above $z = 1$. Even so, the X-ray AGN bias factor should evolve with time, and indeed Yang et al. (2006) found a rapid increase of the bias factor with redshift with $b(z = 0.45) = 0.95 \pm 0.15$ and $b(z = 2.07) = 3.03 \pm 0.83$. Similarly, Allevato et al. (2011) estimated the average bias in the COSMOS AGN survey and found a redshift evolution of the bias factor with $b(z = 0.92) = 2.30 \pm 0.11$ and $b(z = 1.94) = 4.37 \pm 0.27$.

The AGN clustering pattern can also be used for the verification of the unification model, because both obscured and unobscured AGN should have identical correlation function, if the orientation of the torus is the only determining factor of the AGN phenomenology. Gilli et al. (2009) used the 2 sq. deg. XMM-COSMOS field and did not find any significant difference in the spatial distribution of the broad and narrow line AGN. Similarly, Ebrero et al. (2009), studying 1063 *XMM-Newton* observations, found consistent correlation properties for sources with high and low hardness ratios, which mostly correspond to obscured and unobscured AGN, respectively. These results postulate that obscured and unobscured objects populate similar environments, which agrees with the unified model of AGN.

However, the analysis of the 9 sq. deg. Bootes multiwavelength survey showed slightly different clustering properties for the two types of AGN (Hickox et al. 2011). Similarly, Puccetti et al. (2006) investigated the central 0.6 sq. deg. region of the ELAIS-S1 field and found that the correlation amplitude in the hard band ($\theta_0 = 12.8'' \pm 7.8''$) is 2.5 times higher than that in the soft band ($5.2'' \pm 3.8''$), but with a weak significance ($\sim 1\sigma$). Gandhi et al. (2006) used the hardness ratio (HR) and divided the point-like sources in mainly obscured ($HR > -0.2$) and unobscured ($HR < -0.2$) subsamples, finding a positive clustering signal only for the obscured sources in the hard band.

In this work we will revisit these questions by presenting the final results of the point-like source distribution of the *XMM-Newton* Large Scale Structure (XMM-LSS) survey of Pierre et al. (2004). In Gandhi et al. (2006) we presented the AGN clustering results based on the previous release of 4.2 sq. deg. of this survey. A weak positive correlation signal was found in the soft band (angular scale $\theta_0 = 6.3'' \pm 3''$ with a slope $\gamma = 2.2 \pm 0.2$). At present the full XMM-LSS field is one of the widest (~11 sq. deg.) medium-deep surveys. It is part of an even larger project, the XXL, observations of which are currently being implemented (Pierre et al. 2011).

In the following sections we present the description of the XMM-LSS survey (Sect. 2). Results of the numerical simulations of the X-ray point-like sources are presented in Sect. 3. Basic properties of the XMM-LSS field, like its source distribution on the sky and the point-source $\log N$–$\log S$ relation, are shown in Sect. 4. Section 5 includes the method used to produce the random catalogs and the ACF analysis for the different samples. Inverting from angular to spatial clustering and the derived bias of AGN are presented in Sects. 6 and 7, respectively, while the main conclusions are listed in Sect. 8.

2. The sample of X-ray point-like sources

In the present correlation function analysis, we have used point-like X-ray sources from the XMM-LSS field, which consists of 87 pointings with maximum available exposures from 10 to 28 ks. Also we used 7 pointings of the independent deeper Subaru/*XMM-Newton* Deep Survey (SXDS) (Ueda et al. 2008) whose data we reanalyzed with our pipeline because it is fully enclosed in the XMM-LSS area, although with a different spacing pattern. For S01 pointing of SXDS we kept only 40 ks chunk to prevent possible source confusion.

Altogether, the XMM-LSS field is contiguous and contains ~5700 sources in the soft (0.5–2 keV) band and ~2500 in the hard (2–10 keV) band, out of which ~180 are extended (mainly galaxy clusters). Although all extended sources were removed from our analysis, it is interesting to note that they were categorized according to their extension likelihood[1] (EXTlike) and core radius (EXT) into two classes: "C1" which are the true extended sources with EXTlike > 33 and EXT > 5″, containing 54 objects, and "C2" which is a class with almost 50 per cent contamination at 15 < EXTlike < 33 and EXT > 5″, containing 129 objects (see Pacaud et al. 2006 for details).

Separately, we have made use of a more uniform XMM-LSS survey for our analysis which consists of 10 ks chunks. This catalog will be published soon (Chiappetti et al., in prep.)

We considered all point-like sources as AGN, although we do expect a ~3% stellar contamination (Salvato et al. 2009). More details about the source classification will be given in Melnyk et al. (in prep.). The sensitivity limits of the joined sample are near 10^{-15} and 3×10^{-15} erg s^{-1} cm^{-2} for the soft and hard bands, respectively.

The average distances between the centers of adjacent pointings were substantially shorter than the FoV diameter of the EPIC cameras to gain a more homogeneous coverage. This caused overlaps between adjacent pointings. Because each pointing was processed individually, the final merged catalog was produced a posteriori (Pierre et al. 2007; Chiappetti et al., in prep.). As a first possibility, we only considered sources with an off-axis distance <10′. In this way, we did not have to consider boundary sources that are often detected with large errors. The total effective area of the fields was 8.3 sq. deg. The distribution of the corresponding 4066 X-ray sources located within

[1] By the term "likelihood" as used hereinafter, we mean formally the log-likelihood.

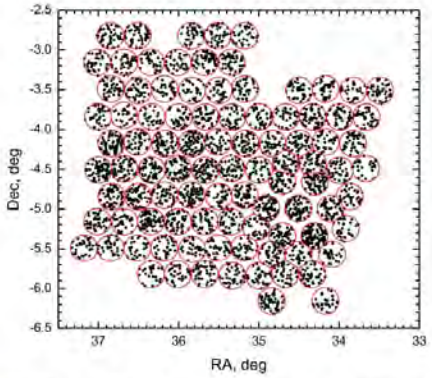

Fig. 1. Distribution of the X-ray point-like sources observed in the soft band within the whole XMM-LSS field with an off-axis distance less than 10′. The red circles represent the borders between the different pointings. Note that even when using the 10′ limitation, we may have some overlapping regions. We discarded these minor overlaps using the Voronoi tessellation method.

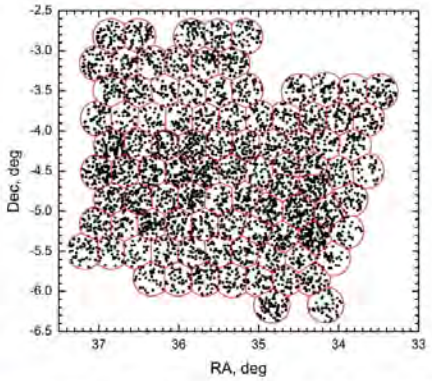

Fig. 2. Distribution of the X-ray point-like sources observed in the soft band within the whole XMM-LSS field with the Voronoi tessellation method. Note that using the Voronoi tessellation we did not exceed the 13′ off-axis distance for any pointing.

the borders is shown in Fig. 1. As an alternative merging possibility we applied a Voronoi boundary delimitation (Matsuda & Shima 1984) without imposing an off-axis cutoff and using sources across the full exposure XMM-LSS field. In other words, in any overlap region among two pointings we only kept those detections in our final catalog that had the shortest off-axis distance. In this way, we were able to use the widest possible area 10.9 sq. deg. of the investigated field. The distribution of the 5093 point-like X-ray sources is shown in Fig. 2. The basic ACF results were checked considering both approaches and it was found that apart from larger uncertainties in the case of the <10′ delimitation method, the results were statistically identical.

3. Simulations of XMM-LSS AGN

For a proper correlation function analysis we need to know the values of the detection probability for each registered source. Therefore we performed extensive simulations of each individual XMM pointing. We briefly describe our procedure and the set of simulations that were used for the representation of the XMM-LSS field.

3.1. Description of the XMM-Newton point-source simulation

The principle of the simulations is similar to the one presented in Pacaud et al. (2006) and Gandhi et al. (2006). The main steps of the procedure consist in i) generating an input source list drawn from a fiducial flux distribution that is randomly distributed across the pointing field of view; ii) simulating images of the field as it would be seen by *XMM-Newton* by reproducing the main instrumental effects (vignetting, PSF distortion, detector masks, background and Poisson noise); iii) detecting sources with the XMM-LSS pipeline (Pacaud et al. 2006) and obtaining their likelihoods and measured count-rates[2]; iv) correlating the detected source list with the input catalog using a 6″ radius and deriving the rates of true and false detections as well as the detection probabilities.

The simulations were performed in the soft and the hard bands. The original source distribution was taken from Moretti et al. (2003) using either their soft or hard band fitting formulae, down to a flux which approximately corresponds to 2 photons on-axis (i.e. below *XMM-Newton* detection limit). This value depends on the exposure time chosen for each particular simulation. Non-resolved AGN photon background was added following Read & Ponman (2003), then we subtracted the contribution of the AGN resolved by our detection algorithm. The constant conversion factor cf between the total count-rates and the physical fluxes S was calculated on the basis of the MOS and PN camera factors provided by Pierre et al. (2007).

Particle background was also added according to values quoted in Read & Ponman (2003) and was subsequently modified by multiplying these values by an arbitrary factor between 0.1 and 8 to allow for pointing-to-pointing background variations. In any case, this component was not vignetted. We summarize our typical background values in Table 1. The PSF model was taken from the *XMM-Newton* medium model calibration files. The vignetting was modeled through its off-axis variation onto each detector.

The detection algorithm provides for each source an estimate of its count-rate on each detector as well as the local background value at the source position. A key parameter is the source detection likelihood. Following Pacaud et al. (2006), this quantity was computed using the C-statistic. Its value is the difference between the likelihood of the best-fitting point-source model and the likelihood of a pure background fluctuation. As such, the source likelihood LH represents the significance of the detection. A value of 15 provides a good balance between contamination and completeness (see Pacaud et al. 2006 and paragraph 3.2 for a discussion of the stability of this criterion).

3.2. Set of simulations

To fully account for the variations of the detection efficiency across the XMM-LSS fields, we simulated 18 900 and 6480 pointings in the soft and the hard bands, respectively. Table 2 details the simulation set. Figure 3 illustrates the influence of exposure time and background ratio value for three

[2] Throughout this paper, count-rates are expressed in terms of total MOS1+MOS2+PN count-rates, corrected for vignetting. That is why two sources with the same count-rate but different off-axis positions will have different probabilities of detection.

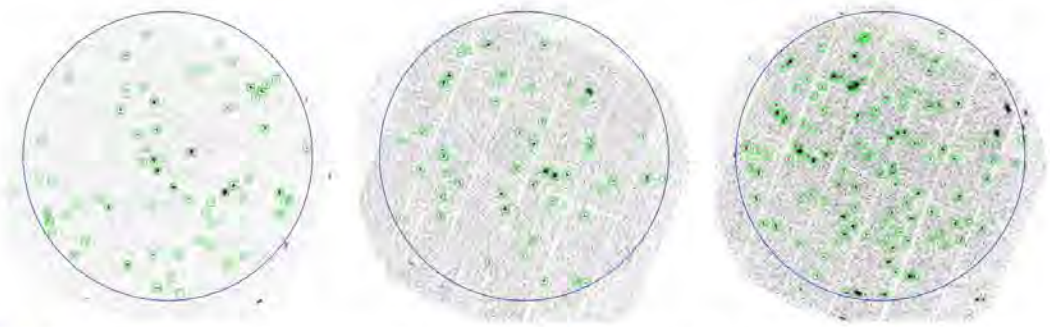

Fig. 3. Examples of simulated *XMM-Newton* pointings in the soft band. The large blue circle indicates the region in which the source detection is performed (13 arcmin maximal off-axis angle). Green boxes indicate the positions of sources detected with a likelihood ML > 15. *Left*: T_{exp} = 10 ks, background ratio = 1; *Middle*: T_{exp} = 10 ks, background ratio = 4; *Right*: T_{exp} = 40 ks, background ratio = 1.

Table 1. Typical background values for the pointing simulations.

	Photon background		Particle background	
	soft band	hard band	soft band	hard band
MOS1	1.21	1.77	0.764	1.16
MOS2	1.32	1.88	0.730	1.09
PN	2.49	3.55	2.80	6.03

Notes. We allowed the particle background to vary from one pointing to the other through a multiplicative factor chosen among 0.1, 0.25, 0.5, 1, 2, 4 and 8. Units for each *XMM-Newton* detector are 10^{-6} cts s^{-1} pixel^{-1}.

Table 2. Summary of the soft and hard band simulation sets.

T_{exp} (ks)	Limiting flux (10^{-16} erg s^{-1} cm^{-2})	Particle background factors	Number of fields
Soft band 0.5–2 keV			
7	1.43	0.1 0.25 0.5 1 2 4 8	7 × 540
10	1	0.1 0.25 0.5 1 2 4 8	7 × 540
20	0.5	0.1 0.25 0.5 1 2 4 8	7 × 540
40	0.25	0.1 0.25 0.5 1 2 4 8	7 × 540
80	0.125	0.1 0.25 0.5 1 2 4 8	7 × 540
Hard band 2–10 keV			
7	14.3	0.1 1 3	3 × 540
10	10	0.1 1 3	3 × 540
20	5	0.1 1 3	3 × 540
40	2.5	0.1 1 3	3 × 540

Notes. The second column refers to the lowest flux of the input simulated sources in the band of interest. Different background levels are accounted for by applying a multiplicative factor to the values from Table 1. This set of simulation encompasses most of the XMM-LSS pointing characteristics.

pointings from our simulation set at 10 and 40 ks and for background ratios 1 and 4.

Thanks to the high number of simulated fields, we were able to bin our results by source off-axis angle. We have chosen six annuli of equal area to obtain approximately the same level of significance in each bin. Values defining the bin bounds are 0, 5.3, 7.5, 9.2, 10.6, 11.9 and 13.0 arcmin.

3.2.1. Completeness/contamination balance

The source selection was based on the detection likelihood value (ML) all detected sources with ML > 15 were included in the final sample of point-like sources. A fraction of these sources comes from false detections. Figure 4 shows the distribution of the recovered sources for three configurations in the innermost off-axis bin (0–5.3 arcmin). We see little dependence of the contamination rate on the background level and exposure time, and the ML = 15 threshold appears as the best choice for homogeneous balance between completeness of the sample and contamination by spurious sources.

We numerically computed the rate of false detections as a function of the off-axis angle, background level and exposure time and in any configuration. The average rate of spurious detections is between 2 and 5 per pointing (up to 13 arcmin off-axis angle). A typical pointing (T_{exp} = 10 ks, background ratio = 1) gives from 40 to 50 detections in the [0–10] arcmin off-axis, which leads to a contamination rate of about 5%.

3.2.2. Detection efficiency as a function of pointing characteristics

We show in Figs. 5–7 the probability curves derived from our simulations. These curves were computed by dividing the number of detected (ML > 15) sources by the number of input sources in a given input count-rate bin and for a given exposure time, background ratio and off-axis bin. The detection efficiency is close to the flux-limited efficiency, whose limit depends on the local pointing characteristics. A strong dependence on the off-axis position is noticeable in Fig. 7 because the effect of vignetting and PSF distortions are growing with off-axis distance. The exposure time dependence (Fig. 5) is compatible with a $\propto\sqrt{T_{exp}}$ improvement factor over the signal-to-noise ratio, while the background level has a milder influence on the detection efficiency. In a typical pointing (T_{exp} = 10 ks, background ratio = 1) the flux limit is 2.5×10^{-15} (4×10^{-15}) erg s^{-1} cm^{-2} at 50% (90%) completeness.

3.2.3. Relating real data to simulations

Sensitivity maps across the entire XMM-LSS field can be derived through interpolation between simulated pointings. The exposure time of a given pointing is a straightforward quantity, as is the off-axis angle at the position of a source. To relate the background ratio quantity to real data, we used estimates of the local background fitted by our detection algorithm

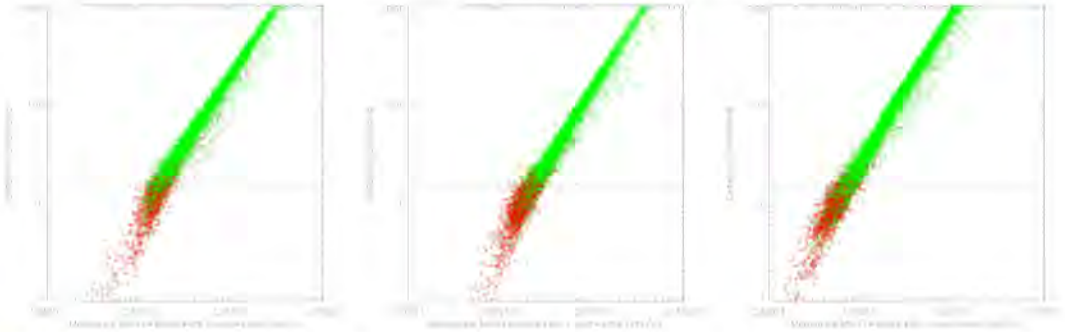

Fig. 4. Examples of likelihood versus count-rate plots for three combinations of pointing exposures and background ratios from our soft band simulation set. Green symbols show detections with a real input counterpart while red points indicate spurious (false) detections. All sources within 5 arcmin from the pointing center are shown here. *Left*: 540 pointings with $T_{\rm exp}$ = 10 ks, background ratio = 1; *Middle*: 540 pointings with $T_{\rm exp}$ = 10 ks, background ratio = 4; *Right*: 540 pointings with $T_{\rm exp}$ = 40 ks, background ratio = 1. The horizontal line corresponds to ML = 15, the threshold above which detected sources are included in the catalog. The separation between false and real detections is relatively independent of the pointing quality.

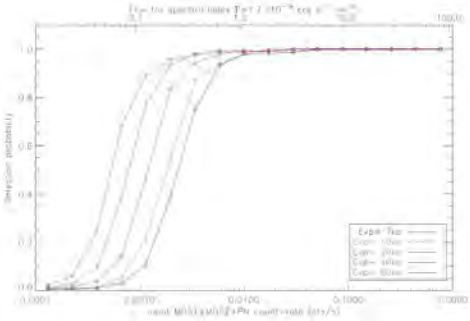

Fig. 5. Efficiency of our source detection algorithm in the innermost annulus (0–5 arcmin) of the simulated soft band XMM observations, as a function of the input source count-rate (or equivalently, flux for a typical AGN spectrum and a galactic hydrogen column density fixed to 2.6×10^{20} cm^{-2}). The exposure time differs from one curve to the other, but not the background rate.

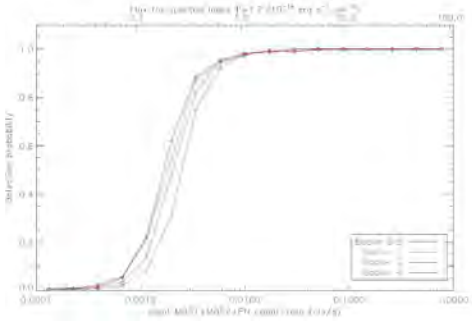

Fig. 6. Same as Fig. 5 for various background rates in the soft band (defined by a multiplicative factor times the values quoted in the 2nd column of Table 1). Exposure time is held at 10 ks in all cases.

at each detected source position (see Pacaud et al. 2006 for a description of the fitting procedure). Estimated numbers of background counts per pixel are put out as two quantities PNT_BG_MAP_MOS and PNT_BG_MAP_PN. Figure 8 shows the relationship between the input background ratio and these quantities as derived from simulations. As expected, local background estimates computed by the detection algorithm are well correlated with the background ratio values introduced in the simulations. We fitted the local background values by PNT_BG_MAP_MOS(PN) using the least-squares method separately for each pointing. With this we determined the background ratio level B, which corresponds to the best parameter of the fitting.

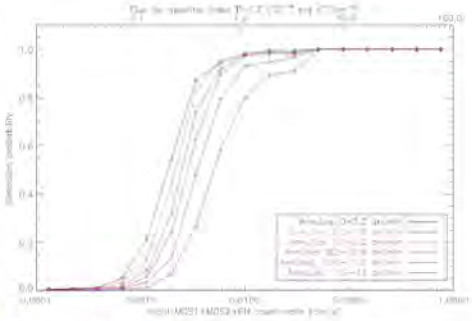

Fig. 7. Same as Fig. 5 for the six off-axis bins in the soft band (see text). Exposure time is held at 10 ks in all cases, and the particle background ratio is set to 1.

4. Sky coverages and log *N*-log *S* distributions

An important characteristic of an X-ray survey is the sky coverage or, in other words, the effective area curve. This indicates the maximum effective area over which we can detect sources brighter than some given flux limit. We have constructed the area curves using the numerically calculated probabilities p to detect sources with a certain flux S, an off-axis distance R in a pointing with some effective exposure T and particle background level B.

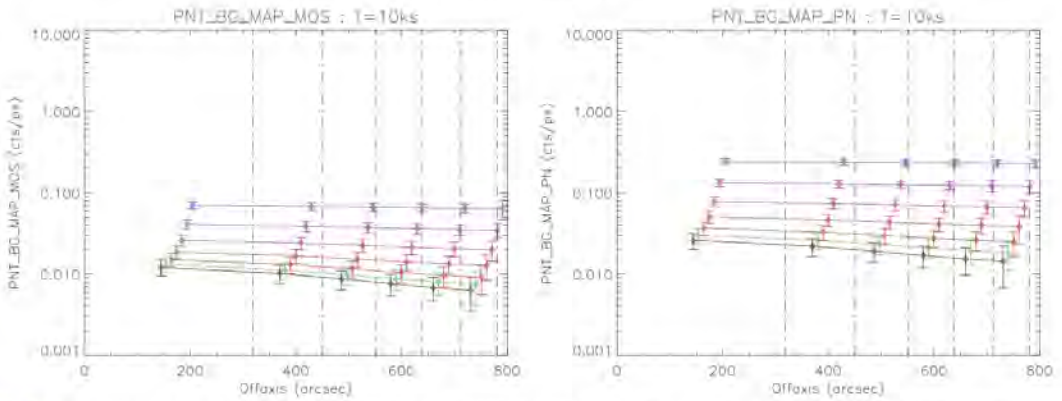

Fig. 8. Pipeline-estimated background values on MOS (*left*) and PN (*right*) detectors, in the soft band, as seen in the simulations. Curves from bottom to top stand for background ratios B equal to 0.1, 0.25, 0.5, 1, 2, 4 and 8. This plot shows how the local background estimate output of the detection algorithm can be related to the background ratio parameter introduced in the simulations. The error bars represent 1-σ standard variation computed from the source sample. The vertical lines correspond to bounds of our equal-area off-axis bins. Only the results for 10 ks are displayed and similar relations are extracted for 7, 20, 40 and 80 ks pointings.

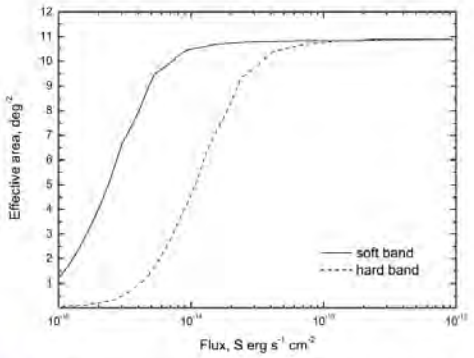

Fig. 9. Effective area curves for the whole XMM-LSS field in the soft (0.5–2 keV) and hard (2–10 keV) bands.

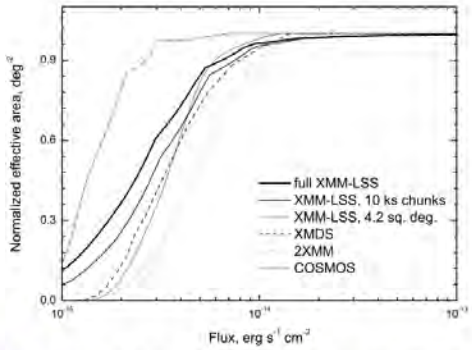

Fig. 10. Comparison of the normalized effective area curves in the soft band for the full exposure XMM-LSS field, the 10 ks version (see Sect. 5.1), the XMM-LSS 4.2 sq. deg. (Gandhi et al. 2006), the XMM Medium Deep Survey (XMDS Chiappetti et al. 2005), the 2XMM (Ebrero et al. 2009) and the COSMOS (Miyaji et al. 2007; Cappelluti et al. 2007).

The effective area $A(S)$ is calculated while integrating over the whole field area Ω:

$$A(S) = \int p(S, R, T, B)\mathrm{d}\Omega. \quad (1)$$

Figure 9 shows the effective area curves for the investigated samples in the soft and hard bands, with a minimum flux 10^{-15} for the soft and 3×10^{-15} erg s^{-1} cm^{-2} for the hard bands. For the construction of the illustrated area curves we used the Voronoi tessellation delimitation method.

Figure 10 shows a comparison between the normalized effective area curves of various recent X-ray surveys. The effective area curve as a function of flux depends mainly on the depth of the source detection (indicated by the signal-to-noise ratio or likelihood thresholds). It also depends on the distributions of the pointing exposures, particle background level and the procedure of handling the pointing overlaps. Evidently, the COSMOS field has the lowest flux limit and the steepest area curve among the considerable surveys with the likelihood limit for the source detection being equal to 6 (Cappelluti et al. 2007).

Our full exposure XMM-LSS survey, having a significant fraction of the contributing pointings with exposures between 10 and 15 ks and a source detection threshold of ML = 15, has the next lowest flux-limit after the COSMOS survey, and a quite steeply increasing area-curve. The corresponding 10 ks XMM-LSS field has its area curve shifted to the right and its flux limit increased by a factor of ~1.2.

Using those area curves and the differential distributions of the sources as a function of their flux, we constructed the log N–log S relation. Note that it is important to take into account the flux boosting. This phenomenon especially affects faint objects with a low detection probability. Owing to Poisson noise, we may detect objects fainter than the flux limit in successful cases and sometimes not detect sources brighter than the flux limit in unsuccessful cases. This may cause the creation of an artificial bump in the log N–log S distribution.

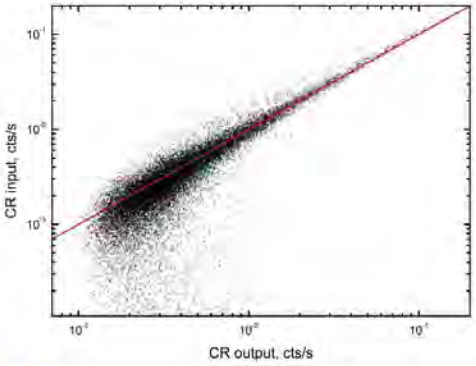

Fig. 11. Example of the dependence between input and output count-rates for the hard band, $T = 20$ ks, $b = 1$. The red line corresponds to $CR_{in} = CR_{out}$.

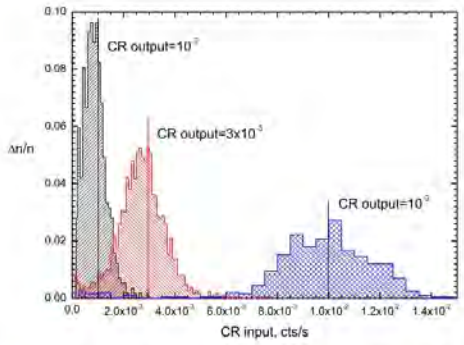

Fig. 12. Distributions of CR_{in} for three detected CR_{out} created on the basis of the simulated distribution in Fig. 11.

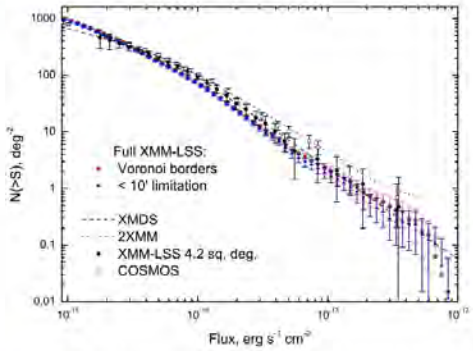

Fig. 13. Log $N-\log S$ distributions in the soft band for the whole XMM-LSS sample and for the two different procedures of handling the pointing overlaps. The results of the XMM Medium Deep Survey (XMDS (Chiappetti et al. 2005), 2XMM (Ebrero et al. 2009), XMM-LSS 4.2 sq. deg. (Gandhi et al. 2006) and COSMOS (Miyaji et al. 2007; Cappelluti et al. 2007) are shown for comparison. The vertical bars denote 1σ uncertainties.

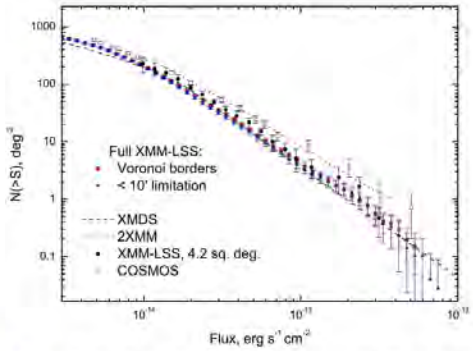

Fig. 14. Log $N-\log S$ distributions in the hard band for the whole sample and for the two different procedures of handling the pointing overlaps. For comparison we present the $\log N-\log S$ distributions for the same samples as in Fig. 13.

To take this effect into account, we used the numerically simulated dependencies between the input CR_{in} and the output CR_{out} count rates individually for each pointing (see Fig. 11 for example). Clearly, when we detect some flux CR_{out}, it corresponds to a real input CR_{in} distributed over a wide range. For each CR_{out} bin we constructed the density probability distribution as a function of CR_{in}. Figure 12 represents the normalized distributions of CR_{in} for three detected CR_{out}. At low flux, we may see an asymmetric shape in the distribution that is shifted toward smaller CR_{in} because of an artificial flux boosting. Therefore, we randomly chose some CR_{in} for each detected source with CR_{out} according to the density probability function. In this way, we carried out Monte-Carlo simulations with the deconvolution of the output into the input rates and constructed $\log N-\log S$ curves for various considered samples (Figs. 13, 14).

The currently estimated $\log N - \log S$ are lower for both bands than those of the 2XMM (Ebrero et al. 2009) and COSMOS (Cappelluti et al. 2007) surveys, with deviations not exceeding the $2–3\sigma$ Poisson level. However, they excellently agree with those derived by Gandhi et al. (2006) and Chiappetti et al. (2005), based on previous releases of XMM-LSS fields. Moreover, the XMDS (Chiappetti et al. 2005) was based on a totally different pipeline used for extracting the X-ray point-like sources. This suggests that the observed deficiency could be an intrinsic characteristic of the XMM-LSS field.

5. The angular correlation function analysis

To determine the ACF, we generated random catalogs in the following way. Firstly, we distributed the fiducial point-like sources with random coordinates over the whole investigated field. Secondly, we chose for each random source a flux according to the $\log N-\log S$ distribution and calculated the probability p of detecting the corresponding point-like source in the relevant pointing, taking into account the exposure time, the particle background level (B) of the pointing and the off-axis distance of the corresponding source. Then, we chose a random number ρ for each random point-like source that is uniformly distributed between 0 and 1. If the ρ value was less than p, we kept the source, if it was higher, we discarded the source. If a random source was closer than 10 arcsec to another one, we removed it because the extension of the EPIC PSF (~6″ minimum, on axis)

prevents one from detecting such close pairs and blends them into a single source. We generated random catalogs in this way that contain 100 times the number of point-like sources in the real source catalog, that was used in the present analysis. The larger the point population of the random catalog, the more accurate the ACF measurement because it suppresses random fluctuations caused by small numbers.

To calculate the ACF, we used two estimators, the Hamilton estimator (Hamilton 1993), as in Gandhi et al. (2006):

$$1 + w(\theta) = f_{\rm H}\frac{DD(\theta)RR(\theta)}{DR^2(\theta)}, \quad (2)$$

and the Landy & Szalay estimator (Landy & Szalay 1993):

$$1 + w(\theta) = f_{\rm LS}\frac{DD(\theta) - 2DR(\theta) + RR(\theta)}{RR(\theta)}, \quad (3)$$

where DD, RR and DR represent the numbers of data-data, random-random and data-random pairs with a separation θ, while $f_{\rm H}$ and $f_{\rm LS}$ are the corresponding normalization factors of the two estimators. In general the two estimators provide consistent results but in any case we will present the results based on both estimators in the correlation function plots.

To speed-up our calculations, we divided the random catalog of those samples with more than 2000 X-ray sources into a maximum of 10 random subcatalogs, and we averaged $w(\theta)$ for each θ bin over the whole random catalogs. Note that we verified by investigating one such sample that the above procedure provides stable correlation results. The $w(\theta)$ uncertainty in each θ-bin is given by

$$\sigma_w = (1 + w)/\sqrt{DD}. \quad (4)$$

The ACF calculations were performed for angular scales in the range: $20'' < \theta < \theta_{\rm max}$, where $\theta_{\rm max} = 12\,000''$. We used $20''$ as our lowest angular-separation limit because of the large size of the *XMM-Newton* PSF near the FoV borders. We verified that pairs, constituted by sources belonging to adjacent pointings, are real only for pair separations $\gtrsim 20''$. We then fitted the resulting ACF with the power-law in the angular range where it was possible, i.e., using only the positive w values:

$$w(\theta) = (\theta_0/\theta)^{\gamma-1}. \quad (5)$$

We analyze here the ACF of the full exposure XMM-LSS field. However, because there are strong indications for a flux-limit dependence of the correlation function amplitude (e.g., Plionis et al. 2008), we also analyzed a homogeneous sample of an effective 10 ks exposure over the whole XMM-LSS region. To this end we cut the event list of the pointings into 10 ks chunks and repeated the source detection procedure from the beginning. We also separately estimated the ACF of samples based on the hardness ratio (HR).

5.1. The whole XMM-LSS field

We first present in Figs. 15 and 16 the ACF results of the full exposure XMM-LSS region for both the soft and hard bands and for the Voronoi delimitation and off-axis angle $<10'$ overlap approaches. In the inset panels we present the 1, 2 and 3σ contours of the fitted parameters in the (θ_0, γ) plane, while in Table 3 we present the corresponding best fit θ_0 and γ parameters and their standard deviation, as well as the value of θ_0 for a fixed slope $\gamma = 1.8$ and the integral ACF signal within separations of 3.3 arcmin, $w(<3.3')$. Evidently, that there are no significant

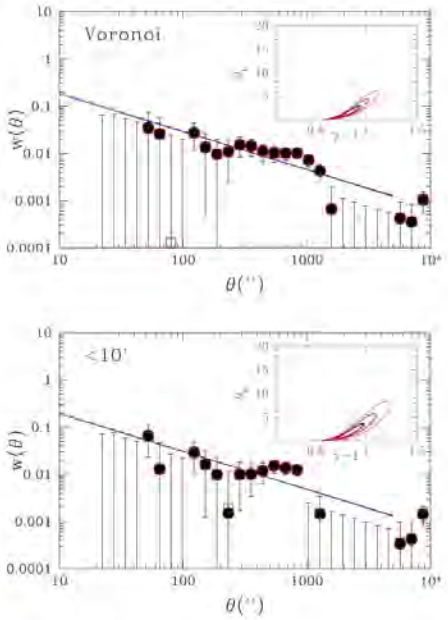

Fig. 15. Soft band ACF for the whole sample: Voronoi delimitation (*top panel*); off-axis angle $<10'$ (*lower panel*). The filled (black) points correspond to the Hamilton estimator while the open (red) squares to the Landy & Szalay estimator. The error bars represent 1σ standard deviation. The dashed line represents the best power-law fit, while the continuous line corresponds to the constant $\gamma = 1.8$ fit. The inset plot presents the 1, 2 and 3σ contours in the fitted (θ_0, γ) parameter space.

Table 3. Soft and hard band correlation functions for the whole XMM-LSS field, as well as for the two possible overlap approaches.

Band	Overlap	N	θ_0''	γ	$\theta''_{0,\gamma=1.8}$	$w(<3.3')$
Soft	Vor.	5093	1.3 ± 0.2	1.94 ± 0.02	1.3 ± 0.2	0.006 ± 0.007
	$<10'$	4066	1.4 ± 0.3	1.81 ± 0.02	1.3 ± 0.2	0.009 ± 0.003
Hard	Vor.	2369	7.5 ± 0.9	2.00 ± 0.03	2.5 ± 0.4	0.075 ± 0.013
	$<10'$	1988	6.5 ± 0.8	1.91 ± 0.03	3.7 ± 0.5	0.080 ± 0.014

Notes. N indicates the number of X-ray sources in the corresponding sample, while the last column shows the integrated ACF signal, and its uncertainty, within $20'' < \theta < 200''$.

differences between the results based on the correlation function estimators (as seen in Figs. 15, 16) or on the two delimitation methods. Therefore we used for the remaining study only the samples based on the space-filling Voronoi delimitation method and the Landy & Szalay ACF estimator (see also Kerscher et al. (2000) for a detailed comparison of different estimators).

Furthermore, we find that the hard band correlation function is slightly but clearly stronger than the corresponding soft band, as can be also verified by comparing the corresponding inset contour plots, which agree with the results of Basilakos et al. (2005), Puccetti et al. (2006) but disagree with those of Ebrero et al. (2009).

As discussed above, to provide a "clean" ACF, that is unaffected by the convolution of (a) the variable flux-limit in the

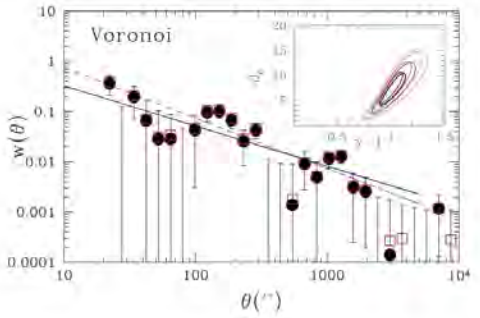

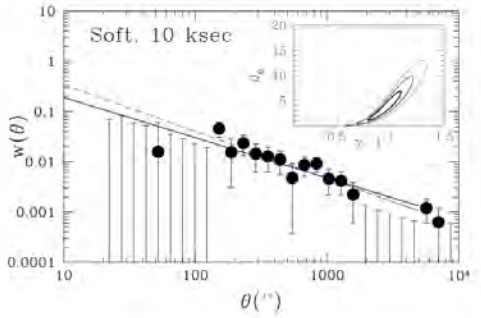

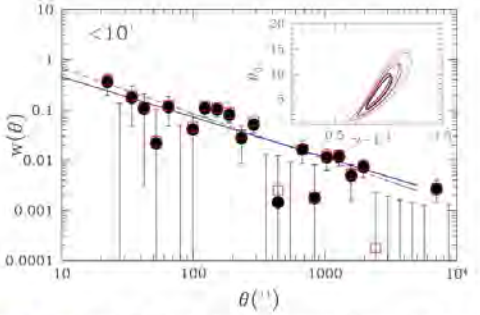

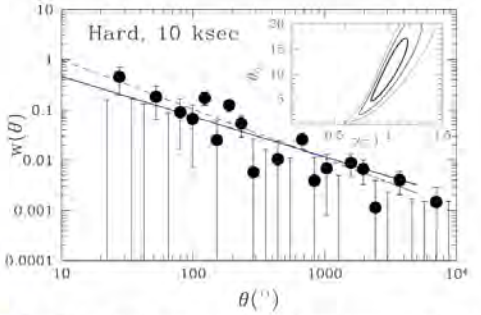

Fig. 16. Hard band ACF for the whole sample: Voronoi delimitation (*upper panel*); off-axis angle <10′ (*lower panel*).

Fig. 17. ACF for the 10 ks sample in the soft band (*upper panel*) and for the hard band (*lower panel*).

Table 4. Correlation function for the 10 ks chunk samples.

Band	N	θ_0''	γ	$\theta''_{0,\gamma=1.8}$	$w(<3.3')$
Soft	4360	3.2 ± 0.5	1.93 ± 0.03	1.3 ± 0.2	0.005 ± 0.007
Hard	1712	9.9 ± 1.4	1.98 ± 0.04	3.8 ± 0.7	0.092 ± 0.019

different parts of the survey and (b) the flux-limit clustering dependence, we considered a sample with a homogeneous 10 ks exposure time across the whole XMM-LSS area. Table 4 and Fig. 17 show the parameters of the ACFs for both bands. The main variation with respect to the previous analysis is that the ACF difference between the soft and hard bands is now even more prominent.

We also investigated the flux-limit dependence of clustering with our homogeneous 10 ks sample. To this end we estimated the angular clustering length, θ_0 for various flux-limited subsamples by keeping the slope of the ACF fixed to its nominal value of $\gamma = 1.8$. Figure 18 shows the corresponding results for the soft and hard bands. Evidently the known dependence is clearly reproduced with our data, and it will be interesting to investigate whether this dependence is present in the spatial correlation length, via Limber's inversion (see further below). Another interesting result is that the amplitude of the hard band ACF is larger than that of the soft band only in the lowest flux-limits. At flux limits $\geq 10^{-14}$ erg s^{-1} cm^{-2} the trend is reversed and the soft band is stronger than the hard band clustering.

How do our results compare with those of other XMM surveys? With respect to our previous release of the 4.2 sq. deg. XMM-LSS survey (Gandhi et al. 2006), our new catalog

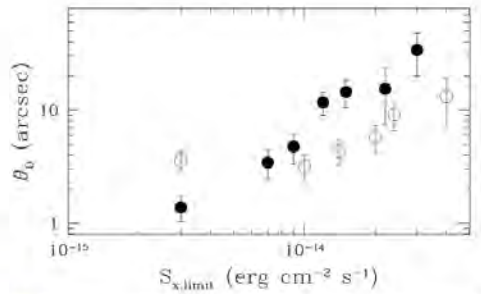

Fig. 18. Best-fit correlation length θ_0 for $\gamma = 1.8$ as a function of the flux limit of the homogeneous 10 ks sample in the soft (filled circles) and the hard bands (open circles).

introduces many improvements. Among them is the wider (by ~2.6 times) sampled area, and the inclusion of a deeper SXDS field. Furthermore, we updated the point-like source detection procedure and introduced a novel definition of the selection function and random-catalog generation procedure.

Our current XMM-LSS area curve is substantially different from that of Gandhi et al. (2006) (see Fig. 10). To investigate the reasons of this difference in detail, we used the 44 pointings common to both studies to compare the corresponding point-like source catalogs in the soft band. The current XMM-LSS catalog contains 2106 objects with off-axis distances less than 10′ and the Gandhi et al. (2006) catalogue contains 1093 such sources,

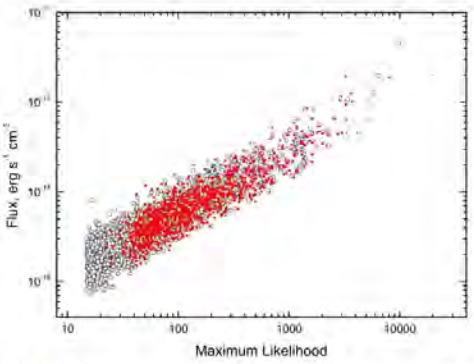

Fig. 19. Dependence between flux and ML in the soft band for the point like sources of 44 pointings from the present XMM-LSS survey (black open circles) and from Gandhi et al. (2006) (red filled circles).

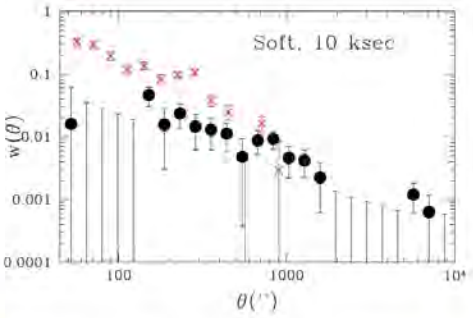

Fig. 20. Soft band ACF comparison between our XMM-LSS survey (filled points) and that of the 2XMM survey (crosses) of Ebrero et al. (2009).

while the common sources are 1048. Figure 19 shows the dependence between flux and ML for both catalogs. Obviously, the chosen ML limit of the Gandhi et al. (2006) catalog is substantially higher than the current limit of ML = 15 and it is equal to ML ~ 40. It is also evident, inspecting Fig. 19, that a value of ML ~ 40 is associated with a significantly higher flux-limit with respect to that of ML = 15, causing the observed difference of the corresponding area curves (see Fig. 10).

The above mentioned changes and improvements, particularly the lower ML detection limit, have resulted in a variation of some of our results with respect to those of Gandhi et al. (2006). Specifically, we found a slightly different clustering signal in the soft band; $\theta_0 = 1.3'' \pm 0.2''$ for $\gamma = 1.81$ vs. $6.3'' \pm 3''$ for $\gamma = 2.2$ in Gandhi et al. (2006). However, at the fixed canonical value of the exponent ($\gamma = 1.8$), the Gandhi et al. (2006) soft band analysis provides a clustering amplitude of $\theta_0 = 1.7'' \pm 0.9''$ versus $1.2'' \pm 0.2''$ for the current XMM-LSS survey. The lower correlation signal of our current XMM-LSS survey should be attributed to the lower ML limit, which introduces a significantly higher fraction of faint sources with respect to the higher ML limit of the Gandhi et al. (2006) catalog. Also, we found a significant clustering signal in the hard band, in contrast to the absence of any significance in Gandhi et al. (2006).

With respect to the COSMOS (Miyaji et al. 2007) and 2XMM (Ebrero et al. 2009) surveys, we find (at fixed canonical $\gamma = 1.8$) a lower soft band correlation function amplitude, $\theta_0 = 1.2'' \pm 0.2''$, compared to $1.9'' \pm 0.3''$ and to $7.7'' \pm 0.1''$ for the COSMOS and the 2XMM surveys, respectively. Our hard band (2–10 keV) XMM-LSS correlation amplitude of $3.6'' \pm 0.7''$ is also lower than the corresponding 2XMM value of $5.9'' \pm 0.3''$, while the COSMOS hard band correlation results are not very significant, probably because they are divided into two sub-bands (2–4.5 and 4.5–10 keV).

Note, however, that the wide contiguous area of the XMM-LSS survey implies that we should have a better estimation of $w(\theta)$ on large angular scales (i.e., $1000'' \lesssim \theta \lesssim 10\,000''$), while COSMOS and 2XMM are limited to ~6000″ and ~1000″, respectively.

In Fig. 20 we compare the soft band $w(\theta)$ of our XMM-LSS and the 2XMM surveys. The large 2XMM $w(\theta)$ amplitude at small angular scales is evident, although at ~1000″ the two correlation functions appear to be consistent. The higher 2XMM correlation amplitude should be attributed to the considerably different mix of faint and bright sources in the two surveys, as shown by their respective area curves (see Fig. 10). The larger part of faint sources in the current XMM-LSS survey causes the lower amplitude of the source angular correlation function with respect to the 2XMM, as expected from the known dependence between clustering and flux-limit (Plionis et al. 2008; Ebrero et al. 2009), a fact which has also been verified by our analysis (Fig. 18).

5.2. Subsamples of sources with soft and hard spectra

An interesting question, that relates to the unification paradigm of AGN, is whether the clustering pattern, among others, of hard and soft-spectrum AGN is comparable. According to the unification paradigm, what determines the appearance of an AGN as obscured or unobscured (type II or I) is its orientation with respect to the observer's line-of-sight. Therefore, there should be no intrinsic difference in their clustering pattern. On this question there have been conflicting results in the literature and we here re-address this with our data.

To this end we compared the correlation function of the hard and soft-spectrum sources by separating them, within each band, using the hardness ratio, HR, indicator defined as

$$\mathrm{HR} = \frac{\mathrm{CR_h} - \mathrm{CR_s}}{\mathrm{CR_h} + \mathrm{CR_s}}, \quad (6)$$

where $\mathrm{CR_s}$ and $\mathrm{CR_h}$ represent the total count rates in the soft and the hard band, respectively. It is known that most of the sources with HR > -0.2 are likely to be obscured (hard-spectrum) AGN; conversely, the sources with HR < -0.2 are mostly (soft-spectrum) unobscured (see Gandhi et al. 2004 for details). Using this criterion, we split the whole sample and derived the log N–log S distributions for each of them in the soft and the hard bands (Fig. 21). Table 5 and Figs. 22, 23 show the parameters and ACFs for the obtained subsamples.

The main result of this analysis is that there is a distinct clustering difference between the sources with hard and soft spectra in the soft band, with the former sources being significantly more clustered. In the hard band the corresponding comparison shows a much weaker difference, in the same direction, but not that significant. However, one also observes that the integrated signal within separations ≤3 arcmin indicates that at least on these small scales the hard-spectrum sources show a stronger clustering signal than the corresponding soft-spectrum ones. Similar

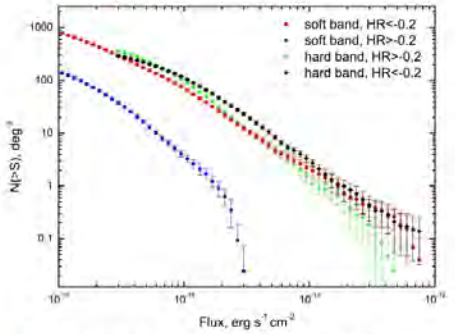

Fig. 21. Log N–log S distributions in the soft and the hard bands for sources with different hardness ratios.

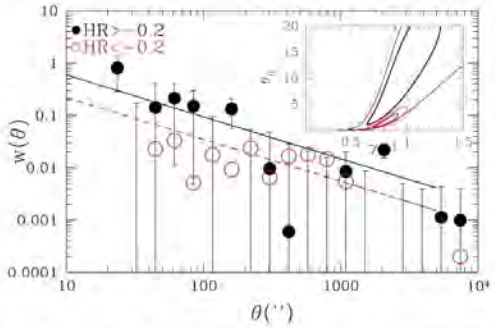

Fig. 22. ACF for the whole XMM-LSS sample in the soft band for sources with HR > −0.2 (filled circles, hard-spectrum AGN), and for sources with HR < −0.2 (open circles; soft-spectrum AGN). Note that for clarity reasons we do not plot the $w(\theta)$ uncertainties of the later sources. The solid line represents the $\gamma = 1.8$ fit to the HR > −0.2 $w(\theta)$, while the dashed line corresponds to the HR < −0.2 $w(\theta)$ fit.

Table 5. Correlation function for the subsamples characterized by their hardness ratio above and below −0.2.

Band	HR	N	θ_0''	γ	$\theta''_{0,\gamma=1.8}$	$w(<3.3')$
Soft	>−0.2	674	10.3 ± 3.3	1.93 ± 0.08	5.2 ± 2.0	0.066 ± 0.048
	<−0.2	4418	1.5 ± 0.2	1.80 ± 0.02	1.5 ± 0.2	0.019 ± 0.005
Hard	>−0.2	1170	10.7 ± 1.7	1.94 ± 0.04	5.5 ± 1.0	0.129 ± 0.028
	<−0.2	1198	13.1 ± 2.4	2.04 ± 0.06	4.4 ± 1.1	0.056 ± 0.026

results were found in Gandhi et al. (2006). Therefore, one may conclude that indeed there are indications for a different clustering pattern between hard-spectrum and soft-spectrum sources, which cannot be attributed to their different flux-limits, since we verified that this result is valid for brighter flux-limits as well. We believe that this result suggests a possible environmental component in the determination of the different types of AGN, beyond their orientation with respect to the observer's line-of-sight. An environmental dependence of the AGN type has also been found in local optical AGN samples (e.g., Koulouridis et al. 2006a,b, 2011, and references therein).

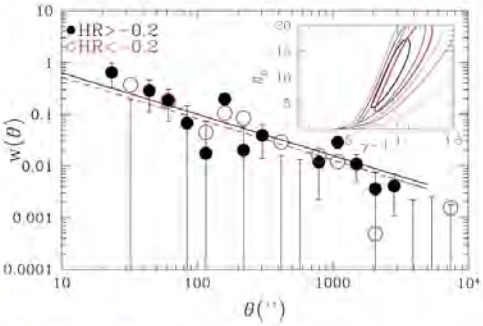

Fig. 23. As in Fig. 22 but for the hard band.

6. Inverting from angular to spatial clustering

We now derive the spatial correlation length that corresponds to the measured angular clustering. To this end we used the usual Limber inversion (Peebles 1980). The main steps are sketched below.

In a spatially flat universe, the ACF $w(\theta)$ can be obtained from the spatial one, $\xi(r)$, by

$$w(\theta) = 2\frac{\int_0^\infty \int_0^\infty x^4\phi^2(x)\xi(r,z)\mathrm{d}x\mathrm{d}u}{[\int_0^\infty x^2\phi(x)\mathrm{d}x]^2}, \quad (7)$$

where the physical separation between any two sources that are separated by an angle θ and considering the small angle approximation, is given by

$$r \simeq \frac{1}{(1+z)}\left(u^2 + x^2\theta^2\right)^{1/2}, \quad (8)$$

while $\phi(x)$ is the selection function (the probability that a source at a distance x is detected in the survey) given by

$$\phi(x) = \int_{L_{\min}(z)}^{\infty} \Phi(L_x, z)\mathrm{d}L, \quad (9)$$

where $\Phi(L_x, z)$ is the redshift-dependent luminosity function of the X-ray selected AGN. A variety of X-ray source luminosity functions are available in the literature, and to investigate the uncertainty that their differences can introduce in the derived value of r_0, we will present results for a number of $\Phi(L_x, z)$. Although the most recent soft/hard band luminosity functions are those of Ebrero et al. (2009), we will also use those of Hasinger et al. (2005) for the soft band, while for the hard band we used those of Ueda et al. (2008) and of La Franca et al. (2005). In all cases we used of course the luminosity-dependent density evolution model of the luminosity function.

The proper distance $x(z)$ is related to the redshift through

$$x(z) = \frac{c}{H_0}\int_0^z \frac{\mathrm{d}y}{E(y)}, \quad (10)$$

with

$$E(z) = [\Omega_\mathrm{m}(1+z)^3 + \Omega_\Lambda]^{1/2} \quad \Omega_\mathrm{m} = 1 - \Omega_\Lambda. \quad (11)$$

In this context, the spatial correlation function can be modeled as in de Zotti et al. (1990)

$$\xi(r,z) = (r/r_0)^{-\gamma} \times (1+z)^{-(3+\epsilon)}, \quad (12)$$

Table 6. Spatial correlation length r_0 (in h^{-1} Mpc), provided by Limber's inversion of the ACF and using different AGN X-ray luminosity functions, for the homogeneous 10 ks sample and for the lowest flux-limit available.

	Soft band		Hard band		
ϵ	Ebrero	Hasinger	Ebrero	La Franca	Ueda
−1.2	6.2 ± 0.7	7.2 ± 0.8	10.1 ± 0.9	9.8 ± 0.9	10.1 ± 0.9
−3	3.2 ± 0.4	3.3 ± 0.4	5.3 ± 0.5	5.2 ± 0.5	5.3 ± 0.5

Notes. The corresponding soft and hard band median redshifts are $\bar{z} \simeq 1.1$ and $\simeq 1$, respectively, while the peaks of the corresponding redshift distributions are at $z \simeq 1$ and 0.7, respectively.

where r_0 is the correlation length in three dimensions and $\epsilon(\equiv\gamma - 3)$ parameterizes the type of clustering evolution. A value of $\epsilon = -1.2$ for $\gamma = 1.8$, indicates a constant clustering in comoving coordinates, while $\epsilon = -3$ indicates a constant clustering in physical coordinates (e.g., de Zotti et al. 1990).

Combining the above system of equations, we obtained the following integral equation for $w(\theta)$

$$w(\theta) = 2\frac{H_0}{c}\int_0^\infty \left(\frac{1}{N}\frac{\mathrm{d}N}{\mathrm{d}z}\right)^2 E(z)\mathrm{d}z \int_0^\infty \xi(r,z)\mathrm{d}u, \quad (13)$$

where $\mathrm{d}N/\mathrm{d}z$ denotes the number of objects in the given survey within a solid angle Ω_s and in the shell $(z, z + \mathrm{d}z)$. It takes the following form:

$$\frac{\mathrm{d}N}{\mathrm{d}z} = \Omega_s x^2 \phi(x)\left(\frac{c}{H_0}\right)E^{-1}(z). \quad (14)$$

Using Eqs. (12), (8) and (13), we find that the amplitude θ_0 in two dimensions is related to the correlation length r_0 in three dimensions through the equation (see Basilakos et al. 2005):

$$\theta_0^{\gamma-1} = H_\gamma r_0^\gamma \left(\frac{H_0}{c}\right)\int_0^\infty \left(\frac{1}{N}\frac{\mathrm{d}N}{\mathrm{d}z}\right)^2 \frac{E(z)}{x^{\gamma-1}(z)}(1+z)^{-3-\epsilon+\gamma}\mathrm{d}z. \quad (15)$$

where $H_\gamma = \Gamma(\frac{1}{2})\Gamma(\frac{\gamma-1}{2})/\Gamma(\frac{\gamma}{2})$.

Following the previous steps, we derived the spatial clustering length scale for fixed $\gamma = 1.8$ and for both values of clustering evolution parameter ($\epsilon = -1.2$ and -3). The results are presented in Table 6. Evidently that all three hard band luminosity functions provide the same r_0 value, while for $\epsilon = -1.2$ there is a difference in the soft band with the Hasinger et al. (2005) $\Phi_s(L)$, providing an r_0 value that is 16% higher than that provided by Ebrero et al. (2009) $\Phi_s(L)$. As we will see, this difference increases proportionally to the flux-limit of the subsample used. In Fig. 24 we present the inverted r_0 values as a function of the different flux limits, as they appear in Fig. 18. We see that for the soft band the two luminosity functions used in the inversion provide r_0 values that diverge with increasing flux-limit.

The dashed lines in Fig. 24 correspond to fits of the data, using for each band results based on all different luminosity functions, of the form:

$$r_0 = A\left(\frac{f_x}{3\times10^{-15}}\right)^\beta, \quad (16)$$

with $(A, \beta) \simeq (6.5, 0.54)$ for the soft band and $(A, \beta) \simeq (9.4, 0.1)$ for the hard band. Evidently, the flux dependence of clustering, once one inverts from angular to 3D space, is preserved mostly in the soft band. In the hard band we see at most a weak dependence and only for fluxes $\gtrsim 2 \times 10^{-14}$ erg s^{-1} cm^{-2}, while a constant

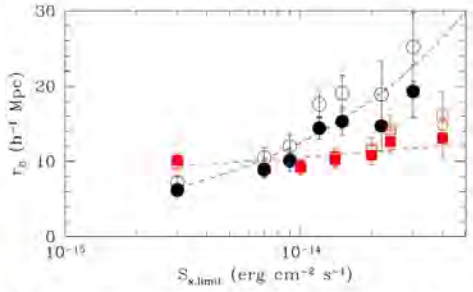

Fig. 24. Spatial correlation length r_0 for $\gamma = 1.8$ and $\epsilon = -1.2$ considering the homogeneous 10 ks based observations as a function of the flux limit of the sample in the soft band (filled and empty circles correspond to the Ebrero and Hasinger $\Phi_s(L)$, respectively) and in the hard band (filled square, open squares and open hexagons correspond to the Ebrero, Ueda and La Franca $\Phi_s(L)$, respectively).

hard band value of $r_0 \simeq 10\ h^{-1}$ Mpc, irrespective of the flux limit, appears also to be consistent with the data. These hard band results agree with those of Ebrero et al. (2009), who found that the weak dependence of θ_0 on the flux-limit translates into a roughly constant r_0 as a function of flux-limit, or equivalently as a function of median redshift or median X-ray luminosity of the sample. However, a relatively strong dependence of the soft band r_0 with respect to the flux-limit disagree with Ebrero et al. (2009), but agrees with Plionis et al. (2008).

7. Bias of the X-ray selected AGN

The concept of biasing between different classes of extragalactic objects and the background matter distribution was introduced by Kaiser (1984) and Bardeen et al. (1986) to explain the higher amplitude of the two-point correlation function of clusters of galaxies with respect to that of galaxies themselves. In our case and within the framework of linear biasing (cf. Kaiser 1984; Benson et al. 2000), the evolution of the bias parameter is usually defined as

$$b^2(z) = \frac{\xi_{\mathrm{AGN}}(8,z)}{\xi_{\mathrm{DM}}(8,z)} = \left[\frac{r_0(z)}{8}\right]^\gamma \frac{1}{\xi_{\mathrm{DM}}(8,z)}, \quad (17)$$

where $\xi_{\mathrm{AGN}}(8,z) = (r_0(z)/8)^\gamma$ and $\xi_{\mathrm{DM}}(8,z)$ are the spatial correlation functions of AGN and dark matter halos evaluated at $8\ h^{-1}$ Mpc, respectively. Notice that the correlation lengths in 3D are presented in Table 6. The correlation function of the DM halos is given by Peebles (1980)

$$\xi_{\mathrm{DM}}(8,z) = \frac{\sigma_8^2(z)}{J_2}, \quad (18)$$

where $J_2 = 72/[(3-\gamma)(4-\gamma)(6-\gamma)2^\gamma]$ and $\sigma_8^2(z)$ is the dark matter density variance in a sphere with a comoving radius of $8\ h^{-1}$ Mpc, which evolves as

$$\sigma_8(z) = \sigma_8 D(z)/D(0). \quad (19)$$

Note that $D(z)$ is the linear growth factor scaled to unity at the present time. For the concordance Λ cosmology[3] the growth factor becomes (see Peebles 1993)

$$D(z) = \frac{5\Omega_{\mathrm{m}}E(z)}{2}\int_z^{+\infty}\frac{(1+y)}{E^3(y)}\,\mathrm{d}y \quad (20)$$

[3] In this work we use $\Omega_{\mathrm{m}} = 1 - \Omega_\Lambda = 0.3$ and $\sigma_8 = 0.80$.

Table 7. Linear bias factor for the lowest flux-limit results of the homogeneous 10 ks XMM-LSS data (and for the same X-ray luminosity functions as in Table 6).

	Soft band		Hard band		
ϵ	Ebrero	Hasinger	Ebrero	La Franca	Ueda
−1.2	2.2 ± 0.2	2.7 ± 0.3	3.3 ± 0.3	3.2 ± 0.3	3.3 ± 0.3
−3	1.2 ± 0.1	1.3 ± 0.1	1.9 ± 0.2	1.8 ± 0.2	1.9 ± 0.2

Finally, inserting Eqs. (19) and (18) into Eq. (17), we obtain the evolution of biasing with epoch as a function of the clustering properties

$$b(z) = \left[\frac{r_0(z)}{8}\right]^{\gamma/2} \frac{J_2^{1/2}}{\sigma_8 D(z)/D(0)}. \quad (21)$$

For angular clustering we may identify the dominant redshift of the sample under study as that predicted by the luminosity function of the sources used and the flux limit of the sample, which predicts the redshift distribution of the sources. We can then obtain from the last equation an estimate of the bias of our X-ray sources (see Table 7). Of course one has to keep in mind that this is a quite crude estimate since we implicitly assume that all detected sources obey the same luminosity function, while in effect luminosity functions are derived from subsamples of all the detected X-ray sources for which optical counterparts are identified.

We see again that although our hard band results roughly agree with those of Ebrero et al. (2009), our soft band results are significantly different, because we found a significantly weaker clustering amplitude than the aforementioned authors.

We can now use a bias evolution model (e.g., Sheth et al. 2001; Basilakos et al. 2008, and references therein) to estimate the halo mass that corresponds to the above estimated bias factors (for $\epsilon = -1.2$), assuming that each halo hosts one AGN source. Using the latter model (see details in Papageorgiou et al., in prep.), we obtain that for the soft band and the Ebrero et al. luminosity function the corresponding halo mass is $M_h \simeq 10^{12.9 \pm 0.3}\ h^{-1}\ M_\odot$, while using the Hasinger luminosity function the corresponding value is $M_h \simeq 10^{13.2 \pm 0.3}\ h^{-1} M_\odot$. For the hard band we find that $M_h \simeq 10^{13.7 \pm 0.3}\ h^{-1} M_\odot$. Note that using the Sheth et al. bias model, we find very similar M_h values (for example, for the hard band results we find $M_h \simeq 10^{13.6}\ h^{-1} M_\odot$).

8. Main conclusions

We have performed a two-point correlation function analysis of the XMM-LSS sample of point sources that contains in total 94 *XMM-Newton* pointings (more than five thousand point-like sources). The observations were made near the celestial equator at high galactic latitudes over ∼11 sq. deg. in the soft (0.5–2 keV) and hard (2–10 keV) bands with effective exposures ranging from 8.1 to 47.3 ks. The minimum flux limits are almost 10^{-15} and 3×10^{-15} erg s^{-1} cm^{-2} for the soft and hard bands, respectively. For the definition of the detection probabilities for each source and for the proper generation of the mock catalogs we performed a series of numerical Monte-Carlo simulations of the *XMM-Newton* observations. The most important points and results of our work are listed below.

To deal with the pointing overlap question, we considered two approaches: that of a 10′ off-axis limitation, and the Voronoi delimitation. No major differences were observed in the derived point-source correlation function between these two approaches. We consequently followed the statistically richer Voronoi delimitation approach, which produces a contiguous field.

The $\log N$–$\log S$ distributions for the soft and hard bands were found to agree well with the results from the previously released XMM-LSS catalog (Gandhi et al. 2006). Using the whole exposure XMM-LSS data, we extended the $\log N$–$\log S$ to lower fluxes, ie., 10^{-15} and 3×10^{-15} erg s^{-1} cm^{-2} for the soft and hard bands, respectively.

The amplitude of the correlation function $w(\theta)$ is significantly higher in the hard band than in the soft band at the lowest fluxes. When analyzing a homogeneous 10 ks extracted sample from the full exposure data, this difference becomes more prominent. At higher fluxes ($f_x \geq 10^{-14}$ erg s^{-1} cm^{-2}) the amplitude of the correlation function becomes higher in the soft band. These results provide a bias factor at a median redshift $\bar{z} \simeq 1.1$ of ∼2.5 for the soft band when inverted to 3D (and for $\epsilon = -1.2$), and at $\bar{z} \simeq 1$ of ∼3.3 for the hard band sources. These bias values correspond to a mass of the halos hosting the AGN sources of $M_h \sim 10^{13 \pm 0.3}\ h^{-1}\ M_\odot$ for the soft band and $M_h \sim 10^{13.7 \pm 0.3}\ h^{-1}\ M_\odot$ for the hard band.

The correlation at degree-scale (≳3000″) nicely extends that observed on an arcmin scale (100–1000″), a result which is obtained thanks to the wide contiguous area covered by the survey.

The hard-spectrum sources show a stronger clustering than the soft-spectrum ones, especially in the soft band. This hints at an environmental dependence of the AGN type.

The amplitude of the spatial correlation function grows with flux limit, but mostly in the soft band. In the hard band there is at most a weak dependence, with a constant value of $r_0 \simeq 10\ h^{-1}$ Mpc, which is consistent with the data.

Acknowledgements. The simulations were performed at the CNRS "Centre de Calcul de l'IN2P3" located in Lyon, France. The authors would like to thank Pierrick Micout for his help regarding the use of the CC-IN2P3. A.E., O.M., E.G. and J.S. acknowledge support from the ESA PRODEX Programme "XMM-LSS", from the "Belgian Federal Science Policy Office" and from the "Communauté française de Belgique – Actions de recherche concertées – Académie universitaire Wallonie-Europe".

References

Akylas, A., Georgantopoulos, I., & Plionis, M. 2000, MNRAS, 318, 1036
Allevato, V., Finoguenov, A., Cappelluti, N., et al. 2011, ApJ, 736, 99
Bardeen, J. M., Bond, J. R., Kaiser, N., & Szalay, A. S. 1986, ApJ, 304, 15
Basilakos, S., & Plionis, M. 2009, MNRAS, 400, L57
Basilakos, S., & Plionis, M. 2010, ApJ, 714, L185
Basilakos, S., Plionis, M., Georgakakis, A., & Georgantopoulos, I. 2005, MNRAS, 356, 183
Basilakos, S., Plionis, M., & Ragone-Figueroa, C., 2008, ApJ, 678, 627
Benson, A. J., Cole, S., Frenk, C. S., Baugh, C. M., & Lacey, C. G. 2000, MNRAS, 311, 793
Brandt, W. N., & Hasinger, G. 2005, ARA&A, 43, 827
Cappelluti, N., Hasinger, G., Brusa, M., et al. 2007, ApJS, 172, 341
Cappelluti, N., Ajello, M., Burlon, D., et al. 2010, ApJ, 716, L209
Carrera, F. J., Ebrero, J., Mateos, S., et al. 2007, A&A, 469, 27
Chiappetti, L., Tajer, M., Trinchieri, G., et al. 2005, A&A, 439, 413
Coil, A. L., Georgakakis, A., Newman, J. A., et al. 2009, ApJ, 701, 1484
Comastri, A., & Brusa, M. 2008, Astron. Nachr., 329, 122
de Zotti, G., Persic, M., Franceschini, A., et al. 1990, ApJ, 351, 22
Ebrero, J., Mateos, S., Stewart, G. C., Carrera, F. J., & Watson, M. G. 2009, A&A, 500, 749
Engels, D., Tesch, F., & Ledoux, C. 1999, Proceedings of the Conference, Highlights in X-ray Astronomy, ed. B. Aschenbach, & M. Freyberg, MPE-Report 272, 218
Gandhi, P., Crawford, C. S., Fabian, A. C., & Johnstone, R. M. 2004, MNRAS, 348, 529
Gandhi, P., Gareet, O., Disseau, L., et al. 2006, A&A, 457, 393
Gareet, O., Gandhi, P., Gosset, E., et al. 2007, A&A, 474, 473
Gilli, R., Daddi, E., Zamorani, G., et al. 2005, A&A, 430, 811
Gilli, R., Zamorani, G., Miyaji, T., et al. 2009, A&A, 494, 33

Hamilton, A. J. S. 1993, ApJ, 417, 19
Hartwick, F. D. A., & Schade, D. 1990, ARA&A, 28, 437
Hasinger, G., Miyaji, T., & Schmidt, M. 2005, A&A, 441, 417
Hickox, R. C., Jones, C., Forman, W. R., et al. 2007, Cosmic Frontiers, ASP Conf. Ser., 379, 181
Hickox, R. C., Myers, A. D., Brodwin, M., et al. 2011, ApJ, 731, 117
Kaiser, N. 1984, ApJ, 284, L9
Kerscher, M., Szapudi, I., & Szalay, A. S. 2000, ApJ, 535, L13
Koulouridis, E., Plionis, M., Chavushyan, V., et al. 2006a, ApJ, 639, 37
Koulouridis, E., Chavushyan, V., Plionis, M., Krongold, Y., & Dultzin-Hacyan, D. 2006b, ApJ, 651, 93
Koulouridis, E., Plionis, M., et al. 2011, ApJ, submitted [arXiv:1111.4084]
Krumpe, M., Miyaji, T., & Coil, A. L. 2010, ApJ, 713, 558
La Franca, F., Fiore, F., Comastri, A., et al. 2005, ApJ, 635, 864
Landy, S. D., & Szalay, A. S. 1993, ApJ, 412, 64
Limber, D. N. 1953, ApJ, 117, 134
Manners, J. C., Johnson, O., Almaini, O., et al. 2003, MNRAS, 343, 293
Mandelbaum, R., Li, C., Kauffmann, G., & White, S. D. M. 2009, MNRAS, 393, 377
Matsuda, T., & Shima, E. 1984, Progr. Theoret. Phys., 71, 855
Miyaji, T., Zamorani, G., Cappelluti, N., et al. 2007, ApJS, 172, 396
Miyaji, T., Krumpe, M., Coil, A. L., & Aceves, H. 2011, ApJ, 726, 83
Moretti, A., Campana, S., Lazzati, D., & Tagliaferri, G. 2003, ApJ, 588, 696
Pacaud, F., Pierre, M., Refregier, A., et al. 2006, MNRAS, 372, 578
Peebles, P. J. E. 1980, The large-scale structure of the universe (Princeton, N.J. Princeton University Press), 435
Peebles, P. J. E. 1993, Principles of Physical Cosmology (Princeton New Jersey: Princeton University Press)
Pierre, M., Valtchanov, I., Altieri, B., et al. 2004, J. Cosm. Astropart. Phys., 9, 11
Pierre, M., Chiappetti, L., Pacaud, F., et al. 2007, MNRAS, 382, 279
Pierre, M., Pacaud, F., Juin, J. B., et al. 2011, MNRAS, 414, 1732
Plionis, M., Rovilos, M., Basilakos, S., Georgantopoulos, I., & Bauer, F. 2008, ApJ, 674, L5
Plionis, M., Terlevich, R., Basilakos, S., et al. 2010, Invisible Universe: Proceedings of the Conference, AIP Conf. Proc., 1241, 267
Puccetti, S., Fiore, F., D'Elia, V., et al. 2006, A&A, 457, 501
Read, A. M., & Ponman, T. J. 2003, A&A, 409, 395
Salvato, M., Hasinger, G., & Ilbert, O. 2009, ApJ, 690, 1250
Sheth, R. K., Mo, H. J., & Tormen, G. 2001, MNRAS, 323, 1
Ueda, Y., Watson, M. G., Stewart, I. M., et al. 2008, ApJS, 179, 124
Yang, Y., Mushotzky, R. F., Barger, A. J., et al. 2003, ApJ, 585, L85
Yang, Y., Mushotzky, R. F., Barger, A. J., & Cowie, L. L. 2006, ApJ, 645, 68

3.2 Вплив оточення на галактики та на активність ядер галактик

Взаємозв'язок між еволюцією материнської галактики та формуванням центральної чорної діри вказує, що має бути залежність між фізичними властивостями АЯГ та оточенням галактики, – цей зв'язок ще не до кінця зрозумілий. Який фактор, що впливає на властивості АЯГ є вирішальним – внутрішня еволюція чи вплив оточення? Чи впливає близьке і далеке оточення АЯГ/галактики на еволюцію чорної діри?

Для пошуку відповідей на ці питання у статтях [13, 33] було розглянуто близьке (<0.4–1 Мпк) та далеке (> 1 Mpc) оточення АЯГ та рентгенівських галактик до z~1 у південному XXL полі (25 кв. град) та частині північного поля XXL XMM-LSS (11 кв. град), відповідно. Головною метою цих робіт було порівняння густини оточення різних типів рентгенівських точкових джерел, попередньо класифікувавши їх у рентгенівському, оптичному, інфрачервоному та радіо діапазонах спектру. У статті [33] було використано методи знаходження фотометричних червоних зміщень для багатохвильових ототожнень рентгенівських об'єктів (~50% з 777). За відсутності червоних зміщень галактик поля, для знаходження надлишків густини біля АЯГ, використовувався оптичний каталог галактик CFHTLS [55]. Пошук надлишків густини проводився у проекції на небесну сферу (2D підхід) – у якості індикатора "сусіда" була застосована різниця видимих величин об'єктів з відповідними K-корекціями. У роботі [13] було також застосовано цей підхід, але всі червоні зміщення для рентгенівських об'єктів було визначено за спектральними спостереженнями, а пошук найближчих сусідів проводився тільки між об'єктами, що мають червоні зміщення. В цій же роботі перколяційним методом було знайдено агломерати АЯГ та скорельовано їхні позиції з розташуванням рентгенівських скупчень галактик.

A&A 620, A6 (2018)
https://doi.org/10.1051/0004-6361/201730479

Astronomy & Astrophysics
Special issue

The XXL Survey: second series

The XXL survey

XXI. The environment and clustering of X-ray AGN in the XXL-South field

O. Melnyk[1,2], A. Elyiv[2], V. Smolčić[1], M. Plionis[3,4,5], E. Koulouridis[6], S. Fotopoulou[7], L. Chiappetti[8], C. Adami[9], N. Baran[1], A. Butler[10], J. Delhaize[1], I. Delvecchio[1], F. Finet[11], M. Huynh[10], C. Lidman[12], M. Pierre[6], E. Pompei[13], C. Vignali[14,15], and J. Surdej[16]

[1] Department of Physics, Faculty of Science, University of Zagreb, Bijenička cesta 32, 1000 Zagreb, Croatia
e-mail: melnykol@gmail.com
[2] Main Astronomical Observatory, Academy of Sciences of Ukraine, 27 Akademika Zabolotnoho St., 03680 Kyiv, Ukraine
[3] Physics Dept., Aristotle Univ. of Thessaloniki, Thessaloniki 54124, Greece
[4] Instituto Nacional de Astrófisica, Óptica y Electrónica, 72000 Puebla, Mexico
[5] IAASARS, National Observatory of Athens, 15236 Penteli, Greece
[6] DSM/Irfu/SAp, CEA Saclay, 91191 Gif-sur-Yvette Cedex, France
[7] Department of Astronomy, University of Geneva, ch. d'Ecogia 16, 1290 Versoix, Switzerland
[8] INAF-IASF Milano, via Bassini 15, 20133 Milano, Italy
[9] Aix Marseille Univ., CNRS, CNES, LAM, Marseille, France
[10] International Centre for Radio Astronomy Research, M468, University of Western Australia, Crawley, WA 6009, Australia
[11] Subaru Telescope, National Astronomical Observatory of Japan, 650 North Aohoku Place, Hilo, HI 96720, USA
[12] Australian Astronomical Observatory, North Ryde, NSW 2113, Australia
[13] European Southern Observatory, Alonso de Cordova 3107, Vitacura, 19001 Casilla, Santiago 19, Chile
[14] Dipartimento di Fisica e Astronomia, Alma Mater Studiorum, Università degli Studi di Bologna, Via Gobetti 93/2, 40129 Bologna, Italy
[15] INAF – Osservatorio Astronomico di Bologna, Via Gobetti 93/3, 40129 Bologna, Italy
[16] Institut d'Astrophysique et de Géophysique, Université de Liège, Allée du 6 Août 19c, 4000 Liège, Belgium

Received 21 January 2017 / Accepted 22 November 2017

ABSTRACT

Context. This work is part of a series of studies focusing on the environment and the properties of the X-ray selected active galactic nuclei (AGN) population from the XXL survey. The present survey, given its large area, continuity, extensive multiwavelength coverage, and large-scale structure information, is ideal for this kind of study. Here, we focus on the XXL-South (XXL-S) field.
Aims. Our main aim is to study the environment of the various types of X-ray selected AGN and investigate its possible role in AGN triggering and evolution.
Methods. We studied the large-scale (>1 Mpc) environment up to redshift $z = 1$ using the nearest neighbour distance method to compare various pairs of AGN types. We also investigated the small-scale environment (<0.4 Mpc) by calculating the local overdensities of optical galaxies. In addition, we built a catalogue of AGN concentrations with two or more members using the hierarchical clustering method and we correlated them with the X-ray galaxy clusters detected in the XXL survey.
Results. It is found that radio detected X-ray sources are more obscured than non-radio ones, though not all radio sources are obscured AGN. We did not find any significant differences in the large-scale clustering between luminous and faint X-ray AGN, or between obscured and unobscured ones, or between radio and non-radio sources. At local scales (<0.4 Mpc), AGN typically reside in overdense regions, compared to non-AGN; however, no differences were found between the various types of AGN. A majority of AGN concentrations with two or more members are found in the neighbourhood of X-ray galaxy clusters within <25–45 Mpc. Our results suggest that X-ray AGN are typically located in supercluster filaments, but they are also found in over- and underdense regions.

Key words. X-rays: galaxies: clusters – galaxies: active – radio continuum: galaxies – quasars: general

1. Introduction

Over the last decade many authors have been studying the local and large-scale environment of active galactic nuclei (AGN), investigating a possible link between nuclear activity, host galaxy properties and environment. For example Gilmour et al. (2009), Constantin et al. (2008), Silverman et al. (2009), Lietzen et al. (2009, 2011), Tasse et al. (2008, 2011), Melnyk et al. (2013), Gendre et al. (2013), and Karouzos et al. (2014a,b) have shown that AGN reside in any type of environment, including underdense and overdense regions. Gilli et al. (2009) did not find any evidence that AGN with broad optical lines cluster differently from AGN without broad optical lines.

On the other hand, others have reported environmental differences between various types of AGN (obscured, unobscured, luminous, faint, FRI, FRII, etc.). In particular, Koulouridis et al. (2006) and Villarroel & Korn (2016) found that Seyfert-2 galaxies (Sy2) have close neighbours more frequently than Seyfert-1 galaxies (Sy1). In addition, these neighbours present evidence of more recent interactions than their Sy1 peers (Koulouridis et al. 2013). Melnyk et al. (2013) found evidence that hard X-ray (obscured) AGN are located in more overdense regions than soft

X-ray (unobscured) ones. Koulouridis et al. (2014) reported a significantly higher frequency of merging for non-hidden broad-line region (HBLR) Sy2s, than for HBLR ones. In an earlier study, Strand et al. (2008) showed that optical luminous AGN inhabit denser environments than low-luminosity ones (however, see Karouzos et al. 2014a).

Gandhi et al. (2006) and Gendre et al. (2013) showed that independently from the radio excitation mode, FRI sources are found to lie in higher density environments than FRII sources. Sabater et al. (2013) outlined the importance of both small-scale and large-scale environmental influence on AGN properties. Low excitation radio galaxies (LERG) or low-to-moderate radiative luminosity AGN (MLAGN) are found in more dense regions than high excitation radio galaxies (HERG) or moderate-to-high radiative luminosity AGN (HLAGN); the modern classification of radio sources can be found in Smolčić et al. (2017). Sabater et al. (2013) explained this by the presence of warmer gas at higher densities than is accreted at low rates in a radiatively inefficient manner, triggering typical low-luminosity radio AGN. The fraction of HERG and optical AGN increases with increasing one-on-one interactions, which can funnel cold gas to the nuclear regions. Similar results were obtained by Ineson et al. (2015).

Differences were also reported for differently selected AGN (optical, IR, radio, or X-ray). Koutoulidis et al. (2013) concluded that X-ray selected AGN reside in significantly more massive dark-matter host halos than optically selected ones. Hickox et al. (2011) and Elyiv et al. (2012) found stronger clustering of obscured than unobscured quasi-stellar object (QSO), contrary to Allevato et al. (2011) and Allevato et al. (2014). However, their samples were differently selected. Karouzos et al. (2014a) compared the environmental properties of X-ray, radio, and IR-selected AGN, and found that X-ray selected AGN reside in more dense environments; radio AGN also prefer overdense regions, but they can be found in a variety of environments. However, a small population of the most luminous radio sources was found in an overdense environment, while the most radio-faint ones were found in underdense regions; IR-selected AGN were found in very local overdensities. Mendez et al. (2016) found that X-ray selected sources are more clustered than IR-selected ones, and linked this difference to their distinct host-galaxy populations. Tasse et al. (2008, 2011) reported that X-ray selected type 2 AGN are located in underdense regions similarly to low-mass radio-loud AGN. However, the high-mass radio-loud AGN prefer overdense regions. Up-to-date observational properties of all AGN types in different electromagnetic bands are summarized in Padovani et al. (2017).

The simplest version of the unified scheme by Antonucci (1993) proposed that different types of AGN, like Seyfert-1 and Seyfert-2 galaxies, as well as broad- and narrow-line AGN/QSOs (i.e. unobscured and obscured AGN) are intrisically the same objects, the only difference being the orientation of an obscuring torus with respect to our line of sight. Therefore, they should present the same environmental properties. However, the reason for the differences reported in the above-mentioned studies might be due to one of the following: 1) selection and observational effects, 2) the intrinsically different properties of different AGN types, or 3) the different evolutionary stages of different AGN types. If cases 2 and 3 are true, the simplest version of the unified scheme cannot fully describe the observational properties of all the different sources and needs to be refined.

To better understand the above issues, the present work is dedicated to the analysis of the small- and large-scale environment and the clustering properties of different types of X-ray selected point-like sources (mainly AGN) in the 25 deg^2 XXL-South (XXL-S) field. This field is now characterized by a homogeneous optical spectroscopic coverage up to $m_i = 21.8$ owing to two recently dedicated spectroscopic campaigns (Lidman et al. 2016, XXL Paper XIV, and Chiappetti et al. 2018, hereafter XXL Paper XXVII). More than 4500 redshifts are available for the optical counterparts of X-ray point-like sources, which mainly consist of AGN. The environmental properties of these AGN are reported for the first time in this field.

In Sect. 2 we present the sample. In Sect. 3, we describe the nearest neighbour analysis, while in Sect. 4 we present the methodology and the results of the optical overdensity analysis around X-ray selected point-like sources. The method of X-ray galaxy cluster matching with AGN agglomerates is described in Sect. 5. Discussion of the main results and a summary are presented in Sect. 6. Throughout this work we use the standard cosmology: $\Omega_0 = 0.27$, $\Omega_\Lambda = 0.73$, and $H_0 = 71$ km s^{-1} Mpc^{-1}.

2. The XXL Survey and the sample

The Ultimate XMM Extragalactic Survey (XXL) is an international project based on the *XMM-Newton* Very Large Programme surveying ~50 deg^2 of the extragalactic sky (Pierre et al. 2016, hereafter XXL Paper I). The XXL survey contains two nominally equal fields at a depth of $\sim 4 \times 10^{-15}$ erg cm^{-2} s^{-1} and $\sim 2 \times 10^{-14}$ erg cm^{-2} s^{-1} in the soft (0.5–2.0 keV) and hard (2.0–10.0 keV) bands, respectively (XXL Paper I, Fig. 4). It comprises 622 XMM pointings with a total exposure >6 Ms, and a median exposure of 10.4 ks (see XXL Paper I for details). The two fields have an extensive multiwavelength coverage from X-ray to radio wavelengths (the detailed descriptions are given in XXL Paper I and Fotopoulou et al. 2016, hereafter XXL Paper VI[1]). Baran et al. (2016; hereafter XXL Paper IX) and Smolčić et al. (2016; hereafter XXL Paper XI) presented radio observations of XXL with the Very Large Array (VLA) and the Australia Telescope Compact Array (ATCA), respectively. Butler et al. (2018a, hereafter XXL Paper XVIII) reported the new observations of the full XXL-S with ATCA.

The XXL-S field is one of the two XXL fields, centred at RA = 23^{h}30 and Dec = −55^{d}00. It occupies an area of ~25 deg^2 containing 11316 X-ray point-like sources[2]. Figure 1 presents the spatial distribution of the X-ray point-like sources with optical counterparts from the Blanco Cosmology Survey[3] (BCS; Desai et al. 2012). Objects in the $0.2 < z < 1.0$ redshift range, which constitute the target sample of this paper, and the radio sources amng them are marked differently on the map. The description of the X-ray–multiwavelength associations is presented in XXL Paper VI. The spectroscopic redshifts were taken from XXL Paper XVI, and have been significantly enriched (52%) by new observations taken in 2016, described in XXL Paper XXVII, and obtained with the AAOmega spectrograph on the Anglo-Australian Telescope. A few tens of redshifts were taken from the Marseille CeSaM database[4], obtained in the frame of the ESO follow-up programme with FORS2[5]. We only considered

[1] The multiwavelength and spectroscopic information of the XXL is summarized on the web page http://xxlmultiwave.pbworks.com
[2] We considered here only point-like sources from the "good" XMM pointings, i.e. with the condition Xbadfield < 3, http://cosmosdb.iasf-milano.inaf.it/XXL/
[3] https://www.noao.edu/survey-archives/bcs/
[4] http://cesam.oamp.fr/xmm-lss/
[5] Focal Reducer and low dispersion Spectrograph for the Very Large Telescope (VLT) of the European Southern Observatory (ESO).

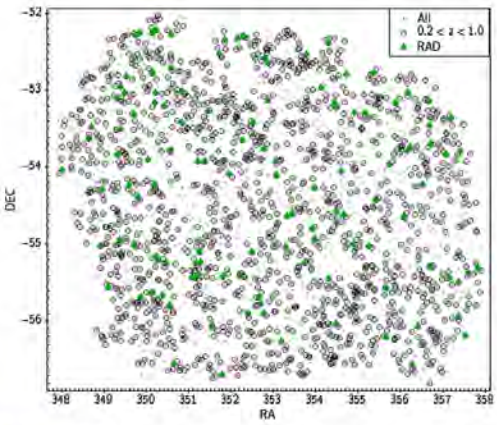

Fig. 1. Distribution of the XXL-S X-ray point-like sources with optical counterparts considering all the redshifts (N = 3280; black dots) and sources with spectroscopic redshifts in the range $0.2 < z < 1.0$ (N = 1592; open circles). The positions of the radio-selected X-ray point-like sources (RAD; N = 270) are marked with green triangles.

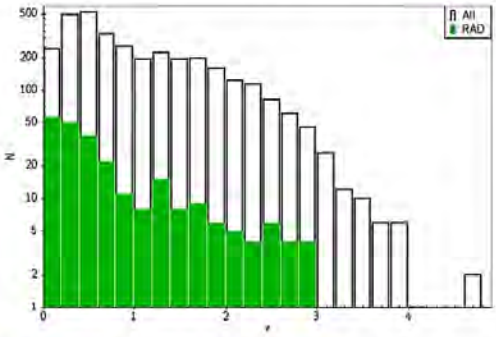

Fig. 2. Redshift distribution of the XXL-S X-ray point-like sources with spectroscopic (N = 3280) redshifts. The green histogram represents the redshift distribution of the radio-selected X-ray point-like sources (RAD; N = 270).

those high-quality spectroscopic redshifts located within 1.1 arcsec around the optical counterparts. The redshift distribution of the sample of 3280 objects is shown in Fig. 2.

For the purposes of the present study we divided our sample into various subsamples as described below and considered them in two redshift ranges: $0.2 < z < 0.6$ and $0.6 < z < 1.0$. Table 1 contains a brief description of each sample.

GAL and AGN. We separated the full sample into two subsamples, X-ray galaxies (GAL) and AGN. We considered a source as an AGN if $L_{\rm X,hard} > 2 \times 10^{42}$ erg s^{-1} (or $L_{\rm X,soft} > 10^{42}$ erg s^{-1} if the X-ray source was detected only in the soft band) following Brusa et al. (2010). We applied a K-correction to the sources following the formula

$$L_X = 4\pi d_L^2 \frac{F_X}{(1+z)^{2-\Gamma_X}}, \quad (1)$$

where $d_{\rm L}$ is the luminosity distance, $F_{\rm X}$ is the X-ray hard band flux, and $\Gamma_{\rm X}$ = 1.7 is the photon spectral index. Typical uncertainties on the single luminosity do not exceed 3% over the whole redshift range.

Table 1. Description of the various subsamples of the X-ray point-like source population (see Sect. 2 for details).

Sample	$N_{0.2<z<0.6}$	$N_{0.6<z<1.0}$	Description
Total	1012	580	All sources in the entire redshift range
GAL	107	0	$L_{\rm X,hard} < 2 \times 10^{42}$ erg s^{-1}. If no hard band $L_{\rm X,soft} < 10^{42}$ erg s^{-1}.
AGN	905	580	$L_{\rm X,hard} > 2 \times 10^{42}$ erg s^{-1}. If no hard band $L_{\rm X,soft} > 10^{42}$ erg s^{-1}.
AGN$_{\rm soft}$	626	486	AGN with $HR < -0.2$
AGN$_{\rm hard}$	279	94	AGN with $HR \geq -0.2$
RAD	88	33	X-ray sources with radio counterparts – from Butler et al. (2018a) catalogue
nRAD	924	547	Sources without radio counterparts
Faint AGN	145	89	1/4 of the sample With lowest $L_{\rm X,hard}$ luminosities
Lum. AGN	140	89	1/4 of the sample With highest $L_{\rm X,hard}$ luminosities

Notes. The indicated number of sources refers to the samples in the $0.2 < z < 0.6$ and $0.6 < z < 1.0$ redshift ranges.

Figure 3 presents the hardness ratio (HR) distribution of the sources over the full redshift range ($0.2 < z < 1.0$), with the subset of radio sources highlighted in green. The HR was calculated as $HR = (H - S)/(H + S)$, where S and H denote the count rate (cts/s) in the soft and hard band, respectively. As in Melnyk et al. (2013), we refer to AGN$_{\rm hard}$ (obscured AGN) when $HR \geq -0.2$ and AGN$_{\rm soft}$ (unobscured AGN) when $HR < -0.2$. This value for separating type 1 and type 2 AGN is a compromise based on previous studies. In particular, Garcet et al. (2007) compared optical and X-ray spectra of AGN in the XMM-LSS[6] field. The authors demonstrated that 69% of the sources with $HR > -0.2$ are optical type 2 AGN and 81% are X-ray type 2 AGN. Similarly, Brusa et al. (2010) showed that 80% of the sources with $HR \geq -0.2$ are X-ray/optically obscured AGN. Based on the analysis of X-ray spectra of the XXL-1000-AGN sample, XXL Paper VI, it was shown that higher values of HR correspond to higher absorption systems (Fig. 6a). Therefore, we first removed GAL (see above) from the AGN sample and then we divided the sample into AGN$_{\rm soft}$ and AGN$_{\rm hard}$ using the HR criterion.

RAD and nRAD. We correlated the positions of the XXL-S 2.1 GHz detected sources from the ATCA catalogue of XXL Paper XVIII with the positions of the optical counterparts of the X-ray point-like sources located within 1.0 arcsec. According to the probability function shown in Butler et al. (2018b, XXL Survey XXXI), at "1", there are ~85% genuine matches and ~15% spurious matches. We found 270 common sources, i.e. 5.5% of the full sample. We separated the sample into two subsamples: radio (RAD) and non-radio (nRAD) sources, i.e. with and without radio counterparts, respectively.

The mean HR values in the interquartile range for the samples of RAD and nRAD are $-0.63^{+0.27}_{-0.37}$ and $-0.49^{+0.33}_{-0.51}$, respectively.

[6] XMM-LSS is included in the XXL-North (XXL-N) field with central coordinates RA = 02$^{\rm h}$20, Dec = −5$^{\rm d}$00.

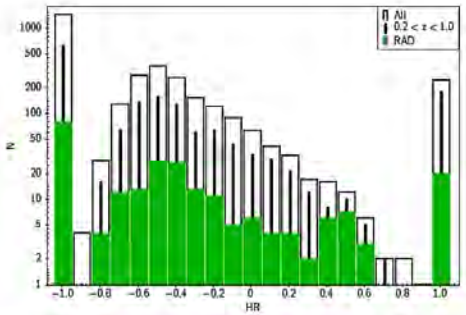

Fig. 3. Hardness ratio (HR) distribution of the XXL-S X-ray point-like sources with spectroscopic (N = 3280) redshifts and those in the $0.2 < z < 1.0$ redshift range. The green histogram represents the HR distribution of the radio-selected X-ray point-like sources (RAD; N = 270).

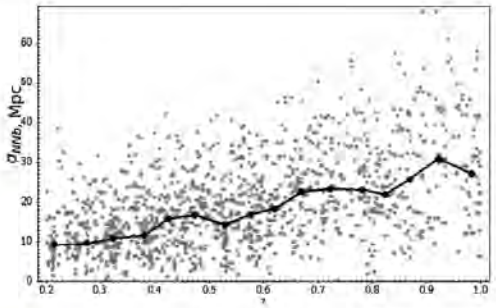

Fig. 4. Nearest neighbour distance vs. redshift for the considered sample. The broken line shows the median values of d_{NNb} in each redshift bin.

Faint and luminous AGN. We only considered sources detected in the hard band and we re-arranged $L_{X,hard}$ values in ascending order. We defined the lowest 1/4 as the "Faint AGN" sample and the highest 1/4 as the "Luminous AGN" sample. In the $0.2 < z < 0.6$ and $0.6 < z < 1.0$ redshift ranges, the $\log L_{X,hard}$ (erg/s) values of the first (third) quartiles are 42.86 (43.42) and 43.57 (44.04). Taking into account typical errors for the luminosity (see Eq. (1)), the samples of faint and luminous AGN do not overlap.

We note that the selection function of the X-ray sources has not been considered in this paper. We have to presume that a number of obscured (hard) sources is not detected within the current flux limit of the survey, even though of the same intrinsic luminosities with detected unobscured (soft) sources. Consequently, at a fixed flux limit the obscured sources are intrinsically more luminous than the unobscured ones. This may introduce a bias to the results, which is partially taken into account by using the random sampling method described in detail in the next section.

3. Large-scale environment: the nearest neighbour distance method

In this section we study the large-scale environment (>1 Mpc[7]) of X-ray point-like sources using the nearest neighbour method, assuming that in general they closely trace the distribution of optical galaxies.

It was mentioned in the previous section that we chose to analyse the distribution of X-ray point-like sources in two redshift ranges: $0.2 < z < 0.6$ and $0.6 < z < 1.0$. We excluded from this analysis 274 objects with $z < 0.2$ since this sample mainly comprises nearby faint galaxies (79%). In order to use consistent samples for the large- and the small-scale analysis, we discarded all sources with $z > 1$ as well. For all these high-redshift objects, we cannot study the fainter environment because of the completeness limit of the optical catalogue (see next section for details).

We located the nearest neighbour of each X-ray source from the XXL-S catalogue and calculated the corresponding value of the nearest neighbour distance (d_{NNb}, Mpc) using comoving coordinates and compared the mean values of d_{NNb} for each pair of sources, i.e. GAL versus AGN, AGN_{hard} versus AGN_{soft}, RAD versus nRAD, and faint versus luminous AGN.

Figure 4 illustrates the dependence of d_{NNb} versus the redshift. Due to the lack of fainter sources at high redshifts (i.e. because of the selection function), the value of d_{NNb} increases with redshift. To perform a more consistent analysis, we studied the properties of the selected sources within the two above-mentioned redshift ranges.

Additionally, to eliminate any possible biases caused by the different redshift distributions of the compared pair samples, we applied the stratified random sampling method. In more detail, we divided the number of sources in bins with step $\delta z = 0.05$. If the number of sources in one sample was larger than in the other for a certain bin, we randomly discarded N number of sources from the larger sample so as to match the distributions. Applying this procedure to all bins, we obtained the new normalized redshift distributions, which are not significantly different according to the Kolmogorov–Smirnov test (the null hypothesis that the two samples are drawn from the same parent population cannot be rejected at any significant statistical level, see Table 2). Figure 5 illustrates this approach for the RAD/nRAD samples comparing the real (initial) distribution (left panel) and new randomized distribution (right panel).

Using a single random sampling might cause an overestimation or underestimation of the real values due to a possible contamination of outliers, especially if the number of counts is small. Therefore, we performed the stratified random sampling technique ten times (cross validation technique), for each redshift range. In Table 2 we report the median values (of the ten realizations) for the redshift z, the hardness ratio HR, and the nearest neighbour distance d_{NNb}. Also, we list the two-sample Kolmogorov–Smirnov results p_{KS}[8] for the z, HR, and d_{NNb} distributions of the pairs. Comparing the corresponding values of d_{NNb}, we conclude that there is no significant difference between the paired distributions. Therefore, the large-scale environment does not noticeably influence the hardness or the radio activity of the sources, the presence or not of an AGN, and the luminosity of an AGN. However, the objects in the faint sample are far more obscured than their luminous peers.

[7] We also have a negligible number of nearest neighbours <1 Mpc; see Fig. 4.

[8] We also computed the t-test probabilities comparing the mean values of all corresponding pairs of parameters. Since we reach the same conclusions, we decided not to present them in the tables.

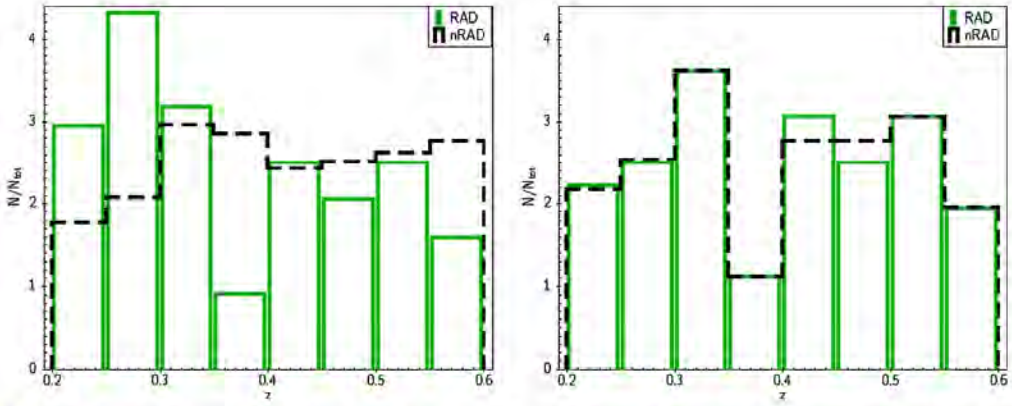

Fig. 5. *Left panel*: redshift distribution of the full radio (RAD) and non-radio (nRAD) samples. *Right panel*: respective randomized samples (single realization).

Table 2. Comparison of the median z, HR, and $d_{\rm NNb}$ values for the paired subsamples.

Samples (1a) (1b)	N (2a) (2b)	z (3a) (3b)	$p_{{\rm KS},z_{1,2}}$ (4)	HR (5a) (5b)	$p_{{\rm KS},HR_{1,2}}$ (6)	$d_{\rm NNb}$ (7a) (7b)	$p_{{\rm KS},d_{\rm NNb1,2}}$ (8)
			$0.2 < z < 0.6$				
AGN_{hard}	237	0.41	0.99	0.56	–	14.28	0.63
AGN_{soft}	537	0.42		–0.74		14.22	
GAL	42	0.31	0.96	–0.94	10^{-15}	11.15	0.80
AGN*	349	0.31		–0.25		11.97	
RAD	72	0.40	0.98	–0.19	0.01	13.84	0.46
nRAD	757	0.40		–0.40		13.61	
Faint	43	0.37	0.68	0.23	10^{-5}	12.83	0.86
Lum.AGN	41	0.38		–0.31		13.52	
			$0.6 < z < 1.0$				
AGN_{hard}	83	0.77	0.99	0.36	–	24.68	0.66
AGN_{soft}	430	0.77		–0.72		24.18	
RAD	20	0.78	0.99	–0.64	0.24	24.38	0.76
nRAD	341	0.78		–0.72		23.95	
Faint	33	0.75	0.65	–0.11	0.03	22.18	0.29
Lum.AGN	33	0.76		–0.40		25.50	

Notes. (*) Comparison of GAL and AGN was made only in the $0.2 < z < 0.45$ redshift range (limit of the GAL sample). Columns are: (1) subsample name; (2) number of members; (3) median values of the mean z; (5) HR; and (7) $d_{\rm NNb}$, Mpc of ten randomized samples and the respective Kolmogorov–Smirnov two-sample test probabilities of the distributions (4, 6, 8).

A significant difference in the HR distributions is also evident between the GAL/AGN, and RAD/nRAD subsamples within the low-redshift range. The reason for the difference between galaxies and AGN is obvious; only the AGN torus can provide this amount of obscuration. The difference between the radio and non-radio sources cannot be readily explained. It implies, however, that the radio sources are more obscured than non-radio X-ray selected sources (although not at the level of the faint subsample).

Therefore, we did not find any significant differences between the populations. We conclude that the large-scale environment does not significantly affect the considered X-ray and radio properties of the sources (see further discussion in Sect. 6.1).

4. Small-scale environment

The reason to study the small-scale environment of the X-ray point-like sources is that we can possibly detect variations (which are not traceable in the large-scale analysis) that may play a role in the type of activity (see e.g. Koulouridis et al. 2006). To this end, we calculated the local (0–0.4 Mpc) optical galaxy overdensities around the sources of our subsamples. Due to the lack of extensive spectroscopic coverage of the normal galaxy population (non X-ray sources) we performed a projected (2D) overdensity analysis, following Melnyk et al. (2013), where we used a similar approach for the XMM-LSS field. We considered the same subsamples and redshift ranges as in the previous sections.

4.1. Methodology

Taking into account the redshift and the angular distance D_A, we estimated the angular sizes of the linear radius 0.4 Mpc at the source rest-frame. Then we counted the number, N_0, of the BCS optical galaxies within a circle of radius 0.4 Mpc and within a range of magnitudes from $m^* - \Delta m$ to m^* (bright environment) and from m^* to $m^* + \Delta m$ (faint environment), where $\Delta m = 1$ and m^* is the apparent magnitude corresponding to the knee of the i'-band luminosity function $[\Phi(L)]$, given by

$$m^* = 5\log_{10} d_L + 25 + M^*_{i'} + Q_{0.1}(z) + K_{0.1}(z), \quad (2)$$

where $M^*_{i'}(= -20.82 + 5\log_{10} h)$ is the absolute magnitude at the knee of the i-band $\Phi(L)$ taken from Blanton et al. (2003); $Q(z)$ and $K(z)$ are the evolution and K-corrections, respectively, taken from Poggianti (1997) and shifted to match their rest-frame shape at $z = 0.1$; and d_L is the luminosity distance. Here, we used the magnitudes as a proxy for the stellar mass. The Δm limits are similar to what is used to evaluate the cluster members (e.g. Martini et al. 2013; Koulouridis et al. 2014; Bufanda et al. 2017).

Next we calculated the galaxy overdensities, δ,

$$\delta = \frac{N_0 A_b}{N_b A_0} - 1, \quad (3)$$

where N_0 is the total number of objects in considered circle with surface area A_0, and N_b is the local background counts estimated in the annulus between 3.1 and 5 Mpc with surface area A_b.

To estimate the σ uncertainties we used the Jackknife resampling technique (Efron et al. 1983). To check the significance of the results we compared the overdensity of galaxies around each sources with that expected from the mock X-ray source distributions. The mock catalogues have random coordinates, but the same fiducial magnitude (m^*) distribution. For the mock randomly distributed sources, we used the same BCS optical catalogue to search for neighbours as we did for the real ones including the Jackknife technique.

For each catalogue we calculated the cumulative overdensity distribution

$$F(>\delta) = N(>\delta)/N_{\rm tot}, \quad (4)$$

which is defined as the percentage of all sources $N_{\rm tot}$ having an overdensity above a given δ value. Finally, we compared the real distributions with the random ones.

4.2. Results

First, we calculated the overdensity distributions for the different randomized subsamples in two redshift ranges for the bright ($m^* - 1 < m < m^*$) and faint ($m^* < m < m^* + 1$) environments and compared them with the mock distributions. We did not study the faint environment of sources in the high-redshift range because of the completeness of the optical BCS catalogue at about $i \sim 23$, which corresponds to our rest frame m^* at $z = 1$.

We used the Kolmogorov–Smirnov (KS) two-sample test to estimate quantitatively the differences between the real and mock overdensity distributions. The typical KS probabilities ($p_{\rm KS}$) of the two corresponding distributions of overdensities being drawn from the same parent population are $<10^{-3}$, meaning that the real and mock distributions are significantly different in the first redshift range. The exceptions are the GAL overdensities in both environments and the luminous and faint AGN in bright environments and in both redshift ranges.

Figures 6 and 7 present the cumulative distributions of overdensities for the real and mock subsamples in the low- and high-redshift range, respectively. In Table 3 we list the value of $F(>\delta)$ at the point $\delta > 0$. We also list the corresponding 1 σ intervals for the real and mock samples. The σ_s indicates the difference (in σ units) that the fraction of real sources at a given overdensity level is higher than the corresponding fraction of the mock sources. For example, in the $0.2 < z < 0.6$ redshift range, the fraction of $\rm AGN_{hard}$ in bright overdense environments with $\delta > 0$ is 66%. This is higher than the random expectations at the 5.6 σ level. In the faint overdense environment, the corresponding fraction is 65%, which is higher than the random expectations at the 4.0 σ level. In the high-redshift range, we find $F(\delta > 0) = 55\%$, which is not significantly different from the random expectations at the 0.3 σ level.

Our results show that, in general, X-ray point-like sources inhabit both dense and underdense environments. However, there are significantly more X-ray sources than in their corresponding mock catalogues which inhabit overdense regions in both redshift ranges (in agreement with Melnyk et al. 2013), especially in the low-redshift range. The difference is less than 3 σ only for GAL, RAD, faint, and luminous AGN in both environments. However, the low significance is most likely due to small sample sizes. At higher redshifts we do not have clear evidence of overdensities (except for the nRAD sample) probably because of the small sample sizes.

Table 3. Comparison of the fraction F of sources with overdensity values $\delta > 0$ in the randomized samples and their respective mock catalogues.

Sample	N	$F_{\rm real(>\delta)} \pm \sigma_{\rm real}$,%	$F_{\rm mock(>\delta)} \pm \sigma_{\rm mock}$,%	σ_s	σ_p
$0.2 < z < 0.6$, bright environment					
$\rm AGN_{hard}$	237	66 ± 3.0	42 ± 3.2	5.6	1.7
$\rm AGN_{soft}$	537	60 ± 2.1	49 ± 2.2	3.7	
GAL	42	46 ± 7.6	37 ± 7.4	0.9	1.6
AGN	349	59 ± 2.6	45 ±3.7	3.8	
RAD	72	66 ±5.5	44 ± 5.8	2.9	1.4
nRAD	757	59 ± 1.8	48 ± 1.8	4.3	
Faint AGN	43	59 ± 7.4	48 ± 7.5	1.3	0.4
Lum. AGN	41	55 ± 7.7	40 ± 7.6	1.3	
$0.2 < z < 0.6$, faint environment					
$\rm AGN_{hard}$	237	65 ± 3.1	47 ± 3.2	4.0	2.0
$\rm AGN_{soft}$	537	58 ± 2.1	46 ± 2.2	3.8	
GAL	42	63 ± 7.3	44 ± 7.6	1.8	0.5
AGN	349	59 ± 2.6	46 ± 2.7	3.4	
RAD	72	62 ± 5.7	47 ± 5.8	1.9	0.5
nRAD	757	59 ± 1.8	47 ± 1.8	4.7	
Faint AGN	43	77 ± 6.1	48 ± 7.5	3.0	2.5
Lum. AGN	41	52 ± 7.7	37 ± 7.4	1.6	
$0.6 < z < 1.0$, bright environment					
$\rm AGN_{hard}$	83	55 ± 5.4	57 ± 5.4	0.3	0.1
$\rm AGN_{soft}$	430	54 ± 2.4	48 ± 2.4	1.8	
RAD	20	50 ± 9.8	50 ± 9.8	0.0	0.5
nRAD	341	55 ± 2.5	44 ± 2.5	3.2	
Faint AGN	33	50 ± 8.6	41 ± 8.5	0.7	1.8
Lum. AGN	33	71 ± 7.6	59 ± 8.4	1.0	

Notes. σ_s is the difference between $F_{\rm real}$ and $F_{\rm mock}$ in units of its typical standard deviation, calculated as $|F_{\rm real} - F_{\rm mock}|/(\sigma^2_{\rm real} + \sigma^2_{\rm rand})^{1/2}$; σ_p is the corresponding difference between pairs of the samples $\rm AGN_{hard}/AGN_{soft}$, etc.

These results are not unexpected given that AGN are known to be clustered. Our main interest, though, is to study the environmental trends for the subsamples defined in Table 1.

In the last column of Table 3 (σ_p) we compare the real samples at the point of $\delta = 0$ in σ units. As can be seen, there are no significant differences for any pair of samples. Therefore, pairs of GAL and AGN, $\rm AGN_{hard}$ and $\rm AGN_{soft}$, radio and non-radio sources, and faint and luminous AGN occupy similar environments.

It is worth mentioning that the small- and large-scale environments of our sources do not correlate, i.e. isolated objects as defined in the large-scale analysis are found in a variety of small-scale environments, not necessarily in isolation.

5. X-ray clusters versus AGN agglomerates

In this section we study the XXL-S AGN-supercluster candidates defined as the super structures comprising X-ray point-like sources. These structures were obtained by applying the classical bottom-up hierarchical clustering method[9] to the sample of X-ray point-like sources using comoving coordinates. To

[9] Linkage of clusters starts by considering each object as a cluster. Then, one by one, it merges all elements into a single cluster. Depending on the input free parameter of clustering radii, the hierarchical tree is cut dividing the sample on clustered and unclustered objects. We used the minimum distance between clusters for linkage.

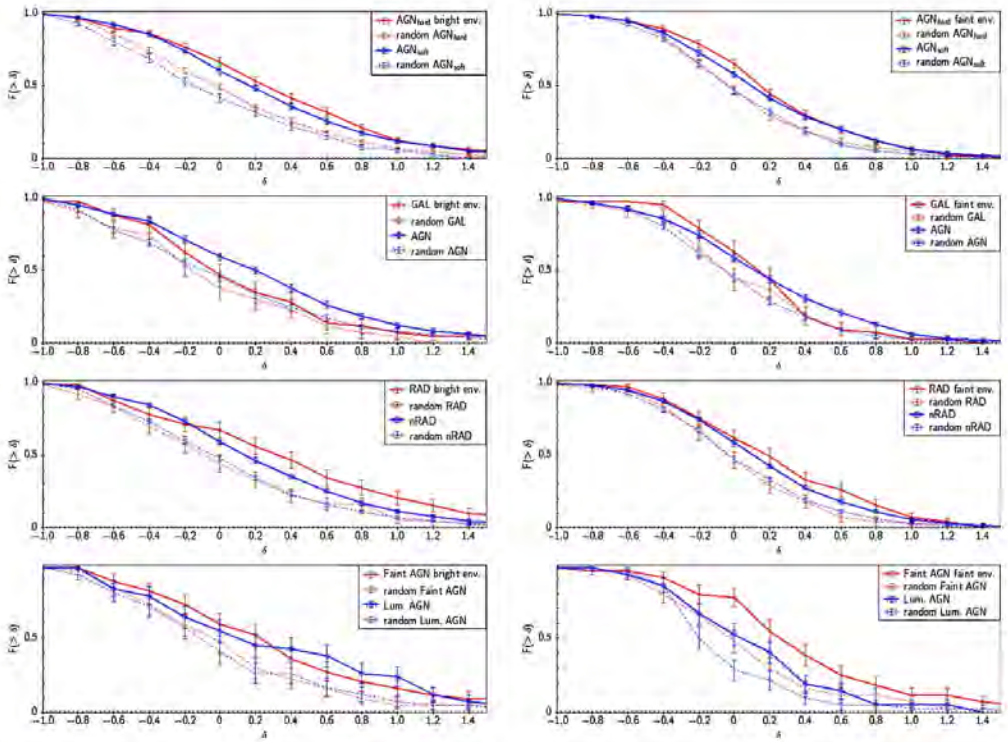

Fig. 6. Cumulative distributions of the overdensities for the randomized and mock samples in the $0.2 < z < 0.6$ redshift bin. The different samples are coded as indicated in the label of each panel. The error bars correspond to 1 σ deviations.

distinguish between X-ray galaxy clusters (i.e. virialized structures that are detected as X-ray extended sources) and the structures which were obtained with the hierarchical method, we use the term "agglomerate". This is in analogy to the study by Karachentsev et al. (2012). Then, we checked if the agglomerates trace the distribution of X-ray galaxy clusters (X-ray extended sources).

In this analysis we defined AGN agglomerates at clustering radii of 16.76 Mpc and 28.32 Mpc in the $0.2 < z < 0.6$ and $0.6 < z < 1.0$ redshift ranges, respectively. Adopting these values, 2/3 of the sources are in agglomerates and 1/3 are isolated in our sample. Here we followed the proportion ~70% of clustered and ~30% unclustered galaxies in the Local Universe (see Karachentsev et al. 2012 and references therein). Figure 8 shows the dependence of the typical distances between the sources in the agglomerates $\langle D \rangle$ versus the number of their X-ray point-like members.

The XXL X-ray cluster sample (C1 and C2 types) is described in Pierre et al. (2016), Pacaud et al. (2016; hereafter XXL Paper II) and Adami et al. (2018, XXL Paper XX). The considered samples of spectroscopically confirmed X-ray galaxy clusters from XXL Paper XX contain $N_{cl} = 81$ and 22 clusters, respectively, in the $0.2 < z < 0.6$ and $0.6 < z < 1.0$ redshift ranges.

To avoid biases related to inhomogeneity of the X-ray point-like sources in the field with respect to cluster positions we have performed the following test. Separately for the two considered redshift ranges around each X-ray cluster within with an angular radius r, we counted the number of all point-like X-ray sources such that $m^* - 2 < m < m^* + 1$, where m is the rest-frame i-band magnitude of a cluster and m^* is the apparent magnitude of an X-ray AGN/galaxy. According to this method, we calculated the number of point-like sources with available spectroscopic redshifts and without it. In Fig. 9 we plotted the ratio between the numbers of X-ray point-like sources with spectro-z and the whole sample for different angular radii around the X-ray clusters. The error bars show the boundaries of the confidence interval at the 95% level. As can be seen, the completeness of the spectroscopic redshifts for the X-ray point-like sources is 78% and 30% of the total population of sources in the $0.2 < z < 0.6$ and $0.6 < z < 1.0$ redshift ranges, respectively. This percentage does not depend significantly on the distance from the X-ray clusters. We conclude that the distribution of the X-ray point-like sources near the X-ray clusters is non-biased.

We also computed the minimum distances between each cluster and all the agglomerates (geometrical centres of the agglomerates). Then we built the distributions of the minimum distances and compared them with the respective distributions of the galaxy clusters and randomly chosen agglomerates. To build the mock catalogues, we chose random coordinates and redshifts from the real sample of the X-ray point-like sources in the corresponding redshift ranges. Therefore, our mock catalogues have the same properties as the real one. The number of the mock agglomerates was 100 times higher than

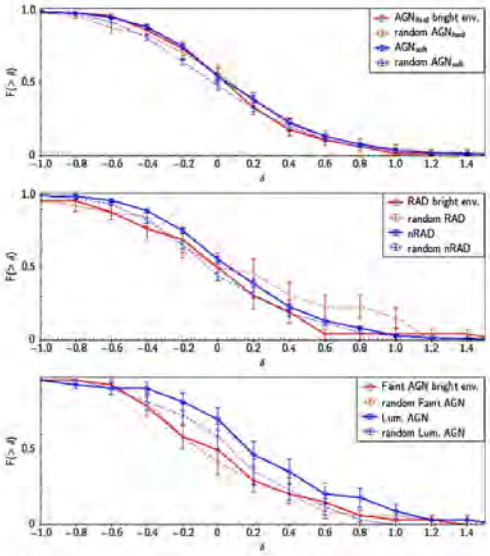

Fig. 7. Cumulative distributions of the overdensities for the randomized and mock samples in the $0.6 < z < 1.0$ redshift bin. The different samples are coded as indicated in the label of each panel. The error bars correspond to 1 σ deviations.

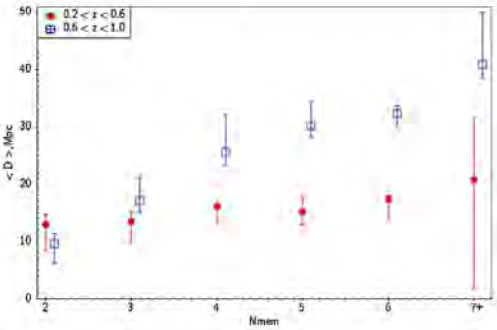

Fig. 8. Median values of the average distances between the members of agglomerate within their interquartile ranges vs. the number of agglomerate members.

the number of the real agglomerates. Comparison between the minimum distance distributions of all the X-ray clusters and the real/mock agglomerates for all the samples are shown in Fig. 10.

Table 4 presents the mean values of the minimum distances between the X-ray clusters and the real or mock AGN agglomerates with different populations: 2+ (two or more members), 3+, 5+, and 10+. In both redshift ranges, the null hypothesis that the real and mock distributions are drawn from the same parent set can be rejected at a high level of significance. In other words, we report significantly smaller distances between the X-ray clusters and the AGN agglomerates with different a number of members than expected from the mock realizations.

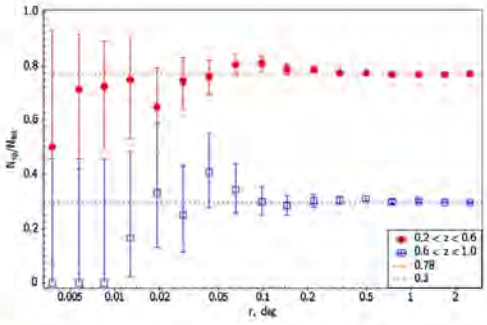

Fig. 9. Ratio between the numbers of X-ray point-like sources with spectroscopic redshifts (N_{sp}) and the whole sample (N_{tot}) for different angular radii r around the X-ray clusters.

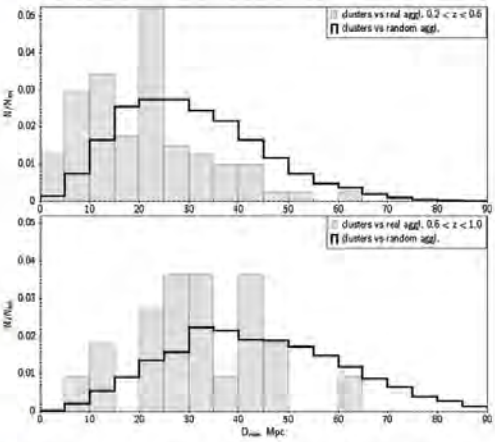

Fig. 10. Distributions of the minimum distances between all the X-ray clusters and all the real/mock agglomerates (2+).

Mainly, the AGN agglomerates follow the distribution of the X-ray clusters at the <25 Mpc scale in the $0.2 < z < 0.6$ and <45 Mpc in the $0.6 < z < 1.0$ ranges, respectively: 73^{+7}_{-8}% and 86^{+9}_{-13}%. The corresponding random expectations are 39^{+1}_{-1}% and 55^{+1}_{-2}%, respectively. The above-mentioned uncertainties correspond to the 95% confidence level, so these results are highly significant.

In Table 5 we present the geometric centres of the most populated agglomerates (>10 members) and their possible associations with X-ray clusters, supercluster candidates, and pairs of clusters from XXL Paper XX. In the columns we indicate the published names of the cluster, supercluster, or pair and the minimum distances between the corresponding galaxy structure and the given agglomerate. We conclude that the most populated concentrations of AGN are associated with supercluster candidates.

6. Discussion and conclusions

We have studied in the present paper the environment and the clustering properties of the X-ray selected point-like sources

Table 4. Kolmogorov–Smirnov p_{KS} and t-test p_t probabilities of the real and mock minimum distance distributions ($D_{min,real}$ and $D_{min,mock}$ in Mpc) and the corresponding mean values between the clusters and the agglomerates with different populations being drawn from the same parent population.

Aggl.	N_{Aggl}	N_{cl}	$\langle D_{min,real} \rangle$ SD	±	$\langle D_{min,mock} \rangle$ SD	±	p_{KS}	p_t
			$0.2 < z < 0.6$					
2+	143	81	21.0 ± 12.3		30.6 ± 14.2		10^{-9}	10^{-9}
3+	84	81	25.0 ± 15.2		37.6 ± 14.9		10^{-10}	10^{-10}
5+	39	81	32.2 ± 20.2		50.1 ± 24.9		10^{-11}	10^{-11}
10+	12	81	55.7 ± 36.2		89.7 ± 59.2		10^{-10}	10^{-10}
			$0.6 < z < 1.0$					
2+	104	22	32.4 ± 13.0		44.3 ± 19.2		10^{-5}	10^{-5}
3+	54	22	43.2 ± 17.8		57.9 ± 26.3		10^{-4}	10^{-4}
5+	20	22	60.5 ± 26.6		88.1 ± 41.8		10^{-6}	10^{-5}
10+	6	22	109.1 ± 75.6		146.7 ± 76.0		10^{-3}	10^{-4}

Notes. For example, 2+ means two or more members in an agglomerate.

with spectroscopic redshifts from the 25 deg^2 XXL-S field in two redshift ranges: 1012 sources with $0.2 < z < 0.6$ and 580 sources with $0.6 < z < 1.0$.

6.1. Small- and large-scale environments of X-ray AGN

It was shown, in general, that the X-ray selected AGN reside in all kinds of environments. This is in agreement with previous works for AGN selected in the optical, X-ray, and radio (cf. Gilmour et al. 2009; Constantin et al. 2008; Silverman et al. 2009; Lietzen et al. 2009, 2011; Tasse et al. 2008, 2011; Melnyk et al. 2013; Hwang et al. 2012; Gendre et al. 2013; Manzer & De Robertis 2014; Karouzos et al. 2014a,b; Song et al. 2016).

On the other hand, according to the small-scale analysis, the Kolmogorov–Smirnov probability that the AGN overdensity distribution is consistent with the mock distribution is less than 10^{-3} in the first redshift range and for both the bright and faint environments. The AGN_{soft} and AGN_{hard} (i.e. unobscured and obscured AGN), radio, and non-radio X-ray sources also prefer the overdense bright or faint environments more frequently than in the mock catalogues at a high level of significance ($>3\,\sigma$). There is also an apparent shift to higher overdensity values at lower redshifts. This result is in agreement with X-ray AGN environmental studies by Melnyk et al. (2013), Silverman et al. (2009), and Karouzos et al. (2014a). It also agrees with some studies for optical AGN, although there are many studies of optical AGN that do not agree. For example, Hwang et al. (2012) and Song et al. (2016) found that the fraction of AGN in the field is higher than in clusters (see also the references in those papers), contrary to Manzer & De Robertis (2014) for whom the AGN fraction increases with decreasing distance to the group centroid. However, Melnyk et al. (2015) and Argudo-Fernández et al. (2016) independently found no difference in the prevalence of optical AGN (mainly type 2) in isolated and paired galaxies.

According to our results, although the majority of AGN are located in small-scale overdensities, their luminosity does not correlate with the environmental density. Karouzos et al. (2014a) obtained similar results, concluding that high-luminosity AGN are not preferentially triggered by mergers. They concluded that AGN likely trace the overdense environment because they inhabit the most massive galaxies and not because they are triggered by interactions, supporting the scenario of secular AGN evolution. Our findings are also in general agreement with recent environmental studies of optically selected AGN. In particular, Sabater et al. (2015) used a sample of about 250 000 galaxies and showed that the effects of the large-scale environment and galaxy interactions are minimal on both the prevalence of optically selected HLAGN and on their luminosity, supporting the scenario of a secular AGN evolution. We are motivated to test the nearest neighbour effect in the XXL-N field in the future, where many spectroscopic redshifts have become available.

The differences between the environment of AGN_{soft} (i.e. mainly unobscured or broad-line AGN, HLAGN, type 1) and AGN_{hard} (mainly obscured AGN, narrow-line, MLAGN, type 2[10]) are also negligible. This is in agreement with the classical unified scheme for AGN by Antonucci (1993). In our previous work for the XMM-LSS field Melnyk et al. (2013), we found some evidence that AGN_{hard} are located in more overdense regions than AGN_{soft}, although the significance level was relatively low ($<3\,\sigma$) and the number of sources was three times lower than in the present study. It is also in agreement with Gilli et al. (2009) and Strand et al. (2008).

We have to note that the considered small-scale overdensities were computed within 400 kpc, while other studies have reported the difference between obscured and unobscured AGN at very small distances, <30–100 kpc (see e.g. Koulouridis et al. 2006, 2013; Koss et al. 2012; Satyapal et al. 2014). Also, we do not consider the host galaxy types in this paper.

We did not find that X-ray radio-selected AGN prefer denser environments than non-radio selected ones, unlike previous studies (Lietzen et al. 2011; Sabater et al. 2013; Karouzos et al. 2014a,b; Ineson et al. 2015; Argudo-Fernández et al. 2016; Bradshaw et al. 2011). However, we found that among the X-ray selected sources, radio detections display significantly higher hardness ratios than radio undetected sources.

We did not find evidence for any influence of the large-scale (>1 Mpc) environment on X-ray or radio properties of the sources. We again note that our assumption here was that the X-ray sources closely trace the distribution of optical galaxies. According to Song et al. (2016), the optical quasar density changes somewhat more slowly than the galaxy density. Nevertheless, taking into account the field galaxies, those authors showed a weak positive correlation between the black hole mass and the large-scale environmental density, and a negative correlation between the optical luminosity and the density. As previously noted, due to very non-homogeneous spectroscopic coverage of the XXL-S field galaxies, we were not able to calculate the environmental density of the field galaxies.

6.2. Large-scale structure of the XXL-S

We find no correlation between the small-scale and large-scale environments of the X-ray sources, implying that there does not seem to be any preferable environment for X-ray sources. Nevertheless, they avoid the most empty regions of galaxies (voids). This is in agreement with the fact that powerful X-ray AGN are rarely observable among isolated galaxies in the Local Universe (Pulatova et al. 2015). In an earlier work by Georgakakis et al. (2007) it was also shown that X-ray selected AGN at $z \sim 1$ avoid underdense regions at the 99.89% confidence level.

We found that X-ray AGN typically reside at relatively small distances from the centres of X-ray clusters (<5 Mpc), which

[10] This classification is not explicit.

Table 5. XXL-S supercluster candidates, the most populated agglomerates, and possible correlations with X-ray clusters.

N_{mem}	RA	Dec	$\langle z \rangle$	D_{max}, Mpc	$\langle D \rangle$, Mpc	XLSSC clusters*	$D_{min,real}$, Mpc	Supercluster**
46	352.179	−54.240	0.21	84.4	37.6	595, 586, 608	12, 13, 12	part S05
38	355.082	−54.440	0.33	80.2	35.2	614, 548, 632, 538	24, 21, 21, 24	part S02
30	352.810	−53.872	0.26	86.1	36.1	–	–	–
24	356.087	−53.811	0.62	135.6	58.2	509	40	–
21	352.315	−54.810	0.28	74.7	32.6	612, 622, 588, 519, 524	16, 22, 19, 22, 21	part S03
17	353.983	−55.115	0.38	72.9	35.5	573, 543	15, 23	–
17	351.601	−54.448	0.61	110.9	50.9	580,611	25, 6	pair, id30
15	352.953	−56.132	0.31	67.1	26.5	–	–	–
14	352.677	−52.489	0.45	63.5	30.5	561, 641	21, 24	pair, id25
13	350.457	−53.179	0.71	90.7	40.7	–	–	–
13	349.393	−54.392	0.87	114.2	49.9	–	–	–
13	349.607	−54.196	0.66	70.65	37.6	–	–	–
11	349.183	−54.948	0.44	41.6	17.1	–	–	–
11	354.043	−54.479	0.53	46.8	26.1	–	–	–
11	350.214	−53.125	0.37	68.3	35.4	547	20	–
10	349.291	−53.780	0.28	34.2	21.9	526, 557, 591	8 ,13, 17	part S06
10	354.541	−56.039	0.47	41.7	20.8	639, 609	17, 8	–
10	349.773	−53.559	0.79	91.1	47.6	560	42	–

Notes. (*) The name of the X-ray cluster given in XXL Paper XX. (**) Supercluster candidates (and also cluster pair) defined in XXL Paper XX as concentrations of X-ray clusters, "part" means that half or more of the members of the supercluster are associated with the corresponding agglomerate. N_{mem} represents the number of members in the agglomerate, RA and Dec are the coordinates of the centre, $\langle z \rangle$ is the average redshift, D_{max} is the maximum distance between members of the agglomerate, $\langle D \rangle$ is the average distance between its members, and $D_{min,real}$ is the distance between a given cluster and its nearest agglomerate.

may refer to the absence of the "AGN suppression" effect which was reported in previous works by Koulouridis & Plionis (2010) and Ehlert et al. (2014). However, our findings are in agreement with Koulouridis et al. (2014), where the effect of AGN suppression in X-ray clusters was not found for the poor clusters in the XMM-LSS field. Koulouridis et al. (2016; XXL Paper XII) argue that the total number of AGN in the vicinity of three superclusters significantly exceeds the field expectations. Although superclusters represent the most extensive concentrations in the Universe, they do not represent the densest environments. We expect that future XXL papers dedicated to studying AGN counts in X-ray clusters will clarify this issue.

In general, there seems to be an anticorrelation between high density and AGN activity. We found that X-ray AGN trace the distribution of X-ray clusters at a <25–45 Mpc scale: the fraction of agglomerates located in the vicinity of X-ray clusters is ~1.5–2 times higher than for randomly distributed agglomerates in both considered redshift ranges. This is in agreement with Arnold et al. (2009) and also with optical AGN studies by Hwang et al. (2012) and Song et al. (2016), where the authors show that the AGN fractions in the field environment are higher than in clusters. Kocevski et al. (2009) found that Seyfert-2 galaxies avoid the densest regions of superclusters and are instead located in intermediate density environments. Moreover, we found that the most populated agglomerates are associated with supercluster candidates (see XXL Paper XX). We interpret our results as showing that X-ray AGN mainly reside in supercluster filaments/field environments.

To summarise our results:

1. The large-scale environment does not correlate with any specific AGN population studied here.
2. Obscured/unobscured AGN, radio, and non-radio sources typically reside in small-scale overdensities, a trend which is stronger at lower redshifts.
3. No correlation was found between small-scale overdensities and X-ray luminosity, nor between environmental density and the type of AGN. Radio sources also prefer the same locally overdense environments as non-radio AGN.
4. A large number of AGN concentrations with two or more members correlates with the presence of X-ray galaxy clusters within <25–45 Mpc.

Acknowledgements. XXL is an international project based around an XMM Very Large Programme surveying two 25 deg^2 extragalactic fields at a depth of ~5 × 10^{-15} erg cm^{-2} s^{-1} in the [0.5–2] keV band for point-like sources. The XXL website is http://irfu.cea.fr/xxl. Multiband information and spectroscopic follow-up of the X-ray sources were obtained through a number of survey programmes, http://xxlmultiwave.pbworks.com/. The research leading to these results has received funding from the European Union Seventh Framework Programme (FP7 2007-2013) under grant agreement 291823 Marie Curie FP7-PEOPLE-2011-COFUND (The new International Fellowship Mobility Programme for Experienced Researchers in Croatia – NEWFELPRO). This article has been written as part of the project "AGN environs in XXL" which has received funding through NEWFELPRO project under grant agreement No83. The Saclay group acknowledges long-term support from the Centre National d'Études Spatiales (CNES). EK thanks CNES and CNRS for support of post-doctoral research. VS, JD, and ID acknowledge funding by the European Unions Seventh Framework programme under grant agreement 337595 (ERC Starting Grant, CoSMass). This research has made use of the XMM-LSS database, operated at CeSAM/LAM, Marseille, France

References

Adami, C., Caretta, C., Faccioli, L., et al. 2018, A&A, 620, A5 (XXL Survey, XX)
Allevato, V., Finoguenov, A., Cappelluti, N., et al. 2011, ApJ, 736, 99
Allevato, V., Finoguenov, A., Civano, F., et al. 2014, ApJ, 796, 4
Argudo-Fernández, M., Shen, S., Sabater, J., et al. 2016, A&A, 592, A30
Arnold, T. J., Martini, P., Mulchaey, J. S., Berti, A., & Jeltema, T. E. 2009, ApJ, 707, 1691
Antonucci, R. 1993, ARA&A, 31, 473
Baran, N., Smolčić, V., Milaković, D., et al. 2016, A&A, 592, A8 (XXL Survey, IX)

Blanton, M. R., Hogg, D. W., Bahcall, N. A., et al. 2003, ApJ, 592, 819
Bradshaw, E. J., Almaini, O., Hartley, W. G., et al. 2011, MNRAS, 415, 2626
Brusa, M., Civano, F., Comastri, A., et al. 2010, ApJ, 716, 348
Bufanda, E., Hollowood, D., Jeltema, T. E., et al. 2017, MNRAS, 465, 2531
Butler, A., Huynh, M., Delhaize, J., et al. 2018a, A&A, 620, A3 (XXL Survey, XVIII)
Butler, A., Huynh, M., Delvecchio, I., et al. 2018b, A&A, 620, A16 (XXL Survey, XXXI)
Chiappetti, L., Fotopoulou, S., Lidman, C., et al. 2018, A&A, 620, A12 (XXL Survey, XXVII)
Constantin, A., Hoyle, F., & Vogeley, M. S. 2008, ApJ, 673, 715
Desai, S., Armstrong, R., Mohr, J. J., et al. 2012, ApJ, 757, 83
Efron, B., & Gong, G., 1983, Am. Stat., 37, 36
Ehlert, S., von der Linden, A., Allen, S. W., et al. 2014, MNRAS, 437, 1942
Elyiv, A., Clerc, N., Plionis, M., et al. 2012, A&A, 537, A131
Fotopoulou, S., Pacaud, F., Paltani, S., et al. 2016, A&A, 592, A5 (XXL Survey, VI)
Gandhi, P., Garcet, O., Disseau, L., et al. 2006, A&A, 457, 393
Garcet, O., Gandhi, P., Gosset, E., et al. 2007, A&A, 474, 473
Gendre, M. A., Best, P. N., Wall, J. V., & Ker, L. M. 2013, MNRAS, 430, 3086
Georgakakis, A., Nandra, K., Laird, E. S., et al. 2007, ApJ, 660, L15
Gilli, R., Zamorani, G., Miyaji, T., et al. 2009, A&A, 494, 33
Gilmour, R., Best, P., & Almaini, O. 2009, MNRAS, 392, 1509
Hickox, R. C., Myers, A. D., Brodwin, M., et al. 2011, ApJ, 731, 117
Hwang, H. S., Park, C., Elbaz, D., & Choi, Y.-Y. 2012, A&A, 538, A15
Ineson, J., Croston, J. H., Hardcastle, M. J., et al. 2015, MNRAS, 453, 2682
Karachentsev, I. D., Karachentseva, V. E., Melnyk, O. V., Elyiv, A. A., & Makarov, D. I. 2012, Astrophys. Bull., 67, 353
Karouzos, M., Jarvis, M. J., & Bonfield, D. 2014a, MNRAS, 439, 861
Karouzos, M., Im, M., Kim, J.-W., et al. 2014b, ApJ, 797, 26
Kocevski, D. D., Lubin, L. M., Lemaux, B. C., et al. 2009, ApJ, 700, 901
Koss, M., Mushotzky, R., Treister, E., et al. 2012, ApJ, 746, L22
Koulouridis, E., & Plionis, M. 2010, ApJ, 714, L181
Koulouridis, E., Plionis, M., Chavushyan, V., et al. 2006, ApJ, 639, 37
Koulouridis, E., Plionis, M., Chavushyan, V., et al. 2013, A&A, 552, A135
Koulouridis, E., Plionis, M., Melnyk, O., et al. 2014, A&A, 567, A83
Koulouridis, E., Poggianti, B., Altieri, B., et al. 2016, A&A, 592, A11 (XXL Survey, XII)
Koutoulidis, L., Plionis, M., Georgantopoulos, I., & Fanidakis, N. 2013, MNRAS, 428, 1382
Lidman, C., Ardila, F., Owers, M., et al. 2016, PASA, 33, e001 (XXL Survey, XIV)
Lietzen, H., Heinämäki, P., Nurmi, P., et al. 2009, A&A, 501, 145
Lietzen, H., Heinämäki, P., Nurmi, P., et al. 2011, A&A, 535, A21
Manzer, L. H., & De Robertis, M. M. 2014, ApJ, 788, 140
Martini, P., Miller, E. D., Brodwin, M., et al. 2013, ApJ, 768, 1
Melnyk, O., Plionis, M., Elyiv, A., et al. 2013, A&A, 557, A81
Melnyk, O., Karachentseva, V., & Karachentsev, I. 2015, MNRAS, 451, 1482
Mendez, A. J., Coil, A. L., Aird, J., et al. 2016, ApJ, 821, 55
Pacaud, F., Clerc, N., Giles, P. A., et al. 2016, A&A, 592, A2 (XXL Survey, II)
Padovani, P., Alexander, D. M., Assef, R. J., et al. 2017, A&AR, 25, 2
Pierre, M., Pacaud, F., Adami, C., et al. 2016, A&A, 592, A1 (XXL Survey, I)
Poggianti, B. M. 1997, A&AS, 122, 399
Pulatova, N. G., Vavilova, I. B., Sawangwit, U., Babyk, I., & Klimanov, S. 2015, MNRAS, 447, 2209
Sabater, J., Best, P. N., & Argudo-Fernández, M. 2013, MNRAS, 430, 638
Sabater, J., Best, P. N., & Heckman, T. M. 2015, MNRAS, 447, 110
Satyapal, S., Ellison, S. L., McAlpine, W., et al. 2014, MNRAS, 441, 1297
Silverman, J. D., Kovač, K., Knobel, C., et al. 2009, ApJ, 695, 171
Smolčić, V., Delhaize, J., Huynh, M., et al. 2016, A&A, 592, A10 (XXL Survey, XI)
Smolčić, V., Delvecchio, I., Zamorani, G., et al. 2017, A&A, 602, A2
Song, H., Park, C., Lietzen, H., & Einasto, M. 2016, ApJ, 827, 104
Strand, N. E., Brunner, R. J., & Myers, A. D. 2008, ApJ, 688, 180
Tasse, C., Best, P. N., Röttgering, H., & Le Borgne, D. 2008, A&A, 490, 893
Tasse, C., Röttgering, H., & Best, P. N. 2011, A&A, 525, A127
Villarroel, B., & Korn, A. J. 2016, A&A, 596, A20

3.3. Пошук гравітаційно-лінзових систем

Гравітаційне лінзування залишається потужним інструментом для вивчення розподілу темної матерії у Всесвіті. Статистика гравітаційних лінз має забезпечити обмеження на космологічні параметри, оскільки оптична глибина лінзування залежить від величини об'єму простору зокрема між квазаром і спостерігачем. Детальні дослідження гравітаційно-лінзових систем, у свою чергу, дають змогу вивчити структуру джерела світла (наприклад, квазара) та розподіл маси в самій лінзі (галактики чи скупчення).

В роботах [9, 10, 27–29] була проведена обробка довготривалих спостережень гравітаційно-лінзованих квазарів для знаходження характеристик мікролінзування. Оскільки рентгенівські точкові джерела можна спостерігати до великих червоних зміщень, ми вважали за доцільне оцінити кількість гравітаційних лінз в полі XXL огляду [8] та провести пошук кандидатів в гравітаційні лінзи серед оптичних ототожнень цих об'єктів [11]. Такий підхід виглядав досить оптимістично, тому що ймовірність того, що рентгенівське точкове джерело є АЯГ або квазаром є досить високою.

Отже, в роботі [8] ми оцінили частоту множинних зображень АЯГ серед оптичних ототожнень рентгенівських точкових джерел огляду XXL. Було отримано очікувані статистичні властивості цієї вибірки, такі як розподіл червоних зміщення лінзових джерел і дефлекторів, які призводять до утворення кількох зображень. Моделювання дефлекторів було проведено з використанням як сферичних, так і еліпсоїдних сингулярних ізотермічних розподілів мас. Мета роботи [11] полягала в тому, щоб визначити кандидатів у гравітаційні лінзи серед приблизно 5500 оптичних ототожнень рентгенівських точкових джерел поля XMM-LSS після візуального перегляду зображень CFHTLS T006 та перевірки показників кольору кандидатів на колір-колір діаграмах.

Monthly Notices of the ROYAL ASTRONOMICAL SOCIETY

MNRAS 452, 1480–1492 (2015) doi:10.1093/mnras/stv1401

Predicted multiply imaged X-ray AGNs in the XXL survey

F. Finet,[1,2,3★] A. Elyiv,[2,4,5] O. Melnyk,[2,6] O. Wertz,[2] C. Horellou[7] and J. Surdej[2†]

[1]*Aryabhatta Research Institute of Observational Sciences (ARIES), Manora Peak, Nainital 263 129, Uttarakhand, India*
[2]*Extragalactic Astrophysics and Space Observations (AEOS), University of Liège, Allée du 6 Août, 17 (Sart Tilman, Bât. B5c), B-4000 Liège, Belgium*
[3]*National Astronomical Observatory of Japan (NAOJ), 650 N. A'Ohoku place, Hilo, HI 96720, USA*
[4]*Main Astronomical Observatory, Academy of Sciences of Ukraine, 27 Akademika Zabolotnoho St., UA-03680 Kyiv, Ukraine*
[5]*Dipartimento di Fisica e Astronomia, Università di Bologna, Viale Berti Pichat 6/2, I-40127 Bologna, Italy*
[6]*Astronomical Observatory, Kyiv National University, 3 Observatorna St., UA-04053 Kyiv, Ukraine*
[7]*Department of Earth & Space Sciences, Chalmers University of Technology, Onsala Space Observatory, SE-439 92 Onsala, Sweden*

Accepted 2015 June 23. Received 2015 June 22; in original form 2014 March 20

ABSTRACT

We estimate the incidence of multiply imaged active galactic nuclei (AGNs) among the optical counterparts of X-ray selected point-like sources in the XXL field. We also derive the expected statistical properties of this sample, such as the redshift distribution of the lensed sources and of the deflectors that lead to the formation of multiple images, modelling the deflectors using both spherical and ellipsoidal singular isothermal mass distributions. We further assume that the XXL survey sample has the same overall properties as the smaller *XMM*-COSMOS sample restricted to the same flux limits and taking into account the detection probability of the XXL survey. Among the X-ray sources with a flux in the [0.5–2] keV band larger than 3.0×10^{-15} erg cm^{-2} s^{-1} and with optical counterparts brighter than an r-band magnitude of 25, we expect ∼20 multiply imaged sources. Out of these, ∼16 should be detected if the search is made among the seeing-limited images of the X-ray AGN optical counterparts and only one of them should be composed of more than two lensed images. Finally, we study the impact of the cosmological model on the expected fraction of lensed sources.

Key words: gravitational lensing: strong – galaxies: active – cosmological parameters – X-rays: galaxies.

1 INTRODUCTION

The XXL survey,[1] carried out by the space-based X-ray observatory *XMM–Newton*, spans over ∼2 × 25 square degrees with near 10 ks exposure in each field and is expected to lead to the detection of ∼25 000 active galactic nuclei (AGNs) down to a limiting flux 10^{-15} erg cm^{-2} s^{-1} in the [0.5–2] keV soft X-ray band (Pierre et al., in preparation). These X-ray data are complemented by multi-wavelength data obtained with the Canada–France–Hawaii Telescope Legacy Survey (CFHTLS) and with the Blanco telescope (Blanco/South Pole Telescope Cosmology Survey) in the (near-) optical u', g, r, i and z bands, down to a limiting AB magnitude of ∼25. Besides the multi-band imaging of the XXL fields, there is a very large on-going effort to obtain optical spectra of XXL sources, through either the matching of existing survey catalogues or dedicated spectroscopic surveys. Among these spectroscopic data acquisition programmes, the VIMOS Public Extragalactic Redshift Survey (Guzzo & Le Fèvre 2010) covers most of the northern field, the southern field being covered using the AAOmega multi-object spectrograph on the Anglo-Australian Telescope, an instrument used for the Galaxy And Mass Assembly project (Driver et al. 2009).

The completeness of this multi-wavelength data base over the entire XXL field provides a unique sample to search for multiply imaged AGNs. We have thus initiated such a search among the optical counterparts of point-like sources in the soft X-ray band. Besides the scientific interest provided by each multiply imaged source, the goal of this project is to construct a statistically clean sample of lensed sources that will be used, in combination with samples of multiply imaged sources from other recent surveys, to independently constrain the cosmological model.

The choice of the soft X-ray point-like sources is motivated by the higher sensitivity of *XMM–Newton* in this band. Furthermore, this spectral band should contain a larger fraction of type-I AGNs than the hard X-ray. On average, type-I AGNs with a detectable optical counterpart are expected to have a higher redshift than type-II AGNs (more absorbed in the visible and thus more difficult to detect in the optical at high redshift). As higher redshift sources have a higher probability of being lensed, this population is more likely to undergo gravitational lensing with the formation of multiple images. The better angular resolution achievable in the optical domain will allow us to unravel the multiply imaged sources.

A search for gravitational lenses among the optical counterparts of X-ray sources has already been carried out for a subset of the

★ E-mail: finet@astro.ulg.ac.be
† Also, Directeur de Recherche honoraire du F.R.S.-FNRS.
[1] http://ifru.cea.fr/xxl

XXL field, the *XMM–Newton* Large-Scale Structure (XMM-LSS) field (Elyiv et al. 2013). For this smaller field, visual inspection of all optical counterparts has been done in order to identify the multiply imaged AGN candidates that are now awaiting spectroscopic confirmation. The search for lensed sources in the larger XXL field is in progress.

In this paper, we present a prospective analysis of the lensed AGN population detectable within the XXL survey, as well as a study of their expected statistical properties. In order to perform this analysis, we have reformulated the mathematical formalism to study the statistical aspects of gravitational lensing, basing the statistical formalism on the observables of the source population.

This paper is structured as follows. We present the mathematical approach in Section 2. Namely, we derive the expression allowing us to calculate the probability for a source to be lensed with the formation of multiple images, modelling the deflector population by means of a spherical mass distribution and then taking into account the internal ellipticity of the deflector mass distribution. We explain how this expression may be averaged over the entire population of sources detected in the survey, thanks to the source joint probability density, with which we derive the expression of the expected fraction of lensed sources in a survey, as well as the expected redshift distribution of the lensed sources and that of the deflectors. Our simulations also account for the inability of the ground-based CFHT and Blanco telescopes to resolve multiple images with too small angular separations.

In Section 3, we present the observational constraints used to estimate the expected properties of the XXL population in the X-ray and optical domains: these were inferred from the deeper (but smaller) XMM-COSMOS field (Brusa et al. 2010). Finally, in Section 4 we present our results, i.e. the expected number of multiply imaged sources in the XXL and the XMM-LSS fields, as well as the expected statistical properties of these lensed sources. We also investigate the fraction of lensing events as a function of their number of lensed images and we investigate how the fraction of multiply imaged sources changes as a function of the cosmological mass density parameter, $\Omega_{\rm m}$.

2 MATHEMATICAL FORMALISM

2.1 Lensing optical depth

Multiple images due to gravitational lensing occur when light rays emitted from a background source are deviated towards the observer by a foreground deflector located near the line of sight. In our case, the amplified lensed sources have to be above the survey flux limit in both the X-ray and the optical domains, and the lensed images have to be resolved in the latter. The probability for a source to be lensed depends on its redshift, its X-ray flux and r-band magnitude. In this section, we derive an expression to calculate the probability for a source to undergo a gravitational lensing event as a function of its redshift and its X-ray flux only, considering the minimal angular separation resolvable in the r band. We will analyse the validity of this simplification in Section 5 by formally including the r magnitude in the calculations.

Let us consider a source with redshift $z_{\rm s}$, with an observed flux $f_{\rm X}$ in the X-ray band, and a lens with a mass distribution characterized by a set of parameters M', located at an intermediate position along the line of sight at redshift $z_{\rm d}$. In the lens plane perpendicular to the line of sight, we can define an area $\Sigma(z_{\rm s}, z_{\rm d}, f_{\rm X}, M')$ centred on the source projected on the lens plane, called the lensing cross-section in which the presence of a deflector leads to the detection of multiple images by the observer (where the multiple images are resolved in the r-band CCD frames). The lensing cross-section is a function of the redshifts of the source and the deflector, the X-ray flux $f_{\rm X}$ of the source and the deflector mass distribution parameters M' (some mass distributions are more efficient at deflecting light rays and thus have a larger lensing cross-section).

The probability $\mathrm{d}\tau(z_{\rm s}, z_{\rm d}, f_{\rm X}, M')$ for this source to be multiply imaged due to the presence of a deflector in the redshift range $[z_{\rm d}, z_{\rm d} + \mathrm{d}z_{\rm d}]$ is given by (Turner, Ostriker & Gott 1984)

$$\mathrm{d}\tau = (1+z_{\rm d})^3\, n_{\rm D}\left(z_{\rm d}, M'\right) \frac{c\mathrm{d}t}{\mathrm{d}z_{\rm d}}\, \Sigma\left(z_{\rm s}, z_{\rm d}, f_{\rm X}, M'\right)\, \mathrm{d}z_{\rm d}, \tag{1}$$

where $n_{\rm D}(z_{\rm d}, M')$ is the volume density in the comoving reference frame of deflectors characterized by the mass parameters M'. The quantity $c\mathrm{d}t/\mathrm{d}z_{\rm d}$ represents the infinitesimal light-distance element at redshift $z_{\rm d}$ per deflector redshift unit, which, in a flat expanding Friedmann-Lemaître-Robertson-Walker (FLRW) universe, is given by (e.g. Peebles 1993)

$$\frac{c\mathrm{d}t}{\mathrm{d}z_{\rm d}} = \frac{c}{H_0\,(1+z_{\rm d})}\, \left[(1+z_{\rm d})^3\, \Omega_{\rm m} + (1-\Omega_{\rm m})\right]^{-1/2}. \tag{2}$$

where $\Omega_{\rm m}$ is the present-day value of the cosmological mass density parameter.

The envelope of the lensing cross-sections at different deflector redshifts $z_{\rm d}$ defines the *lensing volume* in which the presence of a deflector leads to the detection of multiple lensed images of the background source. The probability $\tau(z_{\rm s}, f_{\rm X}, M')$ for a source to be lensed with the formation of multiple images can be calculated by integrating equation (1) over all values of the deflector redshift $z_{\rm d}$, which leads to

$$\tau\left(z_{\rm s}, f_{\rm X}, M'\right) = \int_0^{z_{\rm s}} (1+z_{\rm d})^3\, n_{\rm D}\left(z_{\rm d}, M'\right) \frac{c\mathrm{d}t}{\mathrm{d}z_{\rm d}}\, \Sigma\left(z_{\rm s}, z_{\rm d}, f_{\rm X}, M'\right)\, \mathrm{d}z_{\rm d}. \tag{3}$$

The definition of $\tau(z_{\rm s}, f_{\rm X}, M')$ in equation (3) corresponds to an optical depth, which for small values can be assimilated to a probability. For this reason, we refer to $\tau(z_{\rm s}, f_{\rm X}, M')$ as the source *lensing optical depth* or *lensing probability*, without distinction.

In equation (3), the comoving density $n_{\rm D}(z_{\rm d}, M')$ of deflectors assumes one type of deflectors with similar characteristics defined by the parameters M'. Considering the mass distribution to be characterized by means of deflectors with a central velocity dispersion σ, in the range $[\sigma, \sigma + \mathrm{d}\sigma]$, $n_{\rm D}(z_{\rm d}, \sigma)$ may be expressed by means of the velocity dispersion function (VDF) of galaxies $\Phi_\sigma(\sigma, z_{\rm d})$,

$$n_{\rm D}\left(z_{\rm d}, \sigma\right) = \Phi_\sigma\left(\sigma, z_{\rm d}\right) \mathrm{d}\sigma. \tag{4}$$

To take into account the contribution of all galaxies with different central velocity dispersions, equation (3) has to be integrated over σ. The VDF in equation (4) can be either measured directly or inferred from the luminosity function (LF) of the deflecting galaxies, using the mean Faber–Jackson or Tully–Fisher relationship, depending on the type of galaxies considered. However, Sheth et al. (2003) have shown that neglecting the dispersion of the Faber–Jackson relationship leads to a wrong estimate of the VDF. We thus use the VDF determined directly through observations (thereby following Sheth et al. 2003; Mitchell et al. 2005; Choi, Park & Vogeley 2007; Chae 2010). Sheth et al. (2003) and Choi et al. (2007) have shown that the VDF of early- and late-type galaxies is well fitted by the modified Schechter function

$$\Phi_\sigma\left(\sigma, z_{\rm d}\right) \mathrm{d}\sigma = \Phi_* \left(\frac{\sigma}{\sigma_*}\right)^\alpha \exp\left(-\left(\frac{\sigma}{\sigma_*}\right)^\beta\right) \frac{\beta}{\Gamma\left(\alpha/\beta\right)} \frac{\mathrm{d}\sigma}{\sigma}. \tag{5}$$

where Φ_* and σ_* are the characteristic number density and central velocity dispersion, respectively, α and β are the slope coefficients of the VDF for low and high values of σ, respectively, and where $\Gamma(x)$ is the Gamma function.

Although less numerous, early-type galaxies are much more efficient deflectors than late-type ones, which tend to form multiple images with smaller angular separation. Late-type galaxies contribute by less than 10 per cent to the gravitational lensing events in a typical sample of lensed AGNs selected in the optical or near-infrared (Fukugita & Turner 1991; Maoz & Rix 1993; Keeton, Kochanek & Falco 1998; Kochanek et al. 2000), although in radio-selected samples, thanks to the better angular resolution of the survey, the fraction of lensing events formed by late-type deflectors may be higher (e.g. the CLASS survey where at least 5 of 22 deflectors are late-type galaxies; see Browne et al. 2003). In the present work, because the multiple images will be searched for in the SDSS r band, we consider the deflector population to be only composed of early-type galaxies, and we will study in Section 4 the validity of this assumption.

Constraints from strong-lensing statistics on the evolution of the VDF of early-type galaxies show very little evolution or are consistent with a no-evolution assumption (see e.g. Chae 2003, 2010; Ofek, Rix & Maoz 2003; Oguri et al. 2012). Consequently, throughout this work we assume the deflector VDF to be constant with redshift in the comoving reference frame, or in other words, that there is no impact of the evolution of the deflector population on the VDF and we use the value of the VDF parameters determined in the local Universe by Choi et al. (2007), i.e.

$$[\Phi_*, \sigma_*, \alpha, \beta] = \left[8 \times 10^{-3}\, h^3\,\mathrm{Mpc}^{-3},\ 161\,\mathrm{km\,s}^{-1},\ 2.32,\ 2.67\right].$$

The lensing cross-section in equation (1) depends on the deflector mass distribution parmeters M. For a deflector mass distribution modelled as a singular isothermal sphere (SIS; a spherical mass distribution with a volume density scaling as r^{-2}), the mass distribution is characterized by the line-of-sight velocity dispersion σ and the lensing cross-section $\Sigma(z_\mathrm{s}, z_\mathrm{d}, f_\mathrm{X}, \sigma)$ can be defined as [see Turner et al. (1984) for definition and Claeskens (1999) for the formalism followed in this paper]

$$\Sigma\left(z_\mathrm{s}, z_\mathrm{d}, f_\mathrm{X}, \sigma\right) = b_0^2\left(z_\mathrm{s}, z_\mathrm{d}, \sigma\right) \iint_{S_\mathrm{y}} \frac{N_{f_\mathrm{X}}\left(f_\mathrm{X}/A\left(\mathbf{y}\right)\right)}{N_{f_\mathrm{X}}\left(f_\mathrm{X}\right)} \mathrm{d}\mathbf{y}, \tag{6}$$

where we have introduced the source vector $\mathbf{y} = (y_1, y_2)$ which Cartesian coordinates are projected on the deflector plane, and normalized to the scale factor b_0 (i.e. the Einstein radius in the deflector plane). $A(\mathbf{y})$ is the total amplification of the lensed images formed for a source located at the position $\mathbf{y}$, i.e. the sum of the amplification moduli of each lensed image and $N_{f_\mathrm{X}}(f_\mathrm{X})$ is the differential number counts function (DNCF) as a function of the source flux f_X in the X-ray band. For an SIS deflector, the scale factor is given by (see e.g. Claeskens 1999)

$$b_0\left(\sigma, z_\mathrm{d}, z_\mathrm{s}, \mathrm{UM}\right) = 4\pi\left(\frac{\sigma}{c}\right)^2 \frac{D_\mathrm{OD} D_\mathrm{DS}}{D_\mathrm{OS}}, \tag{7}$$

where D_OD, D_DS and D_OS represent the different angular diameter distances between the observer, the deflector and the source, c is the speed of light and $\mathrm{UM} = (\Omega_\mathrm{m}, H_0)$ is a set of parameter values characterizing the universe model as a flat expanding FLRW one.

The ratio $N_{f_\mathrm{X}}\left(f_\mathrm{X}/A\left(\mathbf{y}\right)\right)/N_{f_\mathrm{X}}\left(f_\mathrm{X}\right)$ in equation (6) is known as the *amplification bias* (Turner 1980; Turner et al. 1984; Fukugita & Turner 1991). It is introduced to take into account a favourable bias when estimating the lensing probability in a flux-limited sample induced by the amplification phenomenon. The amplification may lead to the inclusion of sources in a flux-limited sample that are intrinsically fainter than the flux limit but have undergone a gravitational lensing amplification. Since the ratio of the DNCF in equation (6) at two different X-ray flux levels (i.e. f_X and $f_\mathrm{X}/A\left(\mathbf{y}\right)$) is likely to be slightly dependent on the source redshift, it would certainly be more accurate to consider the redshift dependence of the DNCF. However, at the time of this work, the XXL redshifts are not yet available and we do not have access to a source sample large enough to constrain the redshift dependence of the DNCF (the source sample used is described in Section 3). Consequently, we consider the value of the DNCF ratios averaged over the whole redshift range. Because of the presence of $A\left(\mathbf{y}\right)$ in the amplification bias, the expression of $\Sigma(z_\mathrm{s}, z_\mathrm{d}, f_\mathrm{X}, \sigma)$ is intrinsically linked to the amplification map of the deflector defining the amplification as a function of the source position, itself determined by the mass distribution of the deflector. It is out of the scope of this paper to explain this dependence in detail and the reader may refer to e.g. Hezaveh & Holder (2011) for some further description. Nevertheless, because of the presence of the total amplification A in its argument, the calculation of the amplification bias in equation (6) necessitates the knowledge of $N_{f_\mathrm{X}}\left(f_\mathrm{X}\right)$ for sources fainter than the survey limiting flux. This may be estimated either by extrapolating $N_{f_\mathrm{X}}\left(f_\mathrm{X}\right)$ or by considering a parent source sample accessing fainter fluxes. In this work, we will consider a deeper source sample described in Section 3.

Finally, S_y in equation (6) represents the area in the $\mathbf{y}$ plane, centred on the deflector, in which the presence of a source leads to a *lensing event*, i.e. the lensing cross-section, normalized to the scale factor.

The *lensing event* may be defined in different ways. It may refer to the formation of multiple images or to the formation of a given number of lensed images, or the formation of lensed images with an angular separation sufficiently large to be detected in a survey. Depending on the definition adopted for the lensing event, the integration domain S_y differs and, consequently, this leads to a different definition of the lensing cross-section Σ in equation (6) and of the lensing optical depth in equation (3). In most cases, the integration in equation (6) must be performed numerically.

When modelling the deflector mass distribution by means of an SIS profile, the lensing events can lead to the formation of two images at maximum. We define $\tau_\mathrm{SIS}(z_\mathrm{s}, f_\mathrm{X})$ as the probability for a source to be multiply imaged when the deflectors are modelled by an SIS mass distribution. $\tau_\mathrm{SIS}(z_\mathrm{s}, f_\mathrm{X})$ is thus calculated by inserting equations (4)–(7) into equation (3) and by performing the integration over σ. The integration over σ can be performed analytically, leading to the following expression (Turner et al. 1984; Mitchell et al. 2005 for derivation using the VDF)

$$\tau_\mathrm{SIS}\left(z_\mathrm{s}, f_\mathrm{X}\right) = \Phi_* \frac{\Gamma\left(\left(\alpha+4\right)/\beta\right)}{\Gamma\left(\alpha/\beta\right)} \int_0^{z_\mathrm{s}} \left(1+z_\mathrm{d}\right)^3 \frac{c\mathrm{d}t}{\mathrm{d}z_\mathrm{d}} \Sigma_\mathrm{SIS}\left(z_\mathrm{s}, z_\mathrm{d}, f_\mathrm{X}, \sigma_*\right) \mathrm{d}z_\mathrm{d}. \tag{8}$$

$\Sigma_\mathrm{SIS}(z_\mathrm{s}, z_\mathrm{d}, f_\mathrm{X}, \sigma_*)$ represents the lensing cross-section defined by equation (6), for $\sigma = \sigma_*$, when considering the area S_y for the case of an SIS deflector. The integration in equation (8) must be performed numerically.

The introduction of an internal ellipticity in the mass distribution used to model the deflectors allows us to account for the formation of more than two lensed images. This is the reason why the singular isothermal ellipsoid (SIE) mass distribution has been introduced (Kormann, Schneider & Bartelmann 1994). The ellipticity parameter in the SIE profile is the axial ratio q of the deflector mass

projected on the deflector plane and the mass distribution parameters M' are now σ and q. As for the case of the SIS deflector, we can define the probability $\tau_{\rm SIE}(z_{\rm s}, f_{\rm X})$ for a source to be lensed with the formation of multiple images, irrespectively of the number of the lensed images, when modelling the deflector population with SIE mass distributions (Huterer, Keeton & Ma 2005). On the other hand, we may also define the probability $\tau_{{\rm SIE},i}(z_{\rm s}, f_{\rm X})$ for a source to be lensed with the formation of i images (with $i = 2, 3$ or 4). As the lensing cross-section now depends on the axial ratio q of the deflector (through the dependence of S_i in equation 6), in order to calculate $\tau_{\rm SIE}(z_{\rm s}, f_{\rm X})$ we must also integrate equation (1) over the axial ratio q, using an appropriate probability distribution. Furthermore, the deflector density function in equations (3) and (4) must take into account how the deflector population is distributed as a function of both σ and q, and thus we have to introduce the dependence of $n_{\rm D}$ on the axial ratio q. In equation (4), the density $n_{\rm D}(\sigma, q)$ of deflectors with a central velocity dispersion in the range $[\sigma, \sigma + {\rm d}\sigma]$ and an axial ratio in the range $[q, q + {\rm d}q]$ may be expressed as

$$n_{\rm D}(\sigma, q) = \Phi_\sigma(\sigma)\, d_{q|\sigma}(\sigma, q)\, {\rm d}\sigma = \Phi_\sigma(\sigma)\, d_q(q)\, {\rm d}\sigma {\rm d}q, \quad (9)$$

where $d_{q|\sigma}(\sigma, q)$ represents the normalized axial ratio distribution for the deflectors with a central velocity dispersion σ and $d_q(q)$ is the marginal normalized distribution as a function of q. The last equality arises if we assume that the deflector distributions as a function of σ and q are mutually independent.[2] $\Phi_\sigma(\sigma)$ is given by equation (5), as in the case of the SIS mass model. There are pieces of strong evidence from the study of various gravitational lens samples, that elliptical galaxy isophotes and the mass distribution ellipticities are aligned and have well-correlated values (see Koopmans et al. 2006; Sluse et al. 2012 for independent confirmations). Furthermore, as previously mentioned, there is no evidence for strong evolution effects in the VDF of early-type galaxies from lensing surveys. Thanks to these two observational facts, $d_q(q)$ can be estimated from the distribution of the isophotes of early-type galaxies as measured in the local Universe. We therefore use the axial ratio distribution measured by Choi et al. (2007) from a sample of elliptical galaxies in the local Universe.

$\tau_{\rm SIE}(z_{\rm s}, f_{\rm X})$ can thus be calculated by inserting equations (5) and (9) into equation (1), and by integrating over σ and q. Using equations (6) and (7), and performing the analytical integration over σ, $\tau_{\rm SIE}$ can thus be expressed as

$$\tau_{\rm SIE}(z_{\rm s}, f_{\rm X}) = \Phi_* \frac{\Gamma((\alpha+4)/\beta)}{\Gamma(\alpha/\beta)} \int_0^{z_{\rm s}} (1+z_{\rm d})^3 \frac{c{\rm d}t}{{\rm d}z_{\rm d}} \int_0^1 d_q(q)\, \Sigma_{\rm SIE}(z_{\rm s}, z_{\rm d}, f_{\rm X}, \sigma_*, q)\, {\rm d}q\, {\rm d}z_{\rm d}, \quad (10)$$

where $\Sigma_{\rm SIE}(z_{\rm s}, z_{\rm d}, f_{\rm X}, \sigma_*, q)$ represents the lensing cross-section calculated through numerical integration of equation (6), when considering an SIE deflector with an axial ratio q and a central velocity dispersion σ_*. Similarly, the probability $\tau_{{\rm SIE},i}(z_{\rm s}, f_{\rm X})$ for a source to be lensed with the formation of i images, when modelling the deflectors with SIE profiles, can be calculated using $\Sigma_{{\rm SIE},i}$ in the previous relation and considering in S_i only the area in which a source should be located in order to lead to the formation of i lensed images.

We have developed *Matlab* toolboxes and libraries to perform the numerical integration in the expressions of $\tau_{\rm SIS}(z_{\rm s}, f_{\rm X})$ and $\tau_{\rm SIE}(z_{\rm s}, f_{\rm X})$ from equations (8) and (10), as well as for the calculation of $\tau_{{\rm SIE},i}(z_{\rm s}, f_{\rm X})$, taking into account that lensed images angularly too close to each other cannot be resolved in the survey. The numerical integrations are made in two steps. First, we create a data base of the lensing cross-sections in equation (6), considering $h_0 = 1$, ranging over all possible values of $f_{\rm X}$ and over the ratio $\theta_{\rm min}/\theta_{\rm E}$, where $\theta_{\rm min}$ represents the smallest angular separation for which point-like images of same brightness are resolved in the survey, and also over q for the SIE case. The integration of the double integral in equation (6) is performed by plain Monte Carlo integration, where we randomly generate $\sim 10^6$ source positions $\boldsymbol{y}$, and calculate the position and amplification of the lensed images, which contribute to the integral only if the multiple images can be resolved and brighter than the X-ray limiting flux of the survey. In the second step, the lensing optical depths are calculated by integrating equations (8) and (10) using trapezoidal integration and the data base of lensing cross-sections. We have thus all the tools needed for the calculation of the lensing optical depth of a source with known redshift and apparent X-ray flux, when considering a population of deflectors modelled with SIS or SIE mass distributions.

Similar expressions for the lensing optical depths such as $\tau_{\rm SIS}(z_{\rm s}, f_{\rm X})$, $\tau_{\rm SIE}(z_{\rm s}, f_{\rm X})$ and $\tau_{{\rm SIE},i}(z_{\rm s}, f_{\rm X})$ (equations 8 and 10, respectively), as well as their differential contribution as a function of the deflector redshift ${\rm d}\tau/{\rm d}z_{\rm d}$, have already been derived and used for the analysis of statistical samples of lensed sources, either to constrain the cosmological model (e.g. Turner et al. 1984; Fukugita, Futamase & Kasai 1990; Turner 1990; Fukugita & Turner 1991; Kochanek 1992; Maoz & Rix 1993; Surdej et al. 1993; Cen et al. 1994; Chae et al. 2002; Keeton 2002; Chae 2003; Oguri et al. 2012) or to study the population of deflectors (Keeton 1998; Keeton & Kochanek 1998; Keeton et al. 1998; Kochanek et al. 2000; Chae 2003, 2010; Ofek et al. 2003), some of the work having considered the ellipticity of the mass distribution as well as the effect of external sheer on the statistics (Huterer et al. 2005; Oguri & Marshall 2010; Oguri et al. 2012).

The various expressions derived for the optical depth τ and its differential contribution ${\rm d}\tau/{\rm d}z_{\rm d}$ are considered for a single source. This may be averaged over the whole detected population to derive the mean optical depth through the sample as well as the expected redshift distributions of the lensed sources and deflectors. To average over the population of sources, some previous works have made use of the source LF, and integrate over the absolute magnitude of the source population (e.g. Oguri & Marshall 2010; Oguri et al. 2012) which, for the integration process, necessitates the choice of a universe model.

In the next subsection, we propose a slightly different formulation that allows us to average any function over the entire population of sources detected in a survey, where the averaging is done based on the observables, i.e. the distribution in the $(z_{\rm s}, f_{\rm X})$ plane of the detected sources. Because the formalism is based directly on the observed distribution of sources, it naturally takes into account the detection biases of the sources. We apply this method to derive useful expressions such as the average lensing optical depth in a sample, the redshift distributions of the lensed sources and of the deflectors effectively leading to the formation of multiple lensed images.

[2] Although not strictly justified, this assumption is made because of the lack of observational constraints for the distribution of early-type galaxies in the (σ, q) plane, as well as for calculation time consideration.

2.2 Joint source probability density and fraction of multiply imaged sources

Let us consider a survey characterized by its limiting flux, different biases in the source detection procedure and its angular coverage. Each detected source is characterized by its redshift z_s and its flux f_X in the selected spectral band (in the present case, the [0.5–2] keV band). The detection of a source within the survey may be considered as a random event with respect to the continuous random variables associated with the source redshift and the X-ray flux, respectively.

We can define a probability $P(z_s, f_X)$ that a source detected in the survey is characterized by an observed redshift and flux in the range $[z_s, z_s + \mathrm{d}z_s[$ and $[f_X, f_X + \mathrm{d}f_X[$, respectively. We may then define the joint probability density $d_{\rm obs}(z_s, f_X)$ spanning over the (z_s, f_X) plane, associated with this random event. $P(z_s, f_X)$ and $d_{\rm obs}(z_s, f_X)$ are related through

$$P(z_s, f_X) = d_{\rm obs}(z_s, f_X)\,\mathrm{d}z_s\mathrm{d}f_X. \tag{11}$$

The random variables z_s and f_X associated with a detected source follow the joint distribution described by $d_{\rm obs}(z_s, f_X)$. This function contains all the information about the survey and implicitly takes into account the detection biases. For a sufficiently large number of detected sources, the joint probability density $d_{\rm obs}(z_s, f_X)$ may be directly estimated from the detected source population, by calculating a smoothed histogram of the source distribution in the (z_s, f_X) plane, normalized by the total number $N_{\rm AGN}$ of sources detected within the survey. Ideally, we would have liked to define the source joint probability density $d_{\rm obs}(z_s, f_X, r)$ in the (z_s, f_X, r) space, where r represents the SDSS r magnitude of the optical counterpart(s) of the X-ray sources. However, because of the small number of sources observed in our reference sample (see Section 3), the quantity $d_{\rm obs}(z_s, f_X, r)$ could hardly be accurately determined. When analysing the XXL sample however, the number of detected sources should be sufficient to constrain $d_{\rm obs}$ in the 3D space. We shall therefore postpone such a more detailed study until all optical counterparts of the XXL X-ray sources have been identified.

The normalized marginal probability density distributions associated with the random variables z_s and f_X are closely related to the observations. Indeed, the marginal density distribution obtained by integrating $d_{\rm obs}(z_s, f_X)$ over z_s or f_X represents the normalized source distribution as a function of the flux $N_{f_X}(f_X)/N_{\rm AGN}$ and the redshift $N_{z_s}(z_s)/N_{\rm AGN}$, respectively.

The use of $d_{\rm obs}(z_s, f_X)$ as a weighing function when performing the integration over the entire population of detected sources allows us to calculate the expected mean value of any function of the random variables z_s and f_X. The mathematical expectation $\langle\tau\rangle$ of the lensing optical depth, i.e. the fraction of sources gravitationally lensed within the detected population, can be calculated by integrating $\tau(z_s, f_X)$ over the (z_s, f_X) plane, weighing with $d_{\rm obs}(z_s, f_X)$, i.e.

$$\langle\tau\rangle = \iint \tau(z_s, f_X)\, d_{\rm obs}(z_s, f_X)\,\mathrm{d}z_s\mathrm{d}f_X. \tag{12}$$

Using the expression of $\tau_{\rm SIS}(z_s, f_X)$, $\tau_{\rm SIE}(z_s, f_X)$ or $\tau_{{\rm SIE},i}(z_s, f_X)$ given by equations (8) and (10) for the calculation of the optical depth $\tau(z_s, f_X)$ in equation (12), we are able to calculate the expected fraction of multiply imaged sources, considering a population of deflectors modelled with either the SIS or SIE mass profile. In the latter case, we can also calculate the expected fraction of lensed sources as a function of the number i of lensed images.

Oguri et al. (2008) have also derived an expression for the number of multiply imaged sources using a binning of the redshift–magnitude space (equation 12 in Oguri et al. 2008), and with the number of sources in the bins as a weighing factor. Their expression corresponds to the discrete equivalent of equation (12), integrating in the redshift–magnitude space, rather than the (z_s, f_X) plane. The essential difference between the approach used in these previous works and ours is the use of the source distribution in the (f_X, z_s) rather than using the source LF as a weighing factor in the absolute magnitude–redshift space. Our approach allows us to account directly for the detection bias of the sources and does not necessitate any assumption of a universe model for the calculation of the weighing factor (which is necessary when using absolute magnitudes and the source LF).

2.3 Normalized redshift distributions

It is now straightforward to establish the normalized distribution $w_{Z_d}(z_d)$ of the deflector redshifts expected in the XXL field

$$w_{Z_d}(z_d) = \frac{1}{\langle\tau\rangle}\iint \left\{\frac{\mathrm{d}\tau}{\mathrm{d}z_d}(z_s, z_d, f_X)\, d_{\rm obs}(z_s, f_X)\right\}\mathrm{d}z_s\mathrm{d}f_X, \tag{13}$$

where the differential contribution $\mathrm{d}\tau/\mathrm{d}z_d$ of the redshift z_d to a source lensing optical depth is given by equation (1).

Similarly, the normalized redshift distribution $w_{Z_s}(z_s)$ of the lensed sources is given by

$$w_{Z_s}(z_s) = \frac{1}{\langle\tau\rangle}\int \tau(z_s, f_X)\, d_{\rm obs}(z_s, f_X)\,\mathrm{d}f_X. \tag{14}$$

Oguri et al. (2012) have derived by different means an expression for $w_{Z_d}(z_d)$ and applied it to the sample of the SDSSQLS (see equation 23 in Oguri et al. 2012). This estimation was done by binning the redshift–magnitude plane and using the number of sources in the different bins as a weighing factor. Their relation corresponds to the discrete equivalent of equation (13), where the integration runs over the redshift–magnitude plane, rather than the (z_s, f_X) one.

In Oguri & Marshall (2010), the authors have derived a different expression for the redshift distribution of the lensed sources (equation 7 in Oguri & Marshall 2010), equivalent to equation (14), except that the integration runs over the absolute magnitude and the weighing function used in the integration corresponds to the expression of the joint probability density expressed in terms of the source LF.

Finally, let us note that Mitchell et al. (2005) have also derived an estimation for the redshift distribution of the lensed sources in the CLASS survey, assuming the DNCF of the sources to be expressed as a single power-law expression, i.e. the amplification bias being thus constant for each source. However, this assumption is very restrictive as QSOs usually show a DNCF that presents a break at a critical magnitude, and needs to be modelled by a double power-law expression.

The use of $d_{\rm obs}(z_s, f_X)$ allows an easy calculation of $\langle\tau\rangle$ through the survey, and the calculation of the expected normalized distributions $w_{Z_s}(z_s)$ and $w_{Z_d}(z_d)$, as a function of the redshift of the lensed sources and of the deflectors, respectively. These distributions are calculated without any assumption about the source population, as $d_{\rm obs}(z_s, f_X)$ may be directly estimated from the observed data, naturally including the observational biases.

In the next section, we present the observational constraints used for the estimation of the joint probability density of the XXL survey.

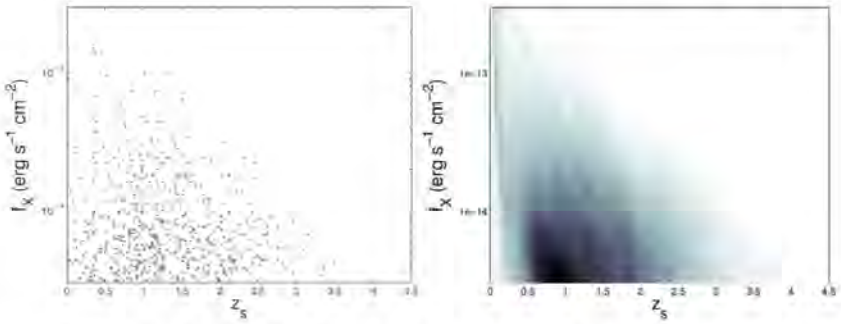

Figure 1. The left-hand panel displays the distribution in the (z_s, f_X) plane of the XMM-COSMOS source population (Brusa et al. 2010), restricted to $F_{[0.5-2]\mathrm{keV}} > 3 \times 10^{-15}$ erg cm^{-2} s^{-1} in the [0.5–2] keV band and with an optical counterpart brighter than $r = 25$, for which a redshift estimate is available. This X-ray band flux limit corresponds to a detection probability of 0.5 in the XMM-LSS field, as defined in Elyiv et al. (2012). The X-ray flux is shown on a logarithmic scale. The right-hand panel displays the joint probability density function $d_{\mathrm{obs}}(z_s, f_X)$ in the (z_s, f_X) plane, corresponding to the XMM-COSMOS source population (Brusa et al. 2010), restricted to the X-ray band flux limit of the XMM-LSS fields.

3 OBSERVATIONAL CONSTRAINTS AND d_{obs} DETERMINATION

Ideally, the joint probability density of the XXL sources should be derived by constructing a histogram of the XXL sources in the redshift–X-ray flux plane. However, the cross-correlation between the X-ray and (near-)optical data and the identification of the source type have not yet been performed. The XXL X-ray sources and their associated multi-wavelength data have characteristics similar to those of one of its sub-fields, the XMM-Large Scale Structure (XMM-LSS), covering 10.9 out of the 44.2 square degrees effectively covered by the XXL survey. The XMM-LSS X-ray sources and their associated multi-wavelength data, presented in Chiappetti et al. (2013), have optical counterparts taken from the CFHTLS W1 catalogue, down to the limiting magnitudes $i' \simeq 25$, $r' \simeq 25$, before correction for Galactic extinction.[3] The X-ray source classification and properties of the XMM-LSS field have already been determined (Melnyk et al. 2013). The survey limiting flux in the soft band is $F_{[0.5-2]\mathrm{keV}} \simeq 3 \times 10^{-15}$ erg s^{-1} cm^{-2} (with a detection probability of 0.5, as defined in Elyiv et al. 2012). Nevertheless, at the time of this work, the redshift estimate in the XMM-LSS sample is still ongoing.

Therefore, to retrieve the properties of the expected population to be detected within the XXL survey and their optical counterparts, we used data from a deeper field (~60 ks exposure, compared to ~10 ks for XMM-LSS): the XMM-COSMOS field, to which we apply the flux cuts of the XXL in the X-ray and the optical, that we assume to be similar to those of the XMM-LSS. The XMM-COSMOS survey, covering a contiguous field of 2 square degrees, is described in Brusa et al. (2010), and has a limiting flux of $F_{[0.5-2]\mathrm{keV}} \simeq 5 \times 10^{-16}$ erg s^{-1} cm^{-2} ($\simeq 1.4 \times 10^{-15}$ considering the flux with 50 per cent effective area coverage; see fig. 6 in Cappelluti et al. 2007). The flux limit at 50 per cent effective area coverage for the XMM-LSS and that for the COSMOS are in good agreement with the exposure time ratios as $3 \times 10^{-15}/1.4 \times 10^{-15} \sim \sqrt{60\,\mathrm{ks}/10\,\mathrm{ks}}$.

[3] After correction, the limiting magnitudes of the CFHTLS W1 catalogue are (expressed in AB magnitudes and considering a 5σ signal-to-noise ratio) $r \simeq 24.8$ and $i \simeq 24.5$. See http://xxlmultiwave.pbworks.com/w/page/54613008/Optical and http://terapix.iap.fr/rubrique.php?id_rubrique=268 for details.

Their optical catalogue with which the cross-correlation was performed contains sources detected in at least one of the Subaru bands (b, v, g, r, i, z) down to an AB magnitude limit of ~27. The COSMOS sample is almost complete down to $F_{[0.5-2]\mathrm{keV}} \simeq 3 \times 10^{-15}$ erg s^{-1} cm^{-2} (X-ray detection probability of $\geq$0.98; cf. Cappelluti et al. 2007, fig. 6), and 98 per cent of the X-ray sources have an optical counterpart.

The joint probability density of the XXL survey is expected to be quite similar to that of the XMM-COSMOS field if we apply to this survey the same X-ray and optical flux cuts and take into account the different probability of detection for sources fainter than 2×10^{-14} erg cm^{-2} s^{-1}. Consequently, we first estimate the COSMOS joint probability density $d_{\mathrm{COSMOS}}(z_s, f_X)$ from a smoothed histogram of the sources from the XMM-COSMOS in the (z_s, f_X) plane, where we apply the X-ray and r-band cutoffs of the XXL. We then take into account the XXL detection probability to determine $d_{\mathrm{obs}}(z_s, f_X)$.

In the left-hand panel of Fig. 1, we have represented the XMM-COSMOS sources in the (z_s, f_X) plane, with fluxes presented along a logarithmic scale. We have only considered sources with a flux larger than $F_{[0.5-2]\mathrm{keV}} = 3 \times 10^{-15}$ erg cm^{-2} s^{-1} in the [0.5–2] keV band and with an optical counterpart brighter than $r = 25$ in the SDSS r band. We have rejected all X-ray sources for which there was no redshift estimate. Whenever available, spectroscopic redshifts were preferred to photometric ones. The XMM-COSMOS catalogue presented in Brusa et al. (2010) contains 1797 sources in the 2 square degrees. After applying the X-ray and r-band cutoff (and excluding sources with no available r magnitude), there are 630 sources of which 6 are excluded because of no available redshift. The final restricted COSMOS source sample contains 624 sources. The density of sources in the (z_s, f_X) plane is larger for the fainter fluxes, near redshift $z \sim 1$. At any given redshift, there are more sources with a lower flux. Finally, let us also point out the absence of sources with a high flux at high redshift.

In order to estimate the joint probability density $d_{\mathrm{COSMOS}}(z_s, f_X)$ of the COSMOS sources, we have calculated a smoothed histogram of the COSMOS source distribution with the XMM cutoff in the X-ray and r band displayed in the left-hand panel of Fig. 1. For the convenience of the developed software, $d_{\mathrm{COSMOS}}(z_s, f_X)$ has been derived using a logarithmic scale for the X-ray fluxes. We have considered redshift intervals of 0.375 with bin centres separated

Table 1. Estimate of (1) the number of sources with an X-ray flux greater than 3×10^{-15} erg cm^{-2} s^{-1} in the [0.5–2] keV range and $r < 25$ and (2) the number of detected multiply imaged sources in the XMM-COSMOS, XMM-LSS and XXL surveys. The estimates of the number of sources are extrapolated from the XMM-COSMOS catalogue taking into account the angular coverage of the different surveys. For the estimate of the number of multiply imaged sources, the numbers in parentheses correspond to the SIS case. Observational data are presented in bold.

Survey	Coverage (deg^2)	Number of sources	Lensed sources ($\theta_{\rm min} = 0$ arcsec) SIE (SIS)	Lensed sources ($\theta_{\rm min} = 0.45$ arcsec) SIE (SIS)	>2 images ($\theta_{\rm min} = 0$ arcsec)	>2 images ($\theta_{\rm min} = 0.45$ arcsec)
XMM-COSMOS	**2**	**621**	–	–	–	–
XMM-COSMOS (with XXL $P_{\rm detection}$)	**2**	**529.5**	–	–	–	–
XMM-LSS	**10.9**	2885	5 (5)	4 (4)	0	0
XXL	**44.2**	11 701	20 (21)	16 (17)	1	1
			$\langle\tau\rangle$ ($\theta_{\rm min} = 0$ arcsec)	$\langle\tau\rangle$ ($\theta_{\rm min} = 0.45$ arcsec)	$\langle\tau_{>2}\rangle/\langle\tau\rangle$ ($\theta_{\rm min} = 0$ arcsec)	$\langle\tau_{>2}\rangle/\langle\tau\rangle$ ($\theta_{\rm min} = 0.45$ arcsec)
SIE			1.698×10^{-3}	1.384×10^{-3}	0.0718	0.0564
SIS			1.788×10^{-3}	1.489×10^{-3}	–	–
SIS (Late)			5.719×10^{-4}	1.629×10^{-6}	–	–

by 0.0625 and logarithmic magnitude intervals of 0.3 separated by bins of 0.05. The derived COSMOS joint probability density is shown in the right-hand panel of Fig. 1. We have intentionally kept the same axis as in the left-hand panel in order to clearly identify the similarities between the two figures. The grey-scale indicates the values of $d_{\rm COSMOS}(z_{\rm s}, f_{\rm X})$; the darker the grey, the higher the probability of finding a source. The normalization factor of $d_{\rm COSMOS}(z_{\rm s}, f_{\rm X})$ is the number of sources (624) detected in the 2 square degrees of the COSMOS field, restricted to the XMM-LSS cutoffs.

To take into account the detection probability of the XXL survey, we multiply the $d_{\rm COSMOS}(z_{\rm s}, f_{\rm X})$ in the right-hand panel of Fig. 1 by the XMM-LSS detection probability as a function of the flux taken from Elyiv et al. (2012, fig. 10), the obtained distribution being $d_{\rm obs}(z_{\rm s}, f_{\rm X})$. The normalization factor of this distribution represents the number of sources (592.5) with $F_{[0.5-2]\rm keV} \gtrsim 3 \times 10^{-15}$ erg cm^{-2} s^{-1} and $r < 25$ that would be detected within the XXL survey in the 2 square degrees of the XMM-COSMOS field. From this normalization factor, we may thus estimate the number of sources to be detected in the XMM-LSS and XXL fields with similar characteristics. The expected numbers of sources in the different surveys are summarized in Table 1. Assuming the final XXL catalogue to have similar characteristics as those of the XMM-LSS, this estimate of $d_{\rm obs}(z_{\rm s}, f_{\rm X})$ is assumed to be valid for both the XMM-LSS and the XXL fields.

As a reliability test of the derived joint probability density $d_{\rm obs}(z_{\rm s}, f_{\rm X})$, we verify its ability to represent the properties of the observed population of AGNs. In the left-hand panel of Fig. 2, we have represented as a continuous grey line the observed cumulative distribution as a function of the redshift of the XMM-COSMOS sources with an X-ray flux larger than $F_{[0.5-2]\rm keV} = 3 \times 10^{-15}$ erg cm^{-2} s^{-1} in the [0.5–2] keV band, with $r < 25$ and a redshift estimation.

In the same figure, we have represented with a dashed dark grey line the cumulative source redshift distribution derived from the COSMOS joint probability distribution when not considering the detection probability of the XXL survey. The cumulative redshift

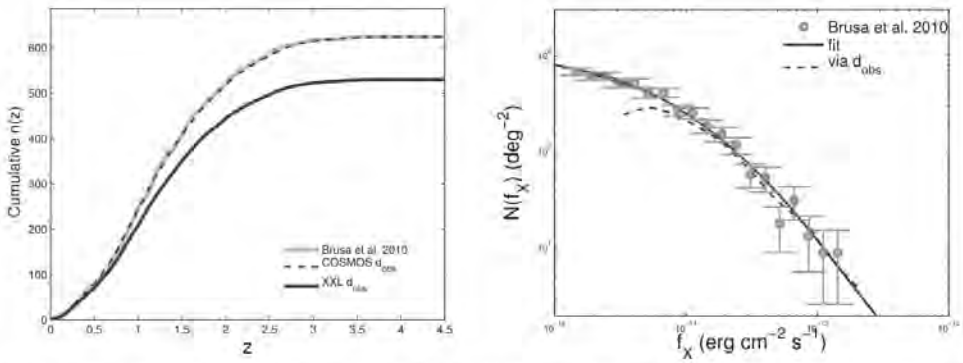

Figure 2. Left-hand panel: cumulative function of the number density $N(z_{\rm s})$ of the sources as a function of the redshift for the XMM-COSMOS sources with $F_{[0.5-2]\rm keV} \gtrsim 3 \times 10^{-15}$ erg cm^{-2} s^{-1} and $r < 25$. We have also represented the cumulative redshift distribution inferred from the marginal distribution of the joint probability density function $d_{\rm COSMOS}(z_{\rm s}, f_{\rm X})$ and $d_{\rm obs}(z_{\rm s}, f_{\rm X})$, with and without considering the XXL detection probability detection (dashed and continuous black curves, respectively). Right-hand panel: differential number counts of the XMM-COSMOS sources as a function of the flux in the soft X-ray band, for all the COSMOS sources, which are used for the amplification bias calculation. We have only represented the X-ray flux range accessible to the XXL survey. We have also represented the marginal distribution obtained from the joint probability density function $d_{\rm COSMOS}(z_{\rm s}, f_{\rm X})$, as well as the DNCF fit used for the calculation of the amplification bias.

distribution is obtained by integrating $d_{\rm COSMOS}(z_{\rm s}, f_{\rm X})$ over $f_{\rm X}$ and by multiplying the number of AGNs detected per square degree in the COSMOS field, where we have applied the XXL cutoffs.

The cumulative redshift distribution inferred from the distribution $d_{\rm COSMOS}(z_{\rm s}, f_{\rm X})$ reproduces very well the observed cumulative source redshift distribution.

In the same figure, we have represented with a dark continuous line the cumulative redshift distribution derived from the final $d_{\rm obs}(z_{\rm s}, f_{\rm X})$ when considering the detection probability of the XMM-LSS survey. We remark very good agreement at low redshift between this distribution and the two previous ones, and a significant deviation above redshift $\sim$1 due to the fact that the XXL survey does not detect all of the fainter sources, more numerous at higher redshifts.

In the right-hand panel of Fig. 2, we have represented the DNCF of the XMM-COSMOS sources as a function of their X-ray soft band flux. The flux is shown along a logarithmic scale and the error bars are estimated considering a Poisson noise. We have here considered all the COSMOS sources brighter than $F_{[0.5\text{-}2]keV} = 1 \times 10^{-15}$ erg cm^{-2} s^{-1}. This DNCF is used to estimate $N_{f_{\rm X}}(f_{\rm X})$ needed when calculating the amplification bias in equation (6). As previously mentioned, the calculation of the lensing optical depth necessitates the knowledge of the DNCF for fluxes fainter than the survey detection limit. We have therefore fitted the observed XMM-COSMOS DNCF $\log_{10}(n(f_{\rm X}))$ with a third-order polynomial in the flux range covered by the XMM-COSMOS and extrapolated the data linearly outside this flux range. The fit is shown as a continuous dark grey line in the right-hand panel of Fig. 2. This polynomial form of the DNCF is used for the calculation of the amplification bias in our simulations.

In the same figure, we have represented with a dashed line the DNCF per unit of solid angle derived from the joint probability density function $d_{\rm obs}(z_{\rm s}, f_{\rm X})$, where we have restricted the COSMOS sources to the XXL cutoffs and taken into account the detection probability of the survey. This is obtained by integrating $d_{\rm obs}(z_{\rm s}, f_{\rm X})$ over $z_{\rm s}$ and by multiplying by the number $N_{\rm AGN}/\Omega$ of AGNs per square degree. This curve is matching fairly well the fitted curve for the brighter sources and is lower for the fainter sources, where the XXL survey only detects part of the sources and where the fraction of excluded sources with $r > 25$ is higher.

The small size of the source sample in the XMM-COSMOS field at low redshift (due to the small survey angular coverage) does not permit a better estimate of $d_{\rm obs}(z_{\rm s}, f_{\rm X})$ at these low redshift values, because of a large scatter in the observed data at low redshift, especially for the brighter sources. Nevertheless, as these very bright and low-redshift sources are very rare in the survey and as their lensing probability is very small (because of their very low redshift), this does not have a large impact on our simulations. These problems will be reduced in the XXL survey, for which the angular coverage is $\sim$20 times larger than that of the XMM-COSMOS field. This confirms, as mentioned earlier, that the COSMOS sample is not large enough to determine the distribution $d_{\rm obs}(z_{\rm s}, f_{\rm X}, r)$ of the sources in the 3D space $(z_{\rm s}, f_{\rm X}, r)$.

4 RESULTS

4.1 Mean lensing optical depth

Using the joint probability density $d_{\rm obs}(z_{\rm s}, f_{\rm X})$ described in Section 3, we have computed the mean lensing optical depth $\langle\tau\rangle$ for the XXL survey, integrating numerically equation (12). As $d_{\rm obs}(z_{\rm s}, f_{\rm X})$ is assumed to be identical for the XXL and the XMM-LSS surveys, the results are valid for both surveys.

To calculate the lensing optical depth, we modelled the deflector population with SIS and SIE mass distributions (equations 8 and 10). We have computed the average optical depth for different values of the minimum image separation $\theta_{\rm min}$ resolvable at optical wavelengths. When calculating the cross-section, we have considered the detection of the lensed images to be achievable down to an angular separation $\theta_{\rm min}$ (independently of their relative amplification). Although this is not strictly accurate, we have made this assumption for the following reason. The regions contributing the most to the lensing cross-section are those where the source is located close to the caustic curves, as these are the most amplified and thus benefit the most from the amplification bias. For these configurations, the lensed images that are the closest to each other (and also the brightest) are those formed on each side of the tangential critical curve. These lensed images have a very similar amplification (Kormann et al. 1994). Consequently, for the detection of these lensed images, the critical parameter is the smallest angular distance under which these point-like images cannot be resolved, independently of their brightness. In practice however, for lensed images close to each other, the minimum angular distance at which the point-like images can be disentangled is dependent on the flux difference between the images, especially at very small angular distances. For the analysis of the final XXL sample, the angular selection function (characterizing the smallest angular distance detectable as a function of the relative amplification of the lensed images) will have to be determined precisely.

Fig. 3 displays the behaviour of the average optical depth $\langle\tau\rangle$ as a function of the minimal image separation $\theta_{\rm min}$ resolvable in the optical survey. We display the results when modelling the deflector population with either SIE or SIS mass profiles. In the former case, we have calculated the total probability of having a multiply imaged source, independently of the number of the lensed images.

For a perfect instrument (i.e. $\theta_{\rm min} = 0$ arcsec), when considering deflectors modelled with SIE mass distributions, we find an average lensing probability $\langle\tau_{\rm SIE}\rangle = 1.698 \times 10^{-3}$. When modelling the

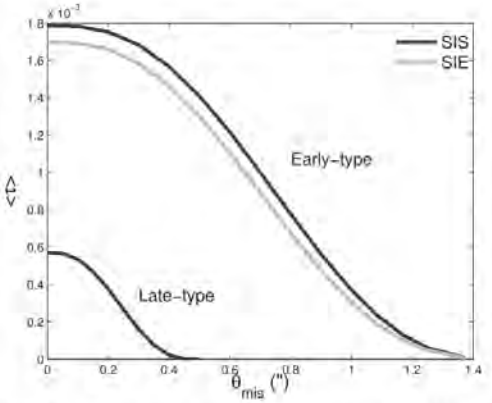

Figure 3. Average lensing probability $\langle\tau\rangle$ calculated for the XXL and XMM-LSS fields as a function of the minimum angular separation $\theta_{\rm min}$ resolvable by the survey in the optical domain, when modelling the deflector population with the SIS and SIE mass distributions. For comparison, we have also computed the case of the late-type galaxies, modelled by means of SIS mass distributions.

deflectors with an SIS mass distribution, the mean lensing probability is $\langle\tau_{\rm SIS}\rangle = 1.788 \times 10^{-3}$. Modelling the deflectors with SIS mass distributions thus leads to a slightly larger average lensing probability by ∼5 per cent. The reason for this is that the SIE mass distribution was introduced in order to preserve the projected mass inside the same area but does not conserve the geometrical cross-section nor the amplification probability distribution. In other words, the area inside the caustic curve of an SIS deflector is always larger than or equal to that included inside the caustic curves of an SIE deflector. When averaging the SIE lensing cross-section over the deflector ellipticity distribution, this leads to an equivalent SIE lensing cross-section smaller than that of the SIS case. Furthermore, for these two types of deflectors, the probability of producing a multiply imaged source with a given total amplification slightly differs. The impact of the amplification bias is thus different for the two deflector models. Consequently, the slight differences between $\langle\tau_{\rm SIS}\rangle$ and $\langle\tau_{\rm SIE}\rangle$ depend on the DNCF as a function of $f_{\rm X}$ for the source population, which varies from one survey to another. The overestimate of $\langle\tau_{\rm SIS}\rangle$ thus has to be estimated independently for each survey. This boost of the average lensing optical depth in the SIS model was studied by Huterer et al. (2005) who concluded that the ellipticity in the deflector mass distribution decreases the mean lensing optical depth. A boost of the SIS model by a few per cent may be expected in a survey with sources showing a steep DNCF.

Both $\langle\tau_{\rm SIE}\rangle$ and $\langle\tau_{\rm SIS}\rangle$ decrease for increasing values of the parameter $\theta_{\rm mis}$. When considering a finite resolution of the instrument, some of the lensed images formed are angularly too close to each other and are detected as a single point-like object. Consequently, the probability of *detecting* the lensed images decreases as $\theta_{\rm mis}$ increases.

In the present case, the multiple lensed images will be searched for among the optical counterparts of the point-like X-ray sources, because of the better angular resolution in the optical domain. The ground-based observations are limited by the atmospheric seeing. In the northern XXL fields, the CFHT in the *r* band has a typical seeing of 0.7 arcsec (Salmon et al. 2009) and for the Southern hemisphere the typical seeing with the Blanco telescope is ∼0.9 arcsec (Desai et al. 2012). We thus considered our full width at half-maximum of the point spread function (PSF) to be homogeneous over the entire sample and equal to ∼0.9 arcsec.

Thanks to PSF fitting techniques, we can hope to resolve multiple point-like lensed images down to half the full width at half-maximum for lensed images with the same amplification, which constitute the configurations contributing the most to the lensing cross-section as previously explained. Consequently, the typical $\theta_{\rm mis}$ value achievable is expected to be $\theta_{\rm mis} \sim 0.45$ arcsec (in practice, as stressed previously, $\theta_{\rm mis}$ depends on the relative amplification of the lensed images, which will have to be taken into account when analysing the final XXL sample). For this value, we have $\langle\tau_{\rm SIE}\rangle = 1.384 \times 10^{-3}$ and $\langle\tau_{\rm SIS}\rangle = 1.489 \times 10^{-3}$. The slight overestimate of the SIS mean lensing value relatively to that of the SIE model thus increases with $\theta_{\rm mis}$ and reaches ∼10 per cent for $\theta_{\rm mis} = 0.45$ arcsec.

For comparison, we have computed the evolution of the mean optical depth as a function of $\theta_{\rm mis}$ for the population of late-type galaxies modelled by means of an SIS mass distribution. As for the case of the early-type galaxies, we have considered the comoving density of late-type galaxies to be constant with the redshift and we have used the VDF parameters determined by Chae (2010) in the local Universe, i.e.

$$[\Phi_*, \sigma_*, \alpha, \beta] = \left[66 \times 10^{-3}\, h^3\,\mathrm{Mpc}^{-3}, 91.5\,\mathrm{km\,s}^{-1}, 0.69, 2.10\right].$$

The results are displayed in Fig. 3. When considering a perfect instrument ($\theta_{\rm mis} = 0$ arcsec), the average lensing optical depth associated with the late-type galaxies is about a third of that of the early-type ones (i.e. $\langle\tau\rangle = 5.719 \times 10^{-4}$). Nevertheless, the decrease of $\langle\tau\rangle$ with $\theta_{\rm mis}$ is steeper than that in the early-type galaxy case. Indeed, late-type galaxies are less massive and lead to smaller typical angular separations of the multiple lensed images, which are not disentangled in the seeing-limited images. For $\theta_{\rm mis} = 0.45$ arcsec, the average lensing optical depth due to late-type galaxies is found to be $\langle\tau\rangle = 1.629 \times 10^{-6}$, three orders of magnitude lower than that of the early-type galaxies. The expected contribution of the late-type galaxies in our sample of gravitationally lensed sources is thus negligible, which validates our assumption of only considering the population of early-type galaxies as the deflectors for the XXL lensed source sample.

Our estimation of the contribution of late-type galaxies to the lensed sources is surprisingly low compared to the observed fraction of late-type lenses in existing samples. Furthermore, it suggests that late-type lenses with image separations larger than 0.5 arcsec are extremely rare, which is also in contradiction with observed samples. Indeed, 2 out of the 13 CLASS lenses from the statistical sample are likely to be produced by late-type galaxies (B0218 and B1933; see Browne et al. 2003) and out of the 26 lensed QSOs of the SDSSQLS statistical sample, one is possibly due to a late-type galaxy (J1313) and has an angular separation larger than 1 arcsec. We do not fully understand the reason for these discrepancies. A possible cause of error is the effect of the lens environment, not considered in this work, which may lead to an additional gravitational shear. Huterer et al. (2005) have shown that the external shear broadens the distribution of angular separation between the lensed images without changing its average value. It may therefore increase the fraction of events with an angular separation larger than 1 arcsec. In the CLASS and SDSSQLS statistical samples, all the lenses produced by late-type galaxies with and angular separation larger than 1 arcsec required external shear to accurately model the position and relative amplification of the lensed images (see Sluse et al. 2012; Suyu et al. 2012 and references therein). Another possible source of discrepancy is the VDF used for late-type galaxies (from Chae 2010) which does not come from direct measurements (as in the case of the early-type VDF; Choi et al. 2007). It is inferred from the local LF of late-type galaxies using the Tully–Fisher relationship (taking into account its dispersion) and assuming a conversion between the circular velocity $v_{\rm c}$ and σ to be that of an SIS profile (i.e. $\sigma = v_{\rm c}/\sqrt{2}$). Chae (2010) stresses that lensing statistics of late-type galaxies might necessitate to consider the circular velocity function (rather than the VDF) and consider more realistic mass distribution models. Furthermore, type-specific LF (and VDF) are still potentially biased by misclassification of the galaxy types and, according to Park & Choi (2005), the work of Chae (2010) has an ∼10 per cent classification mismatch. We therefore advise to use with caution the results concerning the late-type population statistics.

Table 1 summarizes the number of multiply imaged sources expected in the different surveys as well as the expected number of detected events. Assuming that the sources detected in the XXL survey will have the same properties as those in the XMM-COSMOS to which we applied the same flux limits in the X-ray and optical bands (except when estimating the amplification bias) and when accounting for the detection probability of the XXL, we expect the detection of 11 701 sources with $F_{[0.5\text{–}2]\rm keV} > 3 \times 10^{-15}$ erg cm^{-2} s^{-1} and $r < 25$ in the 44.2 square degrees of the survey. Among these sources, we expect 21 (20 in the SIE case) to be

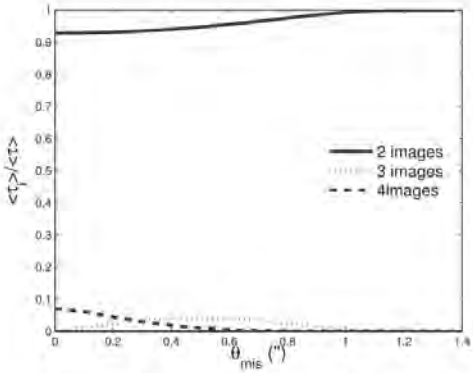

Figure 4. Fraction $\langle \tau_{\mathrm{SIE},i} \rangle / \langle \tau_{\mathrm{SIE}} \rangle$ of the lensing events with a given number $i = 2$, 3 or 4 of images as a function of the survey minimum angular separation θ_{mis}, when modelling the deflector population with the SIE mass distribution. Three-image configurations are quads with two blended point-like images.

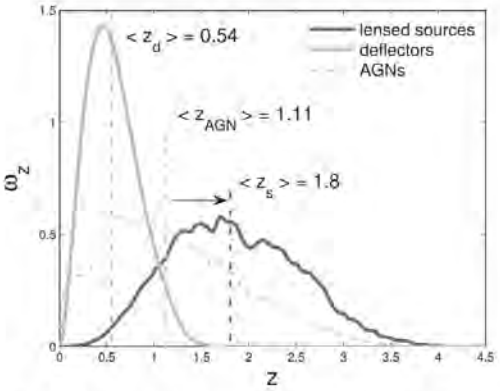

Figure 5. Normalized redshift distributions of the deflectors, the lensed sources and all AGNs. For each distribution, we have indicated the median redshift value.

multiply imaged, out of which 17 (16 in the SIE case) should be detected assuming $\theta_{\mathrm{mis}} = 0.45$ arcsec.

When calculating the lensing probability of a source to be lensed through equation (10), considering a population of deflectors modelled with SIE profiles, we may also calculate the probability $\tau_{\mathrm{SIE},i}$ of a source to be lensed with the formation of a given number i of lensed images. We have calculated the average value of $\langle \tau_{\mathrm{SIE},i} \rangle$ for the population of sources to be detected within the XXL and XMM-LSS fields using equation (12), for different values of the θ_{mis} parameter. The results are displayed in Fig. 4, where we have plotted as a function of the value of the θ_{mis} parameter the fraction of lensing events composed of i lensed images $\langle \tau_{\mathrm{SIE},i} \rangle / \langle \tau_{\mathrm{SIE}} \rangle$ relatively to the total average lensing probability $\langle \tau_{\mathrm{SIE}} \rangle$.

The fraction of lensing events with the formation of two images is always the highest. This is a consequence of the scarcity of very elliptical deflectors (see Choi et al. 2007, fig. 13 for the axial ratio distribution of early-type galaxies). In the case of a perfect instrument (i.e. $\theta_{\mathrm{mis}} = 0$ arcsec), we find that 93 per cent of the lensed sources are composed of two images and this fraction increases with the value of the θ_{mis} parameter.

For a perfect instrument, the lensed sources with formation of more than two images are composed of quads (i.e. four-image configurations). As θ_{mis} increases, some of the four-lensed-image configurations, due to their too small angular separation, have only three point-like images detected (quads with two blended point-like images). Out of the 20 lensed sources formed in the XXL population, only one is expected to be detected with more than two images.

The fraction of lensing systems with more than two images is roughly consistent with the results of Oguri & Marshall (2010) who have calculated the expected number of gravitationally lensed quasars in wide-field optical surveys. For a survey with a limiting magnitude $i = 25$, these authors find a fraction of a little more than ~10 per cent of quads (formation of four images) against ~7 per cent in our simulations. The slight difference is most likely due to the different ellipticity distribution of the deflectors considered [Oguri & Marshall (2010) consider a combination of oblate and prolate three-dimensional deflectors with a Gaussian distribution of their ellipticity] as well as their consideration of an additional external shear due to the lens environment. Hutterer et al. (2005) showed that the external shear increases the fraction of quads in a sample of lensed sources.

4.2 Redshift distributions

Using the joint probability density $d_{\mathrm{obs}}(z_s, f_X)$ described in Section 3, we have computed the mathematical expectation of the normalized redshift distribution of the deflectors $w_{Z_d}(z_d)$ and of the lensed sources $w_{Z_s}(z_s)$, numerically integrating equations (13) and (14), respectively. We have considered $\theta_{\mathrm{mis}} = 0.45$ arcsec and we have modelled the deflectors with SIS mass distributions. The normalized redshift distributions $w_{Z_d}(z_d)$ and $w_{Z_s}(z_s)$ are shown as a function of the redshift in Fig. 5. For comparison, we have represented the marginal distribution as a function of the redshift of the joint probability density, i.e. the normalized distribution as a function of the redshift of all the sources (independently of the fact that they are being lensed).

In this figure, we have also illustrated the median value of the observed redshift for the different distributions. The redshift distribution of the lensed sources is shifted towards a higher redshift compared to that for all the sources. As the source redshift increases, so does its geometrical lensing volume (i.e. the volume in which the presence of a deflector leads to the formation of multiple lensed images). Consequently, sources with a higher redshift tend to have a higher lensing probability. The mathematical expectation for the redshift moves from $\langle z_{\mathrm{AGN}} \rangle \simeq 1.11$ for the entire source population to $\langle z_s \rangle \simeq 1.8$ for the lensed sources.

For redshifts larger than $\langle z_{\mathrm{AGN}} \rangle$, the distribution of the lensed sources does not appear as a smooth function of the redshift, and we clearly see the presence of bumps or redshift ranges with a probability excess compared to a smooth decreasing function of the redshift. These probability overdensities of lensed source detections correspond to redshift ranges in which strong emission lines of the AGNs enter in the optical SDSS r band, in which the optical counterparts are searched for; they are thus a consequence of a selection bias. The presence of the emission lines in the r band increases their probability of being detected, compared to that of a source with only a continuum-like spectrum. For example, the Mg II line at 279.8 nm enters the r-band filter in the redshift range 2–2.42, for which we see an overdensity in the lensed source redshift distribution.

The redshift distribution of the lensed sources corresponds to the probability density from which the detected lensed source redshift may be considered as a random event, thanks to the fact that, in this case, all the lensed sources are detected and may have their redshift estimated. Given a large enough sample of lensed sources, this distribution could be retrieved from a normalized histogram of the lensed sources, as a function of their redshift.

In Fig. 5, we have also represented the normalized distribution ω_{z_d}, as a function of the redshift, for the deflectors involved in the formation of multiply imaged sources. The deflector redshift median value is $\langle z_d \rangle \sim 0.54$ and the most probable value is $z \lesssim 0.5$. The contribution of deflectors with $z \gtrsim 1$ is very small. This comforts our assumption of a non-evolving deflector population in the calculation of the lensing optical depth, as the population involved is mainly located at low redshift.

In the case of the deflector distribution, the observed redshift distribution of the deflectors involved in the formation of multiple images of a source will be highly biased as most of them are not bright enough to be detected.

Oguri & Marshall (2010) have also estimated the expected lens redshift distribution for lensed quasars detected in optical imaging surveys. The deflector redshift distributions are marginally consistent, although the distribution found in this work peaks at lower redshifts [$z_{\max} \sim 0.6$ for Oguri & Marshall (2010) and $z_{\max} \sim 0.5$ in the present work]. The expected source redshift distribution is also shifted towards lower redshift in our study. This difference in the lensed source and deflector redshift distributions comes from the difference in the source distribution: in the present work, the rather bright X-ray flux cutoff tends to reject sources at high redshift, which are included in the sample of Oguri & Marshall (2010).

4.3 Influence of the cosmological model

The probability for a source with a known apparent flux and redshift to be gravitationally lensed with the formation of multiple images depends on the cosmological model. This may be seen for instance through the dependence of the infinitesimal light-distance element $c\mathrm{d}t/\mathrm{d}z$ on the cosmological mass density parameter Ω_m in equation (2), as well as through the dependence of the lensing cross-section on Ω_m (see equations 6 and 7) via the definition of the angular diameter distances. If we consider a flat expanding FLRW universe model, the only dependence of the lensing probability on the universe model is made through the cosmological mass density parameter Ω_m. Indeed, although a flat expanding FLRW is totally characterized by Ω_m and H_0, an increase in the value of H_0 will only act as a scaling factor (decreasing the lensing volume while increasing the density of deflectors). So far, we have considered an FLRW flat universe with $\Omega_\mathrm{m} = 0.3$ and $H_0 = 70$ km s^{-1} Mpc^{-1}. In Fig. 6, we display the behaviour of the average lensing probability $\langle\tau\rangle$ for the XXL sources as a function of Ω_m, for a flat universe with $H_0 = 70$ km s^{-1} Mpc^{-1}. We have computed both $\langle\tau_\mathrm{SIE}\rangle$ and $\langle\tau_\mathrm{SIS}\rangle$. Both models lead to the same behaviour of the mean lensing probability as a function of Ω_m and, here as well, we observe that the SIS mass distribution leads to a slight overestimate of the average lensing probability when compared to that corresponding to the SIE model, whatever the value of Ω_m.

There is a very strong dependence of the expected fraction of lensed sources in the survey on Ω_m. For this reason, the statistics of gravitational lensing in a well-defined sample of sources has been widely used to probe the value of Ω_m and test dark energy models (Turner et al. 1984; Fukugita et al. 1990; Turner 1990; Surdej et al. 1993; Keeton 1998, 2002; Chae et al. 2002; Ofek et al. 2003; Mitchell et al. 2005; Cao et al. 2012).

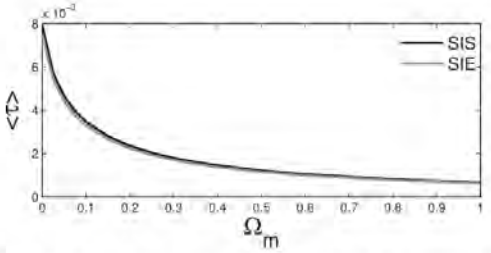

Figure 6. Average lensing probability as a function of the cosmological matter density parameter Ω_m.

The XXL sample on its own will not allow better constraints on the value of Ω_m than recent lens surveys such as the SDSS-LQS. Oguri et al. (2012) for instance constrained Ω_{Λ} to $\Omega_{\Lambda} = 0.79^{+0.06(\mathrm{stat.})}_{-0.07} \pm 0.06(\mathrm{syst.})$ on the basis of 19 lenses from the SDSS-QLS statistical sample. The XXL lensed source sample will thus be combined with other recent surveys (including the SDSS-QLS) to better constrain the cosmological parameters.

5 CONSIDERING THE *r*-BAND CUTOFF

In the previous section, when calculating the amplification bias in equation (6), we have only considered the distribution of the sources as a function of their flux f_X in the X-ray band and we have considered the lensing optical depth $\tau(z_s, f_\mathrm{X})$ to be only a function of the source redshift and its flux in the X-ray band. Ideally, the source r magnitude in the optical domain should also be considered for the calculation of $\tau(z_s, f_\mathrm{X}, r)$ and $d_\mathrm{obs}(z_s, f_\mathrm{X}, r)$ and the calculation of the mean lensing optical depth $\langle\tau\rangle$ in equation (12) should include the integration over r.

The joint probability density $d_\mathrm{obs}(z_s, f_\mathrm{X}, r)$ may be decomposed as

$$d_\mathrm{obs}(z_s, f_\mathrm{X}, r) = d_\mathrm{obs}(z_s, f_\mathrm{X})\, d(r|z_s, f_\mathrm{X}), \tag{15}$$

where $d(r|z_s, f_\mathrm{X})$ is the normalized distribution as a function of r for sources with a redshift and an X-ray flux in the ranges $[z_s, z_s + \mathrm{d}z_s]$ and $[f_\mathrm{X}, f_\mathrm{X} + \mathrm{d}f_\mathrm{X}]$, respectively, and equation (12) remains correct if we consider the optical depth $\tau_{\langle r\rangle}(z_s, f_\mathrm{X})$ averaged over the r magnitudes

$$\tau_{\langle r\rangle}(z_s, f_\mathrm{X}) = \int \tau(z_s, f_\mathrm{X}, r)\, d(r|z_s, f_\mathrm{X})\, \mathrm{d}r. \tag{16}$$

Equivalently, $\tau_{\langle r\rangle}(z_s, f_\mathrm{X})$ can be calculated through equation (3) if we consider an average lensing cross-section $\Sigma_{\langle r\rangle}$

$$\Sigma_{\langle r\rangle} = b_0^2 \iint_{\mathcal{S}_\mathrm{S}} B_{\langle r\rangle}\, \mathrm{d}\mathbf{y}, \tag{17}$$

where we have defined the amplification bias $B_{\langle r\rangle}$ averaged over the r magnitudes

$$B_{\langle r\rangle} = \int \frac{N(z_s, f_\mathrm{X}/A_\mathrm{X}, r + 2.5\log(A_r))}{N(z_s, f_\mathrm{X}, r)}\, d(r|z_s, f_\mathrm{X})\, \mathrm{d}r, \tag{18}$$

where $N(z_s, f_\mathrm{X}, r)$ represents the density of sources with a redshit z_s, having an observed flux f_X in the X-ray and an r-band magnitude r, A_X and A_r are the amplifications due to the lensing event in the X-ray and r band, respectively. If the source is point-like, we may

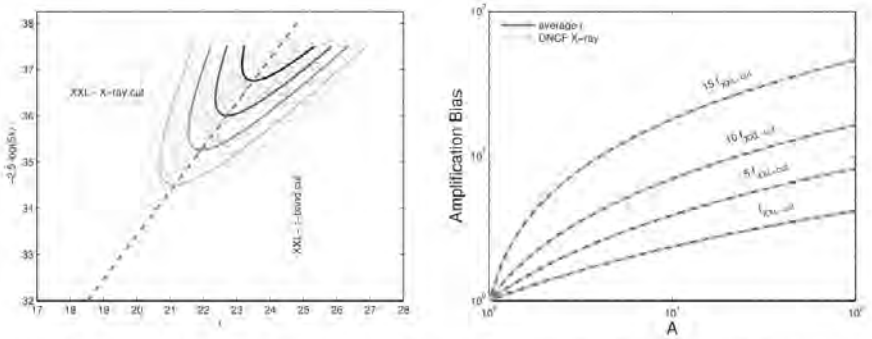

Figure 7. Left: distribution of the COSMOS sources in the (f_X, r) plane. We have represented the X-ray fluxes in terms of the X-ray magnitudes $m_s = -2.5 \log f_X$, and have represented the X-ray and r-band cutoff of the XXL survey. We have also represented the contour plot of the COSMOS source density in the (f_X, r) plane. Right: amplification bias as a function of the total amplification of the lensing event when considering only the DNCF as a function of the X-ray flux f_X (continuous dark grey line) and when averaging over the r-band magnitude distribution of the sources.

then assume that $A_X = A_r$. If not, the ratio A_X/A_r will depend on the size of regions in the AGN emitting the X-ray and the optical fluxes, respectively, as well as the positions of these regions with respect to the caustic curves. The expectation of the ratio A_X/A_r will thus necessitate heavy simulations to be performed. As a first approximation we consider point-like sources.

In this work, the amplification bias $B_{X\text{-ray}}$ has been calculated so far uniquely on the basis of the X-ray flux through the relation

$$B_{X-ray} = \frac{N(f_X/A_X)}{N(f_X)}. \tag{19}$$

where we have neglected the redshift dependence of the sources as a function of their redshift because of a too small source sample to correctly characterize this possible redshift dependence. In the following, we will compare the amplification bias obtained through equations (18) and (19).

To calculate rigorously the amplification bias through equation (18), we thus need to determine the distribution of the source population in the (z_s, f_X, r) space. Our observational data from the COSMOS sample are not large enough to estimate this distribution over the whole area probed by the survey. Consequently, we assume the distributions $N(z_s, f_X, r)$ and $d(r|z_s, f_X)$ to be independent of the redshift.

Let us now estimate the distribution $N(f_X, r)$ on the basis of the distribution of the COSMOS sample in the (f_X, r) plane, represented in the left-hand panel of Fig. 7. We have represented all the COSMOS sources for which the soft X-ray flux and r-band magnitude are given in the sample of Brusa et al. (2010). As 98 per cent of the detected X-ray sources have an optical counterpart in the r band for X-ray sources brighter than the XXL 0.5 detection probability cut, we can consider this sample to be a complete sample of X-ray sources brighter than the X-ray cut, for which we know the optical counterpart.

To estimate $N(f_X, r)$, we have proceeded as follows. We bin in terms of the $m_s = -2.5 \log f_X$ magnitude, with a bin width of $dm_s = 0.5$ and bin centres ranging from 33.5 to 37. In each m_s bin, we construct the histogram of the sources as a function of the r-band magnitude, using bins with a width of $dr = 0.5$ and bin centres ranging from 17 to 28 with step of 0.5. Each histogram as a function of r is fitted by means of a Gaussian profile. The number of sources in each bin is then divided by $dm_s dr$.

We thus obtain the evolution of the Gaussian fit parameters (i.e. the amplitude A_G, the average position r_G and the standard deviation σ_G) as a function of the m_s bin and we fit the dependence of these parameters as a function of m_s by a linear law in the m_s range 33.5–37. We model the density of the sources in the (f_X, r) plane by

$$N(f_X, r) = A_G(m_s) \exp\left(-\left(\frac{r - r_G(m_s)}{2\sigma_G(m_s)}\right)^2\right). \tag{20}$$

The COSMOS data do not have enough bright sources to constrain $N(f_X, r)$ for m_s brighter than 33.5. We have represented the isodensity contours of the calculated function $N(f_X, r)$ in the left-hand panel of Fig. 7, showing very good agreement between the observed distribution of the COSMOS sources and the modelled density function.

We now use the modelled function $N(f_X, r)$ to calculate the amplification bias in equation (18), for sources with different X-ray-to-optical flux ratios. Assuming that the amplification induced by the lensing event in the X-ray and that in the optical are identical, when amplified, a source is displaced in the (m_s, r) parallel to the dashed line shown in the left-hand panel of Fig. 7. Consequently, the amplification bias is calculated thanks to the evolution of $N(f_X, r)$ along this trajectory.

In the right-hand panel, we represent the behaviour of the amplification bias as a function of the total amplification of the lensing event, for four sources with apparent X-ray fluxes equal to the XXL X-ray limiting flux $f_{XXL\text{-}cut}$, and 5, 10 and 15 times the value of the $f_{XXL\text{-}cut}$. The dashed light grey curve represents the amplification bias $B_{X\text{-ray}}$ obtained when only considering the DNCF of the XXL sources as a function the X-ray flux, calculated through equation (19). The continuous black curve corresponds to the average bias $B_{\langle r \rangle}$ calculated thanks to equation (18). We see perfect agreement between these curves and the amplification bias calculated only considering the DNCF as a function of the X-ray flux f_X. Consequently, the amplification bias calculated through equation (6) perfectly corresponds to the amplification bias averaged over the r-band magnitudes.

Thus, assuming a point-like source, we may calculate the amplification bias in the combined X-ray/optical data by considering uniquely the X-ray distribution of a complete and deeper sample, which validates the method introduced in Section 2. Nevertheless,

in the analysis of the final XXL sample, we will have to also consider the redshift dependence of the amplification bias, which will be made possible thanks to the much larger size of the sample.

6 CONCLUSIONS

We have calculated the expected statistical properties of the multiply imaged sources to be detected among the optical counterparts of the XXL point-like sources, modelling the deflectors successively with SIS and SIE mass profiles. We find the following.

(i) One expects the formation of 20 (21 using the SIS model) multiply imaged AGNs out of which 16 (17 for the SIS case) should be detected among the optical counterparts with an angular resolution of 0.45 arcsec, and we only expect the detection of one gravitational lens system composed of more than two lensed images.

(ii) The expectations are consistent when modelling deflectors with SIE and SIS mass distributions, although the SIS model leads to a slight overestimate of the mean lensing probability. This overestimate is a function of the amplification bias and is thus different for each survey.

(iii) The late-type galaxy population should not contribute to the lensed sources to be detected.

(iv) Although the detection is done simultaneously in the X-ray and in the optical domain, the amplification bias may be estimated from the X-ray flux distribution, as long as we consider a complete X-ray sample from a deeper survey and for point-like sources.

In this work, we have considered isothermal profiles to model the deflectors. This has allowed us to get first good estimates of the expected number of lensed AGN in the XXL survey. However, more detailed calculations ought to be carried out. Indeed, Auger et al. (2010) and Koopmans et al. (2009), through the analysis of massive early-type deflectors from the Sloan Lens ACS Survey (SLACS) survey, have found a slight deviation from the isothermal profile, with a steeper slope parameter ($\langle\gamma\rangle = 2.078$ and 2.085, respectively, where the mass distribution evolves as $r^{-\gamma}$). If we consider two mass distributions with the same total mass, a steeper profile would lead to a higher fraction of the lens in the centre, which will increase the Einstein angular radius, therefore leading to an increase in the lensing cross-section of the deflector. This increase in the lensing cross-section with the steepness of the radial mass profile has been put in evidence in a series of papers (Mandelbaum, van de Ven & Keeton 2009; van de Ven, Mandelbaum & Keeton 2009), where the authors studied the impact of galaxy shape and density profile on the selection biases in surveys for the detection of strong lenses. Because isothermal profiles are singular, the authors analysed more realistic profiles in order to define the total mass.

Furthermore, Sonnenfeld et al. (2013) have shown from the study of the CFHTLS-Strong Lensing Legacy Survey (SL2S) galaxy-scale lens sample (with deflectors in the range $0.2 < z < 0.8$) that the mass density profile of early-type galaxies depends on the redshift, lower galaxies showing a steeper average profile. As deflectors with a steeper profile tend to have a higher lensing cross-section, this would favour the deflector redshift distribution to be shifted towards lower redshift.

These effects, along with the redshift dependence of the amplification bias, will have to be considered in the analysis of the final XXL sample.

ACKNOWLEDGEMENTS

The authors would like to acknowledge the Communauté Française de Belgique and the Actions de Recherche Concertées de l'Académie universitaire Wallonie-Europe for their funding during the present research.

REFERENCES

Auger M. W., Treu T., Bolton A. S., Gavazzi R., Koopmans L. V. E., Marshall P. J., Moustakas L. A., Burles S., 2010, ApJ, 724, 511
Browne I. W. A. et al., 2003, MNRAS, 341, 13
Brusa M. et al., 2010, ApJ, 716, 348
Cao S., Pan Y., Biesiada M., Godlowski W., Zhu Z.-H., 2012, J. Cosmol. Astropart. Phys., 3, 16
Cappelluti N. et al., 2007, ApJS, 172, 341
Cen R., Gott J. R., III, Ostriker J. P., Turner E. L., 1994, ApJ, 423, 1
Chae K.-H., 2003, MNRAS, 346, 746
Chae K.-H., 2010, MNRAS, 402, 2031
Chae K.-H. et al., 2002, Phys. Rev. Lett., 89, 151301
Chiappetti L. et al., 2013, MNRAS, 429, 1652
Choi Y.-Y., Park C., Vogeley M. S., 2007, ApJ, 658, 884
Claeskens J.-F., 1999, PhD thesis, Université de Liège, Belgium
Desai S. et al., 2012, ApJ, 757, 83
Driver S. P. et al., 2009, Astron. Geophys., 50, 050000
Elyiv A. et al., 2012, A&A, 537, A131
Elyiv A., Melnyk O., Finet F., Pospieszalska-Surdej A., Chiappetti L., Pierre M., Sadibekova T., Surdej J., 2013, MNRAS, 434, 3305
Fukugita M., Turner E. L., 1991, MNRAS, 253, 99
Fukugita M., Futamase T., Kasai M., 1990, MNRAS, 246, 24p
Guzzo L., Le Fèvre O. eds 2010, AIP Conf. Proc. Vol. 1241, Invisible Universe. Am. Inst. Phys., New York, p. 39
Hezaveh Y. D., Holder G. P., 2011, ApJ, 734, 52
Huterer D., Keeton C. R., Ma C.-P., 2005, ApJ, 624, 34
Keeton C. R., II 1998, PhD thesis, Harvard University
Keeton C. R., 2002, ApJ, 575, L1
Keeton C. R., Kochanek C. S., 1998, ApJ, 495, 157
Keeton C. R., Kochanek C. S., Falco E. E., 1998, ApJ, 509, 561
Kochanek C. S., 1992, ApJ, 384, 1
Kochanek C. S. et al., 2000, ApJ, 543, 131
Koopmans L. V. E., Treu T., Bolton A. S., Burles S., Moustakas L. A., 2006, ApJ, 649, 599
Koopmans L. V. E. et al., 2009, ApJ, 703, L51
Kormann R., Schneider P., Bartelmann M., 1994, A&A, 284, 285
Mandelbaum R., van de Ven G., Keeton C. R., 2009, MNRAS, 398, 635
Maoz D., Rix H.-W., 1993, ApJ, 416, 425
Melnyk O. et al., 2013, A&A, 557, A81
Mitchell J. L., Keeton C. R., Frieman J. A., Sheth R. K., 2005, ApJ, 622, 81
Ofek E. O., Rix H.-W., Maoz D., 2003, MNRAS, 343, 639
Oguri M., Marshall P. J., 2010, MNRAS, 405, 2579
Oguri M. et al., 2008, AJ, 135, 512
Oguri M. et al., 2012, AJ, 143, 120
Park C., Choi Y.-Y., 2005, ApJ, 635, 29
Peebles P., 1993, Principles of Physical Cosmology. Princeton Univ. Press, Princeton, NJ
Salmon D., Cuillandre J.-C., Barrick G., Thomas J., Ho K., Matsushige G., Benedict T., Racine R., 2009, PASP, 121, 905
Sheth R. K. et al., 2003, ApJ, 594, 225
Sluse D., Chantry V., Magain P., Courbin F., Meylan G., 2012, A&A, 538, A99
Sonnenfeld A., Treu T., Gavazzi R., Suyu S. H., Marshall P. J., Auger M. W., Nipoti C., 2013, ApJ, 777, 98
Surdej J. et al., 1993, AJ, 105, 2064
Suyu S. H. et al., 2012, ApJ, 750, 10
Turner E. L., 1980, ApJ, 242, L135
Turner E. L., 1990, ApJ, 365, L43
Turner E. L., Ostriker J. P., Gott J. R., 1984, ApJ, 284, 1
van de Ven G., Mandelbaum R., Keeton C. R., 2009, MNRAS, 398, 607

This paper has been typeset from a TEX/LATEX file prepared by the author.

Monthly Notices of the ROYAL ASTRONOMICAL SOCIETY

MNRAS 434, 3305–3309 (2013) doi:10.1093/mnras/stt1255
Advance Access publication 2013 August 1

Search for gravitational lens candidates in the XMM-LSS/CFHTLS common field

A. Elyiv,[1,2]* O. Melnyk,[1,3] F. Finet,[1] A. Pospieszalska-Surdej,[1] L. Chiappetti,[4] M. Pierre,[5] T. Sadibekova[5] and J. Surdej[1]

[1]*Institut d'Astrophysique et de Géophysique, Université de Liège, 4000 Liège, Belgium*
[2]*Main Astronomical Observatory, Academy of Sciences of Ukraine, 27 Akademika Zabolotnoho St, 03680 Kyiv, Ukraine*
[3]*Astronomical Observatory, Kyiv National University, 3 Observatorna St, 04053 Kyiv, Ukraine*
[4]*INAF, IASF Milano, via Bassini 15, I-20133 Milano, Italy*
[5]*Laboratoire AIM, CEA/ DSM/Irfu/SAp, CEA-Saclay, F-91191 Gif-sur-Yvette Cedex, France*

Accepted 2013 July 5. Received 2013 July 5; in original form 2013 June 4

ABSTRACT

Our aim was to identify gravitational lens candidates among some 5500 optical counterparts of the X-ray point-like sources in the medium-deep ~11 deg^2 *XMM*-LSS survey. We have visually inspected the optical counterparts of each QSOs/AGN using CFHTLS T006 images. We have selected compact pairs and groups of sources which could be multiply imaged QSO/AGN. We have measured the colours and characterized the morphological types of the selected sources using the multiple point spread function fitting technique. We found three good gravitational lens candidates: J021511.4−034306, J022234.3−031616 and J022607.0−040301 which consist of pairs of point-like sources having similar colours. On the basis of a colour–colour diagram and X-ray properties we could verify that all these sources are good QSO/AGN candidates rather than stars. Additional secondary gravitational lens candidates are also reported.

Key words: gravitational lensing: strong.

1 INTRODUCTION

Gravitational lensing remains a powerful tool for studies of dark matter distribution in the Universe. One important application of gravitational lens statistics is to provide strong constraints on the cosmological models and parameters since the lensing optical depth depends on the cosmological volume element (Surdej, Remy & Haubold 1992; Mitchell et al. 2005; Oguri et al. 2008; Jullo et al. 2010; Rozo, Wu & Schmidt 2011).

An ideal set of observations to carry out extragalactic research and especially for searching gravitational lens systems is the CFHTLS photometric survey.[1] Previous investigators have mainly set up automatic procedures to search for gravitational lens systems. Cabanac et al. (2007) have presented 40 strong lens candidates over 28 deg^2 of the CFHTLS field, which consist of galaxy/group deflectors producing conspicuous gravitational arc systems. More et al. (2012) have reported about 127 lens system candidates (Strong Lensing Legacy Survey-ARCS) over 150 deg^2 in the CFHTLS. In that work, they applied semi-automatic techniques to find gravitational arcs with the help of some additional visual inspection. Maturi, Mizera & Seidel (2013) studied the statistical colour properties of gravitational arcs over 37 deg^2 in the CFHTLS-Archive-Research Survey and found 73 new arc candidates. Sygnet et al. (2010) have found three good candidates for edge-on galaxy lens applying their automatic/visual procedure to 30 444 individual CFHTLS relatively bright spirals $18 < i < 21$. Shan et al. (2012) have performed a weak lensing analysis over 64 deg^2 of the CFHTLS fields.

We propose here to search for multiply imaged QSOs/AGN among the counterparts of X-ray point-like sources detected with *XMM*. Therefore contrary to the previous approaches, we have been searching for gravitationally lensed QSOs/AGN at much smaller angular scales (typically 1–4 arcsec).

The search for gravitational lens candidates among the optical counterparts of X-ray-selected QSOs/AGN looked a priori very promising as, first of all, it allows the selection of a sample of QSOs/AGN with very few contaminants. Moreover, as the X-ray QSOs/AGN are bright and distant sources (observed up to a redshift $z \sim 4$), they have a high probability of being multiply imaged due to the presence of a deflector near their line of sight.

From lensing probability calculations over a mock catalogue of X-ray sources (reproducing the redshift distribution and differential number counts of the COSMOS X-ray sources as a function of their flux), where we have assumed a constant comoving density of deflector galaxies modelled as singular isothermal spheres, we expect ~15 QSOs/AGN among the *XMM*-LSS soft X-ray sources

* E-mail: elyiv@astro.ulg.ac.be
[1] Canada France Hawaii Telescope Legacy Survey: http://www.cfht.hawaii.edu/Science/CFHLS/

to have a deflector sufficiently close to their line of sight to lead to the formation of multiple lensed images of their optical counterpart (Surdej et al. 2011; Finet, Elyiv & Surdej 2012).

The contiguous ∼11 deg^2 medium–deep *XMM*-LSS field has been surveyed at high galactic latitudes with the *XMM–Newton* satellite, centred on RA $2^h\,18^m\,00^s$ Dec. $-7^\circ\,00'\,00''$ (J2000). It provides the identification of a homogeneous sample of galaxy clusters and QSOs/AGN (Pierre et al. 2011) and reaches a sensitivity near 10^{-18} W m^{-2} for point-like sources in the soft band (Elyiv et al. 2012). About 80 per cent of the 6000 point-like *XMM*-LSS X-ray sources have (an) optical CFHTLS DR6 counterpart(s) (Chiappetti et al. 2013). Visual inspection of all counterparts led us to classify the sources as being either extended or point-like and reject the wrong associations (Melnyk et al. 2013). In this paper, we describe separately the results of our gravitational lens search among the CFHTLS counterparts of X-ray sources.

In Section 2, we detail the method used to identify multiply imaged QSOs/AGN in the *XMM*-LSS field. In Section 3, we describe the adopted procedure to search for multiply imaged QSOs/AGN, discuss each individual candidate and report their colour measurements as well as their morphology. Section 4 contains the main conclusions.

2 THE SAMPLE OF GRAVITATIONAL LENS CANDIDATES

Our sample of X-ray point-like sources and their optical counterparts consist of objects which have been detected in the soft and/or the hard X-ray band and coming from the multiwavelength catalogue of Chiappetti et al. (2013). The ∼5500 optical counterparts of the X-ray sources were visually inspected on 10 arcsec × 10 arcsec CFHTLS optical images centred on the X-ray sources. The angular separations between the lensed images for a typical galaxy deflector and cosmological redshifts of the source (QSO/AGN) and the lens are typically of the order of 1 or several arcsec (Refsdal & Surdej 1994). Knowing that lensed components should be point-like sources and should have rather similar colour properties (colour difference smaller than 0.1–0.2 mag.), this selection was also carried out using these strict criteria. Contamination by the lens, intrinsic colour variation plus time delay(s) and/or microlensing acting may cause colour differences above typical CFHTLS photometric errors.

The point spread function (PSF) of the *XMM–Newton* telescopes provides a resolution near 4–6 arcsec for a point-like source. A detected point-like X-ray source may therefore be sometimes identified with multiple (more than one) optical counterparts. We have made an in-depth study of these particular cases in order to detect new gravitational lens systems (mostly multiply imaged QSOs/AGN).

We inspected g, r and i CFHTLS direct CCD frames whenever they were available. For visual inspection we used the monochromatic images in logarithmic scale for each band as well as the colour composed images. For better objectivity four independent members of the present team (called hereafter 'inspectors') ranked each counterpart in the following way: 1 – very good candidate, 2 – good lens candidate, 3 – possible lens candidate and 0 – definitely not a candidate. A similar approach has been followed by More et al. (2008) when searching for gravitational lenses in the Extended *Chandra* Deep Field South and by Jackson (2008) in the COSMOS field. We finally retained nearly 300 candidates which were marked with the 1, 2 or 3 rank by at least one inspector. Next we added the ranks from all inspectors and formed a top list of 72 probable lens candidates. We visually inspected this list several times and removed very faint objects, objects which are obvious stars according to their spectra and so on. At the end, we finally selected 18 multiply imaged QSO/AGN candidates which could be potentially strong lens systems, see Fig. 1 and Table 1. They are ranked there from the best to worst according to final morphological and colour selection.

Most of them consist of double sources. For five pairs with an angular separation larger than 3 arcsec we considered their photometry in the g, r and i bands directly from the CFHTLS catalogue. We used available spectroscopic or photometric redshifts from SDSS[2] (Abazajian et al. 2009) and Melnyk et al. (2013). For the remaining more compact systems, we performed a multiple PSF fitting analysis to precise their morphology (point-like or extended source) and accurate magnitude measurement of each component. We adopted the same PSF fitting technique as that used for the analysis of the gravitational lens systems HE 0435−1223 described in Ricci et al. (2011) and UM673 in Ricci et al. (2013).

3 DESCRIPTION OF THE INDIVIDUAL CANDIDATES

3.1 The best candidates

Candidate J021511.4−034306 is seen as a wide pair. Therefore, we took the magnitudes of the two point-like sources from the CFHTLS data base. The components show similar colours: $g - r = 0.39$ and 0.38 for the A and B components, $r - i = 0.00$ and 0.08, respectively. Photometric redshift determination for the A component indicates $z = 0.94$ (Melnyk et al. 2013). We did not find any SDSS spectra but just a note that these two sources are point like. This system thus consists of a good gravitational lens candidate according to the PSF analysis. The components are bright and slightly saturated. Therefore, we encountered some problems when performing the PSF fitting.

Candidate J022234.3−031616 consists of two close faint sources. We have just r- and g-band observations. We performed a PSF fitting analysis and found that this system consists of two point-like sources with very similar colours: $g - r = -0.46$ and -0.36 for A and B, respectively, see Fig. 2. This system thus consists of a good gravitational lens candidate.

Candidate J022607.0−040301 consists of one bright and one faint source. We performed a PSF fitting analysis and found that both of them are point-like sources. However, they have slightly different colours. Note that the presence of a nearby lens, microlensing and/or intrinsic variations with time delay acting could of course account for such different colours. Photo-z for the A component is 0.086 (Rowan-Robinson et al. 2008).

3.2 Candidates found with extended images or with different colours

Candidate J021844.4−044825 contains one bright optical component near the centre of the X-ray emission and two symmetric faint components. The system is wide and we took the magnitudes of each component from the CFHTLS catalogue. The colours of the two symmetric sources are similar: $g - r = 0.78$ and 0.94 for the B and C components, $r - i = 0.53$ and 0.65, respectively. Akiyama et al. (in preparation) on the basis of spectroscopic observations claim that component A is a QSO/AGN with $z = 4.55$. Since the

[2] www.sdss.org

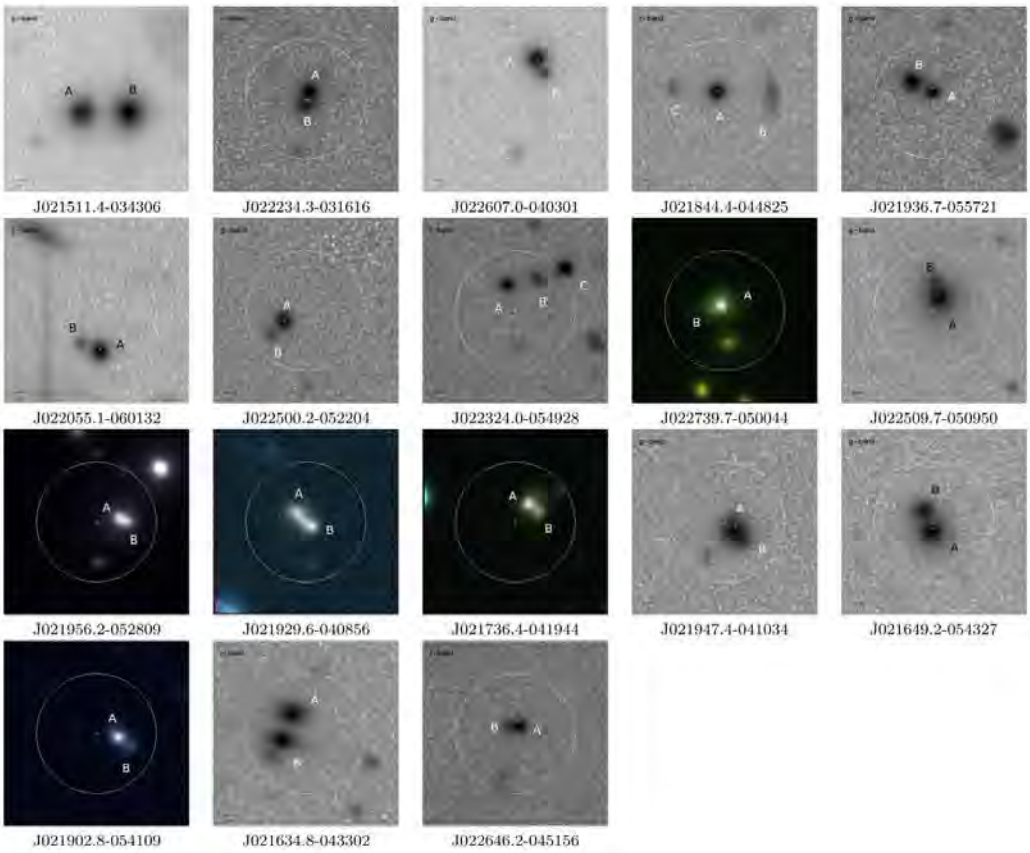

Figure 1. Images of 18 gravitational lens candidates. The cross indicates the centre of the X-ray emission. The radius of the circle around the centre of X-ray emission is 6 arcsec. Here we chose the best illustrative band or colour image for each candidate.

central component A has very high redshift, we do not consider it as a potential deflector. Moreover, the symmetric components B and C are extended, the system J021844.4−044825 does not therefore constitute good gravitational lens candidate.

Candidate J021936.7−055721 consists of two components with an angular separation near 3 arcsec. For these, we took the magnitudes from the CFHTLS data base. The components have similar colours: $g - r = 0.59$ and 0.66 for the A and B components, $r - i = 0.15$ and 0.18, respectively. We performed a PSF fitting analysis of this system. It shows that component A is point like and that B is an extended source.

Candidate J022055.1−060132 also consists of one bright and one faint components. We performed PSF fitting and found that both components are point-like sources. However, they also show very different colours. Given the very different colours and high flux ratio, we do not consider this system to be a good gravitational lens candidate.

Candidate J022500.2−052204 consists of one bright and one faint components. We performed PSF fitting and found that both components are point-like sources. However, they have very different colours. Given the very different colours and high flux ratio, we do not consider this system to be a good gravitational lens candidate.

Candidate J022324.0−054928 is composed of one faint and two symmetric bright components. The system is wide and we took the magnitudes of the components from the CFHTLS catalogue. The colours of those components are very different.

3.3 Candidates found to be extended or not classifiable sources

Candidates J022739.7−050044, J022509.7−050950, J021956.2−052809, J021929.6−040856, J021736.4−041944, J021947.4−041034, J021649.2−054327, J021902.8−054109, J021634.8−043302 and J022646.2−045156 consist of pairs of extended sources according to our PSF fitting analysis.

Candidate J021634.8−043302 consists of a wide pair and we took their magnitudes from the CFHTLS data base. The components show similar colours: $g - r = 1.41$ and 1.33 for the A and B components, $r - i = 0.59$ and 0.62, respectively. From the SDSS data base, the estimated photo-z is 0.38 ± 0.04 and 0.33 ± 0.04 for the A and B components, respectively. In the SDSS data base there is just a note that the two components are galaxies. We performed the PSF fitting of these two components and confirm that they are both extended, see Fig. 2.

Table 1. Properties of the potential strong lens candidates.

ID		Xcatname[a]	RA	Dec.	g	r	i	$g-r$	$r-i$
1	A[c]	J021511.4−034306	2: 15: 11.49	−3: 43: 07.94	18.15	17.76	17.76 ± 0.001	0.39	0.00
	B[c]		−4.69″	+0.03″	17.24	16.86	16.78	0.38	0.08
2	A[c]	J022234.3−031616	2: 22: 34.33	−3: 16: 17.14	21.59 ± 0.02	22.05 ± 0.03		−0.46	
	B[e]		+0.37″	−1.25″	22.28 ± 0.03	22.64 ± 0.04		−0.36	
3	A[c]	J022607.0−040301	2: 26: 06.86	−4: 02: 57.09	19.35 ± 0.01	19.08 ± 0.01	19.00 ± 0.01	0.27	0.08
	B[c]		−1.39″	−2.95″	21.82 ± 0.02	21.47 ± 0.03	21.18 ± 0.02	0.35	0.29
4	A[e]	J021844.4−044825	2: 18: 44.46	−4: 48: 24.69	22.62 ± 0.01	20.81 ± 0.01	19.98 ± 0.002	1.81	0.83
	B[b]		−5.41″	−0.16″	22.97 ± 0.03	22.19 ± 0.03	21.66 ± 0.02	0.78	0.53
	C[b]		+4.51″	+0.44″	24.11 ± 0.05	23.17 ± 0.05	22.52 ± 0.03	0.94	0.65
5	A[c]	J021936.7−055721	2: 19: 36.80	−5: 57: 20.26	22.83 ± 0.02	22.24 ± 0.02	22.09 ± 0.02	0.59	0.15
	B[b]		+2.00″	+1.03″	22.21 ± 0.01	21.55 ± 0.01	21.37 ± 0.01	0.66	0.18
6	A[c]	J022055.1−060132	2: 20: 55.17	−6: 01: 36.51	21.10 ± 0.01	20.44 ± 0.01	20.67 ± 0.02	0.66	-0.23
	B[c]		+1.86″	+0.77″	23.55 ± 0.06	23.47 ± 0.07	23.43 ± 0.06	0.08	0.04
7	A[c]	J022500.2−052204	2: 25: 00.41	−5: 22: 05.50	22.20 ± 0.02	21.73 ± 0.02	21.35 ± 0.03	0.47	0.38
	B[e]		+1.17″	−1.38″	23.90 ± 0.05	23.55 ± 0.06	23.59 ± 0.07	0.35	-0.04
8	A[b]	J022324.0−054928	2: 23: 24.12	−5: 49: 25.13	21.69 ± 0.004	21.64 ± 0.01	21.32 ± 0.01	0.05	0.32
	B[c]		−3.05″	+0.56″	23.11 ± 0.02	22.74 ± 0.04	22.06 ± 0.02	0.37	0.68
	C[c]		−5.76″	+1.53″	21.05 ± 0.003	20.83 ± 0.01	20.76 ± 0.01	0.22	0.07
9	[b]	J022739.7−050044	2: 27: 39.83	−5: 00: 42.99					
10	[b]	J022509.7−050950	2: 25: 09.72	−5: 09: 49.21					
11	[b]	J021956.2−052809	2: 19: 56.12	−5: 28: 08.28					
12	[b]	J021929.6−040856	2: 19: 29.66	−4: 08: 56.75					
13	[b]	J021736.4−041944	2: 17: 36.35	−4: 19: 43.20					
14	[b]	J021947.4−041034	2: 19: 47.40	−4: 10: 34.83					
15	[b]	J021649.2−054327	2: 16: 49.22	−5: 43: 28.45					
16	[b]	J021902.8−054109	2: 19: 02.66	−5: 41: 10.13					
17	A[b]	J021634.8−043302	2: 16: 34.93	−4: 33: 00.13	21.93 ± 0.01	20.52 ± 0.01	19.93 ± 0.004	1.41	0.59
	B[b]		+1.14″	−2.82″	21.77 ± 0.01	20.44 ± 0.01	19.82 ± 0.01	1.33	0.62
18		J022646.2−045156	2: 26: 46.26	−4: 51: 55.45	21.37 ± 0.02[e]	[d]	[b]		

Notes. [a]Identifiers are from Chiappetti et al. (2013). In order to shorten the ID names, we systematically omitted the prefix 2XLSSd before the names of the objects. [b]Extended source. [c]Only for the bright A component. [d]Possibly affected by a cosmic ray. [e]Point-like source.

Candidate J022646.2−045156 looks very different in the various bands. In the g band, it looks like a single point-like source according to the PSF fitting results. In the r band, we see a faint secondary component. However, the bright component looks more compact than the reference star (PSF). This could hint on the presence of a defect or cosmic ray in the r band. It was therefore not possible to correctly define the r magnitude. In the i band, the bright component appears as an extended source according to PSF fitting. The SDSS SED analysis shows that it is a QSO/AGN with z=1.085. It could be that the host galaxy of this QSO/AGN has been detected in the i band.

3.4 Discussion

Using the multiple PSF fitting technique, we found 11 gravitational lens system candidates which consist of extended components: J021844.4−044825, J022739.7−050044, J022509.7−050950, J021956.2−052809, J021929.6−040856, J021736.4−041944, J021947.4−041034, J021649.2−054327, J021902.8−054109, J021634.8−043302 and J022646.2−045156. The candidate J021936.7−055721 consists of two components which have similar colours but one of the components is extended and the other one is point-like. Using magnitudes from the CFHTLS survey or from PSF fitting for the case of compact systems, we found that the following candidates have very different colours: J022055.1−060132, J022500.2−052204 and J022324.0−054928.

The two candidates J021511.4−034306 and J022234.3−031616 consist of pairs of point-like sources having very similar colours. Candidate J021511.4−034306 is very bright in X-ray, 1.1×10^{-13} and 1.5×10^{-16} W m^{-2} in the soft and hard bands, respectively. It corresponds to a hardness ratio $HR = -0.60$ which points to a source being likely an unobscured AGN. Candidate J022234.3−031616 is faint in X-ray and is only seen in the soft band, 6.8×10^{-18} W m^{-2}. The optical counterparts of the J022607.0−040301 candidate have slightly different colours but it could be caused by the presence of a lens, intrinsic colour variation of the AGN combined with a time delay and/or microlensing effects. The system is bright in X-ray, about 1.5×10^{-17} W m^{-2} in both the soft and hard bands. Its corresponding hardness ratio −0.63 indicates that it is a likely unobscured AGN.

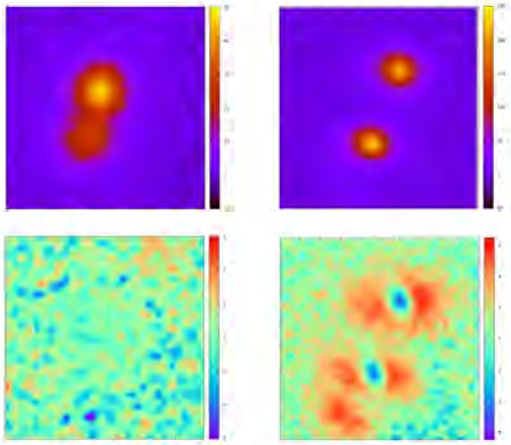

Figure 2. The CFHTLS images are shown at the top and the residuals after subtraction of a double PSF at the bottom. The latter residuals have been normalized to the noise image, in σ unit.

These last three systems (J021511.4−034306, J022234.3−031616 and J022607.0−040301) constitute the best gravitational lens candidates.

From the *XMM*-LSS source catalogue (Chiappetti et al. 2013), we have constructed the colour–colour diagram ($r - i$ versus $g - r$; see Fig. 3) for all spectroscopically confirmed stars and QSO/AGN counterparts of *XMM*-LSS point-like sources (see classification of sources in Melnyk et al. 2013). From this plot we suggest that the J021511.4−034306 and J022607.0−040301 candidates are probably AGN. For the candidate J022234.3−031616 we have only

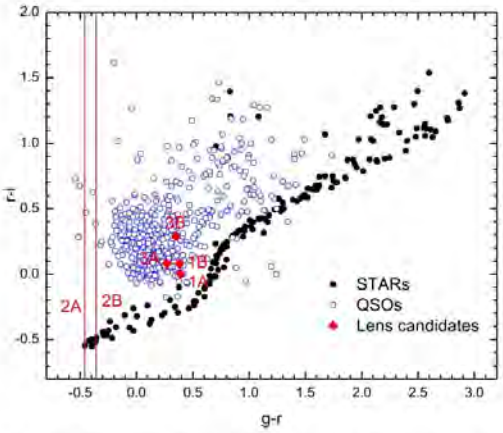

Figure 3. Colour–colour diagram from the templates of stars and spectroscopically confirmed QSOs/AGN in the *XMM*-LSS field, 131 templates are from Pickles (1998), 4 from Bohlin, Colina & Finley (1995), 19 from Bixler, Bowyer & Laget (1991). The components of the three best lens candidates are indicated in red: 1A – J021511.4−034306A, 1B – J021511.4−034306B, 2A – J022234.3−031616A, 2B – J022234.3−031616B, 3A – J022607.0−040301A, 3B – J022607.0−040301B.

magnitudes in g and r bands and we cannot classify them as QSOs/AGN or stars on the sole basis of the colour–colour diagram.

4 CONCLUSION

We have performed a visual inspection of some 5500 optical counterparts of X-ray point-like sources in the *XMM*-LSS/CFHTLS common field. Four independent inspectors have identified 18 compact systems which could be multiply imaged QSO/AGN. Using the PSF fitting technique we have characterized the morphology and colours of the components. As a result, we found three systems (J021511.4−034306, J022234.3−031616 and J022607.0−040301) which met our colour and morphological criteria and are the best gravitational lens candidates. They are point-like source pairs with similar colours. With a high probability they could be QSO/AGN. For a final confirmation we need spectroscopic observations of the multiple components of the selected systems.

ACKNOWLEDGEMENTS

AE (post-doc PRODEX) and JS acknowledge support the ESA Prodex Programme '*XMM*-LSS', from the Belgian Federal Science Policy Office and from the Communauté française de Belgique – Actions de recherche concertées – Académie universitaire Wallonie-Europe. AE is grateful to Stephen Gwyn for help with the CFHTLS images.

REFERENCES

Abazajian K. N. et al., 2009, ApJS, 182, 543
Bixler J. V., Bowyer S., Laget M., 1991, A&A, 250, 370
Bohlin R. C., Colina L., Finley D. S., 1995, AJ, 110, 1316
Cabanac R. A. et al., 2007, A&A, 461, 813
Chiappetti L. et al., 2013, MNRAS, 429, 1652
Elyiv A. et al., 2012, A&A, 537, A131
Finet F., Elyiv A., Surdej J., 2012, Mem. Soc. Astron. Ital., 83, 944
Jackson N., 2008, MNRAS, 389, 1311
Jullo E., Natarajan P., Kneib J.-P., D'Aloisio A., Limousin M., Richard J., Schimd C., 2010, Sci, 329, 924
Maturi M., Mizera S., Seidel G., 2013, A&A, preprint (arXiv:1305.3608)
Melnyk O. et al., 2013, A&A, preprint (arXiv:1307.0527)
Mitchell J. L., Keeton C. R., Frieman J. A., Sheth R. K., 2005, ApJ, 622, 81
More A., McKean J. P., Muxlow T. W. B., Porcas R. W., Fassnacht C. D., Koopmans L. V. E., 2008, MNRAS, 384, 1701
More A., Cabanac R., More S., Alard C., Limousin M., Kneib J.-P., Gavazzi R., Motta V., 2012, ApJ, 749, 38
Oguri M. et al., 2008, AJ, 135, 512
Pickles A. J., 1998, PASP, 110, 863
Pierre M., Pacaud F., Juin J. B., Melin J. B., Valageas P., Clerc N., Corasaniti P. S., 2011, MNRAS, 414, 1732
Refsdal S., Surdej J., 1994, Rep. Prog. Phys., 57, 117
Ricci D. et al., 2011, A&A, 528, A42
Ricci D. et al., 2013, A&A, 551, A104
Rowan-Robinson M. et al., 2008, MNRAS, 386, 697
Rozo E., Wu H.-Y., Schmidt F., 2011, ApJ, 735, 118
Shan H. et al., 2012, ApJ, 748, 56
Surdej J., Remy M., Haubold H., 1992, in Benvenuti P., Schreier E. J., eds, ESO Conf. Workshop Proc. No. 44, Science with the Hubble Space Telescope. European Southern Observatory, Garching, p. 127
Surdej J., Elyiv A., Finet F., Melnyk O., 2011, XXL Consortium Meeting, AGN Gravitational Lensing in the XXL Survey, available at: http://arachnos.astro.ulg.ac.be/RPub/Colloques/XXL2
Sygnet J. F., Tu H., Fort B., Gavazzi R., 2010, A&A, 517, A25

This paper has been typeset from a TEX/LATEX file prepared by the author.

У роботах [9, 10] проведено фотометричний мультиспектральний моніторинг квадрупольного HE0435-1223 та подвійного UM673 квазарів, відповідно, упродовж декількох епох спостережень у різних фільтрах.

Результати, отримані у [9], показують значне зменшення потоку гравітаційно-лінзового квазару між двома спостережуваними 2008–2009 років епохами. Падіння потоку спостерігалося для чотирьох лінзованих компонентів, – ймовірно, воно викликано зміною у власній світності квазара. Було також помічено варіації показників кольору – почервоніння в той час, коли квазар стає слабшим у світності. Подібний ефект зміни кольору у всіх чотирьох компонентах вже спостерігався в попередніх дослідженнях цього квазару. Асинхронна зміна кольорів може вказувати на ефект мікролінзування у цій системі. Потрібно зазначити, що результати даних спостережень квазару HE0435-1223 [9] було використано авторами [86] при моделюванні розподілу темної матерії в цій системі, а авторами [87] у детальному вивченні ефектів мікролінзування.

Результати роботи [10] показали значне зменшення потоку лінзованого компоненту "A" квазара з подвійним зображенням UM673 між сезонами 2008–2009 рр. і меншу варіцію потоку в 2009–2011 рр. у V і R смугах. Дані спостережень було отримано за допомогою датського 1.54-м телескопа. Було також відокремлено внесок потоку лінзованої галактики у слабкіший B компонент системи, що демонструє вплив застосування такої процедури на показник кольору останнього. Зроблено висновок, що внесок лінзової галактики у фотометрію UM673 значний і їм не можна знехтувати. Отже, було незалежно оцінено зміну величини потоку від лінзованої галактики за допомогою даних фотометрії та положень гравітаційно-лінзової системи, отриманих за допомогою Космічного телескопу Габбла (HST). Альтернативна оцінка потоку лінзованої галактики була зроблена в роботі [88].

Крім того, в роботі [28] нами були представлені результати обробки фотометричних спостережень гравітаційно-лінзової системи H1413+117, отримані протягом 2001 - 2008 років, з метою оцінки часових затримок між зображеннями квазара з лінзами та найкращим чином охарактеризувати події мікролінзування, що відбуваються. Було зроблено висновки про можливість пояснення варіацій кольору двома типами подій мікролінзування: мікролінзування для компонентів A, B, C, що відповідає типовим варіаціям $\sim 10^{-4}$ mag d^{-1} протягом усіх сезонів, тоді як компонент D показує надзвичайно сильний ефект мікролінзування з варіаціями до $\sim 10^{-3}$ mag d^{-1} протягом 2004 та 2005 років. Результати цієї роботи було обговорено в роботах [89, 90].

У роботі [29] нами представлено V і R фотометрію гравітаційно лінзованих квазарів WFI 2033-4723 і HE 0047-1756. Спостережувані дані було зібрано в рамках колаборації MiNDSTEP у співпраці з колегами обсерваторії ESO La Silla (1,54-м датський телескоп) за період від 2008 по 2012 роки. Було виявлено параметри зміни світності і кольорів, що було пояснено довготривалими подіями мікролінзування в цих системах. Приклади обговорення результатів цієї роботи можна знайти у [89, 91].

A&A 528, A42 (2011)
DOI: 10.1051/0004-6361/201016188

Astronomy & Astrophysics

Flux and color variations of the quadruply imaged quasar HE 0435-1223⋆

D. Ricci[1,⋆⋆], J. Poels[1], A. Elyiv[1,2], F. Finet[1], P. G. Sprimont[1], T. Anguita[3,4], V. Bozza[5,6], P. Browne[7], M. Burgdorf[8,24], S. Calchi Novati[5,9], M. Dominik[7,⋆⋆⋆], S. Dreizler[10], M. Glitrup[11], F. Grundahl[11], K. Harpsøe[12,25], F. Hessman[10], T. C. Hinse[12,13], A. Hornstrup[14], M. Hundertmark[10], U. G. Jørgensen[12,25], C. Liebig[7,15], G. Maier[15], L. Mancini[5,9,16], G. Masi[17], M. Mathiasen[12], S. Rahvar[18], G. Scarpetta[5,6], J. Skottfelt[12], C. Snodgrass[19,20], J. Southworth[21], J. Teuber[12], C. C. Thöne[22,23], J. Wambsganß[15], F. Zimmer[15], M. Zub[15], and J. Surdej[1,⋆⋆⋆⋆]

[1] Département d'Astrophysique, Géophysique et Océanographie, Bât. B5C, Sart Tilman, Université de Liège, 4000 Liège 1, Belgique
e-mail: ricci@astro.ulg.ac.be
[2] Main Astronomical Observatory, Academy of Sciences of Ukraine, Zabolotnoho 27, 03680 Kyiv, Ukraine
[3] Centro de Astro-Ingeniería, Departamento de Astronomía y Astrofísica, Pontificia Universidad Católica de Chile, Casilla 306, Santiago, Chile
[4] Max-Planck-Institut für Astronomie, Königstuhl 17, 69117 Heidelberg, Germany
[5] Dipartimento di Fisica "E.R. Caianiello", Università degli Studi di Salerno, via Ponte Don Melillo, 84085 Fisciano (SA), Italy
[6] Instituto Nazionale di Fisica Nucleare, Sezione di Napoli, Italy
[7] SUPA, University of St Andrews, School of Physics & Astronomy, North Haugh, St Andrews, KY16 9SS, UK
[8] Deutsches SOFIA Institut, Universitaet Stuttgart, Pfaffenwaldring 31, 70569 Stuttgart, Germany
[9] Istituto Internazionale per gli Alti Studi Scientifici (IIASS), Vietri Sul Mare (SA), Italy
[10] Institut für Astrophysik, Georg-August-Universität Göttingen, Friedrich-Hund-Platz 1, 37077 Göttingen, Germany
[11] Department of Physics & Astronomy, Aarhus University, Ny Munkegade, 8000 Aarhus C, Denmark
[12] Niels Bohr Institute, University of Copenhagen, Juliane Maries vej 30, 2100 Copenhagen Ø, Denmark
[13] KASI – Korea Astronomy and Space Science Institute, 61-1 Hwaam-dong, Yuseong-gu, Daejeon 305-348, Republic of Korea
[14] National Space Institute, Technical University of Denmark, 2800 Lyngby, Denmark
[15] Astronomisches Rechen-Institut, Zentrum für Astronomie, Universität Heidelberg, Mönchhofstraße 12-14, 69120 Heidelberg, Germany
[16] Dipartimento di Ingegneria, Università del Sannio, Corso Garibaldi 107, 82100 Benevento, Italy
[17] Bellatrix Astronomical Observatory, Center for Backyard Astrophysics, Ceccano (FR), Italy
[18] Physics Department, Sharif University of Technology, Tehran, Iran
[19] European Southern Observatory, Casilla 19001, Santiago 19, Chile
[20] Max Planck Institute for Solar System Research, Max-Planck-Str. 2, 37191 Katlenburg-Lindau, Germany
[21] Astrophysics Group, Keele University, Newcastle-under Lyme, ST5 5BG, UK
[22] Dark Cosmology Centre, Niels Bohr Institute, University of Copenhagen, Juliane Maries Vej 30, 2100 Copenhagen, Denmark
[23] INAF – Osservatorio Astronomico di Brera, 23807 Merate, Italy
[24] SOFIA Science Center, NASA Ames Research Center, Mail Stop N211-3, Moffett Field CA 94035, USA
[25] Centre for Star and Planet Formation, Geological Museum, Øster Voldgade 5, 1350 Copenhagen, Denmark

Received 23 November 2010 / Accepted 10 January 2011

ABSTRACT

Aims. We present *VRi* photometric observations of the quadruply imaged quasar HE0435-1223, carried out with the Danish 1.54 m telescope at the La Silla Observatory. Our aim was to monitor and study the magnitudes and colors of each lensed component as a function of time.

Methods. We monitored the object during two seasons (2008 and 2009) in the *VRi* spectral bands, and reduced the data with two independent techniques: difference imaging and point spread function (PSF) fitting.

Results. Between these two seasons, our results show an evident decrease in flux by ≈0.2–0.4 magnitudes of the four lensed components in the three filters. We also found a significant increase (≈0.05–0.015) in their $V - R$ and $R - i$ color indices.

Conclusions. These flux and color variations are very likely caused by intrinsic variations of the quasar between the observed epochs. Microlensing effects probably also affect the brightest "A" lensed component.

Key words. quasars: general – gravitational lensing: weak – techniques: photometric

⋆ Based on data collected by MiNDSTEp with the Danish 1.54 m telescope at the ESO La Silla Observatory. Tables 5–7 are only available in electronic form at the CDS via anonymous ftp to cdsarc.u-strasbg.fr (130.79.128.5) or via http://cdsarc.u-strasbg.fr/viz-bin/qcat?J/A+A/528/A42

⋆⋆ Boursier FRIA.
⋆⋆⋆ Royal Society University Research Fellow.
⋆⋆⋆⋆ Also Directeur de Recherche honoraire du FRS-FNRS.

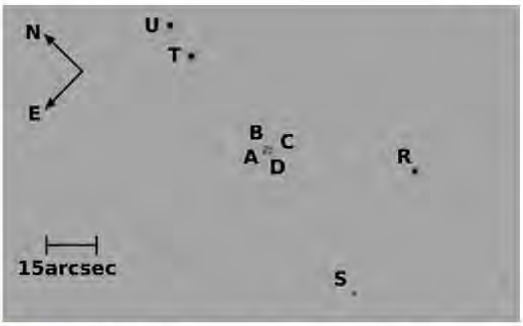

Fig. 1. Zoom of a DFOSC *i* filter image showing the four components of the lensed quasar and four nearby stars. The components are labeled following the notation of Wisotzki et al. (2002): "A" for the brighter component, "B", "C" and"D" clockwise. The stars "R", "S", "T" and "U" were used to search for a suitable reference star. The "R" star was finally chosen. The contrast of the displayed image, on a negative scale, was selected to improve the visibility of the lensed components. The image is a median of the three CCD frames collected on 2008 August 8.

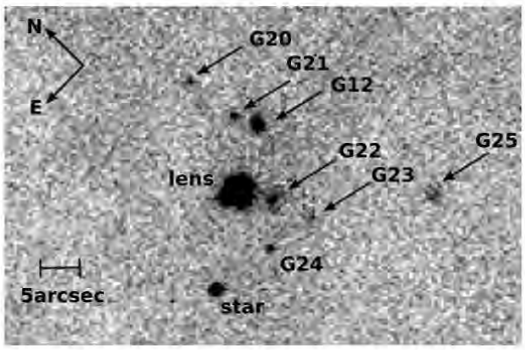

Fig. 2. Zoom of a DFOSC *i* filter image showing the galaxy environment near HE0435-1223. The objects are labeled following the notation of Morgan et al. (2005). The contrast, on a negative scale, was selected to improve the visibility of the galaxies. The image is a median of the three CCD frames collected on 2008 August 8.

1. Introduction

In the framework of the MiNDSTEp (Microlensing Network for the Detection of Small Terrestrial Exoplanets) campaign (Dominik et al. 2010), which has as a main target the systematic observation of bulge microlenses, we developed a parallel project concerning photometric multi-band observations of several lensed quasars[1]. In the present paper we focus on HE0435-1223 (see Fig. 1), a QSO discovered by Wisotzki et al. (2000) in the course of the Hamburg/ESO digital objective prism survey, and confirmed to be a quadruply imaged quasar by Wisotzki et al. (2002). The lensing galaxy was initially identified as an elliptical with a scale length of ≈12 kpc at a redshift in the range $z = 0.3$–0.4. The time delays between the four images (labeled "A", "B", "C", "D", starting from the brighter one and proceeding clockwise) of the quasar were estimated around 10 days, and the quasar itself showed some signs of intrinsic variability (Wisotzki et al. 2002).

More recently, the value of the redshift for the lensing galaxy was estimated as $z = 0.44 \pm 0.20$, and the quasar redshift was confirmed to be $z = 1.6895 \pm 0.0005$, with a Δz between the components of ≈0.0015 rms (Wisotzki et al. 2003). These spectrophotomeric observations showed some possible signature of microlensing effects in the continuum and in the spectral emission lines for the "D" component.

Morgan et al. (2005) provided milliarcsecond astrometry, revised the value of the lens redshift at $z = 0.4546 \pm 0.0002$ with the Low-Dispersion Survey Spectrograph 2 (LDSS2) on the Clay 6.5 m telescope, and studied the galaxy environment of the lens, because it is located in a dense galaxy field. The results do not show any evidence of a cluster for the considered galaxies. However, the nearest galaxies (G20, G21, G22, G23, and G24 in Fig. 2) whose redshifts were not measured, left this scenario open. Nevertheless, the results of a deep investigation concerning the direction of an external shear in the gravitational field of the lens do not show an evident correlation with the position of the near galaxies. As a remaining explanation, Morgan et al. (2005) suggested the presence of substructures in the lensing galaxy.

The first systematic monitoring, which was performed in the *R* filter and covered the years between 2003 and 2005, was carried out by Kochanek et al. (2006): that paper provided astrometric measurements compatible with the previous works, measured the time delays between the images ($\Delta t_{AD} = -14.37$, $\Delta t_{AB} = -8.00$, and $\Delta t_{AC} = -2.10$ days, with errors respectively of 6%, 10% and 35%), and finally confirmed the lensing galaxy as an elliptical with a rising rotation curve.

Furthermore, Mediavilla et al. (2009) observed HE0435-1223 in the framework of a monitoring of 29 lensed quasars, and attributed eventual microlensing events to the normal stellar populations, while Blackburne & Kochanek (2010) focused on the quasar itself, applying a model with a time-variable accretion disk to the object. Mosquera et al. (2011) found clear evidence of chromatic microlensing in the "A" component, and provided an estimate of the disk size in the *R* band in agreement with the simple thin-disk model. Blackburne et al. (2011) used the chromatic microlensing to model the accretion disk, and Courbin et al. (2010) recalculated the time delays with *N*-body realizations of the lensing galaxy, which he thought to belong to the "B component" ($\Delta t_{BA} = 8.4$, $\Delta t_{BC} = 7.8$ and $\Delta t_{BD} = 6.5$ days with errors of 25%, 10%, and 11% respectively). Considering multi-color observations of other lensed quasars, a single-epoch multi-band photometry was used on MG0414+0534 to constrain the accretion disk model and the size of the emission region in the continuum (Bate et al. 2008; Bate 2008; Floyd et al. 2008).

A multi-epoch multi-band photometry, carried out during several years, was used for the quasar Q2237+0305 by Koptelova et al. (2006), who observed the object during five years (1995–2000) in the *VRI* bands. Anguita et al. (2008) combined these data with OGLE observations. Mosquera et al. (2009) monitored the object in eight filters and found evidence for microlensing in the continuum, but not in the emission lines. Furthermore, Q2237+0305 was the object of deep studies focused on the lens galaxy (Poindexter & Kochanek 2010b), and on the inclination of the accretion disk (Poindexter & Kochanek 2010a). Another example of multi-epoch multi-band observations is given by UM673/Q0142–100, observed in the Gunn *i* and Cousins *V* filters between 1998 and 1999 (Nakos et al. 2005)

[1] HE0435-1223, UM673/Q0142-100, Q2237+0305, WFI2033-4723 and HE0047-1756

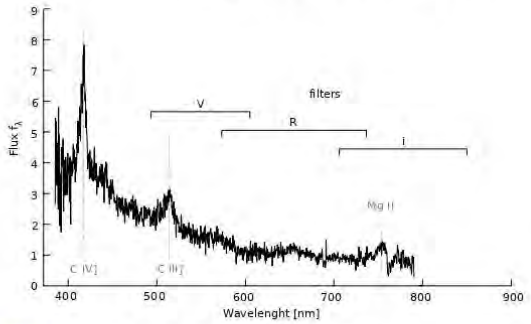

Fig. 3. Position and bandwidth of the *VRi* DFOSC filters superposed on the unresolved spectrum of HE0435-1223. The figure is a composition made from the spectrum shown in the paper of Wisotzki et al. (2002).

Table 1. Parameters of the DFOSC filters used for the photometry [2].

Filter	ESO #	Size [mm]	λ [nm]	$\Delta\lambda$ [nm]
Bessel *V*	451	C60.0	544.80	116.31
Bessel *R*	452	C60.0	648.87	164.70
Gunn *i*	425	C60.0	797.79	142.88

and in the *VRI* bands between 2003 and 2005 (Koptelova et al. 2010). Unlike for these objects, no *systematic* multi-band photometry has ever been carried out for HE0435-1223.

Here, we present two periods of multi-band photometric observations of HE0435-1223, performed in the *VRi* spectral bands with the Danish 1.54 m telescope at the La Silla Observatory.

In Sect. 2 we explain how the observations were carried out; in Sect. 3 we focus on the data reduction, and we describe the two independent techniques: difference imaging and point spread function (PSF) fitting, that were used to construct the light curves. In Sect. 4 we present the results. Finally, in Sect. 5 we summarize the conclusions.

2. Observations and pre-processing

We observed HE0435-1223 during two seasons (2008 and 2009) with the Danish 1.54m telescope at the La Silla Observatory. We used the DFOSC instrument (Danish Faint Object Spectrograph and Camera) for imaging and photometry, with a 2147×2101 CCD device, covering a $13.7' \times 13.7'$ field of view with a resolution of $0.39''$/pixel. The gain of the device is 0.74 electron/ADU in high mode, while the read out noise in this mode is 3.1 electrons (Sørensen 2000).

The data were collected in three different filters: Gunn *i*, Bessel *R* and Bessel *V* (see Table 1 and Fig. 3). We worked with a very homogeneous dataset consisting of 180s exposures.

For almost every night of observation, we also collected bias images and dome flat-fields, which were already treated *in loco* using an automatic IDL procedure, part of the MiNDSTEp pipeline for the observation of bulge microlenses. We then obtained master flat-fields for the different filters and master biases. When these images were not present for the desired date, we coupled the most recent set of master bias and master flat-fields to our science dataset, in the phase of pre-processing.

[2] Information available on the Internet at `http://www.eso.org/lasilla/telescopes/d1p5/misc/dfosc_filters.html`

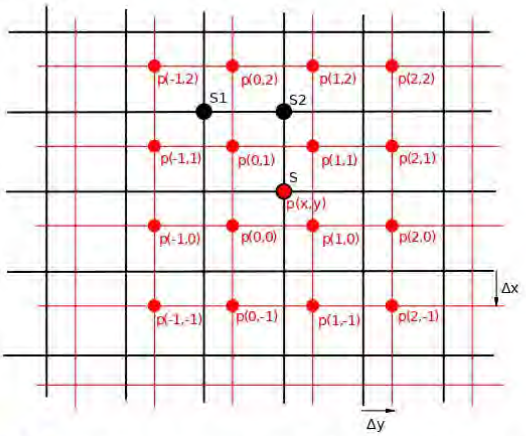

Fig. 4. Scheme for the superposed images of the first (little dots, lighter grid) and second (big dots, bolder grid) stars. The big dots correspond to the knots with known fluxes. The arrows Δx and Δy indicate the shift between the two images.

We collected a total of 391 images during the 2008 season, and 160 images in 2009.

The images were pre-processed (de-biased and flat-fielded), and we used particularly the dome flats. To erase the possible residual halos caused by the inhomogeneous illumination, the sky background was subtracted fitting a 4th degree surface after masking the stars and cosmic rays, and the images were recentered with an accuracy of 1 px.

These steps were performed with a C++ pipeline developed by our team.

We analyzed each image to sort out and then disregard the problematic images in terms of bad tracking, particularly bad seeing (the components were completely unresolved) or bad focusing.

We then obtained 216 images during the 2008 season: 70 in the *i* filter, covering 26 nights, 83 in the *R* filter, covering 32 nights, and 63 in the *V* filter, covering 25 nights, distributed between 2008 July 27 and 2008 October 4.

Concerning the 2009 season, we obtained 116 images: 46 in the *i* filter, covering 17 nights, 37 in the *R* filter, covering 14 nights, and 33 in the *V* filter, covering 12 nights, distributed between 2009 August 20 and 2009 September 19.

3. Data reduction

As a first step, we chose four stars near HE0435-1223, labeled "R", "S", "T" and "U" in Fig. 1, to search for a stable reference star. We examined the ratios between the fluxes of these stars in the *V* band as a function of time, to possibly detect some photometric variations between the two seasons.

For the calculation of the ratio between the fluxes of two selected stars we applied the PSF fitting method that was also subsequently used on the gravitational lens system itself. While using this method, we superposed the image of the first star over the fixed image of the second star as shown in Fig. 4. The red and black grids represent the images of the first and the second star, respectively.

The big dots correspond to the knots for which the counts are known. The values $p(x, y)$ and S correspond to the counts

Table 2. Average V magnitude differences between the two epochs for the four stars near HE0435-1223.

Pair	$\langle V_{2008}\rangle$	$\langle V_{2009}\rangle$
⟨S−R⟩	1,78 ± 0,03	1,77 ± 0,02
⟨S−T⟩	2,04 ± 0,07	1,95 ± 0,07
⟨T−R⟩	−0,41 ± 0,06	−0,40 ± 0,04
⟨U−S⟩	−2,36 ± 0,04	−2,42 ± 0,03
⟨U−R⟩	−0,58 ± 0,04	−0,65 ± 0,03
⟨U−T⟩	−0,34 ± 0,05	−0,31 ± 0,04

for each knot of the first and the second star, respectively. To perform a precise fitting we needed to superpose these images with an accuracy better than 1 pixel. When this was done, the knots of both images did not perfectly coincide with each other as shown in Fig. 4. Therefore we had to calculate intermediate values, for example $p(x, y)$, which we could compare with the value S at the same point. For that we used bicubic interpolation (Press et al. 1992). The intermediate value $p(x, y)$ is expressed by the polynomial

$$p(x, y) = \sum_{i=0}^{3} \sum_{j=0}^{3} a_{i,j} x^i y^j. \quad (1)$$

To derive the values of the 16 coefficients $a_{i,j}$ we resolved this set of equations for 16 knots around the considered point $p(x, y)$. They are shown as red dots in Fig. 4. With this coefficient matrix $a_{i,j}$ we could derive $p(x, y)$ at any point. For the fitting of both images we minimized the quantity

$$\Delta(A, \Delta x, \Delta y) = \sum_k (A p_k(x + \Delta x, y + \Delta y) - S_k)^2, \quad (2)$$

which is the sum over all knots k of the first star image; A is the ratio between the total flux of the second and the first star, Δx and Δy are the relative shifts (fractions of a pixel) between the two superposed images. Before the first iteration, we set the three parameters A, Δx and Δy within reasonable ranges.

We derived the light curves for the reference stars as magnitude differences and calculated the average difference and standard deviations for the two epochs (see Table 2). Obviously the stellar pairs with the star "R" in Table 2 show on average the smallest differences between the two epochs. Moreover the light curves of the "R" star shows on average the least standard deviation σ (see Table 2), and we may reasonably assume that star "R" is the most stable reference star between the two seasons. Therefore we chose star "R" as the reference for all subsequent photometric zero point determinations.

The magnitude of the reference star was taken from the USNO-B1.0 catalog for the i and R filters (16.27 and 16.33 respectively), and from the NOMAD1 catalog for the V filter (17.04).

The light curves for the four components of the gravitational lens system were then calculated with two independent methods treated below: difference imaging and PSF fitting.

3.1. Difference imaging method

The aim of the difference imaging technique is to subtract from each image of our field (indicated as "frame" in the following) one image of the same field (called "reference frame") taken at a different time under the best seeing conditions. This operation produces a set of subtracted frames where only the relative flux variations between the two images (generic frame and reference frame) are visible. Performing aperture photometry on these subtracted frames, and in particular at the positions of the lensed QSO components, we derived the light curves of the four lensed components.

However, differences in seeing, focus, and guiding precision between frames collected at different times may produce variations in the shape of the PSF: trying the subtraction without additional operations would produce high residuals caused by potential PSF slope variations. Several methods have been developed to force the PSF of the images to match (Alard 1999, 2000). These methods are particularly useful in crowded fields such as the galactic bulge, but are less succesful in sparse fields. In this paper we adopt the method proposed by Phillips (1993) which was already successfully applied by Nakos et al. (2005) and is based on FFT (Fast Fourier Transform).

If r is the reference frame and f a generic frame, then $f = r \otimes k$, where k is the convolution kernel describing the differences between the PSF, which are unknown, and $\otimes$ indicates the convolution product. In the Fourier space, the previous equation can be noted as $F = RK$, where F, R and K represents the Fourier transform ($\mathscr{F}$) of the generic frame f, the reference frame r, and the convolution kernel k. Then $k = \mathscr{F}^{-1}(F/R)$.

Phillips (1993) considers the limits of this technique and the solutions adopted to avoid problems with background and high-frequency noise.

We normalized the frames in flux by fixing the magnitude of the reference star in each filter with the values of the catalogs mentioned above. Then we used the difference imaging method on the normalized frames. With this technique, all the not variable objects in the field disappear, which allows us automatically to suppress the contribution of the lensing galaxy, which is an extended and photometrically constant object.

To obtain the light curves, we performed aperture photometry of the residuals, using the positions of the selected reference star and of the lensed components previously derived. But we found for the 2009 images a weak linear dependence between the magnitude and the seeing, which we removed after calibrating this effect.

The procedure described in this paragraph is based on a code developed by our team, written in Python.

The results for the three filters are shown in the left column of Fig. 5. The error bars correspond to the magnitude rms (1σ) of each night of observation.

3.2. PSF fitting method

We also decided to calculate the light curves using PSF fitting as an independent method, which we previously employed to determine the most adequate reference star.

For the fitting of the lens system we used the image of star "R" as the PSF reference. Then we fitted each frame with five adjustable PSF for the four lensed quasar images and the lensing galaxy, taking the relative astrometric coordinates between the components from Kochanek et al. (2006). Note that the faint lensing galaxy is barely resolved on direct HST CCD frames (Morgan et al. 2005)[3]. Therefore, it is legitimate to model it with the PSF of our ground-based observations.

In this way we had seven free parameters: Δx, Δy (coordinates of the gravitational lens system with respect to the reference star "R"), and the central fluxes of the five components.

[3] HST program 9744.

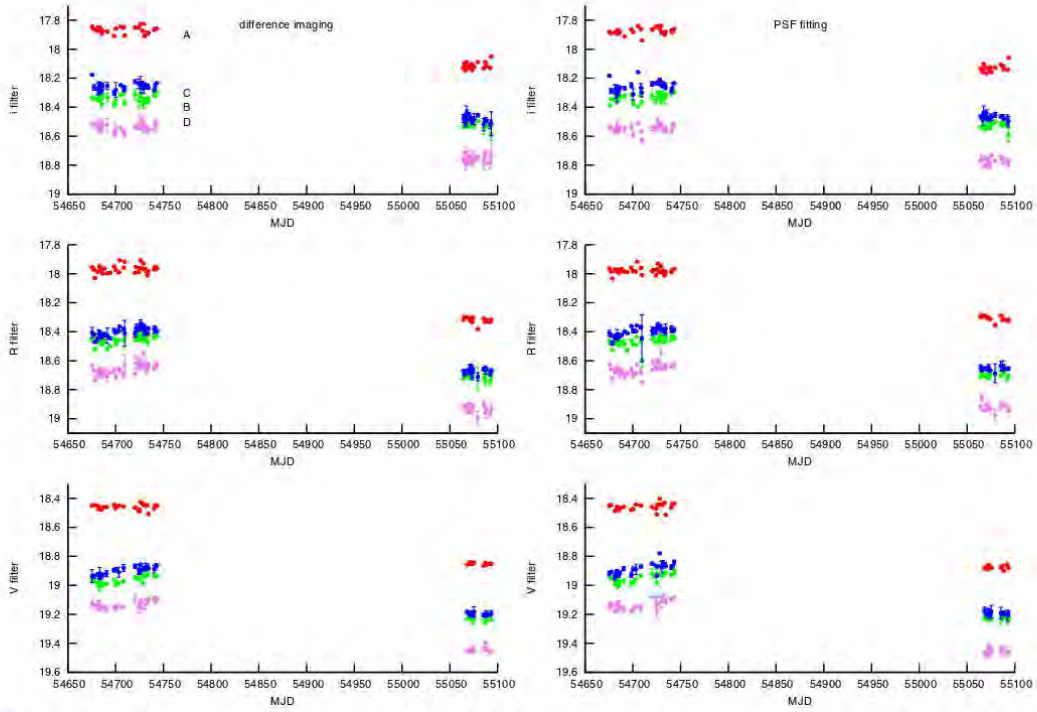

Fig. 5. Light curves of the four lensed components of HE0435-1223. The different graphs illustrate the photometry in the *i*, *R* and *V* bands, calculated using the difference imaging technique (*left*) and the PSF fitting technique (*right*). The error bars correspond to the magnitude rms (1σ) of each night of observation.

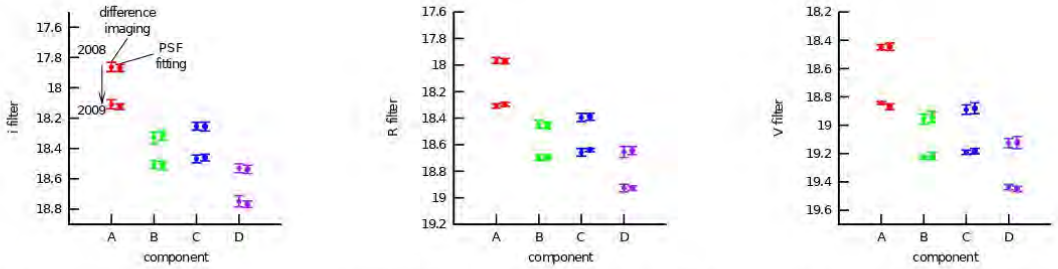

Fig. 6. Average magnitude of each component for the 2008 season (upper symbols) and 2009 (lower symbols), calculated with the difference imaging technique (*left*) and the PSF fitting method (*right*). The error bars correspond to the magnitude rms (1σ) during each epoch of observation.

After minimization of the squared differences between the fluxes of the real lens system image and the simulated image with the five PSF, we derived the seven best-fitting parameters. We used bicubic interpolation for the superposition of the CCD frames to achieve results better than 1 pixel according to our description in Sect. 3. To construct the light curves, we calculated the flux ratios between each component and the reference star "R". The procedure described in this paragraph is based on an Object Pascal code developed by our team.

The results for the three filters are shown in the right column of Fig. 5. The error bars correspond to the magnitude rms (1σ) of each night of observation.

4. Results

Both methods show a significant decrease in flux of the four lensed components between the 2008 and 2009 seasons. The estimated amounts of the decrease are coherent between the two methods (see Fig. 6).

In order to estimate this decrease, we measured the mean and the σ for each component in each filter. The average values for the magnitudes and rms for each component, each filter and the 2008 and 2009 seasons, are reported in Table 3. Specifically, all the four components show a decrease by $\approx$0.2–0.4 magnitudes in each of the filters, although we notice a slightly larger amplitude for component "A" in the *V* band.

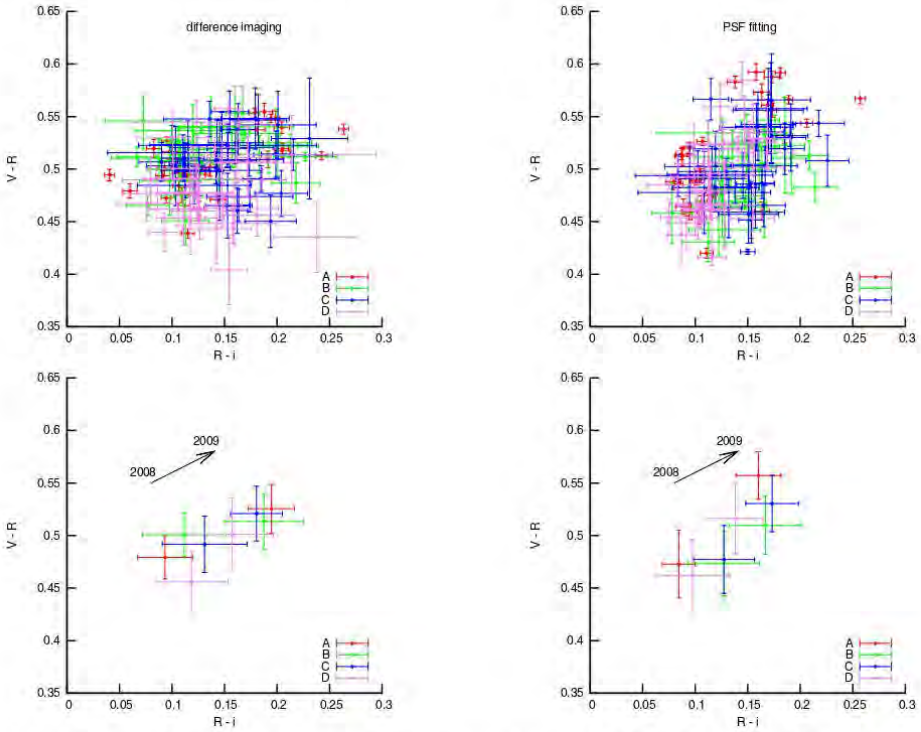

Fig. 7. Color-color diagrams for the four lensed components. The left column shows the $V - R$ vs. $R - i$ diagram calculated with the difference imaging technique: all observations (*upper panel*) and average of the observations for each season (*lower panel*). The right column shows the same diagrams calculated with the PSF fitting technique.

Table 3. *VRi* average magnitudes of the four lensed components of HE0435-1223 during the 2008 and 2009 seasons.

2008	Technique	*A*	*B*	*C*	*D*
i	difference imaging	17.86 ± 0.03	18.33 ± 0.04	18.25 ± 0.03	18.53 ± 0.03
i	PSF fitting	17.87 ± 0.02	18.32 ± 0.03	18.26 ± 0.03	18.54 ± 0.03
R	difference imaging	17.97 ± 0.02	18.46 ± 0.02	18.39 ± 0.03	18.64 ± 0.03
R	PSF fitting	17.97 ± 0.02	18.44 ± 0.03	18.39 ± 0.03	18.65 ± 0.04
V	difference imaging	18.45 ± 0.03	18.94 ± 0.04	18.88 ± 0.04	19.12 ± 0.04
V	PSF fitting	18.45 ± 0.02	18.96 ± 0.03	18.89 ± 0.03	19.13 ± 0.03
2009	Technique	*A*	*B*	*C*	*D*
i	difference imaging	18.11 ± 0.03	18.51 ± 0.02	18.47 ± 0.03	18.75 ± 0.04
i	PSF fitting	18.12 ± 0.02	18.51 ± 0.03	18.46 ± 0.02	18.77 ± 0.02
R	difference imaging	18.30 ± 0.01	18.69 ± 0.02	18.64 ± 0.01	18.93 ± 0.02
R	PSF fitting	18.31 ± 0.02	18.70 ± 0.02	18.66 ± 0.03	18.93 ± 0.03
V	difference imaging	18.87 ± 0.02	19.22 ± 0.03	19.18 ± 0.02	19.45 ± 0.02
V	PSF fitting	18.84 ± 0.01	19.23 ± 0.01	19.19 ± 0.02	19.44 ± 0.02

The corresponding values expressed in sigma units show a shift between ≈11.3σ and ≈13.7σ in the *V* band, except for component "A", which shows a decrease by ≈26.3σ. In the *R* and *i* filters, the shift is between ≈6.5σ and 7.5σ, except for component "A" (≈15.0σ and ≈9.8σ respectively) and component "C" in the *R* band (≈12.0σ).

For the fraction of nights when the object was observed in all *VRi* filters, we were able to build the color-color diagram ($V - R$ vs. $R-i$) for the four components. The results are shown in Fig. 7. With the same technique used to estimate the decrease in flux, we also found a significant increase (≈0.05–0.015) for the color indices $V - R$ and $R - i$ between the two observing seasons. The details are given in Table 4. In particular, component "A" shows the largest shift in color.

The corresponding values expressed in sigma units show a shift in color between ≈1.3σ and ≈2.0σ for the color indices $V - R$ and $R - i$, except for component "A" (3.40σ in $V - R$ and 3.1σ in $R - i$).

Given the short time delays (Kochanek et al. 2006) and because we expect microlensing to lead to uncorrelated flux variations between the four lensed components, these results support the assumption that the observed magnitude and color

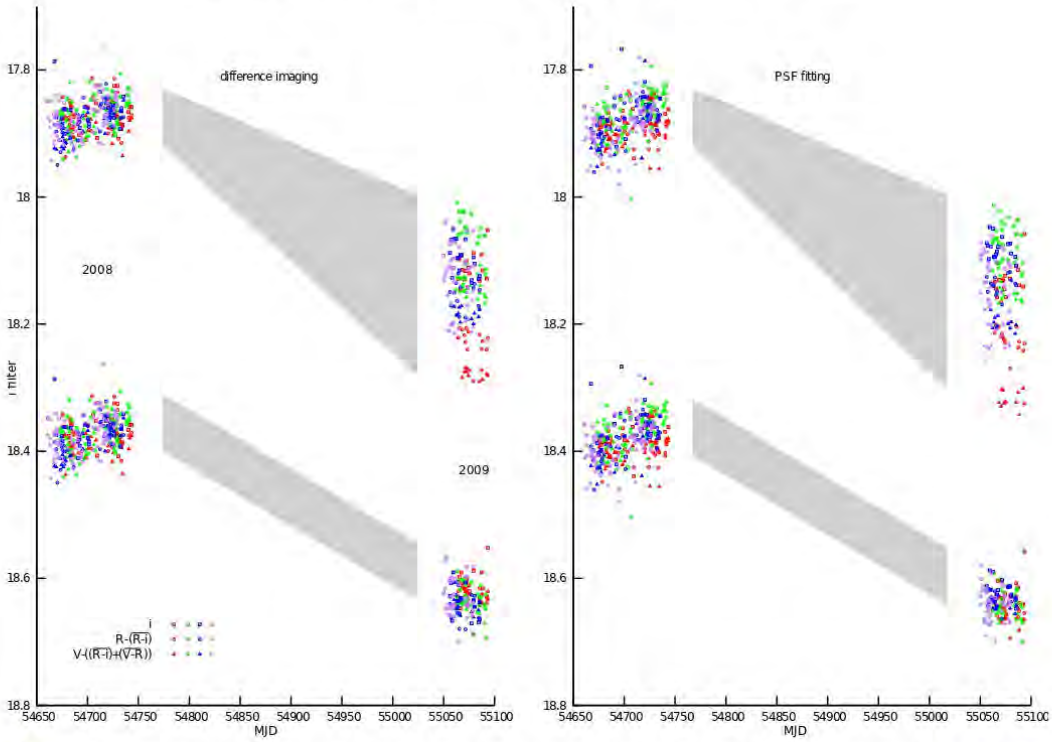

Fig. 8. *Upper light curve*: "global *i*" light curve of the four lensed components of HE0435-1223 obtained after subtracting the average 2008 *i* difference in magnitude from "B", "C", and "D" with respect to component "A"; then corrected for the time delays provided by Kochanek et al. (2006) and finally subtracting from the *R* and the *V* light curves the average 2008 $R-i$ and $(R-i)+(V-R)$ color indices, respectively. *Lower light curve*: "global *i*" light curve obtained repeating the same procedure as for the upper one, but correcting for the average 2008 magnitude and color indices concerning the 2008 data, and for the 2009 average magnitude and color indices concerning the 2009 data. The left panel shows the results obtained with the difference imaging technique, while the right panel shows the results obtained with the PSF fitting technique. The gray quadrilaterals help to connect the two epochs of observation. The lower light curves are arbitrarily shifted in magnitude.

Table 4. Averages and error bars (sigma) characterizing the $V-R$ and $R-i$ color indices of each component for the 2008 and 2009 seasons.

2008	Technique	*A*	*B*	*C*	*D*
$V-R$	difference imaging	0.47 ± 0.03	0.47 ± 0.03	0.48 ± 0.03	0.46 ± 0.03
$V-R$	PSF fitting	0.48 ± 0.02	0.50 ± 0.02	0.49 ± 0.03	0.46 ± 0.03
$R-i$	difference imaging	0.08 ± 0.02	0.13 ± 0.03	0.13 ± 0.03	0.10 ± 0.04
$R-i$	PSF fitting	0.09 ± 0.03	0.11 ± 0.04	0.13 ± 0.04	0.12 ± 0.03
2009	Technique	*A*	*B*	*C*	*D*
$V-R$	difference imaging	0.56 ± 0.02	0.51 ± 0.03	0.53 ± 0.03	0.52 ± 0.03
$V-R$	PSF fitting	0.53 ± 0.02	0.51 ± 0.03	0.52 ± 0.03	0.50 ± 0.03
$R-i$	difference imaging	0.16 ± 0.02	0.17 ± 0.03	0.17 ± 0.03	0.14 ± 0.03
$R-i$	PSF fitting	0.19 ± 0.02	0.19 ± 0.04	0.18 ± 0.02	0.16 ± 0.04

variations are very likely caused by intrinsic variations of the QSO, while the lensed "A" component is probably also affected by microlensing.

As a complementary approach, we decided to construct two "global *i*" light curves to better understand the nature of these different variations in flux and color index.

To construct the first one, we superposed the light curves of the four components by subtracting from "B", "C", and "D" their average 2008 difference in magnitude with respect to the "A" component, and we corrected the data for the time delays provided by Kochanek et al. (2006) (i.e, we applied to the components a shift in the MJD corresponding to the time delays). Then, we superposed the obtained curves (one for each filter) by subtracting from the *R* and the *V* light curves the average 2008 $R-i$ and $(R-i)+(V-R)$ color indices, respectively. The goal of this first "global *i*" light curve is to visualize how the spreads in magnitude and colors evolve between the epochs. The results are shown in Fig. 8 (upper light curves).

To construct the second "global *i*" light curve, we repeated the same procedure, but subtracted from the 2008 data of "B", "C" and "D" the average 2008 difference in magnitude with respect to component "A", and from 2009 data the corresponding

average 2009 difference in magnitude. Similarly, we subtracted from the R and the V light curves the average 2008 and 2009 $R-i$ and $(R-i)+(V-R)$ color indices, respectively. The results are shown in Fig. 8 (lower curves).

After these superpositions, we observe in 2008 a scatter in the data (see Fig. 8) significantly larger than that of the individual light curves (see Fig. 5); and in general a difference in scatter between the two epochs that we attribute to intrinsic variations of the quasar both in magnitude and color.

We also observe a slight brightening of the lensed quasar in 2008, followed by a significant decrease in 2009. Our observations corroborate those recently reported by Courbin et al. (2010). Referring to the PSF-only fitting method, we were also able to estimate the magnitude of the lensing galaxy as 19.87 ± 0.10 in the i band; 20.47 ± 0.13 in the R band; and 21.89 ± 0.24 in the V band. Furthermore, no significant changes in the magnitude of the lensing galaxy were observed between the two epochs. Our results for the V and i filters are coherent with those of Wisotzki et al. (2002) and Morgan et al. (2005).

Proceeding in the same way, we did not find any evident color-shift for the lensing galaxy: we find a value of 1.47 ± 0.33 and 1.36 ± 0.21 for the $V-R$ color index in 2008 and 2009, respectively; and 0.59 ± 0.17 and 0.61 ± 0.14 for the $R-i$ color index.

The stability of the flux of the lensing galaxy over the two epochs enforces the validity of our PSF fitting software. We find that appreciably larger photometric error bars derived for the lensing galaxy are essentially caused by its faintness ($V \approx 21.9$) compared with the four lensed components ($V \in [18.4, 19.5]$).

5. Conclusion

Systematic multi-spectral band photometry of the quadruply imaged quasar HE0435-1223, carried out during two seasons (2008 and 2009), shows a significant decrease in flux of the four lensed components between the two epochs.

The drop in flux observed for the four lensed components between 2008 and 2009 is very likely caused by a change in the intrinsic luminosity of the quasar. This corroborates the previous studies of the HE0435-1223 gravitational lens system by Kochanek et al. (2006) and Courbin et al. (2010).

Concerning the color variations, the intrinsic reddening of a quasar when it becomes fainter in luminosity is an effect already observed in previous studies (Pereyra et al. 2006), and the same trend probably accounts for the similar observed changes in the colors of the four lensed components of HE0435-1223.

This hypothesis is enforced if we suppose that the intrinsic photometric quasar variations in the different colors are not synchronized, which provides an explanation for the differences in scatter between the epochs (see Fig. 8). Microlensing probably provides the additional effect necessary to account for the higher flux variation observed for the "A" component.

The presented observations also show that a well sampled multi-band photometry can help in distinguishing the nature of the variability of multiply imaged objects, in particular gravitationally lensed quasars.

We suggest to couple this technique in the future with integral field spectroscopy to provide an additional way for an even more detailed investigation of the observed phenomena.

Acknowledgements. The research was supported by ARC – Action de recherche concertée (Communauté Française de Belgique – Académie Wallonie-Europe). A.E. is the beneficiary of a fellowship granted by the Belgian Federal Science Policy Office. Astronomical research at Armagh Observatory is funded by the Department of Culture, Arts & Leisure (DCAL), Northern Ireland, UK. Operation of the Danish 1.54 m telescope is supported by the Danish National Science Research Council (FNU). We wish to thank the anonymous referee for the remarks and the suggestions.

References

Alard, C. 1999 [arXiv:astro-ph/9903111]
Alard, C. 2000, A&AS, 144, 363
Anguita, T., Schmidt, R. W., Turner, E. L., et al. 2008, A&A, 480, 327
Bate, N. 2008, in Manchester Microlensing Conference
Bate, N. F., Floyd, D. J. E., Webster, R. L., & Wyithe, J. S. B. 2008, MNRAS, 391, 1955
Blackburne, J. A., & Kochanek, C. S. 2010, ApJ, 718, 1079
Blackburne, J. A., Pooley, D., Rappaport, S., & Schechter, P. L. 2011, ApJ, 729, 34
Courbin, F., Chantry, V., Revaz, Y., et al. 2010, [arXiv:1009.1473]
Dominik, M., Jørgensen, U. G., Rattenbury, N. J., et al. 2010, Astron. Nachr., 331, 671
Floyd, D. J. E., Bate, N. F., & Webster, R. L. 2008, Mem. Soc. Astron. Ital., 79, 1271
Kochanek, C. S., Morgan, N. D., Falco, E. E., et al. 2006, ApJ, 640, 47
Koptelova, E., Oknyanskij, V. L., Artamonov, B. P., & Burkhonov, O. 2010, MNRAS, 401, 2805
Koptelova, E. A., Oknyanskij, V. L., & Shimanovskaya, E. V. 2006, A&A, 452, 37
Mediavilla, E., Muñoz, J. A., Falco, E., et al. 2009, ApJ, 706, 1451
Morgan, N. D., Kochanek, C. S., Pevunova, O., & Schechter, P. L. 2005, AJ, 129, 2531
Mosquera, A. M., Muñoz, J. A., & Mediavilla, E. 2009, ApJ, 691, 1292
Mosquera, A. M., Muñoz, J. A., Mediavilla, E., & Kochanek, C. S. 2011, ApJ, 728, 145
Nakos, T., Courbin, F., Poels, J., et al. 2005, A&A, 441, 443
Pereyra, N. A., Vanden Berk, D. E., Turnshek, D. A., et al. 2006, ApJ, 642, 87
Phillips, A. C. 1993, PhD Thesis, University of Washington
Poindexter, S., & Kochanek, C. S. 2010a, ApJ, 712, 668
Poindexter, S., & Kochanek, C. S. 2010b, ApJ, 712, 658
Press, W., Teukolsky, S., Vetterling, W., & Flannery, B. 1992, Numerical Recipes in C, 2nd edn. (Cambridge, UK: Cambridge University Press)
Sørensen, A. N. 2000, Evaluation of the MAT/EEV 44−82 ser. no. 8171-1-1 Ringo, Tech. Rep., IJAF, Copenhagen University Observatory
Wisotzki, L., Becker, T., Christensen, L., et al. 2003, A&A, 408, 455
Wisotzki, L., Christlieb, N., Bade, N., et al. 2000, A&A, 358, 77
Wisotzki, L., Schechter, P. L., Bradt, H. V., Heinmüller, J., & Reimers, D. 2002, A&A, 395, 17

A&A 551, A104 (2013)
DOI: 10.1051/0004-6361/201118755

Astronomy & Astrophysics

Flux and color variations of the doubly imaged quasar UM673⋆,⋆⋆

D. Ricci[1,30,31], A. Elyiv[1,2], F. Finet[1], O. Wertz[1], K. Alsubai[27], T. Anguita[3,4,32], V. Bozza[5,6], P. Browne[7], M. Burgdorf[8,24], S. Calchi Novati[5,9], P. Dodds[7], M. Dominik[7,⋆⋆⋆], S. Dreizler[10], T. Gerner[15], M. Glitrup[11], F. Grundahl[11], S. Hardis[12], K. Harpsøe[12,25], T. C. Hinse[12,13], A. Hornstrup[14], M. Hundertmark[10], U. G. Jørgensen[12,25], N. Kains[7], E. Kerins[26], C. Liebig[7,15], G. Maier[15], L. Mancini[4,5,16], G. Masi[17], M. Mathiasen[12], M. Penny[26], S. Proft[15], S. Rahvar[18,29], G. Scarpetta[5,6], K. Sahu[28], S. Schäfer[10], F. Schönebeck[15], R. Schmidt[15], J. Skottfelt[12], C. Snodgrass[19,20], J. Southworth[21], C. C. Thöne[22,23], J. Wambsganss[15], F. Zimmer[15], M. Zub[15], and J. Surdej[1,⋆⋆⋆⋆]

(Affiliations can be found after the references)

Received 28 December 2011 / Accepted 31 January 2013

ABSTRACT

Aims. With the aim of characterizing the flux and color variations of the multiple components of the gravitationally lensed quasar UM673 as a function of time, we have performed multiepoch and multiband photometric observations with the Danish 1.54 m telescope at the La Silla Observatory.

Methods. The observations were carried out in the *VRi* spectral bands during four seasons (2008–2011). We reduced the data using the point spread function photometric technique as well as aperture photometry.

Results. Our results show for the brightest lensed component some significant decrease in flux between the first two seasons (+0.09/+0.11/+0.05 mag) and a subsequent increase during the following ones (−0.11/−0.11/−0.10 mag) in the $V/R/i$ spectral bands, respectively. Comparing our results with previous studies, we find smaller color variations between these seasons as compared with previous ones. We also separate the contribution of the lensing galaxy from that of the fainter and close lensed component.

Key words. gravitational lensing: strong – quasars: general – techniques: photometric – quasars: individual: UM673

1. Introduction

Multiply imaged quasars are of great interest in astrophysics due to the possibility, from observed flux and color variations between the lensed components, to distinguish between intrinsic quasar variations caused by the accretion mechanism, and microlensing effects induced by stars in the lens galaxy (Wambsganss 2006).

In previous papers (Ricci et al. 2011b,a), we have studied such variations for the quadruply imaged quasar HE 0435-1223, observed in the framework of a *VRi* multiepoch monitoring of five lensed quasars[1], a parallel project of the Microlensing Network for the Detection of Small Terrestrial Exoplanets (MiNDSTEp) campaign (Dominik et al. 2010).

In the current paper, we focus on UM673/Q0142−100 (see Fig. 1), a doubly imaged quasar discovered by Surdej et al. (1987) during a high resolution imaging survey of HLQs (Highly Luminous Quasars) and subsequently studied by our team (Smette et al. 1990, 1992; Daulie et al. 1993; Nakos et al. 2005).

Surdej et al. (1988) reported a separation of 2.22″ between the components "A" (brighter) and "B" (fainter), and found their V magnitudes to be 16.9 and 19.1 respectively, at a redshift $z = 2.719$. The redshift of the sensibly fainter ($R = 19.2$) lensing galaxy, located very close to the "B" component, was derived to be $z = 0.49$, and the time delay between the two lensed components was estimated around 7 weeks.

A photometric monitoring of UM673 was performed during the years 1987–1993 (Daulie et al. 1993), but the photometry did not show any clear evidence for relative variations over the considered period.

In the framework of the CfA Arizona Space Telescope LEns Survey (CASTLES) project, precise astrometry of the components and of the lens galaxy "G" was obtained[2]. The colors of the lens galaxy were found to match those of a passively evolving early-type galaxy at $z \approx 0.5$ (Muñoz et al. 1998).

Lehár et al. (2000, 2002) reported *Hubble* Space Telescope (HST) observations of UM673 at optical and infrared wavelengths, and Sinachopoulos et al. (2001) observed the lensed quasar in the R filter for six seasons (1995–2000), detecting a significant increase by 0.3 mag of the combined system (lensed components) with respect to the values reported at discovery, with a peak of 0.5 mag during the period 1995–1997. Lehár et al. (2000) performed photometric measurements on HST data taken in the R filter, and obtained magnitudes of 16.67, 18.96, and 19.35 for the "A", "B" components and the lens galaxy, respectively.

After spectrophotometric observations performed in 2002 by Wisotzki et al. (2004), which did not show any evidence of microlensing, the first multifilter monitoring of UM673 was carried out by Nakos et al. (2005) between 1998 and 1999, in the Cousins V and Gunn i filters. Analysis of the light curves was made using three different photometric methods: image

⋆ Based on data collected by MiNDSTEp with the Danish 1.54 m telescope at the ESO La Silla Observatory

⋆⋆ Light curves are only available in electronic from at the CDS via anonymous ftp to cdsarc.u-strasbg.fr (130.79.128.5) or via http://cdsarc.u-strasbg.fr/viz-bin/qcat?J/A+A/551/A104

⋆⋆⋆ Royal Society University Research Fellow.

⋆⋆⋆⋆ Also Directeur de Recherche honoraire du FRS-FNRS.

[1] UM673/Q0142-100, HE0435-1223, Q2237+0305, WFI2033-4723 and HE0047-1756.

[2] http://www.cfa.harvard.edu/castles/Individual/Q0142.html

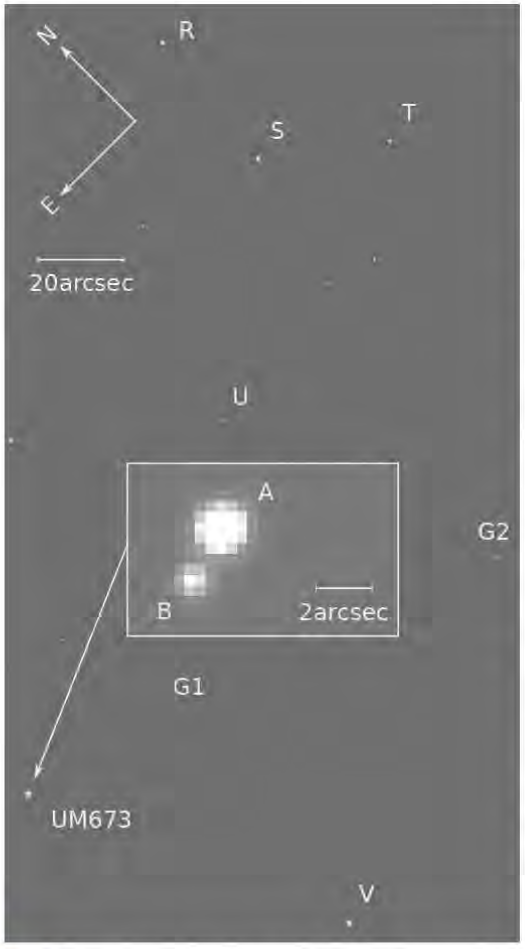

Fig. 1. DFOSC *V* filter image, taken on 2008-08-03, showing the position of UM673 and the stars "R", "S", "T", "U", and "V" used to search for a suitable reference star. The "V" star was finally chosen. "G1" and "G2" are field galaxies. The inset zoom shows the two components "A" and "B" of the lensed quasar.

deconvolution (Magain et al. 2007), point spread function (PSF) fitting, and image subtraction. Nakos et al. (2005) found that component "A" displayed possible evidence for microlensing.

Koptelova et al. (2008, 2010a,b) and Koptelova & Oknyanskij (2010) observed the object in the *VRI* bands and succeeded for the first time in determining a time delay: $150^{+7}_{-18}{}^{+42}_{-36}$ days (at 68% and 95% confidence levels).

Furthermore, Fadely & Keeton (2011) examined the wavelength dependence of the flux ratios for several gravitationally lensed quasars using *K* and *L*′-band images obtained with the Gemini North 8m telescope, detecting no difference between the two flux ratios for the specific case of UM673 ("B"/"A" = 0.128 ± 0.002 in the *K*-band and 0.132 ± 0.006 in the *L*′-band).

Finally, in a recent paper, Koptelova et al. (2012) re-estimated the determination of the time delay to a value of 89 ± 11 days using 2001–2011 VRI observations, and suggested the brightness variations to be mainly due to intrinsic variations of the quasar.

Table 1. Number of CCD images collected for each filter and each year of observation of UM673.

	Images				Nights			
Season	*V*	*R*	*i*	total	*V*	*R*	*i*	total
2008	42	45	43	130	15	15	15	45
2009	34	35	26	95	12	13	9	34
2010	72	78	0	150	23	26	0	49
2011	51	53	9	113	15	16	1	32
total	199	211	78	488	65	70	25	160

Notes. The corresponding number of nights for each filter is also shown.

We present multiepoch photometric monitoring data of UM673 over four seasons (2008–2011), carried out in three filters (*VRi*) with the Danish Faint Object Spectrograph and Camera (DFOSC) instrument of the Danish 1.54 m telescope at the La Silla Observatory.

The observations and the pre-processing of the images are presented in Sect. 2. Section 3 presents the reduction techniques and the results are shown in Sect. 4. Finally, Sect. 5 contains the main conclusions.

2. Observations and pre-processing

We monitored UM673 during four seasons (2008–2011) using the Danish 1.54 m telescope at the La Silla Observatory, equipped with the DFOSC instrument, providing 2147 × 2101 pixel CCD frames over a field of view of 13.7′×13.7′ with a declared resolution of 0.39″/pixel. The RON (read-out-noise) of the CCD camera in high-mode (gain $g = 0.74$ electron/ADU) is 3.1 electrons per pixel. With the exception of the re-aluminization of the primary mirror in 2009, the configuration software/hardware of the telescope did not change over the four seasons of observation. The data were collected in the Bessel *V*, Bessel *R*, and Gunn *i* filters[3].

We obtained a total number of 488 *VRi* images corresponding to 160 nights over the four seasons. The details are given in Table 1.

In 2010, no *i* filter image was taken, as the monitoring was foreseen since the beginning in the only *VR* filters, and the *i* filter images were taken depending on the remaining telescope time with respect to the other MiNDSTEp parallel projects. All the frames were acquired with a 180 s exposure.

We treated the images following the same procedure as those relative to HE 0435-1223 described in a previous paper (Ricci et al. 2011b), with the exception that we used the images already de-biased and flat-fielded *in loco* by the Interactive Data Language (IDL) automatic pipeline used at the Danish Telescope for the daily monitoring of the bulge microlenses.

3. Data reduction

We carefully checked the history of the scale of the images between the various seasons, and we found a constant value of 0.395″/pixel. We froze this angular scale in the data reduction. We also checked the evolution of the position angle

[3] More details are available at http://www.eso.org/lasilla/telescopes/d1p5/misc/dfosc_filters.html

Table 2. Maximum differences of the R filter magnitudes between seasons and in σ units for the stars "R", "S", "T", "U", and "V" in Fig. 1.

Star	Δm_R	$\Delta m_R/\sigma_R$
"R"	0.014	0.67
"S"	0.030	1.29
"T"	0.058	2.69
"U"	0.037	0.84
"V"	0.020	0.90

between the CCD pixel grid and the equatorial coordinate system, finding a change in angle between the seasons: 4.5′ between 2008 and 2009, 5.2′ between 2008 and 2010, and 4.7′ between 2008 and 2011. We took this effect into account in our data reduction.

Finally, we checked the seeing values for all the observations. We decided to fit the "U" star (see Fig. 1) with a two-dimensional Gaussian function, and we found that the R filter images had the best seeing. We then decided to search for a suitable reference star in that filter.

We disregarded all those images for which the two lensed components were unresolved (seeing >2″). Independently we measured the flux ratio between the two bright galaxies "G1" and "G2" (see Fig. 1) using aperture photometry (we integrated a square area of 40×40 pixels centered on each galaxy). In the analysis we only used those images for which this flux ratio was stable, corresponding to a total of 9–18 images per season, depending on the filter.

The reference candidates are the stars "R", "S", "T", "U" and "V" in Fig. 1: we compared the fluxes of these stars with the total flux of the bright galaxies "G1" and "G2" using aperture photometry. For this test we decided to use galaxies because we can be sure of their stability. Table 2 contains the maximum differences of the magnitudes between seasons and in sigma units for the five concerned stars.

On the basis of this analysis, we conclude that star "R" and star "V" are comparably stable. However, star "V" is closer to the lens system, and it is therefore better to use its shape as a reference PSF for the lens fitting. Also, it had been found to be photometrically stable by Sinachopoulos et al. (2001) and Nakos et al. (2003); finally it was already used by Nakos et al. (2005) as a reference for the PSF fitting of UM673.

From all these considerations, we decided to use star "V" as the reference star for the PSF fitting of the lens system. To calibrate the magnitudes in the VRi filters, we used the values of the star "V" provided by Nakos et al. (2003): $m_V = 16.54 \pm 0.01$, $m_R = 16.00 \pm 0.01$, and $m_I = 15.55 \pm 0.01$. Moreover, we calculated the R magnitude of the "G1" and "G2" galaxies with aperture photometry, using "V" as the reference star. We found values of $m_R = 17.47 \pm 0.03$ for "G1", and $m_R = 17.92 \pm 0.05$ for "G2".

We tested if it was possible, on the basis of our data, to measure independently the magnitude of the lens galaxy "G" in each band. We found that the R band images had better quality, and we proceeded using these images. Each image was interpolated with a bicubic spline and every pixel was divided in a grid of 20×20 new sub-pixels. Then we superposed these oversampled images and we summed them up to obtain an oversampled image with a high signal-to-noise ratio (see Fig. 2). We used the "V" reference star as reference PSF. We fitted the gravitational lens system with two PSFs for the "A" and "B" lensed components, fixing their relative astrometry. We then adjusted the scale factors of those two PSFs to retrieve the uncontaminated image of the background lens galaxy. We used aperture photometry to derive its magnitude relatively to the "V" reference star.

To improve the accuracy of the photometry, we added two factors to scale the fluxes of the "A" and "B" lensed components. We varied the factor of the "A" component from 0.94 to 1.1 with a step of 0.0022, and we varied the factor of the "B" component from 0.2 to 1.1 with a step of 0.04.

First we constructed an array of residual maps for these two factor combinations, and for each residual map we calculated the coordinates of the light center of the galaxy "G". As a criterion for the correctness of the obtained galaxy image we chose the distance from its light center to the expected one, provided by the accurate astrometry measurements. The distance between the "B" lensed component and the galaxy "G" provided by HST data is 0.38″, which is ≈20 new sub-pixels. So we assumed that the distance between the obtained and expected light center of "G" should be less than half the distance between the galaxy "G" and the "B" lensed component (<10 new sub-pixels).

We applied the same criterion between the expected and observed position of the maximum of light of the galaxy "G". Indeed, the light center of "G" may be slightly offest from its maximum of light.

We considered that the overlap between the regions where these two conditions are satisfied fixes the region of allowed values for the two scale factors, and the minimum and maximum magnitudes of galaxy "G" which are 19.02 and 19.56, respectively. From that, we then independently calculated the magnitude of the lensing galaxy "G" in the R band as 19.29 ± 0.27. If we calculate this value as an average magnitude over all the allowed values for the two scale factors, we obtain 19.27 ± 0.15. Both these values, within the error bars, are in good agreement with the HST data. An image of the reconstructed galaxy is shown in Fig. 3.

Therefore, in the following analysis we considered the magnitudes of the lens galaxy "G" as being those previously measured with HST. HST results (named $G_{\rm HST}$), obtained using HST filters, were converted to the ground-based photometric system by Lehár et al. (2000) using Holtzman et al. (1995) calibrations. The V, R and i magnitudes that they derived for the galaxy are: $G_V = 20.81 \pm 0.02$, $G_R = 19.35 \pm 0.01$, and $G_I = 18.72 \pm 0.03$.

We applied the PSF fitting technique while accounting for the magnitude of the lens on the best frames previously chosen, by refining the robust method already used in our previous work (Ricci et al. 2011b).

Our method is based on the simultaneous fit of each frame with two PSFs for the "A" and "B" components, and the de Vaucouleurs profile for the lens galaxy "G", fixing the relative astrometry between the components in accordance with measurements from Muñoz et al. (1998). We also fixed the magnitudes of the galaxy "G" to the above mentioned values. For a more accurate fitting, we used a bicubic interpolation of the images.

Koptelova et al. (2010b, 2012) observed UM673 with the VRI filters, and derived the photometry without separately taking into account the magnitude of "B" and that of the lens galaxy "G". As the lens galaxy is located very close to the "B" component, and for comparison with other works, we also calculated the magnitudes of the "B"+"G" components as a simple superposition of their fluxes. Let us label "B+G" the results obtained in this way.

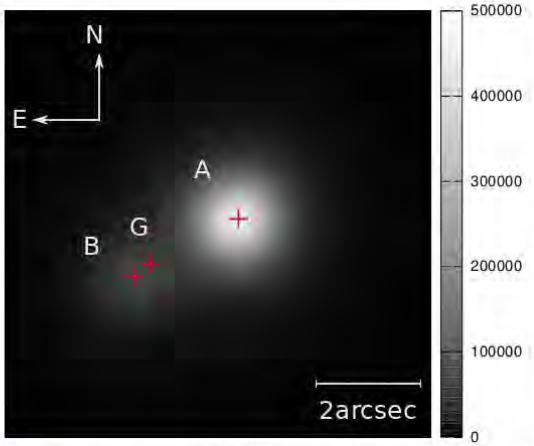

Fig. 2. Composite image of UM673 obtained by superposing the 44 best quality CCD images in the *R* filter, resampled by dividing each pixel in a grid of 20 × 20 subpixels and recentering the images with an accuracy of one new subpixel. The positions of the components, provided by HST, are also shown.

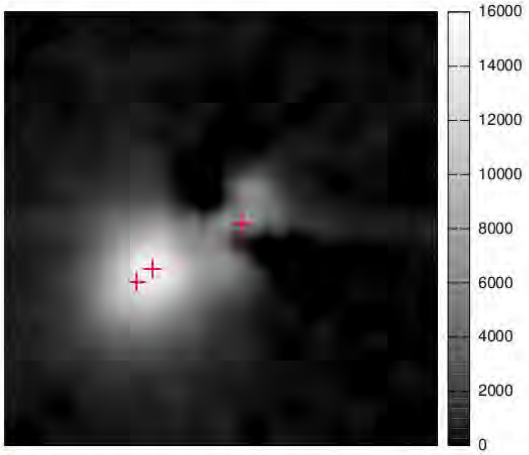

Fig. 3. Reconstructed image of the lens galaxy of UM673. Orientation, pixel scale and marks are the same as those shown in Fig. 2. See the text for the details relative to the reconstruction technique.

4. Results

4.1. Flux variations

The separate light curves of the two lensed components "A" and "B" of UM673 and the "B+G" light curve are shown in Fig. 4.

For a robust measurement of variability, we calculated the average and the standard deviation over each season. Then, we also measured the photometry of the whole system $(A + B + G)_{aperture}$ using aperture photometry. The aperture photometry was calculated using two independent routines: a custom routine set up by our team, and the IRAF `daophot` package. As the results were robust and coherent between each other, we decided to normalize the averaged PSF fitting results to aperture photometry. We then calculated for each year a normalization parameter $k = [(A+B+G)_{aperture} - G_{HST}]/(A_{PSF}+B_{PSF})$, and we corrected all *PSF* magnitudes for k. These averaged results are in agreement with the non normalized results, and are shown in Fig. 5 and in Table 3.

Furthermore, in Table 3 we list the magnitudes of "B+G" as a mere superposition of their fluxes. The contribution due to the galaxy "G" in the total flux of the unresolved component "B+G" is quite important: near 18%, 45% and 52% in the *V*, *R* and *i* bands, respectively.

We see an initial common behavior for the different filters and components: the flux slightly decreases between the 2008 and 2009 seasons, and increases between the 2009 and 2010 seasons. Then, during the 2011 season, the flux of the "A" component keeps increasing, while the "B" component slightly decreases.

In particular, in the *V* filter we notice a decrease in flux by 0.09 mag between the 2008 and 2009 seasons for the "A" component (corresponding to a decrease of 3σ), and an increase in flux by 0.10 mag between the two successive seasons (2009–2011). The flux of the "B" lensed component, as well as of "B+G", slightly decreases in this filter over the four seasons, but not significantly.

Table 3. Average magnitudes for the gravitationally lensed components of UM673 in the *VRi* bands.

Component	Season	*V*	*R*	*i*
A	2008	16.79 ± 0.02	16.48 ± 0.03	16.27 ± 0.03
	2009	16.88 ± 0.04	16.59 ± 0.04	16.32 ± 0.03
	2010	16.84 ± 0.01	16.55 ± 0.02	
	2011	16.77 ± 0.03	16.48 ± 0.03	16.22 ± 0.01
B	2008	19.13 ± 0.06	19.09 ± 0.05	18.80 ± 0.10
	2009	19.20 ± 0.04	19.16 ± 0.05	18.85 ± 0.04
	2010	19.16 ± 0.06	19.10 ± 0.05	
	2011	19.18 ± 0.05	19.22 ± 0.10	18.84 ± 0.06
B+G	2008	18.92 ± 0.07	18.46 ± 0.05	18.01 ± 0.10
	2009	18.98 ± 0.04	18.50 ± 0.05	18.03 ± 0.05
	2010	18.94 ± 0.06	18.47 ± 0.05	
	2011	18.96 ± 0.06	18.53 ± 0.10	18.03 ± 0.07

In the *R* filter the behavior is the same: for the "A" component the flux decreases by 0.11 mag (above 3σ) between the first two seasons and successively increases by 0.11 mag between the 2009 and 2011 seasons. The flux of the "B" lensed component slightly decreases, as well as the flux of "B+G", with a less significant amplitude.

Finally, in the *i* filter we notice less evident trends than detected in the other filters, excepted for the brighter "A" lensed component which presents a smaller decrease in flux between the first two seasons and a further increase by 0.10 mag between 2009 and 2011.

Our results are in good agreement with Koptelova et al. (2012) recent results for the same epochs (see the larger background symbols in Fig. 5). We obtain for the "A" lensed component a magnitude ≈ 0.02–0.08 larger for all the filters. The magnitudes of "B+G" are slightly smaller: within 2σ in the *R* and *i* bands. These differences might derive from using different techniques for PSF fitting and/or setting the photometric zero-points.

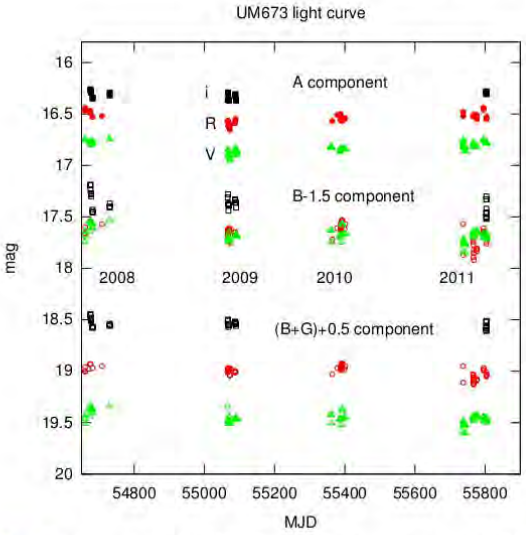

Fig. 4. Light curves in the *VRi* filters of the lensed components "A" and "B" of the gravitationally lensed quasar UM673. The plot also shows the "B+G" values. The "B" and "B+G" light curves have been shifted by −1.5 and 0.5 mag, respectively. Typical errors of individual observations are near 0.02 and 0.05–0.08 mag for the "A" and "B" components, respectively.

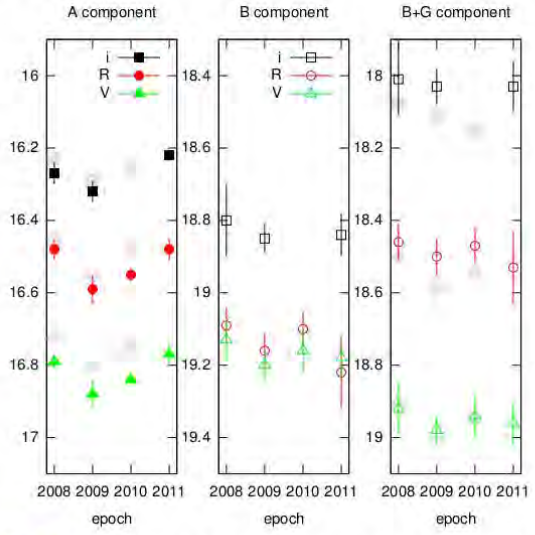

Fig. 5. Average light curves over the four seasons of observation for the two lensed components "A" and "B". The "B+G" average light curve is also shown (see the text for details). The error bars indicate the standard deviation over the epoch. The larger background symbols show recent results independently obtained by Koptelova et al. (2012).

Table 4. Average $R-i$ and $V-R$ color indices for the gravitationally lensed components of UM673.

Component	Season	$R-i$	$V-R$	$V-i$
A	2008	0.21 ± 0.04	0.32 ± 0.04	0.52 ± 0.03
	2009	0.26 ± 0.05	0.29 ± 0.06	0.56 ± 0.05
	2010		0.29 ± 0.02	
	2011	0.26 ± 0.03	0.30 ± 0.04	0.55 ± 0.03
B	2008	0.28 ± 0.11	0.04 ± 0.08	0.32 ± 0.12
	2009	0.32 ± 0.06	0.04 ± 0.06	0.35 ± 0.06
	2010		0.06 ± 0.07	
	2011	0.38 ± 0.11	−0.04 ± 0.11	0.34 ± 0.08
B+G	2008	0.45 ± 0.11	0.46 ± 0.08	0.91 ± 0.12
	2009	0.47 ± 0.07	0.48 ± 0.06	0.95 ± 0.07
	2010		0.48 ± 0.08	
	2011	0.51 ± 0.12	0.43 ± 0.11	0.93 ± 0.09

4.2. Color variations

From the data collected during the 2008, 2009, and 2011 seasons, we were able to build a color-color diagram to search for color variations of the two lensed components and of "B+G" with time. The results are shown in Fig. 6 and in Table 4.

All color variations over each epoch are found to be within the error bars. Our results also show that within these error bars the color indices of the "A" component and of "B+G" are coherent with the work of Koptelova et al. (2010b, 2012) data, and we find small variations with respect to HST data which are relative to 1994.

Moreover, the temporal evolution of the color index between the observations of Koptelova et al. (2010b, 2012) and the current data shows a weak trend indicating that the quasar becomes redder as its flux decreases, as already observed in our multicolor study of the gravitationally lensed quasar HE 0435-1223 (Ricci et al. 2011b).

Galaxy "G" affects quite strongly the color of "B+G". We find a difference of 0.17–0.13 mag between the $R-i$ color index of "B+G" and "B", a difference of 0.42–0.47 mag in $V-R$ and of 0.59–0.60 mag in $V-i$. On the basis of HST data, corresponding differences in colors between the "B+G" and "B" components are 0.17, 0.37 and 0.54 (Lehár et al. 2000). This supports the view that the contribution of galaxy "G" cannot be neglected in any considered band.

Nakos et al. (2005) reduced UM673 data in the V and i filters by using three different techniques: MCS deconvolution, difference imaging, and PSF fitting. The first two techniques allow in principle to get rid of the contribution of "G", while results obtained with PSF fitting are contaminated by the lens galaxy. Despite this, Nakos et al. (2005) results are coherent with each other. We compared their $V-i$ color index obtained by the different methods. Nakos et al. (2005) obtained differences on the $V-i$ color index between "B+G" and the "B" components smaller than 0.04 mag, which is comparable with their photometric errors. This is in contradiction with Lehár et al. (2000) results and our results, which lead to 0.54 and 0.59–0.60 mag, respectively. As it was shown above, the brightness of galaxy "G" cannot be neglected in the V, R or i bands. The contribution of galaxy "G" significantly changes the color of "B+G".

In Fig. 7 we compare the evolution of the $V-i$ color index with time, by using the data collected from HST (Muñoz et al. 1998), Nakos et al. (2005), and Koptelova et al. (2010b). An adaptation of recently published data by Koptelova et al. (2012) is also shown. We find good agreement with their data.

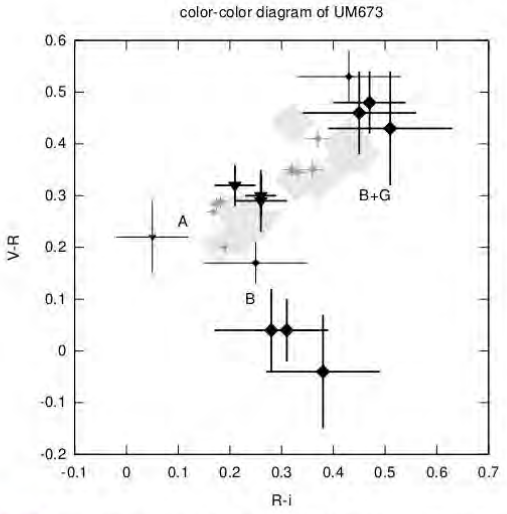

Fig. 6. Color–color diagram for the 2008, 2009 and 2011 seasons (black bold dots) of the two lensed components "A" and "B" of UM673. The "B+G" values are relative to the color indices of the "B" component that includes the contribution of the lens galaxy, as in the approach of Koptelova et al. (2010b). The diagram also includes HST (Muñoz et al. 1998) data (black light points) and Koptelova et al. (2010b) data (little gray points). The larger background symbols refer to the data from Koptelova et al. (2012).

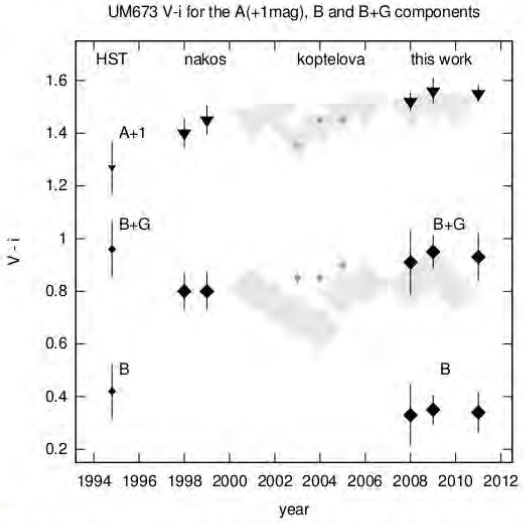

Fig. 7. Evolution of the $V - i$ color index of "A" (triangles), "B" and "B+G" (rhombi) with time, including the data from HST (Muñoz et al. 1998), from Nakos et al. (2005), from Koptelova et al. (2010b) and from the present work. Adaptation of recently published data by Koptelova et al. (2012) is also shown (larger background symbols). The "A" component is shifted by +1 mag.

4.3. "Global *i*" light curve

A "global *i*" light curve which also includes the results of Muñoz et al. (1998), Nakos et al. (2005) and Koptelova et al. (2010b, 2012) is shown in Fig. 8. To construct this figure, first we shifted in time the light curve of "B+G" using the value of the time delay (89 days) provided by Koptelova et al. (2012). Then we calculated for each filter the average 2008 difference in magnitude between the two components, and we corrected the "B+G" light curve for these values. Finally, we corrected the V and R light curves of both components by their average 2008 $V - i$ and $R - i$ color indices, respectively. We chose the 2008 season as a reference only because it represents the beginning of our observations. Figure 8 shows that the flux of the quasar intrinsically varied over the different seasons, with an amplitude of ≈0.6 mag, peak-to-valley over the last two decades.

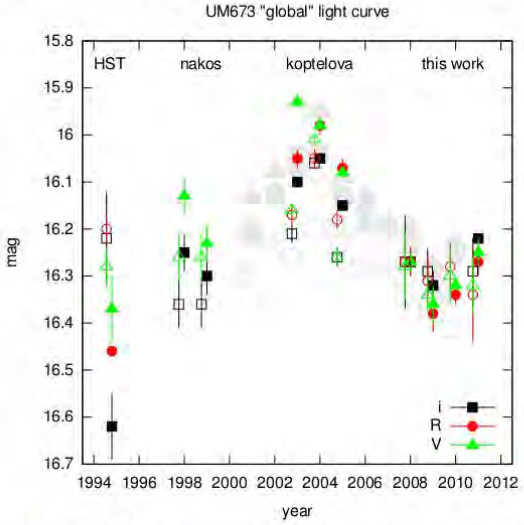

Fig. 8. "Global *i*" light curve of UM673 built by including data from HST (Muñoz et al. 1998), Nakos et al. (2005), Koptelova et al. (2010b) and the present work. An adaptation of recently published data by Koptelova et al. (2012) is also shown (larger background symbols). The technique used to build this curve is explained in detail in Sect. 4.3. In particular, filled and open symbols are used for the "A" and the "B+G" lensed components, respectively.

5. Conclusions

We have presented a photometric monitoring, carried out during four epochs in three different filters, of the doubly imaged quasar UM673.

The results show a significant decrease in flux of the "A" lensed component between the first two seasons (2008–2009), and a smaller increase between the successive three seasons (2009–2011). This behavior is mostly significant in the V and R bands.

Moreover, our observations are in good agreement with the previous works carried out by Muñoz et al. (1998), Koptelova et al. (2010b), and Koptelova et al. (2012) in terms of flux variations and color index. We also separated the contribution of the lens galaxy from the fainter lensed component, showing the effects of this operation on the color index of the latter. We conclude that the contribution of the lens galaxy in the photometry

of UM673 cannot be neglected and we give an independent estimation of the magnitude of the lens galaxy.

Further observations could help in corroborating the separate color variations of the components, and the slight flux trend observed between the seasons.

Acknowledgements. This research was supported by ARC – Action de recherche concertée (Communauté Française de Belgique – Académie Wallonie-Europe). D.R. (boursier FRIA) acknlowledges GLObal Robotic telescopes Intelligent Array for e-Science (GLORIA), a project funded by the European Union Seventh Framework Programme (FP7/2007-2012) under grant agreement number 283783. A.E. is the beneficiary of a fellowship granted by the Belgian Federal Science Policy Office. A.E. is also grateful for partial support in the framework of the NASU Target Program "CosmoMicroPhysics". N.K. received funding from the European Community's Seventh Framework Programme (/FP7/2007-2013/) under grant agreement No 229517. M.D., M.H. and C.L. acknowledge the Qatar Foundation for support from QNRF grant NPRP-09-476-1-078. Operation of the Danish 1.54 m telescope is supported by the Danish National Science Research Council (FNU).

References

Daulie, G., Hainaut, O., Hutsemekers, D., et al. 1993, in Liege International Astrophysical Colloq., 31, eds. J. Surdej, D. Fraipont-Caro, E. Gosset, S. Refsdal, & M. Remy, 181
Dominik, M., Jørgensen, U. G., Rattenbury, N. J., et al. 2010, Astron. Nach., 331, 671
Fadely, R., & Keeton, C. R. 2011, AJ, 141, 101
Holtzman, J. A., Burrows, C. J., Casertano, S., et al. 1995, PASP, 107, 1065
Koptelova, E., & Oknyanskij, V. 2010, The Open Astronomy Journal, 3, 184
Koptelova, E. A., Artamonov, B. P., Bruevich, V. V., Burkhonov, O. A., & Sergeev, A. V. 2008, Astron. Rep., 52, 270
Koptelova, E., Oknyanskij, V., Artamonov, B., & Chen, W. 2010a, Mem. Soc. Astron. It., 81, 138
Koptelova, E., Oknyanskij, V. L., Artamonov, B. P., & Burkhonov, O. 2010b, MNRAS, 401, 2805
Koptelova, E., Chen, W. P., Chiueh, T., et al. 2012, A&A, 544, A51
Lehár, J., Falco, E. E., Kochanek, C. S., et al. 2000, ApJ, 536, 584
Lehár, J., Falco, E. E., Kochanek, C. S., et al. 2002, ApJ, 571, 1021
Magain, P., Courbin, F., Gillon, M., et al. 2007, A&A, 461, 373
Muñoz, J. A., Falco, E. E., Kochanek, C. S., et al. 1998, Ap&SS, 263, 51
Nakos, T., Ofek, E. O., Boumis, P., et al. 2003, A&A, 402, 1157
Nakos, T., Courbin, F., Poels, J., et al. 2005, A&A, 441, 443
Ricci, D., Poels, J., Elyiv, A., et al. 2011a, VizieR Online Data Catalog, J/A+A/528/A42
Ricci, D., Poels, J., Elyiv, A., et al. 2011b, A&A, 528, A42
Sinachopoulos, D., Nakos, T., Boumis, P., et al. 2001, AJ, 122, 1692
Smette, A., Surdej, J., Shaver, P. A., et al. 1990, in Gravitational Lensing, eds. Y. Mellier, B. Fort, & G. Soucail, Lect. Notes Phys. (Berlin: Springer Verlag), 360, 122
Smette, A., Surdej, J., Shaver, P. A., et al. 1992, ApJ, 389, 39
Surdej, J., Magain, P., Swings, J., et al. 1987, Nature, 329, 695
Surdej, J., Magain, P., Swings, J., et al. 1988, A&A, 198, 49
Wambsganss, J. 2006, in Saas-Fee Advanced Course 33: Gravitational Lensing: Strong, Weak and Micro, eds. G. Meylan, P. Jetzer, P. North, et al., 453
Wisotzki, L., Becker, T., Christensen, L., et al. 2004, Astron. Nach., 325, 135

[1] Département d'Astrophysique, Géophysique et Océanographie, Bât. B5C, Sart Tilman, Université de Liège, 4000 Liège 1, Belgium e-mail: ricci@astro.ulg.ac.be
[2] Main Astronomical Observatory, Academy of Sciences of Ukraine, Zabolotnoho 27, 03680 Kyiv, Ukraine
[3] Centro de Astro-Ingeniería, Departamento de Astronomía y Astrofísica, Pontificia Universidad Católica de Chile, Casilla 306, Santiago, Chile
[4] Max-Planck-Institut für Astronomie, Königstuhl 17, 69117 Heidelberg, Germany
[5] Dipartimento di Fisica "E.R. Caianiello", Università degli Studi di Salerno, via Ponte Don Melillo, 84085 Fisciano (SA), Italy
[6] Instituto Nazionale di Fisica Nucleare, Sezione di Napoli, Italy
[7] SUPA, University of St Andrews, School of Physics & Astronomy, North Haugh, St Andrews, KY16 9SS, UK
[8] Deutsches SOFIA Institut, Universitaet Stuttgart, Pfaffenwaldring 31, 70569 Stuttgart, Germany
[9] Istituto Internazionale per gli Alti Studi Scientifici (IIASS), Vietri Sul Mare (SA), Italy
[10] Institut für Astrophysik, Georg-August-Universität Göttingen, Friedrich-Hund-Platz 1, 37077 Göttingen, Germany
[11] Department of Physics & Astronomy, Aarhus University, Ny Munkegade, 8000 Aarhus C, Denmark
[12] Niels Bohr Institute, University of Copenhagen, Juliane Maries vej 30, 2100 Copenhagen Ø, Denmark
[13] KASI – Korea Astronomy and Space Science Institute, 776 Daedukdae-ro, Yuseong-gu, Daejeon 305-348, Republic of Korea
[14] National Space Institute, Technical University of Denmark, 2800 Lyngby, Denmark
[15] Astronomisches Rechen-Institut, Zentrum für Astronomie, Universität Heidelberg, Mönchhofstraße 12–14, 69120 Heidelberg, Germany
[16] Dipartimento di Ingegneria, Università del Sannio, Corso Garibaldi 107, 82100 Benevento, Italy
[17] Bellatrix Astronomical Observatory, Center for Backyard Astrophysics, Ceccano (FR), Italy
[18] Physics Department, Sharif University of Technology, Tehran, Iran
[19] European Southern Observatory, Casilla 19001, Santiago 19, Chile
[20] Max Planck Institute for Solar System Research, Max-Planck-Str. 2, 37191 Katlenburg-Lindau, Germany
[21] Astrophysics Group, Keele University, Newcastle-under Lyme, ST5 5BG, UK
[22] Dark Cosmology Centre, Niels Bohr Institute, University of Copenhagen, Juliane Maries Vej 30, 2100 Copenhagen, Denmark
[23] INAF, Osservatorio Astronomico di Brera, 23807 Merate, Italy
[24] SOFIA Science Center, NASA Ames Research Center, Mail Stop N211-3, Moffett Field CA 94035, USA
[25] Centre for Star and Planet Formation, Geological Museum, Øster Voldgade 5, 1350 Copenhagen, Denmark.
[26] Jodrell Bank Centre for Astrophyics, University of Manchester, UK
[27] Alsubai's Establishment for Scientific Studies, Qatar
[28] Space Telescope Science Institute (STScI), USA
[29] Perimeter Institute for Theoretical Physics, 31 Caroline Street North, Waterloo, Ontario N2L 2Y5, Canada
[30] INAF/Istituto di Astrofisica Spaziale e Fisica Cosmica, Bologna, via Gobetti 101, 40129 Bologna, Italy
[31] Instituto de Astronomía, Universidad Nacional Autónoma de México, Apdo. Postal 877, Ensenada, B.C. 22800, Mexico
[32] Departamento de Ciencias Físicas, Universidad Andrés Bello, Av. República 252, Santiago, Chile

3.4 Висновки до розділу 3

Було проведено аналіз двоточкової кореляційної функції вибірки точкових джерел поля XMM-LSS (11 кв. град) зі 94 спостережуваних полів XMM-Newton (d=30’), що містять понад п’ять тисяч точкових джерел у м’якому (0.5–2 кеВ) та жорсткому (2–10 кеВ) діапазонах із ефективною експозицією від 8.1 до 47.3 кс. Для визначення ймовірностей виявлення кожного джерела та для правильного створення рандомізованого каталогу ми виконали серію чисельних моделювань методом Монте-Карло кожного зі спостережуваних полів (полів зору) XMM-Newton. У такий спосіб ми створили об’єднане поле всіх 94 полів, використовуючи метод Вороного для їхнього розмежування.

Було знайдено, що амплітуда двоточкової кореляційної функції значно більша у жорсткому діапазоні, ніж у м’якому. Показано, що АЯГ з жорстким рентгенівським спектром (здебільшого АЯГ 2 типу) більш кластеризовані, ніж ті, що мають м'який спектр (АЯГ 1 типу). Це може означати, що два основних типи АЯГ перебувають в різних середовищах, а саме АЯГ з м'яким рентгенівським спектром тяжіють до більш розріджених областей Всесвіту, якими є межі космічних войдів.

За амплітудами кореляційних функцій було визначено байєс-фактор ~2.5 для медіанного червоного зміщення 1.1 (при перетворенні у 3D) для м’якого діапазону та ~3.3 для жорсткого діапазону при z = 1. Ці значення байєсу відповідають масі материнського гало АЯГ $M_{\rm h} \sim 10^{13 \pm 0.3}\,{\rm h}^{-1}\,M_{\odot}$ для м’якого діапазону і $M_{\rm h} \sim 10^{13.7 \pm 0.3}\,{\rm h}^{-1}\,M_{\odot}$ для жорсткого.

Досліджувалися властивості близького (<0.4–1 Мпк) та далекого (> 1 Мпк) оточення АЯГ у XMM-LSS полі та південному полі XXL до z = 1. Результати, отримані для двох полів, свідчать, що АЯГ обох типів можуть знаходитися як

у щильному, так і у розрідженому оточенні. Однак, зі значимістю ~ 3σ, для поля XMM–LSS було знайдено, що значна частина АЯГ 2 типу знаходяться у більш населеному оточенні, ніж АЯГ першого типу. Далеке оточення знаходилося, порівнюючи відстані між парами АЯГ різних типів, а близьке оточення – серед оптичних галактик у проекції на небесну сферу. Було знайдено, що рентгенвські АЯГ, що мають також радіо ототожнення, є більш затьмареними (жорсткими у рентгені), ніж джерела, що не випромінюють в радіо діапазоні. Ніякої значної різниці в великомасштабному оточенні різних типів АЯГ (1 та 2 типів, радіо і не радіо об'єктами, світними і тм'яними) знайдено не було. Однак, було підтверджено, що АЯГ здебільшого розташовані у локальних надлишках густини, порівняно з рентгенівськими галактиками. Такі результати підтверджують універсальну схему АЯГ, але не виключають, що оточення може мати вплив на еволюцію АЯГ, оскільки дослідження найближчого оточення є проблематичним.

Використовуючи ієрархічний метод кластеризації, було знайдено агломерати АЯГ кількістю більшою 2 членів. Ці агломерати було скорелювано з положеннями рентгенівських скупчень галактик. Було продемонстровано, що більшість цих агломератів розташовані у безпосередній близькості до скупчень галактик <25–45 Мпк. Ці результати можно інтерпретувати так, що рентгенівські АЯГ здебільшого розташовані у філаментах надскупчень, але вони також можуть бути знайдені в оточенні з великою та малою густиною населення.

Було розраховано очікувані статистичні властивості для виявлення оптичних ототожнень множинних зображень квазарів з ренгенівсього огдяду XXL. Моделювання профілів мас лінзуючих об'єктів було проведено з моделями SIS (сферичний розподіл маси за законом r^{-2}) та SIE (одиночний ізотермічний еліпсоїд). Серед рентгенівських об'єктів в діапазоні [0.5–2] кеВ

з потоком більше, ніж 3.0×10^{-15} ерг $см^{-2}$ $с^{-1}$ та оптичними ототожнення яскравіше за r = 25 mag, очікується існування ∼20 гравітаційно-лінзових квазарів з більше, ніж двома, зображеннями.

Візуальний перегляд оптичних *g, r* та *i* зображень 5500 рентгенівських АЯГ, розташованих на 11 кв. градусах огляду XMM-LSS, дозволив виділити 18 кандидатів в гравітаційні лінзи з видимою величиною r<22.5 mag. Додаткові тести на колір-колір діаграмах залишили у вибірці 3 найкращі кандидати у гравітаційні лінзи: J021511.4−034306, J022234.3−031616 і J022607.0−040301, пари точкових джерел яких мають подібні кольори. Було використано фотометричну апроксимацію кратних зображень за допомогою відомої функції розсіювання точки. Спостереження цих кандидатів з вищою кутовою роздільністю є перспективним для виявлення ефекту сильного гравітаційного лінзування.

Було оброблено результати спотережень датського 1.54-метрового телескопа гравітаційно лінзових систем HE0435-1223, UM673, H1413+117, WFI 2033-4723 і HE 0047-1756. Було детектовано варіації кольору, що вказують на ефекти мікролізування, а для деяких систем було оцінено величину потоку від лінзованих галактик.

Розділ 4. ВИСОКОЕНЕРГЕТИЧНІ ПРОЦЕСИ В ВОЙДАХ

Величина та походження магнітного поля у войдах є важливими для розуміння еволюції Всесвіту [61, 62]. До недавнього часу войди розглядали як абсолютно порожні регіони великомасштабної структури Всесвіту. Такі регіони утворюються як наслідок початковій флуктуації поля густини матерії в місцях з густиною значно меншою за середню. Спектроскопічні спостереження та чисельні моделювання розвитку Всесвіту показують, що войди мають складну форму від сфер, еліпсоїдів, опуклих многогранників до складної піноподібної фрактальної структури. На околицях войдів розміщенні так звані стіни, їхні розміри коливаються від кількох до сотень Мпк [63, 64, 65]. Малочисельні, як правило карликові, галактики у войдах еволюціонують повільно і не відзначаються особливою активністю.

Існують два сценарії походження магнітного поля у войдах. Перший включає астрофізичні процеси руху плазми та утворення магнітного поля у відносно локальній області. Зореутворення в малочисельних галактиках войдів викликає певний потік космічних променів від спалахів наднових, прискорення космічних променів в оболонках залишків наднових. Динамо механізм цих космічних променів призводить до посилення галактичного магнітного поля. Галактичний вітер, підсилений космічними променями, може досягати високих швидкостей, покидати галактичне гало та проникати відповідно у міжгалактичний простір космічної порожнини. Разом з космічними променями переноситься енергія магнітного поля в об’єм войду. Чисельні моделювання показують, що такий механізм може підтримувати індукцію магнітного поля у войдах аж до 10^{-15} Гс з високим ступенем невизначеності, для порівняння магнітне поле в галактиках та скупченнях становить порядку 10^{-6} Гс [62, 66].

Іншим кандидатом на механізм генерації магнітного поля у войдах є космологічні процеси генерації магнітних полів, що поширюються у ранньому Всесвіті. Таке магнітне поле при космологічному розширенні Всесвіту розчиняється у порожнинах і може слугувати зародковим для магнітного поля в галактиках і скупченнях галактик, якщо його напруженість є достатньо сильною. Сценарій первинного магнітного поля природно пояснює ієрархію магнітного поля в галактиках і войдах, тому що адіабатичне стиснення та динамо механізм можуть підсилювати магнітне поле в скупченнях та галактиках. Відповідно магнітне поле у войдах зменшується через їх космічне розширення [67].

Загальноприйнято, що чорні діри перебувають в центрі галактик та генерують струмені заряджених частинок, які можуть транспортувати магнітне поле в міжгалактичне поле. У випадку надмасивної чорної діри в радіогалактиках таке транспортування може відбуватися на відстані кількох Мпк. Проти малі маси галактик та відсутність помітної активності АЯГ у войдах роблять такий сценарій малоймовірним. Проте карликові галактики можуть містити чорні діри проміжних мас, де присутність струменів на масштабі парсек або кілопарсек можуть мати місце. На додаток, високо магнетизовані струмені АЯГ на границях порожнин можуть проникати в основний об'єм та робити свій внесок у магнетизацію [68].

Різні моделі передбачають дуже різні величини магнітних полів у войдах від $\leq 10^{-20}$ Гс аж до $\approx 10^{-9}$ Гс. Спостережувана границя на магнітні поля у войдах $< 10^{-9}$ Гс, яка обговорюється на сьогоднішній день, випливає зі спостережень ефекту Фарадея для емісійних ліній від далеких квазарів. Подібне обмеження накладається зі спостереження мікрохвильового фону.

4.1. Електромагнітні лавини від блазарів та вимірювання магнітного поля в войдах

У роботі здобувача [6] проаналізована можливість вимірювання магнітного поля у войдах, виходячи зі спостережень вторинного випромінювання від електромагнітних лавин, що проходять крізь них. Розглянуто поширення в космічних войдах електромагнітних каскадів, викликаних високоенергетичними гамма-променями від малочисельного підкласу АЯГ – блазарів. Особливістю блазарів є спрямований майже на спостерігача релятивістський джет, який генерує в космічний простір високоенергетичні 10 – 300 ТеВ гамма-промені. Ті, в свою чергу, взаємодіють із інфрачервоним фоном і розпадаються на заряджені електрон-протонні пари, які відхиляються в міжгалактичному магнітному полі та взаємодіють з мікрохвильовим фоном, генеруючи вторинні гамма-промені нижчих енергій (інверс-Комптон реакція). Вторинні гамма промені на енергіях 0.1–10 ТеВ можуть знову генерувати нові електрон-позитронні пари, або безпосередньо спостерігатися черенковськими телескопами. Оскільки магнітне поле в скупченнях галактик та філаментах великомасштабної структури досить високе, тому електрон-позитронні пари там заплутуються, і вторинні гамма-промені ізотропно розсіюються.

Саме в космічних войдах, де напруженість магнітного поля на порядки нижча ніж в скупченнях, електромагнітна лавина розвивається вздовж напрямку руху первинного гамма-фотона та може бути виявлена зі спостережень по гало в гамма-діапазоні. Інтегральний потік гало залежить від того, яка частка об’єму на промені зору заповнена магнітним полем напруженості B, іншими словами, від фактору заповненості ν(B) войдами між блазаром та спостерігачем. З другого боку, на промені зору можуть знаходитися інші

елементи великомасштабної структури, такі як скупчення та філаменти з магнітним полем на порядки вище, ніж у войдах. Значне відхилення чи навіть заплутування електронів та позитронів в частинах лавини, яка проходить через великомасштабні структури, може спричинити пригнічення потоку вторинної лавини в напрямку на спостерігача на фактор $v(B)^{1/3}$.

У роботі [6] також вивчено параметри черенковських телескопів, які зможуть зареєструвати магнітні поля різної величини, а також промодельовано лавину методом Монте-Карло на рівні індивідуальних частинок, використовуючи перерізи реакцій: взаємодії гамма фотонів високих енергій з інфрачервоними фотонами, утворення електропозитивних пар та інверс-Комптон реакції взаємодії електронів та позитронів з мікрохвильовим випромінюванням та генерації вторинних гамма-фотонів. Побудовано детальний профіль лавини, зображення протяжного гало навколо блазарів в гамма діапазоні для різних магнітних полів, для блазарів на різних відстанях від спостерігача. Значний прогрес у розумінні явища блазарів було досягнуто з початком спостережень телескопа Фермі. Комбінування даних Фермі в енергетичній смузі 0.1–10 ГеВ і з даними наземних гамма-телескопів, таких як HESS, MAGIC і VERITAS в діапазоні 100 ГеВ–10 ТеВ забезпечує вивчення детального спектру блазарів [60]. Гамма-промені ТеВ-их енергій, що поглинаються на шляху від первинного джерела, ініціюють електромагнітні каскади в міжгалактичному просторі. Електрон-позитронна компонента електромагнітного каскаду відхиляється позагалактичним магнітним полем. У роботі [7] обговорюються спектральні, часові та морфологічні властивості релятивістських каскадів у джетах блазарів у діапазоні 0.1–1 ГеВ. Дослідження базується на двох незалежних чисельних моделюваннях індукованих γ-променями електромагнітних каскадів у міжгалактичний простір, введений у статтях [61] та [6].

PHYSICAL REVIEW D 80, 023010 (2009)

Gamma-ray induced cascades and magnetic fields in the intergalactic medium

A. Elyiv
Main Astronomical Observatory National Academy of Sciences of Ukraine, 27 Akademika Zabolotnoho Street 03680 Kyiv, Ukraine

A. Neronov
ISDC Data Center for Astrophysics, Chemin d'Ecogia 16, 1290 Versoix, Switzerland and Geneva Observatory, 51 Chemin des Maillettes, CH-1290 Sauverny, Switzerland

D. V. Semikoz
APC, 10 rue Alice Domon et Leonie Duquet, F-75205 Paris Cedex 13, France and Institute for Nuclear Research RAS, 60th October Anniversary Prospect 7a, Moscow, 117312, Russia
(Received 24 March 2009; published 22 July 2009)

We present the results of Monte Carlo simulations of three-dimensional electromagnetic cascade initiated by interactions of the multi-TeV γ rays with the cosmological infrared/optical photon background in the intergalactic medium. Secondary electrons in the cascade are deflected by the intergalactic magnetic fields before they scatter on CMB photons. This leads to extended 0.1°–10° scale emission at multi-GeV and TeV energies around extragalactic sources of very high-energy γ rays. The morphology of the extended emission depends, in general, on the properties of magnetic fields in the intergalactic medium. Using Monte Carlo simulated data sets, we demonstrate that the decrease of the size of extended source with the increase of energy allows to measure weak magnetic fields with magnitudes in the range from $\lesssim 10^{-16}$ G to 10^{-12} G if they exist in the voids of the large scale structure.

DOI: 10.1103/PhysRevD.80.023010 PACS numbers: 95.85.Pw, 98.62.En, 98.80.Es

I. INTRODUCTION

Spectral and timing properties of astronomical sources of very high-energy γ rays could be strongly affected by the development of electromagnetic cascades on the way from the source to the Earth. These cascades could be initiated by interactions of the γ rays with the ambient radiation fields inside the γ-ray source, in the source host galaxy and in the Milky Way galaxy, as well as with cosmological photon fields in the intergalactic space. The ubiquity of particle cascades has twofold consequences. On one, pessimistic, side, they complicate the interpretation of the observational data in the very high-energy (VHE, 0.1–10 TeV) γ-ray band. On the other, optimistic, side, with enough spectral and angular resolution, one can quantify the influence of the cascade on the observed source signal and not only reconstruct the spectrum of the primary γ-ray source, but also use the information about properties of the cascade to study the physical characteristics of the medium in which the cascade has developed.

An illustration of such possibility is given by the observations of the effect of absorption of VHE γ rays on the extragalactic background light (EBL). Observations of this effect in the spectra of distant blazars are now routinely used to constrain the EBL spectrum and, in this way, the models of cosmological evolution of galaxies and stellar populations (see [1] for a recent review).

In the derivation of the constraints on the EBL from the observations of absorption of VHE γ-ray flux from distant blazars one usually adopts an assumption that secondary emission from the e^+e^- pairs, deposited in the intergalactic space by the absorbed γ rays, is not detectable. This assumption is valid if the trajectories of the secondary pairs are significantly deflected by the magnetic fields during their radiative cooling. This is true if the strength of the extragalactic magnetic fields (EGMF) is higher than $\sim 10^{-12}$ G [2–4].

However, the strength of EGMF is not measured (see [5] for a review of measurements of cosmic magnetic fields), so that there is no direct way to check the validity of the assumption of the nondetection of the cascade emission. It is also not possible to constrain the values of EGMF from the cosmological models of the origin of magnetic fields in the Universe.

The problem of the origin of 1–10 μG magnetic fields in galaxies and galaxy clusters is one of the long-standing problems of astrophysics/cosmology (see [6–8] for reviews). On the galaxy scales, such fields are thought to be produced via dynamo mechanism [9,10] from "seed" primordial fields of unknown origin. Recent observations of the presence of strong, ~ 10 μG, magnetic fields in the high-redshift galaxies [11,12] point to the fact that the dynamo mechanism is extremely efficient and/or the seed magnetic fields are quite strong so that the 10 μG magnetic fields are generated already at large redshifts.

The dynamo mechanism could work also on the scales of galaxy clusters [13], although the seed magnetic fields would be amplified by a much smaller factor in this case. The fact that the observed strength of magnetic field in galaxy clusters is comparable to that of the individual

galaxies [14] implies that the seed fields in the galaxy clusters should be orders of magnitude higher than the seed magnetic fields for the galactic dynamos. Recent simulations show that such stronger seed magnetic fields could be produced via magnetized winds from the cluster galaxies [15,16].

The origin of the seed magnetic fields for the galactic dynamos is largely uncertain. All the models of production of such seed fields invoke the difference of mobility of electrons and protons, which results in production of electric currents and of the "battery-like" effects at different stages of cosmological evolution, from the phase transitions in the early Universe, to the formation of first galaxies [7,8]. A common feature of all the theoretical models is a prediction that a larger or smaller fraction of the space outside galaxies, galaxy clusters, and filaments of the large scale structure has to be filled with a very weak magnetic field, with the strength approaching that of the primordial seed fields. Depending on the model, the predictions of the typical strength of the EGMF in the voids of the large scale structure range from $\lesssim 10^{-20}$ G up to $\sim 10^{-9}$ G (see e.g. [7,8,17–19]). A moderate observational limit on the present day strength of EGMF $B < 10^{-9}$ G comes from the limit on rotation measure of emission from distant quasars [7]. A similar restriction comes from the analysis of anisotropies of the cosmic microwave background [20,21].

Gamma-ray observations could, in principle, be used to constrain properties of the EGMF using the imaging [3] and/or timing [22,23] of the γ-ray signal. The idea is to observe or, at least, constrain the properties of the inverse Compton (IC) emission produced by the e^+e^- pairs deposited by the absorbed γ rays in the intergalactic space. If the EGMF strength is below 10^{-12} G (plausible assumption, in the view of the cosmological models of the origin of magnetic fields), one expects that the deflections of the secondary electrons and positrons by EGMF should result in the appearance of an EGMF-dependent extended emission around initially point sources and/or in an EGMF-dependent time delay of the emission from the secondary pairs. If the EGMF is stronger than 10^{-12} G, VHE γ-ray observations still can be used to derive a *lower* limit on the EGMF strength, because strong EGMF $\gg 10^{-12}$ G can still be revealed via the extended emission around VHE sources [2] with properties not directly dependent on the EGMF structure.

In what follows we explore the possibility to measure the EGMF using the data of VHE γ-ray observations of extragalactic sources. In the Sec. II we extend ideas of Ref. [3] on the developent of electromagnetic cascade in the intergalactic medium and find the range of EGMF strengths which lead to observable extended emission around extragalactic γ-ray point sources at GeV and TeV energies. In Sec. III we model the development of the γ-ray induced cascades in the intergalactic medium via Monte Carlo simulations. This allows us to simulate the cascade-induced extended emission around point γ-ray sources and to study the dependence of the properties of this extended emission on the strength of EGMF. Using the simulated data sets, we demonstrate that the assumed strength of EGMF can be calculated from the measurement of the energy dependence of the size of the extended emission. We summarize our results in Sec. IV.

II. ELECTROMAGNETIC CASCADE IN INTERGALACTIC MEDIUM

Multi-TeV γ rays emitted by distant point sources are not able to propagate over large distances because of the absorption in interactions with EBL. The pair production on EBL reduces the flux of γ rays from the source by

$$F(E_{\gamma_0}) = F_0(E_{\gamma_0}) \exp[-\tau(E_{\gamma_0}, z)], \quad (1)$$

where $F(E_{\gamma_0})$ is the detected spectrum, $F_0(E_{\gamma_0})$ is the initial spectrum of the source, and $\tau(E_{\gamma_0}, z)$ is the optical depth with respect to the pair production on EBL, which is a function of the primary photon energy E_{γ_0} and of the redshift of the source z.

The e^+e^- pairs of the energy E_e produced in interactions of multi-TeV γ rays with EBL photons produce secondary γ rays via IC scattering of the cosmic microwave background (CMB) photons to the energies

$$E_\gamma \simeq \epsilon_{\rm CMB} \frac{E_e^2}{m_e^2} \simeq 6 \left[\frac{E_{\gamma_0}}{100\ {\rm TeV}}\right]^2 {\rm TeV}, \quad (2)$$

where $\epsilon_{\rm CMB} = 6 \times 10^{-4}$ eV is the typical energy of CMB photons. In the above equation we have assumed that the energy of the primary γ ray is $E_{\gamma_0} \simeq 2E_e$. Upscattering of the infrared/optical background photons gives a subdominant contribution to the IC scattering spectrum because the energy density of the CMB is much higher than the density of the infrared/optical background.

Deflections of e^+e^- pairs produced by the γ rays, which were initially emitted slightly away from the observer, could lead to "redirection" of the secondary cascade photons toward the observer. This effect leads to the appearance of extended emission around a point source of γ rays.

The cascade electrons lose their energy via IC scattering of the CMB photons within the distance

$$D_e = \frac{3m_e^2c^3}{4\sigma_T U_{\rm CMB} E} \simeq 2.2 \times 10^{22} \left[\frac{E_e}{50\ {\rm TeV}}\right]^{-1} {\rm cm}. \quad (3)$$

Comparing this to the Larmor radius in the magnetic field B,

$$R_L = \frac{E_e}{eB} \simeq 1.7 \times 10^{24} \left[\frac{B}{10^{-13}\ {\rm G}}\right]^{-1} \left[\frac{E_e}{50\ {\rm TeV}}\right] {\rm cm} \quad (4)$$

one can find the typical deflection angle of the cascade photons

$$\Delta = \frac{D_e}{R_L} \simeq 0.7^a \left[\frac{B}{10^{-13}\ \mathrm{G}}\right]\left[\frac{E_e}{50\ \mathrm{TeV}}\right]^{-2}. \quad (5)$$

A simple geometrical calculation [3] shows that the bulk of the IC upscattered cascade γ rays of the energy E_γ arrives within an angle

$$\Theta_{\rm ext} = \frac{D_{\gamma_0}}{D}\Delta \simeq \frac{0.7^\circ}{\tau(E_{\gamma_0}, z)}\left[\frac{E_\gamma}{6\ \mathrm{TeV}}\right]^{-1}\left[\frac{B}{10^{-13}\ \mathrm{G}}\right]. \quad (6)$$

where D is the distance to the source and D_{γ_0} is the mean free path of the primary γ rays. The above expression is valid for $\tau(E_{\gamma_0}, z) > 1$. If the extension of the cascade-induced "glow" around the initial point source is determined by the deflections of the cascade electrons by the EGMF, the extension of the glow, $\Theta_{\rm ext}$ is expected to shrink inversely proportional to the γ-ray energy.

In the above calculations we have assumed that the correlation length of the EGMF, λ_B, is much larger than D_e. In an opposite situation, $D_e \gg \lambda_B$, electrons propagate through many regions with different field orientation during their cooling time. The deflections of electrons by the randomly oriented magnetic fields in different regions could be described as diffusion in angle Δ, with the scattering length equal to the coherence scale of the magnetic field, λ_B. In this case, Δ is estimated as

$$\Delta = \frac{\sqrt{D_e \lambda_B}}{R_L} \simeq 0.3^\circ \left[\frac{E_e}{50\ \mathrm{TeV}}\right]^{-3/2}\left[\frac{B}{10^{-13}\ \mathrm{G}}\right]\left[\frac{\lambda_B}{1\ \mathrm{kpc}}\right]^{1/2}. \quad (7)$$

Smaller deflections of electrons result in a smaller size of the extended source

$$\Theta_{\rm ext} \simeq \frac{0.3^\circ}{\tau(E_{\gamma_0}, z)}\left[\frac{E_\gamma}{6\ \mathrm{TeV}}\right]^{-3/4}\left[\frac{B}{10^{-13}\ \mathrm{G}}\right]\left[\frac{\lambda_B}{1\ \mathrm{kpc}}\right]^{1/2}. \quad (8)$$

If $\tau(E_{\gamma_0}, z) > 1$, most of the power of the primary photon beam at the energy E_{γ_0} is transferred to the power of electromagnetic cascade, so that the total flux of the extended source is of the order of the primary source flux at the energy E_{γ_0}. The extended source flux at a given energy E_γ is further modified by the absorption on the way toward the Earth, so that the resulting flux of the extended source at the energy E_γ is $F_{\rm ext}(E_\gamma, \Theta_{\rm ext}) \simeq (e^{\tau(E_{\gamma_0}, z)} - 1)e^{-\tau(E_\gamma, z)}F(E_{\gamma_0})$, where $F(E_{\gamma_0})$ is the observed point source flux at the energy E_{γ_0}.

The above estimate of the flux of the extended source is obtained under the assumption that the magnetic field of the strength B fills most of the intergalactic medium between the source and observer on the Earth. On the other hand, the line of sight can be intersected by the elements of the large scale structure, in which the magnetic field is much stronger than the typical EGMF. Strong deflections of electrons in the parts of the cascade traversing the large scale structure could lead to the suppression of the secondary cascade flux in the direction of the observer. To take into account this effect, it is convenient to introduce the "volume filling factor," $\mathcal{V}(B)$, of the field of particular strength B. The fraction of the path along the line of sight, occupied by the field of the strength B is $[\mathcal{V}(B)]^{1/3}$ and the

$$F_{\rm ext}(E_\gamma, \Theta_{\rm ext}) \simeq [\mathcal{V}(B)]^{1/3}\frac{(e^{\tau(E_{\gamma_0}, z)} - 1)}{e^{\tau(E_\gamma, z)}}F(E_{\gamma_0}). \quad (9)$$

Combining Eqs. (6) and (9), one can see that a measurement of the total flux and of the energy-dependent size of the cascade emission around an extragalactic point source enables to extract the information about the parameters of extragalactic magnetic field, B, $\mathcal{V}(B)$, along the line of sight.

It is easier to detect an extended emission around a given point source if the angular size of the extended source is not too large. The energy of the detected γ rays, E_γ, and the EGMF, B, enter in Eq. (6) for the source size through a combination E_γ/B. This means that stronger magnetic fields could be measured by the instruments sensitive at higher energies. At the highest energies, the sensitivity of a telescope is determined mostly by the effective collection area $A_{\rm eff}(E_\gamma)$. Let us consider, as a reference, a source at the redshift $z \simeq 0.03$, producing a flux $F(E_{\gamma_0}) \sim 10^{-12}$ erg/cm^2 s. If $E_{\gamma_0} \sim 100$ TeV, the optical depth $\tau(E_{\gamma_0}, z) \sim 10$, so that all the primary γ-ray power is transferred to the extended source emission at the energy $E_\gamma \simeq 6$ TeV. The statistics of the extended emission signal is

$$N_\gamma \simeq 2 \times 10^3\left[\frac{F(E_{\gamma_0})}{10^{-12}\ \mathrm{erg/cm^2\,s}}\right]\left[\frac{A_{\rm eff}(E_\gamma)}{10\ \mathrm{km^2}}\right] \times \left[\frac{T_{\rm exp}}{50\ \mathrm{hr}}\right]\left[\frac{E_\gamma}{6\ \mathrm{TeV}}\right]^{-1}. \quad (10)$$

The statistics sufficient for the extended source analysis is thus achieved within the exposure time $T_{\rm exp} \sim 50$ hr (typical for the current generation ground-based γ-ray telescopes) with a telescope with an effective area $A_{\rm eff} \sim 10$ km^2. Such an effective area is achievable with the planned next-generation Cherenkov telescope array, optimized for the observations in the 10 TeV energy band [24]. Otherwise, a comparable signal statistics is achievable with a much smaller collection area, $A_{\rm eff} \sim 0.1$ km^2, provided that the exposure time is $T_{\rm exp} \sim 1$ yr. This is achievable with the next-generation HAWC water Cherenkov telescope [25].

Extremely weak magnetic fields $B \leq 10^{-16}$ G could be detectable through the degree-scale extended emission in the GeV, rather than TeV energy band, see Eq. (6). The primary photons which lead to the production of extended emission in the GeV band have energies $E_{\gamma_0} \sim 1$–3 TeV, see Eq. (2). The mean free path of such photons is much larger than that of the $\sim$100 TeV photons, so that detectable extended emission is expected around distant ($z \gg 0.1$), rather than nearby, sources in this case. Even smaller

fields can be probed with timing analysis of the observed signal, as was discussed in Ref. [23].

The extended emission in the GeV energy band has to be detected on top of the diffuse γ-ray background (DGRB). The characteristics of this background are uncertain at present. Previous measurements done by EGRET [26,27] indicate that a significant part of DGRB can be due to unresolved point sources (e.g. blazars). The true DGRB should contain at least a contribution from cosmic ray interactions with the CMB, but this contribution can be significantly below the EGRET value [28]. In the near future *Fermi* [29] will provide a new measurement of DGRB. Assuming that the intensity of the DGRB measured by *Fermi* will be by a factor $f_{\rm Fermi} < 1$ lower than the EGRET measurement, we can estimate the sensitivity of *Fermi* for the detection of extended emission around high-redshift sources in the GeV energy band. The number of DGRB γ rays within a $\theta \sim 1$ degree region on the sky is

$$N_b \simeq 10^2 f_{\rm Fermi}\left[\frac{E_\gamma}{1\ {\rm GeV}}\right]^{-1}\left[\frac{A_{\rm eff}}{1\ {\rm m}^2}\right]\left[\frac{T_{\rm exp}}{1\ {\rm yr}}\right]\left[\frac{\theta}{1^\circ}\right]^2. \quad (11)$$

Rescaling Eq. (10) for a brighter blazar $F(E_{\gamma_0}) \sim 10^{-11}$ erg/cm^2 s one finds that the signal statistics is in this case:

$$N_\gamma \simeq 2\times 10^3\left[\frac{F(E_{\gamma_0})}{10^{-11}\ {\rm erg/cm^2\,s}}\right]\left[\frac{A_{\rm eff}(E_\gamma)}{1\ {\rm m}^2}\right]\left[\frac{T_{\rm exp}}{1\ {\rm yr}}\right] \times\left[\frac{E_\gamma}{1\ {\rm GeV}}\right]^{-1}. \quad (12)$$

Assuming the exposure time $T_{\rm exp} \sim 1$ yr, one finds that a moderate collection area $A_{\rm eff} \leq 1$ m^2, typical for the space-born γ-ray telescopes, like *Fermi*, is sufficient for the study of expected extended emission.

Assuming that the sensitivity of a telescope is sufficient for the detection of extended emission, one can estimate the maximal measurable magnetic field from the condition that the source extension $\Theta_{\rm ext}(E_\gamma)$ does not exceed the size of the telescope's field of view (FoV) $\Theta_{\rm FoV}$. Taking the source size at the energy $E_\gamma \simeq 1$ TeV as a reference, and substituting $\Theta_{\rm FoV}$ at the place of $\Theta_{\rm ext}$ in Eq. (6), one can find that the maximal measurable field is

$$B_{\rm max} \simeq 3\times 10^{-13}\left[\frac{\Theta_{\rm FoV}}{1.5^\circ}\right]\left[\frac{E_\gamma}{1\ {\rm TeV}}\right]\left[\frac{\tau(E_{\gamma_0}, z)}{10}\right]\ {\rm G} \quad (13)$$

in the case of the fields with large correlation length $\lambda_B \gg D_e$ and

$$B_{\rm max} \simeq 1.3\times 10^{-12}\left[\frac{\Theta_{\rm FoV}}{1.5^\circ}\right]\left[\frac{E_\gamma}{1\ {\rm TeV}}\right]^{3/4}\left[\frac{\lambda_B}{1\ {\rm kpc}}\right]^{-1/2} \times\left[\frac{\tau(E_{\gamma_0}, z)}{10}\right] \quad (14)$$

in the case $\lambda_B \ll D_e$ (see Eq. (8)).

An increase of the size of the FoV, expected with next-generation ground-based γ-ray telescopes, such as the Cherenkov telescope array optimized for the 10 TeV energy band [24], or the next-generation wide field Cherenkov telescope array AGIS [30], will provide, apart from a better sky coverage, an improvement of sensitivity for the detection of stronger EGMF.

The weakest magnetic fields which can be probed are found from the observation that $\Theta_{\rm ext}$ cannot be measured if it becomes smaller than the size of the point spread function of the telescope, $\theta_{\rm PSF}$. Since $\Theta_{\rm ext} \sim E_\gamma^{-1}$ (see (6)), the largest source extension is achieved at lowest energies. Assuming $\theta_{\rm PSF} \sim 0.1^\circ$ (typical for the Cherenkov telescope arrays and for *Fermi*), one finds from (6)

$$B_{\rm min} \simeq 2\times 10^{-16}\left[\frac{\tau(E_{\gamma_0}, z)}{1}\right]\left[\frac{E_\gamma}{0.1\ {\rm TeV}}\right]\left[\frac{\theta_{\rm PSF}}{0.1^\circ}\right]\ {\rm G} \quad (15)$$

in the case of the fields with large correlation length $\lambda_B \gg D_e$ and

$$B_{\rm min} \simeq 1.5\times 10^{-15}\left[\frac{\theta_{\rm PSF}}{0.1^\circ}\right]\left[\frac{E_\gamma}{0.1\ {\rm TeV}}\right]^{3/4}\left[\frac{\lambda_B}{1\ {\rm kpc}}\right]^{-1/2} \times\left[\frac{\tau(E_{\gamma_0}, z)}{1}\right] \quad (16)$$

in the case $\lambda_B \ll D_e$ (see Eq. (8)).

The characteristics of a setup optimized for the detection of weakest EGMF $B \sim 10^{-16}$ G, should be quite different from the one optimized for the detection of stronger EGMF, $B \sim 10^{-12}$ G. In this case, high sensitivity at low energies $E_\gamma \leq 0.1$ TeV and good angular resolution are required. These can be achieved with the planned next-generation low-energy extensions of the ground-based Cherenkov telescope arrays, like HESS-II [31], MAGIC-II [32], and CTA [33] or with *Fermi* [29]. Another important difference between the approaches for detection of strong and weak EGMF is a different choice of sources. Strong EGMF could be detected via a study of extended emission around nearby ($z < 0.1$) extragalactic TeV sources, while weak EGMF could be detected via studies of extended emission around sources of sub-TeV γ rays in the distant Universe ($z > 0.1$).

III. NUMERICAL SIMULATIONS

The EGMF-determined energy dependence of the size of the extended emission in the TeV energy band, given by Eq. (6), provides a possibility to extract the information on the properties of the EGMF from the observational data. In the qualitative discussion of the previous section we have assumed, for the sake of simplicity, that each primary γ ray produces the electron and positron of energies equal to one-half of the primary γ-ray energy, $E_e = E_\gamma/2$, and that the electron and positron emit IC photons of energies equal to $(E_e/m_e)^2\epsilon_{\rm CMB}$. In other words, we have adopted a "monochromatic approximation" for the production spectra of e^+e^- pairs and of the IC scattered photons. A scatter of the energies of cascade particles can, in principle, lead to

the "blurring" of the energy dependence of the surface brightness profiles of the extended source, thus preventing the possibility of the measurement of magnetic field via the study of the source extension. Besides, both spectrum and morphology of the extended emission could depend on the spectrum of the primary source. This dependence could lead to the loss of the characteristic E_γ^{-1} behavior of the source extension and to the loss of information about the properties of EGMF.

In order to study these problems in more detail, we have developed a Monte Carlo code for the modeling of γ ray-induced electromagnetic cascades in the intergalactic space, with account of the EGMF.

A. Primary γ rays

We consider, as a reference case, an extragalactic source that injects γ rays with a power-law energy distribution, $dN_{\gamma_0}/dE_{\gamma_0} \sim E_{\gamma_0}^{-\Gamma} \exp(-E_{\gamma_0}/E_{\rm cut})$ with the power-law index $\Gamma = 2$ and cutoff energy $E_{\rm cut} = 300$ TeV. The calculations presented below can be generalized (repeated) for an arbitrary assumption about the primary source spectrum. As it is explained below, an analysis of the real data sets aimed at the measurement of EGMF has to include Monte Carlo simulations of the properties of the extended sources produced by the primary point sources with different spectra.

To calculate the pair production by the primary γ rays in the intergalactic space, we assume the energy dependence of the mean free path of the γ rays calculated in Ref. [34] for the "nominal" cosmic infrared background (CIB) model.[1] We take into account the uncertainty of the measurements of the CIB by allowing for different overall normalizations of the CIB. The pair production on the CMB becomes important at the energies above ~50 TeV. Since our calculations extend to the primary γ rays with energies above 50 TeV we also take into account the CMB photon background.

If the mean free path of the γ rays of the energy E_{γ_0} is D_{γ_0}, the probability density of the creation e^+e^- pair at a distance x from the source is

$$P(x) = \frac{1}{D_{\gamma_0}} \int_0^x \exp\left(-\frac{x'}{D_{\gamma_0}}\right) dx' \tag{17}$$

so that the distances x_i at which the ith γ ray creates an e^+e^- pair could be expressed through a random number P_i distributed in the interval $0 < P_i < 1$ as

$$x_i = -D_{\gamma_0} \cdot \ln(P_i). \tag{18}$$

[1] A known uncertainty of a factor of ~2 in the normalization of the CIB [35,36] introduces an uncertainty by the same factor in the γ-ray mean free path D_{γ_0}. This, in turn, introduces a factor of ~2 uncertainty in the expected size of the extended emission, see Eq. (6), and in the measured magnetic field strength.

Using the production spectrum of the e^-e^+ pairs, $dN(E_e)/dE_e = f(\omega_0, E_{\gamma_0}, E_e)$, where ω_0 is the energy of the background photon, we calculate the energy of the electron, produced by the ith primary γ ray, taking into account that the probability for an electron to have energy $E_{e,i}$ is

$$P(E_{e,i}) = \int_0^{E_{e,i}} f(\omega_0, E_{\gamma 0,i}, E_e) dE_e. \tag{19}$$

Having calculated the electron energy $E_{e,i}$ we calculate the positron energy as $E_{e^+,i} = E_{\gamma_0} - E_{e,i}$. Initial directions of motion of the electron and positron $\mathbf{v}_{e^\pm}$ coincide with the primary photon direction.

B. e^+e^- pairs

We model the propagation of both electrons and positrons in the EGMF by solving the equations of motion,

$$\gamma_e m_e \frac{d\mathbf{v}_e}{dt} = \pm e \mathbf{v}_e \times \mathbf{B} \tag{20}$$

where γ_e is the Lorentz factor of e^- or e^+, m_e, e are, respectively, the electron mass and charge and $\mathbf{v}_e$ is its velocity.

The IC scattering of the background photons is treated in a way similar to the one used for the pair production, via calculation of the distance of emission of each next IC γ ray, using an equation similar to (18) with a substitution $D_{\rm IC} = (\sigma_T n_{\rm CMB})^{-1}$, where σ_T is the Thomson cross section, at the place of D_{γ_0}. The energy of each subsequent upscattered photon is calculated based on the differential cross section of IC scattering [37], in a way similar to the calculation of the energies of the e^+e^- pairs, described above. Having calculated the energy of an IC γ ray, E_γ, we decrease the electron/positron energy, $E_e \to E_e - E_\gamma$. We repeat the generation of the IC γ rays for all branches of the cascade until energies of electrons/positrons become less than 0.1 TeV.

The secondary cascade γ rays produced via the IC scattering process by the e^+e^- pairs could themselves be absorbed by interactions with CIB photons and inject additional e^+e^- pairs. We take this possibility into account in our calculations. We do not include the cosmological evolution of the CMB and CIB, because we consider only the relatively nearby extragalactic γ-ray sources, situated at the distances ~100 Mpc.

C. Extragalactic magnetic field

The energy attenuation length of the e^+e^- pairs in the intergalactic medium is short compared to the coherence length of the EGMF, $D_{\rm EGMF} \sim 1$ Mpc, estimated to be of the order of the typical distance between the galaxies [5,38]. This means that one can assume that electrons and positrons propagate in an ordered magnetic field (rather than diffuse in a random field) during their radiative

cooling. In our modeling we divide all the space into a grid of cubic cells with the side length 1 Mpc. In each cell we choose a constant magnetic field with random orientation. We assume, for simplicity, that the strength of EGMF is the same in each cell and leave the investigation of the effect of variations of the EGMF strength along the lines of sight toward individual extragalactic sources for future work.

D. Properties of γ ray-induced cascades in intergalactic space

The results of typical runs of our code are presented in Figs. 1 and 2. Figure 1 compares the cascades induced by the γ rays of the energy $E_{\gamma_0} = 300$ TeV emitted from a source at the distance $D = 120$ Mpc. The three cases shown with black color in the figure correspond to different choices of the strength of EGMF. For comparison, we show in the same figure in red a cone with an opening angle $\Theta_{\rm jet} = 5^\circ$ which is believed to be a typical opening angle of the blazar jets ($\Theta_{\rm jet} \simeq 1/\Gamma_{\rm jet}$, where $\Gamma_{\rm jet} \sim 10$ is the bulk Lorentz factor of the jet). The leftmost black-colored cascade develops in the EGMF of the strength $B = 10^{-14}$ G, the cascade in the middle develops in EGMF $B = 10^{-15}$ G, while the cascade on the right develops in a magnetic field $B = 10^{-16}$ G. One can clearly see that the increase of the strength of the magnetic field leads to the increase of the opening angle of the cascade. Also the opening angle of the cascade becomes larger than the typical jet opening angle at a certain distance from the source. This distance depends on the EGMF strength.

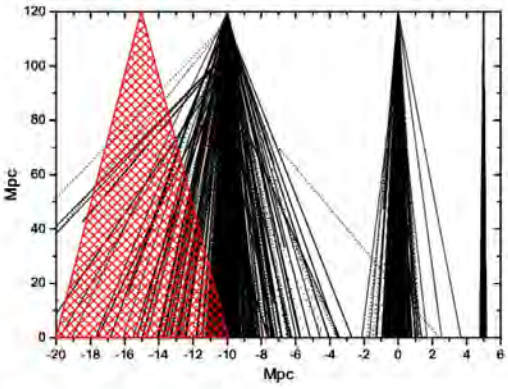

FIG. 1 (color online). Examples of showers from γ rays with primary energy $E_0 = 300$ TeV developing in the EGMF of the strength 10^{-14} (left), 10^{-15} (middle), and 10^{-16} G (right). Only photon tracks with energies above 0.1 TeV are shown. The mean free paths of the electrons and positrons are much shorter ($\sim$ 1 kpc) than the cascade development scale and they are not visible in the figure. The red-hatched cone shows a cone with an opening angle of $\Theta_{\rm jet} = 5^\circ \sim 1/\Gamma_{\rm jet}$, which is (minimal possible) the opening angle of the blazar jet with bulk Lorentz factor $\Gamma_{\rm jet} \simeq 10$.

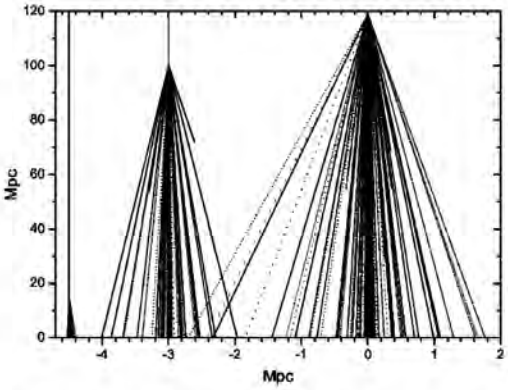

FIG. 2. Examples of showers from γ photons with different primary energies 10 (left), 30 (middle), and 100 TeV (right) in EGMF 10^{-15} G.

Figure 2 shows the dependence of the geometrical properties of the cascade on the energy of the primary γ ray. The left, middle, and right cascades are initiated by the γ rays of the energies 10, 30, and 100 TeV, respectively. The decrease of the mean free path of the primary γ ray with the increase of energy is evident from this figure. The decrease of the mean free path leads to the earlier onset of the electromagnetic cascade.

E. Extended emission around an extragalactic point source

To model the detection of the γ ray-induced cascades by the space- or ground-based γ-ray telescope, we adopt the following procedure, illustrated by Fig. 3.

Simulations of electromagnetic cascades initiated by the primary γ rays injected by an isotropically emitting source or by a source emitting into a jet with a certain opening angle take a lot of computing time. Besides, most of the cascade photons initially emitted at large angles with respect to the line of sight would never reach the detector, so that the machine time spent on their calculation would be wasted. Taking this fact into account, we inject all the primary photons in the same direction. We save the coordinates and arrival directions of all the cascade photons with energies above 0.1 TeV, which crossed the sphere with center at the location of the source and with radius D equal to the distance to the detector.

Next, to take into account the characteristics of the detector, we choose a circle of the angular radius $d_{\rm PSF} = D\theta_{\rm PSF}$ where $\theta_{\rm PSF}$ is the angular resolution of the detector. To calculate the extended emission produced by an isotropically emitting source, we place the detector circle at a set of random positions on the sphere and sum all the

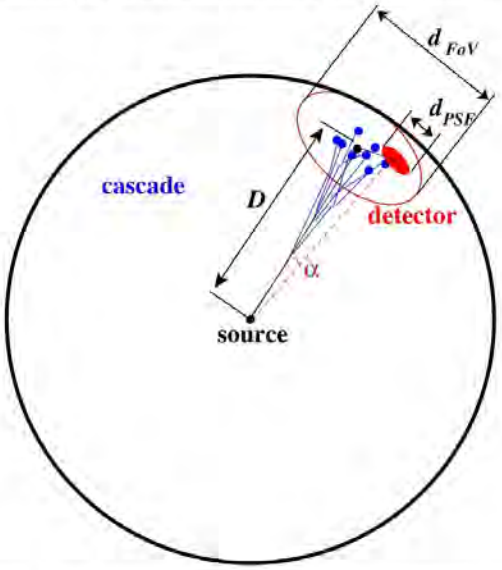

FIG. 3 (color online). Scheme of Monte Carlo calculations of the extended emission.

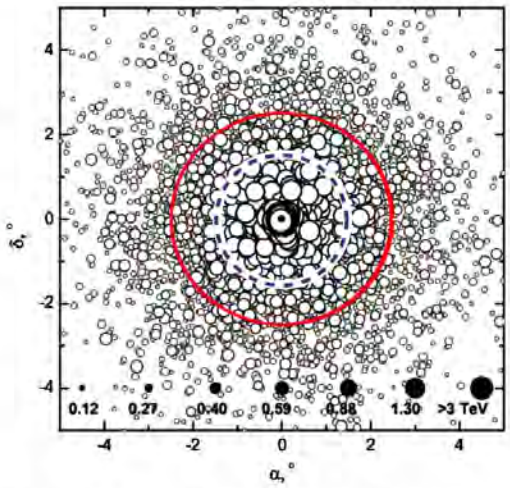

FIG. 4 (color online). The arrival directions of the primary and secondary cascade γ rays (circles) from a source at a distance $D = 120$ Mpc. The EGMF strength is 10^{-14} G. The sizes of the circles representing each photon are proportional to the photon energies. The blue dashed circle has radius 1.5°, equal to the radius of the FoV or MAGIC telescope. The radius of the red solid circle is 2.5°, which corresponds to the size of the FoV of the HESS telescope.

cascade photons which pass through the detector circle at a given angle with respect to the normal to the sphere. This procedure is equivalent to the injection of primary photons in different directions at a fixed detector but is more time efficient. For the sake of simplicity, we restrict our calculations here to the case when the source emits γ rays isotropically. In this case the effects of distortion of the circular symmetry of the surface brightness of the extended source due to the finite opening angle of the blazar jet and misalignment of the jet with respect to the line of sight do not affect the measurement of EGMF strength. We leave the investigation of the distortions of the morphology of extended emission caused by specific geometries of the jet for future investigation.

The results of numerical calculation of the energy-dependent morphology of extended emission are shown in Figs. 4 and 5 for a source at a distance $D = 120$ Mpc (equal to the distance of the blazar Mrk 421).

In the case of the calculation shown in Fig. 4 the EGMF strength is assumed to be $B = 10^{-14}$ G. One can see that strong deflections of the cascade electrons by the EGMF lead in this case to a very large size of the extended emission at the energies ~0.1 TeV, with significant contribution to the signal extending up to ~4° from the source. Obviously, the extended emission at these energies cannot be detected by a typical Cherenkov telescope array, which has a FoV with the diameter ~5° (HESS) or ~3° (MAGIC) (shown as, respectively, solid and dashed circles in Fig. 4). The extension of the source becomes smaller than the size of HESS and MAGIC FoVs only at the energies above ~1 TeV.

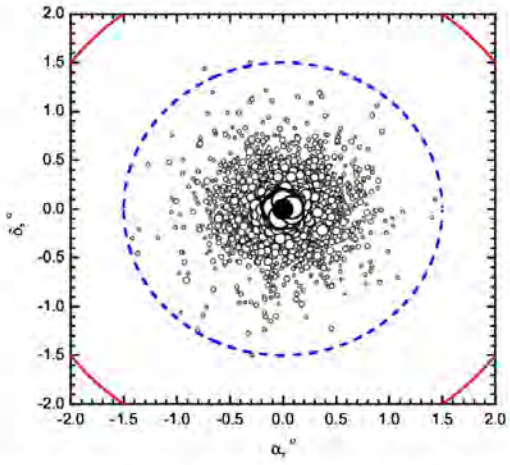

FIG. 5 (color online). The same as Fig. 4 but for the EGMF strength 10^{-15} G.

The extended emission is more compact if the strength of the EGMF is weaker. This is illustrated in Fig. 5 which shows the result of the calculation of extended emission around the same point source as in Fig. 4, but assuming the EGMF strength $B = 10^{-15}$ G. One can see that in this case most of the extended emission down to the energies ~ 0.1 TeV fits into the FoVs of both HESS and MAGIC telescopes.

Figure 6 shows the radial surface brightness profiles of the extended sources shown in Figs. 4 and 5 in different energy bands. One can see that in each energy band the profiles of the extended emission produced by the cascade in a weaker magnetic field (open diamonds) are always more concentrated toward the central source than the profiles of extended emission produced by a cascade in a stronger magnetic field (filled diamonds), the magnetic field is 10^{-14} G. The details of the shape of the surface brightness profile at the angular scale $\theta \sim 0.1^\circ \sim \theta_{\rm PSF}$ close to the size of the PSF of a telescope could be calculated only if the details of the response of the telescope are known.

In our calculations we do not model the telescope's PSF and, instead, assume that γ rays from a point source are homogeneously distributed within a disk of the radius $\theta_{\rm PSF} = 0.1^\circ$. This explains the appearance of a "plateau" in the surface brightness profiles. Comparing the normalization of the plateau with the one of the extended emission, one can judge, if the sensitivity of a telescope is sufficient for the detection of extended emission around a point source at a given level of the significance of detection of the source for a particular telescope. It is important to note that, in spite of the much lower normalization of the surface brightness profiles of extended emission, as compared to the point source emission, the total flux of the extended source (integrated over the telescope's field of view) could be comparable to the one of the point source.

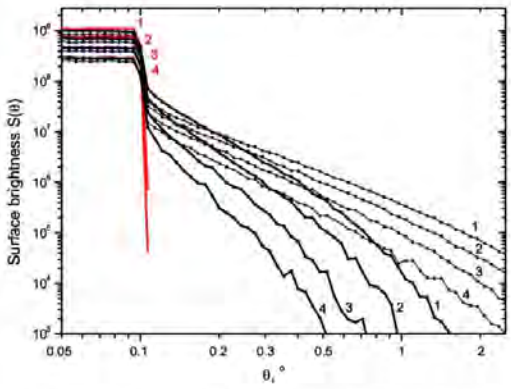

FIG. 6 (color online). Surface brightness profiles of emission in different energy bands (1 – 0.10–0.12 TeV, 2 – 0.12–0.18 TeV, 3 – 0.18–0.27 TeV, 4 – 0.27–0.40 TeV) produced by the cascades in the EGMF of the strength 10^{-14} G (thin lines) and 10^{-15} G EGMF (thick lines) and without magnetic field (red lines).

The qualitative discussion of the model radial brightness profile of the extended emission, presented in the previous section, adopted simplifying assumptions (such as e.g. the monochromatic spectrum of the primary γ-ray source and monochromatic approximation for the spectrum of IC emission from the cascade e^+e^- pairs). Although useful for the qualitative understanding of the method of measurement of EGMF, these assumptions do not hold in a realistic situation. In a more general case, the shape of the radial surface brightness profile of extended source, $S(\theta, E)$, could be derived from the results of our numerical calculations.

In the particular case of a power-law primary γ-ray spectrum with the photon index $\Gamma = 2$, which we consider as an example, the radial brightness profiles of an extended source shown in Fig. 6 can be approximated as power-law with an exponential cutoff:

$$\frac{dn_\gamma(E_\gamma)}{d\theta} \propto \theta S(\theta, E_\gamma) \propto \left(\frac{\theta}{\Theta_{\rm cut}(E_\gamma)}\right)^\alpha \exp\left(-\frac{\theta}{\Theta_{\rm cut}(E_\gamma)}\right), \tag{21}$$

with the slope $\alpha \simeq -1$. The energy-dependent parameter $\Theta_{\rm cut}(E_\gamma)$ characterizes the extension of the source at a given energy E. This parameter is an analog of the parameter $\Theta_{\rm ext}$, which would characterize the size of the extended source in the case of the monochromatic primary source spectrum.

F. Measurement of EGMF strength

Since the parameter $\Theta_{\rm cut}$, which appears in Eq. (21), is a direct analog of the parameter $\Theta_{\rm ext}$ for the case of a source emitting a power-law spectrum of primary γ rays, one expects that, similarly to $\Theta_{\rm ext}$, $\Theta_{\rm cut}$ should decrease inversely proportionally to the energy. Figure 7 shows that this is indeed the case.

The energy dependence of the size of the extended source, $\Theta_{\rm cut}(E_\gamma)$, is determined by the strength of the EGMF along the line of sight. Therefore, measuring this energy dependence, one can extract information about the properties of the EGMF from the observational data. In the simplest case of a monochromatic point source of γ rays, the dependence of the source extension on the EGMF strength could be found analytically (6). It is clear that if the primary γ rays from the source are distributed within a certain energy range, a superposition of the extended sources produced in result of the absorption of the primary γ rays of different energies will lead to the changes of the normalization coefficient $N = N(\Gamma, E_{\rm cut})$ depending on the spectral model of the primary source. Then Eq. (6) can be rewritten for the case of power-law injection spectrum via the substitution $\Theta_{\rm ext} \to \Theta_{\rm cut}$ and introduction of

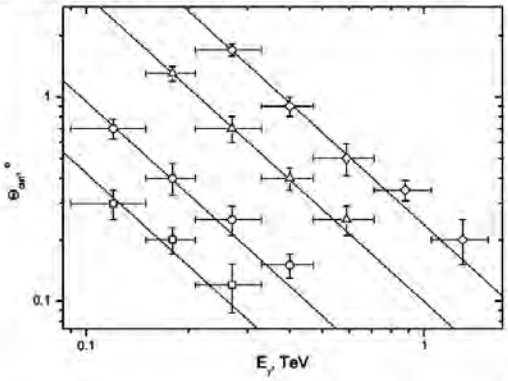

FIG. 7. Θ_{cut} as function of energy E_γ for several values of EGMF, 10^{-15} G (squares), 2×10^{-15} (circles), 5×10^{-15} (triangles), 10^{-14} (diamonds). Solid lines correspond to the fits of the data points with $\Theta_{cut} \sim E_\gamma^{-1}$.

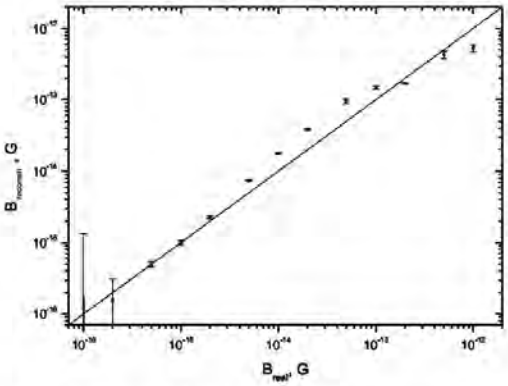

FIG. 8. Comparison of the EGMF strength reconstructed from the measurement of extended emission in simulated data sets, $B_{reconstr}$, with the real value of the magnetic field strength assumed for the simulations, B_{real}. The line corresponds to $B_{real} = B_{reconstr}$.

$N(\Gamma, E_{cut})$:

$$\Theta_{cut}(E_\gamma, B) = \frac{N(\Gamma, E_{cut})}{\tau(E_{\gamma_0}(E_\gamma), z)} \left[\frac{E_\gamma}{6\ \mathrm{TeV}}\right]^{-1} \left[\frac{B}{10^{-13}\ \mathrm{G}}\right]. \quad (22)$$

Using a numerically calculated $N(\Gamma, E_{cut})$, one would be able to derive the strength of the EGMF from the observationally measured $\Theta_{cut}(E_\gamma)$.

To illustrate the implementation of the algorithm described above, we consider the case of a primary γ-ray source with the photon index $\Gamma = 2$ and exponential high-energy cutoff at $E_{cut} = 300$ TeV. We derive the value of the normalization coefficient $N(\Gamma = 2, E_{cut} = 300\ \mathrm{TeV})$ from a fit of the energy dependence of $\Theta_{cut}(E_\gamma)$ using the simulated properties of the extended emission for a (arbitrarily chosen) reference EGMF $B = 10^{-15}$ G. Once the value of the normalization coefficient N is fixed, one can resolve Eq. (22) with respect to B and use the measurements of $\Theta_{cut}(E_\gamma)$ to infer the value of B from the simulated data sets produced for different choices of EGMF strength.

The result of such a procedure of the "reconstruction" of B from the simulated data sets is shown in Fig. 8. The y axis of the plot shows the reconstructed value of the EGMF strength, while the initially assumed EGMF strength is plotted along the x axis. Since the normalization coefficient N is found from the simulations assuming the "reference" magnetic field, the reconstructed magnetic field is exactly equal to the assumed magnetic field at the reference point $B = 10^{-15}$ G.

From Fig. 8 one can see that the assumed value of the EGMF can be reconstructed from the data in a satisfactory way only in a certain range of EGMF strengths (10^{-16} G $< B < 10^{-12}$ G). This range is determined by the assumed characteristics of the γ-ray telescopes and/or by the intrinsic properties of the cascade.

When the field strength gets close to 10^{-16} G, the size of the extended source at the energies above $\sim$0.1 TeV approaches the assumed angular resolution of the telescope, $\theta_{PSF} = 0.1°$. Under these conditions, the extended emission becomes indistinguishable from the point source and measurement of $\Theta_{cut}(E)$ becomes impossible. This is reflected in a large error bar of the point at 10^{-16} G in Fig. 8. Obvious ways to extend the range of accessible EGMF strengths toward still weaker fields is to improve the angular resolution and/or to extend the observed energy band to the energies below 0.1 TeV. Another possibility is to observe such a field with *Fermi* at the energies 1–100 GeV.

If the EGMF along the line of sight is stronger than 10^{-14} G, the size of the extended source at the energy $\sim$0.1 TeV becomes comparable to the size of the FoV of the current generation Cherenkov telescope arrays, $\theta_{FoV} \sim 2°$. Under these conditions, the measurement of $\Theta_{cut}(E)$ is still partially possible at the energies much larger than $\sim$0.1 TeV, but the precision of determination of $\Theta_{cut}(E)$ rapidly drops when the field becomes larger than $\sim 10^{-14}$ G. One should note that, in a realistic situation, the measurement of the radial brightness profile of the extended source becomes problematic already when the source size is smaller, but comparable to the size of the field of view. The difficulty is that the source signal has to be disentangled from the cosmic ray background, in the camera, with intensity depends on the off-axis angle.

In our calculations we have ignored these difficulties and assumed that (a) the telescope FoV is not limited and (b) that an arbitrary large source (with extension up to $\sim 10°$) could be detected. One can see that with a large FoV, high sensitivity telescope the field strength can be

reconstructed from the measurement of characteristics of the extended emission up to the EGMF strengths $\sim 10^{-12}$ G, at which the energy dependence of the source size on the EGMF gets lost because of the too strong deflections of the cascade electrons and positrons.

In principle, an energy-dependent size of the extended source is predicted also when the strength of the EGMF is larger than 10^{-12} G, within the model of extended emission discussed in Ref. [2]. However, in this case the size of the source is determined by the mean free path of the 10–100 TeV γ rays through the cosmological infrared/optical background. The angular extension of the source in this model can be readily estimated to be $\Theta(E_\gamma) \sim [\tau(E_{\gamma_0})]^{-1}$. Taking into account the fact that in a limited energy range $\tau(E_{\gamma_0})$ could be approximated by a linear function, one finds that the size of the extended source is also expected to shrink with energy. Contrary to the case of the EGMF-dependent source size, the size of the halos considered in Ref. [2] decreases as $\Theta(E_\gamma) \sim E_{\gamma_0}^{-1} \sim E_\gamma^{-1/2}$ (see Eq. (2)). This means that the energy dependence of the size of extended halos around extragalactic sources considered in Ref. [2] could be readily distinguished from the one expected if the extended source size is determined by the EGMF. Systematic detection of the extended emission with the characteristic $E_\gamma^{-1/2}$ dependence of the source extension on the energy would provide a strong argument in favor of the existence of strong EGMFs, $B \gg 10^{-12}$ G.

At the end of this section, we would like to comment on the implementation of the proposed method for the analysis of the data of the real γ-ray observations of extragalactic sources. In a realistic situation the primary source spectrum is (a) not known in advance and is (b) strongly modified at the highest energies by the effect of absorption on the EBL. This means that, in general, one cannot assume a particular spectral model of the primary sources for the EGMF search analysis, as it is done above for the analysis of the Monte Carlo simulated data sets. Instead, the measurement of the EGMF has to be done simultaneously with the measurement of the parameters of the high-energy emission spectrum of the primary source. This implies the following analysis procedure. First, using the Monte Carlo simulations described above, one has to produce a "look-up table" of the normalization coefficients $N(\Gamma, E_{\rm cut}, \ldots)$ for a set of parameters $(\Gamma, E_{\rm cut}, \ldots)$ of different possible spectral models of the γ-ray source. Next, using these look-up tables, one can simultaneously find the best-fit values for the spectral model parameters $(\Gamma, E_{\rm cut}, \ldots)$ and for the EGMF strength B, via a multiparameter fitting the spectral and morphological characteristics of the extended emission.

IV. SUMMARY AND CONCLUSIONS

In this paper we have used Monte Carlo simulations of the development of γ ray-induced electromagnetic cascade in the intergalactic space to study the properties of extended emission around extragalactic point sources of VHE γ rays. We have demonstrated that the properties of the cascade and, as a consequence, the properties of the expected extended emission around extragalactic γ-ray sources strongly depend on the strength of the (largely uncertain) EGMF along the line of sight toward the source.

The dependence of the properties of the cascades on the EGMF strength could be used to reveal the presence of extremely weak magnetic fields in the intergalactic medium and to measure (or, at least, estimate) the strength of these fields. Such a measurement would enable to distinguish between existing competing cosmological models of the origin of magnetic fields in the Universe, which widely differ (by more than 10 orders of magnitude) in their predictions of the EGMF strength.

We have demonstrated that if the typical magnetic field strength along the line of sight is in the range 10^{-16} G $\leq B \leq 10^{-12}$ G, the cascade emission could be detected as an energy-dependent extended glow around the point source (see Figs. 4 and 5) by the ground-based γ-ray telescopes. Telescopes optimized for the searches of stronger and weaker magnetic fields should have quite different characteristics. The large effective collection area and large size of the telescope's field of view are needed for the detection of stronger magnetic fields $B \sim 10^{-12}$ G. At the same time, high sensitivity at low γ-ray energies (below 0.1 TeV) and good angular resolution are important for the detection of weaker $B \sim 10^{-16}$ G fields. Still weaker fields $B \leq 10^{-16}$ G should reveal themselves through the extended emission around extragalactic γ-ray sources in the *Fermi* energy band, $E_\gamma \sim$ 1–100 GeV.

The extension of the γ-ray glow around extragalactic point sources appears to decrease inversely proportionally to the energy (Figs. 6 and 7). The measurement of the energy dependence of the source size enables to derive a constraint on the strength of the extragalactic magnetic field from the data (Monte Carlo simulated data in our case), using Eqs. (21) and (22). We have described the algorithm of reconstruction of the EGMF strength from the data. Figure 8 presents the results of the implementation of the algorithm for the analysis of the simulated data sets. The proposed algorithm could be directly used for the analysis of the real data of ground and space-based γ-ray telescopes.

Apart from the measurement of the EGMF, a study of the properties of extended emission around extragalactic point sources enables to constrain the properties of the primary γ-ray source spectrum at the energies above 10 TeV at which the flux from the source is strongly suppressed by absorption on the extragalactic background light. We have argued that, in fact, in the analysis of the real data, the constraints on the spectral characteristics of

the primary source have to be found simultaneously with the constraints on the EGMF strength.

When this paper was finished, we became aware of a paper which analyzes the properties of extended emission around extragalactic γ-ray sources by Dolag *et al.* [39], which presents results complementary to our study. Contrary to our study, Ref. [39] concentrates on the analysis of the properties of the EGMF-dependent extended emission assuming different spectral and morphological characteristics of the primary γ-ray source, fixing a particular model of the EGMF.

ACKNOWLEDGMENTS

A. E. and A. N. are grateful to the Ukrainian Virtual Roentgen and Gamma-Ray Observatory VIRGO.UA and computing clusters of Main Astronomical Observatory and Bogolyubov Institute for Theoretical Physics, for using their computing resources. This work was supported by the Swiss National Science Foundation and the Swiss Agency for Development and Cooperation in the framework of the program SCOPES—Scientific cooperation between Eastern Europe and Switzerland.

[1] F. A. Aharonian *et al.*, Rep. Prog. Phys. **71**, 096901 (2008).
[2] F. A. Aharonian, P. S. Coppi, and H. J. Volk, Astrophys. J. **423**, L5 (1994).
[3] A. Neronov and D. V. Semikoz, JETP Lett. **85**, 473 (2007).
[4] P. D'Avezac, G. Dubus, and B. Giebels, Astron. Astrophys. **469**, 857 (2007).
[5] R. Beck, AIP Conf. Proc. **1085**, 83 (2009).
[6] P. P. Kronberg, Rep. Prog. Phys. **57**, 325 (1994).
[7] D. Grasso and H. R. Rubinstein, Phys. Rep. **348**, 163 (2001).
[8] L. M. Widrow, Rev. Mod. Phys. **74**, 775 (2002).
[9] Y. B. Zeldovich, A. A. Ruzmaikin, and D. D. Sokoloff, *Magnetic Fields in Astrophysics* (McGraw-Hill, New York, 1980).
[10] E. N. Parker, *Cosmological Magnetic Fields* (Clarendon, Oxford, 1979).
[11] M. L. Bernet, F. Miniati, S. J. Lilly, P. P. Kronberg, and M. Dessauges-Zavadsky, Nature (London) **454**, 302 (2008).
[12] A. M. Wolfe, R. A. Jorgenson, T. Robinshaw, C. Heiles, and J. X. Prochaska, Nature (London) **455**, 638 (2008).
[13] P. C. Tribble, Mon. Not. R. Astron. Soc. **263**, 31 (1993).
[14] C. L. Carilli and G. B. Taylor, Annu. Rev. Astron. Astrophys. **40**, 319 (2002).
[15] S. Bertone, C. Vogt, and T. Enlin, Mon. Not. R. Astron. Soc. **370**, 319 (2006).
[16] J. Donnert, K. Dolag, H. Lesch, and E. Müller, Mon. Not. R. Astron. Soc. **392**, 1008 (2009).
[17] G. Sigl, F. Miniati, and T. A. Ensslin, Phys. Rev. D **68**, 043002 (2003); **70**, 043007 (2004).
[18] K. Dolag, D. Grasso, V. Springel, and I. Tkachev, JETP Lett. **79**, 583 (2004); J. Cosmol. Astropart. Phys. 01 (2005) 009.
[19] M. Bruggen, M. Ruszkowski, A. Simionescu, M. Hoeft, and C. D. Vecchia, Astrophys. J. **631**, L21 (2005).
[20] J. D. Barrow, P. G. Ferreira, and J. Silk, Phys. Rev. Lett. **78**, 3610 (1997).
[21] P. Blasi, S. Burles, and A. V. Olinto, Astrophys. J. **514**, L79 (1999).
[22] R. Plaga, Nature (London) **374**, 430 (1995).
[23] K. Murase, K. Takahashi, S. Inoue, K. Ichiki, and S. Nagataki, arXiv:0806.2829.
[24] A. V. Plyasheshnikov, F. A. Aharonian, and H. J. Volk, J. Phys. G **26**, 183 (2000).
[25] See details of detection possibilities on the HAWC official site: http://hawc.umd.edu.
[26] P. Sreekumar *et al.*, Astrophys. J. **494**, 523 (1998).
[27] A. W. Strong, I. V. Moskalenko, and O. Reimer, Astrophys. J. **613**, 956 (2004).
[28] O. E. Kalashev, D. V. Semikoz, and G. Sigl, Phys. Rev. D **79**, 063005 (2009).
[29] See details of detection possibilities on the Fermi official site: http://fermi.gsfc.nasa.gov/.
[30] J. Buckley *et al.*, arXiv:0810.0444.
[31] See details of detection possibilities on the H.E.S.S. official site: http://www.mpi-hd.mpg.de/hfm/HESS.
[32] See details of detection possibilities on the MAGIC official site: http://wwwmagic.mppmu.mpg.de.
[33] See details of detection possibilities on the CTA official site: http://www.cta-observatory.org.
[34] A. F. Aharonian, arXiv:astro-ph/0112314.
[35] T. M. Kneiske *et al.*, Astron. Astrophys. **413**, 807 (2004).
[36] A. Franceschini *et al.*, Astron. Astrophys. **487**, 837 (2008).
[37] G. R. Blumenthal and R. J. Gould, Rev. Mod. Phys. **42**, 237 (1970).
[38] D. Harari, S. Mollerach, E. Roulet, and F. Sanchez, J. High Energy Phys. 03 (2002) 045.
[39] K. Dolag, M. Kachelriess, S. Ostapchenko, and R. Tomas, arXiv:0903.2842.

The Astrophysical Journal Letters, 719:L130–L133, 2010 August 20 doi:10.1088/2041-8205/719/2/L130

DEGREE-SCALE GeV "JETS" FROM ACTIVE AND DEAD TeV BLAZARS

A. Neronov[1], D. Semikoz[2,3], M. Kachelriess[4], S. Ostapchenko[4,5], and A. Elyiv[6,7]
[1] ISDC Data Centre for Astrophysics, Ch. d'Ecogia 16, Versoix, Switzerland
[2] APC, 10 rue Alice Domon et Leonie Duquet, F-75205 Paris Cedex 13, France
[3] Institute for Nuclear Research RAS, 60th October Anniversary Prospect 7a, Moscow 117312, Russia
[4] Institutt for fysikk, NTNU, Trondheim, Norway
[5] D. V. Skobeltsyn Institute of Nuclear Physics, Moscow State University, Russia
[6] Institut d'Astrophysique et de Geophysique, Universite de Liege, 4000 Liege, Belgium
[7] Main Astronomical Observatory, Academy of Sciences of Ukraine, 27 Akademika Zabolotnoho St., 03680 Kyiv, Ukraine
Received 2010 February 26; accepted 2010 July 6; published 2010 July 28

ABSTRACT

We show that images of TeV blazars in the GeV energy band should contain, along with point-like sources, degree-scale jet-like extensions. These GeV extensions are the result of electromagnetic cascades initiated by TeV γ-rays interacting with extragalactic background light and the deflection of the cascade electrons/positrons in extragalactic magnetic fields (EGMFs). Using Monte Carlo simulations, we study the spectral and timing properties of the degree-scale extensions in simulated GeV band images of TeV blazars. We show that the brightness profile of such degree-scale extensions can be used to infer the light curve of the primary TeV γ-ray source over the past 10^7 yr, i.e., over a time scale comparable to the lifetime of the parent active galactic nucleus. This implies that the degree-scale jet-like GeV emission could be detected not only near known active TeV blazars, but also from "TeV blazar remnants," whose central engines were switched off up to 10 million years ago. Since the brightness profile of the GeV "jets" depends on the strength and the structure of the EGMF, their observation provides additional information about the EGMF.

Key words: galaxies: active – galaxies: jets – gamma rays: galaxies – methods: numerical

Online-only material: color figures

1. INTRODUCTION

Significant progress in understanding the activity of blazars, i.e., active galaxies with relativistic jets aligned with the line of sight (LOS), was achieved with the start of operation of the *Fermi* telescope. The combination of data from *Fermi* in the 0.1–10 GeV energy band and from ground-based γ-ray telescopes such as HESS, MAGIC, and VERITAS in the 100 GeV–10 TeV band provides detailed simultaneous spectral and timing information for the most extreme representatives of the blazar population (Abdo et al. 2009).

The TeV γ-ray flux from distant blazars is significantly attenuated by pair production on the infrared/optical extragalactic background light (EBL; Kneiske et al. 2004; Stecker et al. 2006; Franceschini et al. 2008; Primack et al. 2008). TeV γ-rays that are absorbed on the way from the primary γ-ray source initiate electromagnetic cascades in the intergalactic space. The charged component of the electromagnetic cascade is deflected by the extragalactic magnetic field (EGMF). Potentially observable effects of such electromagnetic cascades in the EGMF include the "echoes" of multi-TeV γ-ray flares (Plaga 1995; Murase et al. 2008) and the appearance of extended emission around initially point-like γ-ray sources (Aharonian et al. 1994; Neronov & Semikoz 2007; Dolag et al. 2009; Elyiv et al. 2009).

TeV γ-ray emission from blazars is believed to be relativistically beamed into a narrow cone (jet) with an opening angle $\Theta_{\rm jet} \sim \Gamma^{-1} \sim 5^\circ[\Gamma/10]$, where Γ is the bulk Lorentz factor of the γ-ray emitting plasma. Blazars are a special type of γ-ray emitting active galactic nuclei (AGNs) for which the angle between the LOS and the jet axis, $\theta_{\rm obs}$, is $\theta_{\rm obs} \lesssim \Theta_{\rm jet}$; see Figure 1 (Urry et al. 1991).

In general, the number of blazars with a given jet-LOS misalignment angle is expected to scale as $dN/d\theta_{\rm obs} \sim \theta_{\rm obs}$ in the range $0 < \theta_{\rm obs} \lesssim \Theta_{\rm jet}$. Thus most observed TeV blazars should have $\theta_{\rm obs} \sim \Theta_{\rm jet}$, rather than $\theta_{\rm obs} \simeq 0$. Consequently, the TeV γ-ray emission pattern is not symmetric with respect to the axis source observer. In sources with $\theta_{\rm obs} \sim \Theta_{\rm jet}$, most multi-TeV γ-rays are preferentially emitted on one side of the LOS, as is shown in Figure 1. As a result, the extended emission from the cascade initiated by the absorption of TeV γ-rays in interactions with EBL photons should appear as a one- or two-sided jet-like extension next to the primary point source (Aharonian 2004), rather than as a previously discussed extended axially symmetric halo (Aharonian et al. 1994; Neronov & Semikoz 2007, 2009; Dolag et al. 2009; Elyiv et al. 2009).

In what follows, we discuss the spectral and timing properties of such jet-like cascade extensions in the 0.1–1 GeV images of TeV blazars. Our study is based on two independent Monte Carlo codes for γ-ray induced electromagnetic cascades in the intergalactic space, introduced by Dolag et al. (2009) and Elyiv et al. (2009).

2. BASIC FORMULAE

Before presenting our numerical results, we discuss the basic physics of the phenomenon in a simplified picture. In particular, we assume that the electromagnetic cascade consists of two steps only and replace probability distributions by their means. Then the mean free path of very high energy γ-rays through the EBL can be approximated by $D_\gamma(E_{\gamma_0}) = \kappa[E_{\gamma_0}/1\ {\rm TeV}]^{-1}$ Gpc, where the numerical factor $\kappa = \kappa(E_{\gamma_0}, z) \sim \mathcal{O}(1)$ includes the uncertainties of the EBL modeling. Pair production on EBL reduces the flux of γ-rays from the source by a factor $\exp[-\tau(E_{\gamma_0})]$, where $\tau \simeq D/D_\gamma$ is the optical depth with respect to pair production and D is the distance to the source.

Electron–positron pairs created in interactions of multi-TeV γ-rays with EBL photons produce secondary γ-rays via inverse Compton (IC) scattering on cosmic microwave background

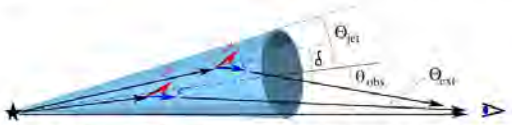

Figure 1. Geometry of the propagation of direct and cascade γ-rays from the source (on the left) to the observer (on the right).

(A color version of this figure is available in the online journal.)

(CMB) photons. Typical energies of the IC photons reaching the Earth are $E_\gamma = (4/3)\epsilon_{\rm CMB} E_e^2/m_e^2 \simeq 0.8[E_{\gamma_0}/1\ {\rm TeV}]^2$ GeV, where $\epsilon_{\rm CMB} = 6 \times 10^{-4}$ eV is the typical energy of CMB photons.

Deflections of e^+e^- pairs produced by the γ-rays, which were initially emitted away from the observer, can redirect secondary photons toward the observer. This effect leads to the appearance of extended emission around an initially point source of γ-rays (Neronov & Semikoz 2007; Dolag et al. 2009; Elyiv et al. 2009).

In the absence of perfect alignment of the jet axis with the LOS, the extended cascade emission might be strongly asymmetric. It might appear as a jet-like feature next to the primary γ-ray source. The maximal angular size of this jet-like feature can be estimated as the size of the projected γ-ray mean free path as $\Theta_{\rm ext,max} \simeq D_\gamma \theta_{\rm obs}/(D - D_\gamma)$, if $D_\gamma < D$ (i.e., $\tau > 1$). If $\tau(E_{\gamma_0}) < 1$, the cascade emission from the TeV γ-ray beam can extend to very large angles $\Theta_{\rm ext,max} \sim \pi/2$.

The jet-like extended emission can be observed only if deflections of the cascade e^+e^- pairs are sufficiently large to redirect the cascade emission toward the observer. If the correlation length of the EGMF is larger than the electron cooling distance $D_e = 3m_e^2c^3/(4\sigma_T U_{\rm CMB} E_e) \simeq 0.7[E_e/0.5\ {\rm TeV}]^{-1}$ Mpc, where σ_T denotes the Thomson cross section and $U_{\rm CMB}$ the energy density of the CMB photons, then the deflection angle can be estimated as (Neronov & Semikoz 2009) $\delta = D_e/R_L \simeq 3^\circ[B/10^{-17}\ {\rm G}][E_e/0.5\ {\rm TeV}]^{-2}$ with R_L being the Larmor radius of electrons and positrons.

If the correlation length λ_B of the EGMF is much smaller than the electron cooling distance D_e, the deflection angle can be estimated using the diffusion approximation as $\delta = \sqrt{D_e \lambda_B}/R_L \simeq 3^\circ[E_e/0.5\ {\rm TeV}]^{-3/2}[B/10^{-17}\ {\rm G}][\lambda_B/0.7\ {\rm Mpc}]^{1/2}$. If the EGMF is weak, electron/positron trajectories are not strongly deflected during one cooling time, and thus secondary cascade γ-rays are emitted within a cone with an opening angle of order $\mathcal{O}(\delta)$. In this case, only a part of the cascade emission could be observed. If the mean free path of the primary γ-rays is much shorter than the distance to the source, the angular extension could be estimated from the simple geometrical consideration of Figure 1 as $\sin(\Theta_{\rm ext}(B)) = (D_\gamma/D)\sin\delta$. Otherwise, the angular size of the source is found from the sum of the angles of triangle with vertices at the source, at the pair production point and at the position of the observer (see Figure 1) as $\Theta_{\rm ext}(B) = \delta - \theta_{\rm obs}$.

Most of the known TeV blazars have moderate distances so that $\tau(E_{\gamma_0} = 1\ {\rm TeV}) \leqslant 1$. In this case, $\Theta_{\rm ext,max} \sim \pi/2$ and $\Theta_{\rm ext}(B) = \delta - \theta_{\rm obs}$. A measurement of $\Theta_{\rm ext} \ll \Theta_{\rm ext,max}$ thus provides a measurement of δ and, in this way, gives a constraint on the parameters of the EGMF, i.e., B and λ_B.

The difference in the path length between the direct and cascade γ-rays leads to a significant time delay of the cascade emission signal. For a given jet misalignment angle $\theta_{\rm obs}$, the time delay of emission coming from the direction θ away from the source is $T_{\rm delay} \sim \frac{D}{c}\left(\frac{\sin\theta + \sin(\theta_{\rm obs}+\Theta_{\rm jet})}{\sin(\theta+\theta_{\rm obs}+\Theta_{\rm jet})} - 1\right) \simeq \frac{D\theta(\theta_{\rm obs}+\Theta_{\rm jet})}{2c} \simeq 3 \times 10^6\left[\frac{(\theta_{\rm obs}+\Theta_{\rm jet})}{5^\circ}\right]\left[\frac{\theta}{5^\circ}\right]$ yr. Comparing this time scale with the typical time scale of AGN activity, $T_{\rm AGN} \sim 10^7$ yr, one sees that degree-scale extended emission in the GeV energy range depends on the TeV γ-ray luminosity of the blazar integrated over its lifetime.

3. RESULTS OF NUMERICAL MODELING

To model the asymmetric extended emission from the γ-ray-initiated electromagnetic cascade in intergalactic space, we have extended our two Monte Carlo codes such that they now follow the three-dimensional trajectories of individual cascade particles moving through the EGMF. The turbulent component of the EGMF has been calculated following the algorithm of Giacalone & Jokipii (1994).

To produce an image of the γ-ray-induced electromagnetic cascade, as it would be detected by a γ-ray telescope, we use the algorithm described by Elyiv et al. (2009). We have verified that the results obtained using the two different codes are compatible with each other.

We record positions and directions of all secondary γ-rays that cross a sphere of the radius $R = D$ around the source. We choose the directions of primary γ-rays to be distributed within a cone with an opening angle $\Theta_{\rm jet}$. We consider a primary γ-ray beam with a Gaussian profile, so that the probability for a primary γ-ray to have a direction misaligned by an angle Θ with respect to the jet axis is $p(\Theta) \sim \exp(-\Theta^2/\Theta_{\rm jet}^2)$.

For simplicity, we consider a monochromatic primary γ-ray beam with all the primary γ-rays having the same energy $E_{\gamma_0} = 1$ TeV. This is sufficient to demonstrate the existence of the effect discussed here for the first time, namely, degree-scale jet-like extensions in *Fermi* images of TeV blazars. The EBL background is taken from the calculations of Kneiske et al. (2004). We fix the distance to the source as $D = 400$ Mpc, so that $\tau(E_{\gamma_0}) \sim 1$. The EGMF is chosen to have a correlation length of the order of several Mpc, with its power spectrum sharply peaked at the wavenumber $k \simeq 1\ {\rm Mpc}^{-1}$. Our results could be generalized in a straightforward way to the case of an arbitrary primary γ-ray spectrum, arbitrary distance to the source and different EBL models, when considering extended emission from particular TeV blazars with known TeV band spectra and known redshift.

Figure 2 shows the effect of the misalignment of the primary γ-ray beam with the LOS on the morphology of the extended emission. The left panel of the figure corresponds to the situation $\theta_{\rm obs} = 0$, which is equivalent to the axially symmetric case considered by Dolag et al. (2009) and Elyiv et al. (2009). An axially symmetric extended "halo" around the primary point source is clearly visible. The other panels of the figure show the cases of a jet with an opening angle $\Theta_{\rm jet} = 3^\circ$ misaligned by angles $\theta_{\rm obs} = 3^\circ$, 6°, and 9°, respectively. It is clear that the misalignment of the jet axis with the LOS leads to the appearance of an extended jet-like feature on one side of the source. The ratio of the point source flux to the flux of the extension grows with the increase of the misalignment angle $\theta_{\rm obs}$.

The angular extension of the cascade emission depends on the strength of the EGMF as long as the trajectories of e^+e^- pairs are not completely randomized. The morphological properties of the jet-like emission are practically independent from the properties of the EGMF, when the EGMF strength is such that the deflection angle $\delta \geqslant 2\pi$. Figure 3 shows the growth of the source extension with the increase of the EGMF strength.

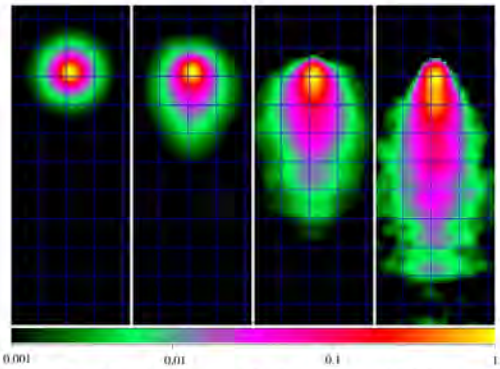

Figure 2. $E > 1$ GeV band images of the sky region around TeV blazars with jets inclined at $\theta_{\rm obs} = 0^\circ$, $\theta_{\rm obs} = 3^\circ$, $\theta_{\rm obs} = 6^\circ$, and $\theta_{\rm obs} = 9^\circ$ (left to right). The jet opening angle is $\Theta_{\rm jet} = 3^\circ$ and the EGMF strength is $B = 10^{-16}$ G. The spacing of the coordinate grid is 2°; the color scale is logarithmic in surface brightness: yellow corresponds to the maximal surface brightness and black corresponds to the surface brightness less than 10^{-3} of the maximal value.

(A color version of this figure is available in the online journal.)

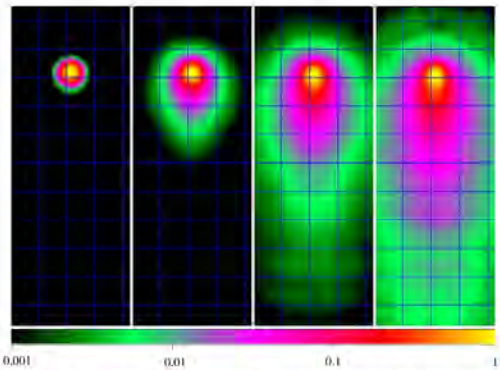

Figure 3. $E > 1$ GeV band images of the sky region around TeV blazars with $\Theta_{\rm jet} = \theta_{\rm obs} = 3^\circ$ for different values of the EGMF strength. From left to right: 10^{-17} G, 10^{-16} G, 10^{-15} G, 10^{-14} G.

(A color version of this figure is available in the online journal.)

For magnetic fields stronger than $B \sim 10^{-15}$ G, the size of the extended source reaches ten(s) of degrees. In this case, the extended source could significantly contribute to the diffuse γ-ray background.

Cascade emission coming from regions with angular distance $\theta \gtrsim 1^\circ$ to the primary source is delayed by $T_{\rm delay} \sim 10^5$–10^7 yr compared to the direct emission from the source. This means that "echoes" from periods of enhanced activity of the source (e.g., an enhanced accretion rate following major merger episodes), which happened all along the lifetime of an AGN some time T ago, could enhance the flux at the distance $\theta \simeq 1.^\circ 7[T/10^6\ {\rm yr}][(\theta_{\rm obs} + \Theta_{\rm jet})/5^\circ]$ from the source.

Figure 4 shows a time sequence of $E > 1$ GeV band images of the sky region around a TeV source at different times after a short episode of TeV γ-ray emission. One can clearly see that the emission at large angular distances is delayed by up to 10^7 yr.

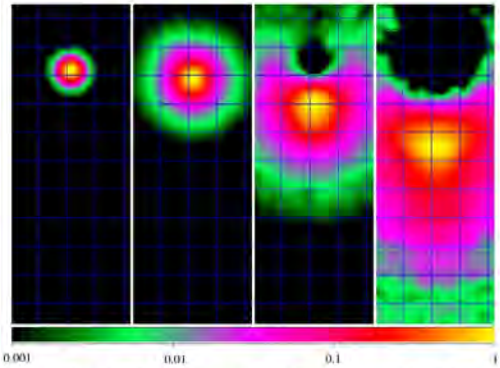

Figure 4. $E > 1$ GeV band images of the sky region around a TeV blazar with $\Theta_{\rm jet} = \theta_{\rm obs} = 3^\circ$ at different times following instantaneous injection of 1 TeV γ-rays at the source. From left to right: images in time intervals $0 < T_{\rm delay} < 10^5$ yr, 10^5 yr $< T_{\rm delay} < 10^6$ yr, 10^6 yr $< T_{\rm delay} < 3 \times 10^6$ yr, and 3×10^6 yr $< T_{\rm delay} < 10^7$ yr after the outburst. $B = 10^{-16}$ G.

(A color version of this figure is available in the online journal.)

The flux coming from the region at an angular distance θ from the point source is proportional to the source flux averaged over the period $T_{\rm delay}$. Therefore, it is possible that GeV γ-rays are detectable today from an AGN which was active some 10^7 yr ago, but at present it is no longer active. In this case, a GeV source would be classified as "unidentified": the parent AGN (1) could not be identified as an AGN in the optical, X-ray, and TeV γ-ray bands or (2) the GeV source is displaced from the position of the parent AGN. The characteristic feature of such an unidentified "AGN remnant" is the absence of counterparts at lower energies: If the GeV γ-rays are produced by e^+e^- pairs deposited in the intergalactic medium by primary TeV γ-rays, the only energy loss mechanism for the pairs is IC scattering on CMB photons.

4. DISCUSSION

The presence of extended jet-like emission at degree scales should be a generic feature of GeV band images of TeV blazars. The total flux of the jet-like extended source is proportional to the source luminosity in the TeV energy band. Taking into account the fact that TeV blazars have hard γ-ray spectra, the primary source luminosity in the TeV band could be much larger than its GeV luminosity, so that the overall extended source luminosity could be higher than the primary source luminosity in the GeV band. This means that the best candidates for the search of extended emission are TeV blazars with hard intrinsic spectra.

This does not automatically mean that the extended emission should be readily detectable in *Fermi* images of TeV blazars. In spite of the larger luminosity, the extended source flux might be suppressed if the EGMF is strong enough to randomize the trajectories of e^+e^- pairs before they lose their energy to the GeV band via IC emission. The maximal possible suppression of the extended source flux is by a factor of $\Theta_{\rm jet}^{-2} \sim 100$.

Another potential problem for the detection of jet-like extended emission next to TeV blazars is that the extended source has to be identified on top of the diffuse γ-ray background. The minimal detectable flux for extended sources increases roughly as $\theta^{1/2}$, where θ is the angular length of the jet-like extended

source. Thus, sources at larger distances, for which the jet-like extensions appear more compact, are better candidates for the search of extended emission in the *Fermi* energy band.

Finally, the detectability of extended emission close to TeV blazars strongly depends on the angular resolution of the Large Area Telescope (LAT). At low energies, $E_\gamma \sim 0.1$ GeV, the LAT angular resolution is relatively poor, $\theta_{\rm PSF} \simeq 10^\circ$. It is clear that only very large angular size jet-like extensions with an angular diameter $\theta \sim \theta_{\rm PSF}$ could be detected. However, the detectability of such large extended sources would be complicated by the high level of diffuse sky background within the $\sim 10^\circ$ region around the source. At the same time, the size of the point-spread function (PSF) decreases to $\theta_{\rm PSF} \leqslant 1^\circ$ above GeV energies. This dramatically improves the sensitivity of the telescope for the search of extended emission: extensions of much smaller angular size could be detected on top of a strongly reduced background. This favors the search of extended emission at energies above $\sim$1 GeV.

As an example, we consider a blazar with the TeV band luminosity $L_0(E_{\gamma_0}) \sim 10^{43}$ erg s^{-1} beamed in a cone with an opening angle $\Theta_{\rm jet} = 3^\circ$, so that the equivalent isotropic luminosity of the source is $L_{\rm iso} \simeq 10^{45}$ erg s^{-1}. In the absence of absorption, the source would give a flux $F_{\rm iso,0} \simeq 10^{-10}[D/300\ {\rm Mpc}]^{-2}$ erg (cm^2 s)$^{-1}$. At energies E_γ such that $\tau(E_{\gamma_0}) \gtrsim 1$ the overall luminosity of the cascade emission is comparable to the primary source luminosity at energy E_{γ_0}, so that in the case of small EGMFs ($\delta \leqslant \Theta_{\rm jet}$), i.e., at the level of the lower bounds $B \sim 10^{-17}$–10^{-16} G derived from *Fermi* observations (Neronov & Vovk 2010; Tavecchio et al. 2010), the flux in the cascade is $F_{\rm cascade} \sim F_{\rm iso,0}$. In this case, the cascade emission is readily detectable in the GeV band by *Fermi*. In the opposite case, the cascade emission is completely isotropized and the cascade flux is suppressed by a factor of $1/\Theta_{\rm jet}^2 \sim 4 \times 10^2$, so that it is marginally below the minimal detectable flux for extragalactic *Fermi* point sources in the GeV band, $F_{\rm min} \sim 10^{-12}$ erg (cm^{2}s)$^{-1}$.

Thus, in the most pessimistic case jet-like extensions are detectable only for the brightest blazars with the observed steady-state flux at the level of $F_{\rm iso} \simeq \exp(-\tau)F_{\rm iso,0} \sim 3 \times 10^{-11}$ erg (cm^2 s)$^{-1}$ (assuming $\tau \simeq 1$). Only several extragalactic sources with sufficient steady-state flux are detected by *Fermi* above 100 GeV (Neronov et al. 2010a). Among these sources, 3C 66A, 1ES 0502+675, PG 1553+113, and, possibly, PKS 2155–304 are at sufficiently large redshifts for strong cascade emission in the GeV energy range. These sources should be considered as primary candidates for the search of the jet-like extended emission. By contrast, all sources with sufficiently high flux at few $\times$ 100 GeV (Neronov et al. 2010b) are viable candidates for the detection of the extended jet-like emission, if the EGMF is weak.

The number of detectable "blazar remnants" also strongly depends on the EGMF. If the EGMF is so weak that $T_{\rm delay} \ll T_{\rm AGN}$, blazar remnants would not exist, since cascade and direct emission would be observed together. If typical deflection angles of electrons emitting in the GeV band are several degrees ($B \sim 10^{-17}$ G for large λ_B), the number of blazar remnants observable in the GeV band should be comparable to the number of active TeV blazars, since $T_{\rm delay} \sim T_{\rm AGN}$. If the EGMF is much stronger, the number of potentially observable blazar remnants grows because the cascade emission is emitted in a wider cone than emission from the parent blazar. However, the typical flux of the blazar remnants decreases because of the same effect. Thus, for strong EGMFs, the number of blazar remnants above the *Fermi* sensitivity limit might be very small. The strong dependence of the observability of blazar remnants on the EGMF strength implies that constraints on the EGMF could be deduced from their source statistics.

To summarize, we have shown that GeV band images of TeV blazars should possess degree-scale jet-like extended features. These features trace the direction of the TeV γ-ray beam emitted by the blazar. They are produced as results of electromagnetic cascades initiated by TeV γ-rays interacting with EBL photons. We have performed Monte Carlo simulations of three-dimensional electromagnetic cascades developing in the EGMF. Using these Monte Carlo simulations, we have derived the properties of the GeV jet-like extended emission near TeV blazars. We have investigated the dependence of the characteristics of the jet-like extended sources (the angular size, the brightness profile) on the strength of the EGMFs and on the opening angle and orientation of the primary TeV γ-ray beam from the blazar. We have also demonstrated that the γ-ray signal in the jet-like extended emission is delayed up to 10^7 yr compared to the direct γ-ray signal from the primary point source. The very long time delay of the cascade emission means that the extended GeV source could be detected next to a blazar that is no longer active as a blazar.

A.E. is supported by a fellowship from the Belgium Federal Science Policy Office, A.N. by the Swiss National Science Foundation project PP00P2_123426/1, and S.O. by a Marie Curie IEF fellowship from the European Community and by the Romforskning program of Nork Forskningsradet.

REFERENCES

Abdo, A. A., et al. (Fermi LAT Collaboration) 2009, ApJ, 707, 1310
Aharonian, F. A. 2004, Very High Energy Cosmic Gamma Radiation: A Crucial Window on the Extreme Universe (River Edge, NJ: World Scientific)
Aharonian, F. A., Coppi, P. S., & Völk, H. J. 1994, ApJ, 423, L5
Dolag, K., Kachelrieß, M., Ostapchenko, S., & Tomàs, R. 2009, ApJ, 703, 1078
Elyiv, A., Neronov, A., & Semikoz, D. V. 2009, Phys. Rev. D, 80, 023010
Franceschini, A., Rodighiero, G., & Vaccari, M. 2008, A&A, 487, 837
Giacalone, J., & Jokipii, J. R. 1994, ApJ, 430, L137
Kneiske, T. M., Bretz, T., Mannheim, K., & Hartmann, D. H. 2004, A&A, 413, 807
Murase, K., Takahashi, K., Inoue, S., Ichiki, K., & Nagataki, S. 2008, ApJ, 686, L67
Neronov, A., & Semikoz, D. V. 2007, JETP Lett., 85, 473
Neronov, A., & Semikoz, D. V. 2009, Phys. Rev. D, 80, 123012
Neronov, A., Semikoz, D. V., & Vovk, I. 2010a, A&A, in press (arXiv:1003.4615)
Neronov, A., Semikoz, D. V., & Vovk, I. 2010b, A&A, submitted (arXiv:1004.3767)
Neronov, A., & Vovk, I. 2010, Science, 328, 73
Plaga, R. 1995, Nature, 374, 430
Primack, J. R., Gilmore, R. C., & Somerville, R. S. 2008, AIP Conf. Proc., Vol. 1085, High Energy Gamma-ray Astronomy, ed. F. A. Aharonian, W. Hofmann, & F. Rieger (Melville, NY: AIP), 71
Stecker, F. W., Malkan, M. A., & Scully, S. T. 2006, ApJ, 648, 774
Tavecchio, F., Ghisellini, G., Foschini, L., Bonnoli, G., Ghirlanda, G., & Coppi, P. 2010, MNRAS, 406, L70
Urry, C. M., Padovani, P., & Stickel, M. 1991, ApJ, 382, 501

4.2. Властивості та стійкість електромагнітних лавин у войдах

У роботі [4] проаналізована стабільність релятивістських пучків електрон-позитронних пар низької щільності, що утворюються у міжгалактичному середовищі від гамма-фотонів ТеВ-них енергій. Проблема актуальна для вимірювання магнітного поля в космічних порожнинах через спостереження в гамма діапазоні. Крім того, розсіювання таких пучків може істотно впливати на теплову історію войдів. Ми використали метод Монте-Карло для кількісної оцінки властивостей електромагнітного потоку, зокрема зміну Лоренц-фактора і кутового розкиду пучка електрон-позитронних пар породжених потоків, залежно від відстані від самого блазара.

У роботі [5] детально проаналізовано взаємодію первинних високоенергетичних гамма-фотонів, індукованих ТеВ-ними блазарами з оптичним та інфрачервоним фоновим ізотропним випромінюванням у космічних войдах. Фонові фотони мають енергії більше, ніж на 10 порядків нижчі за взаємодіючий з ними фотон ТеВ-них енергій. Результати аналітичних розрахунків було перевірено чисельним моделюванням.

The Astrophysical Journal, 770:54 (9pp), 2013 June 10 doi:10.1088/0004-637X/770/1/54

RELAXATION OF BLAZAR-INDUCED PAIR BEAMS IN COSMIC VOIDS

Francesco Miniati[1] and Andrii Elyiv[2,3]
[1] Physics Department, Wolfgang-Pauli-Strasse 27, ETH-Zürich, CH-8093 Zürich, Switzerland; fm@phys.ethz.ch
[2] Institut d'Astrophysique et de Géophysique, Université de Liège, B-4000 Liège, Belgium
[3] Main Astronomical Observatory, Academy of Sciences of Ukraine, 27 Akademika Zabolotnoho St., 03680 Kyiv, Ukraine
Received 2012 August 4; accepted 2013 April 25; published 2013 May 23

ABSTRACT

The stability properties of a low-density ultrarelativistic pair beam produced in the intergalactic medium (IGM) by multi-TeV gamma-ray photons from blazars are analyzed. The problem is relevant for probes of magnetic field in cosmic voids through gamma-ray observations. In addition, dissipation of such beams could considerably affect the thermal history of the IGM and structure formation. We use a Monte Carlo method to quantify the properties of the blazar-induced electromagnetic shower, in particular the bulk Lorentz factor and the angular spread of the pair beam generated by the shower, as a function of distance from the blazar itself. We then use linear and nonlinear kinetic theory to study the stability of the pair beam against the growth of electrostatic plasma waves, employing the Monte Carlo results for our quantitative estimates. We find that the fastest growing mode, like any perturbation mode with even a very modest component perpendicular to the beam direction, cannot be described in the reactive regime. Due to the effect of nonlinear Landau damping, which suppresses the growth of plasma oscillations, the beam relaxation timescale is found to be significantly longer than the inverse Compton loss time. Finally, density inhomogeneities associated with cosmic structure induce loss of resonance between the beam particles and plasma oscillations, strongly inhibiting their growth. We conclude that relativistic pair beams produced by blazars in the IGM are stable on timescales that are long compared with the electromagnetic cascades. There appears to be little or no effect of pair beams on the IGM.

Key words: gamma rays: general – instabilities – intergalactic medium – plasmas – radiation mechanisms: non-thermal – relativistic processes

Online-only material: color figures

1. INTRODUCTION

Streaming relativistic particles are common in tenuous astrophysical plasma and their propagation and stability properties are a recurrent theme. The examples include type III solar radio burst (Benz 1993), quasars' jets (Lesch & Schlickeiser 1987), cosmic rays streaming out of star-forming galaxies (Miniati & Bell 2011), and cosmic-ray transport in the intracluster medium (Ensslin et al. 2011). Propagation and stability properties, related in particular to the excitation of plasma waves, are a subject of attentive investigation as they can play a crucial role in the interpretation of observational data.

Ultrarelativistic beams of e^+e^- pairs are also generated in the intergalactic medium (IGM) by very high energy gamma rays from distant blazars by way of photon–photon interactions with the extragalactic background light (EBL; Gould & Schréder 1967; Schlickeiser et al. 2012). While blazars' spectra, and in particular their multi-TeV cutoff features, have been studied in detail to constrain the EBL (e.g., Aharonian et al. 2006), recently multi-GeV and TeV blazar observations have also been used to constrain magnetic field in cosmic voids for the first time (Neronov & Vovk 2010; Tavecchio et al. 2011). In fact, for a flat enough blazar spectra, the electromagnetic cascade should produce an observable spectral bump at multi-GeV energies. The absence of such a bump in a number of observed blazars is ascribed to the presence of a sufficiently strong magnetic field, $B_{\rm v} \gtrsim 10^{-16}$ G, to deflect the pairs in less than an inverse Compton length, $\ell_{\rm IC} \simeq {\rm Mpc}\,(E_\pm/{\rm TeV})^{-1}(1+z)^{-4}$, where z is the cosmological redshift (Plaga 1995; Neronov & Semikoz 2009). When the time variability of the blazars is taken into account, the above lower limit is relaxed to a more conservative value of $B_{\rm v} \gtrsim 10^{-18}$ G (Dermer et al. 2011; Taylor et al. 2011). The required filling factor of the magnetic field is about 60% (Dolag et al. 2011). Other potential effects of a magnetic field in voids on the electromagnetic cascades have also been investigated, including extended emission around gamma-ray point-like sources (Aharonian et al. 1994; Neronov & Semikoz 2007; Dolag et al. 2009; Elyiv et al. 2009; Neronov et al. 2010a) and the delayed echoes of multi-TeV gamma-ray flares or gamma-ray bursts (Plaga 1995; Takahashi et al. 2008; Murase et al. 2008; Murase 2009).

However, in principle the pair beam is subject to various instabilities, in particular microscopic plasma instabilities of the two-stream family. On this account, Broderick et al. (2012) conclude that transverse modes of the two-stream instability act on much shorter timescales than inverse Compton scattering, effectively inhibiting the cascade and invalidating the above magnetic field measurements. In addition, as a result of the beam's relaxation, a substantial amount of energy would be deposited into the IGM, with dramatic consequences for its thermal history (Chang et al. 2012; Pfrommer et al. 2012).

In this paper, we reanalyze the stability of blazar-induced ultrarelativistic pair beams. In particular, we use a Monte Carlo model of the electromagnetic shower to quantify the beam properties at various distances from the blazar, and analyze the stability of the produced beam following the work of Breizman, Rytov, and collaborators (reviewed in Breizman & Ryutov 1974; Breizman 1990). We find that even for very modest perpendicular components of the wavevector, the analysis of the instability requires a kinetic treatment. We thus estimate the maximum growth rate of the instability and find that for bright blazars (with an equivalent isotropic gamma-ray luminosity of

10^{45} erg s^{-1}) it is suppressed by Coulomb collisions at distances $D \gtrsim 50$ and 20 physical Mpc at redshifts 0 and 3, respectively. Importantly, the growth rate of plasma oscillations is found to be severely suppressed by nonlinear Landau damping so that even at closer distances to the blazar, the beam relaxation timescale remains considerably longer than the inverse Compton cooling time. Finally, the resonance condition cannot be maintained in the presence of density inhomogeneities associated with cosmological structure formation, which also act to dramatically suppress the instability. Thus, our findings support the magnetic field based interpretation of the gamma-ray observational results and rule out effects of the blazar beam on the thermal history of the IGM. Broderick et al. (2012) did not consider the role of density inhomogeneities and concluded that nonlinear Landau damping is unimportant, although they did not present a quantitative analysis of the process.

The rest of this paper is organized as follows. Section 2 summarizes the physical properties of pair beams produced by blazars and present the results of the Monte Carlo model. The two-stream instability in both the reactive and kinetic regimes is discussed in Section 3, where the maximum growth rate of the instability is also given and compared to the collisional rate. Nonlinear effects are considered in Section 4, where the timescales for the beam relaxation are derived. Finally, Section 5 briefly summarizes the results.

2. PAIR BEAMS IN VOIDS

In order to carry out the analysis of the stability of ultrarelativistic pair beams produced by blazars, we need to estimate characteristic quantities of the beam, including its density contrast to the IGM, the Lorentz factor, and the angular and velocity spread. These quantities are derived from the energy and number density of the pair producing photons, i.e., the blazar's spectral flux, F_γ, and the EBL model. Pair production has been studied extensively in the literature (e.g., Gould & Schréder 1967; Bonometto & Rees 1971; Schlickeiser et al. 2012) and in the following we briefly summarize its qualitative features, which we then use to describe the results of our Monte Carlo model of a blazar-induced cascade.

2.1. Basic Qualitative Features

Pairs are most efficiently created just above the energy threshold for production, i.e., where

$$s \equiv E_\gamma E_{\rm EBL}(1-\cos\phi)/2m_e^2c^4 \geqslant 1, \tag{1}$$

with ϕ the angle between the interacting photons, E_γ and $E_{\rm EBL}$ the energy of the incident and target EBL photon, respectively, and the relativistic invariant, s, the center of mass energy square in units $m_e^2c^4$. The mean free path for the process depends on the details of the EBL model (Kneiske et al. 2004; Franceschini et al. 2008) but is approximately

$$\ell_{\gamma\gamma} \simeq 0.8\left(\frac{E_\gamma}{\rm TeV}\right)^{-1}(1+z)^{-\zeta}\ {\rm Gpc}, \tag{2}$$

with $\zeta = 4.5$ for $z \leqslant 1$, $\zeta = 0$ otherwise (Neronov & Semikoz 2009; Broderick et al. 2012). The particle number density of the beam, n_b, is set by the balance of pair production rate, $2F_\gamma/\ell_{\gamma\gamma}$, evaluated close to production threshold, and energy loss rate. If inverse Compton losses dominate then, at a distance D from the blazar such that $F_\gamma = L_\gamma/4\pi D^2$,

$$n_b \simeq 2\frac{F_\gamma}{c}\frac{\ell_{\rm IC}}{\ell_{\gamma\gamma}} \simeq 3\times10^{-25}\,{\rm cm}^{-3}\left(\frac{E_\gamma L_\gamma}{10^{45}\,{\rm erg\,s}^{-1}}\right)\times\left(\frac{D}{\rm Gpc}\right)^{-2}\left(\frac{E_\gamma}{\rm TeV}\right)(1+z)^{\zeta-4}, \tag{3}$$

where $E_\gamma L_\gamma$ is an estimate of the blazar's equivalent isotropic gamma-ray luminosity for a source at distance D (see Broderick et al. 2012). Each pair particle carries about half the energy of the incident gamma ray, so the beam Lorentz factor is

$$\Gamma = \frac{E_\gamma}{2m_ec^2} \sim 10^6\left(\frac{E_\gamma}{\rm TeV}\right). \tag{4}$$

Another important characteristic quantity of the beam is its angular spread, $\Delta\theta$, determined by the distribution of angles θ between the pair produced particles and the parent photon's direction. This can be found to be related to Γ and the relativistic invariant as

$$\Delta\theta \leqslant \frac{s}{\Gamma}\left(1-\frac{1}{s}\right)^{\frac{1}{2}}. \tag{5}$$

2.2. Monte Carlo Model

In this section, we compute the characteristic quantities of a blazar-induced pair beam, using a Monte Carlo model of the electromagnetic cascade, fully described in Elyiv et al. (2009) and also applied in Neronov et al. (2010). For this purpose, the blazar's spectral emission is a typical power-law distribution of primary gamma-ray photons, $dn_\gamma/dE_\gamma \propto E_\gamma^{-q}$, in the range $10^3 \leqslant E_\gamma/m_ec^2 \leqslant 10^8$ and with $q = 1.8$ (Abdo et al. 2010). In addition, we use the *nominal* model of Aharonian (2001) for the EBL in the range 0.1–1000 μm. For the cosmic background radiations beyond 0.1 μm we used data from Hauser & Dwek (2001). Contrary to Elyiv et al. (2009), we did not consider the deflection of e^+e^- pairs in the extragalactic magnetic field as well as the inverse Compton interactions with cosmic microwave background (CMB) photons. Here we took into account pair distributions resulting from just the first double photon collisions. The energy distribution and cross section of the relevant reactions were taken from Aharonian (2003).

Given the primary gamma-ray photon spectrum, we generated random gamma–photon interaction events. These are characterized by the random distance from the blazar at which the double photon collision occurs based on the EBL dependent mean free path of the high-energy photons. Next, we randomly generated the energies $E_\pm$ of the produced e^+e^- pairs and evaluated the proper angle θ between each pair and the direction of the incident gamma-ray photon. For these quantities we used the analytical expressions for $\mu_e = \cos(\theta)$ in Schlickeiser et al. (2012).

The results of the calculation are shown in Figure 1 for a blazar with equivalent isotropic gamma-ray luminosity of 10^{45} erg s^{-1}. The top panel shows the spectral energy distribution of the production rate of the pairs at several distances from the blazar, ranging from 3.5 Mpc (top, black line) to 1 Gpc (bottom, yellow line). The bottom panel shows the peak (dashed line) and mean (solid line) energy of the generated pairs, in units of m_ec^2, as a function of distance from the blazar. The Lorentz factor of the pairs is a monotonically decreasing function of distance in the range $\Gamma = 10^5$–10^6 up to a Gpc away from the

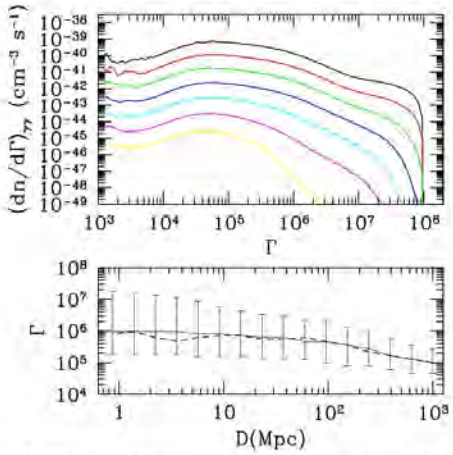

Figure 1. Top: energy distribution of the beam pairs generated at distances, from top to bottom, 3.5 (black), 9.1 (red), 23.3 (green), 60 (blue), 153 (cyan), 390 (magenta), and 1000 (yellow) Mpc from a blazar with equivalent isotropic gamma-ray luminosity of 10^{45} erg s^{-1}. Bottom: peak (dashed line) and mean (solid line) pair beam energy as a function of distance from the blazar for an equivalent isotropic gamma-ray luminosity of 10^{45} erg s^{-1}. The vertical bars correspond to 68% of the energy spread about the median.

(A color version of this figure is available in the online journal.)

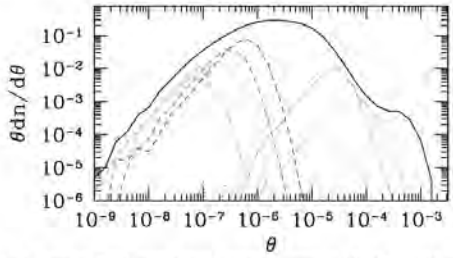

Figure 2. Angular distribution of beam pairs generated at 244 Mpc (solid curve) from the blazar. The colored curves, from right to left, indicate the contribution to the angular distribution from pairs in the energy range 10^3–2.1×10^3 (dotted green), 2.1×10^3–4.6×10^3 (dotted cyan), 4.6×10^3–10^4 (dotted red), and 10^4–2.15×10^4 (dotted blue), which dominate the large-angle end, and 10^6–2.1×10^6 (dash blue), 2.1×10^6–4.6×10^7 (dash red), 4.6×10^7–10^8 (dash cyan), and 10^8–2.15×10^8 (dash green), which dominate the small-angle end.

(A color version of this figure is available in the online journal.)

blazar. This shows that pair production typically peaks at near-infrared ($E_{\rm EBL} \simeq 0.1$ eV) EBL target photons interacting with gamma rays with energy $E_\gamma \sim (0.1$–$1)$ TeV. The vertical bars indicate the energy range encompassing 68% of the particles. In fact, there is considerable energy spread about the mean value, which decreases toward larger distances as the energy range of gamma-ray photons interacting with the EBL is also reduced. However, the beam particles always remain ultrarelativistic, a detail relevant in the analysis below.

Figure 2 shows the angular distribution of beam pairs at distances 244 Mpc (black dash) from the blazar. The beam angular spread is of order $\Delta\theta \simeq 10^{-5}$, consistent with Equation (5) and the value of Γ estimated above. The colored (dashed and dotted) curves show the angular distribution of pairs in eight different energy bins, indicating that the beam angular spread is primarily determined by pairs with $\Gamma \sim 10^4$–10^6.

Table 1
Beam Basic Properties from Monte Carlo Model

D (Mpc)	n_b (cm^{-3})	$\langle\Gamma^{-1}\rangle^{-1}$ (10^4)	$\langle\Gamma\rangle$ (10^5)	$\langle\Gamma^2\rangle/\langle\Gamma\rangle$ (10^6)	$\Delta\theta$ (10^{-5})
0.87	2.81e-18	1.52	1.56	5.65	6.43
1.39	1.17e-18	1.28	1.53	5.50	8.30
2.22	4.73e-19	1.48	1.52	5.13	6.06
3.55	1.79e-19	1.39	1.48	4.65	6.32
5.68	7.48e-20	1.32	1.39	4.01	7.07
9.09	2.93e-20	1.33	1.35	3.28	7.60
14.55	1.14e-20	1.35	1.28	2.55	7.75
23.28	4.48e-21	1.28	1.20	1.94	7.50
37.25	1.65e-21	1.30	1.13	1.50	7.29
59.60	5.25e-22	1.44	1.11	1.26	8.76
95.37	1.86e-22	1.39	1.00	0.99	9.14
152.59	6.31e-23	1.34	0.86	0.75	8.88
244.14	2.03e-23	1.27	0.72	0.52	9.67
390.63	6.13e-24	1.19	0.58	0.32	11.0
625.00	1.75e-24	1.12	0.47	0.18	11.0
1000.00	4.71e-25	1.04	0.39	0.12	11.8

The distribution that we use for the analysis of the pair beam stability below is the steady state one obtained by balancing the production rate given in Figure 1 with inverse Compton losses, i.e.,

$$f(\Gamma) = \int_0^\Gamma \frac{\tau_{\rm IC}(\varepsilon)}{\varepsilon} \left(\frac{dn(\varepsilon)}{d\varepsilon}\right)_{\gamma\gamma} d\varepsilon, \quad (6)$$

where $\tau_{\rm IC}(\Gamma) = \ell_{\rm IC}/c$ is the energy dependent timescale for inverse Compton losses.

In Table 1, we report as a function of distance, D, from the blazar, the main properties of the beam, which are relevant to the analysis below. These include the number density of the beam pairs, n_b; the mean value of the inverse of the pairs' Lorentz factor, $\langle\Gamma^{-1}\rangle^{-1}$, which enters the estimate of the maximum growth rate of the instability; the mean value of the pairs' Lorentz factor, $\langle\Gamma\rangle$, which determines the mean energy of the beam; the mean square value of the pairs' Lorentz factor divided by the mean value of the same, $\langle\Gamma^2\rangle/\langle\Gamma\rangle$, which enters the estimate of the inverse Compton timescale; and the rms of the opening angle of the pairs, $\Delta\theta$, which also enters the growth rate of the instability. These Lorentz gamma factors differ considerably, and they all monotonically decrease with distance as in the bottom panel of Figure 1.

Although the results in this and the next sections assume a blazar equivalent isotropic gamma-ray luminosity of 10^{45} erg s^{-1}, they can be generalized to other luminosities by rescaling the pair beam number density according to $n_b \to n_b(E_\gamma L_\gamma/10^{45}$ erg s$^{-1})$.

2.3. IGM in Voids

The analysis of the pair beam instability also depends on the thermodynamic properties of the plasma in cosmic voids, namely, the number density of free electrons and their temperature. The number density of free electrons can be expressed as $n_e \simeq 2 \times 10^{-7}(1+\delta)(1+z)^3$ cm^{-3}. The typical overdensity δ is taken to be the value at which the cumulative distribution of the IGM gas is 0.5. Using the simulation results presented in Section 4.2, and in particular the insets in Figure 9, we estimate as representative value for the voids $\delta_v = -0.9(1+z)$, where the redshift dependence is approximate but sufficient for our

purposes. Note that this implies a redshift evolution of the bulk IGM density in voids, $n_v \propto (1+z)^4$. As for the gas temperature, we assume $T_v \simeq$ a few $\times 10^3$ K $(1+z)^{1.5}$, which reproduces the IGM temperature at mean density of a few $\times 10^4$ at redshift 3. This redshift dependence, while again a rough approximation, is acceptable for our purposes.

3. BEAM INSTABILITY: REACTIVE VERSUS KINETIC

The blazar-induced pair beam is subject to microscopic instabilities, in particular two-stream-like instabilities, of both electrostatic and electromagnetic nature. The beam is neutrally charged so no return current is induced. In the following, we assume a sufficiently weak magnetic field, such that $\omega_H \ll \omega_p$, where ω_H is the cyclotron frequency, $\omega_p = (4\pi n_v e^2/m_e)^{1/2}$ is the plasma frequency of the IGM in voids, and e is the electron's charge. In this case, the instability is predominantly associated with Cherenkov emission of Langmuir waves, which operates under the resonant condition

$$\omega - \mathbf{k}\cdot\mathbf{v} = 0, \tag{7}$$

where $\mathbf{k}$ is the wavevector of the perturbation mode and $\mathbf{v}$ is the beam particle velocity. The pair particles contribute equally to the dielectric function as they have the same mass, number density, velocity distribution, and plasma frequency, $\omega_{p,b} = (4\pi n_b e^2/m_e)^{1/2}$. After separating the contributions from the background plasma and the beam particles, the dispersion relation for Langmuir waves, valid in the relativistic case, can be written as (Breizman 1990)

$$1 - \frac{\omega_p^2}{\omega^2} - \frac{4\pi e^2}{k^2}\int \frac{\mathbf{k}\cdot\partial f/\partial \mathbf{p}}{\mathbf{k}\cdot\mathbf{v}-\omega} d\mathbf{p} = 0, \tag{8}$$

where $f(\mathbf{p})$ is the distribution function of the beam particles. There are two important regimes that characterize the unstable behavior of the beam, namely, reactive and kinetic. In the reactive case, the beam's velocity spread, $\Delta\mathbf{v}$, is negligible so all particles can participate in the unstable behavior and the growth rate of the instability is therefore fastest. In the kinetic regime, on the other hand, the velocity spread is considerable and only the resonant particles contribute to the growth of Langmuir waves, so the growth rate is slower than in the reactive case. Formally, the reactive regime is applicable when (Breizman & Ryutov 1971)

$$|\mathbf{k}\cdot\Delta\mathbf{v}| \ll \gamma_r, \tag{9}$$

where γ_r is the reactive growth rate. In this case, the integral in Equation (8) can be solved in a simplified way, which involves neglect of the velocity spread around the mean value. This leads to the estimate of the reactive growth rate that, maximized along the longitudinal component of the wavevector, reads (Fainberg et al. 1970)

$$\gamma_r \simeq \omega_p \left(\frac{n_b}{\Gamma n_v}\right)^{\frac{1}{3}} \left(\frac{k_\parallel^2}{k^2\Gamma^2} + \frac{k_\perp^2}{k^2}\right)^{\frac{1}{3}}, \tag{10}$$

with $k_\parallel = \omega_p/v$ and $k_\parallel, k_\perp$ being the components of the wavevector parallel and perpendicular to the beam direction, respectively. It is well known that, for an ultrarelativistic beam ($\Gamma \gg 1$), the fastest growing modes in the reactive regime are those quasi-perpendicular to the beam. This is due to the large suppression caused by relativistic inertia along the longitudinal direction (Fainberg et al. 1970). However, as shown later, for quasi-perpendicular directions of the wavevector, the reactive regime is not applicable.

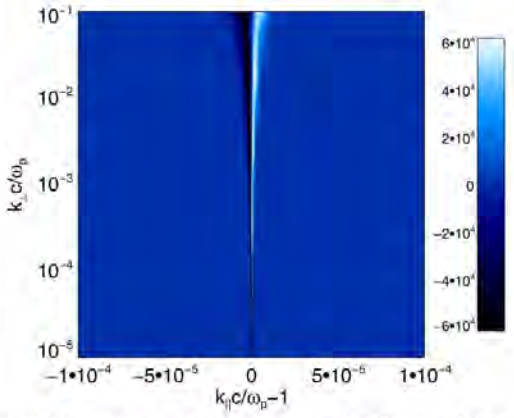

Figure 3. Normalized growth rate, $\gamma_k/\pi\omega_p(n_b/n_v)$, from Equation (12) in the plane $k_\parallel c/\omega_p - k_\perp c/\omega_p$. The bright region is positive, dark is negative, and the uniformly colored region is zero, as it lies outside the resonant region.
(A color version of this figure is available in the online journal.)

When the approximation (Equation (9)) is not valid, the growth rate is evaluated from a pole of the integrand in the dispersion relation (Equation (8)), namely,

$$\gamma_k = \omega_p \frac{2\pi e^2}{k^2}\int \mathbf{k}\cdot\frac{\partial f}{\partial \mathbf{p}}\,\delta(\omega_p - \mathbf{k}\cdot\mathbf{v})\,d\mathbf{p}. \tag{11}$$

If, as is the case here, despite the energy spread the particles remain ultrarelativistic and $|\mathbf{v}| = c$ can be assumed, the above integral can be simplified to (Breizman & Mirnov 1970)

$$\gamma_k = -\omega_p \pi \frac{n_b}{n}\left(\frac{\omega_p}{kc}\right)^3 \int_\mu^{\mu_+} d\mu \frac{2g + \left(\mu - \frac{k_\parallel c}{\omega_p}\right)\frac{\partial g}{\partial \mu}}{|(\mu_+ - \mu)(\mu - \mu_-)|^{\frac{1}{2}}}, \tag{12}$$

where the integration variable μ is the angle between the particles and the beam direction, and

$$\mu_\pm = (\omega_p/kc)\left(k_\parallel/k \pm k_\perp/k\sqrt{k^2c^2/\omega_p^2 - 1}\right), \tag{13}$$

$$g(\theta) = \frac{m_e c}{n_b}\int p f(p,\theta) dp \simeq \langle\Gamma^{-1}\rangle \frac{1}{\Delta\theta^2} e^{-\frac{\theta^2}{\Delta\theta^2}}. \tag{14}$$

The second equality for $g(\theta)$ in Equation (14) is found to be a good approximation based on results of the Monte Carlo model of the cascade. The integral for the growth rate in Equation (12) can be evaluated numerically. The *qualitative* behavior of the growth rate, γ_k, on the plane $k_\parallel$–$k_\perp$ is summarized in Figure 3 (Breizman & Ryutov 1971) for a beam at a Gpc from the blazar. Outside the narrow resonant region of k-space, corresponding in the plot to the uniform color, the growth rate is effectively null. In the narrow resonant region around $k_\parallel = \omega_p/c$, the growth can be positive (bright), negative (dark), and null, and for large enough values of $k_\perp$, it carries the sign of $\omega_p/k_\parallel - c$ (see below). Within the resonant region, the growth rate as a function of $k_\parallel$ has typically two extrema, a maximum and a minimum. This is shown in Figure 4 for values of $k_\perp$ of interest, i.e., where

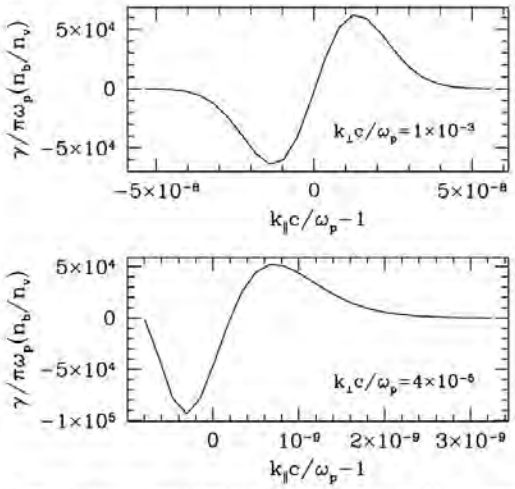

Figure 4. Normalized growth rate as a function of $k_\parallel c/\omega_p$ inside the resonant region for values of $k_\perp$ where γ_k reaches its maximum values.

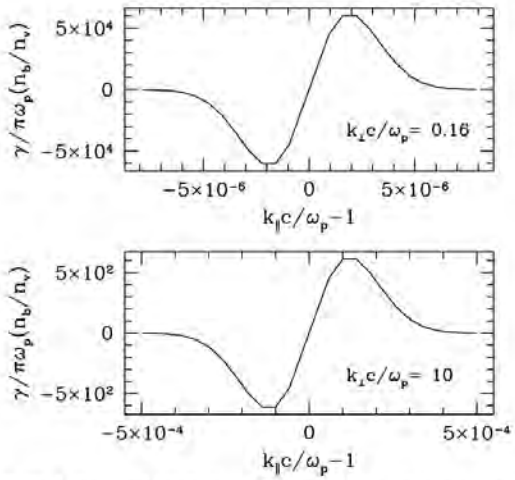

Figure 5. Normalized growth rate as a function of $k_\parallel c/\omega_p$ inside the resonant region for large values of $k_\perp$ where γ_k starts to drop compared with its maximum value.

γ_k reaches its maximum values. The growth rate has its largest values where $k_\perp c/\omega_p \lesssim 1$, and decays rapidly in the opposite limit. This can be seen from Figure 5 where γ_k is plotted for values of $k_\perp$ close to and much larger than ω_p/c (cf. scale of y-axis). Finally, we find that the growth rate, maximized with respect to $k_\parallel$ and as a function of $k_\perp$, can be well approximated by the following expression by Breizman & Ryutov (1971):

$$\gamma_k \simeq \omega_p \langle\Gamma^{-1}\rangle \frac{n_b}{n_v}\frac{1}{\Delta\theta^2}\frac{\omega_p^2}{\omega_p^2+k_\perp^2c^2}, \tag{15}$$

which we will be using in the following.

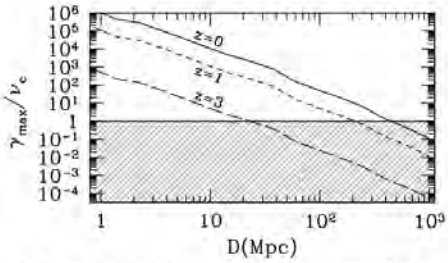

Figure 6. Ratio of instability maximum growth rate, $\gamma_{\max}$, to Coulomb collision rate, ν_c, for redshifts $z=0$ (solid curve), $z=1$ (short dashed curve), and $z=3$ (long dashed curve). The shaded area corresponds to the absolutely stable region where $\gamma_{\max} \lesssim \nu_c$.

3.1. Fastest Growing Modes versus Coulomb Collisions

For particles of an ultrarelativistic beam with modest angular spread, $\Delta\theta \ll 1$, we can assume $v_\parallel \simeq c$ and $v_\perp \simeq c\Delta\theta$. If the energy spread $\Delta E/E \lesssim 1$, then the longitudinal velocity spread of the beam is

$$\Delta v_\parallel \simeq c\frac{\Delta E}{\langle\Gamma\rangle^2 E} + c\Delta\theta^2. \tag{16}$$

Thus, for the angular spread and Lorentz factor characteristic of the blazar-induced beam, the longitudinal velocity spread is negligible with respect to the perpendicular velocity spread. It turns out that the first and second terms in Equation (16) are comparable to within a factor of a few, so for the sake of simplicity in the following we retain the second term only, neglecting any fudge factor. If we then use Equations (9) and (16), with the estimates for the beam angular spread and bulk Lorentz factor from the previous section, we find that virtually all modes require a kinetic description unless

$$\frac{k_\perp}{k} \lesssim \times 10^{-5}\left(\frac{n_b/n_v}{10^{-15}}\right)\left(\frac{\langle\Gamma\rangle}{10^5}\right)^{-1}\left(\frac{\Delta\theta}{10^{-5}}\right)^{-3}. \tag{17}$$

The maximum growth rate occurs at $k_\perp$ provided by the above estimate. For smaller values, we enter the reactive regimes and relativistic inertia increases. For larger values, we are in the kinetic regime where the growth rate decreases due to the increasing velocity spread along $\mathbf{k}$ although the decrease becomes significant only for $k_\perp \gtrsim \omega_p/c$. The fastest growth rate for modes with $k_\perp \lesssim \omega_p/c$ is therefore given by

$$\gamma_{\max} \simeq \omega_p\langle\Gamma^{-1}\rangle\frac{n_b}{n_v}\frac{1}{\Delta\theta^2} = 4\times10^{-12}\,\mathrm{s}^{-1}\left(\frac{n_v}{2\times10^{-8}\,\mathrm{cm}^{-3}}\right)^{-\frac{1}{2}} \times\left(\frac{\langle\Gamma^{-1}\rangle}{10^{-4}}\right)^{-1}\left(\frac{\Delta\theta}{10^{-4}}\right)^{-2}\left(\frac{D}{\mathrm{Gpc}}\right)^{-2}, \tag{18}$$

where we have taken $n_b \simeq 10^{-24}$ cm^{-3} at a Gpc from a blazar of luminosity $E_\gamma L_\gamma = 10^{45}$ erg s^{-1}. A basic condition for the growth of an instability is that its growth rate exceeds the collisional damping rate, i.e., $\gamma_{\max} \gg \nu_c$, where (Huba 2009)

$$\nu_c \simeq 10^{-11}\,\mathrm{s}^{-1}\left(\frac{n_v}{2\times10^{-8}\,\mathrm{cm}^{-3}}\right)\left(\frac{T_v}{3\times10^3\,\mathrm{K}}\right)^{-\frac{3}{2}}, \tag{19}$$

and for the Coulomb logarithm we have used $\Lambda_c = 27.4$ (Huba 2009). In Figure 6, we plot the ratio $\gamma_{\max}/\nu_c$ as a function of distance from the blazar, using the values reported in Table 1.

which again applies for a blazar of equivalent isotropic gamma-ray luminosity of 10^{45} erg s^{-1}. The solid, dashed, and long-dashed curves correspond to redshifts $z = 0$, $z = 1$, and $z = 3$, respectively. The redshift dependence is obtained by using the void average density and temperature redshift dependences discussed in Section 2.3, together with the redshift dependence of n_b given in Section 2.1. The shaded area corresponds to the region where the instability is inhibited by collisions. The plot shows that the instability can only develop at distances of less than a 50 Mpc at redshift $z = 0$ and about 20 physical Mpc $z = 3$.

4. BEAM STABILIZATION

As shown in the previous section, pair beams within a certain distance of the parent blazar may be unstable due to the excitation of Langmuir waves. In this section we further analyze these unstable conditions. In particular, we consider nonlinear effects on plasma waves due to scattering off thermal ions and density inhomogeneities. We begin, however, with a brief outline of the main features of the relaxation process (for a detailed description, see, e.g., Melrose 1989; Breizman & Ryutov 1974). An important assumption in what follows is that the level of plasma turbulence remains low compared to the plasma thermal energy so that a perturbative approach is valid. This will be verified at the end of the analysis.

The presence of excited plasma waves causes the beam particles to diffuse in momentum space. This continues until the particle momentum distribution has flattened, and Cherenkov emission ($\propto \partial f/\partial p$) is suppressed. According to the calculations of Grognard (1975), this process of quasilinear relaxation takes about 50–100 instability growth timescales to complete. In general, however, other processes occur that reduce the energy of resonant waves the particles interact with, thus stabilizing the beam. Spatial transport effects may contribute in two ways. On the one hand, waves drift along the energy density gradient at the group velocity, $v_g \simeq 3v_i^2/c$. For the case of interest here, this process is negligible due to the smallness of the group velocity and spatial gradients of the wave energy. In addition, however, if the plasma frequency is not constant in space due to plasma inhomogeneities, the wavevector will change in time, destroying the particle–wave resonant conditions. This effect turns out to be important and will be considered further below.

In the limit of weak turbulence, second-order effects can also play an important role (Melrose 1989; Breizman & Ryutov 1974). In short, these are described in terms of three-wave interactions and particle-wave scattering. Three-wave interactions involve, in addition to Langmuir waves, at least one electromagnetic wave because the frequency resonance condition cannot be fulfilled with three Langmuir waves alone. Compared with other processes discussed below, however, they are of order $k_B T/m_e c^2$, so they turn out to be negligible for the conditions of interest here. As for particle-wave scattering, Langmuir waves can undergo induced scattering either by electrons or ions, into either Langmuir waves or electromagnetic waves. The latter process is suppressed in the presence of inhomogeneities, so it will be neglected in the following. Furthermore, as we are considering waves with wavelength larger than the Debye length, the scattering by thermal ions is considerably more important than thermal electrons. This is because for thermal ions only, the superposed effects of the bare and shielding charge (basically an electron of opposite charge as the bare charge) do not cancel out due to the much larger mass of the ion compared with the electron. Therefore, with regard to second-order nonlinear effects in the following we only consider induced scattering off thermal ions.

4.1. Nonlinear Landau Damping

In this section, we consider in some detail the main process that we believe compensates the growth of Langmuir waves, i.e., induced scattering off plasma ions, also known as nonlinear Landau damping (Tsytovich & Shapiro 1965; Breizman et al. 1972; Lesch & Schlickeiser 1987). In this process, a thermal ion, with characteristic velocity v_{ti}, interacts with the beam wave produced by two Langmuir oscillations, $\omega(\boldsymbol{k})$, $\omega(\boldsymbol{k}')$, under the condition for Cherenkov interaction, i.e.,

$$\omega(\mathbf{k}) - \omega(\mathbf{k}') = (\mathbf{k} - \mathbf{k}') \cdot \mathbf{v}_{ti}. \tag{20}$$

The rate of induced scattering of Langmuir waves off thermal ions in a Maxwellian plasma with number density n and ion/electron temperature T_i/T_e, respectively, is (e.g., Melrose 1989)

$$\gamma_{\rm nl}(\mathbf{k}) = \frac{3(2\pi)^{\frac{1}{2}}}{2}\frac{T_i T_e}{(T_i+T_e)^2}\int \frac{d^3\mathbf{k}'}{(2\pi)^3}\frac{\hat{W}(k')}{nm_e v_{ti}} \times \left(\frac{\mathbf{k}\cdot\mathbf{k}'}{kk'}\right)^2 \frac{k'^2-k^2}{|\mathbf{k}'-\mathbf{k}|}\exp\left[-\frac{1}{2}\left(\frac{3}{2}\frac{v_{te}^2}{\omega_p v_{ti}}\frac{k'^2-k^2}{|\mathbf{k}'-\mathbf{k}|}\right)^2\right], \tag{21}$$

where $\hat{W}(k)$ indicates the spectral energy density of Langmuir waves. The growth rate, $\gamma_{\rm nl}(\mathbf{k})$, bears the sign of $(k'-k)$. This indicates that as a result of induced scattering, Langmuir waves cascade toward regions of phase space of lower wavevectors, i.e., lower energies, the energy difference being absorbed by the thermal ions. Eventually, the wave energy is transferred to modes with wavenumber, k, small enough that the wave phase-speed, $\omega/k > c$, exceeds the speed of light, and resonance with the beam particles is lost. The wavenumbers allowed in the scattering process are constrained by the integral expression in Equation (21). In particular, the following condition must be fulfilled:

$$\frac{|k'^2-k^2|}{|\mathbf{k}'-\mathbf{k}|} \leqslant \omega_p \frac{v_{ti}}{v_{te}^2} \simeq 35 \times \frac{\omega_p}{c}\left(\frac{T_{\rm v}}{3\times 10^3\,{\rm K}}\right)^{-\frac{1}{2}}. \tag{22}$$

The above constrain is satisfied for the case of differential scattering, i.e., $\Delta k/k \ll 1$, whereby $k \sim k'$ and $\mathbf{k}' \sim -\mathbf{k}$. In this case, Langmuir waves, generated with wavenumber, $k \sim \omega_p/c$, parallel to the beam, are isotropized. This reduces the level of resonant energy density by a factor $\sim\Delta\theta^2/4\pi$, somewhat increasing the lifetime of the beam. However, given the low temperature of the IGM in voids, the more efficient integral scattering, with $k' \ll k$, is also allowed. In this case, Langmuir waves are mostly kicked out of resonance in a single scattering event, dramatically reducing the level of resonant energy density and suppressing the instability.

The general solution for the evolution of the energy density in plasma waves is a non-trivial task as it requires solving for integro-differential equations that describe the detailed energy transfer of the wave energy across different modes. However, for a conservative estimate, we can neglect differential scattering and evaluate the rate of induced integral scattering from Equation (21) using the condition $k' \ll k$. We thus obtain

$$\gamma_{\rm nl} \simeq \omega_p \frac{W_{\rm nr}}{n_{\rm v} k_B T_{\rm v}}\frac{v_{te}^2}{v_{ti}\,c}, \tag{23}$$

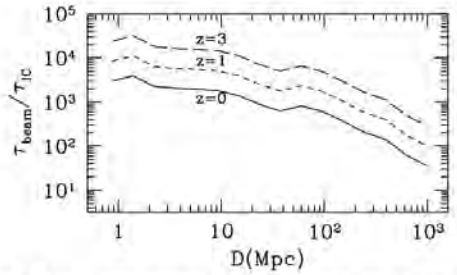

Figure 7. Ratio of beam relaxation timescale, τ_{beam}, to inverse Compton loss time, τ_{IC}, for redshifts $z = 0$ (solid line), $z = 1$ (short dashed line), and $z = 3$ (long dashed line).

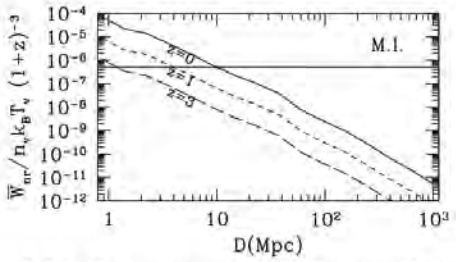

Figure 8. Ratio of non-resonant waves to thermal energy as a function of distance from our reference blazar for redshifts $z = 0$ (solid line), $z = 1$ (short dashed line), and $z = 3$ (long dashed line). The horizontal line corresponds to the threshold for the onset of the modulation instability.

where W_{nr} is the total energy density in Langmuir waves at $k \ll \omega_p/c$, i.e., non-resonant with the beam. This energy density is excited by the nonlinear scattering process and for the most part is dissipated by Coulomb collisions at a rate ν_c (see further discussion below). Thus it evolves according to

$$\frac{\partial W_{nr}}{\partial t} = 2\tilde{\gamma}_{nl} W_{nr} W_r - \nu_c W_{nr}, \tag{24}$$

where we have used $\tilde{\gamma}_{nl} \equiv \gamma_{nl}/W_{nr} = \omega_p(1/n_v k_B T_v)(v_{te}^2/v_{ll}c)$ and W_r is the total energy density in Langmuir waves at $k \sim \omega_p/c$, i.e., resonant with the beam. The latter obviously evolves according to

$$\frac{\partial W_r}{\partial t} = 2\gamma_{max} W_r - 2\tilde{\gamma}_{nl} W_{nr} W_r, \tag{25}$$

where we have neglected the role of collisions (i.e., we assume $\gamma_{max} \gg \nu_c$, as required for the existence of the instability). Equations (24) and (25) form a well-known Lotka–Volterra system of coupled nonlinear differential equations, which has stable periodic solutions, with the following average values for the energy densities:

$$\overline{W}_{nr} = \frac{\gamma_{max}}{\tilde{\gamma}_{nl}}, \quad \overline{W}_r = \frac{\nu_c}{2\tilde{\gamma}_{nl}}. \tag{26}$$

In this regime, the transfer rate of Langmuir waves out of resonance by nonlinear Landau damping equals on average their production rate, i.e., $\gamma_{nl} \simeq \gamma_{max}$. Thus, the beam emission of Langmuir waves is only linear in time, with an average power $P(W_r) = 2\overline{\gamma}_{max} W_r$, and the beam relaxation timescale at redshift $z = 0$ is

$$\tau_{beam} \simeq \frac{n_b \langle\Gamma\rangle m_e c^2}{2\gamma_{max}\overline{W}_r} = 1.5 \times 10^9\,\mathrm{yr}\left(\frac{n_v}{2\times 10^{-8}\,\mathrm{cm}^{-3}}\right)^{-1} \times \left(\frac{\langle\Gamma^{-1}\rangle}{10^{-4}}\right)\left(\frac{\langle\Gamma\rangle}{10^5}\right)\left(\frac{\Delta\theta}{10^{-4}}\right)^2\left(\frac{T_v}{3\times 10^3\,\mathrm{K}}\right). \tag{27}$$

The above timescale should be compared with the pairs' cooling time on the CMB, $\tau_{IC} = \ell_{IC}/c \simeq 3 \times 10^6 (E_\pm/\mathrm{TeV})^{-1}(1+z)^{-4}$ yr. The ratio of these timescales is plotted in Figure 7 using the values reported in Table 1 as a function of distance from our reference blazar with isotropic gamma-ray luminosity of 10^{45} erg s^{-1}. At redshift $z = 0$ (solid line), the beam appears to be stable on significantly longer timescales than the inverse Compton emission energy loss timescale, particularly within 100 Mpc from the blazar, where the average value of Γ of the pairs tends to be higher. This conclusion is reinforced at higher redshifts (dashed line for $z = 3$), where the redshift dependence is inferred as in Section 3.1.

The above analysis works in the weak turbulence regimes, which require that the energy density of resonant Langmuir waves be a small fraction of the beam energy density. For the typical values of IGM gas and beam parameters used above, this requirement is readily fulfilled as $\overline{W}_{nr}/n_b\Gamma m_e c^2 \simeq 3 \times 10^{-6}$, warranting our approach limited to second-order processes.

Another consistency check to be performed concerns the assumption of collisional dissipation of the long-wavelength Langmuir waves. In fact, accumulation of energy in these non-resonant waves can generate modulation instability of the background plasma if (Breizman 1990)

$$\frac{\overline{W}_{nr}}{n_v k_B T_v} \gtrsim k^2\lambda_D^2 \sim k_B T_v/mc^2. \tag{28}$$

In Figure 8, the ratio on the left-hand side of the above equation is plotted as a function of distance from our reference blazar using the values in Table 1. The solid line corresponds to redshift $z = 0$ and the horizontal line is the nominal threshold value for the onset of the modulation instability. For redshifts higher than $z = 0$, we plot for comparison with the same threshold line the same ratio on the left-hand side of Equation (28) but divided by a factor $(1+z)^3$ to account for the IGM temperature redshift dependence (see Section 2.3).

The plot shows that the assumption of collisional dissipation of the long-wavelength Langmuir waves is always valid except at short distances from low-redshift blazars. The modulation instability deserves more attention than the scope of the current paper can afford. Here we notice that, while the modulation instability could help stabilize the beam (Nishikawa & Ryutov 1976), it could also provide an effective dissipation rate that is more efficient than collisions. In this case, the level of energy density of resonant waves, W_r, will increase with consequent reduction of the beam lifetime (see Equations (26) and (27)). However, because the threshold condition for triggering the modulation instability depends quadratically on the temperature (see Equation (28)), should the background plasma suffer even modest heating caused by the beam relaxation, the modulation instability will quickly stabilize, restoring the conditions for collisional dissipation of the non-resonant waves.

Therefore, in conclusion, from the above analysis together with the findings in Section 3.1, it appears that the beam is stable at basically all relevant distances from the blazar, and the beam

instability plays only a secondary role on the electromagnetic shower, the beam dynamics, and the thermal history of the IGM.

4.2. Plasma Inhomogeneities

In addition to the kinetic effects described above, the energy density of the plasma waves evolves in time due to spatial gradient effects according to (Kaplan & Tsytovich 1973)

$$\frac{d}{dt}\hat{W}(x,t,k) = \frac{\partial \hat{W}}{\partial t} + \mathbf{v}_g \nabla_{\mathbf{x}} \hat{W} - \nabla_{\mathbf{x}}\omega \cdot \nabla_{\mathbf{k}} \hat{W}. \quad (29)$$

where for the rate of change of the wavevector we have used the equation of geometric optics

$$\frac{d\mathbf{k}}{dt} = -\nabla_{\mathbf{x}}\omega. \quad (30)$$

The first and second terms on the right-hand side of Equation (29) describe, as usual, explicit time dependence and the effects of spatial gradients discussed at the beginning of Section 4. The last term describes the change in $\hat{W}$ associated with modifications of the waves' wavevector as a result of inhomogeneities. This term is important because, just like induced scattering by thermal ions, it transfers the excited Langmuir waves to wavemodes that are out of resonance with the beam particles, therefore suppressing the instability (Breizman & Ryutov 1971; Nishikawa & Ryutov 1976).

For Langmuir waves, the most important contribution to $\nabla_{\mathbf{x}}\omega$ comes from density inhomogeneities. In addition, the beam stabilization mainly results from changes in the longitudinal component of the wavevector. Therefore, we restrict our analysis to this case only, and write

$$\frac{dk_\parallel}{dt} \simeq \frac{1}{2}\frac{\omega_p}{\lambda_\parallel}, \quad (31)$$

with $\lambda_\parallel = n_\vee/(\bar{\nabla} n_\vee)_\parallel$, the length scale of the density gradient along the beam.

In order to estimate the scale lengths of IGM density gradients, λ, we have carried out a cosmological simulation of structure formation including hydrodynamics, dark matter, and self-gravity as described in Miniati & Colella (2007). For the cosmological model, we adopted a flat ΛCDM universe with the following parameters: total mass density, normalized to the critical value for closure, $\Omega_m = 0.2792$; normalized baryonic mass density, $\Omega_b = 0.0462$; normalized vacuum energy density, $\Omega_\Lambda = 1 - \Omega_m = 0.7208$; Hubble constant $H_0 = 70.1$ km s^{-1} Mpc^{-1}; spectral index of primordial perturbation, $n_s = 0.96$; and rms linear density fluctuation within a sphere of comoving radius of 8 h^{-1} Mpc, $\sigma_8 = 0.817$, where $h \equiv H_0/100$ (Komatsu et al. 2009). The computational box has a comoving size $L = 50\,h^{-1}$ Mpc, which is discretized with 512^3 comoving cells, corresponding to a nominal spatial resolution of 100 h^{-1} comoving kpc. The collisionless dark matter component is represented with 512^3 particles with mass $6 \times 10^5\, h^{-1}\, M_\odot$.

Figure 9 shows the range of scale lengths of IGM density gradients as a function of IGM gas overdensity for three different cosmological redshifts, $z = 0$ (top), $z = 1$ (middle), and $z = 3$ (bottom). Accordingly, the distance covered by the beam particles during the fastest growth time, $\sim c\gamma_{\max}^{-1} \simeq 1$ kpc, is much shorter than the typical scale length of density gradients. This corresponds to the case of regular, as opposed to random, inhomogeneities.

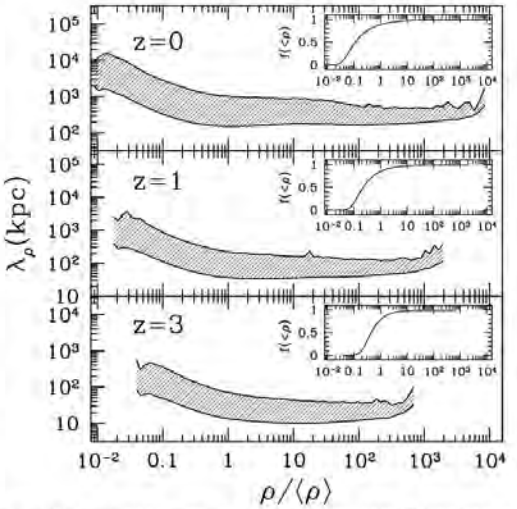

Figure 9. Characteristic length scale of density gradient in the IGM as a function of IGM gas overdensity. The shaded area covers ±1 root-mean-squared value about the average. The inset shows the gas cumulative distribution as a function of overdensity.

It is clear that in order for the excited waves to have an effect on the beam, the beam–wave interaction under resonant conditions must continue for a sufficiently long time. Therefore, the condition for wave excitation is expressed as (Breizman & Ryutov 1971)

$$\gamma_{\max}\frac{\Delta k_\parallel}{|dk_\parallel/dt|} = \gamma_{\max}\frac{2\lambda_\parallel \Delta k_\parallel}{\omega_p} > \Lambda_c, \quad (32)$$

where Λ_c is the Coulomb logarithm and $\Delta k_\parallel$ the change in longitudinal component of the wavevector allowed by the resonant condition (Equation (7)). Using Equation (7) (and neglecting the term $\Delta E/E\,\Gamma^2$) to obtain $\Delta k_\parallel \lesssim (\omega_p/c)\Delta\theta^2 + k_\perp \Delta\theta$, Equation (32) can be solved to express the condition for wave excitation in terms of $\lambda_\parallel$, i.e.,

$$\lambda_\parallel \gtrsim \frac{c}{2\omega_p}(\Gamma^{-1})\frac{n_\vee}{n_b}\Lambda_c\left(1 + \frac{k_\perp}{k_\parallel \Delta\theta}\right)^{-1} > 10^6\,\mathrm{kpc} \times \left(\frac{D}{\mathrm{Gpc}}\right)^2 \left(\frac{(\Gamma^{-1})}{10^{-4}}\right)\left(\frac{\Delta\theta}{10^{-4}}\right)\left(\frac{\Lambda_c}{30}\right)(1+z)^2, \quad (33)$$

where in the second inequality we have used $\kappa_\perp \simeq \kappa_\parallel$, which corresponds to the most favorable case for the instability growth in the presence of inhomogeneities, and again the redshift dependence is derived as described in Section 3.1. We can again plot the minimal values of $\lambda_\parallel$ allowed for the growth of the beam instability using the parameter values for the beam from Table 1. This is shown by the oblique lines in Figure 10 for redshifts $z = 0$ (solid line), $z = 1$ (dashed line), and $z = 3$ (long dashed line). For the same redshifts (and with line-style matching that of the corresponding oblique lines), the three horizontal thin lines represent the mean scale length of density inhomogeneities at typical void overdensity (i.e., where the cumulative gas distribution function is 0.5), extracted from Figure 9. The figure shows that the growth of Langmuir waves

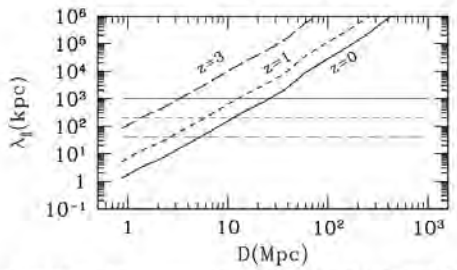

Figure 10. Oblique line corresponds to minimal values of $\lambda_{\parallel}$ allowed for the growth of the beam instability as a function of distance from the blazar obtained using values in Table 1. The horizontal thin lines correspond to the mean scale length of density inhomogeneities at typical void overdensity (i.e., where the cumulative gas distribution function is 0.5), extracted from Figure 9. The solid, dashed, and long dashed lines correspond to redshifts $z = 0$, $z = 1$, and $z = 3$, respectively.

is constrained by the presence of inhomogeneities, to distances $D < 30, 6,$ and1 Mpc from the blazar, for $z = 0, 1,$ and 3, respectively. Inhomogeneities provide another independent argument against the growth of Langmuir waves and the unstable behavior of the pair beam. While nonlinear Landau damping weakens with distance from the blazar (see Figure 6), the impact of inhomogeneities becomes stronger (see Figure 10), so that the stabilization effects of the two processes compensate each other at different distances.

5. CONCLUSION

We have considered the stability properties of a low-density ultrarelativistic pair beam produced in the IGM by multi-TeV gamma-ray photons from blazars. The physical properties of the pair beam are determined through a Monte Carlo model of the electromagnetic cascade. The stability analysis is based on linear and nonlinear kinetic plasma theory. In summary, we find that the combination of kinetic effects, nonlinear Landau damping, and density inhomogeneities appear to considerably stabilize blazar-induced ultrarelativistic beams over the inverse Compton loss timescale, so that the electromagnetic cascade remains mostly unaffected by the beam instability. This implies that the lack of a bumpy feature at multi-GeV energies in the gamma-ray spectrum of distant blazars cannot be attributed to such instabilities and can in principle be related to the presence of an intergalactic magnetic field. Finally, heating of the IGM by pair beams appears negligible.

We are thankful to an anonymous referee for valuable comments on the manuscript. F.M. acknowledges useful discussions with B. N. Breizman and A. Benz, and comments from D. D. Ryutov and R. Schlickeiser. We are grateful to D. Potter for making `grafic++` package available for cosmological initial conditions. This work was supported by a grant from the Swiss National Supercomputing Center (CSCS) under Project ID S275.

REFERENCES

Abdo, A., Ackermann, M., Ajello, M., et al. 2010, A&A, 710, 1271
Aharonian, F. A., Coppi, P. S., & Volk, H. J. 1994, ApJL, 423, L5
Aharonian, F. A. 2001, arXiv:astro-ph/0112314
Aharonian, F. A. 2003, Very High Energy Cosmic Gamma Radiation (Singapore: World Scientific)
Aharonian, F. A., Akhperjanian, A. G., Bazer-Bachi, A. R., et al. 2006, Natur, 440, 1018
Benz, A. 1993, Plasma Astrophysics (Kluwer: Dordrecht)
Bonometto, S., & Rees, M. R. 1971, MNRAS, 152, 21
Breizman, B. N. 1990, RvPP, 15, 61
Breizman, B. N., & Mirnov, V. V. 1970, Ge&Ae, 10, 34
Breizman, B. N., & Ryutov, D. D. 1971, JETP, 33, 220
Breizman, B. N., & Ryutov, D. D. 1974, NucFu, 14, 873
Breizman, B. N., Ryutov, D., & Chebotaev, P. Z. 1972, JETP, 35, 72
Broderick, A. E., Chang, P., & Pfrommer, C. 2012, ApJ, 752, 22
Chang, P., Broderick, A. E., & Pfrommer, C. 2012, ApJ, 752, 23
Dermer, C. D., Cavadini, M., Razzaque, S., et al. 2011, ApJL, 733, L21
Dolag, K., Kachelrieß, M., Ostapchenko, S., & Tomas, R. 2009, ApJ, 703, 1078
Dolag, K., Kachelriess, M., Ostapchenko, S., & Tomàs, R. 2011, ApJL, 727, L4
Elyiv, A., Neronov, A., & Semikoz, D. V. 2009, PhRvD, 80, 023010
Ensslin, T. A., Pfrommer, C., Miniati, F., & Subramanian, K. 2011, A&A, 527, A99
Fainberg, Ya. B., Shapiro, V. D., & Shevchenko, V. I. 1970, JETP, 30, 528
Franceschini, A., Rodighiero, G., & Vaccari, M. 2008, A&A, 487, 837
Gould, R. J., & Schréder, G. P. 1967, PhRvL, 16, 252
Grognard, R. J.-M. 1975, AuJPh, 28, 731
Hauser, M., & Dwek, E. 2001, A&A, 39, 249
Huba, J. D. 2004, NRL Plasma Formulary, NRL/PU/679009-523 (Washington, DC: Naval Research Laboratory)
Kaplan, S. A., & Tsytovich, V. N. 1973, Plasma Astrophysics (Oxford: Pergamon)
Kneiske, T. M., Bretz, T., Mannheim, K., & Hartmann, D. H. 2004, A&A, 413, 807
Komatsu, E., Dunkley, J., Nolta, M. R., et al. 2009, ApJS, 180, 330
Lesch, H., & Schlickeiser, R. 1987, A&A, 179, 93
Melrose, D. B. 1989, Instabilities in Space and Laboratory Plasmas (Cambridge: Cambridge Univ. Press)
Miniati, F., & Bell, A. R. 2011, ApJ, 729, 73
Miniati, F., & Colella, P. 2007, JCoPh, 227, 400
Murase, K. 2009, PhRvL, 103, 081102
Murase, K., Takahashi, K., Inoue, S., Ichiki, K., & Nagataki, S. 2008, ApJL, 686, L67
Neronov, A., & Semikoz, D. V. 2007, JETP Lett., 85, 473
Neronov, A., & Semikoz, D. 2009, PhRvD, 80, 123012
Neronov, A., Semikoz, D., Kachelriess, M., Ostapchenko, S., & Elyiv, A. 2010, ApJL, 719, L130
Neronov, A., & Vovk, I. 2010, Sci, 328, 7
Nishikawa, K., & Ryutov, D. D. 1976, JPSJ, 41, 1757
Pfrommer, C., Chang, P., & Broderick, A. E. 2012, ApJ, 752, 24
Plaga, R. 1995, Natur, 374, 430
Schlickeiser, R., Elyiv, A., Ibscher, D., & Miniati, F. 2012, ApJ, 758, 101
Takahashi, K., Murase, K., Ichiki, K., Inoue, S., & Nagataki, S. 2008, ApJL, 687, L5
Tavecchio, F., Ghisellini, G., Bonnoli, G., & Foschini, L. 2011, MNRAS, 414, 3566
Taylor, A. M., Vovk, I., & Neronov, A. 2011, A&A, 529, A144
Tsytovich, V. N., & Shapiro, V. D. 1965, NucFu, 5, 228

The Astrophysical Journal, 758:101 (18pp), 2012 October 20 doi:10.1088/0004-637X/758/2/101

THE PAIR BEAM PRODUCTION SPECTRUM FROM PHOTON–PHOTON ANNIHILATION IN COSMIC VOIDS

R. Schlickeiser[1,2], A. Elyiv[3,4], D. Ibscher[1], and F. Miniati[5]
[1] Institut für Theoretische Physik, Lehrstuhl IV: Weltraum- und Astrophysik, Ruhr-Universität Bochum, D-44780 Bochum, Germany; rsch@tp4.rub.de, ibscher@tp4.rub.de
[2] Research Department Plasmas with Complex Interactions, Ruhr-Universität Bochum, D-44780 Bochum, Germany
[3] Institut d'Astrophysique et de Géophysique, Université de Liège, B-4000 Liège, Belgium; elyiv@astro.ulg.ac.be
[4] Main Astronomical Observatory, Academy of Sciences of Ukraine, 27 Akademika Zabolotnoho St., 03680 Kyiv, Ukraine
[5] Physics Department, Wolfgang-Pauli-Strasse 27, ETH-Zürich, CH-8093 Zürich, Switzerland; fm@phys.ethz.ch
Received 2012 May 27; accepted 2012 August 26; published 2012 October 5

ABSTRACT

Highly beamed relativistic $e^{\pm}$-pair energy distributions result in double photon collisions of the beamed gamma rays from TeV blazars at cosmological distances with the isotropically distributed extragalactic background light (EBL) in the intergalactic medium. The typical energies $k_0 \simeq 10^{-7}$ in units of $m_e c^2$ of the EBL are more than 10 orders of magnitude smaller than the observed gamma-ray energies $k_1 \geqslant 10^7$. Using the limit $k_0 \ll k_1$, we demonstrate that the angular distribution of the generated pairs in the lab frame is highly beamed in the direction of the initial gamma-ray photons. For the astrophysically important case of power-law distributions of the emitted gamma-ray beam up to the maximum energy M interacting with Wien-type $N(k_0) \propto k_0^q \exp(-k_0/\Theta)$ soft photon distributions with total number density N_0, we calculate analytical approximations for the electron production spectrum. For distant objects with luminosity distances $d_L \gg r_0 = (\sigma_T N_0)^{-1} = 0.49 N_0^{-1}$ Mpc (with Thomson cross section σ_T), the implied large values of the optical depth $\tau_0 = d_L/r_0$ indicate that the electron production spectra differ at energies inside and outside the interval $[(\Theta \ln \tau_0)^{-1}, \tau_0/\Theta]$, given the maximum gamma-ray energy $M \gg \Theta^{-1}$. In the case $M \gg \Theta^{-1}$, the production spectrum is strongly peaked near $E \simeq \Theta^{-1}$, being exponentially reduced at small energies and decreasing with the steep power law $\propto E^{-1-p}$ up to the maximum energy $E = M - (1/2)$.

Key words: cosmic rays – diffuse radiation – gamma rays: general – radiation mechanisms: non-thermal – relativistic processes

1. INTRODUCTION

Intergalactic space is transparent to radiation in most of the electromagnetic spectrum. However, gamma rays above GeV energies cannot travel cosmological distances (Aharonian et al. 1994; Neronov & Vovk 2010) as they are converted into electron–positron pairs, $e^{\pm}$, by way of photon–photon interactions with the extragalactic background light (EBL). The mean free path for a gamma-ray photon with energy E_γ is roughly $l_{\gamma\gamma} \sim 80(E_\gamma/10\,\mathrm{TeV})^{-1}(1+z)^{-\xi}$ Mpc, with $\xi = 4.5$ for redshifts $z \leqslant 1$, $\xi = 0$ otherwise (Kneiske et al. 2004; Franceschini et al. 2008; Neronov & Semikoz 2009), and the exact value depending on the uncertain details of the EBL. This photon absorption process produces a cutoff in the multi-TeV part of the radiation spectrum of distant blazars, a subclass of active galactic nuclei with high-energy photon emission from relativistic jet emission preferentially aligned to the observer's line of sight. Figure 1 depicts the physical situation.

Currently, about 30 blazars with strong TeV photon emission have been detected by the new generation of air Cherenkov TeV γ-ray telescopes such as H.E.S.S., MAGIC, and VERITAS (Hinton & Hofmann 2009). The most distant ones are 3C66A at redshift $z = 0.444$ and 1ES 0414+009 (Abramowski et al. 2012) at redshift $z = 0.287$. Any blazars more distant than $z = 0.16$ produce energetic pair beams.

The study of blazars at TeV energies provides important constraints on the properties of the EBL (Aharonian et al. 2006); it can also be used to probe magnetic fields in cosmic voids (Neronov & Vovk 2010). Each particle of the initially gamma ray produced $e^{\pm}$ pair beam carries about half the energy of the parent gamma ray. Those pairs with typical Lorentz factors $\gamma = 10^6\gamma_6$ are expected to inverse Compton (IC) scatter on the cosmic microwave background (CMB) radiation, on a typical length scale $l_{\mathrm{IC}} \sim 0.75\gamma_6^{-1}(1+z)^{-4}$ Mpc, thus producing gamma rays with energy of the order of 100 GeV. Given the still relatively short IC interaction length l_{IC}, both pair production and IC emission occur primarily in cosmic voids, which fill most of the cosmic volume. The IC-scattered gamma rays then are still energetic enough for further pair production interactions, which give rise to a full electromagnetic cascade. Knowing the initial blazar's photon spectrum and the EBL, the full electromagnetic cascade can be computed. The total multi-GeV flux, from both the intrinsic and cascade components, contributes to the point-source emission, provided no magnetic field deflects the $e^{\pm}$ pairs on the distance ℓ_{IC}.

However, the pair beam is subject to two-stream-like instabilities of both electrostatic and electromagnetic nature. It has been argued that in this case the cascade would not contribute to the multi-GeV flux and the pair beam energy would be transferred to the intergalactic medium (IGM) with important consequences for its thermal history (Broderick et al. 2012). Another possibility is that the instability saturates early on due to nonlinear effects, leaving a marked footprint on the energy distribution of the beam particles. This has important observational consequences for the cascade (Schlickeiser et al. 2012).

In the first part of this study, we investigate in detail the relaxation of charged pair beams generated by beamed blazar TeV gamma-ray emission in the partially ionized electron–proton IGM. We show that the angular distribution of the generated pairs is highly beamed along the direction of the incoming gamma rays. The analytical form of the energy spectrum of beamed pairs is determined and compared with numerical simulation results. We also demonstrate that the final pair energy distribution is relatively narrow and peaks at $m_e c^2/\Theta$, where

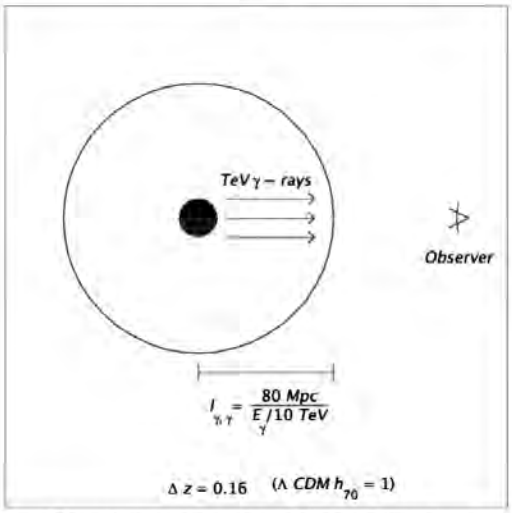

Figure 1. Intergalactic pair beam production: TeV photons from any blazar more distant than $z = 0.16$ produce relativistic pairs by double photon collisions with the EBL soft photons. The mean free path for a gamma-ray photon $l_{\gamma\gamma} \sim 80(E_\gamma/10\,\mathrm{TeV})^{-1}$ Mpc has been converted to a redshift adopting a ΛCDM universe with the Hubble constant $H_0 = 70\,h_{70}$ km s^{-1} Mpc^{-1}.

Θmc^2 with $\Theta \ll 1$ denotes the mean energy of the soft target photons.

Using these and other results from this paper, in the second part of this project (Schlickeiser et al. 2012) we calculate the maximum linear growth rates of the obliquely propagating electrostatic waves and the aperiodic filamentation instability.

The rest of the paper is organized as follows: In Sections 2–4, we derive the injected pair distribution function from the double-photon pair production of blazar gamma radiation with the EBL. The single gamma-ray pair production optical depth is calculated in Section 5. In Sections 6–8, we analytically calculate the electron pair production energy spectrum, starting from the general expression for arbitrary input blazar gamma-ray spectra and arbitrary EBL photon spectra (Section 6), and then specializing to power-law-distributed gamma rays and Wien-type soft photon distributions (Section 7). In Section 8, we provide the pair production spectra in different energy regimes. The results are summarized in Sections 9 and 10.

2. RELATIVISTIC KINEMATICS OF PAIR PRODUCTION BY DOUBLE PHOTON COLLISION

The rest frame of the IGM is chosen as the laboratory (lab) frame. Photon and particle energies and momenta are defined in units of $m_e c^2$ and m_{ec}, respectively. A high-energy ($k_1 \gg 1$) gamma ray with four-momentum $P_1 = k_1(1, \boldsymbol{e}_1)$, where the unit vector $\boldsymbol{e}_1$ defines its direction, interacts with a soft ($k_2 \ll 1$) photon of the EBL with four-momentum $P_2 = k_2(1, \boldsymbol{e}_2)$. The four-momenta of the produced positron and negatron are $P_+ = (E_+, \boldsymbol{p}_+)$ and $P_- = (E_-, \boldsymbol{p}_-)$, respectively, with $E_\pm^2 = p_\pm^2 + 1$.

As usual (Hagedorn 1973) we also introduce the center-of-momentum (CM) frame, defined by

$$k_1^* \boldsymbol{e}_1^* + k_2^* \boldsymbol{e}_2^* = 0. \tag{1}$$

Using the Lorentz invariance of scalar products of four-vectors, we calculate the invariant as

$$s = \frac{1}{4}(P_1 + P_2)^2 = \frac{1}{4}(P_1^* + P_2^*)^2 = \frac{k_1 k_2}{2}(1 - \mu) = \frac{1}{4}(k_1^* + k_2^*)^2, \tag{2}$$

with $\mu = \cos\theta = \boldsymbol{e}_1 \cdot \boldsymbol{e}_2$, where θ denotes the angle between the two photon directions in the lab frame. For head-on ($\mu = -1$) collisions, the invariant s attains its maximum value $s_m = k_1 k_2$. The threshold energy for the creation of pairs in the CM frame is $E_{\mathrm{th}}^* = 2$ and requires values of $s \geqslant 1$, providing in the laboratory frame

$$k_1 k_2 \geqslant 1. \tag{3}$$

Pair production then occurs for values of

$$1 \leqslant s \leqslant s_m = k_1 k_2. \tag{4}$$

Energy and momentum conservation of the $\gamma_1 + \gamma_2 \rightarrow e_+ + e_-$ interaction in the CM-frame require

$$k_1^* + k_2^* = E_+^* + E_-^* \tag{5}$$

and $\boldsymbol{p}_+^* + \boldsymbol{p}_-^* = 0$. The last relation provides

$$\boldsymbol{p}_+^* = -\boldsymbol{p}_-^* = \boldsymbol{p}_0^* = p_0^* \boldsymbol{e}_0^*, \tag{6}$$

so that $E_+^* = E_-^* = E_0^*$ are equal. With Equations (1) and (2), condition (5) then becomes

$$E_0^* = \frac{k_1^* + k_2^*}{2} = s^{1/2}, \tag{7}$$

implying $p_0^* = \sqrt{E_0^{*2} - 1} = \sqrt{s - 1}$, so that

$$\boldsymbol{p}_+^* = -\boldsymbol{p}_-^* = \boldsymbol{p}_0^* = \sqrt{s-1}\,\boldsymbol{e}_0^*. \tag{8}$$

The CM velocity as seen from the laboratory frame is

$$\boldsymbol{\beta}_{\mathrm{CM}} = \frac{k_1 \boldsymbol{e}_1 + k_2 \boldsymbol{e}_2}{k_1 + k_2}, \tag{9}$$

so that

$$\beta_{\mathrm{CM}}^2 = \frac{k_1^2 + k_2^2 + 2k_1 k_2 \mu}{(k_1 + k_2)^2} = 1 - \frac{2k_1 k_2(1 - \mu)}{(k_1 + k_2)^2} \tag{10}$$

and

$$\gamma_{\mathrm{CM}} = \left(1 - \beta_{\mathrm{CM}}^2\right)^{-1/2} = \left[\frac{(k_1 + k_2)^2}{2k_1 k_2(1 - \mu)}\right]^{1/2}. \tag{11}$$

So far, all relations are exact and no approximations have been made.

Given that the EBL photon energies $k_2 \ll 1$ are very small, the threshold condition (3) requires $k_1 \geqslant k_2^{-1} \gg 1$. We therefore approximate relation (10) by (Bonometto & Rees 1971; Aharonian et al. 1983; Cerutti et al. 2009)

$$\beta_{\mathrm{CM}}^2 \simeq 1 - \frac{2k_1 k_2(1 - \mu)}{k_1^2} = 1 - \frac{4s}{k_1^2}, \tag{12}$$

providing

$$\beta_{\mathrm{CM}} \simeq \beta_C \equiv \sqrt{1 - \frac{4s}{k_1^2}}, \quad \gamma_{\mathrm{CM}} \simeq \gamma_C = \frac{k_1}{2s^{1/2}}$$

and

$$\beta_{\rm CM}\gamma_{\rm CM} \simeq \sqrt{(\gamma_C - 1)(\gamma_C + 1)}, \quad (13)$$

where we used the invariant (2).[6] With the same approximation $k_1 \gg k_2$, Equation (9) provides $\boldsymbol{\beta}_{\rm CM} \parallel \boldsymbol{e}_1$, i.e.,

$$\boldsymbol{\beta}_{\rm CM} \simeq \beta_C \boldsymbol{e}_1 = \sqrt{1 - \frac{4s}{k_1^2}}\,\boldsymbol{e}_1, \quad (14)$$

so that the CM frame propagates along the same direction as the high-energy gamma ray. This implies that the gamma-ray direction is unchanged $\boldsymbol{e}_1 = \boldsymbol{e}_1^*$ in the two frames of reference.

Finally we have to calculate the pair energies and momentum vectors in the laboratory frame with the appropriate Lorentz transformations of Equations (6) and (7). For the pair energies we obtain

$$\begin{aligned} E_\pm &= \gamma_C[E_0^* \pm \boldsymbol{\beta}_C \cdot \boldsymbol{p}_0^*] \\ &= \frac{k_1}{2s^{1/2}}\left[s^{1/2} \pm \left(1 - \frac{4s}{k_1^2}\right)^{1/2}(s-1)^{1/2}\boldsymbol{e}_1 \cdot \boldsymbol{e}_0^*\right] \\ &= \frac{k_1}{2}[1 \pm F(s,k_1)\mu_e^*] \end{aligned} \quad (15)$$

with

$$F(s,k_1) = \left(\left(1 - \frac{4s}{k_1^2}\right)\left(1 - \frac{1}{s}\right)\right)^{1/2} \quad (16)$$

and $\mu_e^* = \boldsymbol{e}_1 \cdot \boldsymbol{e}_0^* = \boldsymbol{e}_1^* \cdot \boldsymbol{e}_0^*$ denoting the cosine of the angle between the positron and the incoming gamma ray in the CM system. Equation (15) readily yields the relation

$$\mu_e^* = \pm\frac{\frac{2E_\pm}{k_1} - 1}{F(s,k_1)}, \quad (17)$$

Likewise

$$\begin{aligned} \boldsymbol{p}_\pm &= \boldsymbol{p}_\pm^* + \boldsymbol{\beta}_C\gamma_C\left[\tfrac{\gamma_C}{\gamma_C+1}\boldsymbol{\beta}_C \cdot \boldsymbol{p}_\pm^* + E_0^*\right] \\ &= \pm(s-1)^{1/2}\boldsymbol{e}_0^* + \beta_C\gamma_C s^{1/2}\boldsymbol{e}_1\left[1 \pm \tfrac{\beta_C\gamma_C\left(1-\frac{2}{s}\right)^{1/2}}{\gamma_C+1}\boldsymbol{e}_1 \cdot \boldsymbol{e}_0^*\right] \\ &= \pm(s-1)^{1/2}\boldsymbol{e}_0^* + \tfrac{k_1}{2}\left(1 - \tfrac{4s}{k_1^2}\right)^{1/2}\boldsymbol{e}_1\left[1 \pm \tfrac{k_1}{k_1+2s^{1/2}}F(s,k_1)\mu_e^*\right]. \end{aligned} \quad (18)$$

Taking the scalar product of the last equation with $\boldsymbol{e}_1$, we find for the cosine of the angle between the outgoing electrons and the incoming gamma ray $\mu_e = \boldsymbol{e}_1 \cdot \boldsymbol{p}_\pm/p_\pm$ in the laboratory frame

$$\begin{aligned} \mu_e p_\pm = \pm(s-1)^{1/2}\mu_e^* \\ + \frac{k_1}{2}\left(1 - \frac{4s}{k_1^2}\right)^{1/2}\left[1 \pm \frac{k_1 F(s,k_1)\mu_e^*}{k_1 + 2s^{1/2}}\right], \end{aligned} \quad (19)$$

where we infer from Equation (15)

$$p_\pm = \sqrt{E_\pm^2 - 1} = \frac{k_1}{2}\left[(1 \pm F(s,k_1)\mu_e^*)^2 - \frac{4}{k_1^2}\right]^{1/2}. \quad (20)$$

[6] As an aside, we note that these approximations give very accurate results—as the more general study, avoiding these assumptions, has demonstrated; see Böttcher & Schlickeiser (1997).

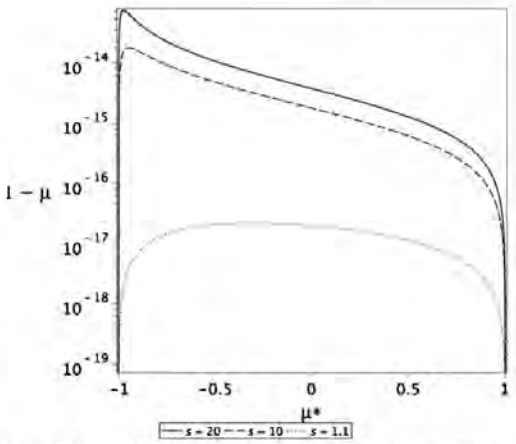

Figure 2. Forward beaming of the generated electrons in the laboratory frame. Shown are the deviations from the forward direction ($\mu = \mu_e = 1$) of electrons in the laboratory frame as a function of the isotropic electron direction in the center-of-momentum frame ($\mu^* = \mu_e^*$) for three values of $s = 1.1$, $s_m/2$, and s_m, where $s_m = k_1k_2 = 20$ denotes the maximum value of the invariant s, corresponding to a monoenergetic gamma-ray beam $k_2 = 10^8$ (51.1 TeV) interacting with a monoenergetic soft photon $k_0 = 2 \times 10^{-7}$ (corresponding 0.1 eV) of EBL.

Combining the last two equations we obtain

$$\begin{aligned} \mu_e = \left[\frac{1 - \frac{4s}{k_1^2}}{(1 \pm F(s,k_1)\mu_e^*)^2 - \frac{4}{k_1^2}}\right]^{1/2} \\ \times \left(1 \pm \mu_e^*\left[\frac{k_1 F(s,k_1)}{k_1 + 2s^{1/2}} + 2\sqrt{\frac{s-1}{k_1^2 - 4s}}\right]\right). \end{aligned} \quad (21)$$

3. FORWARD BEAMING OF PAIR-PRODUCED ELECTRONS

Because we cannot distinguish between negatrons and positrons, we infer from Equation (21) that electrons are produced with values of

$$\begin{aligned} \mu_e = \left[\frac{1 - \frac{4s}{k_1^2}}{(1 + F(s,k_1)\mu_e^*)^2 - \frac{4}{k_1^2}}\right]^{1/2} \\ \times \left(1 + \mu_e^*\left[\frac{k_1 F(s,k_1)}{k_1 + 2s^{1/2}} + 2\sqrt{\frac{s-1}{k_1^2 - 4s}}\right]\right) \end{aligned} \quad (22)$$

for $\mu_e^* \in [-1, 1]$. In Figure 2, we calculate the resulting electron angular distribution in the laboratory frame $\mu_e(\mu_e^*)$ for the three values of $s = 1.1$, $s_m/2$, and s_m, where $s_m = k_1k_2$ denotes the maximum value of the invariant s. We adopt a 50 TeV gamma ray ($k_1 = 10^8$) and a 0.1 eV EBL photon ($k_2 = 2 \times 10^{-7}$) so that $s_m = 20$. In all three cases, the resulting electron angular distribution is highly beamed in the forward ($\mu_e = 1$) direction. For electrons produced at threshold ($s = 1$), we note $F(1, k_1) = 0$, so that Equation (22) reduces to $\mu_e = 1$ for all values of μ_e^*. With $1 - \mu_e \simeq \theta_e^2/2$ for small angles and $1 - \mu_e \leqslant 10^{-13}$, from Figure 2 we find that the angular spread of the initially generated electrons is less than 5×10^{-7} rad with respect to the incoming gamma-ray direction.

4. ELECTRON ENERGY SPECTRUM

According to Equation (7), the energy of the produced electrons in the CM frame is $E^* = s^{1/2} = (1-\beta^{*2})^{-1/2}$, so that the electron velocity is

$$\beta^* = \left[1 - \frac{1}{s}\right]^{1/2}. \tag{23}$$

Following earlier work (Bonometto & Rees 1971; Cerutti et al. 2009), the probability of a single gamma ray of energy k_1 being absorbed between the path length l and $l+dl$, yielding an electron of energy between E and $E+dE$ and a positron of energy between $k_1 - E - dE$ and $k_1 - E$, in the lab frame is given by

$$\begin{aligned} g(E) &= \int_0^{2\pi} d\phi \int_{-1}^{1} d\mu \int_0^{\infty} dk_2 \frac{dn}{dk_2 d\phi d\mu}(1-\mu)\frac{d\sigma_{\gamma\gamma}}{dE} \\ &= \frac{4}{k_1^2}\int_0^{2\pi} d\phi \int_0^{\infty} \frac{dk_2}{k_2^2} \\ &\quad \times \int_0^{k_1 k_2} ds\, s H[s-1] \frac{dn}{dk_2 d\phi d\mu(s)} \frac{d\sigma_{\gamma\gamma}}{dE}, \end{aligned} \tag{24}$$

where we replaced the μ-integration according to Equation (2) with the corresponding s-integration and where the step function $H[s-1]$ accounts for the threshold condition (4). The differential cross section is given by

$$\frac{d\sigma_{\gamma\gamma}}{dE} = \frac{d(\beta^*\mu_e^*)}{dE}\frac{d\sigma_{\gamma\gamma}}{d(\beta^*\mu_e^*)} \tag{25}$$

with (Jauch & Rohrlich 1955; Gould & Schreder 1967; Bonometto & Rees 1971)

$$\begin{aligned} \frac{d\sigma_{\gamma\gamma}}{d(\beta^*\mu_e^*)} &= \frac{3\sigma_T}{16}(1-\beta^{*2}) \\ &\quad \times \frac{1-(\beta^*\mu_e^*)^4 + 2(1-\beta^{*2})[\beta^{*2} - (\beta^*\mu_e^*)^2]}{[1-(\beta^*\mu_e^*)^2]^2}, \end{aligned} \tag{26}$$

where $\sigma_T = 6.65 \times 10^{-25}$ cm^2 denotes the Thomson cross section. Equation (15), used in the form

$$E = \frac{k_1}{2}[1 + F(s,k_1)\mu_e^*] \tag{27}$$

with Equation (23), readily provides

$$\begin{aligned} \frac{d(\beta^*\mu_e^*)}{dE} &= \left[1-\frac{1}{s}\right]^{1/2}\frac{d\mu_e^*}{dE} \\ &= \frac{2\left[1-\frac{1}{s}\right]^{1/2}}{k_1 F(k_1,s)} = \frac{2}{k_1\left[1-\frac{4s}{k_1^2}\right]^{1/2}}. \end{aligned} \tag{28}$$

With

$$A = 1 - \frac{2E}{k_1} \tag{29}$$

we find

$$\beta^*\mu_e^* = \frac{\left(\frac{2E}{k_1}-1\right)\left[1-\frac{1}{s}\right]^{1/2}}{F(k_1,s)} = -\frac{A}{\left[1-\frac{4s}{k_1^2}\right]^{1/2}}, \tag{30}$$

so that the probability (24) becomes

$$\begin{aligned} g(E) &= \frac{3\sigma_T}{2k_1^3}\int_0^{2\pi} d\phi \int_{k_1^{-1}}^{\infty} \frac{dk_2}{k_2^2} \\ &\quad \times \int_1^{k_1 k_2} ds \frac{dn}{dk_2 d\phi d\mu} M(A,s) \end{aligned} \tag{31}$$

with

$$\begin{aligned} &M(A,s) = \\ &\frac{\left(1-\frac{4s}{k_1^2}\right)^{1/2}}{1-A^2-\frac{4s}{k_1^2}}\left[\frac{2+s}{s} + \frac{A^2}{1-\frac{4s}{k_1^2}} - \frac{2\left(1-\frac{4s}{k_1^2}\right)}{s^2\left[1-A^2-\frac{4s}{k_1^2}\right]}\right]. \end{aligned} \tag{32}$$

According to Equation (27), with $-1 \leqslant \mu_e^* \leqslant 1$, the electron energies are restricted to the range

$$\begin{aligned} &E_- \leqslant E \leqslant E_+ \\ &E_\pm = \frac{k_1}{2}[1 \pm F(s,k_1)], \end{aligned} \tag{33}$$

corresponding with the definition (29)

$$A^2 = \left(1-\frac{2E}{k_1}\right)^2 \leqslant F^2(s,k_1) = 1 + \frac{4}{k_1^2} - \left(\frac{1}{s} + \frac{4s}{k_1^2}\right). \tag{34}$$

The last equation yields

$$W(k_1,E) \geqslant s + \frac{k_1^2}{4s} \tag{35}$$

with

$$W(k_1,E) = 1 + k_1 E - E^2 = \frac{k_1^2}{4}(1-A^2) + 1. \tag{36}$$

Because the right-hand side of Equation (35) is always greater than or equal to its minimum value k_1 at $s_0 = k_1/2$, we require $W(k_1,E) \geqslant k_1$, so that

$$1 \leqslant E \leqslant k_1 - 1 \tag{37}$$

is the maximum possible energy range of the generated electrons. Because $W \geqslant k_1$, Equation (36) is well approximated by

$$W(k_1,E) = 1 + k_1 E - E^2 = \frac{k_1^2}{4}(1-A^2). \tag{38}$$

Moreover, for soft photon energies $k_2 \ll 1/2$, the upper s-integration limit $k_1 k_2$ in Equation (31) is much smaller than s_0, so we approximate Equation (35) by

$$W(k_1,E) \geqslant \frac{k_1^2}{4s}, \tag{39}$$

providing with approximation (38) the constraint

$$s \geqslant \frac{1}{1-A^2} \geqslant 1, \tag{40}$$

which for all allowed energy values (37) is larger unity. The probability (31) then becomes

$$\begin{aligned} g(E) &\simeq \frac{3\sigma_T}{2k_1^3}\int_0^{2\pi} d\phi \int_{k_1^{-1}}^{1/2} \frac{dk_2}{k_2^2} \\ &\quad \times \int_{\frac{1}{1-A^2}}^{k_1 k_2} ds \frac{dn}{dk_2 d\phi d\mu} M(A,s), \end{aligned} \tag{41}$$

Finite values of the last integral only result if

$$\frac{1}{1-A^2} \leqslant k_1 k_2$$

or

$$k_2 \geqslant \frac{1}{k_1(1-A^2)} \geqslant k_1^{-1}. \quad (42)$$

Consequently, we obtain

$$g(E) = \frac{3\sigma_T}{2k_1^3} \int_0^{2\pi} d\phi \int_{\frac{1}{k_1(1-A^2)}}^{1/2} \frac{dk_2}{k_2^2} \times \int_{\frac{1}{1-A^2}}^{k_1 k_2} ds \frac{dn}{dk_2 d\phi d\mu} M(A,s). \quad (43)$$

4.1. Gyrotropic and Isotropic Soft Photon Distributions

For the important case of gyrotropic and isotropic soft photon distributions

$$\frac{dn}{dk_2 d\phi d\mu} = \frac{N(k_2)}{4\pi}, \quad (44)$$

the probability (43) reads

$$g(E) = \frac{3\sigma_T}{4k_1^3} \int_{\frac{1}{k_1(1-A^2)}}^{1/2} dk_2 \frac{N(k_2)}{k_2^2} \times \int_{\frac{1}{1-A^2}}^{k_1 k_2} ds\, M(A,s). \quad (45)$$

Substituting $s = k_1^2 x/4$, we obtain

$$g(E) = \frac{3\sigma_T}{16k_1} \int_{\frac{1}{k_1(1-A^2)}}^{1/2} dk_2 \frac{N(k_2)}{k_2^2} I(E,k_1,k_2) \quad (46)$$

with the integrals

$$I(E,k_1,k_2) = \int_{4/k_1^2(1-A^2)}^{4k_2/k_1} dx\, M(A,x) \quad (47)$$

and

$$M(A,x) = \frac{(1-x)^{1/2}}{1-A^2-x}\left[1 + \frac{8}{k_1^2 x} - \frac{32}{k_1^4 x^2} + \frac{A^2}{1-x} - \frac{32A^2}{k_1^4 x^2(1-A^2-x)}\right]. \quad (48)$$

Straightforward, but tedious, integrations, carried out in Appendix A, provide the exact result

$$I(E,k_1,k_2) = R\left[\frac{4k_2}{k_1}\right] - R\left[\frac{4}{k_1^2(1-A^2)}\right], \quad (49)$$

with

$$R[x] = 2(1-x)^{1/2}\left[\frac{16[1-A^2-(A^2+1)x]}{(1-A^2)^2 k_1^4 x(1-A^2-x)} - 1\right] + 4|A|\left[1 + \frac{4}{(1-A^2)k_1^2} - \frac{8(A^2+3)}{(1-A^2)^3 k_1^4}\right] \times \operatorname{artanh}\left(\frac{(1-x)^{1/2}}{|A|}\right) + \frac{16}{(1-A^2)k_1^2}\left[\frac{2(1+3A^2)}{(1-A^2)^2 k_1^2} - 1\right] \times \operatorname{artanh}(1-x)^{1/2}. \quad (50)$$

Instead of using the exact results (49), we approximate the function (48) for small values of $x \leqslant 4k_0/k_1 \ll 1$ by

$$M_0(A,x) = M(A, x \ll 1) = \frac{1}{1-A^2}\left[1 + A^2 + \frac{8}{k_1^2 x} - \frac{32}{k_1^4(1-A^2)x^2}\right]. \quad (51)$$

We readily obtain

$$I(E,k_1,k_2) \simeq \frac{4k_2}{(1-A^2)k_1}\left[\left(1 + A^2 - \frac{2}{k_1 k_2}\right)\left(1 - \frac{1}{k_1 k_2(1-A^2)}\right) + \frac{2}{k_1 k_2}\ln[k_1 k_2(1-A^2)]\right], \quad (52)$$

so that the electron production probability from a single gamma ray of energy k_1 in gyrotropic and isotropic soft photon distributions becomes

$$g(E) = \frac{3\sigma_T}{4k_1^2(1-A^2)} \int_{\frac{1}{k_1(1-A^2)}}^{1/2} dk_2 \frac{N(k_2)}{k_2} \times \left[\left(1 + A^2 - \frac{2}{k_1 k_2}\right)\left(1 - \frac{1}{k_1 k_2(1-A^2)}\right) + \frac{2}{k_1 k_2}\ln[k_1 k_2(1-A^2)]\right]. \quad (53)$$

Here the dependence on the electron energy is contained in $A = 1 - (2E/k_1)$. The production spectrum (53) holds for arbitrary soft photon energy distributions $N(k_0)$.

Introducing the electron energy variable

$$y = \frac{E}{k_1/2} - 1 = -A, \quad (54)$$

the probability (53) can be written as

$$g(y) = \frac{3\sigma_T}{4k_1^2(1-y^2)} \int_{\frac{1}{k_1(1-y^2)}}^{1/2} dk_2 \frac{N(k_2)}{k_2} \times \left[\left(1 + y^2 - \frac{2}{k_1 k_2}\right)\left(1 - \frac{1}{k_1 k_2(1-y^2)}\right) + \frac{2}{k_1 k_2}\ln[k_1 k_2(1-y^2)]\right], \quad (55)$$

which, irrespective of the soft photon energy distributions $N(k_0)$, is symmetric in y, i.e., $g(-y) = g(y)$.

In the following subsections we investigate special soft photon energy distributions.

4.2. Monochromatic Soft Photon Distribution

For the monochromatic soft photon distribution

$$N(k_2) = N_0 \delta(k_2 - k_0) \quad (56)$$

finite values from the general distribution (55) require

$$\frac{1}{k_1(1-y^2)} \leqslant k_0 \leqslant 1/2. \quad (57)$$

The left-hand side of this inequality restricts the allowed electron energies to

$$E_{\min} \leqslant E \leqslant E_{\max} \quad (58)$$

with

$$E_{\max,\min} = \frac{k_1}{2}\left[1 \pm \sqrt{1 - \frac{1}{k_1 k_0}}\right]. \quad (59)$$

This implies

$$y \in [-m, m], \quad m = \sqrt{1 - \frac{1}{k_1 k_0}}, \quad (60)$$

so that

$$1 - y^2 \in \left[\frac{1}{k_1 k_0}, 1\right]. \quad (61)$$

We find

$$g(-m \leqslant y \leqslant m) = \frac{3\sigma_T N_0}{4k_1^2 k_0 (1-y^2)} H\left[\tfrac{1}{2} - k_0\right] H\left[k_0 - \tfrac{1}{k_1}\right] \times \left[\left(1 + y^2 - \tfrac{2}{k_1 k_0}\right)\left(1 - \tfrac{1}{k_1 k_0 (1-y^2)}\right) + \tfrac{2}{k_1 k_0} \ln\left[k_1 k_0 (1-y^2)\right]\right], \quad (62)$$

or

$$g(E_{\min} \leqslant E \leqslant E_{\max}) = \frac{3\sigma_T N_0 H\left[\frac{1}{2} - k_0\right] H\left[k_0 - \frac{1}{k_1}\right]}{8k_0 E(k_1 - E)} \times \left[\frac{1}{k_1 k_0} \ln \frac{4k_0 E(k_1 - E)}{k_1} + \left(\frac{E^2 + (k_1 - E)^2}{k_1^2} - \frac{1}{k_1 k_0}\right) \times \left(1 - \frac{k_1}{4k_0 E(k_1 - E)}\right)\right]. \quad (63)$$

which is shown in Figure 3 for the case $k_1 = 10^8$ and $k_0 = 2 \times 10^{-7}$ in comparison with the electron production probability obtained from the numerical Monte Carlo simulation of the electromagnetic cascade described in detail in Elyiv et al. (2009). We did not include the effects of the extragalactic magnetic field as well as the IC interactions with CMB photons, calculating instead only the generated pair energy distribution resulting from the first double photon collisions. As can be seen, the agreement is perfect. The probability exhibits symmetry with respect to $E = (k_1/2)$, and at energies well below k_1 the leading energy dependence of the electron production spectrum is $g(E \ll k_1) \propto E^{-1}$. Moreover, we note that despite its different analytical form, the probability (63) agrees perfectly with the earlier derived expression of Aharonian and coworkers (Aharonian et al. 1983; Aharonian 2003).

4.3. Arbitrary Soft Photon Distribution

For the arbitrary soft photon distribution $N(k_0)$, we find with Equation (63) for the electron production probability from a single gamma-ray photon,

$$n(E, k_1) = \int_0^\infty dk_0 \frac{N(k_0)}{N_0} g\left(E_{\min} \leqslant E \leqslant E_{\max}\right). \quad (64)$$

The requirement $E_{\min} \leqslant E \leqslant E_{\max}$ demands

$$k_0 \geqslant \frac{k_1}{4E(k_1 - E)}, \quad (65)$$

so that

$$n(E, k_1) = \frac{3\sigma_T H\left[k_1 - \frac{2E^2}{2E-1}\right]}{8E(k_1 - E)} \int_{\frac{k_1}{4E(k_1-E)}}^{1/2} dk_0 \frac{N(k_0)}{k_0} \times \left[\frac{1}{k_1 k_0} \ln \frac{4k_0 E(k_1 - E)}{k_1} + \left(\frac{E^2 + (k_1 - E)^2}{k_1^2} - \frac{1}{k_1 k_0}\right) \times \left(1 - \frac{k_1}{4k_0 E(k_1 - E)}\right)\right]. \quad (66)$$

Substituting $k_0 = k_1 t/[4E(k_1 - E)]$, we obtain

$$n(E, k_1) = \frac{3\sigma_T H\left[k_1 - \frac{2E^2}{2E-1}\right]}{8k_1^2 E(k_1 - E)} \int_1^{\frac{2E(k_1-E)}{k_1}} \frac{dt}{t} \times N\left(k_0 = \frac{k_1 t}{4E(k_1 - E)}\right)\left[\frac{4E(k_1 - E)}{t}\left(\ln t - 1 + \frac{1}{t}\right) + \left(k_1^2 - 2E(k_1 - E)\right)\left(1 - \frac{1}{t}\right)\right]. \quad (67)$$

The electron energy dependence on $E(k_1 - E)$ guarantees the symmetry of the probability dependence, generated by a single gamma ray, around $E = k_1/2$ for arbitrary soft photon distributions.

4.4. Pair Density

The number of pairs with energy E created per unit length path depends on the electron production probability (67) and on the probability of the incoming gamma rays remaining unabsorbed up to the point of observation (Cerutti et al. 2009)

$$\frac{dN_e}{dl dE} = 2n(E, k_1) e^{-\tau(k_1, l)}, \quad (68)$$

with the optical depth

$$\frac{d\tau(k_1, l)}{dl} = \int_0^\infty dE\, n(E, k_1), \quad (69)$$

so that the integration of Equation (68) over all electron energies provides

$$\frac{dN_e}{dl} = 2\frac{d\tau(k_1, l)}{dl} e^{-\tau(k_1, l)}. \quad (70)$$

The total number of pairs produced by a single gamma ray traversing a soft photon radiation field along the path l up to the distance r then is

$$N_e(k_1, r) = 2[1 - e^{-\tau(k_1, r)}] \simeq \begin{cases} 2\tau(k_1, r) & \text{for } \tau(k_1, r) \ll 1 \\ 2 & \text{for } \tau(k_1, r) \gg 1. \end{cases} \quad (71)$$

A differential gamma-ray photon spectrum $I_1(k_1)$ in units of photons cm^{-2} s^{-1} eV^{-1} corresponds to the gamma-ray photon density $m_e c^2 k_1 I_1(k_1)/c$, implying for the number density of produced pairs

$$n_e(k_1, r) = \frac{m_e c^2 k_1 I_1(k_1) N_e(k_1, r)}{c} = \frac{2m_e c^2 k_1 I_1(k_1)}{c}[1 - e^{-\tau(k_1, r)}]. \quad (72)$$

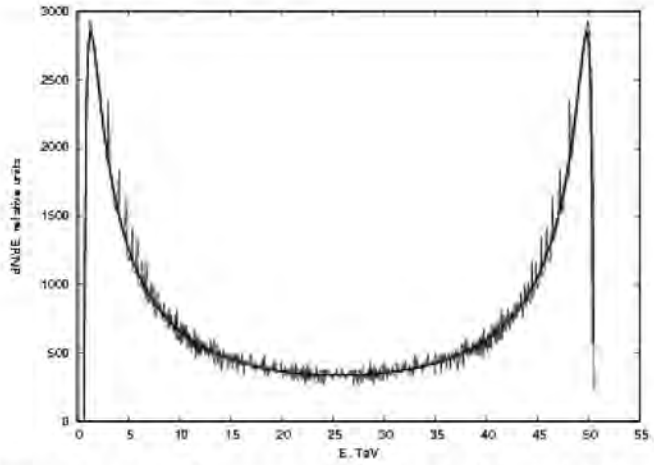

Figure 3. Probability of a single gamma ray of energy $k_1 = 10^8$ (corresponding to 51.1 TeV) being absorbed between the path length l and $l + dl$, yielding an electron of energy between E and $E + dE$, when interacting with monoenergetic isotropically distributed soft photons $k_0 = 2 \times 10^{-7}$ (corresponding 0.1 eV) of EBL. The analytical result (63) (thick line) agrees perfectly with the result from the numerical simulations (thin line). The simulations were done for the same conditions using the Monte Carlo method detailed in Elyiv et al. (2009).

For spatially uniformly distributed soft photon distribution, the optical depth is given by

$$\tau(k_1, r) = r \int_0^\infty dE\, n(E, k_1). \tag{73}$$

Likewise, the integration of Equation (68) over all path lengths yields the differential energy spectrum of the produced pairs from a single gamma ray traversing a soft photon radiation field along the path l up to the distance r as

$$\begin{aligned}\frac{dN_e}{dE}(E, k_1, r) &= 2n(E, k_1) \int_0^r dl\, \exp\left[-l \int_0^\infty dE\, n(E, k_1)\right] \\ &= \frac{2rn(E, k_1)}{\tau(k_1, r)}[1 - e^{-\tau(k_1, r)}] \\ &= N_e(k_1, r) \frac{n(E, k_1)}{\int_0^\infty dE\, n(E, k_1)} \\ &\simeq \begin{cases} 2rn(E, k_1) & \text{for } \tau(k_1, r) \ll 1 \\ \frac{2rn(E, k_1)}{\tau(k_1, r)} & \text{for } \tau(k_1, r) \gg 1. \end{cases}\end{aligned} \tag{74}$$

5. SINGLE GAMMA-RAY PAIR PRODUCTION OPTICAL DEPTH

The calculation of the optical depth (73) of a single gamma-ray photon requires the integration of Equation (66) over all electron energies

$$\begin{aligned}\tau(k_1, r) &= r \int_{E_{\min}}^{E_{\max}} dE \int_0^\infty dk_0 \frac{N(k_0)}{N_0} g(E_{\min} \leqslant E \leqslant E_{\max}) \\ &= \frac{3\sigma_T r}{8} \int_{E_{\min}}^{E_{\max}} \frac{dE}{E(k_1 - E)} \int_{\frac{1}{k_1 E(k_1 - E)}}^{1/2} dk_0 \frac{N(k_0)}{k_0} \\ &\quad \times \left[\frac{1}{k_1 k_0} \ln \frac{4k_0 E(k_1 - E)}{k_1}\right. \\ &\quad \left. + \left(\frac{E^2 + (k_1 - E)^2}{k_1^2} - \frac{1}{k_1 k_0}\right) \right. \\ &\quad \left. \times \left(1 - \frac{k_1}{4k_0 E(k_1 - E)}\right)\right].\end{aligned} \tag{75}$$

Using the electron energy variable (54) and Equation (60), we obtain

$$\tau(k_1, r) = \frac{3\sigma_T r H[k_1 - 2]}{4k_1} \int_{k_1^{-1}}^{1/2} dk_0 \frac{N(k_0)}{k_0} \int_0^m dy\, K(y) \tag{76}$$

with the function

$$\begin{aligned}K(y) = \frac{1}{1 - y^2}\Big(&1 + m^2 - 2(1 - m^2)\ln(1 - m^2) - (1 - y^2) \\ &- \frac{2m^2(1 - m^2)}{1 - y^2} + 2(1 - m^2)\ln(1 - y^2)\Big).\end{aligned} \tag{77}$$

The step function in Equation (76) arises from the condition that $k_1^{-1} \leqslant (1/2)$. Using

$$\int_0^m \frac{dy}{(1 - y^2)^2} = \frac{1}{2}\left[\frac{m}{1 - m^2} + \operatorname{artanh} m\right] \tag{78}$$

and the integral (evaluated in Appendix B)

$$\begin{aligned}I_7(m) &= \int_0^m dy \frac{\ln(1 - y^2)}{(1 - y^2)} \\ &= \frac{1}{4}[\ln^2(1 + m) - \ln^2(1 - m) + 2\ln(1 - m)\ln(1 + m)] \\ &\quad - \ln 2 \ln(1 + m) - \mathrm{Li}\left[\frac{1}{2}, \frac{1 + m}{2}\right]\end{aligned} \tag{79}$$

with the dilogarithm (Abramowitz & Stegun 1972)

$$\mathrm{Li}[a, b] = \int_a^b ds \frac{\ln(1 + s)}{s}, \tag{80}$$

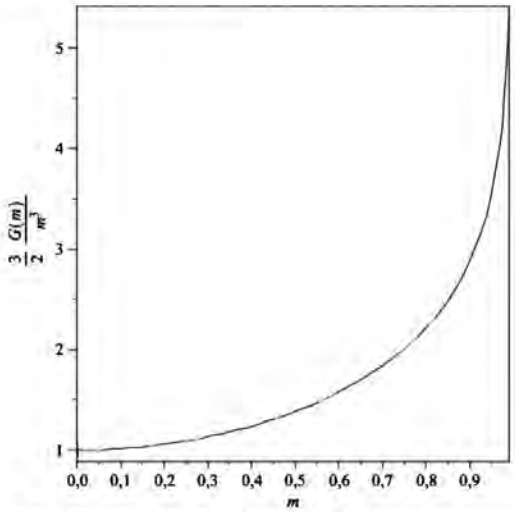

Figure 4. Ratio between the exact variation (82) and its lowest order approximation (84) of the function $G(m)$.

which cannot be expressed as a finite combination of elementary functions (Gradshteyn & Ryzhik 1980), we obtain

$$\tau(k_1, r) = \frac{3\sigma_T r H[k_1 - 2]}{4k_1} \int_{k_1^{-1}}^{1/2} dk_0 \frac{N(k_0)}{k_0} G(m) \qquad (81)$$

with

$$G(m) = \int_0^m dy\, K(y) = [1 + m^4 - 2(1 - m^2)\ln(1 - m^2)]\operatorname{artanh} m - m(1 + m^2) + 2(1 - m^2)H_7(m). \qquad (82)$$

Substituting in Equation (81) m from Equation (60), we find

$$\tau(k_1, r) = \frac{3\sigma_T r H[k_1 - 2]}{2k_1} \times \int_0^{\sqrt{1-\frac{2}{k_1}}} dm\, \frac{mG(m)}{1 - m^2} N\left(\frac{1}{k_1(1 - m^2)}\right). \qquad (83)$$

For small values of $m \ll 1$, we note the asymptotic behavior

$$G(m \ll 1) \simeq \frac{2}{3}m^3\left[1 + \frac{7}{5}m^2\right]. \qquad (84)$$

As Figure 4 illustrates, this approximations agrees reasonable well with the exact variation $G(m)$ for all values of $m < 1$, so that we use it to find for the optical depth (83)

$$\tau(k_1, r) \simeq \frac{\sigma_T r H[k_1 - 2]}{k_1} \int_0^{\sqrt{1-\frac{2}{k_1}}} dm\, \frac{m^4}{1 - m^2} N \times \left(\frac{1}{k_1(1 - m^2)}\right). \qquad (85)$$

5.1. Wien-type Soft Photon Distribution

We now specify the soft photon distribution by the generalized Wien-type spectrum

$$N_W(k_0) = \frac{N_0}{\Gamma(q + 1)\Theta^{1+q}} k_0^q e^{-k_0/\Theta}, \qquad (86)$$

characterized by its power-law index $q > -1$ and the dimensionless temperature $\Theta = k_B T_W / m_e c^2$. N_0 denotes the total number of soft photons and $\Gamma(x)$ denotes the Gamma function. For the optical depth (85) we then derive

$$\tau(k_1, r) \simeq \frac{\sigma_T N_0 r H[k_1 - 2]}{\Gamma(q + 1)(\Theta k_1)^{q+1}} \int_0^{\sqrt{1-\frac{2}{k_1}}} dm \times \frac{m^4}{(1 - m^2)^{q+1}} e^{-\frac{1}{\Theta k_1(1-m^2)}}. \qquad (87)$$

The substitution $t = 1/(1 - m^2)$ provides

$$\tau(k_1, r) \simeq \frac{\sigma_T N_0 r H[k_1 - 2]}{2\Gamma(q + 1)(\Theta k_1)^{q+1}} \Omega(\Theta, k_1, q) \qquad (88)$$

with the integral

$$\Omega(\Theta, k_1, q) = \int_1^{k_1/2} dt\, (t - 1)^{3/2} t^{q-5/2} e^{-\frac{t}{\Theta k_1}} = \Gamma\left(\frac{5}{2}\right) e^{-\frac{1}{\Theta k_1}} U\left(\frac{5}{2}, q + 1, \frac{1}{\Theta k_1}\right) - \int_{k_1/2}^{\infty} dt\, (t - 1)^{3/2} t^{q-5/2} e^{-\frac{t}{\Theta k_1}} \qquad (89)$$

expressed in terms of the confluent hypergeometric function of the second kind (Abramowitz & Stegun 1972). For values $k_1 \gg 2$ the remaining integral is approximated as

$$\int_{k_1/2}^{\infty} dt\, (t - 1)^{3/2} t^{q-5/2} e^{-\frac{t}{\Theta k_1}} \simeq \int_{k_1/2}^{\infty} dt\, t^{q-1} e^{-\frac{t}{\Theta k_1}} = (\Theta k_1)^q \int_{\frac{1}{2\Theta}}^{\infty} ds\, s^{q-1} e^{-s} \simeq (\Theta k_1)^q (2\Theta)^{1-q} e^{-\frac{1}{2\Theta}} = 2^{1-q}\Theta k_1^q e^{-\frac{1}{2\Theta}} \ll 1, \qquad (90)$$

where in the penultimate step we used the smallness of $\Theta \ll 1$. This contribution is negligibly small. We then obtain

$$\Omega(\Theta, k_1, q > 1) \simeq \Gamma\left(\frac{5}{2}\right) e^{-\frac{1}{\Theta k_1}} U\left(\frac{5}{2}, q + 1, \frac{1}{\Theta k_1}\right), \qquad (91)$$

providing for the optical depth (88)

$$\tau(k_1, r) \simeq \frac{\Gamma(5/2)\sigma_T N_0 r H[k_1 - 2]}{2\Gamma(q + 1)(\Theta k_1)^{q+1}} e^{-\frac{1}{\Theta k_1}} U\left(\frac{5}{2}, q + 1, \frac{1}{\Theta k_1}\right). \qquad (92)$$

For small gamma-ray energies $k_1 \ll \Theta^{-1}$, we obtain the approximation

$$\tau(k_1 \ll \Theta^{-1}, r) \simeq \frac{\Gamma(5/2)\sigma_T N_0 r H[k_1 - 2]}{2\Gamma(q + 1)} (\Theta k_1)^{\frac{1}{2}-q} e^{-\frac{1}{\Theta k_1}}. \qquad (93)$$

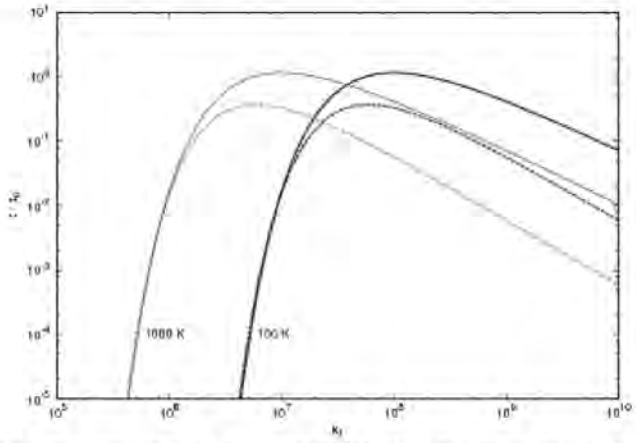

Figure 5. Comparison of the analytical approximation (96) of the optical depth (dashed lines) with the numerically calculated one (solid lines) for a Wien-type soft photon distribution with $q = 2$ and two temperatures $T_W = 100$ and 1000 K.

This is reduced exponentially because for these gamma-ray energies only soft photons in the exponential tail of the Wien distribution overcome the threshold for pair production.

For large gamma-ray energies $k_1 \gg \Theta^{-1}$ the asymptotic behavior of the confluent hypergeometric function depends on the power-law index value q of the Wien distribution, or

$$U\left(\frac{5}{2}, q+1, \frac{1}{\Theta k_1}\right) \simeq \begin{cases} \frac{\Gamma(q)}{\Gamma(5/2)(\Theta k_1)^q} & \text{for } q > 0 \\ \frac{1}{\Gamma(5/2)}[\ln(\Theta k_1) - 2.258] & \text{for } q = 0 \\ \frac{1}{\Gamma(7/2)} & \text{for } q = -1 \\ \frac{\Gamma(-q)}{\Gamma\left(\frac{5}{2}-q\right)} & \text{for } -1 < |q| < 0. \end{cases} \quad (94)$$

For the corresponding optical depth at large photon energies, we then obtain

$$\tau(k_1 \gg \Theta^{-1}, r) \simeq \frac{\sigma_T N_0 r H[k_1 - 2]}{2\Gamma(q+1)(\Theta k_1)^{1+q}} \times \begin{cases} \Gamma(q)(\Theta k_1)^q & \text{for } q > 0 \\ [\ln(\Theta k_1) - 2.258] & \text{for } q = 0 \\ \frac{2}{5} & \text{for } q = -1 \\ \frac{\Gamma(-q)\Gamma(\frac{5}{2})}{\Gamma(\frac{5}{2}-q)} & \text{for } -1 < |q| < 0. \end{cases} \quad (95)$$

For values of $q > 0$, we use the approximation

$$\tau(k_1, r) \simeq \frac{\tau_0}{\Theta k_1 e^{\frac{1}{\Theta k_1}}} \quad (96)$$

with

$$\tau_0 = \frac{\sigma_T N_0 r H[k_1 - 2]}{2q} \quad (97)$$

at all gamma-ray energies. In Figure 5, we compare the analytical single gamma-ray pair optical depth (96) with the numerically calculated one, using the cross section from Aharonian (2003) and Wien-type soft photon distribution with $q = 2$ and the two temperatures $T_W = 100$ K and $T_W = 1000$ K. As can be seen, the agreement is very good for gamma-ray energies below the maximum optical depth. At higher energies the dependences on photon energy agree well, although the analytical calculations underestimate the numerical values by a factor 3–10.

6. ARBITRARY GAMMA-RAY ENERGY DISTRIBUTION

For an extended differential gamma-ray number density distribution $I(k_1) = m_e c^2 I_1(k_1)$ below the maximum energy $k_1 \leqslant k_{1,\max} = M$, now in units of photons per $\mathrm{cm}^{-2}\,\mathrm{s}^{-1}(dk_1)^{-1}$, we obtain with Equation (74) the differential energy spectrum of the produced pairs at the distance r as

$$\frac{dN_e}{dE}(E, r) = \int_0^M dk_1\, I(k_1) \frac{dN_e}{dE}(E, k_1, r) = 2r \int_0^M dk_1\, I(k_1) n(E, k_1) \frac{1 - e^{-\tau(k_1, r)}}{\tau(k_1, r)}. \quad (98)$$

Inserting Equation (67) then provides

$$\frac{dN_e}{dE}(E, r) = \frac{3r\sigma_T}{4} \int_{\frac{2E^2}{2E-1}}^M \frac{dk_1}{k_1^2} I(k_1) \frac{1 - e^{-\tau(k_1, r)}}{\tau(k_1, r)} \times \left[4 \int_1^{2E(1-\frac{E}{k_1})} dt\, N\left(\frac{t}{4E\left(1-\frac{E}{k_1}\right)}\right) \times \frac{\ln t + t^{-1} - 1}{t^2} + \left[\frac{k_1}{E\left(1-\frac{E}{k_1}\right)} - 2\right] \times \int_1^{2E(1-\frac{E}{k_1})} dt\, N\left(\frac{t}{4E\left(1-\frac{E}{k_1}\right)}\right) \frac{t-1}{t^2}\right]. \quad (99)$$

Provided the maximum gamma-ray energy $M \geqslant 2$, electrons are produced in the energy range

$$\frac{M}{2}\left[1 - \sqrt{1 - \frac{2}{M}}\right] \leqslant E \leqslant \frac{M}{2}\left[1 + \sqrt{1 - \frac{2}{M}}\right]. \quad (100)$$

Equation (99) is the general analytical expression of the energy spectrum of electrons produced from the annihilation interactions of a beam of high-energy gamma rays with arbitrary differential number density distribution $I(k_1)$ below $k_1 \leqslant M$ with an isotropically distributed soft photon gas with arbitrary differential number density distribution $N(k_0)$.

6.1. Power-law-distributed Gamma Rays

Blazar observations often indicate power-law distributions of the emitted gamma-ray beam with $I(k_1) = I_0 k_1^{-p}$ for $k_1 \leqslant M$. In this case the electron spectrum (99) reduces to

$$\frac{dN_e}{dE}(E,r) = \frac{3r\sigma_T I_0}{4}\int_{\frac{2E^2}{2E-1}}^{M} dk_1\, k_1^{-(p+2)}\frac{1-e^{-\tau(k_1,r)}}{\tau(k_1,r)} \times\left[4\int_1^{2E\left(1-\frac{E}{k_1}\right)} dt\, N\left(\frac{t}{4E\left(1-\frac{E}{k_1}\right)}\right) \times\frac{\ln t + t^{-1}-1}{t^2} + \left[\frac{k_1}{E\left(1-\frac{E}{k_1}\right)}-2\right] \times\int_1^{2E\left(1-\frac{E}{k_1}\right)} dt\, N\left(\frac{t}{4E\left(1-\frac{E}{k_1}\right)}\right)\frac{t-1}{t^2}\right], \tag{101}$$

In the next section, we will investigate the astrophysically relevant soft photon Wien energy distribution (86) with spectral index $q > 0$.

7. WIEN-TYPE SOFT PHOTON DISTRIBUTION AND POWER-LAW-DISTRIBUTED GAMMA RAYS

7.1. Optical Depth Influence

We first approximate the factor

$$\frac{1-e^{-\tau(k_1,r)}}{\tau(k_1,r)} \simeq \frac{1}{1+\tau(k_1,r)} \tag{102}$$

for all values of τ, noting that for $\tau \ll 1$ and $\tau \gg 1$ the left-hand and right-hand sides of Equation (102) approach the same values 1 and τ^{-1}, respectively. Limiting our discussion to Wien distributions with $q > 1$, the optical depth (96) then provides

$$\frac{1-e^{-\tau(k_1,r)}}{\tau(k_1,r)} \simeq \frac{1}{1+\tau(\Theta k_1)} \tag{103}$$

with

$$\tau(x) = \tau_0 x^{-1} e^{-\frac{1}{x}} \simeq \tau_0 \begin{cases} e^{-x^{-1}} & \text{for } x \ll 1 \\ x^{-1} & \text{for } x \gg 1. \end{cases} \tag{104}$$

The function $\tau(x)$ attains its maximum value $\tau_{\max} = \tau_0 e^{-1} = 0.37\tau_0$ at $x = 1$, is exponentially reduced at small values of x, and decreases proportional to x^{-1} at large values of x.

The limit of large path length

$$r \gg r_0 = (N_0\sigma_T)^{-1} = \frac{0.49}{N_0}\ \text{Mpc}, \tag{105}$$

where $N_0^{\rm EBL} \simeq 1$ is of order unity, corresponds to values of $\tau_0 \gg 1$, so that the factor (103) varies approximately as

$$\frac{1}{1+\tau(x)} \simeq \begin{cases} 1 & \text{for } x \leqslant \frac{1}{\ln\tau_0} \\ \frac{x e^{\frac{1}{x}}}{\tau_0} & \text{for } \frac{1}{\ln\tau_0} \leqslant x \leqslant \tau_0 \\ 1 & \text{for } x > \tau_0. \end{cases} \tag{106}$$

7.2. Further Reduction of the Electron Spectrum

Substituting $k_1 = Ez/(z-1)$, we obtain for the electron spectrum (101)

$$\frac{dN_e}{dE}(E,r) = \frac{3r\sigma_T I_0 H[M-2]}{4E^{1+p}}\int_{\frac{M}{M-1}}^{2E}\frac{dz}{z^2}\frac{\left(1-\frac{1}{z}\right)^p}{1+\tau(k_1(z),r)} \times\left[4\int_1^{\frac{2E}{z}} dt\, N\left(\frac{zt}{4E}\right)\frac{\ln t + t^{-1}-1}{t^2} + \frac{z^2-2z+2}{z-1}\int_1^{\frac{2E}{z}} dt\, N\left(\frac{zt}{4E}\right)\frac{t-1}{t^2}\right]. \tag{107}$$

Using the Wien distribution (86), we find

$$\frac{dN_e}{dE}(E,r) = \frac{3r\sigma_T I_0 N_0 H[M-2]}{4^{q+1}\Gamma(1+q)\Theta^{1+q}E^{1+q+p}} \times\int_{\frac{1}{1-\frac{E}{M}}}^{2E} dz\, e^{-\frac{z}{4\Theta E}}\frac{z^{q-2}\left(1-\frac{1}{z}\right)^p}{1+\tau_0\left(\frac{1-\frac{1}{z}}{\Theta E}\right)e^{-\frac{1-\frac{1}{z}}{\Theta E}}}J(E,\Theta,z) \tag{108}$$

with the integral

$$J(E,\Theta,z) = 4\int_0^{\frac{2E}{z}-1} dy\,(1+y)^{q-3}[(1+y)\ln(1+y)-y]e^{-\frac{y}{4\Theta E}} + \frac{z^2-2z+2}{z-1}\int_0^{\frac{2E}{z}-1} dy\, y(1+y)^{q-2}e^{-\frac{y}{4\Theta E}}, \tag{109}$$

where we substituted $t = 1 + y$ in the two second integrals of Equation (107). Using Equation (97) for the factor $r\sigma_T N_0$, we obtain

$$\frac{dN_e}{dE}(E,r) = \frac{3\tau_0 I_0 H[M-2]}{2^{2q-1}\Gamma(q)\Theta^{1+q}E^{1+q+p}} \times\int_{\frac{1}{1-\frac{E}{M}}}^{2E} dz\,\frac{z^{q-2}\left(1-\frac{1}{z}\right)^p e^{-\frac{z}{4\Theta E}}}{1+\tau_0\left(\frac{1-\frac{1}{z}}{\Theta E}\right)e^{-\frac{1-\frac{1}{z}}{\Theta E}}}J(E,\Theta,z). \tag{110}$$

The most interesting feature of this equation is the dependence on τ_0. For distant blazars with luminosity distances $d_L \gg r_0 \simeq 0.49N_0^{-1}$ Mpc, τ_0 attains values larger than 10^3, so that one could take the formal limit of $\tau_0 \to \infty$. In this limit the τ_0-dependence of the spectrum (110) cancels out, providing

$$\frac{dN_e}{dE}(E,\tau_0 \gg 1) = \frac{3I_0 H[M-2]e^{\frac{1}{4\Theta E}}}{2^{2q+1}\Gamma(q)\Theta^q E^{q+p}} \times\int_{\frac{1}{1-\frac{E}{M}}}^{2E} dz\, z^{q-2}\left(1-\frac{1}{z}\right)^{p-1}e^{-\frac{\frac{1}{2}+z}{4\Theta E}}J(E,\Theta,z) \tag{111}$$

subject to the additional constraint from $\tau(E,z) > 1$ and, implying from Equation (106),

$$\frac{1}{\ln\tau_0} \leqslant \frac{\Theta E}{1-\frac{1}{z}} \leqslant \tau_0 \tag{112}$$

Because $z \gg 2$ for all values of E, we ignore the small z-dependence of this constraint, which then provides the electron energy restriction

$$\frac{1}{\Theta \ln \tau_0} \leqslant E \leqslant \frac{\tau_0}{\Theta} \tag{113}$$

for the spectrum (111), i.e.,

$$\frac{dN_e}{dE}\left(\frac{1}{\Theta \ln \tau_0} \leqslant E \leqslant \frac{\tau_0}{\Theta}, \tau_0 \gg 1\right) \simeq \frac{3I_0 H[M-2] e^{\frac{1}{\Theta E}}}{2^{2q+1}\Gamma(q)\Theta^q E^{q+p}} \times \int_{\frac{1}{1-\frac{2}{M}}}^{2E} dz\, z^{q-2}\left(1-\frac{1}{z}\right)^{p-1} e^{-\frac{1}{\Theta z}} J(E,\Theta,z). \tag{114}$$

This energy spectrum is only determined by the number (I_0) of incoming gamma rays and independent on the actual value of τ_0, if this is large enough. This behavior reflects the fact that any incoming single gamma ray can at most produce only two electrons.

Outside of the energy interval (113) we neglect the τ_0-dependence under the integral in Equation (110) and obtain

$$\frac{dN_e}{dE}\left(E \leqslant \frac{1}{\Theta \ln \tau_0}, \tau_0 \gg 1\right) = \frac{dN_e}{dE}\left(E > \frac{\tau_0}{\Theta}, \tau_0 \gg 1\right) = \frac{3\tau_0 I_0 H[M-2]}{2^{2q+1}\Gamma(q)\Theta^{1+q}E^{1+q+p}} \int_{\frac{1}{1-\frac{2}{M}}}^{2E} dz\, z^{q-2}\left(1-\frac{1}{z}\right)^p e^{\frac{-1}{\Theta E z}} J(E,\Theta,z). \tag{115}$$

Here the production spectrum increases with τ_0 as the electrons are produced by gamma rays with energies such that $\tau(\Theta k_1) < 1$.

Both electron production spectra (114) and (115) depend on the same integral $J(E, \Theta, z)$ that we evaluate approximately in Appendix C as

$$J(E,\Theta,z) \simeq \left[z-1+\frac{1}{z-1}\right]\begin{cases} \frac{\alpha^2}{2} & \text{for } \alpha \ll 1 \\ \frac{\alpha^q}{q} & \text{for } \alpha \gg 1, \end{cases} \tag{116}$$

where

$$\alpha = \frac{4\Theta E}{z}. \tag{117}$$

8. ELECTRON PRODUCTION SPECTRA

In this section we calculate the electron production spectra for electron energies outside and inside the interval $[1/\Theta \ln \tau_0, \tau_0/\Theta]$.

The electron production spectra (115) is determined by the last remaining integral

$$T_1(E,\Theta) = \int_{\frac{1}{1-\frac{2}{M}}}^{2E} dz\, z^{q-2}\left(1-\frac{1}{z}\right)^p e^{-\frac{1}{\Theta E z}} J\left(\frac{4\Theta E}{z}\right). \tag{118}$$

With the asymptotics (116) we find

$$T_1(E,\Theta) \simeq \int_{\frac{M}{M-2}}^{2E} dz\, z^{q-(2+p)}[(z-1)^{p+1}+(z-1)^{p-1}] \times \left[\frac{(4\Theta E)^q}{q z^q} H[4\Theta E - z] + \frac{(4\Theta E)^2}{2z^2} H[z-4\Theta E]\right] e^{-\frac{1}{\Theta E z}}. \tag{119}$$

Because the upper integration limit $2E$ is always larger than $4\Theta E$ for $\Theta < (1/2)$, the behavior of Equation (119) depends on the value of $4\Theta E$ in comparison to the lower ($L = M/(M-E) \geqslant 2$) integration limit. We introduce their ratio as the function

$$X(E) = \frac{L}{4\Theta E} = \frac{M}{4\Theta E(M-E)}. \tag{120}$$

For electron energy values $E \ll \Theta^{-1}$, regardless of the value of M, we always have $4\Theta E \ll L$, corresponding to $X \gg 1$, so that

$$T_1(E \ll \Theta^{-1}) \simeq \frac{(4\Theta E)^2}{2} H[X-1] \int_{\frac{M}{M-2}}^{2E} dz\, z^{q-(4+p)} \times [(z-1)^{p+1}+(z-1)^{p-1}] e^{-\frac{1}{4\Theta E z}}. \tag{121}$$

Likewise, for large electron energies $\Theta^{-1} \ll E < M$, we find

$$T_1(E \gg \Theta^{-1}) \simeq H[1-X] \times \left(\frac{(4\Theta E)^2}{2}\int_{4\Theta E}^{2E} dz\, z^{q-(4+p)}[(z-1)^{p+1}+(z-1)^{p-1}] e^{-\frac{1}{4\Theta E z}} + \frac{(4\Theta E)^q}{q}\int_{\frac{M}{M-2}}^{4\Theta E} dz\, z^{-(2+p)}[(z-1)^{p+1}+(z-1)^{p-1}]\right), \tag{122}$$

where in the second term we approximated $\exp[-z/(4\Theta E)] \simeq 1$.

For the following analysis it is convenient to introduce the dimensionless electron energy variable

$$E = \frac{M}{2}\epsilon, \tag{123}$$

where, according to Equation (100),

$$1-\sqrt{1-\frac{2}{M}} \leqslant \epsilon \leqslant 1+\sqrt{1-\frac{2}{M}}. \tag{124}$$

The function (120) reads

$$X(\epsilon) = \frac{1}{\Theta M \epsilon(2-\epsilon)}. \tag{125}$$

The function $X(\epsilon)$ is symmetric with respect to $\epsilon = 1$, where it attains its minimum value

$$X_{\min} = \frac{1}{\Theta M}. \tag{126}$$

At the minimum and maximum electron energies (125), $X(\epsilon_{\min,\max}) = X_{\max} = 1/(2\Theta) \gg 1$.

Likewise, the electron production spectrum (115) becomes

$$\frac{dN}{d\epsilon}(\epsilon) = \frac{3\tau_0 I_0 H[M-2]}{2^{q-p+1}\Gamma(q)\Theta^{1+q}M^{q+p}\epsilon^{1+q+p}} T_1(\epsilon), \tag{127}$$

with

$$T_1\left(\epsilon \ll \frac{2}{M\Theta}\right) \simeq 2(\Theta M\epsilon)^2 H[X-1] \times \int_{\frac{1}{2-\epsilon}}^{M\epsilon} dz\, z^{q-(4+p)}[(z-1)^{p+1}+(z-1)^{p-1}] e^{-\frac{2}{\Theta M z}} \tag{128}$$

and

$$T_1\left(\epsilon \gg \frac{2}{M\Theta}\right) \simeq H[1-X] \times \left(\frac{(2\Theta M\epsilon)^2}{2}\int_{2\Theta M\epsilon}^{M\epsilon} dz\, z^{q-(4+p)}[(z-1)^{p+1}+(z-1)^{p-1}]e^{-\frac{2}{\Theta M z}} + \frac{(2\Theta M\epsilon)^q}{q}\int_{\frac{2}{2-\epsilon}}^{2\Theta M\epsilon} dz\, z^{-(2+p)}[(z-1)^{p+1}+(z-1)^{p-1}]\right). \quad (129)$$

In terms of ϵ the overriding energy restrictions $E \leqslant (1/\Theta \ln \tau_0)$ and $E > \tau_0/\Theta$ correspond to

$$\epsilon \leqslant \frac{2}{M\Theta \ln \tau_0} < \frac{2}{M\Theta}, \quad (130)$$

provided $\ln \tau_0 > 1$, and

$$\epsilon > \frac{2\tau_0}{M\Theta} > \frac{2}{M\Theta}, \quad (131)$$

provided $\tau_0 > 1$.

8.1. Electron Production Spectrum for $E \ll (\Theta \ln \tau_0)^{-1}$

Here we substitute in Equation (128) $z = t/(1-(\epsilon/2))$ to obtain

$$\begin{aligned} V_1(\epsilon) &= \frac{T_1\left(\epsilon \ll \frac{2}{M\Theta}\right)H[X-1])}{2(\Theta M\epsilon)^2} \\ &= \left(1-\frac{\epsilon}{2}\right)^{3+p-q}\int_1^{\frac{1}{2\Theta X}} dt\, t^{q-(4+p)} \times \left[\left(\frac{t}{1-\frac{\epsilon}{2}}-1\right)^{p+1}+\left(\frac{t}{1-\frac{\epsilon}{2}}-1\right)^{p-1}\right]e^{-Xt} \\ &= \left(1-\frac{\epsilon}{2}\right)^{2-q}e^{-X}\int_0^{\frac{1}{2\Theta X}-1} dy\,(1+y)^{q-(4+p)} \times \left[\left(y+\frac{\epsilon}{2}\right)^{p+1}+\left(1-\frac{\epsilon}{2}\right)^2\left(y+\frac{\epsilon}{2}\right)^{p-1}\right]e^{-Xy}, \end{aligned} \quad (132)$$

where we substituted $t = 1+y$ in the last step. Replacing the exponential function by unity for $y < X^{-1} < 1$ and zero otherwise, we obtain to leading order in $(1/X)$,

$$\begin{aligned} V_1(\epsilon) &\simeq \left(\frac{\epsilon}{2}\right)^p\left(1-\frac{\epsilon}{2}\right)^{2-q}e^{-X} \times \left[\left(\frac{\epsilon}{2}\right)^2\frac{\left(1+\frac{2}{\epsilon X}\right)^{p+2}-1}{p+2}+\left(1-\frac{\epsilon}{2}\right)^2\frac{\left(1+\frac{2}{\epsilon X}\right)^p-1}{p}\right] \\ &= \left(\frac{\epsilon}{2}\right)^p\left(1-\frac{\epsilon}{2}\right)^{2-q}e^{-X}\left[\left(\frac{\epsilon}{2}\right)^2\frac{(1+2\Theta M(2-\epsilon))^{p+2}-1}{p+2} + \left(1-\frac{\epsilon}{2}\right)^2\frac{(1+2\Theta M(2-\epsilon))^p-1}{p}\right]. \end{aligned} \quad (133)$$

With Equations (132) we then obtain for the electron production spectrum at small energies

$$\frac{dN}{d\epsilon}\left(\epsilon \ll \frac{2}{M\Theta\ln\tau_0}\right) \simeq \frac{3\tau_0 I_0}{4\Gamma(q)M^p\Theta} \times X^{q-2}e^{-X}H[X-1]Y(\epsilon) \quad (134)$$

with the function

$$Y(\epsilon) = \epsilon^{-1}\left[\left(\frac{\epsilon}{2}\right)^2\frac{(1+2\Theta M(2-\epsilon))^{p+2}-1}{p+2} + \left(1-\frac{\epsilon}{2}\right)^2\frac{(1+2\Theta M(2-\epsilon))^p-1}{p}\right]. \quad (135)$$

The production spectrum (134) at low electron energies is the product of a power law with an exponential cutoff in the symmetric energy variable $X(E)$, which reflects the adopted Wien soft photon spectrum, times the distribution function $Y(\epsilon)$, which reflects the incoming gamma-ray power-law distribution.

Depending on the maximum gamma-ray energy M being smaller or larger than Θ^{-1}, we derive its approximations as

$$Y(\epsilon, M\Theta \ll 1) \simeq \frac{1}{X}\left[1-\frac{2}{\epsilon}+\frac{2}{\epsilon^2}\right] \quad (136)$$

(independent of the incoming gamma-ray energy distribution) and

$$Y(\epsilon, M\Theta \gg 1) \simeq \frac{2^p}{p+2}\epsilon^{-(1+p)}X^{-(p+2)} \quad (137)$$

(strongly dependent on the incoming gamma-ray energy distribution).

The constraint $X > 1$ corresponds to

$$\epsilon(2-\epsilon) < \frac{1}{\Theta M} \quad (138)$$

and is always fulfilled when $M\Theta < 1$. In the opposite case of $M\Theta > 1$, the constraint only allows electron energies between $1 \leqslant E \leqslant (1/4\Theta)$, in agreement with our initial assumption $4\Theta E \ln\tau_0 \ll 1$.

8.2. Electron Production Spectrum for $E \gg \tau_0\Theta^{-1}$

The first integral in Equation (122) can be approximated as

$$\begin{aligned} j_1 &= \int_{4\Theta E}^{2E} dz\, z^{q-(4+p)}[(z-1)^{p+1}+(z-1)^{p-1}]e^{-\frac{2}{\Theta M z}} \\ &\simeq \int_{4\Theta E}^{2E} dz\, z^{q-3}\left[1-\frac{p+1}{z}\right]e^{-\frac{2}{\Theta M z}} \end{aligned} \quad (139)$$

because in this energy range $z \geqslant 4\Theta E \gg 1$. We obtain

$$j_1 \simeq (4\Theta E)^{q-2}\frac{2c_1(q)}{q} \quad (140)$$

with the constant of order unity

$$c_1(q) = \frac{q}{2}e^{-1}U(1, q-1, 1) = \frac{q\Gamma(q-2,1)}{2}, \quad (141)$$

which is tabulated in Table 1.

We find for the second integral in Equation (122) with the substitution $z = 1/w$

$$\begin{aligned} j_2(p) &= \int_{\frac{M}{M-2}}^{4\Theta E} dz\, z^{-(2+p)}[(z-1)^{p+1}+(z-1)^{p-1}] \\ &= \int_{\frac{1}{4\Theta E}}^{\frac{M-2}{M}} \frac{dw}{w}\left[(1-w)^{p+1}+w^2(1-w)^{p-1}\right]. \end{aligned} \quad (142)$$

Table 1
The Constant $c_1(q)$ for Different Values of q

q	$c_1(q)$
1.0	0.074
1.5	0.134
2.0	0.219
2.5	0.349
3.0	0.552
3.5	0.889
4.0	1.472

For integer values of $p = 1, 2, \ldots$, the integral $j_2(p)$ can be solved exactly, e.g.,

$$j_2(1) = \ln\frac{1}{X} - \frac{1}{2\Theta E}\left(\frac{1}{X} - 1\right) + \frac{1}{(4\Theta E)^2}\left(\frac{1}{X^2} - 1\right). \quad (143)$$

For general values of p we use the expansion for $w < 1$

$$(1-w)^{p+1} + w^2(1-w)^{p-1} \simeq 1 - (p+1)w + \frac{p^2+p+2}{2}w^2, \quad (144)$$

yielding the approximation

$$j_2(p) \simeq \ln\frac{1}{X} - \frac{p+1}{4\Theta E}\left(\frac{1}{X} - 1\right) + \frac{p^2+p+2}{4(4\Theta E)^2}\left(\frac{1}{X^2} - 1\right). \quad (145)$$

which for $p = 1$ agrees exactly with Equation (143).

Collecting terms, we obtain for Equation (122)

$$T_1(E \gg \tau_0\Theta^{-1}) \simeq \frac{(4\Theta E)^q}{q} H[1-X] \times \left[\ln\frac{1}{X} + \frac{p+1}{4\Theta E}\left[1 - \frac{1}{X}\right] + c_1(q)\right]. \quad (146)$$

or

$$T_1\left(\epsilon \gg \frac{2}{\Theta M}\right) \simeq \frac{(2\Theta M)^q}{q} H[1-X]\epsilon^q \times \left[\ln\frac{1}{X} + \frac{p+1}{2\Theta M\epsilon}\left[1 - \frac{1}{X}\right] + c_1(q)\right]. \quad (147)$$

The electron production spectrum (127) at high energies then becomes

$$\frac{dN}{d\epsilon}\left(\epsilon \gg \frac{2\tau_0}{\Theta M}\right) \simeq \frac{3\tau_0 I_0 H[1-X]}{\Gamma(q)\Theta M^p}\epsilon^{-(1+p)}S(\epsilon) \quad (148)$$

with the function

$$S(\epsilon) = \frac{2^{p-1}}{q}\left[c_1(q) + \ln\frac{1}{X} + \frac{p+1}{2\Theta M\epsilon}\left[1 - \frac{1}{X}\right]\right]. \quad (149)$$

The electron production spectrum at high energies is the product of the power law ($\propto \epsilon^{-(p+1)}$), reflecting the incoming gamma-ray energy spectrum, and the distribution $S(\epsilon)$.

The constraint $X < 1$ for $\Theta M \gg 1$ corresponds to electron energies between $1/(4\Theta) \leqslant E \leqslant M - (1/4\Theta)$, which agrees with our original assumption $4\Theta E \gg 1$.

8.3. Electron Production Spectra at Intermediate Energies $(1/\Theta \ln\tau_0) \leqslant E \leqslant \tau_0/\Theta$

The details of the approximations are given in Appendix D. We derive approximately

$$\frac{dN}{d\epsilon}(\epsilon, q=2) \simeq \frac{3\pi^{1/2} I_0 \Theta^{\frac{1}{2}} H[M-2]\epsilon^{-(p-\frac{1}{2})}}{2^{3-p}M^{p-\frac{1}{2}}}. \quad (150)$$

9. SUMMARY OF THE DERIVED ELECTRON PRODUCTION SPECTRA

Summarizing the main results of the last two sections, we notice that the approximations of the electron production spectrum depend on the value of the maximum gamma-ray energy M with respect to $M_c = \Theta^{-1}$, which is determined by the inverse soft photon temperature Θ^{-1}.

9.1. Maximum Gamma-ray Energies $2 \ll M \ll M_c$

In the case $2 \ll M \ll M_c$, only soft photons in the exponential tail of the Wien distribution overcome the threshold for pair production. As a result the maximum electron energy $E_{\max} \simeq M - (1/2)$ is well below $(\Theta \ln\tau_0)^{-1}$ and the electron production spectrum is given by Equations (134) and (136) providing

$$\frac{dN}{d\epsilon}\left(1 - \sqrt{1-\frac{2}{M}} \leqslant \epsilon \leqslant 1 + \sqrt{1-\frac{2}{M}}, \Theta M \ll 1\right) \simeq A_0(\Theta M)^{3-q}\epsilon^{1-q}(2-\epsilon)^{3-q}[1+(1-\epsilon)^2]e^{-\frac{1}{\Theta M\epsilon(2-\epsilon)}}, \quad (151)$$

with the abbreviation

$$A_0 = \frac{3\tau_0 I_0}{4\Gamma(q)\Theta M^p}. \quad (152)$$

Due to the dominating exponential function

$$e^{-\frac{1}{\Theta M\epsilon(2-\epsilon)}} \leqslant e^{-(\Theta M)^{-1}} = e^{-(M_c/M)} \ll 1, \quad (153)$$

the pair production spectrum in this case is strongly peaked at $\epsilon = 1$. This corresponds to half of the maximum gamma-ray energy ($E = M/2$), though it is strongly exponentially reduced (see Figure 6), as indicated by the extremely small numbers at the vertical scale.

9.2. Ultrahigh Maximum Gamma-ray Energies $M \gg M_c$

In the opposite case $M \gg M_c$ most of the low-energy soft photons from the power-law part of the Wien distribution also overcome the threshold for pair production. Here the electron production spectrum is more involved; it is given by the still exponentially reduced Equations (134) and (137) at electron energies $E \leqslant (\Theta \ln\tau_0)^{-1}$, Equation (150) at electron energies $E \in [(\Theta \ln\tau_0)^{-1}, \tau_0/\Theta]$, and Equation (148) at electron energies $(\tau_0/\Theta) \leqslant E \leqslant M - (1/2)$.

As a rough analytical expression, to reproduce all essential features of these three different approximations, we use in the case of $q = 2$, for which we derived approximation (150),

$$\frac{dN}{d\epsilon}\left(1 - \sqrt{1-\frac{2}{M}} \leqslant \epsilon \leqslant 1 + \sqrt{1-\frac{2}{M}}, \Theta M \gg 1\right) \simeq A_1 e^{-\frac{2}{\Theta M\epsilon \ln\tau_0}} \frac{\epsilon^{\frac{1}{2}-p}}{1 + \frac{\pi^{1/2}}{2\tau_0 c_1(2)}(\Theta M\epsilon)^{3/2}} = A_1 e^{-\frac{2}{\Theta M\epsilon \ln\tau_0}} \frac{\epsilon^{\frac{1}{2}-p}}{1 + \frac{\pi}{\tau_0}(\Theta M\epsilon)^{3/2}}, \quad (154)$$

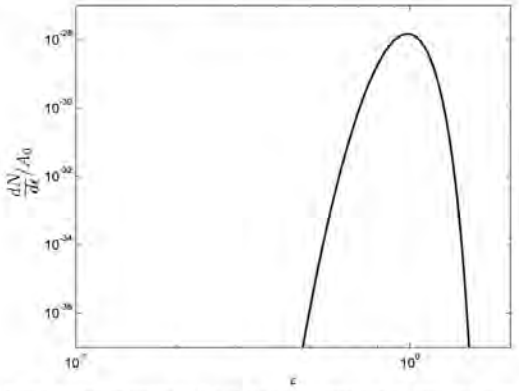

Figure 6. Approximation (151) of the energy spectrum of generated pairs $N(\epsilon)/A_0$ from a power-law-distributed gamma-ray beam $\propto k_1^{-3}H[M-k_1]$ below the maximum gamma-ray energy $M = 10^5$ interacting with isotropically distributed soft photons with a Wien distribution with spectral index $q = 2$ and temperature $\Theta = 1.6 \times 10^{-7}$ (corresponding to 0.08 eV), so that $M_c = 1/\Theta = 6 \times 10^6$. Because M is a factor of 60 smaller than M_c in this example, only soft photons in the exponential tail of the Wien distribution overcome the threshold for pair production, so that the generated pair production spectrum is exponentially reduced (see the small numbers at the vertical axis).

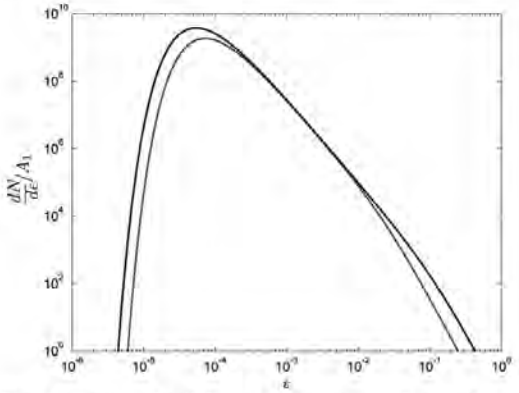

Figure 7. Approximation (154) of the energy spectrum of generated pairs $N(\epsilon)/A_1$ from a power-law-distributed gamma-ray beam $\propto k_1^{-3}H[M-k_1]$ for the maximum gamma-ray energy $M = 10^{10}$ interacting with isotropically distributed soft photons with a Wien distribution with spectral index $q = 2$ and temperature $\Theta = 1.6 \times 10^{-7}$ (corresponding to 0.08 eV), so that $M_c = 1/\Theta = 6 \times 10^6$. Two different values of the optical depth, $\tau_0 = 10^3$ (dotted line) and $\tau_0 = 10^4$ (full line), are adopted. Note that at intermediate electron energies $\epsilon \in [\epsilon_1, \epsilon_2] = 1.2 \times 10^{-3}[(\ln \tau_0)^{-1}, \tau_0]$ the production spectrum is independent of the actual value of τ_0.

with the abbreviation

$$A_1 = \frac{3\pi^{1/2} I_0 \Theta^{\frac{1}{2}}}{2^{3-p} M^{p-\frac{1}{2}}}. \tag{155}$$

This spectrum is shown in Figure 7 for the two values of $\tau_0 = 10^3$ and $\tau_0 = 10^4$. In both cases the low-energy part below $\epsilon < \epsilon_1 = (2M_e/M \ln \tau_0)$ exhibits a strong exponential cutoff, whereas the spectrum at very high energies $\epsilon > \epsilon_1 = 2M_e\tau_0/M$ exhibits the steep power law $\propto \epsilon^{-1-p}$. At intermediate energies the production spectrum is independent of the actual value of

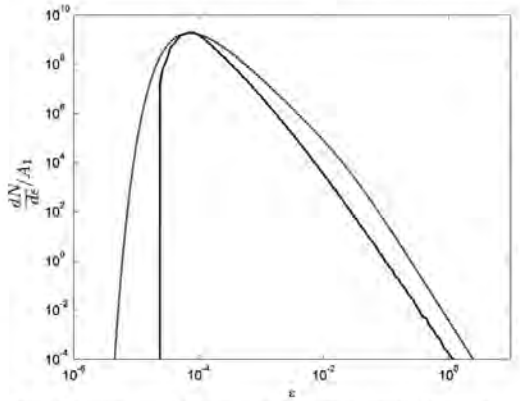

Figure 8. Comparison of the analytically calculated (dotted line) with the numerically calculated (full line) production spectrum of generated pairs from a power-law-distributed gamma-ray beam $\propto k_1^{-3}H[M-k_1]$ for the maximum gamma-ray energy $M = 10^{10}$ interacting with isotropically distributed soft photons with a Wien distribution with spectral index $q = 2$ and temperature $\Theta = 1.6 \times 10^{-7}$ (corresponding to 0.08 eV). An optical depth of $\tau_0 = 10^3$ is adopted.

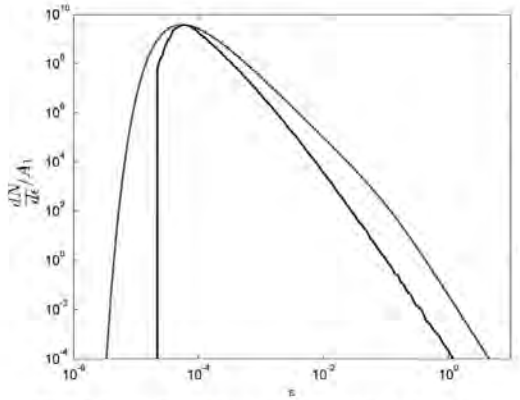

Figure 9. Same as Figure 8 for an adopted optical depth of $\tau_0 = 10^4$.

τ_0, as discussed in Section 7.2. However, the extension of the energy spectrum depends on the value of τ_0 as $\epsilon_1 \propto (\ln \tau_0)^{-1}$ and $\epsilon_2 \propto \tau_0$ become smaller and larger with increasing τ_0, respectively. The energy spectrum peaks near ϵ_1, corresponding to $E_1 = M\epsilon_1/2 = M_e/\ln \tau_0$ for gamma-ray spectral indices $p > 0.5$, and at ϵ_2, corresponding to $E_2 = M\epsilon_2/2 = M_e\tau_0$ for $p < 0.5$. In Figures 8 and 9, we compare our analytical production spectrum (from Figure 7) with the numerically calculated production spectrum using the code of Elyiv et al. (2009) for optical depths $\tau_0 = 10^3$ (Figure 8) and $\tau_0 = 10^4$ (Figure 9), respectively. In this simulation we do not include the effects of the extragalactic magnetic field as well as the IC interactions with CMB photons, instead calculating only the generated pair energy distribution resulting from the first double photon collisions. The analytical and numerical curves have been normalized at the maximum of the production spectrum. Apart from very low gamma-ray energies, the level of agreement is remarkably high: the spectral form and the

location of the maximum are identical. These agreements justify a posteriori the assumptions that allowed our analytic approximation.

10. SUMMARY AND CONCLUSIONS

The detection of about 30 blazars at cosmological distances with strong TeV photon emission has renewed interest in the production of relativistic pairs in double photon collisions of the beamed gamma rays with the isotropically distributed EBL in the IGM. The generated pair beams can probe cosmological magnetic fields in cosmic voids; their deposited energy might also affect the thermal history of the IGM.

The typical energies $k_0 \simeq 10^{-7}$ in units of $m_e c^2$ of the EBL are more than 10 orders of magnitude smaller than the observed gamma-ray energies $k_1 \geqslant 10^7$. Using the limit $k_0 \ll k_1$, we demonstrated from the relativistic kinematics that the angular distribution of the generated pairs from the double photon collision processes in the lab frame is highly beamed in the direction of the initial gamma-ray photons, an obvious expected result but one proven explicitly here.

We also analytically calculated anew the energy spectrum (Equation (63)) of the generated pairs from a monoenergetic beamed gamma ray interacting with a monoenergetic, gyrotropically and isotropically distributed soft photon distribution. Despite its different analytical form, it agrees perfectly with the earlier derived production spectrum of Aharonian et al. (1983) and with the numerically computed energy spectrum based on the work of Elyiv et al. (2009). The analytic energy spectrum (63) serves as a kernel to derive analytically by two integrations the electron energy production spectrum (101) for arbitrary gamma-ray energy distributions and arbitrary soft photon energy distributions.

As blazar observations often indicate power-law distributions of the emitted gamma-ray beam with $I(k_1) = I_0 k^{-\mu}$ for $k_1 \leqslant M$, we studied this case in more detail, adopting a Wien-type $N(k_0) \propto k_0^q \exp(-k_0/\Theta)$ soft photon energy distribution, which represents both graybody distributed target photons and flat ($q > -1$) power-law target photons with an exponential cutoff. For the astrophysically important case of the Wien distribution with $q > 1$, the two integrals of the production spectrum (101) can be evaluated approximately in closed form—providing the analytical approximations for the electron production spectrum. For distant objects with luminosity distances $d_L \gg r_0 = 0.49 N_0^{-1}$ Mpc, the implied large values of the optical depth $\tau_0 = d_L/r_0$ indicate that the electron production spectra differ at energies E inside and outside the interval $[(\Theta \ln \tau_0)^{-1}, \tau_0/\Theta]$, provided the maximum gamma-ray energy $M \gg \Theta^{-1}$. Outside this interval the electron production takes place in the optically thin limit with respect to pair production, whereas inside this interval the electron production becomes independent of τ_0, as any gamma-ray photon can only generate two electrons. For maximum gamma-ray energies $M \ll \Theta^{-1}$ this optically thick behavior does not occur. Here the pair production spectrum is strongly peaked at half of the maximum gamma-ray energy ($E = M/2$), but also strongly exponentially reduced, as only soft photons in the exponential tail of the Wien distribution overcome the threshold for pair production.

In the opposite case $M \gg \Theta^{-1}$ low-energy soft photons from the power-law part of the Wien distribution also participate in the pair production process. Here the production spectrum is strongly peaked near $E \simeq \Theta^{-1}$, the inverse of the soft photon temperature, which is exponentially reduced at small energies and decreasing with the steep power law $\propto E^{-1-\mu}$ up to the maximum energy $E = M - (1/2)$.

We are grateful to the referee for a very constructive report on a difficult manuscript. R.S. and D.I. gratefully acknowledge partial support of this work by the German Ministry for Education and Research (BMBF) through Verbundforschung Astroteilchenphysik grant 05A11PCA and the Deutsche Forschungsgemeinschaft through grant Schl 201/23-1. A.E. is the beneficiary of a fellowship granted by the Belgian Federal Science Policy Office.

APPENDIX A

THE INTEGRAL (49)

With $B = 1 - A^2$ the integral (47) reads

$$I(E, k_1, k_0) = (1 - B) I_0 + I_1 + \frac{8}{k_1^2} I_2 - \frac{32}{k_1^4} I_3 - \frac{32(1 - B)}{k_1^4} I_4, \tag{A1}$$

with

$$I_0 = \int_{x_2(T)}^{4k_0/k_1} dx \, \frac{1}{\sqrt{1 - x}(B - x)}, \tag{A2}$$

$$I_1 = \int_{x_2(T)}^{4k_0/k_1} dx \, \frac{\sqrt{1 - x}}{B - x}, \tag{A3}$$

$$I_2 = \int_{x_2(T)}^{4k_0/k_1} dx \, \frac{\sqrt{1 - x}}{x(B - x)}, \tag{A4}$$

$$I_3 = \int_{x_2(T)}^{4k_0/k_1} dx \, \frac{\sqrt{1 - x}}{x^2(B - x)}, \tag{A5}$$

and

$$I_4 = \int_{x_2(T)}^{4k_0/k_1} dx \, \frac{\sqrt{1 - x}}{x^2(B - x)^2} = -\frac{\partial I_3}{\partial B}. \tag{A6}$$

Using

$$\frac{1}{x(B - x)} = \frac{1}{B}\left[\frac{1}{x} + \frac{1}{B - x}\right]$$

provides

$$B I_2 = I_1 + I_5,$$
$$I_5 = \int_{x_2(T)}^{4k_0/k_1} dx \, \frac{\sqrt{1 - x}}{x} = -I_1(B = 0), \tag{A7}$$

so that

$$I(E, k_1, k_0) = (1 - B) I_0 + \left(1 + \frac{8}{B k_1^2}\right) I_1 + \frac{8 I_5}{B k_1^2} + \frac{32}{k_1^4}\left[(1 - B)\frac{\partial I_3}{\partial B} - I_3\right]. \tag{A8}$$

For I_3 we write Equation (A7)

$$I_3 = \frac{1}{B}\int_{x_2(T)}^{4k_0/k_1} dx \, \frac{\sqrt{1 - x}}{x^2(B - x)}(B - x + x) = \frac{1}{B}[I_6 + I_2] = \frac{I_6}{B} + \frac{1}{B^2}[I_1 + I_5] \tag{A9}$$

with

$$I_6 = \int_{x_2(T)}^{4k_0/k_1} dx\,\frac{\sqrt{1-x}}{x^2} = -I_2(B=0). \quad \text{(A10)}$$

The remaining anti-derivatives are (Gradshteyn & Ryzhik 1980)

$$I_0(B) = \frac{1}{(1-B)^{1/2}}\ln\frac{(1-B)^{1/2}+(1-x)^{1/2}}{(1-B)^{1/2}-(1-x)^{1/2}} = \frac{2}{(1-B)^{1/2}}\,\mathrm{artanh}\left(\frac{1-x}{1-B}\right)^{1/2} \quad \text{(A11)}$$

and

$$I_1(B) = (1-B)^{1/2}\ln\frac{(1-B)^{1/2}+(1-x)^{1/2}}{(1-B)^{1/2}-(1-x)^{1/2}} - 2(1-x)^{1/2} = 2(1-B)^{1/2}\,\mathrm{artanh}\left(\frac{1-x}{1-B}\right)^{1/2} - 2(1-x)^{1/2}, \quad \text{(A12)}$$

so that

$$I_5 = -I_1(B=0) = 2(1-x)^{1/2} - \ln\frac{1+(1-x)^{1/2}}{1-(1-x)^{1/2}} = 2(1-x)^{1/2} - 2\,\mathrm{artanh}\,(1-x)^{1/2}. \quad \text{(A13)}$$

Likewise,

$$I_6 = \frac{1}{2}\ln\frac{1+(1-x)^{1/2}}{1-(1-x)^{1/2}} - \frac{(1-x)^{1/2}}{x} = \mathrm{artanh}\,(1-x)^{1/2} - \frac{(1-x)^{1/2}}{x}. \quad \text{(A14)}$$

For Equation (A9) we obtain

$$I_3(B) = \frac{2(1-B)^{1/2}}{B^2}\,\mathrm{artanh}\left(\frac{1-x}{1-B}\right)^{1/2} - \frac{2-B}{B^2}\,\mathrm{artanh}\,(1-x)^{1/2} - \frac{(1-x)^{1/2}}{Bx}, \quad \text{(A15)}$$

so that

$$\frac{\partial I_3}{\partial B} = \frac{(B-2x)(1-x)^{1/2}}{B^2x(B-x)} + \frac{4-B}{B^3}\,\mathrm{artanh}\,(1-x)^{1/2} + \frac{3B-4}{(1-B)^{1/2}B^3}\,\mathrm{artanh}\left(\frac{1-x}{1-B}\right)^{1/2}. \quad \text{(A16)}$$

This provides for

$$(1-B)\frac{\partial I_3}{\partial B} - I_3(B) = \frac{[B+(B-2)x](1-x)^{1/2}}{B^2x(B-x)} + \frac{4-3B}{B^3} \times \left[\mathrm{artanh}\,(1-x)^{1/2} - \frac{(4-B)(1-B)^{1/2}}{B^3}\,\mathrm{artanh} \times \left(\frac{1-x}{1-B}\right)^{1/2}\right]. \quad \text{(A17)}$$

The integral (A8) finally becomes

$$I(E,k_1,k_0) = R[4k_0/k_1] - R[x_2(T)], \quad \text{(A18)}$$

with

$$R[x] = 4(1-B)^{1/2}\left[1+\frac{4}{Bk_1^2} - \frac{8(4-B)}{B^3k_1^4}\right]\mathrm{artanh}\left(\frac{1-x}{1-B}\right)^{1/2} + \frac{16}{Bk_1^2}\left[\frac{2(4-3B)}{B^2k_1^2} - 1\right]\mathrm{artanh}\,(1-x)^{1/2} + 2\left[\frac{16[B+(B-2)x]}{B^2k_1^4x(B-x)} - 1\right](1-x)^{1/2}. \quad \text{(A19)}$$

With $B = 1 - A^2$, Equation (50) is obtained.

APPENDIX B

THE INTEGRAL (79)

The integral (79) reads

$$I_7(m) = \int_0^m dy\,\frac{\ln(1-y)+\ln(1+y)}{(1-y)(1+y)} = \frac{1}{2}\left[\int_0^m dy\,\frac{\ln(1+y)}{1+y} + \int_0^m dy\,\frac{\ln(1-y)}{1-y} + \int_0^m dy\,\frac{\ln(1+y)}{1-y} + \int_0^m dy\,\frac{\ln(1-y)}{1+y}\right]. \quad \text{(B1)}$$

The first two integrals can be directly solved. Partially integrating the forth integral we find

$$I_7(m) = \frac{1}{4}[\ln^2(1+m) - \ln^2(1-m)] + \frac{1}{2}\ln(1-m)\ln(1+m) - I_8(m) \quad \text{(B2)}$$

with

$$I_8(m) = \int_0^m dy\,\frac{\ln(1+y)}{y-1} = \int_1^{1+m} dx\,\frac{\ln(x+2)}{x}. \quad \text{(B3)}$$

Substituting $x = 2s$ yields

$$I_8(m) = \ln 2\int_1^{1+m}\frac{dx}{x} + \int_{\frac{1}{2}}^{\frac{1+m}{2}} dx\,\frac{\ln(s+1)}{s} = \ln 2\ln(1+m) + \mathrm{Li}\left[\frac{1}{2},\frac{1+m}{2}\right]. \quad \text{(B4)}$$

Collecting terms in Equation (B2) then provides the result (79).

APPENDIX C

APPROXIMATIVE EVALUATION OF THE INTEGRAL (109)

All y-integrals not involving the $\ln(1+y)$-function can be expressed as the difference of two incomplete gamma functions. However, for small nonrelativistic value of the dimensionless soft photon temperature $\Theta \ll 1$, we evaluate the integral (111) here approximately. For values of

$$\frac{4\Theta E}{z} \geqslant \frac{2E}{z} - 1,$$

corresponding to

$$z \geqslant 2E(1-2\Theta) \simeq 2E, \quad \text{(C1)}$$

the exponential functions in the integral (109) can be well approximated by unity. However, this case is of no relevance here because z is limited in the integrals (114) and (115) to $2E$. The opposite case

$$z \leqslant 2E(1-2\Theta) \simeq 2E \tag{C2}$$

holds over the whole range of z-values, and allows us to approximate the exponential functions in the integral (109) by unity for $y \leqslant \alpha = 4\Theta E/z$ and for zero otherwise. Consequently, we obtain

$$\begin{aligned} J(E,\Theta,z) &\simeq J(\alpha) \\ &= 4\int_0^\alpha dy\,(1+y)^{q-3}[(1+y)\ln(1+y)-y] \\ &\quad + \frac{z^2-2z+2}{z-1}\int_0^\alpha dy\,y(1+y)^{q-2} \end{aligned} \tag{C3}$$

with

$$\alpha = \frac{4\Theta E}{z}. \tag{C4}$$

After straightforward, but tedious, integrations we derive

$$\begin{aligned} J(\alpha) &= 4(1+\alpha)^{q-2}\left[\frac{(1+\alpha)\ln(1+\alpha)}{q-1} - \frac{\alpha}{q-2}\right] \\ &\quad + \frac{4}{(q-2)(q-1)^2}[(1+\alpha)^{q-1}-1] \\ &\quad + \frac{z^2-2z+2}{(q-1)(z-1)}\left[\alpha(1+\alpha)^{q-1} - \frac{(1+\alpha)^q-1}{q}\right] \end{aligned} \tag{C5}$$

with the asymptotics

$$J(\alpha) \simeq \left[z-1+\frac{1}{z-1}\right]\begin{cases} \frac{\alpha^2}{2} & \text{for } \alpha \leqslant 1 \\ \frac{\alpha^q}{q} & \text{for } \alpha > 1. \end{cases} \tag{C6}$$

APPENDIX D

ELECTRON PRODUCTION SPECTRA AT INTERMEDIATE ENERGIES $(1/\Theta \ln \tau_0) \leqslant E \leqslant \tau_0/\Theta$

Here the electron production spectrum (114) reads

$$\frac{dN}{d\epsilon}(\epsilon) = \frac{3I_0H[M-2]e^{\frac{1}{\Theta M\epsilon}}}{2^{q+2-p}\Gamma(q)\Theta^q M^{p+q-1}\epsilon^{q+p}} T_2(\epsilon), \tag{D1}$$

with the integral

$$T_2(\epsilon) = \int_{\frac{2}{2-\epsilon}}^{M\epsilon} dz\, z^{q-p}(z-1)^{p-1} e^{-\frac{(z+\frac{2}{z})}{2\Theta E}} J\left(\frac{2\Theta M\epsilon}{z}\right). \tag{D2}$$

We restrict the analysis to the Wien power-law spectral index $q = 2$, so that the asymptotics (116)

$$J(\alpha) = \left[z-1+\frac{1}{z-1}\right]\frac{\alpha^2}{2} \tag{D3}$$

hold for all values of α. We find

$$\begin{aligned} T_2(\epsilon, q=2) &= 2(\Theta M)^2\epsilon^2 \\ &\quad \times \int_{\frac{2}{2-\epsilon}}^{M\epsilon} dz\, z^{-p}[(z-1)^p + (z-1)^{p-2}] e^{-\frac{(z+\frac{2}{z})}{2\Theta M\epsilon}}, \end{aligned} \tag{D4}$$

so that

$$\frac{dN}{d\epsilon}(\epsilon, q=2) = \frac{3I_0H[M-2]\epsilon^{-p}e^{\frac{2}{\Theta M\epsilon}}}{2^{3-p}M^{p-1}} T_3(\epsilon) \tag{D5}$$

with the integral

$$\begin{aligned} T_3(\epsilon) &= \int_{\frac{2}{2-\epsilon}}^{M\epsilon} dz\, z^{-p}[(z-1)^p + (z-1)^{p-2}] e^{-\frac{(z+\frac{2}{z})}{2\Theta M\epsilon}} \\ &\simeq \int_{\frac{2}{2-\epsilon}}^{M\epsilon} dz \left[1-\frac{p}{z}\right] e^{-\frac{(z+\frac{2}{z})}{2\Theta M\epsilon}} = \int_{\frac{2}{2-\epsilon}}^{M\epsilon} dz\, \exp[-F(z)], \end{aligned} \tag{D6}$$

where

$$F(z) = \frac{z+\frac{2}{z}}{2\Theta M\epsilon} = w\left[\frac{1}{z}+\frac{z}{4}\right] \tag{D7}$$

with

$$w = \frac{2}{\Theta M\epsilon}. \tag{D8}$$

In the approximation (D6) we used $z \geqslant 2$. The remaining integral (D6) is solved by the method of steepest descent.

The function $F(z)$ attains its minimum value $F(z_0) = w$ at $z_0 = 2$. With the approximation

$$F(z) \simeq F(z_0) + \frac{1}{2}F''(z_0)(z-z_0)^2 = w + \frac{w}{8}(z-2)^2 \tag{D9}$$

inserted, we obtain for the integral (D6)

$$\begin{aligned} T_3(w) &\simeq \sqrt{\frac{2\pi}{w}}e^{-w}\left(\mathrm{erf}\left[\sqrt{\frac{w}{8}}(M\epsilon-2)\right]\right. \\ &\quad \left. + \mathrm{erf}\left[\sqrt{\frac{w}{2}}\frac{1-\epsilon}{2-\epsilon}\right]\right) \end{aligned} \tag{D10}$$

in terms of the error function. We find for the electron production spectrum (D5)

$$\epsilon^{p-\frac{1}{2}}\frac{dN}{d\epsilon}(\epsilon, q=2) = \frac{3\pi^{1/2}I_0\Theta^{\frac{1}{2}}H[M-2]}{2^{3-p}M^{p-\frac{1}{2}}} T_4(w) \tag{D11}$$

with the function

$$\begin{aligned} T_4(w) &= \mathrm{erf}\left[\sqrt{\frac{w}{2}}\left(\frac{M\epsilon}{2}-1\right)\right] + \mathrm{erf}\left[\sqrt{\frac{w}{2}}\frac{1-\epsilon}{2-\epsilon}\right] \\ &= \mathrm{erf}\left[\frac{1-\Theta w}{\sqrt{2w\Theta}}\right] + \mathrm{erf}\left[\sqrt{\frac{w}{2}}\frac{1-\frac{2}{\Theta M w}}{2-\frac{1}{\Theta M w}}\right]. \end{aligned} \tag{D12}$$

In this electron energy range the function w varies between $w \in [1/\ln\tau_0, \tau_0]$. Given the extreme smallness of $\Theta \ll 1$; the argument of the first error function in Equation (D12) is large compared to unity. This allows us to approximate $T_4(w) \simeq 1$, as the argument of the second error function is a factor $\Theta w/2$ smaller than the argument of the first error function. We then obtain for the electron production spectrum (D11) at intermediate energies

$$\frac{dN}{d\epsilon}(\epsilon, q=2) \simeq \frac{3\pi^{1/2}I_0\Theta^{\frac{1}{2}}H[M-2]\epsilon^{-(p-\frac{1}{2})}}{2^{3-p}M^{p-\frac{1}{2}}}. \tag{D13}$$

REFERENCES

Abramowitz, M., & Stegun, I. A. 1972, Handbook of Mathematical Functions (Washington, DC: NBS)

Abramowski, A., Acero, F., Aharonian, F., et al. (HESS Collaboration), 2012, A&A, 538, A103

Aharonian, F. A. 2003, Very High Energy Cosmic Gamma Radiation (Singapore: World Scientific), Equations (3–25)

Aharonian, F. A., Akhperjanian, A. G., Bazer-Bachi, A. R., et al. (HESS Collaboration), 2006, Nature, 440, 1018

Aharonian, F. A., Atoyan, A. M., & Nagapetian, A. M. 1983, Astrofizika (Astrophysics), 19, 187

Aharonian, F. A., Coppi, P. S., & Völk, H. J. 1994, ApJ, 423, L5

Bonometto, S., & Rees, M. J. 1971, MNRAS, 152, 21

Böttcher, M., & Schlickeiser, R. 1997, A&A, 325, 866

Broderick, A. E., Chang, P., & Pfrommer, C. 2012, ApJ, 732, 22

Cerutti, B., Dubus, G., & Henri, G. 2009, A&A, 507, 1217

Elyiv, A., Neronov, A., & Semikoz, D. V. 2009, Phys. Rev. D, 80, 023010

Franceschini, A., Rodighiero, G., & Vaccari, M. 2008, A&A, 487, 837

Gould, R. J., & Schreder, G. P. 1967, Phys. Rev., 155, 1404

Gradshteyn, I. S., & Ryzhik, I. M. 1980, Tables of Integrals, Series and Products (New York: Academic)

Hagedorn, R. 1973, Relativistic Kinematics (Reading, MA: Benjamin)

Hinton, J. A., & Hofmann, W. 2009, ARA&A, 47, 523

Jauch, J. M., & Rohrlich, F. 1955, Theory of Photons and Electrons (Reading, MA: Addison-Wesley)

Kneiske, T. M., Bretz, T., Mannheim, K., & Hartmann, D. H. 2004, A&A, 413, 807

Neronov, A., & Semikoz, D. 2009, Phys. Rev. D, 80, 123012

Neronov, A., & Vovk, I. 2010, Science, 328, 73

Schlickeiser, R., Ibscher, D., & Supsar, M. 2012, ApJ, 758, 102

4.3 Висновки до розділу 4

Було знайдено, що властивості електромагнітної лавини та зображення блазарів в гамма-променях сильно залежать від магнітного поля в космічних войдах, через які поширюється лавина, та від частки об'єму Всесвіту, зайнятої войдами. Така залежність може бути використана для виявлення та оцінки екстремально малого магнітного поля в космічних порожнинах. Запропонований алгоритм у [6], випробуваний на чисельних даних, може бути використаний на реальних даних при спостереженнях гамма-телескопами. Такі вимірювання дозволять вибрати коректну космологічну модель походження магнітного поля у Всесвіті, оскільки різні моделі дають дуже різні оцінки напруженості поля (більше ніж на 10 порядків розходження).

Було вивчено морфологічні властивості гамма зображень блазарів. За допомогою чисельних моделювань показано, що витягнута струменеподібна структура форми зображення зумовлена невеликим зміщенням (порядку кількох градусів) напрямку генерації первинних фотонів із блазара від променя зору. Досліджено характеристики протяжного зображення, а саме форму, розподіл поверхневої яскравості та їхню залежність від характеристик міжгалактичного магнітного поля. Показано, що гамма випромінювання від протяжної частини зображення затримується близько на 10 млн. років по відношенню до прямих фотонів від джерела. Така довга затримка означає, що протяжні гало можуть спостерігатися навколо блазарів, які вже не активні.

Показано, що комбінація кінетичних ефектів, нелінійного загасання Ландау та неоднорідностей густини середовища стабілізують електрон-позитронні пучки. Енергія пучка не витрачається на генерування нестабільностей в плазмі. Тобто, пучок у космічних войдах є стабільний на

масштабах набагато більших, ніж час розвитку електромагнітного каскаду. З цього також випливає, що електрон-позитронні пучки від блазарів не впливають на міжгалактичне середовище.

Доведено, що кутовий розподіл генерованих електрон-позитронних пар від подвійної фотонної взаємодії в лабораторній системі відліку є сильно концентрованим в напрямку руху первинного гамма-фотону. Аналітично виведено рівняння для енергії електрон-позитронних пар для різних енергетичних спектрів як фонового випромінювання, так і первинного гамма-випромінювання. Отримані аналітичні вирази було перевірено на чисельних моделюваннях.

У роботі [92] досліджено обмеження на величину напруженості позагалактичних магнітних полів. Автори використали результати моделювання [7] як доказ того, що космічна Фермі-лабораторія не зможе задетектувати протяжні гало навколо блазарів для моделі магнітного поля, розглянутій в їхній роботі. В статтях [93, 94] автори відмітили важливість врахування потоку фотонів від згаслих АЯГ за прикладом моделювання [7], а у огляді [95] – важливість визначення нижньої межи на величину напруженості магнітного поля за спостереженнями протяжних гало навколо блазарів. У роботах [96–97, 105] відзначено важливість підходу Монте-Карло симуляцій, застосованого в роботах [6, 7], оскільки аналітичний підхід не здатен врахувати всі особливості електромагнітної лавини від блазарів. У роботі [98] автори використали результат числельних моделювань напрямків приходу первинних та вторинних гама променів від блазарів при різних значеннях напруженості магнітних полів [6] для валідації своїх результатів. Результати робіт [4–7] широко обговорюються у великому огляді [99], де проведено аналіз походження, еволюції та особливостей спостережень позагалактичних магнітних полів.

Крім того, на результати робіт дисертації, висвітлених у цьому розділі, посилаються багато авторів, що доводить їх актуальність і сьогодні. Зокрема, результати роботи [6] відзначені у роботах [100, 115, 116], а висновки [6, 7] обговорюються у роботах [100, 101, 106], в статтях [102–105, 108] згадуються результати, опубліковані у [7]. Також, у роботі [107] розглянуті обмеження на міжгалактичне магнітне поле, використовуючи факт анізотропії протяжних ореолів у діапазоні ГеВ-них енергій навколо блазарів, запропонований у роботі [7]. У роботах [109, 114] підтверджено, що достатньо сильне магнітне поле зменшує потік вторинних частинок електромагнітного каскаду нижче спостережуваної границі, встановленої обмеженнями спостережуваних приладів, що в узгодженні з роботами [4, 6]. У роботах [111–113] досліджувалась стабільність електромагнітного пучка від блазарів у позагалактичному середовищі: авторами були використані наближення, опубліковані в наших роботах [4, 5], а також результати чисельних моделювань з роботи [6].

ВИСНОВКИ

Дисертаційна робота присвячена дослідженню космічних войдів, або порожнин, – областей у Всесвіті з низькою концентрацією галактик, а також аналізу оточення і населення войдів та процесів, які відбуваються у войдах та навколо них у широкому спектральному діапазоні. Серед таких об'єктів великомасштабної структури Всесвіту – галактики, АЯГ, блазари, скупчення галактик. Серед інших досліджених важливих чинників – магнітне поле войдів, ефекти гравітаційного лінзування на квазарах, методи визначення відстаней до галактик та виділення малонаселених систем галактик за різними критеріями ізольованості. Найважливіші отримані результати такі:

1. Вперше запропоновано два методи пошуку войдів, які базуються на *динамічних* критеріях виділення порожнин у лагранжевих координатах: LZVF, що використовує наближення Лагранжа-Зельдовича для відстеження зворотних у часі орбіт галактик та UVF, який використовує метод послаблення кореляційної функції галактика-галактика для доведення розподілу об'єктів до однорідного. В обох випадках порожнини визначаються як області негативної дивергенції зміщень, які можна розглядати як стоки трейсерів маси. Значимість сигналу дивергенції в центральних частинах войдів, отриманих з обидвох шукачів, на 60 % вища, ніж для надлишку профіля густини, отриманим геометричним методом.

2. Показано, що запропоновані шукачі войдів є перспективними альтернативами до існуючих і є ефективними для покращення точності космологічних тестів, що базуються на статистиці войдів та вимірюванні асиметричностей накладених войдів, наприклад, тесту Алькока-Пачинського для уточнення космічних параметрів, насамперед густини матерії Ω_{m}.

3. Було застосовано п'ять моделей машинного навчання для визначення модуля відстані галактик за їхніми спостережуваними даними, такими як видимі зоряні величини у кількох смугах, кутовий діаметр, поверхнева яскравість, показники кольору та координати галактик, променева швидкістю, а також відомий модуль відстані. Було показано, що модель регресії нейронної

мережі з двома прихованими шарами дає точніший результат, ніж інші моделі. Показано, що запропонована модель є конкурентоспроможною у порівнянні з загальновживаними вторинними методами вимірювань модуля відстані, такими як метод Фундаментальної площини та відношення Таллі-Фішера.

4. Вперше проведено аналіз двоточкової кореляційної функції вибірки точкових джерел поля XMM-LSS (11 кв. град) зі 94 спостережуваних полів XMM-Newton (d=30’), що містять понад п’ять тисяч точкових джерел у м’якому (0.5– 2 кеВ) та жорсткому (2–10 кеВ) діапазонах. Було знайдено, що амплітуда двоточкової кореляційної функції значно більша у жорсткому діапазоні, ніж у м’якому. Показано, що АЯГ з жорстким рентгенівським спектром (здебільшого АЯГ 2 типу) більш кластеризовані, ніж ті, що мають м'який спектр (АЯГ 1 типу). Це може означати, що два основних типи АЯГ перебувають в різних середовищах, а саме АЯГ з м'яким рентгенівським спектром тяжіють до більш розріджених областей Всесвіту, якими є межі космічних войдів.

5. Дослідження властивостей близького (<0.4-1 Мпк) та далекого (>1 Мпк) оточення рентгенівських АЯГ поля XXL до z = 1 показало, що АЯГ обох типів можуть знаходитися як у тісному, так у розрідженому оточенні. Було знайдено, що рентгенівські АЯГ, що мають також радіо ототожнення є більш затьмареними (жорсткими у рентгені), ніж джерела, що не випромінюють в радіо діапазоні. Ніякої значної різниці у великомасштабному оточенні різних типів АЯГ (1 та 2 типів, радіо і не радіо об’єктами, світними і тм’яними) знайдено не було. Однак, було підтверджено, що АЯГ здебільшого розташовані у локальних надлишках густини, порівняно з рентгенівськими галактиками. Такі результати підтверджують універсальну схему АЯГ, але не виключають, що оточення може мати вплив на еволюцію АЯГ.

6. Вперше було застосовано геометричний метод Вороного вищих порядків для виділення галактик, пар та триплетів з вибірки огляду SDSS. Було знайдено, що галактики в ізольованих парах та триплетах мають світність у два рази вищу, ніж ізольовані галактики. Також, групи галактик у більш тісному

оточені, наприклад, що знаходяться у скупченнях, мають більшу дисперсію швидкостей та відношення маси до світності.

7. Було розраховано очікувані статистичні властивості для виявлення оптичних ототожнень множинних зображень квазарів з рентгенівського огляду XXL, враховуючи параметри спостережень супутника XMM-Newton. Серед 11 тисяч квазарів очікується знайти ∼20 гравітаційно-лінзових квазарів з більше ніж двома зображеннями. Візуальний перегляд оптичних *g, r* та *i* зображень 5500 рентгенівських АЯГ, розташованих на 11 кв. градусах огляду XMM-LSS та аналіз кольорів дозволив знайти 3 кандидати у лінзовані АЯГ.

8. Вперше доведено ряд властивостей магнітного поля в войдах. Знайдено, що властивості електромагнітної лавини та зображення блазарів в гамма-променях сильно залежать від магнітного поля в космічних войдах, через які поширюється лавина, та від частки об'єму Всесвіту, зайнятої войдами. Така залежність може бути використана для виявлення та оцінки екстремально малого магнітного поля в космічних порожнинах. Було вивчено морфологічні властивості гамма зображень блазарів методами чисельних моделювань. Досліджено характеристики протяжного зображення, а саме форму, розподіл поверхневої яскравості та їхню залежність від характеристик міжгалактичного магнітного поля. Показано, що гамма випромінювання від протяжної частини зображення затримується близько на 10 млн. років по відношенню до прямих фотонів від джерела. Така довга затримка означає, що протяжні гало можуть спостерігатися навколо блазарів, які вже не активні. Доведено, що електрон-позитронні пучки в космічних порожнинах є стабільними на масштабах набагато більших, ніж час розвитку електро-магнітного каскаду. З цього випливає, що електрон-позитронні пучки від блазарів не впливають на міжгалактичне середовище.

Дослідження, представлене у розділі 1 «Войди як складник великомасштабного розподілу небесних об’єктів Всесвіту», ґрунтується на роботі з розробки динамічних шукачів войдів [1] із основного списку здобувача та [36, 41, 44]; представлене у розділі 2 «Модуль відстані до галактик та оцінки ізольованості малонаселених систем галактик» ґрунтується на роботах з використанням методів машинного навчання [2] і мозаїк Вороного вищих порядків [12] із основного списку здобувача та статтях [30–35, 37], а також висвітлено в матеріалах і тезах конференцій [38, 39, 42, 44]; представлене у розділі 3 «Галактики з активними ядрами та особливості їхнього великомасштабного розподілу» ґрунтується на роботах [3, 8–11, 13] із основного списку здобувача та додатково висвітлено в роботах у співавторстві з колегами по колаборації XXL та MiNDSTEp [14–29, 33, 37] і тезах конференцій [40, 43]; представлене у розділі 4 «Високоенергетичні процеси у войдах» ґрунтується на роботах [4–7].

ПОДЯКИ

Я хотів би подякувати усім своїм співавторам, робота з ними була для мене задоволенням: я дуже вдячний проф. Jean Surdej, людині з рідкісними людськими якостями, за надану можливість працювати в XXL та MiNDSTEp колаборациях, що дозволило мені знайти колег і друзів у багатьох країнах, а також взяти участь у спостереженнях в Чилі (ESO); доктору фіз.-мат. наук Караченцевій Валентині Юхимівні та доктору фіз.-мат. наук, проф. Караченцеву Ігорю Дмитровичу за можливість працювати разом, а Валентині Юхимівні за цінні поради та настанови до першого варіанту дисертації. Особливо вдячний моєму науковому консультанту, доктору фіз.-мат. наук, члену-кореспонденту НАН України Вавиловій Ірині Борисівні за мотивацію, а також всебічну допомогу на всіх етапах співпраці та роботи над дисертацією, її внесок дійсно неоціненний. Дуже дякую канд. фіз.-мат. наук Добричевій Дар'ї за співпрацю, допомогу та дружбу.

А найбільше я вдячний своїй дружині Ользі Мельник за постійну підтримку і натхнення.

СПИСОК ВИКОРИСТАНИХ ДЖЕРЕЛ

1. Elyiv, A., Marulli, F., Pollina, G. et al., 2015. Cosmic voids detection without density measurements. MNRAS, 448, pp. 642–653.

2. Elyiv, A. A., Melnyk, O. V., Vavilova, I. B. et al., 2020. Machine-learning computation of distance modulus for local galaxies. A&A, 635A, 124E (7 pp.).

3. Elyiv, A., Clerc, N., Plionis, M. et al., 2012. Angular correlation functions of X-ray point-like sources in the full exposure XMM-LSS field. A&A, 537, id. A131 (14 pp.).

4. Miniati, F., Elyiv, A., 2012. Relaxation of Blazar-induced Pair Beams in Cosmic Voids. ApJ, 770, 1 (9 pp.).

5. Schlickeiser, R., Elyiv, A., Ibscher, D., Miniati, F., 2012. The pair beam production spectrum from photon-photon annihilation in cosmic voids. ApJ, 758, 101 (18 pp.).

6. Elyiv, A., Neronov, A., Semikoz, D.V., 2010. Gamma-ray induced cascades and magnetic fields in the intergalactic medium, Phys. Rev. D., 80, 023010(11 pp.).

7. Neronov, A., Semikoz, D., Kachelriess, M., Ostapchenko, S., Elyiv, A., 2010. Degree- scale GeV "Jets" from Active and Dead TeV Blazars. ApJ Journal Letters, 719, pp. L130-L133.

8. Finet, F., Elyiv, A., Melnyk, O. et al., 2015. Predicted multiply imaged X-ray AGNs in the XXL survey. MNRAS, 452, pp. 1480-1492.

9. Ricci, D., Poels, J., Elyiv, A. et al., 2011. Flux and color variations of the quadruply imaged quasar HE 0435-1223. A&A, 528, id.A49, (16 pp.).

10. Ricci, D., Elyiv, A., Finet, F. et al., 2013. Flux and color variations of the doubly imaged quasar UM673. A&A, 551, id.A104 (7 pp.).

11. Elyiv, A., Melnyk, O., Finet, F. et al., 2013. Search for gravitational lens candidates in the XMM-LSS/CFHTLS common field. MNRAS, 434, pp. 3305–3309.

12. Elyiv, A., Melnyk, O., Vavilova, I., 2009. High-order 3D Voronoi tessellation for identifying isolated galaxy pairs and triplets. MNRAS, 394, pp. 1409 - 1418.

13. Melnyk, O., Elyiv, A., Smolčić, V. et al., 2018. The XXL Survey. XXI. The environment and clustering of X-ray AGN in the XXL-South field. A&A, 620, id.A6 (14 pp.).

14. Nwaokoro, E., Phillipps, S., Young, A. J. … Elyiv, A. et al., 2021. GAMA/XXL: X-ray point sources in low-luminosity galaxies in the GAMA G02/XXL-N field. MNRAS, 502, pp. 3101-3112.

15. Koulouridis, E., Ricci, M., Giles, P.… Elyiv, A. et al., 2018. The XXL Survey. XXXV.The role of cluster mass in AGN activity. A&A, 620, id.A20 (10 pp.).

16. Chiappetti, L., Fotopoulou, S., Lidman, C. … Elyiv, A. et al., 2018. The XXL Survey: XXVII. The 3XLSS point source catalogue, A&A, 620, A12 (18 pp.).

17. Guglielmo, V., Poggianti, B. M., Vulcani, B. … Elyiv, A. et al., 2018. The XXL Survey: XXX. Characterisation of the XLSSsC N01 supercluster and analysis of the galaxy stellar populations. A&A, 620, id. A15 (15 pp.).

18. Guglielmo, V., Poggianti, B. M., Vulcani, B. … Elyiv A. et al., 2018. The XXL Survey: XXII. The XXL-North spectrophotometric sample and galaxy stellar mass function in X-ray detected groups and cluster. A&A, 620, id.A7 (20 pp.).

19. Pierre, M., Adami, C., Birkinshaw, M. … Elyiv, A. et al., 2017. The XXL survey: First results and future, Astronomische Nachrichten, 338, pp. 334-341.

20. Lavoie, S., Willis, J. P., Démoclès, J. … Elyiv, A. et al., 2016. The XXL survey XV: evidence for dry merger driven BCG growth in XXL-100-GC X-ray clusters. MNRAS, 2016, 462, pp. 4141–4156.

21. Koulouridis, E., Poggianti, B., Altieri, B. ... Elyiv, A. et al., 2016. The XXL Survey. XII. Optical spectroscopy of X-ray-selected clusters and the frequency of AGN in superclusters. A&A, 592, id. A11 (11 pp.).

22. Fotopoulou, S., Pacaud, F., Paltani, S. … Elyiv, A. et al., 2016. The XXL Survey. VI.The 1000 brightest X-ray point sources. A&A, id.A5 (30 pp.).

23. Pierre, M., Pacaud, F., Adami, C. … Elyiv, A. et al., 2016. The XXL Survey. I. Scientific motivations – XMM-Newton observing plan – Follow-up observations and simulation program. A&A, 592, id.A1 (16 pp.).

24. Lidman, C., Ardila, F., Owers, M. … Elyiv, A. et al., 2016. The XXL Survey XIV. AAOmega Redshifts for the Southern XXL Field, Publications of the Astronomical Society of Australia, 33, e001 (7 pp.).

25. Koulouridis, E., Plionis, M., Melnyk, O., Elyiv, A. et al., 2014. X-ray AGN in the XMM-LSS galaxy clusters: no evidence of AGN suppression. A&A, 567, id. A83 (15 pp.).

26. Chiappetti, L., Clerc, N., Pacaud, F. … Elyiv, A. et al., 2013. The XMM-Large Scale Structure catalogue - II. X-ray sources and associated multiwavelength data. MNRAS, 429, pp. 1652–1673.

27. Finet, F., Elyiv, A., & Surdej, J., 2012. Detection of bright imaged quasar with Gaia. Memorie della Societa Astronomica Italiana. 83, pp. 944-988. **

28. Akhunov, T. A., Wertz, O., Elyiv, A. et al., 2017. Adaptive PSF fitting - a highly performing photometric method and light curves of the GLS H1413+117: time delays and micro-lensing effects, MNRAS, 465, pp. 3607–3621.

29. Giannini, E., Schmidt, R. W., Wambsganss, J. .. Elyiv, A. et al., 2017. MiNDSTEp differential photometry of the gravitationally lensed quasars WFI 2033-4723 and HE 0047-1756: microlensing and a new time delay, A&A, 597, 16.

30. Vavilova I.B., Dobrycheva D.V., Vasylenko M.Yu., Elyiv A.A. et al., 2021. Machine learning technique for morphological classification of galaxies from the SDSS I. Photometry-based approach, A&A, 648, A122 (14 pp.).

31. Vavilova I.B., Khramtsov V., Dobrycheva D.V., Vasylenko M.Yu., Elyiv A.A., Melnyk O.V., 2022. Machine learning technique for morphological classification of galaxies from SDSS. II. The image-based morphological catalogs of galaxies at $0.02<z<0.1$, Space Science & Technology, 28(1), pp. 03–22.

32. Dobrycheva, D.V., Melnyk, O.V., Vavilova, I.B., Elyiv, A.A., 2015. Environmental Density vs. Colour Indices of the Low Redshifts Galaxies, Astrophysics, 58, pp. 168–180.

33. Melnyk, O., Plionis, M., Elyiv, A. et al., 2013. Classification and environmental properties of X-ray selected point-like sources in the XMM-LSS field. A&A, 557, id. A81 (14 pp.)

34. Elyiv A.A., Melnyk O.V., Vavilova I.B., 2015. Dark and baryonic matter distribution in the sparsely populated galaxy groups. In: Vavilova I.B., Bolotin Yu.L., Boyarsky A.M. et al. Dark matter: Observational manifestation and experimental searches. Kyiv: Akademperiodyka, 2015, 375 p., Vol. 3 of the “Dark energy and dark matter in the Universe”, in three volumes, Ed. V. Shulga. p.129–158.

35. Vavilova I., Elyiv A., Dobrycheva D., Melnyk O., 2021. The Voronoi Tessellation Method in Astronomy. In: Zelinka I., Brescia M., Baron D. (eds). Intelligent Astrophysics. Emergence, Complexity and Computation, vol 39. Springer, Cham. Chapter 3, p. 57–79.

36. Vavilova I., Dobrycheva D., Vasylenko M., Elyiv A., Melnyk O. Multi-wavelength Extragalactic Surveys: Examples of Data Mining Knowledge Discovery in Big Data from Astronomy and Earth Observation, 1st Edition. Edited by Petr Skoda and Fathalrahman Adam. Elsevier, 2020, p. 307–323.

37. Vavilova I., Pakuliak L., Babyk I., Elyiv A. et al., 2020. Surveys, Catalogues, Databases, and Archives of Astronomical Data Knowledge Discovery in Big Data from Astronomy and Earth Observation, 1st Edition. Edited by Petr Skoda and Fathalrahman Adam. Elsevier, 2020, p. 57–102.

38. Vavilova I.B., Elyiv A.A., Dobrycheva D.V., Melnyk O.V. Voronoi tessellation in a spatial galaxy distribution. Abstracts of the Institute of Mathematics Conferences, Sixth International Con-ference on Analytic Number Theory and Spatial Tessellations, 24-28 Sept., 2018, Kyiv, Ukraine. P. 68.

39. Dobrycheva D., Melnyk O., Elyiv A., Vavilova I. Environmental density of galaxies from SDSS via Voronoi tessellation The Zeldovich Universe: Genesis and Growth of the Cosmic Web, Proceedings of the International Astronomical Union, Cambridge: Cambridge University Press, 2016, Vol. 308, pp. 248–249.

40. Elyiv A. X-ray surveys - Correlation function analyses of X-ray point-like sources in the XMM-LSS and XXL fields Half a Century of X-ray Astronomy, Proceedings of the conference held 17-21 September, 2012 in Mykonos Island, Greece. Online at http://www.astro.noa.gr/xcosmo/, id.107.

41. Dobrycheva D.V., Melnyk O.V., Vavilova I.B., Elyiv A.A. Environmental properties of galaxies at z<0.1 from the SDSS via the Voronoi tessellation. Odessa Astronomical Publications, 2014, 27, no 1, p. 26–27.

42. Melnyk O.V., Elyiv A.A., Vavilova I.B. 3-D Voronoi's Tessellation as a Tool for Identifying Galaxy Groups. In: Galaxy Evolution Across the Hubble Time, Edited by F.Combes and J. Palous, Proceedings of the International Astronomical Union, Cambridge: Cambridge University Press, 2007, Vol. 235, p. 223.

43. Melnyk O., Elyiv A. Clustering and environmental studies of AGN in the XMM - LSS and XXL fields. Абстракти “Астрономія та фізика космосу в Київському університеті”, Міжнар. конференція в рамках VIII Всеукраїнського фестивалю науки, 27-30 травня 2014 року, Київ. с.29.

44. Dobrycheva D., Vavilova I., Elyiv A., Melnyk O. Scaling properties of new sample of galaxies with z<0.1 from SDSS DR9. Абстракти “Астрономія та фізика космосу в Київському університеті”, Міжнар. конференція в рамках VIII Всеукраїнського фестивалю науки, 27-30 травня 2014 року, Київ. с.18.

45. Alcock, C., Paczynski, B., 1979. An evolution free test for non-zero cosmological constant. Nature, 281, pp. 358–359.

46. Nadathur, S., Hotchkiss, S., Diego, J. M. et al., 2015. Self-similarity and universality of void density profiles in simulation and SDSS data. MNRAS, 449, pp. 3997–4009.

47. Neyrinck, M. C. 2008, ZOBOV: a parameter-free void-finding algorithm. MNRAS, 386, pp. 2101–2109.

48. Riess, A. G., Fliri, J., & Valls-Gabaud, D., 2012. Cepheid Period-Luminosity Relations in the Near-infrared and the Distance to M31 from the Hubble Space Telescope Wide Field Camera 3. ApJ, 745, pp. 156-162.

49. Steer, I., Madore, B.F., & Mazzarella, J.M. et al., 2017. Redshift-independent Distances in the NASA/IPAC Extragalactic Database: Methodology, Content, and Use of NED-D. AJ, 153, pp. 37-57.

50. Makarov, D., Prugniel, P., Terekhova, N. et al., 2014. HyperLEDA. III. The catalogue of extragalactic distances. A&A, 570, id.A13 (12 pp.)

51. Antonucci, R., 1993. Unified models for active galactic nuclei and quasars. Annual Rev. Astron. Astrophys., 31, pp. 473-521.

52. Miyaji, T., Hasinger, G., Schmidt, M., 1999. Evolution of the ROSAT AGN Luminosity Function. Highlights in X-ray astronomy. Symposium proceedings. Eds. B. Aschenbach & M. J. Freyberg. Garching : Max-Planck-Institut für extraterrestrische Physik, 1999. (MPE report, No. 272, ISSN 0178-0719), p.222.

53. Bongiorno, A., Merloni, A., Brusa, M. et al., 2012. Accreting supermassive black holes in the COSMOS field and the connection to their host galaxies. MNRAS, 427, pp. 3103–3133.

54. Wolf, J., Nandra, K., Salvato, M. et al., 2021. First constraints on the AGN X-ray luminosity function at z 6 from an eROSITA-detected quasar. A&A, 647, id.A5, (16 pp.).

55. Cuillandre, J.-C. J., Withington, K., Hudelot, P. et al., 2012. Introduction to the CFHT Legacy Survey final release (CFHTLS T0007). Observatory Operations: Strategies, Processes, and Systems IV. Proceedings of the SPIE, 8448, article id. 84480M, (6 pp.).

56. Voronoi, G.F., 1908. Nouvelles applications des paramètres continus à la théorie de formes quadratiques. Journal für die reine und angewandte Mathematik, 134, pp. 198-287.

57. Icke, V., van de Weygaert, R., 1987. Fragmenting the universe. A&A, 184, pp. 16-32.

58. Coles, P., Barrow, J. D., 1990. Microwave background constraints on the Voronoi model of large-scale structure. MNRAS, 244, pp. 557-562.

59. Melnyk, O.V., Elyiv A. A., Vavilova I.B., 2006. The structure of the Local Supercluster of galaxies detected by three-dimensional Voronoi's tessel-lation method. Kinematika i Fizika Nebesnykh Tel, 22, no. 4, pp. 283-296.

60. Abdo, A. A., Ackermann, M., Ajello, M. et al, 2009. Fermi Observations of TeV-Selected Active Galactic Nuclei. Astrophys. J., 707, pp. 1310-1333.

61. DeLavallaz, A., Fairbairn, M., 2012. Voids as Alternatives to Dark Energy and the Propagation of γ Rays through the Universe. Physical Review Letters, 108, id. 171301, (4 pp.).

62. Beck, A. M., Hanasz, M., Lesch, H. et al., 2013. On the magnetic fields in voids. MNRAS, 429, pp. L60-L64.

63. Joeveer, M., Einasto, J., & Tago, E., 1978. Spatial distribution of galaxies and of clusters of galaxies in the southern galactic hemisphere. MNRAS, 185, pp. 357-370.

64. Huchra, J. P., Geller, M. J., de Lapparent, V., Burg, R. 1988, The CFA Redshift Survey. Large Scale Structures of the Universe, Proceedings of the IAU. Eds J. Audouze, M.-C. Pelletan and A. Szalay. Vol. 130, Kluwer Academic Publishers, Dordrecht, p.105.

65. Geller, M. J., Huchra, J. P., 1989. Mapping the Universe. Science, 246, pp. 897-903.

66. Geng, A., Kotarba, H., Burzle, F. et al., 2012. Magnetic field amplification and X-ray emission in galaxy minor mergers. MNRAS, 419, pp. 3571-3589.

67. Kahniashvili, T., Maravin, Y., Natarajan, A. et al., 2013. Constraining Primordial Magnetic Fields through Large-scale Structure. ApJ, 770, id. 47, (7 pp.).

68. Bertone, S., Vogt, C., Enßlin, T., 2006. Magnetic field seeding by galactic winds. MNRAS, 370, pp. 319-330.

69. van de Weygaert, R., Platen, E. 2011. Cosmic Voids: Structure, Dynamics and Galaxies. International Journal of Modern Physics: Conference Series. 1, pp. 41–66.

70. Pollina, G., Hamaus, N., Dolag, K. et al., 2017. On the linearity of tracer bias around voids. MNRAS, 469, pp.787-799.

71. Ruiz, A. N., Paz, D. J., Lares, M. et al., 2015. Clues on void evolution - III. Structure and dynamics in void shells. MNRAS, 448, pp.1471-1482.

72. Contarini S., Ronconi T., Marulli, F. et al., 2019. Cosmological exploitation of the size function of cosmic voids identified in the distribution of biased tracers. MNRAS, 488, pp. 3526-3540.

73. Cousinou, M. C., Pisani, A., Tilquin, A. et al., 2019. Multivariate analysis of cosmic void characteristics. Astronomy and Computing, 27, id. 53., (10 pp.).

74. Mosleh, M., Tavasoli, S., Tacchella, S. 2018. Stellar Mass Profiles of Quiescent Galaxies in Different Environments at z ∼ 0. ApJ, 861, id. 101, (pp. 12).

75. Perico, E. L. D., Voivodic, R., Lima, M., Mota, D. F. 2019. Cosmic voids in modified gravity scenarios. A&A, 632, id.A52, (pp.14.).

76. Correa, C.M., Paz, D.J., Sánchez, A. G. et al., 2021. Redshift-space effects in voids and their impact on cosmological tests. Part I: the void size function. MNRAS, 500, pp. 911-925.

77. Kreisch, C. D., Pisani, A., Villaescusa-Navarro, F. et al., 2022. The GIGANTES Data Set: Precision Cosmology from Voids in the Machine-learning Era. ApJ, 935, id.100, (pp. 19.).

78. Pollina, G., Baldi, M., Marulli, F. et al., 2016. Cosmic voids in coupled dark energy cosmologies: the impact of halo bias. MNRAS, 455, pp.3075-3085.

79. Rezaei, Z. 2020. Dark Matter-Dark Energy Interaction and the Shape of Cosmic Voids. ApJ, 902, id.102, (pp. 6.).

80. Ronconi, T., Contarini, S., Marulli, F. et al., 2019. Cosmic voids uncovered - first-order statistics of depressions in the biased density field. MNRAS, 488, p.5075-5084.

81. Dressler, A. 1980. Galaxy morphology in rich clusters: implications for the formation and evolution of galaxies. ApJ, 236, pp. 351-365.

82. Way, M.J., Gazis, R., Scargle, J.D. 2011. Structure in the three-dimensional galaxy distribution. I. Methods and example results. ApJ, 727, 48 (32pp)

83. O'Mill, A., L., Duplancic, F., Garcia, L. et al., 2012. Galaxy triplets in Sloan Digital Sky Survey Data Release 7 - I. Catalogue, MNRAS. 421, pp. 1897-1907.

84. Argudo-Fernández, M., Verley, S., Bergond, G. et al., 2013. The AMIGA sample of isolated galaxies. XII. Revision of the isolation degree for AMIGA galaxies using the SDSS. A&A, 560, id.A9, 14pp.

85. Melnyk, O., Mitronova, S., Karachentseva, V. 2014. Colours of isolated galaxies selected from the Two-Micron All-Sky Survey. MNRAS, 438, p. 548–556.

86. Nierenberg, A. M., Treu, T., Brammer, G. et al., 2017. Probing dark matter substructure in the gravitational lens HE 0435−1223 with the WFC3 grism. MNRAS, 471, pp. 2224–2236.

87. Motta, V., Mediavilla, E., Rojas, K. et al., 2017. Probing the Broad-Line Region and the Accretion Disk in the Lensed Quasars HE 0435- 1223, WFI 2033-4723, and HE 2149-2745 Using Gravitational Microlensing. ApJ, 835, 132, 13pp.

88. Koptelova, E., Chiueh, T., Chen, W. P. et al., 2014. New near-infrared observations and lens-model constraints for UM673. A&A, 566, A36, 10 pp.

89. Millon, M., Courbin, F., Bonvin, V. et al., 2020. COSMOGRAIL XIX. Time delays in 18 strongly lensed quasars from 15 years of optical monitoring? A&A, 640, A105, 31 pp.

90. Okoshi, K., Minowa, Y., Kashikawa, N. et al., 2021. Multiple Mg II Absorption Systems in the Lines of Sight to Quadruply Lensed Quasar H1413+1143. AJ, 162:175, 19 pp.

91. Millon, M., Courbin, F., Bonvin, V. et al., 2020. TDCOSMO II. Six new time delays in lensed quasars from high-cadence monitoring at the MPIA 2.2 m telescope? A&A, 642, A193, 14 pp.

92. Dolag, K., Kachelriess M., Ostapchenko, S., Tomas, R. 2011. Lower limit on the strength and felling factor of extragalactic magnetic fields. ApJ Letters, 727:L4, 4pp.

93. Berezinsky, V., Gazizov, A., Kachelrie, M., Ostapchenko, S., 2011. Restricting UHECRs and cosmogenic neutrinos with Fermi-LAT. Physics Letters B, 695, p. 13-18.

94. Murase, K., Dermer, C. D., Takami, H., Migliori G. 2012. Blasars as ultra-high-energy cosmic-ray sources: implications for TEV gamma-ray observations.

95. Ackermann, M., Ajello, M., Allafort, A. et al., 2012. The Imprint of the Extragalactic Background Light in the Gamma-Ray Spectra of Blazars. Science, 338, pp. 1190-2012.

96. Tavecchio, F., Ghisellini, G., Bonnoli. G., Foschini, L. 2011. Extreme TeV blazars and the intergalactic magnetic field. MNRAS, 414, p. 3566–3576.

97. Kachelrieß, M., Ostapchenko, S., Tomàs, R. ELMAG: A Monte Carlo simulation of electromagnetic cascades on the extragalactic background light and in magnetic fields. Computer Physics Communications, 183, p. 1036-1043.

98. Sol, H., Zech, A., Boisson, C. et al., CTA Consortium. 2013. Active Galactic Nuclei under the scrutiny of CTA. Astroparticle Physics, 43, p. 215-240.

99. Durrer, R., Neronov, A. 2013. Cosmological magnetic fields: their generation, evolution and observation. A&A Rev., 21, id. 62

100. Timothy, C. A., Vladimir, V. V., Thomas, W. et al., 2014. Intergalactiv magnetic fields and gamma-ray observations of extreme TeV blazars. ApJ, 796, id.18, 18pp.

101. Fitoussi, T., Belmont, R., Malzac, J. et al., 2017. Physics of cosmological cascades and observable properties. MNRAS, 466, 3472–3487 pp.

102. Meyer, M., Conrad, J., Dickinson, H. 2016. Sensitivity of the Cherenkov telescope array to detection of intergalactic magnetic fields. ApJ, 827, 147, 10pp.

103. Veres, P., Dermer, C. D., Dhuga, K.S. 2017. Properties of the Intergalactic Magnetic Field Constrained by Gamma-Ray Observations of Gamma-Ray Bursts. ApJ, 847, id. 39, 7pp.

104. Tiede, P., Broderick, A. E., Shalaby, M. et al., 2017. Bow Ties in the Sky. II. Searching for Gamma-Ray Halos in the Fermi Sky Using Anisotropy. ApJ, 850, id. 157, 27 pp.

105. Ackermann, M., Ajello, M., Baldini, L. et al., 2018. The Search for Spatial Extension in High-latitude Sources Detected by the Fermi Large Area Telescope. ApJ Suppl. Ser., 237, id. 32, 36 pp.

106. Broderick, A.E., Tiede, P., Chang, P. et al., 2018. Missing Gamma-Ray Halos and the Need for New Physics in the Gamma-Ray Sky. ApJ,868, id. 87, 17pp.

107. Tiede, P., Broderick, A. E., Shalaby, M. et al., 2020. Constraints on the Intergalactic Magnetic Field from Bow Ties in the Gamma-Ray Sky. ApJ, 892, id. 123, 11pp.

108. Korochkin, A., Neronov, A., Lavaux, G., Ramsøy, M., Semikoz, D. 2022. Detectability of large correlation length inflationary magnetic field with Cherenkov telescopes. Journal of Experimental and Theoretical Physics, 134, p.498-505.

109. Alawashra, M., Pohl, M. 2022. Suppression of the TeV Pair-beam–Plasma Instability by a Tangled Weak Intergalactic Magnetic Field. ApJ, 929, id. 67, 8pp.

110. Toomey, M. W., Oikonomou, F., Murase, K. 2020. Gamma-ray counterparts of 2WHSP high-synchrotron-peaked BL Lac objects as possible signatures of ultra-high-energy cosmic ray emission. MNRAS, 497, p. 2455–2468.

111. Vafin, S., Deka, P. J., Pohl, M., Bohdan, A. 2019. Revisit of Nonlinear Landau Damping for Electrostatic Instability Driven by Blazar-induced Pair Beams. ApJ, 873, id. 10, 12pp.

112. Yan, D., Zhou, J., Zhang, P., Zhu, Q., Wang, J. 2019. Impact of Plasma Instability on Constraint of the Intergalactic Magnetic Field. ApJ, 870, id. 17, 5pp.

113. Vafin, S., Rafighi, I., Pohl, M. et al.. 2018. The Electrostatic Instability for Realistic Pair Distributions in Blazar/EBL Cascades. ApJ, 857, id. 43, 12pp.

114. Archambault, S., Archer, A., Benbow, W. et al., 2017. Search for Magnetically Broadened Cascade Emission from Blazars with VERITAS. ApJ, 835, id. 288, 12 pp.

115. Alves Batista, R., Saveliev, A., Sigl, G., Vachaspati, T., 2016. Probing intergalactic magnetic fields with simulations of electromagnetic cascades Phys. Rev. D, 94, id.083005.

116. Berezinsky, V., Kalashev, O., 2016. High-energy electromagnetic cascades in extragalactic space: Physics and features. Phys. Rev. D, 94, id.023007, 21pp.

ДОДАТОК А. СПИСОК ОПУБЛІКОВАНИХ ПРАЦЬ

ЗА ТЕМОЮ ДИСЕРТАЦІЇ

Основні наукові праці (у реферованих журналах першого квартилю (Q1) відповідно до класифікації SCImago Journal and Country Rank або Journal Citation Reports)

Скорочення: A&A - “Astronomy and Astrophysics”; MNRAS - Monthly Notices of the Royal Astronomical Society; ApJ - Astrophysical Journal; Phys. Rev. D - Physical Review D.

1. **Elyiv, A.**, Marulli, F., Pollina, G., Baldi, M., Branchini, E., Cimatti, A., Moscardini, L., 2015. Cosmic voids detection without density measurements. MNRAS, 448, pp. 642-653.
2. **Elyiv, A. A.**, Melnyk, O. V., Vavilova, I. B., Dobrycheva, D. V., Karachentseva, V. E., 2020. Machine-learning computation of distance modulus for local galaxies. A&A, 635A, 124E (7 pp.).
3. **Elyiv, A.**, Clerc, N., Plionis, M., Surdej, J., Pierre, M., Basilakos, S., Chiappetti, L., Gandhi, P. , Gosset, E., Melnyk, O., Pacaud, F., 2012. Angular correlation functions of X-ray point-like sources in the full exposure XMM-LSS field. A&A, 537, id. A131 (14 pp.).
4. Miniati, F., **Elyiv, A.**, 2012. Relaxation of Blazar-induced Pair Beams in Cosmic Voids. ApJ, 770, 1 (9 pp.).
5. Schlickeiser, R., **Elyiv, A.**, Ibscher, D., Miniati, F., 2012. The pair beam production spectrum from photon-photon annihilation in cosmic voids. ApJ, 758, 101 (18 pp.).
6. **Elyiv, A.**, Neronov, A., Semikoz, D. V., 2010. Gamma-ray induced cascades and magnetic fields in the intergalactic medium, Phys. Rev. D., 80, 023010 (11 pp.).
7. Neronov, A., Semikoz, D., Kachelriess, M., Ostapchenko, S., **Elyiv, A.,** 2010. Degree- scale GeV "Jets" from Active and Dead TeV Blazars. ApJ Journal Letters, 719, pp. L130-L133.
8. Finet, F., **Elyiv, A.**, Melnyk, O., Wertz, O., Horellou, C., Surdej, J., 2015. Predicted multiply imaged X-ray AGNs in the XXL survey. MNRAS, 452, pp. 1480-1492.
9. Ricci, D., Poels, J., **Elyiv, A.**, Finet, F., Sprimont, P. G., Anguita, T., Bozza, V., Browne, P. , Burgdorf, M., Calchi, Novati, S., Dominik, M., Dreizler, S., Glitrup,,M., Grundahl, F., Harpsøe, K., Hessman, F., Hinse, T. C., Hornstrup, A., Hundertmark, M., Jørgensen, U. G., Liebig, C., Maier, G., Mancini, L., Masi, G., Mathiasen, M., Rahvar, S., Scarpetta, G., Skottfelt, J., Snodgrass, C., Southworth, J., Teuber, J., Thöne, C. C., Wambsganß, J., Zimmer, F., Zub, M., Surdej, J., 2011. Flux and color variations of the quadruply imaged quasar HE 0435-1223. A&A, 528, id.A49, (16 pp.).
10. Ricci, D., **Elyiv, A.**, Finet, F., Wertz, O., Alsubai, K., Anguita, T., Bozza, V., Browne, P., Burgdorf, M., Calchi Novati, S., Dodds, P., Dominik, M., Dreizler, S., Gerner, T., Glitrup, M., Grundahl, F., Hardis, S., Harpsøe, K., Hinse, T. C., Hornstrup, A., Hundertmark, M., Jørgensen, U. G., Kains, N.,

Kerins, E., Liebig, C., Maier, G., Mancini, L., Masi, G., Mathiasen, M., Penny, M., Proft, S., Rahvar, S., Scarpetta, G., Sahu, K., Schäfer, S., Schönebeck, F., Schmidt, R., Skottfelt, J., Snodgrass, C., Southworth, J., Thöne, C. C., Wambsganss, J., Zimmer, F., Zub, M., Surdej, J., 2013. Flux and color variations of the doubly imaged quasar UM673. A&A, 551, id.A104 (7 pp.).

11. **Elyiv, A.**, Melnyk, O., Finet, F., Pospieszalska-Surdej, A., Chiappetti, L., Pierre, M., Sadibekova, T., Surdej, J., 2013. Search for gravitational lens candidates in the XMM-LSS/CFHTLS common field. MNRAS, 434, pp. 3305–3309.

12. **Elyiv, A.**, Melnyk, O., Vavilova, I., 2009. High-order 3D Voronoi tessel-lation for identifying isolated galaxy pairs and triplets. MNRAS, 394, pp. 1409 - 1418.

13. Melnyk, O., **Elyiv, A.**, Smolčić, V., Plionis, M., Koulouridis, E., Foto-poulou, S., Chiappetti, L., Adami, C., Baran, N., Butler, A., Delhaize, J., Delvecchio, I., Finet, F., Huynh, M., Lidman, C., Pierre, M., Pompei, E., Vignali, C., Surdej, J., 2018. The XXL Survey. XXI. The environment and clustering of X-ray AGN in the XXL-South field. A&A, 620, id.A6 (14 pp.).

Наукові праці, які додатково висвітлюють тему дисертації:

а) Наукові праці у реферованих журналах першого квартилю (Q1) відповідно до класифікації SCImago Journal and Country Rank або Journal Citation Reports, крім статтей з * (Q3), ** (Q4) та *(Scopus, WoS)**

14. Nwaokoro, E., Phillipps, S., Young, A. J., Baldry, I., Bongiorno, A., Bremer, M. N., Brown, M. J. I., Chiappetti, L., De Propris, R., Driver, S. P., **Elyiv, A.**, Fotopoulou, S., Giles, P. A., Hopkins, A. M., Maughan, B., McGee, S., Pacaud, F., Pierre, M., Plionis, M., Poggianti, B. M., Vignali, C., 2021. GAMA/XXL: X-ray point sources in low-luminosity galaxies in the GAMA G02/XXL-N field. MNRAS, 502, pp. 3101-3112.

15. Koulouridis, E., Ricci, M., Giles, P., Adami, C., Ramos-Ceja, M., Pierre, M., Plionis, M., Lidman, C., Georgantopoulos, I., Chiappetti, L., **Elyiv, A.**, Ettori, S., Faccioli, L., Fotopoulou, S., Gastaldello, F., Pacaud, F., Paltani, S., Vignali, C., 2018. The XXL Survey. XXXV. The role of cluster mass in AGN activity. A&A, 620, id. A20 (10 pp.).

16. Chiappetti, L., Fotopoulou, S., Lidman, C., Faccioli, L., Pacaud, F., **Elyiv, A.**, Paltani, S., Pierre, M., Plionis, M., Adami, C., Alis, S., Altieri, B., Baldry, I., Bolzonella, M., Bongiorno, A., Brown, M., Driver, S., Elmer, E., Franzetti, P., Grootes, M., Guglielmo, V., Iovino, A., Koulouridis, E., Lefèvre, J. P., Liske, J., Maurogordato, S., Melnyk, O., Owers, M., Poggianti, B., Polletta, M., Pompei, E., Ponman, T., Robotham, A., Sadibekova, T., Tuffs, R., Valtchanov, I., Vignali, C., Wagner, G., 2018. The XXL Survey: XXVII. The 3XLSS point source catalogue, A&A, 620, A12 (18 pp.).

17. Guglielmo, V., Poggianti, B. M., Vulcani, B., Moretti, A., Fritz, J., Gastaldello, F., Adami, C., Caretta, C. A., Willis, J., Koulouridis, E., Ramos, Ceja, M. E., Giles, P., Baldry, I., Birkinshaw, M., Bongiorno, A., Brown, M., Chiappetti, L., Driver, S., **Elyiv, A.**, Evrard, A., Grootes, M., Guennou,

L., Hopkins, A., Horellou, C., Iovino, A., Maurogordato, S., Owers, M., Pacaud, F., Paltani, S., Pierre, M., Plionis, M., Ponman, T., Robotham, A., Sadibekova, T., Smolčić, V., Tuffs, R., Vignali, C., 2018. The XXL Survey: XXX. Characterisation of the XLSSsC N01 supercluster and analysis of the galaxy stellar populations. A&A, 620, id. A15 (15 pp.).

18. Guglielmo, V., Poggianti, B. M., Vulcani, B., Adami, C., Gastaldello, F., Ettori, S., Fotoupoulou, S., Koulouridis, E., Ramos, Ceja, M. E., Giles, P., McGee, S., Altieri, B., Baldry, I., Birkinshaw, M., Bolzonella, M., Bongiorno, A., Brown, M., Chiappetti, L., Driver, S., **Elyiv A.**, Evrard, A., Garilli, B., Grootes, M., Guennou, L., Hopkins, A., Horellou, C., Iovino, A., Lidman, C., Liske, J., Maurogordato, S., Owers, M., Pacaud, F., Paltani, S., Pierre, M., Plionis, M., Ponman, T., Robotham, A., Sadibekova, T., Scodeggio, M., Sereno, M., Smolčić, V., Tuffs, R., Valtchanov, I., Vignali, C., Willis J., 2018. The XXL Survey: XXII. The XXL-North spectrophotometric sample and galaxy stellar mass function in X-ray detected groups and cluster. A&A, 620, id.A7 (20 pp.).

19. Pierre, M., Adami, C., Birkinshaw, M., Chiappetti, L., Ettori, S., Evrard, A., Faccioli, L., Gastaldello, F., Giles, P., Horellou, C., Iovino, A., Koulouridis, E., Lidman, C., Le Brun, A., Maughan, B., Maurogordato, S., McCarthy, I., Miyazaki, S., Pacaud, F., Paltani, S., Plionis, M., Reiprich, T., Sadibekova, T., Smolcic, V., Snowden, S., Surdej, J., Tsirou, M., Vignali, C., Willis, J., Alis, S., Altieri, B., Baran, N., Benoist, C., Bongiorno, A., Bremer, M., Butler, A., Cappi, A., Caretta, C., Ciliegi, P., Clerc, N., Corasaniti, P. S., Coupon, J., Delhaize, J., Delvecchio, I., Democles, J., Desai, Sh., Devriendt, J., Dubois, Y., Eckert, D., **Elyiv, A**., Farahi, A., Ferraril, C., Fotopoulou, S., Forman, W., Georgantopoulos, I., Guglielmo, V., Huynh, M., Jerlin, N., Jones, Ch., Lavoie, S., Le Fevre, J.-P., Lieu, M., Kilbinger, M., MaruIli, F., Mantz, A., McGee, S., Melin, J.-B., Melnyk, O., Moscardini, L., Novak, M., Piconcelli, E., Poggianti, B., Pomarede, D., Pompei, E., Ponman, T., Ramos, Ceja, M. E., Rana, P., Rapetti, D., Raychaudhury, S., Ricci, M., Rottgering, H., Sahlen, M., Sauvageot, J.-L., Schimd, C., Sereno, M., Smith, G. P., Umetsu, K., Valageas, P., Valotti, A., Valtchanov, I., Veropalumbo, A., Ascaso, B., Barnes, D., De Petris, M., Durret, F., Donahue, M., Ithana, M., Jarvis, M., Johnston-Hollitt, M., Kalfountzou, E., Kay, S., La Franca, F., Okabe, N., Muzzin, A., Rettura, A., Ricci, F., Ridl, J., Risaliti, G., Takizawa, M., Thomas, P., Truong, N., 2017. The XXL survey: First results and future, Astronomische Nachrichten, 338, pp. 334-341*.

20. Lavoie, S., Willis, J. P., Démoclès, J., Eckert, D., Gastaldello, F., Smith, G. P., Lidman, C., Adami, C., Pacaud, F., Pierre, M., Clerc, N., Giles, P., Lieu, M., Chiappetti, L., Altieri,B., Ardila, F., Baldry, I., Bongiorno, A., Desai, S., **Elyiv, A.**, Faccioli, L., Gardner, B., Garilli, B., Groote, M. W., Guennou, L., Guzzo, L., Hopkins, A. M., Liske, J., McGee, S., Melnyk, O., Owers, M. S., Poggianti, B., Ponman, T. J., Scodeggio, M., Spitler, L., Tuffs, R. J., 2016. The XXL survey XV: evidence for dry merger driven BCG growth in XXL-100-GC X-ray clusters. MNRAS, 2016, 462, pp. 4141-4156.

21. Koulouridis, E., Poggianti, B., Altieri, B., Valtchanov, I., Jaffé, Y., Adami, C., **Elyiv, A.**, Melnyk, O., Fotopoulou, S., Gastaldello, F., Horellou, C., Pierre, M., Pacaud, F., Plionis, M., Sadibekova, T., Surdej, J., 2016. The XXL Survey. XII. Optical spectroscopy of X-ray-selected clusters and the frequency of AGN in superclusters. A&A, 592, id. A11 (11 pp.).

22. Fotopoulou, S., Pacaud, F., Paltani, S., Ranalli, P., Ramos-Ceja, M. E., Faccioli, L., Plionis, M., Adami, C., Bongiorno, A., Brusa, M., Chiappetti, L., Desai, S., **Elyiv, A.**, Lidman, C., Melnyk, O., Pierre, M., Piconcelli, E., Vignali, C., Alis, S., Ardila, F., Arnouts, S., Baldry, I., Bremer, M., Eckert, D., Guennou, L., Horellou, C., Iovino, A., Koulouridis, E., Liske, J., Maurogordato, S., Menanteau, F., Mohr,J. J., Owers M., Poggianti B., Pompei E., Sadibekova, T., Stanford, A., Tuffs, R., Willis, J., 2016. The XXL Survey. VI.The 1000 brightest X-ray point sources. A&A, id.A5 (30 pp.).

23. Pierre, M., Pacaud, F., Adami, C., Alis, S., Altieri, B., Baran, N., Benoist, C., Birkinshaw, M., Bongiorno, A., Bremer, M. N., Brusa, M., Butler, A., Ciliegi, P., Chiappetti, L., Clerc, N., Corasaniti, P. S., Coupon, J., De Breuck, C., Democles, J., Desai, S., Delhaize, J., Devriendt, J., Dubois, Y., Eckert, D., **Elyiv, A.**, Ettori, S., Evrard, A., Faccioli, L., Farahi, A., Ferrari, C., Finet, F., Fotopoulou, S., Fourmanoit, N., Gandhi, P., Gastaldello, F., Gastaud, R., Georgantopoulos, I., Giles, P., Guennou, L., Guglielmo, V., Horellou, C., Husband, K., Huynh, M., Iovino, A., Kilbinger, M., Koulouridis, E., Lavoie, S., Le Brun, A. M. C., Le Fevre, J. P., Lidman, C., Lieu, M., Lin, C. A., Mantz, A., Maughan, B. J., Maurogordato, S., McCarthy, I. G., McGee, S., Melin, J. B., Melnyk, O., Menanteau, F., Novak, M., Paltani, S., Plionis, M., Poggianti, B. M., Pomarede, D., Pompei, E., Ponman, T. J., Ramos-Ceja, M. E., Ranalli, P., Rapetti, D., Raychaudury, S., Reiprich, T. H., Rottgering, H., Rozo, E., Rykoff, E., Sadibekova, T., Santos, J., Sauvageot, J. L., Schimd, C., Sereno, M., Smith, G. P., Smolčić, V., Snowden, S., Spergel, D., Stanford, S., Surdej, J., Valageas, P., Valotti, A., Valtchanov, I., Vignali, C., Willis, J., Ziparo, F., 2016. The XXL Survey. I. Scientific motivations - XMM-Newton observing plan - Follow-up observations and simulation program. A&A, 592, id.A1 (16 pp.).

24. Lidman, C., Ardila, F., Owers, M., Adami, C., Chiappetti, L., Civano, F., **Elyiv, A.**, Finet, F., Fotopoulou, S., Goulding, A., Koulouridis, E., Melnyk, O., Menanteau, F., Pacaud, F., Pierre, M., Plionis, M., Surdej, J., Sadibekova, T., 2016. The XXL Survey XIV. AAOmega Redshifts for the Southern XXL Field, Publications of the Astronomical Society of Australia, 33, e001 (7 pp.).

25. Koulouridis, E., Plionis, M., Melnyk, O., **Elyiv, A.**, Georgantopoulos, I., Clerc, N., Surdej, J., Chiappetti, L., Pierre, M., 2014. X-ray AGN in the XMM-LSS galaxy clusters: no evidence of AGN suppression. A&A, 567, id. A83 (15 pp.).

26. Chiappetti, L., Clerc, N., Pacaud, F., Pierre, M., Guéguen, A., Paioro, L., Polletta, M., Melnyk, O., **Elyiv, A.**, Surdej, J., Faccioli, L., 2013. The XMM-Large Scale Structure catalogue - II. X-ray sources and associated multiwavelength data. MNRAS, 429, pp. 1652–1673.

27. Finet, F., **Elyiv, A.**, & Surdej, J., 2012. Detection of bright imaged quasar with Gaia. Memorie della Societa Astronomica Italiana. 83, pp. 944-988. **

28. Akhunov, T. A., Wertz, O., **Elyiv, A.**, Gaisin, R., Artamonov, B. P., Dudi-nov, V. N., Nuritdinov, S. N., Delvaux, C., Sergeyev, A. V., Gusev, A. S., Bruevich, V. V., Burkhonov, O., Zheleznyak, A. P., Ezhkova, O., Surdej, J., 2017. Adaptive PSF fitting - a highly performing photometric method and light curves of the GLS H1413+117: time delays and micro-lensing effects, MNRAS, 465, pp. 3607–3621.

29. Giannini, E., Schmidt, R. W., Wambsganss, J., Alsubai, K., Andersen, J. M., Anguita, T., Bozza, V., Bramich, D. M., Browne, P., Calchi, Novati, S., Damerdji, Y., Diehl, C., Dodds, P., Dominik, M., **Elyiv, A.**, Fang, X., Figuera, Jaimes, R., Finet, F., Gerner, T., Gu, S., Hardis, S., Harpsøe, K., Hinse, T. C., Hornstrup, A., Hundertmark, M., Jessen-Hansen, J., Jørgensen, U. G., Juncher, D., Kains, N., Kerins, E., Korhonen, H., Liebig, C., Lund, M. N., Lundkvist, M. S., Maier, G., Mancini, L., Masi, G., Mathiasen, M., Penny, M., Proft, S., Rabus, M., Rahvar, S., Ricci, D., Scarpetta, G., Sahu, K., Schäfer, S., Schönebeck, F., Skottfelt, J., Snodgrass, C., Southworth, J., Surdej, J., Tregloan-Reed, J., Vilela, C., Wertz, O., Zimmer, F., 2017. MiNDSTEp differential photometry of the gravitationally lensed quasars WFI 2033-4723 and HE 0047-1756: microlensing and a new time delay, A&A, 597, 16.

30. Vavilova I.B., Dobrycheva D.V., Vasylenko M.Yu., **Elyiv A.A.**, Melnyk O.V., Khramtsov V., 2021. Machine learning technique for morphological classification of galaxies from the SDSS I. Photometry-based approach, A&A, 648, A122 (14 pp.).

31. Vavilova I.B., Khramtsov V., Dobrycheva D.V., Vasylenko M.Yu., **Elyiv A.A**., Melnyk O.V., 2022. Machine learning technique for morphological classification of galaxies from SDSS. II. The image-based morphological catalogs of galaxies at $0.02<z<0.1$, Space Science & Technology, 28(1), pp. 03–22.***

32. Dobrycheva, D.V., Melnyk, O.V., Vavilova, I.B., **Elyiv, A.**A., 2015. Environmental Density vs. Colour Indices of the Low Redshifts Galaxies, Astrophysics, 58, pp. 168–180.**

33. Melnyk, O., Plionis, M., **Elyiv, A.**, Salvato, M., Chiappetti, L., Clerc, N., Gandhi, P., Pierre, M., Sadibekova, T., Pospieszalska-Surdej, A., Surdej, J., 2013. Classification and environmental properties of X-ray selected point-like sources in the XMM-LSS field. A&A, 557, id. A81 (14 pp.)

б) Розділи у монографіях

34. **Elyiv A.A**., Melnyk O.V., Vavilova I.B. Dark and baryonic matter distribution in the sparsely populated galaxy groups. In: Vavilova I.B., Bolotin Yu.L., Boyarsky A.M. et al. Dark matter: Observational manifestation and experimental searches. K.: Akademperiodyka, 2015, 375 p., Vol. 3 of the “Dark energy and dark matter in the Universe”, in three volumes, Ed. V. Shulga. p.129–158. ISBN 978-966-360-287-5

35. Vavilova I., **Elyiv A**., Dobrycheva D., Melnyk O. (2021). The Voronoi Tessellation Method in Astronomy. In: Zelinka I., Brescia M., Baron D. (eds). Intelligent Astrophysics. Emergence, Complexity and Computation, vol 39. Springer, Cham. Chapter 3, p. 57–79. ISBN 978-3-030-65867-0

36. Vavilova I., Dobrycheva D., Vasylenko M., **Elyiv A.**, Melnyk O. Multi-wavelength Extragalactic Surveys: Examples of Data Mining Knowledge Discovery in Big Data from Astronomy and Earth Observation, 1st Edition. Edited by Petr Skoda and Fathalrahman Adam. Elsevier, 2020, p. 307–323**.** ISBN 978-0-128-19154-5.

37. Vavilova I., Pakuliak L., Babyk I., **Elyiv A**., Dobrycheva D., Melnyk O. Surveys, Catalogues, Databases, and Archives of Astronomical Data Knowledge Discovery in Big Data from Astronomy and Earth Observation, 1st Edition. Edited by Petr Skoda and Fathalrahman Adam. Elsevier, 2020, p. 57–102. ISBN 978-0-128-19154-5.

в) Матеріали і тези конференцій

38. Vavilova I.B., **Elyiv A.A.**, Dobrycheva D.V., Melnyk O.V. Voronoi tessellation in a spatial galaxy distribution. Abstracts of the Institute of Mathematics Conferences, Sixth International Conference on Analytic Number Theory and Spatial Tessellations, 24-28 Sept., 2018, Kyiv, Ukraine. P. 68.

39. Dobrycheva D., Melnyk O., **Elyiv A.**, Vavilova I. Environmental density of galaxies from SDSS via Voronoi tessellation The Zeldovich Universe: Genesis and Growth of the Cosmic Web, Proceedings of the International Astronomical Union, Cambridge: Cambridge University Press, 2016, Vol. 308, pp. 248–249 (Scopus).

40. **Elyiv A**. X-ray surveys - Correlation function analyses of X-ray point-like sources in the XMM-LSS and XXL fields Half a Century of X-ray Astronomy, Proceedings of the conference held 17-21 September, 2012 in Mykonos Island, Greece. Online at http://www.astro.noa.gr/xcosmo/, id.107.

41. Dobrycheva D.V., Melnyk O.V., Vavilova I.B., **Elyiv A.A**. Environmental properties of galaxies at z<0.1 from the SDSS via the Voronoi tessellation. Odessa Astron. Publ., 2014, 27, no 1, p. 26–27.

42. Melnyk O.V., **Elyiv A.A**., Vavilova I.B. 3-D Voronoi's Tessellation as a Tool for Identifying Galaxy Groups. In: Galaxy Evolution Across the Hubble Time, Edited by F.Combes and J. Palous, Proceedings of the International Astronomical Union, Cambridge: Cambridge University Press, 2007, Vol. 235, p. 223.

43. Melnyk O., **Elyiv A.** Clustering and environmental studies of AGN in the XMM - LSS and XXL fields. Абстракти "Астрономія та фізика космосу в Київському університеті", Міжнародна конференція в рамках VIII Всеукраїнського фестивалю науки, 27-30 травня 2014 року, Київ. с.29.

44. Dobrycheva D., Vavilova I., **Elyiv A**., Melnyk O. Scaling properties of new sample of galaxies with z<0.1 from SDSS DR9. Абстракти "Астрономія та фізика космосу в Київському університеті", Міжнародна конференція в рамках VIII Всеукраїнського фестивалю науки, 27-30 травня 2014 року, Київ. с.18.